



**HAL**  
open science

# Nature and origin of sedimentary deposits in the Ecuador subduction trench : paleoseismological implications

Miguel Gonzalez

► **To cite this version:**

Miguel Gonzalez. Nature and origin of sedimentary deposits in the Ecuador subduction trench : paleoseismological implications. Earth Sciences. Université de Rennes, 2018. English. NNT : 2018REN1B009 . tel-02173709

**HAL Id: tel-02173709**

**<https://theses.hal.science/tel-02173709v1>**

Submitted on 4 Jul 2019

**HAL** is a multi-disciplinary open access archive for the deposit and dissemination of scientific research documents, whether they are published or not. The documents may come from teaching and research institutions in France or abroad, or from public or private research centers.

L'archive ouverte pluridisciplinaire **HAL**, est destinée au dépôt et à la diffusion de documents scientifiques de niveau recherche, publiés ou non, émanant des établissements d'enseignement et de recherche français ou étrangers, des laboratoires publics ou privés.

# THESE DE DOCTORAT DE

L'UNIVERSITE DE RENNES 1

COMUE UNIVERSITE BRETAGNE LOIRE

ECOLE DOCTORALE N° 600

*Ecole doctorale Ecologie, Géosciences, Agronomie et Alimentation*

Spécialité : Sciences de la Terre et de l'Environnement

Par

**Miguel Gonzalez**

**Nature and origin of sedimentary deposits in the Ecuador subduction trench :**

Paleoseismological Implications

**Thèse soutenue et présentée à Rennes, le 20 avril 2018**

**Unité de recherche : Géosciences RENNES - UMR 6118**

## Rapporteurs avant soutenance :

Sébastien MIGEON      Professeur, Université Paris VI  
Jean Frédéric LEBRUN    Professeur, Université des Antilles

## Composition du Jury :

**Président :**  
Olivier Dauteuil      Directeur de recherche CNRS, Rennes

**Examineurs :**  
Carlos Martillo      Maître de conférence, ESPOL, Guayaquil

**Rapporteurs :**  
Sébastien MIGEON      Professeur, Université Paris VI  
Jean Frédéric LEBRUN    Professeur, Université des Antilles

**Directeur de thèse :**  
Jean-Noël Proust      Directeur de recherche au CNRS

**Co-directeur de thèse :**  
François Michaud      Maître de conférence, Université Paris VI

**Invité :**  
Jean Yves Collot      Directeur de recherche émérite IRD, Nice





# Table of Contents

List of Figures .....	VI
Chapter 1.....	1
Sedimentation and gravity processes along active continental margins .....	1
1.1 Introduction .....	1
1.2 Continental margins.....	2
1.2.1 Passive margins .....	3
1.2.2 Active margins .....	4
1.2.2.1 Accretionary margins .....	5
1.2.3 Morphology of the active margins .....	9
1.2.3.1 <i>General frame</i> .....	9
1.2.3.2 <i>Destabilization of the inner-wall of the trenches</i> .....	10
1.2.3.3 <i>Subduction of seamounts</i> .....	11
1.2.3.4 <i>Roll-over fold associated to regional detachment fault</i> .....	12
1.2.4 Dynamic of the trench sedimentary fill along the active margins .....	13
1.2.4.1 <i>Sedimentary infill geometry</i> .....	13
1.2.4.2 <i>Sedimentary infill thickness lateral variations</i> .....	14
1.2.4.3 Sedimentary infill residence time into the trench .....	16
1.2.4.4 Role of the trench sedimentary infill into the plate interface .....	18
1.3 Processes and products of deep-sea sedimentary deposits .....	20
1.3.1 Pelagic and hemipelagic sedimentation .....	21
1.3.2 Ocean bottom currents (contour currents) .....	22
1.3.3 Gravity-driven processes .....	24
1.3.3.3 Debris Flow deposits .....	27
1.3.3.4 Homogenites .....	27
1.3.3.5 Mass-Transport Deposits .....	28
1.3.3.6 Turbidites.....	29
1.4 Triggering Mechanisms .....	31
1.4.1 Sediment Accumulation.....	31
1.4.2 Erosion .....	31

1.4.3 Earthquakes .....	31
1.4.4 Volcanoes .....	32
1.4.5 Waves .....	32
1.4.6 Gas and Gas Hydrates .....	33
1.4.7 Groundwater seepage .....	33
1.4.8 Diapirism .....	33
1.4.9 Human Activities.....	34
References .....	35
Chapter 2.....	51
Geological setting of the Ecuadorian margin .....	51
2.1 Geodynamic context of the Ecuadorian active margin.....	51
2.2 Main controls of the regional detrital trench sedimentary supply .....	52
2.3 Morphologic segmentation of the slope .....	53
2.3.1 Southern segment of the margin.....	54
2.3.2 Central segment of the margin .....	55
2.3.3 Northern segment of the margin .....	56
2.4 The trench: morphology and sediments distribution .....	58
2.5 Seismological segmentation of the Ecuadorian active margin.....	62
2.6 Paleo-seismological studies and time recurrence of the mega-earthquakes ..	63
2.7 Partial conclusions: objectives and organization of this work .....	66
References .....	70
Chapter 3.....	76
Materials and Methods.....	76
3.1 Introduction .....	76
3.2 Materials.....	77
3.2.1 Bathymetry .....	77
3.2.2 Seismic data.....	78
3.2.3 Deep Sea Sedimentary Cores .....	81
3.3 Methods .....	81
3.3.1 Bathymetric analysis.....	81
3.3.2 Core Description .....	83
3.3.2.1 Split cores Observations .....	83

3.3.2.2 Petrophysical parameters and High-resolution Photography.....	83
3.3.2.3 X-ray Images.....	84
3.3.2.4 Geochemical Analysis.....	84
3.3.2.5 Age Dating.....	84
References.....	86
Chapter 4.....	87
<b>Sedimentary filling of the Ecuadorian subduction trench: An overview.....</b>	<b>87</b>
4.1 Introduction.....	87
4.2 Geologic and Tectonic Settings.....	88
4.3 Data and Methods.....	91
4.4 Results.....	92
4.4.1 Bathymetry data.....	92
4.4.2 Low resolution seismic data.....	95
4.4.3 High resolution CHIRP seismic data.....	99
4.4.4 Piston core data.....	99
4.4.5 Correlation of the core data with the seismic data: sedimentary facies distribution.....	102
4.4.6 Age dating of the sediments in cores.....	105
4.5 Conclusion.....	106
Acknowledgments.....	108
Chapter 5.....	115
<b>Nature and controls on the frontal erosion of the subduction margin of Ecuador:     The example of the Ayampe area.....</b>	<b>115</b>
5.1 Introduction.....	115
5.2 Geological setting.....	116
5.3 Data and methods.....	119
5.3.1 Bathymetric data.....	119
5.3.2 Seismic data.....	119
5.3.3 Core data.....	120
5.4 Results.....	121
5.4.1 Seafloor morphology.....	121
5.4.2 Tectonic structures.....	122
5.4.3 Seismic Facies.....	124

5.4.3.1 The chaotic facies (Ch) .....	126
5.4.3.2 The layered facies (Ly).....	126
5.4.3.3 The semi-transparent facies (St).....	127
5.4.4 Seismic facies architecture.....	127
5.4.4.1 The LTR mega-sequence.....	128
5.4.4.2 The MTR mega-sequence .....	129
5.4.4.3 The UTR mega-sequence .....	129
5.4.5 Sedimentary Facies .....	133
5.4.5.1 Core KAT12-15 .....	133
5.4.5.2 Core KAT12-14 .....	135
5.5 Discussion .....	138
5.5.1 The frontal erosion in Ayampe Basin area .....	138
5.5.1.1 Scars .....	138
5.5.1.2 Landslides .....	141
5.5.1.3 Repetitive surficial erosion and sedimentation.....	141
5.5.2 Frontal erosion triggers in Ayampe area.....	141
5.5.3 A permanent landslide triggering.....	144
5.6 Conclusion.....	144
Acknowledgments.....	145
Chapter 6.....	153
<b>Morpho-tectonic control and sedimentation modalities of mass transport deposits and mega-turbidites: example from the Ecuadorian northern trench .....</b>	<b>153</b>
6.1 Introduction .....	153
6.2 Geodynamic Setting of the Ecuador North Margin .....	155
6.3 Data Sets.....	158
6.4 Results .....	160
6.4.1 Morphologies and structures .....	160
6.4.1.1 The slope .....	160
6.4.1.2 The trench:.....	163
6.4.2 Trench stratigraphy and sedimentation .....	163
6.4.2.1 Hemipelagites.....	171
6.4.2.2 Muddy Turbidites .....	171

6.4.2.3 Megaturbidites.....	172
6.4.2.4 Volcanoclastic deposits .....	173
6.4.2.5 Debrites / Mass Transport Deposits (MTDs).....	174
6.4.3: Distribution of gravity flow deposits .....	174
6.4.3.1 Deep seismic MTD .....	174
6.4.3.2 Chirp MTD and Megaturbidites .....	175
6.4.4 Sedimentation rate model and MT dating from Atacames cores .....	182
6.5 Discussion .....	184
6.5.1 Sources of gravity deposits (Turbidites, Megaturbidites and MTD).....	184
6.5.1.1 Spatial distribution.....	185
6.5.1.2 Composition .....	186
6.5.2 Preconditioning factors for slope instability of the lower slope .....	186
6.5.2.1 Stratigraphy .....	186
6.5.2.2 Tectonics .....	187
6.5.3 Distribution and style of failure along the strike of the margin .....	187
6.5.4 Ages of MTs/MTDs and earthquake occurrence .....	189
6.5.5 Hydrodynamic conditions for emplacement of megaturbidites .....	189
6.5.5.1 Triggering multiple sedimentary destabilizations ?.....	189
6.5.5.2. Tsunami and / or Seiche effect? .....	190
6.5.5.3: Reflections of turbidity currents? .....	193
6.6 Conclusions.....	193
Chapter 7.....	202
General conclusions .....	202
Annexe 1: Core sites.....	205
Annexe 2: Facies Diagrams.....	220
Annexe 3: Sedimentary cores .....	224
Annexe 4: Age dating.....	255

## List of Figures

FIG. 1. 1 MAP SHOWING THE LOCATIONS OF ACTIVE AND PASSIVE CONTINENTAL MARGINS (SOURCE <a href="https://www.bluehabitats.org/?page_id=1660">HTTPS://WWW.BLUEHABITATS.ORG/?PAGE_ID=1660</a> ). .....	3
FIG. 1. 2 SCHEMATIC DIAGRAM SHOWING THE MORPHOLOGY OF A TYPIC PASSIVE MARGIN (CHISTIANSSEN AND HAMBLIN, 2009). THIS DIAGRAM SHOWS THAT A PASSIVE MARGIN IS STRUCTURED BY TILTED BLOCKS FORMED DURING INITIAL RIFTING .....	4
FIG. 1. 3 SCHEMATIC DIAGRAM SHOWING THE MORPHOLOGY OF A TYPIC ACTIVE MARGIN.....	4
FIG. 1. 4 LEFT: DIAGRAMMATIC STRUCTURAL-STRATIGRAPHIC CROSS SECTIONS OF TYPICAL SEGMENTS OF SEDIMENTARY TRENCH INFILL. EXAMPLES FROM THE NORTH PACIFIC TRENCHES (FROM SCHOLL, 1974). RIGHT: IDEALIZED FACIES-DISTRIBUTION IN A TRENCH (FROM PIPER ET AL., 1973).....	5
FIG. 1. 5 SCHEMATIC DIAGRAM SHOWING THE TWO BASIC TYPES OF ACTIVE MARGIN: A) ACCRETIONARY ACTIVE MARGIN, WITH UNDERPLATED AND FRONTALLY ACCRETED SEDIMENTS, AND B) EROSION ACTIVE MARGIN, CHARACTERIZED BY NORMAL FAULTING AND SUBDUCTION OF TECTONICALLY ERODED MATERIAL (CLIFT ET AL., 2004). .....	6
FIG. 1. 6 (A) ESTIMATION OF SUBSIDENCE FROM DRILLING (VON HUENE ET AL., 1988); AND (B) ESTIMATION OF SUBSIDENCE FROM NAUTILE DIVES AND DIRECT OBSERVATIONS (SOSSON ET AL., 1994). .....	8
FIG. 1. 7 ILLUSTRATION OF EVIDENCES OF REGIONAL SUBSIDENCE ALONG THE ACTIVE MEXICAN MARGIN (MICHAUD ET AL., 1995; MERCIER ET AL., 1997). RIGHT AND TOP: LOCALIZATION OF THE NAUTIMATE DIVES ALONG THE INNER WALL OF THE MEXICAN TRENCH AND SYNTHETIC LOG SHOWING THE EXTENSION OF A REGIONAL UNCONFORMITY OF LATE-MIOCENE. LEFT AND TOP: PLUTONIC ROCKS LARGELY OUTCROP ALONG THE INNER WALL AT DEPTH RANGING FROM 3950 TO 2820M. CONGLOMERATES LIE IN UNCONFORMITY ON THE PLUTONIC ROCKS AND 700 TO 1000M WELL-BEDDED SANDSTONES AND SILTSTONES AFFECTED BY NORMAL FAULTS CHARACTERIZE THE UPPER UNIT. THE BENTHIC ASSEMBLAGES INDICATE OF THESE SEDIMENTS PALEO BATHYMETRY OF DEPOSITION SITUATED IN THE UPPER TO MIDDLE BATHYAL WATER DEPTH ZONE. LEFT AND BOTTOM: SUBSIDENCE CURVE DURING THE NEOGENE SHOWING A SUBSIDENCE OF MORE THAN 4000M SINCE 8 MA. ....	9
FIG. 1. 8 THE ROLE OF THE SEAMOUNT ON THE DESTABILIZATION OF THE SLOPE ALONG ACTIVE MARGIN. LEFT: DIAGRAMMATIC SECTIONS ACROSS THE NICOYA SLUMP SHOWING A SEQUENCE OF SEAMOUNT SLIDE DEVELOPMENT. THE PROCESS STARTS WITH THE DESTRUCTION OF THE FRONTAL PRISM AND UPLIFT OF THE SEAFLOOR, AND THEN THE TUNNELING BENEATH THE WEDGE AND THE REBUILD OF THE FRONTAL PRISM; APPARITION OF NORMAL FAULTING AND SLUMPS (VON HUENE, 2004). RIGHT: (A) PERSPECTIVE VIEW AND TECTONIC INTERPRETATION OF AN EXPERIMENT OF CONICAL SEAMOUNT SUBDUCTION, (B) TECTONIC INTERPRETATION OF A CONICAL SEAMOUNT SUBDUCTION SHOWING THE RELATIONS BETWEEN THE DIFFERENT FRACTURE NETWORKS, (C, D) PERSPECTIVE VIEWS OF A SANDBOX EXPERIMENT SHOWING THE RELATIONS BETWEEN SLIP-LINE BACKTHRUST DEVELOPMENT AND SUBDUCTING SEAMOUNT SHAPES. (DOMINGUEZ ET AL., 1998) .....	12
FIG. 1. 9 THE ROLE OF THE DETACHMENT FAULT ON THE DESTABILIZATION OF THE SLOPE ALONG ACTIVE MARGIN (FROM BOURGOIS ET AL., 1993). LEFT 3-D DIAGRAM SHOWING MASS WASTING AFFECTING THE MIDDLE SLOPE OF THE PERU TRENCH. USS : UPPER SLOPE SCARP; MSS MIDDLE SLOPE SCARP, SS SUBDUCTION SCARP. RIGHT TECTONIC EVOLUTION OF THE MIDDLE SLOPE AREA SINCE 400 KA. A ROLL-OVER FOLD FORM DURING THE DEVELOPMENT OF A DEEP DETACHMENT FAULT. CONSEQUENTLY, THE SLOPE ANGLE INCREASE ALONG THE SEAWARD FLANK OF THE ROLL-OVER FOLD AND GRAVITY FAILURE OCCURS. ....	13
FIG. 1. 10 ILLUSTRATION SHOWING SEDIMENTARY WEDGE GEOMETRY CHARACTERISTIC OF THE SEDIMENTARY TRENCH. SEISMIC LINES CROSSING THE CHILE TRENCH ARE FROM GEERSEN ET AL., 2011. DRAWINGS BELOW THE TWO SEISMIC SECTIONS HIGHLIGHT THE FEATURES THAT ARE DISCUSSED IN THE TEXT, PARTICULARLY THE TWO PRINCIPAL CONTRASTING TRENCH DEPOSITS. ....	14
FIG. 1. 11 EXAMPLE OF VARIATIONS OF THICKNESS ALONG A TRENCH (PERU-CHILE TRENCH, FROM VON HUENE, 1974). .....	15
FIG. 1. 12 ILLUSTRATION OF THE LATERAL TRENCH FILL VARIATION AND FACTORS CONTROLLING THESE VARIATIONS (FROM VOLKER ET AL., 2013). LEFT (A) ISOPACH MAP OF THE TRENCH FILL WITHIN THE LIMITS DEFINED BY THE OUTER RISE AND THE TOE OF THE	

CONTINENTAL SLOPE; ISOPACH CONTOURS ARE 400 M. RIGHT: SCHEMATIC REPRESENTATION OF THE DOMINATING FACTORS OF THE TWO OPPOSED ENDMEMBER MODELS FOR SEDIMENT TRANSPORT INTO THE TRENCH AND WITHIN THE TRENCH. ....15

FIG. 1. 13 MAP PROPOSED BY HEURET ET AL. [2011], SHOWING THE VARIABILITY OF PRESENT THICKNESS ALONG THE TRENCH AROUND THE PACIFIC OCEAN. ....16

FIG. 1. 14 LEFT: DIAGRAMMATIC TRANSVERSE SHOWING THE PARAMETERS WITH CONTROLS THE SEDIMENTARY WEDGES INTO THE TRENCHES (FROM THORNBURG AND KULM, 1987). RIGHT: SEDIMENT BUDGET OF ACCRETIONARY WEDGES AS A FUNCTION OF SEDIMENTARY RATE (SR) IN THE TRENCH, CONVERGENCE RATE (CR) AND ANGLE DIP (B) OF THE SUBDUCTING PLATE. W = WIDTH OF THE TRENCH. TOC = THICKNESS OF THE SEDIMENTS SCRAPPED OFF FROM THE SUBDUCTION OCEANIC PLATE (IN C). IN A AND B B AND CR ARE CONSTANT (FROM EINSELE, 2013). ....17

FIG. 1. 15 TRENCH SEDIMENTARY FILLS MODELS FROM PICKERING AND HISCOTT (2016). ....17

FIG. 1. 16 MODEL SHOWING A POSSIBLE INTERPLAY BETWEEN THE AMOUNT OF SEDIMENT INTO THE TRENCH, THE ASPERITY OF THE OCEANIC PLATE AND THE GENERATION OF GREAT EARTHQUAKES (FROM CLOOS AND SHREVE, 1996). TOP: THE SUBDUCTION CHANNEL INCREASES IN SIZE AND THE ASPERITIES WILL BE BLOCKED NEAR THE TRENCH: THIS IMPLY NUMEROUS EARTHQUAKES BU OF LOW MAGNITUDE. BOTTOM: THE SUBDUCTION CHANNEL DECREASES IN SIZE AND THE ASPERITIES WILL BE BLOCKED FURTHER FROM THE TRENCH: THIS IMPLY FEW EARTHQUAKES BUT HIGH MAGNITUDE (> 7.9) MEDIUM (7-7.5) .....18

FIG. 1. 17 DIAGRAMS ILLUSTRATING HOW THE PRESENCE OR ABSENCE OF SIGNIFICANT TRENCH INFILL COULD AFFECT THE PROCESS OF SUBDUCTION (LAMB AND DAVIES, 2003). IN BOTH CASES THE CONVERGENCE VELOCITY “V” IS ABOUT THE SAME. A) EXTENSIVE UNDERMINING OF THE TOE OF THE SEDIMENT-STARVED TRENCHES, MAY DRAG CHAOTIC AND COARSE DEBRIS INTO THE SUBDUCTION ZONE, BUT THIS PROBABLY ACCUMULATES AND RISES NEAR THE UP-DIP EDGE OF THE SZ AS SLUMPING STRIPS OFF THE OVERLYING PRISM, HELPING TO COOL THE PLATE INTERFACE AS WELL AS LIMITING FURTHER DOWN-DIP MOVEMENT OF THE SEDIMENT. HIGH-ANGLE LANDWARD-DIPPING NORMAL FAULTS, TYPICAL OF THIS TYPE OF MARGIN, MAY BE THE COASTAL EXPRESSION OF THIS. B) TRENCHES FULL OF WELL-STRATIFIED FINE-GRAINED SEDIMENT MAY RESULT IN “WELL LUBRICATED” AND SMOOTH SUBDUCTION ZONES BECAUSE THE WET SEDIMENT MAY FORM A WEAK DETACHMENT EXTENDING FAR DOWN THE PLATE INTERFACE. BLANKETING OF THE OCEANIC BASEMENT BY SEDIMENT WILL ALSO HELP TO WARM THE SUBDUCTED OCEANIC BASEMENT. ....19

FIG. 1. 18 LEFT: EVOLUTION OF DIFFERENT PARAMETERS SINCE 50 MA (FROM ONCKEN ET AL., (2006) ALONG THE CENTRAL ANDES. BASED ON THIS EVOLUTION, THE RANGE OF EXPECTED TRENCH FILL THICKNESS IS CALCULED, ASSUMING THAT PLATE INTERFACE STRENGTH SHOWS INVERSE CORRELATION WITH THE AMOUNT OF INCOMING SEDIMENT. RIGHT: MAJOR GLOBAL CLIMATIC TRENDS, AND ANDEAN TECTONIC EVOLUTION AT ~20° S (FROM LAMB AND DAVIS, 2003) POSTULATED PHASES OF SEDIMENT STARVATION IN THE PERU–CHILE TRENCH (C) ALONG THE CENTRAL ANDES DURING PERIODS OF HIGH COASTAL ARIDITY (A) ARE BROADLY IN LINE WITH MEAN ELEVATION HISTORY OF THE ALTIPLANO AND WESTERN MARGIN OF THE EASTERN CORDILLERA IN THE BOLIVIAN ANDES (BASED ON A SELF-CONSISTENT INVERSION OF ESTIMATES FROM GEOMORPHOLOGICAL DATA COMBINED WITH CRUSTAL-THICKENING ESTIMATES AND THEIR TIMINGS FROM CRUSTAL-SHORTENING DATA) .....20

FIG. 1. 19 TERNARY DIAGRAM SHOWING THE THREE MAIN SEDIMENTARY PROCESSES THAT CAN BE FOUND OPERATING IN DEEP SEA (INSIDE THE TRIANGLE) AND THE FACIES MODELS CORRESPONDING TO THEIR RESPECTIVE DEPOSITIONAL PRODUCTS (REBESCO, 2014).....21

FIG. 1. 20 THIS DIAGRAM SHOWS A COMBINATION OF MUDDY, SILTY AND SANDY CONTOURITES IN A NEGATIVE-POSITIVE GRADED SEQUENCE. (FROM GONTHIER, FAUGERES AND STOW, 1984; STOW, 1994) .....24

FIG. 1. 21 DIAGRAM SHOWING FOUR MOST COMMON TYPES OF GRAVITY-DRIVEN PROCESSES THAT CARRY SEDIMENTARY MATERIAL TO DEEP-WATER ENVIRONMENTS. (SHANMUGAM ET AL. 1994) .....25

FIG. 1. 22 (A) DIAGRAM OF A MODERN SLUMP SHOWING TENSIONAL GLIDE PLANE IN THE UPSLOPE DETACHMENT AREA AND COMPRESSIONAL FOLDING AND THRUSTING IN THE DOWNDIP FRONTAL ZONE (AFTER LEWIS, 1971; TAKEN FROM SHANMUGAM, 2006), (B) CORE PHOTOGRAPH SHOWING ALTERNATION OF CONTORTED AND UNCONTORTED SILTSTONE (LIGHT COLOR) AND CLAYSTONE (DARK COLOR) LAYERS OF SLUMP ORIGIN. PALEOCENE, NORTH SEA (SHANMUGAM, 2006) .....26

FIG. 1. 23 FIG. 1.23 SUMMARY OF FEATURES ASSOCIATED WITH SLUMP DEPOSITS OBSERVED IN CORES (SHANMUGAM, 2006) .....27

FIG. 1. 24 FIG. 1.24 NEAR-BOTTOM 4 KHZ SEISMIC-REFLECTION PROFILE SHOWING A HOMOGENITE LAYER (ACOUSTICALLY TRANSPARENT INTERVAL) WITHIN AND ON A BASIN FLOOR IN THE SURROUNDINGS OF THE ISLAND OF THERA, IN THE SOUTHERN AEGEAN SEA, GREECE. (KASTENS AND CITA, 1981) .....28



FIG. 1. 25 DIAGRAM SHOWING THE CONTINUITY OF DEPOSITS FROM A HYPERCONCENTRATED FLOW REPRESENTED BY THE BASE OF LOWE SEQUENCE (LOWE, 1982), A CONCENTRATED FLOW REPRESENTED BY THE TRANSITION FROM THE TOP OF LOWE SEQUENCE TO TA INTERVAL OF BOUMA SEQUENCE (BOUMA, 1962) AND FINALLY A TURBULENT FLOW (TURBIDITE) REPRESENTED BY THE TRANSITION FROM Tb-E INTERVALS OF BOUMA SEQUENCE TO STOW AND SHANMUGAM SEQUENCE (STOW AND SHANMUGAM, 1980), EQUIVALENCE WITH TERMINOLOGY OF MULDER AND ALEXANDER (2001A). FIGURE TAKEN FROM MULDER, 2011 WHICH IS A MODIFICATION FROM SHANMUGAM, 2000 .....30

FIG. 2. 1 GEODYNAMIC CONTEXT OF THE ECUADORIAN MARGIN. THIS AREA IS CHARACTERIZED BY THE SUBDUCTION OF THE CARNEGIE RIDGE AND THE NORTHWARD MOTION, RESPECT TO THE SOUTH AMERICAN PLATE, OF THE NORTH ANDEAN BLOCK. (BASE MAP FROM RYAN ET AL., 2009; BOUNDARIES OF THE FOREARC BASINS FROM DENIAUD, 2000; JAILLARD ET AL., 2009 AND WITT ET AL., 2017) .....51

FIG. 2. 2 THE WESTERN CORDILLERA OF THE ANDES IS CONSIDERED THE MAIN SOURCE OF DETRITAL MATERIAL TRANSPORTED TO THE TRENCH. THE COASTAL CORDILLERA ACTS LIKE A NATURAL BARRIER FOR ALL DRAINAGE COMING FROM THE ANDES, THUS THIS IS DIVERTED I) TO THE ESMERALDAS RIVER IN THE NORTH WHICH TRANSFER THE SEDIMENTS THROUGH THE ESMERALDAS CANYON, AND II) TO THE GUAYAS RIVER IN THE SOUTH WHICH TRANSFER THE SEDIMENTS THROUGH THE GUAYAQUIL CANYON. WHITE DASHED LINES SHOW SEDIMENT PATHWAYS; WHITE STARS REPRESENT SITES OF SEDIMENT ACCUMULATION. CONVERGENCE VELOCITY AFTER TRENKAMP ET AL., 2002. BATHYMETRY FROM MICHAUD ET AL., 2006. IMAGE FROM MICHAUD ET AL., 2015. ....53

FIG. 2. 3 FROM (COLLOT ET AL., 2009): LEFT = MAP OF THE DIFFERENT MORPHOLOGIC SEGMENTS ALONG THE MARGIN. RIGHT = GEOLOGICAL AND STRUCTURAL INTERPRETATION SHOWING THE VARIABILITIES OF THE TRENCH INFILL ALONG THE MARGIN. ....54

FIG. 2. 4 BATHYMETRY MAP, WITH CONTOUR LINES EACH 50 M, OF THE SOUTHERN SEGMENT OF THE ECUADORIAN MARGIN. IN THIS MAP, WE CAN NOTE THE NORTHERN END OF THE PERUVIAN TRENCH, THE GRIJALVA FRACTURE ZONE, THE SALINAS SEAMOUNTS AND THE GUAYAQUIL AND SANTA ELENA CANYONS. S = SCARS OF LANDSLIDE SURFACES; A, B AND C REPRESENT FAULT-CONTROLLED CANYONS (COLLOT ET AL., 2009).....55

FIG. 2. 5 THE SOUTHERN PART OF THE CENTRAL SEGMENT. BATHYMETRY MAP WITH CONTOUR LINES EACH 50 M OF THE CENTRAL SEGMENT OF THE ECUADORIAN MARGIN OFFSHORE BETWEEN PUNTA SALINAS AND CABO SAN LORENZO (FROM COLLOT ET AL., 2009). SOUTH OF THE LATITUDE 1°35'S THE SLOPE MORPHOLOGY IS HIGHLY IRREGULAR, MEANWHILE NORTHWARD THE SLOPE MORPHOLOGY TENDS TO BE SMOOTHER. THERE ARE ALSO E-W ORIENTED SEAMOUNTS SUBDUCTING THE SOUTH AMERICAN PLATE. S = MAIN SCARS OF LANDSLIDE SURFACES.....56

FIG. 2. 6 THE NORTHERN PART OF THE CENTRAL SEGMENT. BATHYMETRY MAP WITH CONTOUR LINES EACH 50 M OFFSHORE BETWEEN CABO PASADO AND PUNTA GALERA, (FROM COLLOT ET AL., 2009). WHERE WE CAN SEE THE NORTHEAST EXTREME OF THE CARNEGIE RIDGE AND THE ATACAMES AND GALERA SEAMOUNTS. THE TRENCH AXIS SHOWS A "EN-ÉCHELON" DISPOSITION (BLACK DOTTED LINE), AND NUMEROUS PLATE BENDING-RELATED NORMAL FAULTS, ASSOCIATED TO SUBDUCTION, ARE AFFECTING THE OUTER WALL OF THE TRENCH. NOTE THAT OFFSHORE PUNTA GALERA THE CONTINENTAL SHELF IS VERY NARROW AND AFFECTED BY LARGE RE-ENTRANTS, AND ALSO THE LOWER SLOPE IS DOMINATED BY IRREGULAR STEEP SCARPS (S) FORMING A SPUR-LIKE TOPOGRAPHIC FEATURE IN THE NORTH WHERE THE GALERAS SEAMOUNTS COLLIDE WITH THE SLOPE. A=SMOOTH MORPHOLOGY, P REPRESENTS A PROMONTORY OVERLIE BY A SEAMOUNT (D'ACREMON ET AL., 2005).....57

FIG. 2. 7 LEFT : FIRST REPRESENTATION OF THE ECUADORIAN TRENCH BATHYMETRY AS IT IS SHOWN BY LONSDALE (1978).....58

FIG. 2. 8 A) MAP WITH THE LOCATION OF SOME PUBLISHED SEISMIC PROFILES ILLUSTRATING THE LATERAL VARIATIONS OF THE THICKNESSES OF THE SEDIMENTARY INFILL ALONG THE TRENCH. B) SEISMIC LINE SHOWING THE THICKNESS OF THE SEDIMENTARY FILL ALONG THE SOUTHERN SEGMENT OF THE MARGIN. GEOLOGICAL INTERPRETATION OF THE SEISMIC LINE SIS-72. TSC= TOP OF SUBDUCTION CHANNEL REFLECTION, TOC= TOP OF OCEANIC CRUST REFLECTION (CALAHORRANO ET AL, 2008). ....59

FIG. 2. 9 ILLUSTRATION OF THE THICKNESS OF THE TRENCH SEDIMENTARY INFILL ALONG THE CENTRAL SEGMENT OF THE ECUADORIAN MARGIN FRONT OF THE CARNEGIE RIDGE (LOCATION OF THE PROFILES ON FIGURE 2.8). FROM SOUTH TO NORTH, (A) SISTEUR

- CRUISE SEISMIC PROFILE FROM SAGE ET AL., 2006; (b) SISTEUR CRUISE SEISMIC PROFILE FROM COLLOT ET AL., 2017 AND (c) SISTEUR CRUISE SEISMIC PROFILE FROM COLLOT ET AL., 2004. WITH THIS SEISMIC RESOLUTION PROFILES, THE TRENCH IS EMPTY. 60
- FIG. 2. 10 ILLUSTRATION OF THE THICKNESS OF THE TRENCH SEDIMENTARY FILL NORTH OF LATITUDE 0° OF THE ECUADORIAN MARGIN (LOCATION OF THE PROFILES ON FIGURE 8.). THE THICKNESS IS LESS THAN 1 STWTT. ....61
- FIG. 2. 11 LEFT: ISOPACH MAP OF THE SEDIMENT THICKNESS INTO THE TRENCH, CLOSE TO THE FOOT OF THE MARGIN, WHERE THE DEEP-SEA FAN OF THE ESMERALDAS CANYON FORMS THE THICKNESS REACHES MORE THAN 4 KMS (MARCAILLOU ET AL., 2008). RIGHT: SEISMIC PROFILE 42 OF THE SISTEUR CRUISE SHOWING THE TRENCH FILL THICKNESS (UP TO 2STWTT (MARCAILLOU ET AL., 2006), LOCATION ON FIGURE 8. ....62
- FIG. 2. 12 GREAT EARTHQUAKES AND COUPLING AREAS ALONG THE ECUADORIAN TRENCH. LEFT: LOCATION OF THE GREAT EARTHQUAKES ALONG THE ECUADORIAN MARGIN (FROM CHLIEH ET AL., 2014) (BLACK STAR = THE EPICENTER OF THE GREAT 1906 EVENT; WHITE STARS = THE EPICENTERS OF THE Mw>7.0 1942–1998 SEISMIC SEQUENCE). GREY SHADED ELLIPSES = HIGH SLIP REGION OF THE 1942, 1958, 1979 AND 1998 SEISMIC SOURCES. RED DASHED CONTOURS = RELOCATED AFTERSHOCKS AREAS OF THE 1942, 1958 AND 1979 EVENTS. RIGHT: DISTRIBUTION OF THE INTER-SEISMIC COUPLING (ISC) ALONG THE ECUADORIAN SUBDUCTION ZONE DERIVED FROM THE INVERSION OF THE INTER-SEISMIC GPS VELOCITIES (FROM CHLIEH ET AL., 2014). RED–YELLOW PATCHES = HIGHLY LOCKED ASPERITIES AND WHITE–BLUE PATCHES = HIGHLY CREEPING REGIONS OF THE MEGATHRUST INTERFACE. ARROWS REPRESENT RESPECTIVELY THE INTER-SEISMIC GPS DATA (BLACK) AND SYNTHETIC (RED). RED DOTTED LINES ARE THE 10-KM ISO-DEPTH CONTOURS OF THE SLAB INTERFACE (FONT ET AL., 2013). IN THE RUPTURE AREA OF THE GREAT 1906 EARTHQUAKES (BLACK DASHED LINE), THE COUPLING IS CONFINED WITHIN THE FIRST 35KM DEPTH OF THE SLAB INTERFACE. A LARGE CREEPING CORRIDOR LIES IMMEDIATELY SOUTH OF THE SHALLOW AXIS OF THE CARNEGIE RIDGE TRACK (CRT). SOUTHWEST OF MANTA, THE PERMANENT GPS STATION OF LA PLATA ISLAND (ISPT) SUGGESTS A HIGHLY-COUPLED PATCH CONFINED BETWEEN THE TRENCH AXIS AND 15-KM DEPTH. IN SOUTH ECUADOR, THE ISC IS WEAK AND SHALLOW. ....63
- FIG. 2. 13 FROM RATZOV ET AL., 2012 LEFT: (A) SLOPE GRADIENT MAP OF THE NORTH ECUADOR TRENCH WITH 500M ISOBATHS CONTOURS SUPERIMPOSED FROM RATZOV ET AL., (2012). THICK DASHED LINES ARE STRUCTURAL RIDGES (R1–R3) SB1–7 ARE TRENCH SUB-BASINS. (B) ZOOM SHOWING THE DETAILED BATHYMETRY WITH SLOPE SCARPS AND RE-ENTRANTS INTERPRETED AS POSSIBLE SOURCE AREAS (S1 TO S3) FOR MTDs. ARROWS INDICATE LIKELY TRANSPORT DIRECTIONS. RIGHT: 3.5 KHZ SEISMIC LINE ACROSS TRENCH SHOWING THREE CHARACTERISTIC ECHOFACIES. FACIES 1: CORRESPONDING TO HEMIPELAGIC AND TURBIDITIC TRENCH FILL; FACIES 2: INTERPRETED AS DOMINANTLY HEMIPELAGIC DEPOSITS INTERBEDDED WITH RARE AND VERY FINE GRAINED TURBIDITES, AND FACIES 3: INTERPRETED AS MTDs (US1 TO US3). (B) INTERPRETED CORE COLUMN FROM GRANULOMETRY, VISUAL DESCRIPTION AND X-RAY VIEWS (RX). TURBIDITES (GREY IN INTERPRETED COLUMN) ARE GRADED UPWARD, AND EXHIBIT A DARK LAMINATED RX FACIES AT THEIR BASE (COARSER MATERIAL WITH LAMINAE), AND LIGHTER RX FACIES UPWARD (FINE GRAINED MATERIAL). HEMIPELAGIC LITHOLOGY (WHITE IN INTERPRETED COLUMN) IS OUTLINED BY A POORLY SORTED GRAIN SIZE DISTRIBUTION (1–2), WHILST TURBIDITE LITHOLOGY (3–4) SHOWS WELL SORTED GRAIN SIZE DISTRIBUTION. ....64
- FIG. 2. 14 SYNTHETIC BATHYMETRIC CROSS SECTION ALONG THE NORTH ECUADORIAN TRENCH SHOWING THE SEVEN IDENTIFIED MTDs. SB1 TO SB7=TRENCH SUB-BASINS 1 TO 7, R1 TO R3=STRUCTURAL RIDGES. DEPOT CENTERS OF SUB-BASINS 1 TO 3 AND 7 ARE UNCONNECTED BECAUSE OF THE STRUCTURALLY UPLIFTED SEDIMENT IN THE TRENCH SADDLE (SB4–SB5). DATED MTDs SUGGEST THAT U1, U2 AND US1 WERE TRIGGERED LOCALLY, WHEREAS THE PAIRED UNITS US2–U3, AND US3–U4 POSSIBLY RESULTED FROM TWO REGIONAL EVENTS, LIKELY EARTHQUAKES, AT ~15.4 KYR AND ~22.6 KYR. (RATZOV ET AL., 201) ....65
- FIG. 2. 15 LEFT: LOCATION OF THE CORE KAMA 21 ALONG WHICH 4 SEDIMENTARY RECORDS OF THE MEGA-EARTHQUAKE WHERE IDENTIFIED. RIGHT: GRAPHIC-CORE LOG OF THE FIRST (TOP) 150 CM OF CORE KAMA21 INTO THE ESMERALDAS TURBIDITES SYSTEM (MIGEON ET AL., 2016). THE X-RAY IMAGE AND ITS INTERPRETATIVE DRAWING REVEAL THE PRESENCE OF FOUR MAIN COARSE-GRAINED LAYERS (B1 TO B4) INTERPRETED AS EARTHQUAKE-TRIGGERED DEPOSITS. THE AGE MODEL IS BASED ON 210Pb EXCESS. THE

FOUR MAIN EARTHQUAKES THAT AFFECTED THE NORTH ECUADOR/SOUTH COLOMBIA MARGIN DURING THE 20TH CENTURY ARE LOCATED ON THE AGE MODEL. ....	66
FIG. 2. 16 ILLUSTRATION WHICH RESUMES THE SEGMENTATION OF THE ECUADORIAN MARGIN. IN THIS FIGURE, WE HAVE LOCATED THE NEW DATA OF ATACAMES (DARK COLORS AND WHITE LINES). THE NEW CORES ARE WHITE CIRCLES. THE THIN BLACK LINES CORRESPOND TO SHE SEISMIC LINES. THE LOCATIONS OF THE MEGA-EARTHQUAKES EPICENTERS CORRESPOND TO THE STARS (FROM NOCQUET ET AL., 2014). THE THICK RED DOTTED-LINE CORRESPONDS TO THE RUPTURE ZONE OF 1906 EARTHQUAKE. ....	68
FIG. 3. 1 LOCATION OF THE ATACAMES NAVIGATION TRACK. IN DARK SHADE, MULTIBEAM FROM THE ATACAMES CRUISE (GRID SPACING 50M). IN THE GULF OF GUAYAQUIL GEMAC CAMPAIGN DATA, COLLECTED BY INOCAR IN 2009, ARE ADDED. NUMBERS CORRESPONDS TO THE LOCATION OF CORE. ....	76
FIG. 3. 2 THIS DIAGRAM SHOWS THE EMISSION AND RECEPTION BASICS OF THE EM122 AND EM710 SYSTEMS. THE ACOUSTIC WAVE IS REFLECTED BY THE SEABED BACK TO THE ANTENNAS, WHICH MEASURE THE SIGNAL IN THE FORM OF A NARROW FAN SHAPE IN THE TRANSVERSE DIRECTION (MICHAUD ET AL, 2012).....	77
FIG. 3. 3 A) MAP SHOWING THE DISTRIBUTION OF THE 2D SEISMIC REFLECTION LINES OF THE SCAN CAMPAIGN (PROPRIETY OF SHE) . RED LINE SHOWS LOCATION OF THE SEISMIC LINE MR08-0980_N, (MODIFIED FROM MARTILLO, 2016). B) SEISMIC REFLECTION LINE MR08_0980_N COLLECTED DURING THE SCAN CAMPAIGN FROM THE NORTHERN PART OF THE ECUADORIAN TRENCH .....	78
FIG. 3. 4 ILLUSTRATION OF THE DIFFERENCE OF RESOLUTION BETWEEN CHIRP AND SEISMIC DATA CROSSING THE ECUADORIAN TRENCH. A) EXAMPLE OF THE CHIRP LINE 0093 ACQUIRED ALONG THE NORTHERN PART OF THE ECUADORIAN TRENCH, B) EXAMPLE OF SEISMIC REFLECTION LINE 1032 (PROPRIETY OF THE SHE) CROSSING THE CHIRP LINE AT0093. THE BLACK RECTANGLE CORRESPONDS TO THE VERTICAL PENETRATION OF THE CHIRP IMAGE. THIS ILLUSTRATION SHOWS THAT THE CHIRP DATA ALLOWS US TO STUDY THE MORE RECENT SEDIMENTARY TRENCH FILL WITH HIGH RESOLUTION; MEANWHILE THE SEISMIC DATA ALLOWS US TO STUDY THE ENTIRE TRENCH FILL BUT WITH LOW RESOLUTION. ....	80
FIG. 3. 5 <b>Fig. 3.5</b> THIS DIAGRAM SHOWS THE MAIN CHARACTERISTICS OF THE KULLEMBERG CORER AND IT WORKS. (ILLUSTRATION BY FRITZ HEIDE, WHOI <a href="http://www.whoi.edu/instruments/gallery.do?mainid=17288&amp;iid=8087">HTTP://WWW.WHOI.EDU/INSTRUMENTS/GALLERY.DO?MAINID=17288&amp;IID=8087</a> ) .....	81
FIG. 3. 6 COMPARISON ALONG A TRENCH SEGMENT OF THE MULTIBEAM BATHYMETRY BEFORE ATACAMES AND AFTER ATACAMES : TO THE LEFT MULTIBEAM DATA BEFORE 2012 (150M GRID PUGU-SALIERI-AMADEUS) ; TO THE RIGHT, MULTIBEAM DATA AFTER 2012 (50M GRID ATACAMES). THE HIGHEST RESOLUTION ALLOWS US TO DISTINGUISH SOME KILOMETER-SIZE BLOCK ON THE TRENCH SEAFLOOR (SEE FOLLOWING PARAGRAPH ABOUT THE RESULTS).....	82
FIG. 3. 7 BATHYMETRY DATA FROM PREVIOUS CAMPAIGNS WAS USED TO BUILD THE 30-M BATHYMETRIC GRID OF THE ECUADORIAN MARGIN. (MARTILLO, 2016). THE DIFFERENT STEPS OF CONSTRUCTION OF THE GRID USED IN THIS STUDY.....	83
FIG. 4. 1 GEODYNAMIC SETTING OF THE NORTH ANDEAN MARGIN (MODIFIED FROM GUTSCHER ET AL., 1999) .....	88
FIG. 4. 2 BATHYMETRIC MAP OF THE ACTIVE SUBDUCTION MARGIN OF ECUADOR SHOWING THE MAIN MORPHO-TECTONIC ELEMENTS PARTICULARLY THE THREE DIFFERENT SEGMENTS.....	90
FIG. 4. 3 BATHYMETRIC MAP OF THE ECUADORIAN TRENCH SHOWING THE LOCATION OF THE CORES, THE HIGH-RESOLUTION CHIRP SEISMIC LINES AND THE LOW-RESOLUTION SCAN LINES.....	91
FIG. 4. 4 TOPOGRAPHIC PROFILE OF THE TRENCH FLOOR PASSING THROUGH THE CORE SITES. THE CORE SITES IN SLOPE BASINS ARE PROJECTED TO THE MAIN LINE. ....	93
FIG. 4. 5 THICKNESS AND DISTRIBUTION OF THE SEDIMENT IN THE ECUADORIAN TRENCH FROM THE ANALYSIS OF THE LOW-RESOLUTION SEISMIC DATA (SCAN). ....	96
FIG. 4. 6 EXAMPLES OF LOW-RESOLUTION SEISMIC PROFILES SHOT ACROSS THE TRENCH IN THE NORTHERN (A), THE CENTRAL (B) AND SOUTHERN (C) SEGMENTS OF THE MARGIN. THE PROFILES SHOW THE ACOUSTIC BASEMENT, THE CARBONATE OZES COVERING OF THE OCEANIC CRUST AND THE TRENCH FILL. THE TRENCH FILL IS COMPOSED OF THREE MAIN UNCONFORMITY—BOUNDED SEISMIC UNITS OR “SEQUENCES” ONLAPPING THE ACOUSTIC BASEMENT AND THE CARBONATE OOZE. WE CAN FOLLOW UP THE THREE SEQUENCES IN ALL DEPOCENTERS ALONG THE MARGIN. ....	98

FIG. 4. 7 HIGH-RESOLUTION CHIRP SEISMIC FACIES, (A) TRANSPARENT FACIES AT NORTHERN SEGMENT OF THE TRENCH, (B) LAYERED FACIES AT NORTHERN SEGMENT OF THE TRENCH, AND (C) CHAOTIC FACIES WITH DIFFRACTIONS AT NORTHERN SEGMENT OF THE TRENCH .....	99
FIG. 4. 8 OVERSIMPLIFIED REPRESENTATION OF THE SEDIMENTARY FACIES OBSERVED IN THE CORES COLLECTED IN THE TRENCH AND IN THE LOWER SLOPE BASINS TOGETHER WITH THEIR SEISMIC FACIES AND APPROXIMATE AGES. SEE THE FULL DATASET IN ANNEXES 1, 2, 3 AND 4 AND A BLOWOUT OF THIS FIGURE IN ANNEX 3 .....	104
FIG. 5. 1 (A) GEODYNAMIC SETTING OF THE NORTH ANDEAN MARGIN (MODIFIED FROM GUTSCHER ET AL., 1999), AND (B) MAP OF THE STUDY AREA WITH THE LOCATION OF THE SEISMIC LINES USED IN THIS STUDY .AND THE SUBDUCTING SEAMOUNTS (=SMT) NUMBERING IS FROM SANCLEMENTE (2014) FIGURE 7.3. ....	117
FIG. 5. 2 BATHYMETRIC MAP OF THE STUDY AREA SHOWING THE MAIN MORPHOSTRUCTURAL ELEMENTS AT THE SEAFLOOR.....	118
FIG. 5. 3 LINE DRAWING OF THE LOW RESOLUTION SEISMIC LINE MR08-788-S (SEE LOCATION ON FIGURE 5.2) .	123
FIG. 5. 4 A) CHIRP LINE ATACP104, WITHOUT INTERPRETATION, SHOWING DETAILS OF THE SEDIMENTARY BASIN (MODIFIED FROM MARTILLO, 2016), B) INTERPRETATION OF THE SEDIMENTARY BASIN SHOWED IN (A) (MARTILLO, 2016), AND C) INTERPRETATION ALONG HOLE SEISMIC LINE ATAC-104 (SEE LOCATION ON FIGURE 5.2).....	125
FIG. 5. 5 OVERSIMPLIFIED DRAWING SHOWING THE LATERAL DISTRIBUTION OF THE GRAVITATIONAL SEDIMENTARY EVENTS ALONG A VIRTUAL CONTINENTAL SLOPE. MODIFIED FROM SHANMUGAN ET AL, 1994. ....	128
FIG. 5. 6 HIGH RESOLUTION CHIRP SEIMIC LINE AT0067 IN THE AYAMPE BASIN (SEE LOCATION ON FIGURE 2).....	131
FIG. 5. 7 HIGH RESOLUTION CHIRP SEISMIC LINE AT0064 IN THE TRENCH (SEE LOCATION ON FIGURE 2) .....	132
FIG. 5. 8 A) SYNTHETIC LITHOSTRATIGRAPHIC COLUMN OF CORE KAT-12-15 (AYAMPE BASIN) WITH PETROPHYSICAL PARAMETERS (DENSITY AND MAGNETIC SUSCEPTIBILITY), X-RAY FLUOROSCOPY AND X-RAY FLUORESCENCE OF TWO LITHOFACIES. B) CORE PROJECTED ON THE SEISMIC PROFILE AT0067. C) LOCATION OF THE CORE ON THE MAP (FIG.4).....	134
FIG. 5. 9 KAT-12-14, A) SYNTHETIC LITHOSTRATIGRAPHIC COLUMN OF KAT-12-14 CORE (TRENCH) WITH PHYSICAL PARAMETERS (DENSITY AND MAGNETIC SUSCEPTIBILITY), X-RAY RADIOGRAPHY AND XR FLUORESCENCE OF TWO LITHOFACIES. B) CORE PROJECTED ON THE AT0064 SEISMIC PROFILE, AND C) LOCATION OF THE CARROT ON THE MAP.....	137
FIG. 5. 10 MAP VIEW OF THE LATERAL DISTRIBUTION OF THE SCARS, SEAMOUNTS AND HIGHS IN AYAMPE AREA. ....	140
FIG. 6. 1 BATHYMETRIC MAP OF THE NORTHERN SEGMENT OF THE ECUADORIAN TRENCH (FROM MICHAUD ET AL., 2009 INCLUDING THE NEW ATACAMES DATA). NEW HIGH SWATH BATHYMETRY WAS RECORDED ALONG THE ATACAMES CRUISE (RED LINES). A GEODYNAMIC FRAMEWORK FROM MICHAUD ET AL., 2015. B) STUDY AREA; STRONG DOTTED WHITE LINE = RUPTURE ZONE OF THE MAIN EARTHQUAKES FROM FONT ET AL., 2013. BLACK RECTANGLE = LOCATION OF THE FIG. 2. ....	157
FIG. 6. 2 MORPHOSTRUCTURAL MAP OF THE STUDY AREA (FROM COLLOT ET AL., 2009, MODIFIED). STRONG WHITE DOTTED LINE = ISOBATH -150M. ....	159
FIG. 6. 3 DEEP SEIMIC PROFILES ACROOS THE MARGIN (LOCATION ON FIGURE 1B AND FIGURE 2). PROPRIETY OF THE SHE (ECUADOR). ....	162
FIG. 6. 4 KM-SCALE FALLEN BLOCKS (BATHYMETRY AND DEEP SEISMIC PROFILE) .....	164
FIG. 6. 5 STRATIGRAPHIC LOG AND DEPOSITS INTERPRETATION OF CORE KAT-21 .....	165
FIG. 6. 6 FIG. 6.6: STRATIGRAPHIC LOG AND DEPOSITS INTERPRETATION OF CORE KAT22 .....	166
FIG. 6. 7 STRATIGRAPHIC LOG AND DEPOSITS INTERPRETATION OF CORE KAT23.....	167
FIG. 6. 8 DETAILED FACIES DESCRIPTION.....	168
FIG. 6. 9 FIG. 6.9: DETAILED FACIES DESCRIPTION.....	169
FIG. 6. 10 DETAILED FACIES DESCRIPTION.....	170
FIG. 6. 11 DEEP SEISMIC PROFILES (PROPRIETY OF THE SHE) CROSSING THE TRENCH (LOCATION ON FIGURE 6.2).....	176
FIG. 6. 12 ATACAMES CHIRP PROFILE ACROSS THE SADDLE AREA (LOCATION ON FIGURE 2). TWO REGIONAL UNITS ARE DISTINGUISHED. THE DOTTED COLORED LINES REPRESENT REMARKABLE SEISMIC REFLECTORS (F, S, K, Q) USED TO REFINE THE STRATIGRAPHICAL CORRELATION BETWEEN THESE TWO UNITS AND BETWEEN THE MTDS.....	177

FIG. 6. 13 ATACAMES CHIRP PROFILE ACROSS THE SB-1 AND SB-2 AREA (LOCATION ON FIGURE 2). WE HAVE IDENTIFIED MORE MTDs THAN RATZOV ET AL., 2010 AND THE THICK MTD U2 IS CONFINED IN THE SB1...178

FIG. 6. 14 ATACAMES CHIRP PROFILE ACROSS THE SB7AND SB6 SUB-BASINS AREA (LOCATION ON FIGURE 2). ..181

FIG. 6. 15 FIG. 6.15: REPARTITION OF THE MTDs ALONG THE NORTHERN ECUADORIAN SEGMENT. ABOVE FROM RATZOV ET AL., 2010; BELOW THIS WORK. THE BATHYMETRIC PROFILE IN BLUE IS ALONG THE ATACAMES CHIRP PROFILE. ....184

FIG. 6. 16 CONCEPTUAL CARTOONS OF A CROSS SECTION OF SUBMARINE SLOPE. ABOVE FAULT CONTROL SLOPE GENERATING ROCK AVALANCHE, COHESION LESS SLUMP WITH DEPOSITS CONTAINING LARGE BLOCKS. BELOW SEAMOUNT SUBDUCTION CONTROLLED SLOPE, WITH FREQUENT THINNER MTD OR LARGE HUGE SLIDE. ....188

FIG. 6. 17 MODELS OF HYDRODYNAMIC CONDITIONS FOR THE SETTLING OF MEGATURBIDITES WITH AMALGAMATED STOW SEQUENCES OBSERVED IN A CONFINED TRENCH. A: TRIGGERING MULTIPLE DESTABILIZATIONS. B: OSCILLATION OF THE WATER COLUMN FOLLOWING A TSUNAMI, C: REFLECTION OF TURBIDITY CURRENTS ALONG THE ESCARPMENTS AND THE SLOPE.....192

## Abstract

Recent deep marine sedimentation in subduction trenches is characterized by the inter-stratification of hemipelagic and turbidite sediments locally interbedded with debris flow, which can result from continental slope shaking triggered by large earthquakes. Sedimentary deposits along the active margin of Ecuador are the consequence of strong tectonic erosion that contributes to the formation of a deep trench filled by a complex suite of sedimentary facies. Gravity flow sedimentation is ubiquitous along the margin and facies range from laterally continuous m-thick mass transport deposits to isolated cm-thick turbidites intercalated with hemipelagite, volcanoclastics and tephra layers. However, the nature and architecture of those deposits remain not clear.

In this study interpretation of detailed swath bathymetry, high-resolution seismic profiles and petrophysical data from sedimentary cores are shown. Most of the information was collected during the scientific campaign “ATACAMES”, onboard the R/V L’Atalante (2012). The objectives of this study are to describe the morphologic complexity on the Ecuadorian margin of the Nazca tectonic plate where a set of deep marine asperities is subducting at different scales, and analyze the consequences on the lateral distribution of the sediments in the various sub-basins.

The Ecuadorian active margin comprises three geomorphological segments: The northern segment, located northward of the Carnegie Ridge, is characterized by a wide (5-10 km) and deep trench (3800 – 4000 m), a gentler gullied continental slope and a shelf (10-40 km wide) with active subsidence. The central segment facing the Carnégie Ridge, is strongly affected by the subduction of the Carnegie ridge which induced a narrow (0–5 km wide) and relatively shallow trench (3100 – 3700 m depth), a steep and gullied slope with no canyons and a 15–40 km wide shelf characterized by areas with active subsidence and uplift. Finally, the southern segment, located southward of the Carnegie Ridge, presents a wide (5–10 km) and deep (4000–4700 m) trench, a starved continental slope with well-defined canyon systems and a wide subsiding shelf (20–50 km).

The sedimentary dynamics along the margin is evaluated by the analysis of 15 sediment cores from which visual description, high-resolution colored photographs, X-Ray imagery, XRF data and measurement of petrophysical properties (gamma density, magnetic susceptibility, resistivity) led to the identification of 11 sedimentary facies that characterize seven sedimentary processes: turbidite beds (turbidity currents), hemipelagites (continuous marine sedimentation), tephtras (airfall ash layers consecutive to volcanic eruptions), debris flow deposits (cohesive debris flows), homogenite (large-scale and/or hybrid gravity flows), slump deposits (mass wasting), and ooze carbonate deposits (bioclastic marine sedimentation). The chronostratigraphy of the deposits is defined by radiocarbon age dating of well-identified hemipelagite sediments. Ages range from 500 to 48,000 years BP over the topmost 10m of the trench deposits.

High-resolution seismic profiles allow definition of three echo-facies: transparent, layered and chaotic. The transparent echo-facies is mainly associated to homogenite deposits,

the layered echo-facies is associated to the turbiditic-hemipelagic interbedded very recent deposits and the chaotic echofacies is associated to reworked gravity flow deposits.

The trench fill represents a lacunar but important record of the history of the subduction margin. Large eastward stepping debris flows in the identified lower two sequences of the trench fill are provided by the outer wall of the trench as a results of slope failures along large normal faults due to the downward bending of the subducting oceanic plate. The sediment of the upper sequence of the trench fill draping the trench floor, are more largely provided by the inner trench wall with a strong control of the Carnegie Ridge. As a result, the depth, frequency, thickness, composition and lateral disposition of the sedimentary deposits vary greatly from those in the north to those in the south. Those large, simple mega-beds like slump, debris flows and homogenites are located in the northern and in the southern segments. They are triggered by large regional fault scarps, in the North and enhanced by the activity of sets of splay faults in the South overhanging the seafloor, at the toe of the slope. Small-size, fluid rich (slump) events are triggered by the subduction of isolated seamounts at the edges of the Carnegie Ridge due to frequent but small destabilizations of an inner trench wall "preconditioned" by the repeated impacts of the successive seamounts. Sets of thick partly volcanoclastic turbidites in the central segment might have been triggered by the complex interaction of slope and continental platform deformation due to seamount subduction and large plinian eruption. These results show the complexity of the sedimentation in the trench of subduction margins that can only be clarified by a precise age dating of the sedimentary events.

## Resumé

La sédimentation marine récente dans les fosses de subduction est caractérisée par l'interstratification de sédiments hémipélagiques, de turbidites et localement de coulées de débris, qui peuvent résulter de la destabilisation des pentes continentales par de grands tremblements de terre. La marge active d'Equateur est constituée par une forte érosion tectonique qui contribue à la formation d'une fosse profonde remplie d'une suite complexe de faciès sédimentaires. La sédimentation par écoulements gravitaires est omniprésente le long de la marge et les faciès vont de dépôts de transport de masse d'épaisseur métriques latéralement continus à des turbidites d'épaisseur centimétriques isolées intercalées avec des couches d'hémipélagites, de volcanoclastiques et de téphras. Cependant, la nature et l'architecture de ces dépôts ne sont pas claires.

Dans cette étude, nous présentons l'interprétation de la bathymétrie détaillée, des profils sismiques à haute résolution et des données pétrophysiques des carottes sédimentaires. La plupart des informations ont été collectées lors de la campagne scientifique "ATACAMES", à bord du R / V L'Atalante (2012). L'objectif de cette étude est de décrire la complexité morphologique à la frontière équatorienne de la plaque tectonique de Nazca où un ensemble d'aspérités marines profondes ont subducté à différentes échelles, et ses conséquences sur la distribution latérale des sédiments dans les différents sous-bassins.

La marge active équatorienne comprend trois segments géomorphologiques: Le segment nord, situé au nord de la Ride de Carnegie, est caractérisé par une large (5-10 km) et profonde fosse (3800 - 4000 m), une pente continentale ravinée et une plate-forme (10 - 40 km de large) avec subsidence active. Le segment central en face de la ride de Carnegie montre une fosse étroite (0-5 km de large) et relativement peu profonde (3100-3700 m de profondeur), une pente escarpée et ravinée, sans canyons, un plateau continental étroit de 15 à 40 km de large caractérisé par des zones d'affaissement et de soulèvement actifs. Enfin, le segment sud, situé au sud de la crête Carnegie, présente une large (5-10 km) et profonde fosse (4000-4700 m), une pente continentale pauvre en sédiments avec des systèmes de canyons bien définis et une large plate-forme subsidente (20-50 km).

La dynamique sédimentaire le long de la marge est évaluée par l'analyse de 15 carottes sédimentaires dont la description visuelle, les photographies à haute résolution, l'imagerie par rayons X, les données XRF et la mesure des propriétés pétrophysiques (densité gamma, susceptibilité magnétique, résistivité) conduisent à l'identification de 11 faciès sédimentaires caractérisant 7 processus sédimentaires: dépôts de turbidite (courants de turbidité), hémipélagites (sédimentation marine continue), téphras (couches de cendres aériennes consécutives à des éruptions volcaniques), dépôts de coulées de débris (coulées de débris cohésifs), homogénites (écoulements de gravité hybrides), des slumps (dépôts en masse) et des dépôts de base carbonate (sédimentation marine bioclastique). La chronostratigraphie des dépôts est définie par la datation au radiocarbone des sédiments hémipélagiques bien identifiés. Les âges vont de 500 à 48 000 ans BP sur les 10 premiers mètres des dépôts de la fosse.



Les profils sismiques à haute résolution permettent de définir 3 echo-faciès: transparent, stratifiés et chaotiques. Le facies transparent est principalement associé aux dépôts d'homogénites, le facies stratifié est associé aux dépôts interstratifiés turbiditique-hémipélagique et le facies chaotique est associé à des dépôts gravitaires grossiers.

Le remplissage de la fosse représente un enregistrement lacunaire mais important de l'histoire de la marge de subduction. De grandes coulées de débris se déplaçant vers l'est dans les deux séquences inférieures du remplissage de la fosse sont initiées le long de la paroi extérieure de la fosse, le long de grandes failles normales dues à la flexion de la plaque océanique subductante. Les sédiments de la séquence supérieure du remplissage de la fosse qui nappent la fosse sont plus largement fournis par la paroi interne de la fosse mais avec un fort contrôle de la ride de Carnegie. En conséquence, la profondeur, la fréquence, l'épaisseur, la composition et la disposition latérale des dépôts sédimentaires varient grandement entre le nord et le sud.

Les grands méga-lits simples, les slumps, les coulées de débris et les homogénites sont situés dans les segments nord et sud. Ils sont déclenchés par de grands escarpements de failles régionales, dans le Nord et par l'activité des séries de failles inverses dans le Sud surplombant le fond marin, au pied de la pente. Les événements de petite taille, riches en fluides (slumps) sont déclenchés par la subduction de monts sous-marins isolés sur les bords de la ride Carnegie en raison de déstabilisations fréquentes de la pente interne de la fosse «préfracturée» par les impacts répétés des monts sous-marins successifs. Des ensembles de turbidites épaisses partiellement volcanoclastiques dans le segment central pourraient avoir été déclenchés par l'interaction complexe de la déformation de la pente et de la plate-forme continentale par la subduction du mont sous-marin et les apports de grandes éruptions pliniennes. Ces résultats montrent la complexité de la sédimentation dans la fosse de la marge de subduction qui ne pourra être clarifiée que par une datation précise des événements sédimentaires.

## Résumé étendu

# Nature et origine des dépôts sédimentaires de la fosse de subduction d'Equateur : Implications paléosismologiques

### Introduction

Les marges continentales, passives ou actives, sont le lieu principal de transfert sédimentaire entre continents et bassins océaniques. De ce fait, elles sont la voie préférentielle des transferts sédimentaires terre-mer au cours du temps. Plus particulièrement les pentes continentales sont le siège de processus d'érosion/dépôt soumises à des processus gravitaires érosifs qui sont des processus majeurs d'érosion et de sédimentation sous-marines sur la pente continentale et dans le bassin profond. De nombreuses études ont montré que ces instabilités, instantanées pour la plupart, impliquent des volumes variés, de quelques mètres cubes, à plus de 1000 km<sup>3</sup> dans les cas extrêmes. Deux processus gravitaires sont considérés comme dominants: les glissements en masse et les écoulements gravitaires turbulents. Les premiers consistent en une cicatrice d'arrachement et le dépôt de corps sédimentaires déstructurés pouvant atteindre plusieurs mètres à centaines de mètres d'épaisseur; les seconds sont générés de façon quasi continue au cours du temps et sont responsables du dépôt de strates individuelles centimétriques à métriques.

Sur la pente continentale, ces glissements peuvent se propager librement, ou bien être canalisés le long de canyons sous-marins qui entaillent la pente continentale. La sédimentation gravitaire dans le domaine marin profond des marges continentales archive alors les traces des grands événements tectoniques, ou climatiques passés sous forme d'une succession de dépôts plus ou moins continus. En effet, sur une marge, les facteurs de déstabilisation et de déclenchement des glissements peuvent impliquer des surpressions de fluides, une surcharge sédimentaire, une pente raide, l'action des vagues, ou une accélération sismique. Sur une marge active, la tectonique, et en particulier l'accélération sismique, sont des facteurs prépondérants dans le déclenchement des glissements.

L'étude de la segmentation de la déformation et de la stratigraphie le long des marges actives est importante à mener. Par exemple la réponse à un fort séisme en termes de glissements, et donc d'enregistrement d'un événement sismologique, va dépendre de nombreux paramètres comme la quantité des apports sédimentaires re-mobilisables, la stratigraphie ou encore le degré de fragmentation, en particulier là où des aspérités topographiques rentrent en subduction, provoquant localement une fragilisation accrue du matériel constituant la marge.

Dans cette étude, nous présentons une interprétation détaillée de la bathymétrie, des profils sismiques à haute résolution et des données obtenues sur les carottes sédimentaires collectées lors de la campagne scientifique "ATACAMES", à bord du N/O L'Atalante (2012). L'objectif de cette étude est de décrire la complexité morphologique à

différentes échelles de la zone de subduction d'Equateur où un ensemble d'aspérités marines profondes ont régulièrement subducté, et la distribution latérale des sédiments dans les différents sous-bassins de la fosse qui témoignent de la déstabilisation d'une pente continentale particulièrement soumise aux tremblements de terre.

Ce mémoire débute par un premier chapitre consacré à l'état des connaissances des processus gravitaires qui se produisent le long des marges continentales (chapitre 1). Il est suivi par une présentation du contexte géodynamique régional et de l'état des connaissances de la marge d'Equateur (chapitre 2). Dans un troisième chapitre, il est brièvement détaillé l'ensemble des données et les méthodes d'analyse des carottes qui ont été utilisés dans ce travail. Dans le quatrième chapitre, nous présentons à l'échelle régionale, la distribution de la sédimentation dans la fosse qui est mise en relation avec l'impact de la ride de Carnegie. Dans un cinquième chapitre, nous précisons l'enregistrement, à l'échelle locale, de la subduction de monts sous-marins qui perturbe et renforce l'effet de déformation régionale de la ride de Carnegie. Finalement, dans un sixième chapitre, nous essayons de déterminer quels sont les indicateurs paléo-sismologiques dans le segment Nord de la fosse, là où les grands séismes historiques sont répertoriés, Puis, nous présentons les conclusions générales de ce travail (chapitre 7).

## **Chapitre 1- Processus géodynamiques et sédimentation gravitaire le long des marges continentales actives**

Dans ce chapitre, nous parlons des caractéristiques des marges continentales passives et actives et nous nous concentrons sur les marges actives puisque la marge de l'Equateur est une zone de ce type. Nous décrivons la morphologie des marges actives, leurs caractéristiques d'accrétion et d'érosion, la subduction des monts sous-marins et les processus de déstabilisation qui peuvent être générés le long de leurs pentes.

Morphologiquement les marges actives sont composées d'un plateau continental, de la pente ou de la paroi interne du côté du continent, de la fosse, de la paroi externe ou de la pente du côté vers l'océan, et des « seamounts » montagnes sous-marines qui subductées dans la zone de la fosse. Lors de leur subduction, les seamounts provoquent des déformations morpho-structurales qui affectent principalement la zone de la fosse et la pente. Il s'agit principalement de réentrants morphologiques et d'escarpements contrôlés par des failles normales et inverses. Toutes ces déformations produisent des matériaux sédimentaires qui remplissent la fosse mais de manière différente le long des marges d'accrétion ou le long des marges d'érosion. Dans les marges érosives, les indentations de la pente persistent longtemps après la subduction sous-marine (Dominguez et al., 1998, Laursen et al., 2002, Hampel et al., 2004), tandis que dans la marge d'accrétion, elles sont rapidement remplies de sédiments.

Dans ces environnements, trois principaux groupes de processus sont capables d'éroder, de transporter et de déposer des matériaux terrigènes, biogènes et volcanoclastique : la décantation en milieu pélagique, les courants dans la fosse et sur les pentes adjacentes et les processus gravitaires. Les sédiments pélagiques sont des matériaux très fins qui

s'accumulent par décantation dans la colonne d'eau, très loin des zones terrestres et généralement à des vitesses de sédimentation de quelques millimètres à un ou deux centimètres par millier d'années. Les sédiments hémipélagiques sont formés de la même manière que les sédiments pélagiques, mais le long des marges continentales où il y a un plus grand mélange avec les matériaux terrigènes et des taux de sédimentation plus élevés. Les courants de fond sont générés par les différences de densité causées par les changements de température et de salinité le long dans la colonne d'eau. Ce type de courants s'écoule le long du fond de l'océan parallèlement aux contours bathymétriques et une grande partie des sédiments moyens et fins de la marge continentale a été retravaillée par ces courants. Son effet est plus perceptible dans les zones marines profondes puisque dans les eaux superficielles son effet est altéré par l'effet des vagues, des marées et des tempêtes. Les événements gravitaires rencontrés sur le fond marin sont: les slides, les slumps, les écoulements de débris et les turbidites.. Ces événements sont provoqués par la gravité et dépendent de la stabilité de la pente et d'un événement déclenchant. Parmi eux les plus intéressants pour cette étude sont les turbidites. Les turbidites sont des dépôts de fonds marins formées par des ruptures massives de la pente (USGS, 2018). Les turbidites déposées peuvent avoir une épaisseur de quelques millimètres à quelques dizaines de mètres. Sur les marges actives, les canyons sous-marins déversent des turbidites dans les bassins d'avant-arc sur la pente ou dans des fosses profondes où ils peuvent s'étendre le long de l'axe du canyon. Les turbidites peuvent se trouver dans les parties inférieures des canyons sous-marins et plus loin vers le large dans les chenaux profonds, mais la plupart se déposent dans de larges cônes sédimentaires. Les turbidites sont composées de sables, de silts ou de graviers interstratifiés avec des argiles pélagiques. Elles sont généralement caractérisées par un granoclassement normal et peuvent ou non afficher des séquences complètes de Bouma. Les turbidites sont largement réparties dans les océans modernes sur les marges passives et dans les régions arc-arrière et avant-arc des marges actives.

## **Chapitre 2- Contexte géologique de la marge Equatorienne**

Dans le chapitre 2, nous présentons le cadre géologique de la marge active équatorienne, les principales sources de sédiments déposés dans la fosse et les principaux contrôles régionaux de la fourniture de ces matériaux au plateau continental, à la pente et à la fosse.

Sur la base des données bathymétriques, la pente de la marge équatorienne est divisée en trois segments géomorphologiques bien définis : Le segment nord, situé au nord de la ride de Carnegie, est caractérisé par une large (5-10 km) et profonde fosse (3800 - 4000 m), une pente continentale ravinée et une plate-forme (10 -40 km de large) avec subsidence active. Le segment central en face de la ride de Carnégie montre une fosse étroite (0-5 km de large) et relativement peu profonde (3100-3 700 m de profondeur), la pente escarpée est ravinée, sans canyons, et le plateau continentale y est étroit de 15 à 40 km de large caractérisé par des zones d'affaissement et de soulèvement actifs. Enfin, le segment sud, situé au sud de la ride de Carnegie, présente une large (5-10 km) et profonde fosse (4000-4700 m), une pente continentale pauvre en sédiments avec des systèmes de canyons bien définis et une large plate-forme subsidente (20-50 km).

Si la marge d'Equateur est une marge très segmentée du point de vue morphologique elle l'est aussi que du point de vue de la source et de la quantité des apports sédimentaires à la fosse. En effet, la présence d'une chaîne côtière fait que les matériaux sédimentaires provenant des Andes sont évacués soit vers le nord dans le canyon d'Esmeraldas et soit vers le sud de la chaîne dans le canyon de Guayaquil. Par conséquent, en face de la ride de Carnegie très peu de matériaux clastiques atteignent la fosse. Il faut donc s'attendre à ce que l'enregistrement sédimentaire en réponse à un grand séisme ne soit pas identique et uniforme tout au long de la fosse. En effet, les hétérogénéités tant stratigraphiques que tectoniques de la pente continentale, vont produire des zones de faiblesses localisées, qui stimulées par un séisme vont favoriser et guider les déstabilisations. La nature des roches, leur teneur en fluides, et leur style de déformation sont des paramètres importants qui vont, en termes de glissement (fréquence, volume, répartition, nature), se traduire par une réponse hétérogène le long de la pente continentale

Par ailleurs, la marge est fortement influencée par la subduction de la ride de Carnegie et sismiquement segmentée. Au nord de grands tremblements de terre ont eu lieu tandis qu'au sud aucun séisme majeur n'a été signalé. Les séismes historiques enregistrés au cours des 800 dernières années ont une récurrence qui varie de 280 à 40-70 ans ou moins pour les tremblements de terre du 20ème siècle. La comparaison des turbidites générées par ces tremblements de terre avec les turbidites générées par le tremblement de terre survenu en 1906 suggère qu'un ou deux tremblements de terre similaires à 1906 ont eu une occurrence d'environ 600 ans

### **Chapitre 3 – Données et méthodes d'analyse**

L'essentiel des données ont été collectées lors de la campagne scientifique ATACAMES en 2012. Les données comprennent de la bathymétrie, de la sismique haute résolution, du sondeur de sédiment et 15 carottes sédimentaires. La bathymétrie a été réalisée avec les systèmes EM710D et EM122. Le système EM710D a été utilisé pour effectuer des mesures dans des eaux peu profondes, jusqu'à une profondeur approximative de 1000 mètres et le système de EM122 a été utilisé pour effectuer des mesures des fonds marins à des profondeurs allant jusqu'à 4300 mètres environ. Les données bathymétriques ATACAMES ont été complétées par des données bathymétriques des projets Pugu-Salieri-Amadeus (2005), Gemac (2009) et la bathymétrie monocanale de l'Institut océanographique de la Marine de l'Equateur (différentes années). Les données sismiques haute résolution de la campagne Atacames ont été complétées à partir des données de sismique réflexion de plus basse résolution acquise lors de la campagne Scan (2009) transverses au plateau continental et à la fosse équatorienne. Les données sismiques haute résolution sont complétées par celles d'un sondeur de sédiment (CHIRP 1.8-5.3 Khz).

Nous utilisons également 15 carottes sédimentaires prélevées à l'aide d'un dispositif de type Kulleberg. Les carottes ont varié entre 3 et 10 mètres de long et ont été prises le long de la zone de la fosse et dans les bassins de pente. La bathymétrie a été traitée

avec le logiciel Caribes v3.8 et a été principalement utilisée pour reconnaître et décrire les caractéristiques géomorphologiques de la fosse, de la pente et d'une partie du plateau continental. Les carottes sédimentaires ont été coupées en deux moitiés, l'une a été utilisée pour faire la description visuelle, les photographies et les mesures pétrophysiques, la radiographie, la fluorescence aux rayons X et prélever des échantillons pour les datations. L'autre moitié est conservée pour archive. Les analyses pétrophysiques ont été réalisées dans le laboratoire de sédimentologie de l'Université de Rennes 1 à l'aide de l'équipement Géotek (MSCL). Les datations 14 ont été réalisées par la plateforme CNRS-INSU ARTEMIS.

#### **Chapitre 4 – Remplissage sédimentaire de la fosse de subduction Équatorienne: un aperçu**

Dans le chapitre 4, nous présentons une analyse du remplissage sédimentaire de la fosse de subduction. Les sédiments dans la fosse proviennent de la couverture de la plaque océanique subductante, de l'avant arc de la plaque chevauchante et des apports latéraux dans l'axe de la fosse provenant des canyons d'Esmeraldas et de Guayaquil.

La plaque océanique est recouverte d'une couche carbonatée de 400-500m d'épaisseur avec une cémentation basale du chert qui subduit sous une plaque de chevauchement composée d'un ensemble complexe de terrains accrétés. La plaque en subduction montre une topographie très irrégulière avec une ride de Carnegie orientée EW, et 2000 m de haut, qui exerce un fort contrôle sur les flux morpho-dynamiques et sédimentaires globaux de la marge. Les données bathymétriques montrent que la paroi interne de la fosse du segment central face à la ride de Carnegie est sensiblement plus lisse que la pente des segments nord et sud, particulièrement fortement déstabilisés en bordure de la ride de Carnegie (zones Atacames et Ayampe) où les monts sous-marins entrent en collision avec la pente inférieure.

La topographie de la fosse imite de façon caractéristique la topographie de la plaque de subduction. La fosse fait 4800m de profondeur au sud, 4300m de profondeur au nord et environ 3700m de profondeur en face de la ride de Carnegie où le fond est très accidenté, avec quelques reliefs locaux de quelques centaines à 600 m de haut. Les dépocentres les plus épais sont situés dans les segments nord (c.400m) et sud (c.300m) de la marge lorsque, en face de la ride de Carnegie, la fosse montre de petits dépocentres de 100m de profondeur entre les reliefs. Les grandes parties de la fosse dépourvues de tout sédiment présentent des caractéristiques d'érosion prononcées causées par les courants de fond canalisés par les parois de la fosse.

Le remplissage sédimentaire comprend trois grandes séquences de dépôt probablement d'âge Pléistocène. Les deux couches inférieures présentent des séquences de déplacement de masse exceptionnellement grandes (200 m d'épaisseur et 5-10 km de large), tandis que la couche supérieure recouvre le fond de la fosse de dépôts turbidites et hémipélagiques en couches minces bien stratifiées. Selon les données sismiques à haute résolution, trois types de faciès sismiques peuvent y être définis: transparent, stratifié et chaotique. Selon les carottes du fond marin, 11 faciès sédimentaires ont été

identifiés regroupés en cinq groupes: hémipélagique (faciès 1), turbidites silteuses (faciès 2 à 6), turbidites volcanoclastiques (faciès 7 et 8), Mass transport Deposits MTD (faciès 9 et 10), et carbonatés (faciès 11). En corrélant ces données avec la sismique haute résolution, il a été possible de décrire les principales caractéristiques de la distribution de la sédimentation le long de la fosse. Les sédiments les plus anciens (48kyrs) correspondent à des coulées de débris provenant de la paroi externe de la fosse et aussi des matériaux provenant de la paroi interne de la fosse à travers le canyon de Santa Elena (39kyrs). La plupart des matériaux qui composent les mégas couches ont des âges qui varient entre 12 et 23 kyrs, dans les segments nord et sud, et les plus récents (entre 6,5 et 7,8 kyrs) se trouvent dans la région d'Ayampe à la limite sud de la ride de Carnegie.

## **Chapitre 5 – Nature et contrôle de l'érosion frontale de la marge de subduction de l'Equateur: l'exemple de la région d'Ayampe**

Le chapitre 5 décrit l'érosion frontale de la marge active d'Equateur affectée par la subduction de monts sous-marins à partir de l'exemple du secteur d'Ayampé. La rugosité de la plaque de subduction y augmente localement l'instabilité de la pente continentale avec d'importants effondrements gravitaires. Cette érosion frontale de la marge et les apports sédimentaires dans la fosse affectent la dynamique de subduction et la sismogénèse le long du contact interplaque.

Le bassin d'Ayampe fait face à l'extrémité sud de la ride de Carnegie, un endroit où apparaissent des monts sous-marins de 100 m de haut et 10-15 km de large. Ici, la fosse mesure 10 km de large, comprend quelques monts sous-marins dont un conique et un à plusieurs pics. La fosse est disséquée par des failles orientées NNE-SSW qui plongent vers le sud à l'échelle régionale. Dans cette zone, la fosse recule activement et la pente subit un effondrement gravitaire global. L'érosion frontale y est très active. De nombreuses petites cicatrices (nx100m à km de large) affectent la pente dans sa partie inférieure et trois grandes (cicatrices S1, S2, S3, nx10 km de large) dans sa partie médiane à supérieure disposés en quinconce à 8, 16 et 32 km de la fosse.

Trois grands glissements de terrain composent le remplissage sédimentaire de la plus grande cicatrice S2. Les glissements de terrain sont de base à en haut LTR 850m-, MTR 250m- et UTR 950m d'épaisseur. Le glissement de terrain du LTR glisse le long de la pente sur 30 km vers le large alors que UTR tronque les deux autres glissements de terrain. Les turbidites et les dépôts de transport de masse scellent le pied des glissements de terrain tandis que les contourites et les hyperpicnites remplissent les bassins en têtes de blocs inclinés juste au-delà du bord de la plate-forme, à leur sommet. Les trois glissements de terrain datent de 1031-1530ka, 1031-790ka et 790-712ka. Les glissements de terrain ont sculpté la cicatrice S2 par l'ablation rotationnelle successive de la pente le long de grandes failles listriques enracinées à l'interface de la plaque.

En comparant la distance des cicatrices de la fosse, le décalage latéral en raison de la dérive vers le nord de la plaque supérieure, l'âge des événements de gravité et l'emplacement de monts sous-marins reconnus sur l'interface de la plaque, nous proposons que les grandes cicatrices observées aujourd'hui sur la pente, peuvent avoir

été découpées ou réactivées par la subduction de seamounts à 57-130ka (S1, Smt7), 337-424ka (S3, SMT6) et 620-712ka (S2, Smt5). Les glissements de terrain sont beaucoup plus anciens et aucune trace des monts sous-marins de ces âges ne peut plus être représentée sur l'interface de la plaque profonde. Néanmoins, trois sommets topographiques bien définis sur la plate-forme à 35, 48 et 72 km de l'axe de la fosse pourraient correspondre à des monts sous-marins responsables de la mise en place des trois glissements principaux.

## **Chapitre 6 - Modalités de contrôle morpho-tectonique et de sédimentation des dépôts de transport de masse et des méga-turbidites: exemple de la fosse nord équatorienne**

Dans le chapitre 6 nous essayons de déterminer quels sont les indicateurs paléosismologiques dans le segment Nord de la fosse, là où les grands séismes historiques sont répertoriés. D'un point de vue sismique la marge d'Equateur présente au Nord une zone fortement couplée sur au moins 300 km de long où plusieurs grands ( $7.7 < M_w < 8.8$ ) séismes historiques ont été enregistrés. A l'inverse elle présente au Sud une zone globalement découplée où ce type de grand séisme n'a pas été reconnu. En 1906, la subduction a provoqué un séisme de magnitude 8.8 (Kelleher, 1972) rompant le contact inter-plaque sur ~500 km. Cette zone a été à nouveau partiellement rompue par une séquence de 4 séismes distincts et adjacents en 1942 ( $M_w$  7.8), 1958 ( $M_w$  7.7), 1979 ( $M_w$  8.1), 2016 ( $M_w$  7.8), 1979 ( $M_w$  8.1) et 2016 ( $M_w$  7.8). Le long de la marge convergente d'Equateur des campagnes océanographiques successives ont été menées (Sisteur (2000), Salieri (2000), Amadeus et Esmeraldas (2006) et Atacames (2012)).

Dans cette zone, nous observons une grande variété de dépôts qui pourraient avoir été déclenchés par des tremblements de terre. Ceux-ci comprennent des slumps, des blocs, des dépôts de transport de masse (MTD), des mégaturbidites et des turbidites. Les dépôts de transport de masse proviennent principalement du nord dans la zone des grands escarpements de la pente interne et au sud, dans la région des monts sous-marins d'Atacames. Les âges de  $720 \pm 50$  yr BP et  $1250 \pm 160$  yr BP déterminés pour les plus récents MTDs sont compatibles avec le supercycle sismique de ~600 ans auquel appartient le tremblement de terre de 1906 ( $M_w = 8,8$ ). Au nord, dans la partie de la pente affectée par de grandes failles régionales linéaires, nous observons des glissements gravitaires et des blocs rares mais volumétriquement importants alors qu'au sud, dans la partie affectée par la collision monts sous marins, la pente est plus fracturée, les glissements sont plus petits, plus homogènes, nombreux et fréquents - la pente y est affectée par une fracturation persuasive et associée à la circulation des fluides.

Nous discutons aussi dans ce chapitre des conditions hydrodynamiques spécifiques observées dans cette fosse confinée qui pourraient expliquer la mise en place des mégaturbidites. Celles-ci comprennent A) plusieurs courants de turbidité et une morphologie confinée empêchant la dispersion du panache à grains fins; B) une oscillation de la colonne d'eau associée à un tsunami cosismique: l'énergie est apparemment insuffisante pour remettre en suspension les dépôts de fond marin comme proposé ailleurs, mais suffisante pour maintenir un transport de charriage déjà initié; C)



des réflexions multiples des courants de turbidité le long des parois des fosses intérieures et extérieures.

## **Chapitre 7 –Conclusion générale**

Cette étude a porté sur l'analyse d'un jeu de données nouvelles de bathymétrie multifaisceaux, de sismique réflexion HR, de sondeur de sédiments, et de carottes sédimentaires, récolté lors de la campagne ATACAMES le long de la marge d'Equateur. Dans cette étude, ces données haute résolution et superficielles ont été complétées par l'utilisation de données de sismiques pétrolières qui recoupent chaque 4 kilomètres la fosse (données qui sont propriété de la Secretaría de Hidrocarburos del Ecuador, et accessibles au travers d'une convention avec l'IRD).

Cette étude est centrée sur l'analyse du remplissage sédimentaire de la fosse de subduction en relation avec les processus gravitaires le long de la marge d'Equateur. Il s'agissait de caractériser la déformation de la marge à court terme (plusieurs cycles sismiques) et à moyen terme (à l'échelle du Quaternaire). Cette étude confirme que la marge d'Equateur qui s'étend sur seulement 600 kms de long est une marge fortement segmentée aussi bien du point de vue morphologique (arrivée de la ride de Carnegie), de la source et de la quantité des apports sédimentaires à la fosse, que du point de vue de l'enregistrement dans les sédiments de la fosse des grands séismes. Cette étude illustre que les sédiments des fosses de subduction sont d'excellents enregistreurs de la déformation des marges actives.

Cette étude nous a permis :

- De préciser la nature et la distribution des sédiments du remplissage sédimentaire de la fosse. L'étude de la morphologie à l'échelle régionale et du remplissage de la fosse (profils pétroliers) nous a permis d'identifier trois segments: un segment nord et un segment sud caractérisés par une pente continentale avec de nombreux marqueurs morphologiques de déstabilisations et un remplissage sédimentaire conséquent de la fosse. Un segment central avec une pente lisse, ravinée mais avec peu de déstabilisations importantes et un remplissage sédimentaire de la fosse très peu important, voir parfois absent. Dans un deuxième temps, l'étude des carottes combinée avec l'interprétation des profils Chirp révèlent dans la fosse, depuis le dernier maximum glaciaire, des dépôts variés (turbidites, hémipélagites, dépôts volcanoclastiques, homogénites, slumps et flux de débris). Les hémipélagites, les turbidites et les homogénites sont présents dans tous les segments. Les turbidites sont plus grossières et plus sableuses avec une fréquence plus élevée dans le segment central. Les dépôts de transport de masse sont localisés principalement dans les segments nord et sud alors que les dépôts volcano-clastiques sont principalement présents dans le segment central. La distribution de ces faciès sédimentaires le long de la fosse est liée à la subduction de la ride de Carnegie qui contrôle l'individualisation des trois segments, ainsi que la nature et la distribution latérale des sédiments dans la fosse. En raison de conditions de dépôt moins profondes, le segment central face à la ride Carnegie,

comporte principalement des turbidites sableuses et limoneuses dans une proportion de 2/1 par rapport aux autres segments. Sa position par rapport aux volcans de l'arc volcanique (plus proche), pourrait expliquer la concentration des dépôts volcanoclastiques. Les segments méridionaux et septentrionaux, affectés par la subduction de monts sous-marins isolés, montrent plus de coulées de débris et de dépôts de transport de masse.

- De montrer l'importance de la déstabilisation de la pente pour la sédimentation dans la fosse. Une reconstitution dans le détail de la mise en place et de la chronologie de la déstabilisation de la marge et des glissements gravitaires massifs associés a été réalisée dans un secteur de subduction successive de monts sous-marins. Nous avons précisé le rôle de l'impact de la subduction de monts sous-marins sur la sédimentation de la marge en étudiant la formation, l'évolution et le remplissage du bassin d'Ayampe, un profond réentrant créé dès 1.45 Ma. Ce bassin est caractérisé par une flexuration de la pente continentale accompagnée de failles normales et d'une tectonique gravitaire initiée par des niveaux de décollement. Dans cette zone, la séquence d'évènements gravitaires a été identifiée, reconstituée et datée. Elle est constituée de dépôts en masse, de débris flows, de mégaturbidites et de turbidites corrélée à la subduction successive de quatre reliefs sous-marins qui accentuent localement l'érosion frontale. Cette étude a permis de mieux comprendre la dynamique de l'érosion frontale et de discuter les relations entre les mécanismes de déformation et la sédimentation le long des marges actives en subduction. L'analyse des glissements et leur datation montre une déstabilisation quasi permanente de toute la pente en liaison avec la compression au front de la marge.
- Dans le secteur Nord de la fosse nous avons dans un premier temps préciser les modalités des transferts sédimentaires en masse. L'analyse des profils sismiques pétroliers couplée à une analyse détaillée de la morphologie nous a permis de préciser la distribution, la source des masses glissées et leur relation avec l'état déformation de la marge. L'analyse des profils pétroliers révèle que les roches constituant les escarpements majeurs, qui nourrissent les glissements les plus volumineux, n'ont pas subi la même séquence de déformation. Au Sud la subduction des seamounts de la chaîne d'Atacames a fracturé de façon « pervasive » sur une vaste zone et une grande épaisseur les roches. Cette fracturation diffuse des roches, lors du passage d'un seamount en subduction, associées à une intense circulation de fluides, va fortement fragiliser les roches sur une grande surface et une grande épaisseur. Au Nord, les escarpements sont au contraire contrôlés par des failles et la fracturation et la fragilisation des roches apparaissent donc limitées dans l'espace aux zones de failles. Entre les failles, la structure originelle des dépôts est conservée, suggérant que les roches conserveraient leurs structures, leur cohérence et seraient moins fragilisées. Les quelques glissements mis en évidence dans ce secteur nord, plus haut sur la pente, n'ont pas atteint la fosse mais se sont arrêtés à mi-pente traduisant probablement une nature assez cohésive des matériaux impliqués, avec peu de fluides, et donc un trajet court sur la pente. De même au Nord du segment les

MTDs sont volumineux et peu nombreux et l'un d'entre eux montre des blocs de taille kilométrique. Au Sud les MTDs sont plus fréquents et moins volumineux. Nous avons donc observé lors de notre étude une segmentation très nette le long de ce segment de marge à la fois des escarpements, de la déformation des roches le long de ces derniers et de la signature dans la fosse des produits de glissements résultants. La pente continentale inférieure est la principale source des MTDs. La subduction des seamounts et les failles régionales sont sans doute l'un des principaux facteurs de pré-conditionnement de l'instabilité des pentes. Ces deux contextes tectoniques répondent probablement différemment aux occurrences de tremblements de terre et peuvent expliquer l'hétérogénéité des enregistrements sédimentaires dans ce segment de fosse.

- Dans le secteur Nord de la fosse nous avons dans un deuxième temps rechercher la présence d'éventuels indicateurs paléo-sismologiques dans la fosse là où les grands séismes historiques sont répertoriés. Au droit de la zone de rupture de 1942 et 2016, aucune rivière majeure n'approvisionne en sédiment la pente et la fosse de telle sorte que la pente continentale, pourrait ne pas être suffisamment rechargée en sédiment entre deux séismes, résultant en une archive paléo-sismique incomplète. L'analyse du Chirp et des carottes nous a permis d'identifier 13 MTD et/ou mega-turbidites qui se distribuent en quatre séries spatialement déconnectées. Un modèle préliminaire de taux de sédimentation établie à partir de datation radiocarbone des carottes nous a permis de proposer de nouvelles corrélations des MTD/mégaturbidites le long du segment nord de la marge ; en particulier U0, U1 et U2 pourraient être liées à la récurrence des grands séismes de 600-700 ans proposée dans la littérature par Migeon et al., 2017. Des datations complémentaires sont nécessaires pour confirmer cette séquence. Enfin, l'analyse sédimentaire des mégaturbidites montre une séquence complexe qui implique plusieurs étapes de mise en place. Nous présentons trois hypothèses (déclenchement de multiples déstabilisations sédimentaires, tsunamis et/ou effet de seiche) sans pouvoir proposer un modèle qui arrive à concilier toutes les observations.

## General Introduction

Continental margins, passives or actives, are the main site of sedimentary transfer between continents and ocean basins. As a result, they are the preferred route of land-sea sediment transfers over time. More particularly, the continental slopes are the site of erosion / deposition processes subjected to erosive gravitational processes that are major underwater erosion and sedimentation processes on the continental slope and in the deepsea basin. Numerous studies have shown that these instabilities, mostly instantaneous, involve varied sedimentary volumes, from a few cubic meters, to more than 1000 km<sup>3</sup> in extreme cases. Two gravity processes are considered dominant: mass landslides and gravity flows. The former consists of an extraction scar and the deposition of unstructured sedimentary bodies up to several meters to hundreds of meters thick; the latter are generated almost continuously over time and are responsible for the deposition of individual centimeter to metric strata.

On the continental slope, these landslides can spread freely, or can be channeled along submarine canyons that cut the continental slope. The gravitational sedimentation in the deep marine domain of the continental margins then records the traces of the great tectonic or climatic events passed in the form of a succession of more or less continuous deposits. Indeed, on a margin, the factors of destabilization and triggering of the slides can involve fluid overpressures, sedimentary overload, steep slope, the action of the waves, or a seismic acceleration. On an active margin, tectonics and seismic acceleration are major factors in triggering landslides.

The active margins in subduction, therefore constitute a privileged environment for the study of tectonics associated with gravitational sedimentation. Earthquakes of great magnitude are at the origin of slope instabilities, generating turbiditic deposits and debris flows. These catastrophic events are recorded in the stratigraphy of the slope basins and the trench of the subduction margin. These sedimentary records provide a unique opportunity to extend local seismic catalogs from the pre-historic Holocene period, thus providing a broad base for probabilistic seismic hazard study. This then documents the return time, spatial distribution and magnitude of subduction earthquakes, as well as their potentially destructive impact on marine and coastal environments.

In parallel, is important to make the study of the segmentation of the deformation and stratigraphy along the active margins. For example, the response to a strong earthquake in terms of landslides, and therefore the recording of a seismological event, will depend on many parameters such as the quantity of sedimentary inputs that can be re-mobilized, and stratigraphy or degree of fragmentation, in particular where topographic asperities fall into subduction, locally causing increases of the fragilization of the material constituting the margin.

The last receptacle of gravity deposits affecting the slope is located at the foot of the active margins in the subduction trench. The sedimentary filling of the subduction trench is thus one of the places where the gravitational processes affecting the slope are recorded in a privileged way.

From a seismic point of view, the Ecuadorian margin in the North has a strongly coupled zone over at least 300 km long where several large ( $7.7 < M_w < 8.8$ ) historical earthquakes have been recorded. Conversely, in the South, it presents a globally decoupled zone where this type of major earthquakes has not been recognized (Collot et al., 2004, Font et al., 2013, Chlieh et al., 2014, Nocquet et al., 2014). Northward, in 1906, the subduction caused an earthquake of magnitude 8.8 (Kelleher, 1972) breaking the inter-plate contact over  $\sim 500$  km. This area was again partially broken by a sequence of 4 separate and adjacent earthquakes in 1942 ( $M_w$  7.8), 1958 ( $M_w$  7.7), 1979 ( $M_w$  8.1), and 2016 ( $M_w$  7.8).

Along the convergent margin of Ecuador successive oceanographic campaigns have been conducted (Sisteur (2000), Salieri (2000), Amadeus and Esmeraldas (2006) and Atacames 2012). These campaigns at sea, with the parallel observation of land deformations (GPS, seismometers, accelerometers) and earthquake analysis (DNA project funded by the ANR), have provided a multi-scale spatial and temporal references of the morphology and structure of the margin.

Initially, this study was focused on the study of the deep structure of the margin and its segmentation (Collot et al., 2004). This work has shown that the margin is characterized by spatial variability, evolving from a tectonic erosion regime in the south (Calahorrano, 2005, Sage et al., 2006) to a tectonic accretion with a complex morphology to the north (Collot et al., 2009, Agudelo et al., 2009, Marcaillou et al., 2008).

Secondly, the work was focused on the study of the relationships between structures and seismogenesis in relation to the entry of the sediments into subduction (Marcaillou, 2003, Marcaillou et al., 2006, Calaharano et al., 2008). or topographies carried by the diving plate (Marcaillou et al., 2016, SanClemente, 2015, Collot et al., 2017). This work continued with a first analysis of the destabilization of the continental slope and the sedimentary record of major earthquakes along the northern segment of the trench (Ratzov et al., 2010, 2012, Migeon et al., 2017).

Thirdly, the work focused on the study of superficial deformations from the sismo-stratigraphic analysis of the sediments preserved on the platform and the upper slope. This allowed to explore the impact of climate variability and deformation on the stratigraphic organization of sediments during the Pleistocene (Michaud et al., 2015, Proust et al., 2016, and Martillo, 2016) in relation with the effect of regional deformation of the subduction of the Carnegie ridge.

All these studies have shown that the Ecuadorian margin, over a short length (about 400 km), is characterized by a wide variety of tectonic and seismological environments. This work focused on the study of the sedimentary filling of the subduction trench and the recording of gravitational deposits. This study has the following main objectives: 1) to clarify the nature and distribution of the sediment filling of the trench; 2) to study in detail the settle and chronology of the destabilization of the margin and associated gravitational landslides, as part of the successive subduction of seamounts; 3) determine the paleo-

seismological indicators in the trench and their distribution. The objective is to specify the sedimentary record of large known historical earthquakes; and whether large earthquakes have also been recorded over the entire trench, or whether sedimentation indicators are only distributed where large earthquakes are historically recognized. In order to meet these objectives, the Atacames (2012) campaign collected unprecedented bathymetry data on the entire trench, as well as sediment sounder profiles, and sedimentary cores. Additionally to this information access to high-quality oil seismic data was granted through the IRD – “Secretaria de Hidrocarburos del Ecuador” agreement.

This thesis begins with a first chapter devoted to the state of knowledge of the gravity processes that occur along continental margins (Chapter 1). It is followed (chapter 2) by a presentation of the regional geodynamic context and the state of knowledge of the Ecuadorian margin. In the third chapter, a brief description of the dataset used in this work and the core analysis methods implemented is made. In the fourth chapter, we present on a regional scale, the distribution of sedimentation in the trench that is related to the impact of the Carnegie Ridge. In a fifth chapter, we detail the local recording of subduction of seamounts that disrupts and enhances the regional deformation effect of the Carnegie Ridge. Finally, in the sixth chapter, we try to determine what are the paleo-seismological indicators in the northern segment of the trench, where large historical earthquakes have been recorded.

# Chapter 1

## Sedimentation and gravity processes along active continental margins

### 1.1 Introduction

Investigation of deep sea sediments began with the voyage of HMS Challenger (1872-1876) which established the general morphology of the ocean basins and the types of sediment they contained. These first researchers believed that only pelagic clays and biogenic oozes were found in the deep sea and thus, during the 19<sup>th</sup> century, and for most of the first half of the 20<sup>th</sup> century, oceans were considered to have quiet, undisturbed floors where only pelagic and hemipelagic sediments could be deposited. No gravity processes had been considered at this time and all sandstones were thought to have been deposited in shallower water. Soon after the Challenger expedition, geologists working in Scotland, the Caribbean, the Alps and elsewhere, in the late 19<sup>th</sup> and early 20<sup>th</sup> centuries, claimed recognition of deep-sea deposits on land. The occurrence of oceanic sediments within continental settings was established. A similar debate occurred around the occurrence of sands and sandstones which were considered initially almost universally to be shallow water.

In 1950, Kuenen and Migliorini (1950) brought together the flume experiments on turbidity currents (Kuenen, 1937, 1950) and Migliorini's observations on graded sand beds in the Italian Apennines to suggest that many graded sandstones in ancient successions had been deposited by high-density turbidity currents. For more than 10 years the turbidity current hypothesis held way as a cause of graded beds, and it was until about 1960 that the word "turbidite" was introduced for the product of a turbidity current. In 1962 Bouma reported that there was a preferred sequence of sedimentary structures in each graded bed although many had the top or bottom of the sequence missing. From then on, all deep-water sands and gravels were interpreted in terms of their transporting, depositional and post depositional processes. However, research through the 1970s showed that the Bouma sequence was strictly applicable to medium-grained sand mud turbidites. Consequently, parallel sequence models were developed for both coarse-grained (conglomeratic) turbidites (Lowe, 1982) and fine-grained (mud rich) turbidites (Stow and Shanmugam, 1980).

In 1959, Gorsline and Emery (1959) delineated the three principal environments of deposition that we still recognize: basin floor, submarine fan and slope apron. In the mid-1960s the submarine fan model was first applied to ancient turbidites (R.G. Walker, 1966a; Jacka et al., 1968). Mutti and Ricci Lucchi (1972) then formulated a more general deep-water depositional model that could be applied to a wider range of ancient sequences. This suggested the types of sequence to be expected not only in an ancient submarine fan, where inner fan, middle fan and outer fan facies associations were recognized, but also in ancient slopes and in deep-water basin plains.

In the 1980s, the universality of the single point source model was questioned with the development of multiple sourced submarine ramp models (Chan & Dott, 1983; Heller & Dickinson, 1985). Stow (1985, 1986) proposed three fan types (the elongate or mud-rich, radial or sand-rich, and fan delta or gravel-rich fans), but also emphasized the importance of different types of slope-apron and basin-plain systems.

Starting in the 1960s, an alternative to the turbidite hypothesis was put forward as an explanation for deep sea sands. This hypothesis proposed that sands could be transported and deposited by deep-ocean bottom currents that travelled transversely along the continental rise, following the contours (Heezen, Hollister & Ruddiman, 1966; Hollister & Heezen, 1967). The sediments deposited by bottom currents became known as contourites and specific sedimentological criteria were proposed for their identification (Hollister & Heezen, 1972). Many attempts were made to discover contourites in the ancient record, but some reports were almost certainly misinterpretations of either shelf sediments or distal turbidites. As giant contourite drifts were drilled and cored it was appreciated that they were generally composed of fine-grained sediments. Facies models for sandy and muddy contourites were put forward by Stow and Lovell (1979) and Stow (1982), and a composite facies model for contourite sequences was developed by Stow, Faugeres and Gonthier (1986). The recognition of outcrop examples of contourites and ancient drift systems is still a matter for debate (e.g. Faugeres & Stow, 1993; Shanmugam, Spalding & Rofheart, 1993).

More recently, sediment transport in deep-water sedimentary systems have been receiving intensive attention during recent decades, because of their crucial importance for natural resource (e.g., deep-sea mineral deposits and hydrocarbon reservoirs) and academic research (e.g., paleoceanography and paleoclimatology) (Mulder, 2011). The dynamic processes driven by downslope transport play a significant role in the construction and shaping of continental margins. Therefore, after this short historical review about submarine gravity processes and associated turbidites gravity-flow deposits, we present the continental margins, where these processes occur very frequently.

## **1.2 Continental margins**

The transition between oceanic crust and continental crust depends on the global tectonic regime and takes place along the margins. There are two types of continental margins (Fig. 1.1): (1) Passive margins, which are derived from oceanic expansion. They are the place of an important subsidence which allows the accumulation of imposing volumes of sediments. (2) Active margins, which are created in areas of lithospheric convergence. The Subduction (or collision) implies an important compressive tectonism associated with high seismicity which can provoke slope destabilization and fall down of important quantities of sediments.



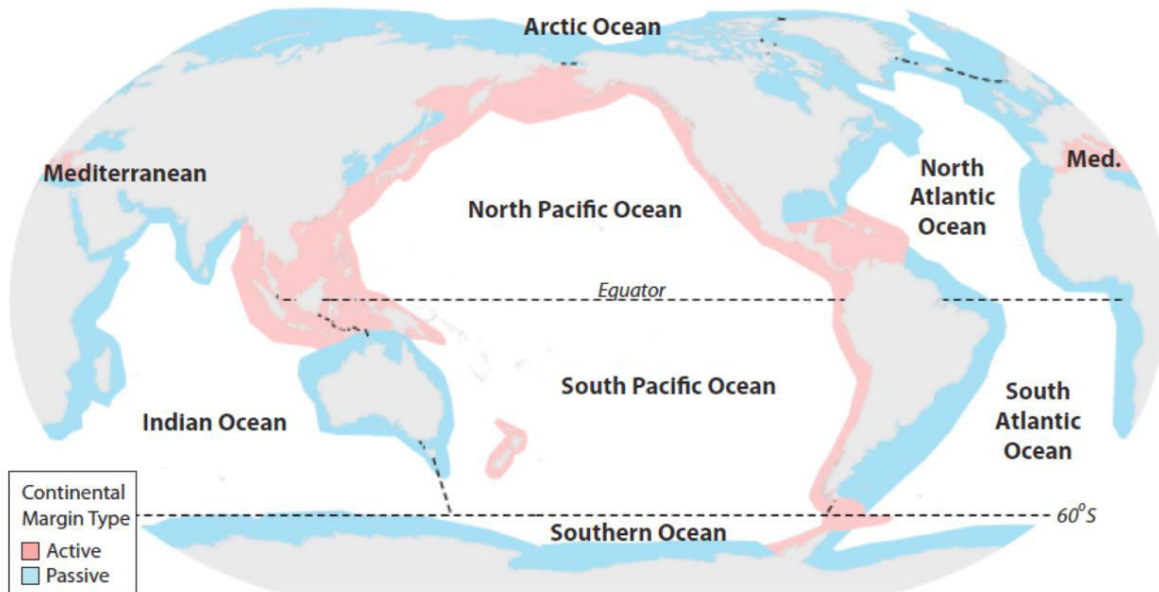


Fig. 1. 1 Map showing the locations of active and passive continental margins (source [https://www.bluehabitats.org/?page\\_id=1660](https://www.bluehabitats.org/?page_id=1660)).

### 1.2.1 Passive margins

Passive margins (also known as rifted margins) mark the sites where continents have rifted apart to become separated by an ocean. Thus, passive margins consist of a seaward tapering wedge of continental crust that is dissected by faults, overlain by sedimentary basins and juxtaposed with oceanic crust (Fig. 1.2). At many margins, magmatic products extruded during continental breakup occupy the outer parts of the margin. The juxtaposition with oceanic crust occurs at the so-called continent-ocean boundary. The coastal parts of many passive margins are marked by mountainous escarpments of variable height. The formation of such mountains is highly debated. Our knowledge of rifted margins has increased greatly in the last few years as the higher quality of long-offset reflection seismic and other geophysical data has led to better imaging of rifted margins at depth. In the majority of cases, these are marked by a continental shelf 70 to 80 km wide on average, but which may exceed several hundred kilometers (for example > 200 km off the state of Maine, > 350 km off Argentina). The continental shelf is located at a depth of less than 150 m. Beyond, the margin is characterized by a slope break localized between 120 and 130 m of depth from which begins the continental slope, dipping average 3 to 5°. The continental slope ends with the glacis, along which the dip softens, at an average depth of 3000 to 4000 m. The highest depths are attained in the almost horizontal Abyssal Plains, beyond 4000 m deep, directly above the oceanic crust.

The morphology of a passive margin comprises a regular slope with a dip relatively constant. Due to their economic importance (they are among the world's most prolific sources of oil and gas) passive margins are much studied and debated among geologists.

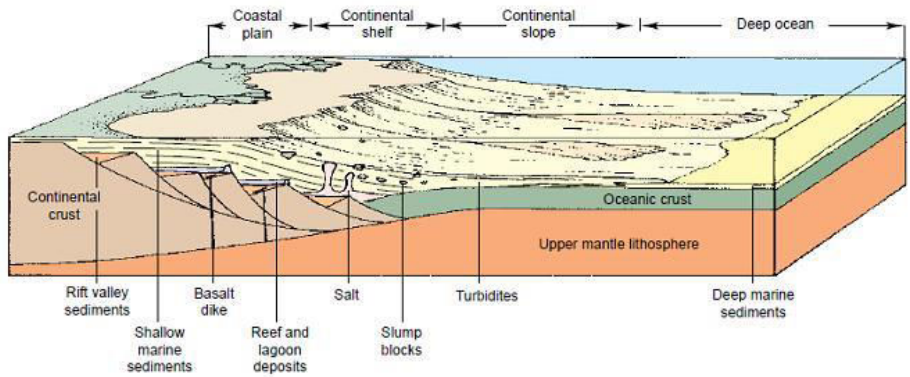


Fig. 1. 2 Schematic diagram showing the morphology of a typical passive margin (Chistiansen and Hamblin, 2009). This diagram shows that a passive margin is structured by tilted blocks formed during initial rifting

### 1.2.2 Active margins

These margins are manifested by subduction zones (dipping of one plate to another) and collision zones (direct confrontation of two plates of the same type). The active margins record deformations related to subduction and therefore have a more complex morphology than passive margins (Fig. 1.2 and 1.3).

On the mainland, they are characterized by the presence of a volcanic arc, and usually by a forearc basin fed by the continental erosion. The forearc basin is not only present on land, but also at the sea. Unlike passive margins, the continental slope ends in an oceanic trench. Beyond the trench, the topography is hilly and irregular, often dotted with rugged volcanic seamounts. The depth of the shelf break may be equivalent to that on passive margins (~150 m), but it can be also deeper, depending of the regional tectonic context. Continental slope descends abruptly into a deep-ocean trench with a depth up to 11,000 m as in the case of The Mariana trench (Aleshire, 2007), or about 4000 m as in the Ecuadorian trench.

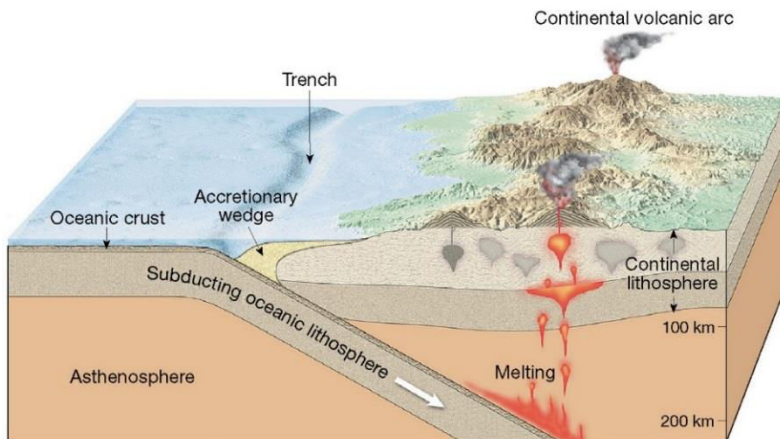


Fig. 1. 3 Schematic diagram showing the morphology of a typical active margin.

The deep-ocean trenches are long and relatively narrow features which represent the deepest parts of the ocean. The in-filling sedimentary sequences can commonly be divided into two groups, an older one of landward-dipping pelagic hemipelagic sequences and a younger, overlying terrigenous sequence of flat-lying turbidite beds (Burk and Drake, 1974; Scholl, 1974; Pickerind and Huscott, 2016); the trench wedge contains sandy turbidites onlapping the outer trench slope (Fig. 1.4).

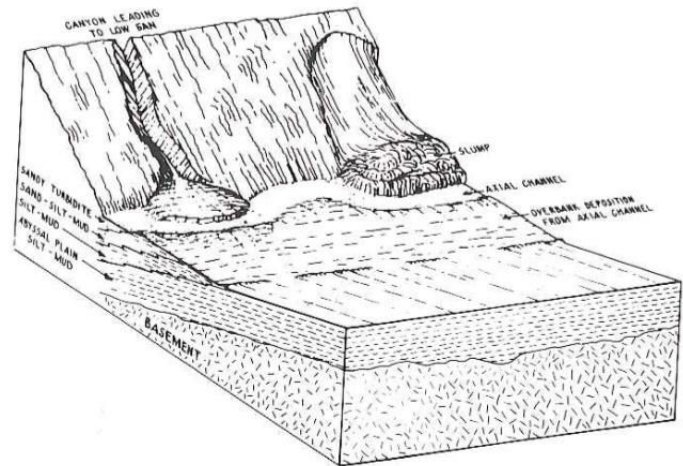
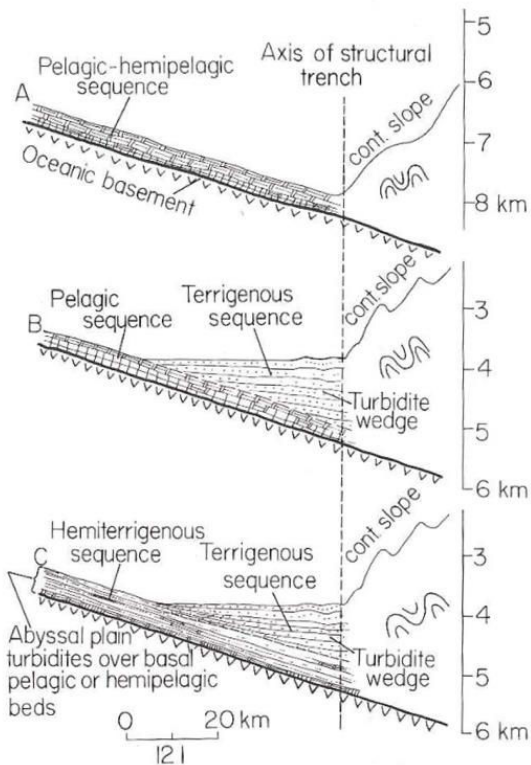


Fig. 1. 4 Left: Diagrammatic structural-stratigraphic cross sections of typical segments of sedimentary trench infill. Examples from the north Pacific trenches (from Scholl, 1974). Right: Idealized facies-distribution in a trench (from Piper et al., 1973)

The general morphology of the continental slope may vary, and there are two main active margin categories (von Huene and Scholl, 1991; Clift and Vannucchi, 2004): (a) Accretionary margins, and (b) Erosive margins. These two categories are characterized by differences in the mechanical properties of the subduction process resulting in a different surface morphology. But it must be recognized that in any given system both processes may be occurring, either switching through time or at the same time in different parts of the subduction zone (Clift et al, 2004)

### 1.2.2.1 Accretionary margins

A margin is considered accretionary only whether it has experienced net accretion over long periods of time in the recent geologic past, i.e., a margin in which a fixed point on the fore-arc migrates upward and/or landward over long periods of geological time (Clift et al, 2004).

These areas are characterized by a margin front bordered by an accretionary wedge consisting of overlapping sediments derived from the trench and the slope. The accretionary wedges have variable width ranging from several tens to hundreds of kilometers. The resulting morphology is smooth, and the mean slope of the entire margin is therefore relatively low ( $2^{\circ}$  -  $4^{\circ}$ ) (Fig. 1.5). However, along the anticline folds, dips may be locally greater than  $20^{\circ}$  (McAdoo et al, 2000). Moreover, the accretionary wedges make also possible the entrapment of sediments derived from the forearc basin.

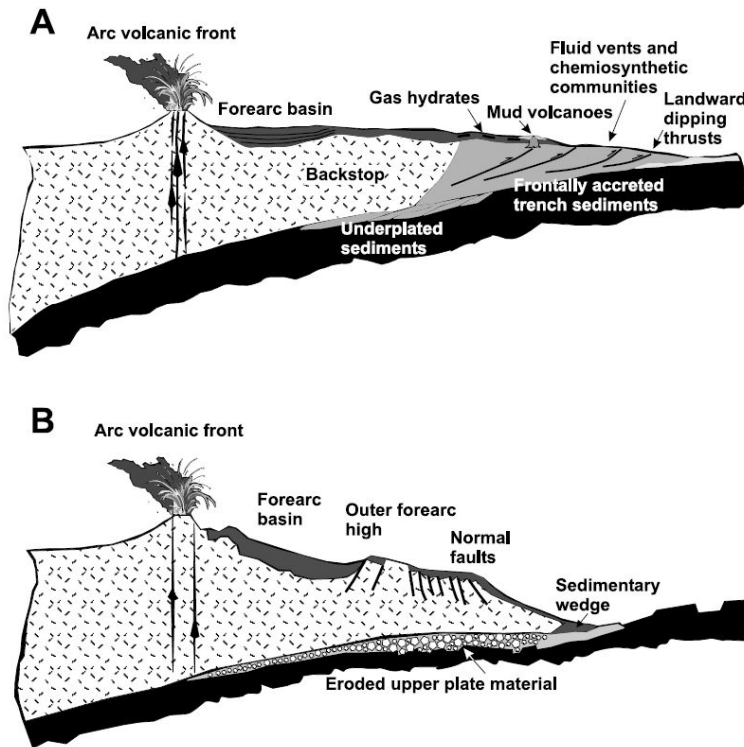


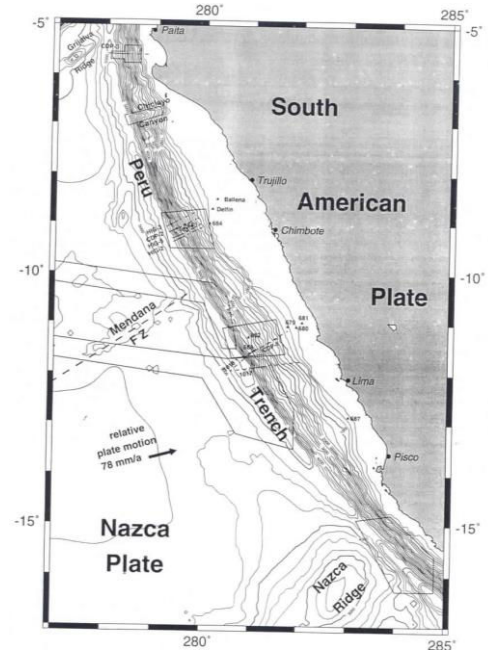
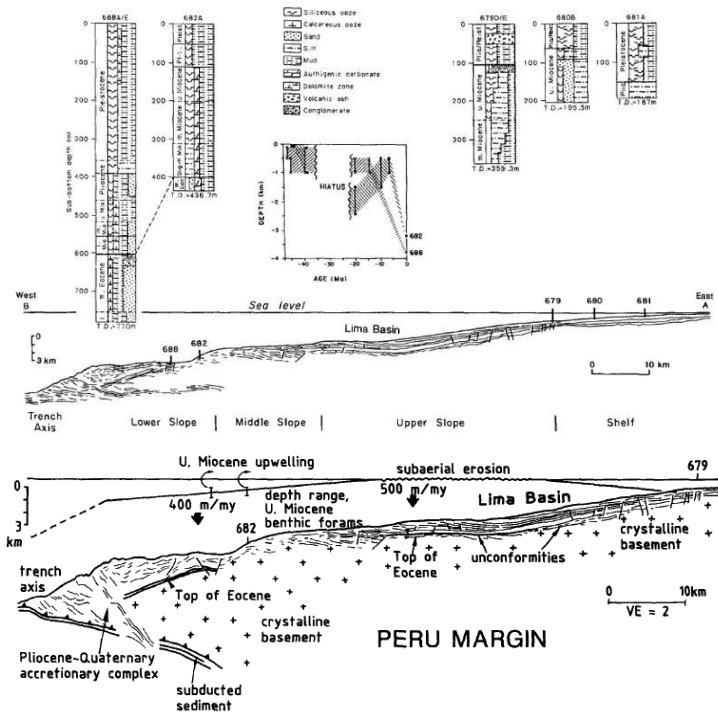
Fig. 1. 5 Schematic diagram showing the two basic types of active margin: a) accretionary active margin, with underplated and frontally accreted sediments, and b) erosive active margin, characterized by normal faulting and subduction of tectonically eroded material (Clift et al., 2004).

### 1.2.2.2 Erosive margins

Contrasting with accretionary margins, erosive margins are progressively destroyed by the subduction process, thus resulting in margin seafloor subsidence (Scholl et al., 1980 ; von Huene et al., 1988, Bourgois et al., 1993; Mercier de Lepinay et al., 1997; Sage et al., 2006) and landward migration of the trench axis and volcanic arc, as a result of net crustal loss through tectonic erosion, regardless of whether there is accretion at the trench axis itself (von Huene et al, 1991; Clift et al, 2004; Wang et al., 2010). The Middle America trench off Guatemala was one of the first sites where subduction without accretion was documented (Aubouin et al., 1982), along the transect proposed by Seely et al. (1974) to be the model of accretion along a convergent margin. The combined results of DSDP Legs 67 and 84 (Von Huene et al., 1980; Aubouin et al., 1982), during which holes along a transect were drilled across the Middle America Trench, provided evidence to propose the Guatemala margin as an end-member model of a new type of convergent margin: the "convergent-extensional margin" (Aubouin et al., 1984; Bourgois et al., 1984), where

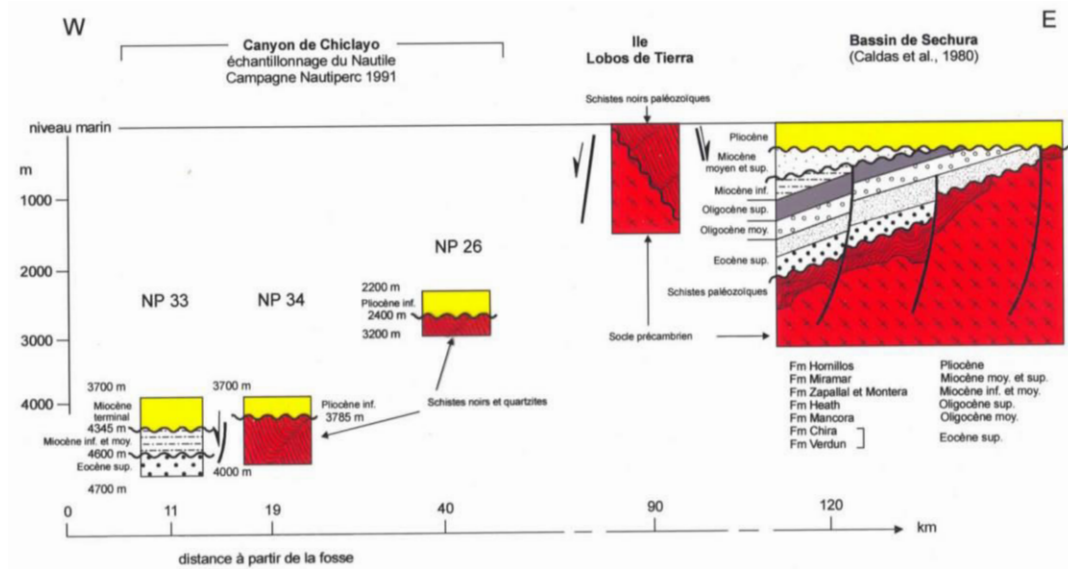
extensional tectonic features occur in association with subsidence (Glaçon and Bourgois, 1985). It is now established that erosive margins (Figure 1.8b) are not systematically linked to subduction of an oceanic asperity and are common in the Circum-Pacific region (Clift and Vannucchi, 2004) where they are marked by steep trench slopes underlain by volcanic, plutonic and mantle rocks and a quasi-absence of an accretionary wedge (Clift et al., 2009).

This subsidence is linked to long-term deformation (Fig.1.5) and presence of normal faults that may affect the base of the entire margin (von Huene et al., 1988; Sage et al. Al., 2006). The resulting average slope is thus high and can reach average values above 7°-8°, as is the case for the margins of Costa Rica (Ranero and von Huene, 2000), Peru (Sosson et al., 1994) (Fig. 1.6) or Mexico (Michaud et al., 1995; Mercier et al., 1997) (Fig. 1.7).



(a)





(b)

Fig. 1. 6 (a) Estimation of Subsidence from drilling (von Huene et al., 1988); and (b) Estimation of subsidence from Nautilite Dives and direct observations (Sosson et al., 1994).

Fig. 1.6: Illustration of the regional subsidence along the Peru which is associated to subduction erosion. Top and right: bathymetric map of the Peru trench; on this map, we have located the two areas of interest; one off Lima (Leg ODP 112, von Huene et al., 1988) and one off the Chiclayo canyon (Sosson et al., 1994). Top and left: During Leg 112, sediments of the basal Pliocene were drilled (site 688) revealing deposition characteristics between 150m and 500 m depths. The integrated interpretation of the seismic profile and the ODP wells along the margin of the trench in Peru (from von Huene et al., 1988, ODP 112) allow to propose subsidence values which are based on the presence of benthic foraminifers and unconformities associated with hiatus (Bottom: During dives revealed that the basement extends less than 19 km from the axis of the trench. The basal Pliocene erosional discordance on basement is regional and it is interpreted by many authors as an episode of sub-aerial erosion. This allows the authors to evaluate a subsidence rate between 713 and 452 m / Ma (at 19 km less from the trench, the margin that was at 0 m in depth is now at 3785 m in depth).

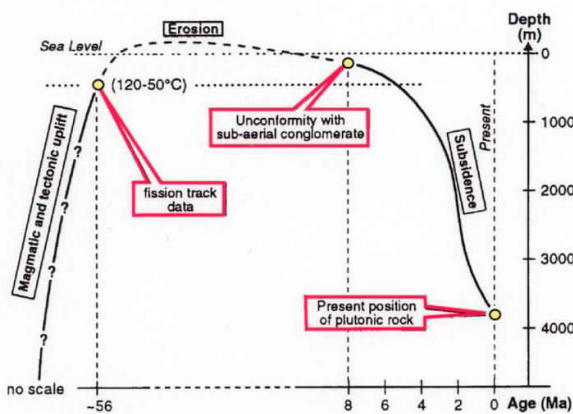
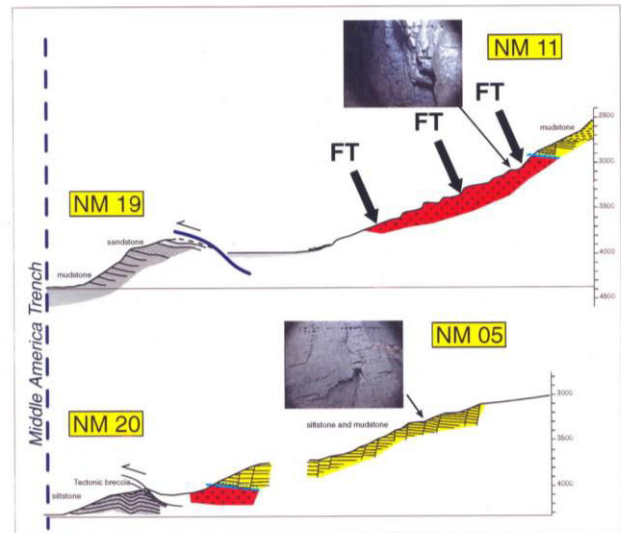
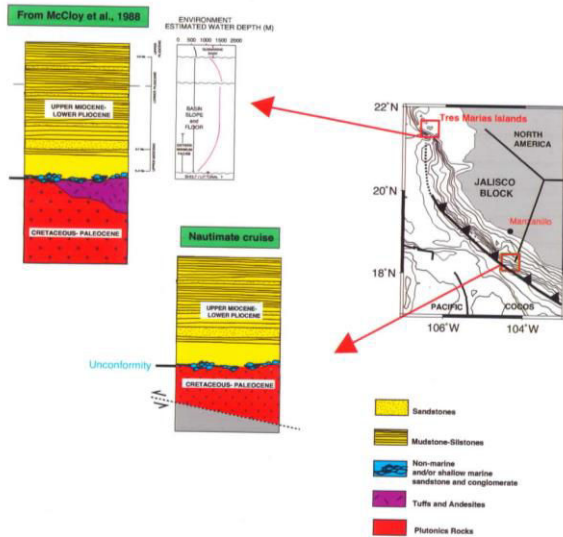


Fig. 1. 7 Illustration of evidences of regional subsidence along the active Mexican margin (Michaud et al., 1995; Mercier et al., 1997). Right and top: localization of the Nautimate dives along the inner wall of the Mexican trench and synthetic log showing the extension of a regional unconformity of late-Miocene. Left and top: Plutonic rocks largely outcrop along the inner wall at depth ranging from 3950 to 2820m. Conglomerates lie in unconformity on the plutonic rocks and 700 to 1000m well-bedded sandstones and siltstones affected by normal faults characterize the upper unit. The benthic assemblages indicate of these sediments paleo bathymetry of deposition situated in the upper to middle bathyal water depth zone. Left and bottom: subsidence curve during the Neogene showing a subsidence of more than 4000m since 8 Ma.

**1.2.3 Morphology of the active margins**

**1.2.3.1 General frame**

Continental slopes of the active margins typically have slope angles of between 2° and 10° with no continental rise. Nevertheless, they are physiographically significant, as they contrast with the very low gradients of continental shelves and the flat ocean floor. Continental slopes extend from the shelf edge, about 200m below sea level, to the basin floor at 4000 or 5000m depth and may be up to a hundred kilometers across in a downslope direction. Continental slopes are commonly cut by submarine canyons (Ratzov et al., 2012; Coste, 2014), which, like their counterparts on land, are steep-sided erosional features. Submarine canyons are deeply incised, sometimes into the bedrock of the shelf, and may stretch all the way back from the shelf edge to the shoreline. They

act as conduits for the transfer of water and sediment from the shelf, sometimes feeding material directly from a river mouth. The presence of canyons controls the formation and position of submarine fans into the trench.

The generally flat surface of the ocean floor is interrupted in places by seamounts, underwater volcanoes located over isolated hotspots. Seamounts may be wholly submarine or may build up above water as volcanic islands, such as the Hawaiian island chain in the central Pacific. The flanks of the volcanoes are commonly unstable and give rise to very large-scale submarine slides and slumps that can involve several cubic kilometers of material (Urgeles et al., 1999). Bathymetric mapping and sonar images of the ocean floor around volcanic islands such as Hawaii in the Pacific and the Canary Islands in the Atlantic have revealed the existence of very large-scale slump features. Mass movements on this scale would generate tsunamis around the edges of the ocean, inundating coastal areas.

The deepest parts of the oceans are the trenches formed in regions where subduction of an oceanic plate is occurring. Trenches can be up to 10,000 m deep. Where they occur adjacent to continental margins (e.g. the Peru–Chile Trench west of South America) they are filled with sediment supplied from the continent, but mid-ocean trenches, such as the Mariana Trench in the west Pacific, are far from any source of material and are unfilled, starved of sediment. Ocean trenches are elongate, gently curving troughs that form where an oceanic plate bends as it enters a subduction zone (Heuret et al., 2011). The inner margin of the trench is formed by the leading edge of the overriding plate of the arc–trench system. The outer margin of the trench is controlled by the plate flexural bending of the oceanic plate. During subduction, the downgoing plate flexes in response to various types of tectonic forces. The flexural bending produces distinct seafloor sloping towards the trench axis, as well as gentle upward seafloor bulging near the outer-rise region seaward of the trench. Furthermore, as flexural deformation becomes significant, this could cause pervasive faulting in the upper plate (Ranero et al., 2005). Trench depth increase with fault dip angle, and age of oceanic lithosphere just prior to subduction. Age of the lithosphere and fault dip angle exert the first-order control on trench depth (Zhong and Gurnis, 1999).

The bottoms of modern trenches are up to 10,000 m below sea level, twice as deep as the average bathymetry of the ocean floors. They are also narrow, sometimes as little as 5 km across, although they may be thousands of kilometers long. Trenches formed along margins flanked by continental crust tend to be filled with sediment derived from the adjacent land areas. Intra-oceanic trenches are often starved of sediment because the only sources of material apart from pelagic deposits are the islands of the volcanic arc. Transport of coarse material into trenches is by mass flows, especially turbidity currents that may flow for long distances along the axis of the trench (Underwood & Moore 1995).

### ***1.2.3.2 Destabilization of the inner-wall of the trenches***

To generate mass wasting along a continental margin by tectonic process, the slope angle needs to be perturbed and increases until over-steeping an angle value, above



which gravity failure occurs. Subduction erosion at depth, change in the angle of subduction, development of relief on the subducting plate, and compressional forces within the sedimentary sequence of the margin may have acted separately or together to increase the slope angle of the slope margin. Several processes were described along the active margin.

### **1.2.3.3 Subduction of seamounts**

Seamounts are omnipresent features of the seafloor (Chapel and Small, 1996). As plate tectonics goes on, seamounts are bound to be transported into subduction zones (Fig. 1.8) affecting the morphology and internal structure of the wedge (Dominguez et al., 1998; Watts A. et al, 2010). Deep seismic reflection has permitted to identify coherently subducted seamounts at different depths: in Nankai as deep as 7-8 km (Bangs et al., 2006) and 10-15 km (Kodaria et al., 2000); in Sumatra a seamount is interpreted around 30-40 km in depth (Singh et al., 2012) and in Ecuador (Collot et al., 2017).

The analogic / physical modeling of the subduction of seamounts beneath an accretionary margin shows the range of deformations that can appear on the overriding plate (Dominguez et al., 1998a). The main morphostructural deformations are the followings (Fig. 1.8):

- A morphological re-entrant at the base of the slope. This re-entrant is filled by landslides and hemi-pelagic sedimentation. On accretionary margins this filling is faster than on erosive margins.
- A sub-vertical scarp on the middle slope. The height of the scarp is proportional to the height of the seamount. Sediments progressively cover the scarp during the subduction of the seamount
- A set of (back) thrust faults deep in a seaward direction, propagates in a landward direction and associated with a local uplift. It forms a circular knoll whose geometry and volume are controlled by the shape and size of the asperity.
- A set of normal and strike-slip faults. Normal faults are present principally around the scarp provoking landslides. The strike-slip faults occur on the right and left sides of the re-entrant in the wake of the subducting seamount, accommodating the deflection of the margin caused by the asperity.

The rate of the filling of the re-entrant caused by a seamount is different along the accretionary and along erosive margins. In erosive margins the slope indentations remain for a long time after the seamount subduction (Dominguez et al., 1998; Laursen et al., 2002; Hampel, et. al., 2004), while in the accretionary margin the re-entrant are swiftly filled by sediments.

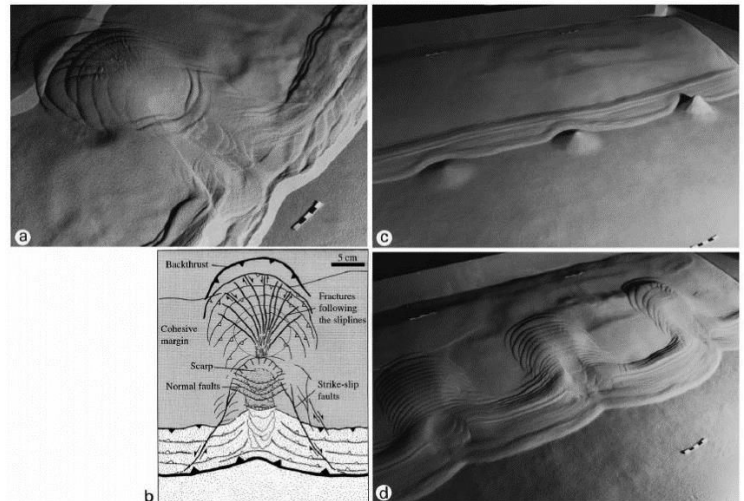
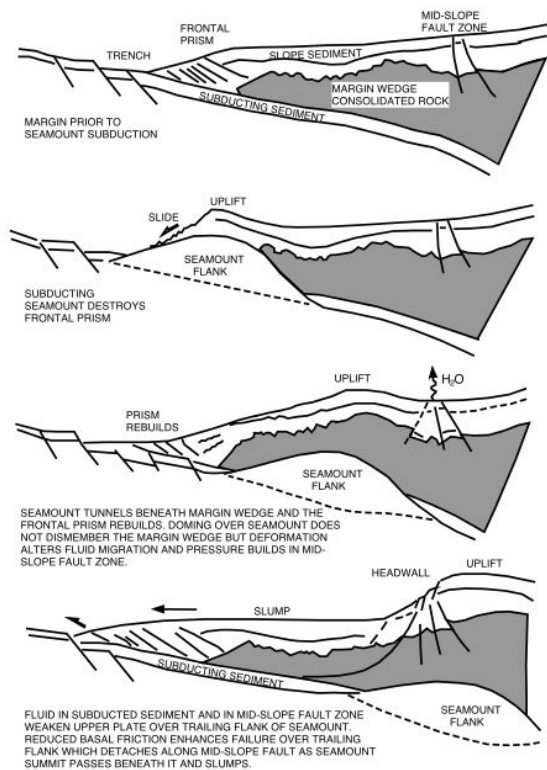


Fig. 1. 8 The role of the seamount on the destabilization of the slope along active margin. Left: Diagrammatic sections across the Nicoya Slump showing a sequence of seamount slide development. The process starts with the destruction of the frontal prism and uplift of the seafloor, and then the tunneling beneath the wedge and the rebuild of the frontal prism; apparition of normal faulting and slumps (von Huene, 2004). Right: (a) Perspective view and tectonic interpretation of an experiment of conical seamount subduction, (b) tectonic interpretation of a conical seamount subduction showing the relations between the different fracture networks, (c, d) perspective views of a sandbox experiment showing the relations between slip-line backthrust development and subducting seamount shapes. (Dominguez et al., 1998)

#### 1.2.3.4 Roll-over fold associated to regional detachment fault.

The seamount subduction is not the only tectonic process that allow massive gravity failure at convergent margin (Fig. 1.9). Along the Peru trench, extensional tectonic features occur in association with subsidence that is assumed to be related to subduction erosion (Bourgeois et al., 1993; Sosson et al., 1994). These last authors propose that a long-term evolution detachment fault affecting the middle slope, has caused important mass wasting along the slope. Estimating the beginning of the detachment fault formation at 400 k, they have associated is activity with the formation of a large roll-over fold. From 400 ka to present time, they estimated that the landward flank of the roll-over fold has rotated landward; consequently, in this area the slope became more stable, with a slope angle evolving from 7° to 2°. On the contrary and during the same time, the seaward flank of the middle slope roll-over fold rotated 5° seaward; consequently, the slope in this area over steepened dramatically the point of gravity failure, and a catastrophic debris avalanche occurred between 16.5 and 11.1 ka removed the seaward flank of the middle slope roll-over fold.

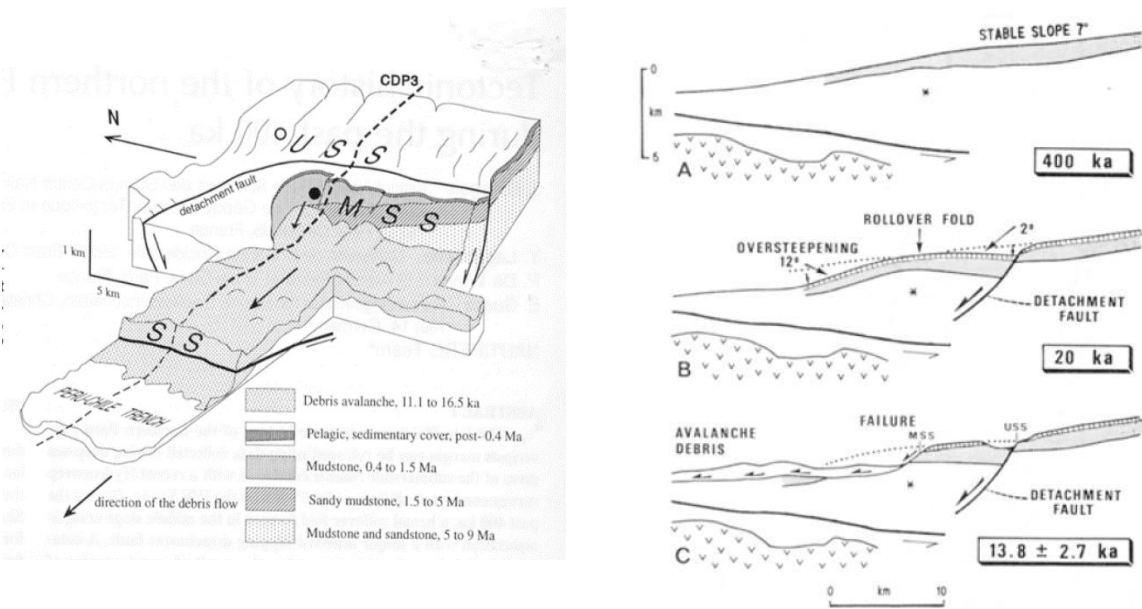


Fig. 1. 9 The role of the detachment fault on the destabilization of the slope along active margin (from Bourgeois et al., 1993). Left 3-D diagram showing mass wasting affecting the middle slope of the Peru trench. USS : Upper slope scarp; MSS middle slope scarp, SS subduction scarp. Right Tectonic evolution of the middle slope area since 400 ka. A roll-over fold form during the development of a deep detachment fault. Consequently, the slope angle increase along the seaward flank of the roll-over fold and gravity failure occurs.

## 1.2.4 Dynamic of the trench sedimentary fill along the active margins

Sedimentary fills of deep-sea trenches are sensitive recorders of long-term tectonics, shorter-term changes in surface processes, and even seismic cycles operating on very short (centennial) geological time scales at active plate margins.

### 1.2.4.1 Sedimentary infill geometry

Three separate sources may be at the origin of the deep-marine trench sediment (Pickering and Hiscott, 2016): oceanic plates sediments passively conveyed by plate motions into the trench during subduction; lateral input from the forearc; and axial transport of sediments along the trench from distant areas. The combination of the two last sources results of the development of a sedimentary wedge along the foot of the outer-wall of the trench (Fig. 1.10). This wedge is developed by the lateral input which produce two principal contrasting trench deposits (Fig.1.10): Blocky and debris flow deposits locally derived from the lower and middle slope of the inner-wall of the trench, or from more distant source as the upper slope and shelf break; and relatively fine-grained deposits supplied by turbidity currents. This sediments infill and drape uneven topography of the oceanic plate and tend towards sheet system with onlap peripheral outer-wall slope.

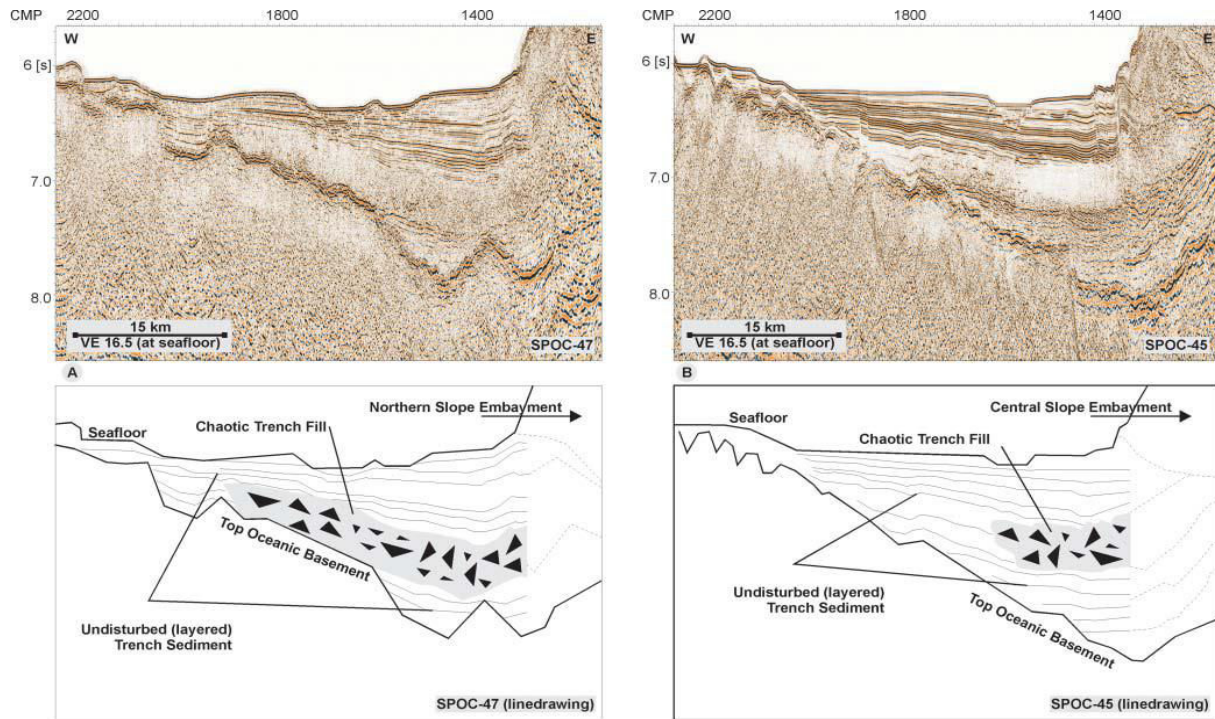


Fig. 1. 10 Illustration showing sedimentary wedge geometry characteristic of the sedimentary trench. Seismic lines crossing the Chile trench are from Geersen et al., 2011. Drawings below the two seismic sections highlight the features that are discussed in the text, particularly the two principal contrasting trench deposits.

#### 1.2.4.2 Sedimentary infill thickness lateral variations

In trenches, sediment thickness varies enormously. The first studies in the 70s shown that the thickness of trench sedimentary fill is variable along the trench (Fig. 1.11). Many factors control the thickness and the distribution of the sediment along the trenches where latitudinal variation in sedimentary processes is important (Völker et al., 2006). More recently, Volker et al., 2013 have computed the total amount and the regional distribution of trench sediment volumes along the Chile trench (Fig. 1.12). They conclude that the sediment fill reflects latitudinal variations in climate as well as in the morphology and geology of Chile margin, but also of sediment transport processes to the trench and within the trench. This is confirmed and illustrated by Heuret, 2011 which has proposed a map of the thickness all along the Pacific trenches (Fig. 1.13). At larger scale, Heuret, et al., 2011 have illustrated this lateral variation of the sedimentary infill thickness all along the Pacific trenches.

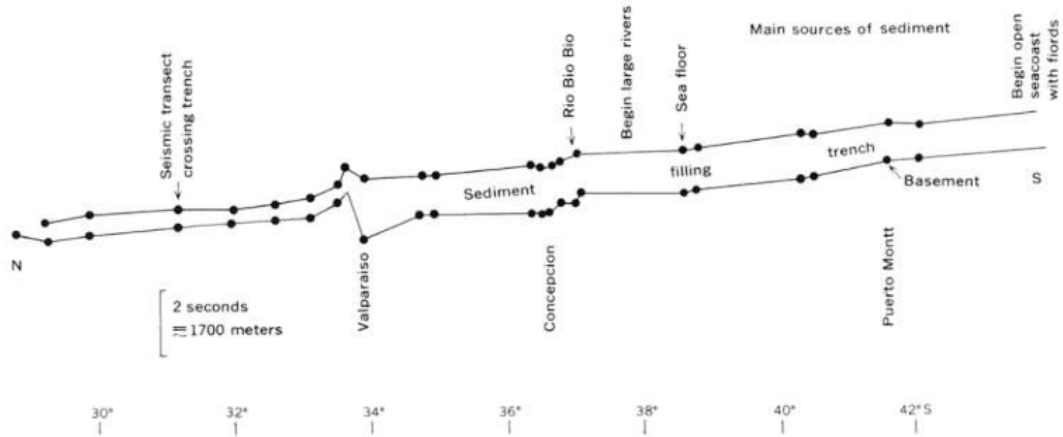


Fig. 1. 11 Example of variations of thickness along a trench (Peru-Chile trench, from von Huene, 1974).

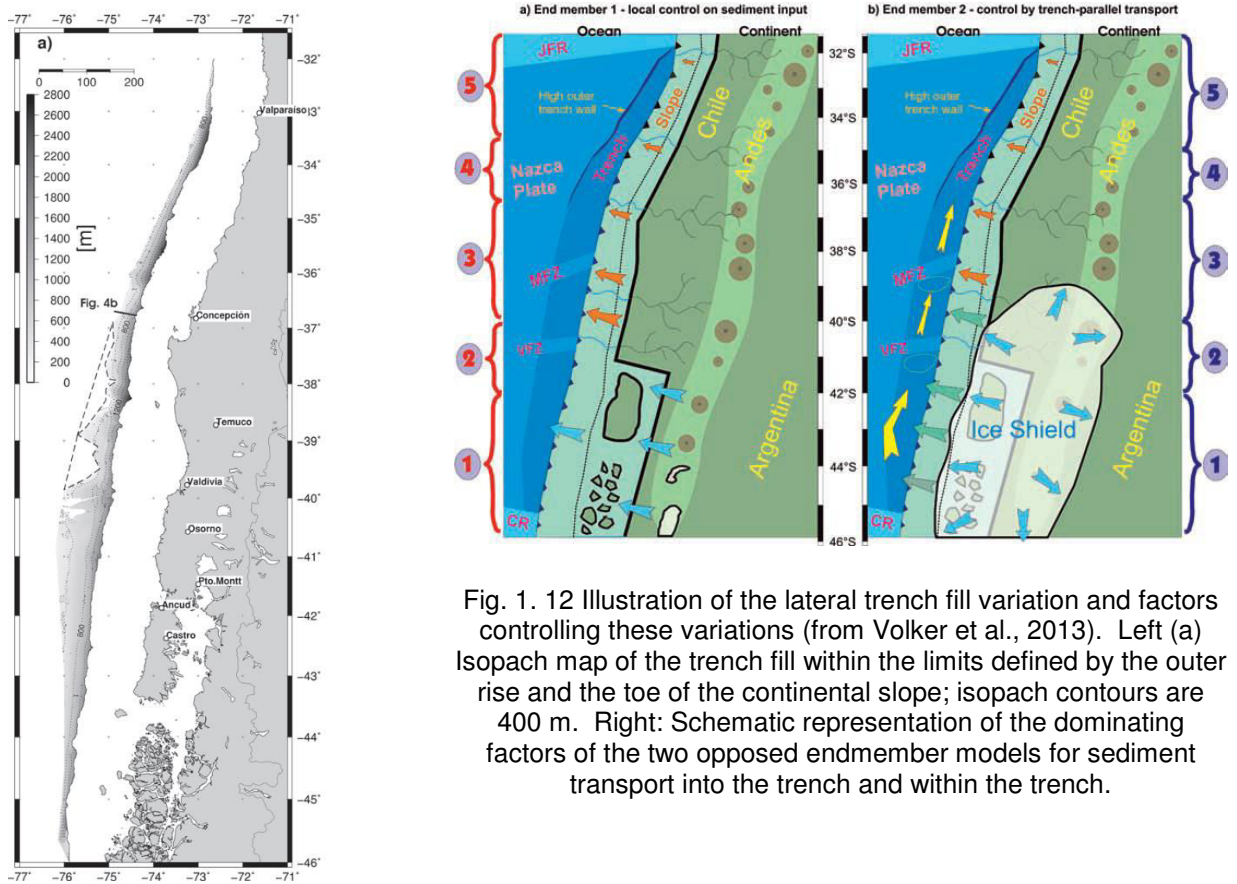


Fig. 1. 12 Illustration of the lateral trench fill variation and factors controlling these variations (from Volker et al., 2013). Left (a) Isopach map of the trench fill within the limits defined by the outer rise and the toe of the continental slope; isopach contours are 400 m. Right: Schematic representation of the dominating factors of the two opposed endmember models for sediment transport into the trench and within the trench.



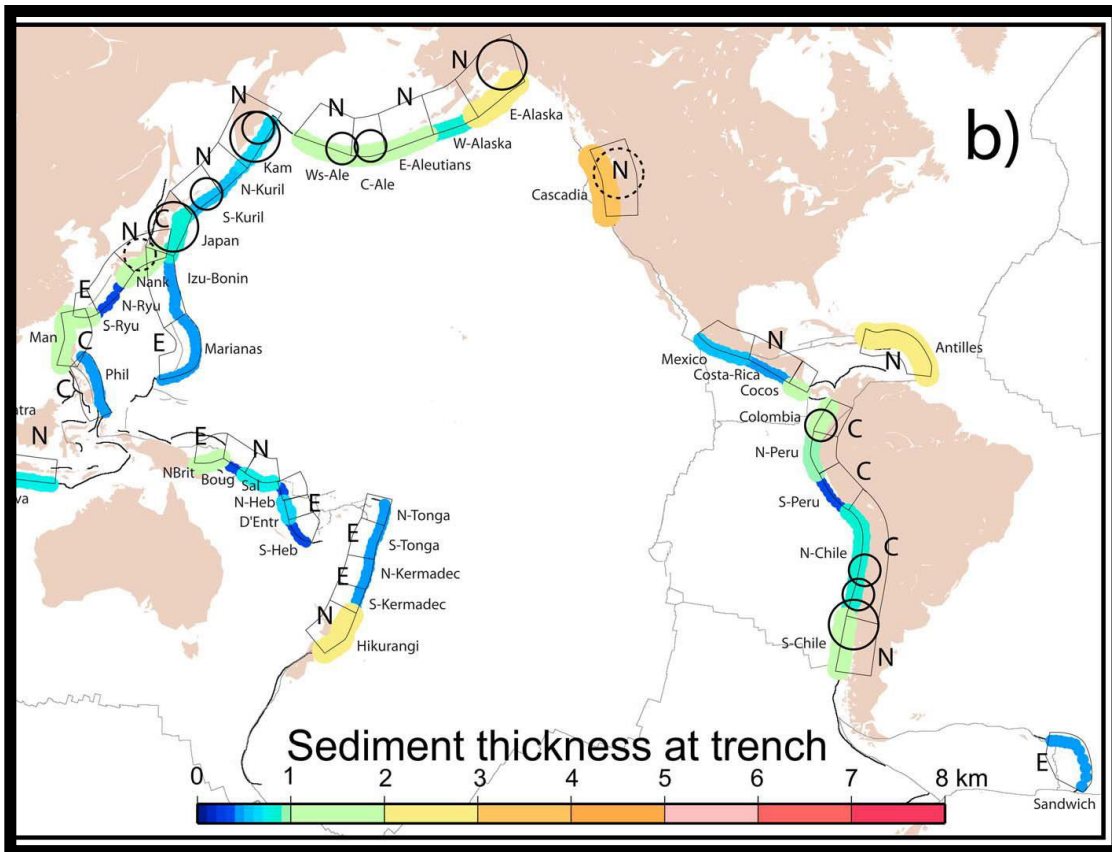


Fig. 1. 13 Map proposed by Heuret et al. [2011], showing the variability of present thickness along the trench around the Pacific Ocean.

### 1.2.4.3 Sedimentary infill residence time into the trench

Moreover, the sediments in a deep-sea trench have little chance of being preserved in their original position because they are continuously scraped off by the overriding accretionary wedge or incorporated into the subduction complex. The residence time of sediments in the deep-sea trench is a function of the convergence rate, the width of the trench and the angle of dip of the oceanic plate (Thornburg and Kulm, 1987) (Fig 1.14). For example, sediment deposited in a 20-km wide trench subject to a convergent rate of 5 cm/a would have a maximum residence time of only 400 000 years (Einsele, 2013). Indeed, the present trench fill (Fig. 1.14) is only a part of the sediment that has been deposited in the trenches because earlier trench fill must have been incorporated into the continental slope or subducted.

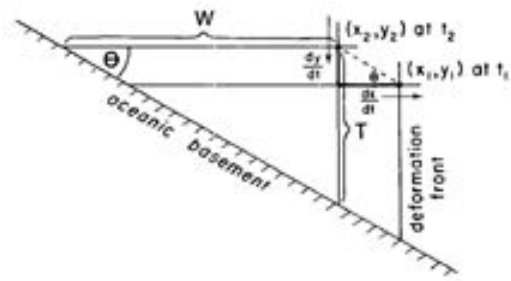


Fig. 1. 14 Left: diagrammatic transverse showing the parameters with controls the sedimentary wedges into the trenches (from Thornburg and Kulm, 1987). Right: sediment budget of accretionary wedges as a function of sedimentary rate (SR) in the trench, convergence rate (CR) and angle dip (B) of the subducting plate. W = width of the trench.  $T_{oc}$  = Thickness of the sediments scraped off from the subduction oceanic plate (in c). In a and b B and CR are constant (from Einsele, 2013).

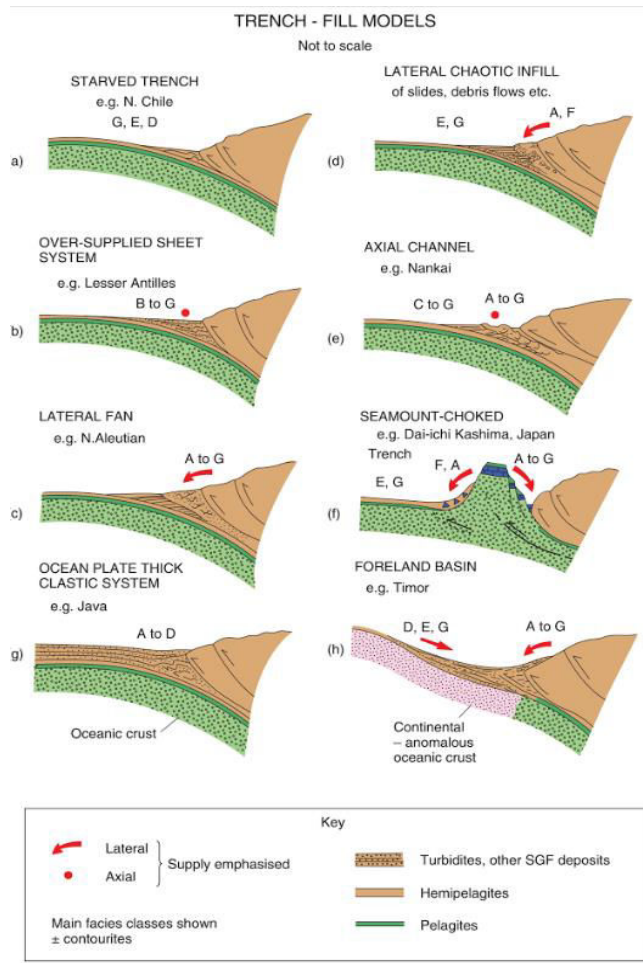
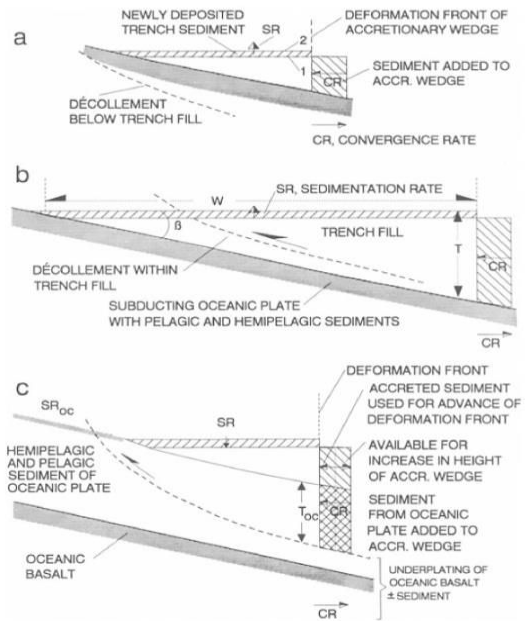


Fig. 1. 15 Trench sedimentary fills models from Pickering and Hiscott (2016).

Based on all these considerations and on definition of several trench sedimentary facies, Pickering and Hiscott (2016) have been proposed tentatively, a classification for the trench fills (Fig.1.15); eight principal type are considered from starved trench until oceanic plate thick clastic system model. The eight types are not mutually exclusive and one trench may contain all the types at different place along the trench.

#### 1.2.4.4 Role of the trench sedimentary infill into the plate interface

Part of the sediments cumulated in the trench is commonly dragged with the downgoing plate beneath the margin to form the so-called subduction channel (Fig. 1.16), a poorly consolidated and fluid-rich layer that is structurally squeezed between upper and lower plates (Shreve and Cloos, 1986). Physical and mechanical properties of subducting material strongly influence the shape and tectonic deformation of the margin (Lallemand et al., 1994). Such deformation processes include frontal accretion, wedge thickening by out-of-sequence thrusting, subduction erosion, and underplating (Cloos and Shreve, 1988). Lallemand et al., (1994) and Clift and Vannucchi (2004) observed that trench fill is a key parameter affecting the subduction erosion of the upper plate. On average, circum-Pacific convergent margins switch from subduction erosion to subduction accretion, with development of an accretionary wedge, when trench fill thickness exceeds ca 1000 m. Decreasing sediment thickness should therefore promote subduction erosion.

The subducting material contains pore-filling fluids in variable amounts depending on the nature and thickness of the underthrust sediment deposit (Cloos and Shreve, 1996). Fluid pressure variations are believed to play a major role in controlling deformation processes and fault dynamics along subduction zone megathrusts (Moore and Saffer, 2001; Sage et al., 2006).

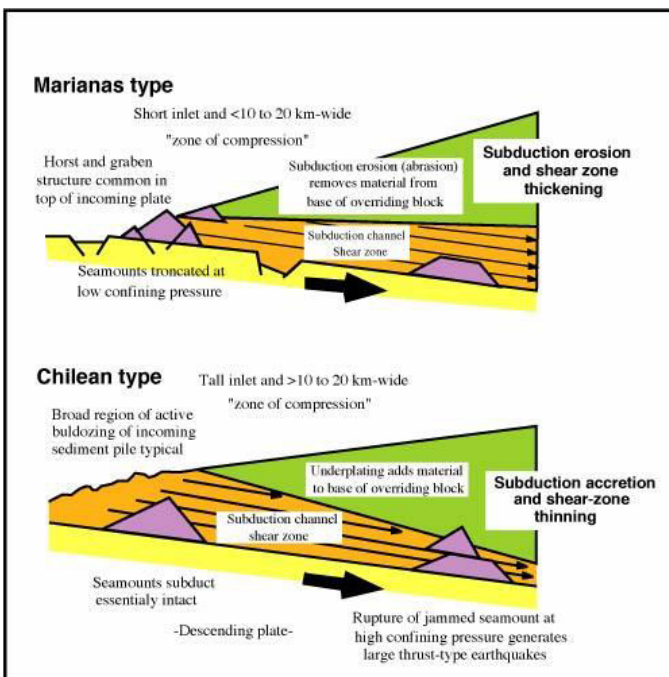


Fig. 1. 16 Model showing a possible interplay between the amount of sediment into the trench, the asperity of the oceanic plate and the generation of great earthquakes (from Cloos and Shreve, 1996). Top: The subduction channel increases in size and the asperities will be blocked near the trench: this imply numerous earthquakes bu of low magnitude. Bottom: The subduction channel decreases in size and the asperities will be blocked further from the trench: this imply few earthquakes but high magnitude (> 7.9) medium (7-7.5)



Some authors consider that the sediments lubricate the interplate contact (Shreve and Cloos 1986) while others think that they increase the coupling (Ruff, 1989). Cloos and Shreve, (1996) have suggested a model where the amount of sediments and the asperities of the oceanic plate interplay and have an important role (Fig. 1.16).

Based on these later considerations, many authors believe that the presence or absence of significant trench sediment fill provides the explanation for lithological or compositional variations in the plate interface on the appropriate length scale (Lamb and Davis, 2003; Oncken et al., 2006). For these authors, higher trenchward sediment flux reduced coupling at the plate interface (Fig. 1.17), resulting in slowed shortening and enhanced slab rollback. And because high sediment flux and transfer of convergence into upper plate shortening constitute a negative feedback, they suggest that interruption of this feedback is critical for sustaining high shortening transfer, as observed for the Andes (Fig. 1.18). As a consequence, the control of the sediment amount into the trench depending of the reliefs along the subduction zone and of the climate end-members models claim that the climate is a major factor controlling the Andes. Taking into account the evolution of the Andes during the last 40 Ma, Oncken et al., (2006) have calculated the expected thickness into the trench (Fig. 1.18) from this assumption that plate interface strength as inverse correlation with the amount of incoming sediment. And they try to correlate the variations of sediment amount with global climate fluctuations.

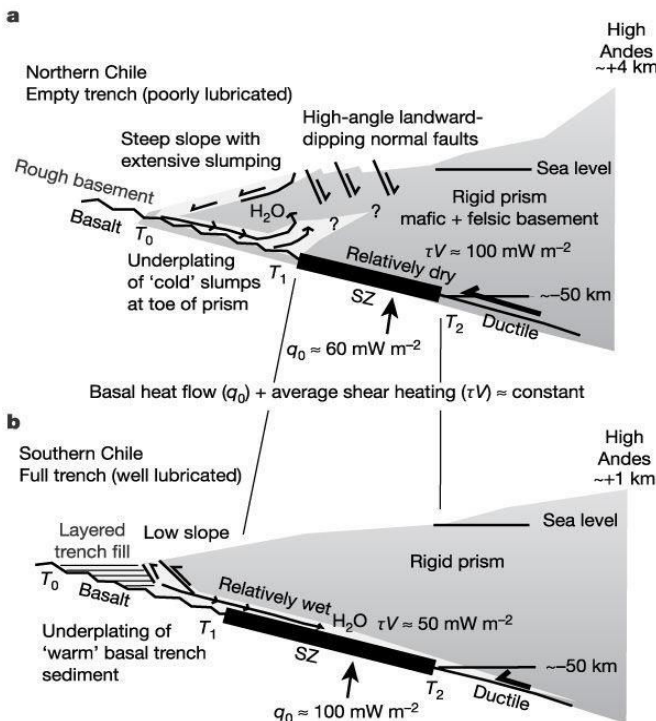


Fig. 1. 17 Diagrams illustrating how the presence or absence of significant trench infill could affect the process of subduction (Lamb and Davies, 2003). In both cases the convergence velocity "V" is about the same. a) extensive undermining of the toe of the sediment-starved trenches, may drag chaotic and coarse debris into the subduction zone, but this probably accumulates and rises near the up-dip edge of the SZ as slumping strips off the overlying prism, helping to cool the plate interface as well as limiting further down-dip movement of the sediment. High-angle landward-dipping normal faults, typical of this type of margin, may be the coastal expression of this. b) trenches full of well-stratified fine-grained sediment may result in "well lubricated" and smooth subduction zones because the wet sediment may form a weak detachment extending far down the plate interface. Blanketing of the oceanic basement by sediment will also help to warm the subducted oceanic basement.

In conclusion, this paragraph shows that the amount and nature of trench sediment is very important in the subduction process. Next, we expose in more details how the sedimentary fill is produced and built in the subduction trenches.

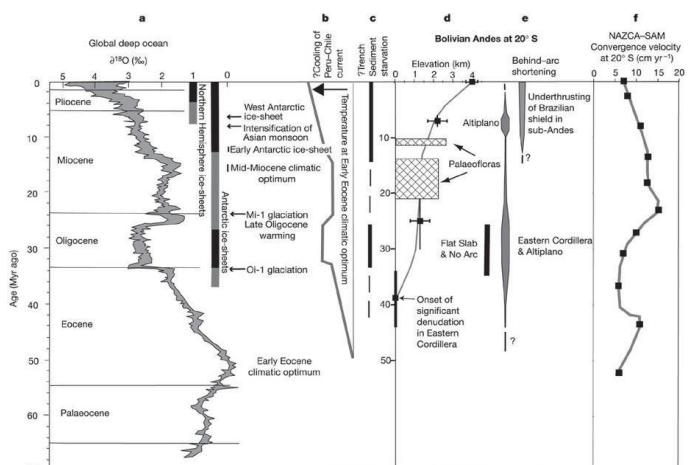
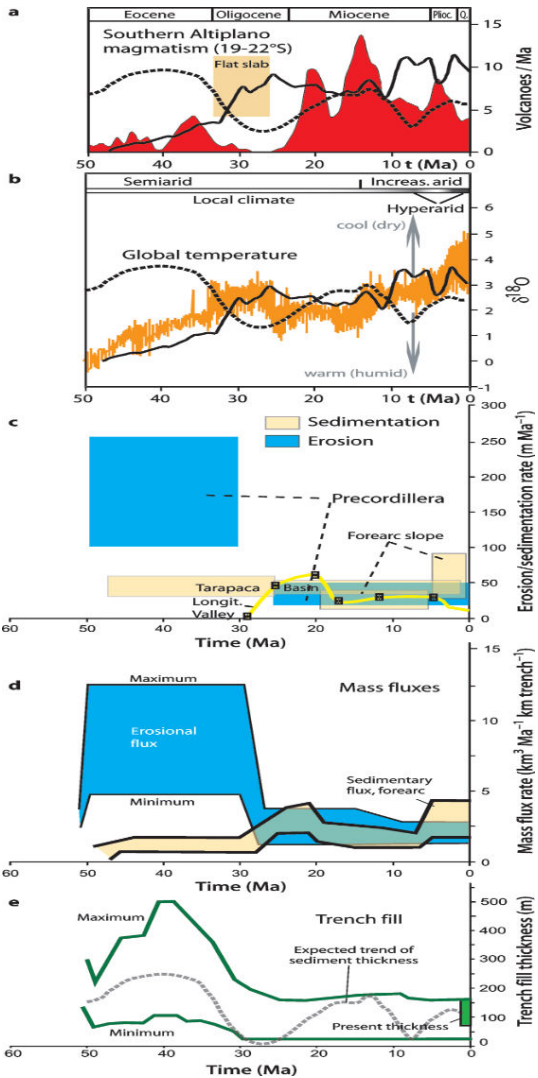


Fig. 1. 18 **Left:** Evolution of different parameters since 50 Ma (from Oncken et al., (2006) along the central Andes. Based on this evolution, the range of expected trench fill thickness is calculated, assuming that plate interface strength shows inverse correlation with the amount of incoming sediment. **Right:** Major global climatic trends, and Andean tectonic evolution at ~20° S (from Lamb and Davis, 2003) Postulated phases of sediment starvation in the Peru–Chile trench (c) along the central Andes during periods of high coastal aridity (a) are broadly in line with mean elevation history of the Altiplano and western margin of the Eastern Cordillera in the Bolivian Andes (based on a self-consistent inversion of estimates from geomorphological data combined with crustal-thickening estimates and their timings from crustal-shortening data)

### 1.3 Processes and products of deep-sea sedimentary deposits

Within an oceanic environment it has been noted that three main groups of processes are capable of eroding, transporting and depositing terrigenous, biogenic, volcanoclastic and other particulate materials (Fig. 1.19): **pelagic settlements, bottom currents and gravity-driven processes**. From them just the first one can generate processes that become dominant only in very remote abyssal areas. On the contrary, all episodic and high-energy density flows are commonly superimposed over or they can interact with relatively permanent flows of bottom currents around many continental margins. There is increasing recognition that contour currents can be a very important factor that transport and control much of deep-sea sedimentation. During the analysis of this processes there is always a certain temptation to simplify the nature of all processes that operate in the deep sea and also try to relate them to resulting deposits. However, the more we learn from measurement and observation, the more the true complexity of processes, from

initiation to deposition, and their relationship to depositional products becomes apparent (Fig. 1.19).

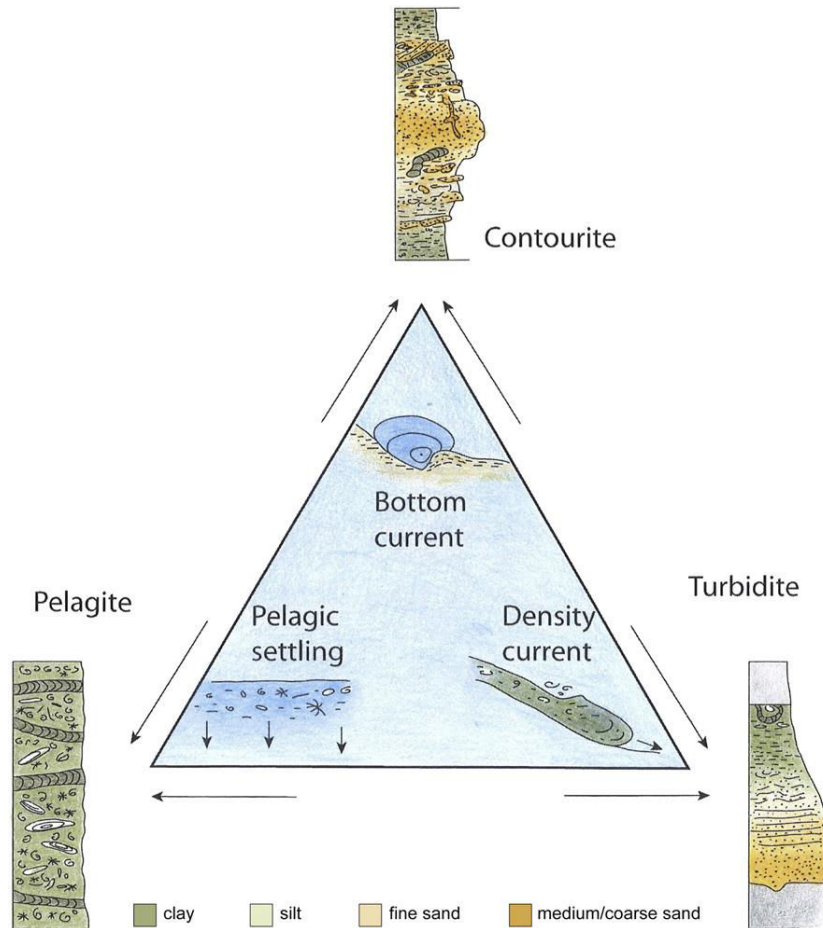


Fig. 1. 19 Ternary diagram showing the three main sedimentary processes that can be found operating in deep sea (inside the triangle) and the facies models corresponding to their respective depositional products (Rebesco, 2014)

### 1.3.1 Pelagic and hemipelagic sedimentation

Pelagic sediments are fine-grained material which accumulate mainly by settling of particles from the overlying water column, far from land, and generally at cumulative rates of a few millimeters to one or two centimeters per thousand years. Hemipelagic sediments are formed in a similar way but along continental margins or shelf settings where there may also be substantial admixtures of terrigenous debris and more rapid sedimentation of pelagic micro-organisms due to higher productivity. Consequently, hemipelagic sedimentation rates are usually much higher, on the order of tens to hundreds of centimeters per thousand years. Because they can form only in areas where they are not diluted by other kinds of sediment, pelagic and hemipelagic sediments commonly are deposited in deep water settings somewhat removed from land areas and shallow shelves.

Pelagic and hemipelagic sediments cover more than half of the earth's surface (pelagic calcareous ooze alone covers about 25% of the planet's surface); volumetrically they are the most abundant type of sediments (Bogs, 2006). Four types of components constitute the bulk of pelagic\hemipelagic sediments: 1) terrigenous detrital particles, 2) biogenic grains, 3) organic matter, and 4) authigenic-diagenetic minerals (Bogs, 2006). The latter two are usually minor constituents and most of the classifications of pelagic\hemipelagic are based on the relative proportions of the first two categories. Other very minor components are volcanic particles and cosmic dust (Nichols, 2009). When the pelagic sediment consists of at least 30% of microfossil shells, either calcareous or siliceous planktonic organisms, the sediment is called "ooze" (Reading, 1996). Based on the composition of the ooze, there are three main types of pelagic sediments: siliceous ooze, calcareous ooze and red clays (Nichols, 2009).

All oozes accumulate extremely slowly at no more than a few centimeters per millennium (Miall, 1997). According to Reading (1996) oozes are commonly strongly bioturbated, but there is no bioturbation when the deposit is completely formed by micro-skeletons. Zoophycos, Planolites and Chondrites are the most common ichnogenera in deep water forming ooze deposits (Bogs, 2006). In deep sea deposits most of the pelagic and hemipelagic deposits are found interbedded with turbidites and other resedimented deposits where they form only a small proportion of the sedimentary materials, and they can be also found associated with contourite drifts; therefore, in many cases it is very difficult to make a distinction between muddy contourites and hemipelagites (e.g. Kidd, Ruddiman et al., 1986). However, there are areas where pelagic and hemipelagic deposits form all, or nearly all, of the sediment column (Nichols, 2009). Thus, it is possible to recognize four different settings in which they dominate: (i) spreading ridges; (ii) aseismic volcanic structures; (iii) ocean basins and abyssal hills; and (iv) continental margins, banks and basins (Bogs, 2006).

### **1.3.2 Ocean bottom currents (contour currents)**

In a general way ocean currents can be divided into 1) surface currents, 2) vertical currents and 3) bottom currents (Rebesco, 2014) Surface currents operate throughout the water column, from the sea surface to a depth of about 4000 m (Shanmugam, 2006). Ocean surface currents are diverted to the right in the Northern hemisphere and to the left in the Southern hemisphere due to the Coriolis Force (Mulder, 2013). Surface currents originated by wind can be considered as an important source of bottom currents. Vertical upwelling currents are caused either by surface waters moving away from each other or by surface water moving offshore (Mulder, 2013). Upwelling along the coast brings cold, nutrient-rich waters to the surface from below. Ocean bottom currents are mainly driven by density differences caused by changes in temperature and salinity. According to Shanmugam (2006) there are three types of deep-water bottom currents: 1) thermohaline-induced geostrophic bottom currents, 2) wind-driven bottom currents, and 3) deep-marine tidal bottom currents.

The formation of ocean bottom currents is one of the results of the oceanic thermohaline circulation, this type of currents flow along the sea floor parallel to, or nearly parallel to, the bathymetric contours of the continental margin and the fine to medium size sediments delivered to the ocean floor are reworked by these bottom currents (Rebesco, 2014). The effects of these currents on the sedimentary deposits are most noticeable in deep waters, since in shallower waters they are masked by the influence of tides, waves and storms (Nichols, 2009). According to literature it has been noted that thermo-haline currents are typically weaker than storm and tidal currents but they transport much more volume, they mainly move clay and silt in suspension and fine sands as bedload (Nichols, 2009).

Shanmugam (2006) makes an interesting comparison of the deposits that can be obtained from bottom currents and turbidity currents. These differences are exposed below as they are appearing in his text:

- *“Bottom currents are driven by thermohaline, wind, or tidal forces, whereas turbidity currents are driven by sediment gravity*
- *Bottom currents may flow parallel to the strike of the regional slope, in circular motions (gyres) unrelated to the slope, and may flow up and down the submarine canyons, whereas turbidity currents always flow downslope*
- *Bottom currents may occur on the shelf, slope, and basinal environments, whereas turbidity currents are more common on the slope and basinal environments*
- *Bottom currents persist for long periods of time and can develop equilibrium conditions, whereas turbidity currents are episodic or surge-type events that fail to develop equilibrium conditions*
- *Bottom currents are free of sediment, and for this reason, they are termed as ‘clear water currents’ (Bouma and Hollister, 1973, p. 82); whereas turbidity currents cannot exist without entrained sediment*
- *Bottom currents show oscillating energy conditions, whereas turbidity currents exhibit waning energy conditions*
- *Bottom currents transport sand primarily by traction (i.e., bed load movement by sliding, rolling, and saltation; Allen, 1984), whereas turbidity currents transport fine-grained sand and mud in suspension*
- *Traction structures (e.g., parallel and ripple laminae and cross beds) are common in bottom-current deposits, whereas normal grading is the norm in turbidites*
- *Bottom-current deposits exhibit sharp upper contacts, whereas turbidites show gradational upper contacts*
- *Bottom currents can result in well-sorted sand with good porosity and permeability because of reworking and winnowing away of mud, whereas turbidity currents do not form well-sorted sand. Turbidites are mud-rich facies”.*

Three clastic contourite facies end-members result from deposition by bottom currents: *muddy contourites, silty contourites and sandy contourites* (Stow et al., 1994) (Fig. 1.20).

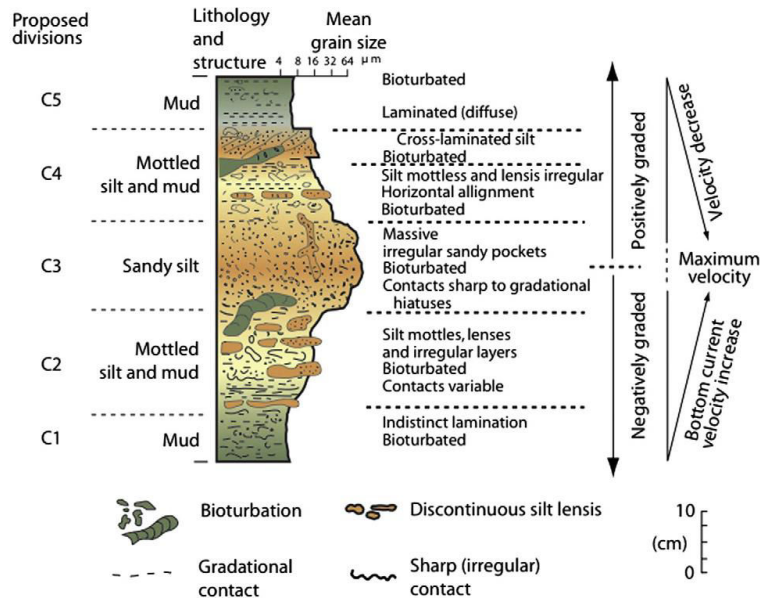


Fig. 1. 20 This diagram shows a combination of muddy, silty and sandy contourites in a negative-positive graded sequence. (from Gonthier, Faugeres and Stow, 1984; Stow, 1994)

### 1.3.3 Gravity-driven processes

Gravity driven processes, such as slides, slumps, debris flows and turbidity currents (Fig. 1.21) are important agents for transporting sediments downslope into deep-marine environments from an original shallow-water setting. All these processes are depending of the down-slope component of gravity which acts upon material stored on or moving down a slope (Reading, 1994). Only rock falls and slides are not considered in this classification. It has been considered that shelf-edge sediment failures are responsible for generating gravity-driven processes, they are triggered initially by one or more of the following external or internal causes such as eustatic changes in sea level, submarine volcanic activity, earthquakes, salt movements in intraslope basins, glacial loading on margins, over steepening of submarine slope near the mouth of rivers, high sedimentation in the delta front setting, tsunamis, storm waves, biologic erosion of submarine canyon walls and generation of gas (Shanmugam, 2006).

It has been noted that most downslope movement of sediments results from general or local decreases, or total loss, of shear strength, as a result the sediment-water mass or some particular layer within it is no longer able to resist the downslope gravitational shear. Such instability is favored by: (i) high slope gradients; (ii) high rates of sedimentation, particularly of fine grained sediment; (iii) repeated cyclical stress, commonly due to seismic shocking but also due to storm and wave action; (iv) high biological productivity and/or bottom water anoxia leading to high organic content in the sediment; which in turn may lead to (v) gas generation due to organic decay and clathrate decomposition.



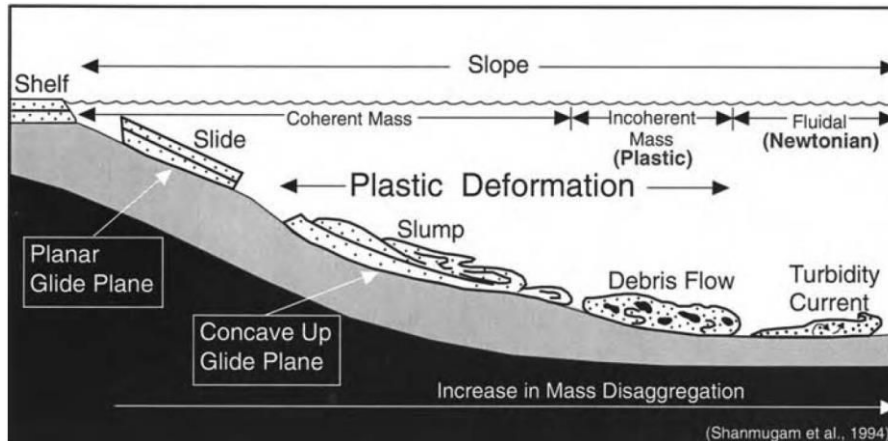


Fig. 1. 21 Diagram showing four most common types of gravity-driven processes that carry sedimentary material to deep-water environments. (Shanmugam et al. 1994)

### 1.3.3.1 Slides

A slide represents a coherent translational mass transport of large blocks or lithified, or partially lithified, strata on a planar glide plane (shear surface) without internal deformation as all the shear is concentrated on basal slip surfaces (Shanmugam, 1994). Submarine slides can travel hundreds of kilometers. They are common in fjords because the submerged sides of glacial valleys are steep and because the rate of sedimentation is high due to sediment-laden rivers that drain glaciers into fjords (Lee et al., 1993).

The term “slide” is used for both a process and a deposit (Shanmugam, 2006). With downslope movement, slide masses may show progressive fragmentation. Slide deposits may make major contributions to the deposits of continental slopes and are characterized by large, often isolated blocks of material, often limestones, in otherwise fine-grained background sediments. Shanmugam (2006) makes a description of general characteristics of slide deposits: 1) they use to range from gravel to mud lithofacies, 2) transported shallow-water blocks encased in deep-water strata (Twenhofel, 1932), 3) primary basal glide plane, 4) they have a basal zone of shearing, 5) there are also secondary internal glide planes, 6) it is possible to find upslope areas with tensional faults, 7) usually they occur on slopes of 1-4° (Booth et al., 1993), 8) frequently there is transformation of slides into debris flows in frontal zone, 9) associated clastic injections, 10) usually they have sheet-like geometry, 11) large-scale slides may be recognized in high resolution seismic profiles of modern systems, finally 12) they are common in areas of tectonic activity, earthquakes, steep gradients, salt movements and rapid sedimentation.

### 1.3.3.2 Slumps

A slump is a coherent mass of sediment that moves on a concave-up glide plane and undergoes rotational movements causing internal deformation (Shanmugam, 2006) (Fig. 1.21). They share many of the features of the slides and are gradational with them. In

practice, distinguishing slides from slumps can be difficult (Shanmugam, 2006). The term “slump” is used for both a process and a deposit. They may occur on very low-gradient slopes, especially where sedimentation rates of fine-grained sediment are high (Reading et al, 1996). Shanmugam (2006) mention some general characteristics of slump deposits: 1) they range from gravel to mud lithofacies, 2) they have a basal zone of shearing (Fig. 1.22a), 3) it is possible to find upslope areas with tensional faults (Fig. 1.22a), 4) it is also possible to see downslope edges with compressional folding or thrusting (Fig. 1.22a), 5) there are slump folds overlain by undeformed strata at outcrop scale, 6) contorted layers interbedded with uncontorted layers at core scale (Fig. 1.22b), 7) upper contact used to be irregular, 8) it is possible to find chaotic layers in heterolithic facies steeply dipping and truncated layers, associated sand injections and lenticular to sheet-like geometry with irregular thickness, and 9) this kind of modern slumps can be recognized as chaotic facies in high-resolution seismic profiles (Fig. 1.23).

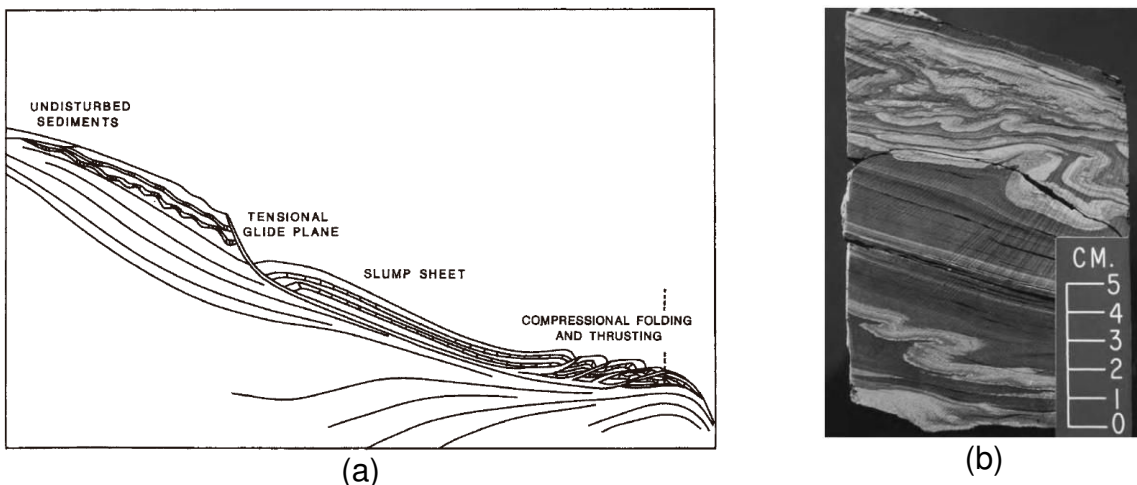
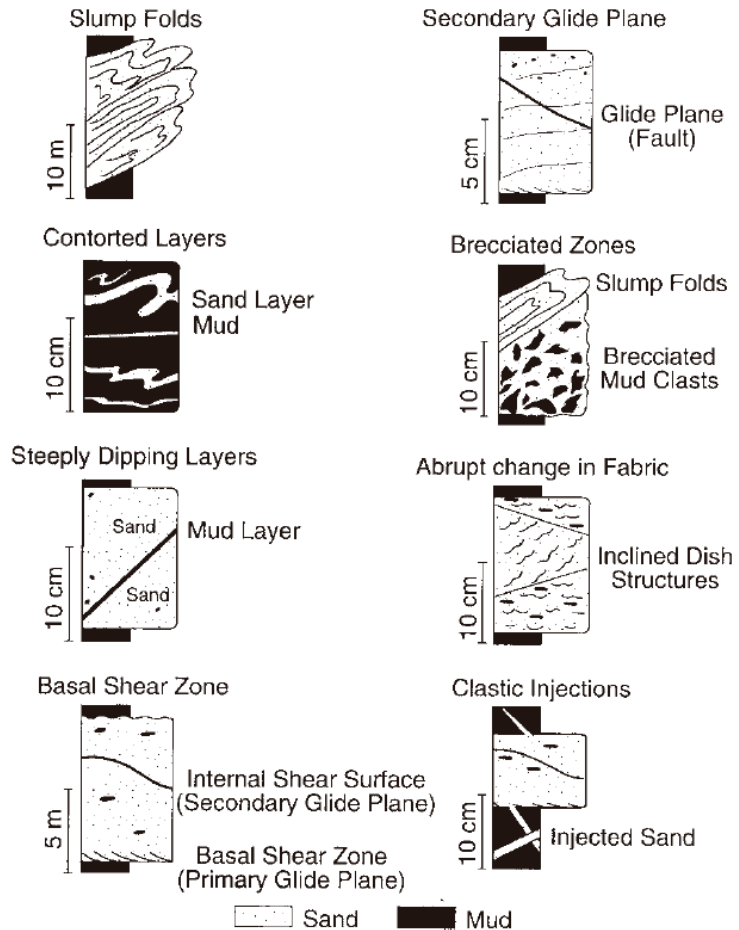


Fig. 1. 22 (a) Diagram of a modern slump showing tensional glide plane in the upslope detachment area and compressional folding and thrusting in the downdip frontal zone (after Lewis, 1971; taken from Shanmugam, 2006), (b) Core photograph showing alternation of contorted and uncontorted siltstone (light color) and claystone (dark color) layers of slump origin. Paleocene, North Sea (Shanmugam, 2006)



Fig. 1. 23 Fig. 1.23 Summary of features associated with slump deposits observed in cores (Shanmugam, 2006)



### 1.3.3.3 Debris Flow deposits

Debris flow deposits are plastic flows in which sediment and water are fully mixed and where any original bedding and lamination has been destroyed (Reading, 2009). It has been noted that unlike a debris flow on land, an underwater flow has the opportunity to deeply mix with water and in doing so it becomes much more dilute and this can lead to a change in the flow mechanism and finally to a transition into a turbidity current. The top layers of a deep-sea debris flow deposit will typically grade up into finer deposits mainly due to dilution of the upper part of the flow. Large debris flows of material are known from the Atlantic off northwest Africa (Masson et al. 1996) and examples of thick, extensive debris-flow deposits are also known from the stratigraphic record (Johnson, 1984). Great debris-flow deposits with tens of metres thick and extending for tens of kilometres can be referred to as megabeds.

### 1.3.3.4 Homogenites

Homogenites are homogeneous mud beds with a thickness ranging from several centimetres to several metres (Mulder, 2011) (Fig. 1.24). There is no presence of bioturbation (Mulder, 2011). The base of this kind of deposits shows an erosive to sharp contact with normally graded base composed of sand to sandy silt (Cita et al., 1984). On

seismic profiles, they use to appears as an acoustically transparent facies (Chapron, 1999). On field outcrops, the massive beds show rare sedimentary structures including hummocky cross-stratification like structures interpreted as antidune deposits (Mulder et al., 2009b; Prave & Duke, 1990).

Homogenites have been interpreted as the result of erosion and liquefaction of a superficial sedimentary bed after the passage of a tsunami wave (Cita et al., 1996). Megabeds deposited consecutively to the Santorini eruption in Cretan Basin (South Aegean Sea; Anastasakis, 2006) lead to the interpretation of similar beds as the distal part of megaturbidites (Mulder, 2011). A similar interpretation with the addition of ponding in the restricted Flysch Basque Basin is provided by Mulder et al. (2009b) for the North Pyrenean Megaturbidite (SW France). In a restricted basin, the sediment is put into suspension by oscillation of the whole water column by the ponding of turbidity currents (internal seiche) (Mulder, 2011). The main difference between homogenites and fine-grained turbidites is usually the thickness of the deposits, in particular, the fine ungraded upper part (Mulder, 2011). McCave and Jones (1988) suggested that deposition could occur by freezing in these thick dense mud suspensions by suppression of the turbulence.

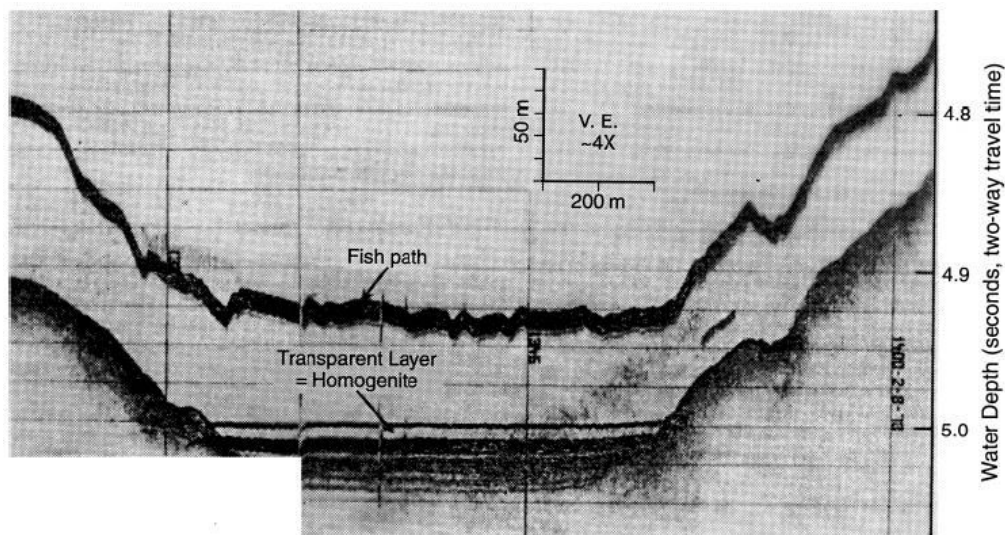


Fig. 1. 24 Fig. 1.24 Near-bottom 4 kHz seismic-reflection profile showing a homogenite layer (acoustically transparent interval) within and on a basin floor in the surroundings of the island of Thera, in the southern Aegean Sea, Greece. (Kastens and Cita, 1981)

### 1.3.3.5 Mass-Transport Deposits

Most of the mass-transport deposits (MTDs) correspond to debris avalanches with a volume varying from a few cubic metres to thousands of cubic kilometres (Mulder, 2011). For example, in the Mississippi turbidite system, where they have been defined, they represent 10-20% of the stratigraphic sequences (Weimer, 1989, 1990). In the Nile turbidite system, the thicknesses of the MTDs vary between 55 and 425 m, suggesting that the base of the transported material involves consolidated sediments or rocks. In the

Amazon turbidite system, two major MTDs have been identified with a probable simultaneous triggering (Western and Eastern MTDs: Piper et al., 1997). The volume of the western MTD is close to 2000 km<sup>3</sup>, and its thickness varies between 100 and 200 m (Damuth and Embley, 1981; Piper et al., 1997). The volume of the eastern MTD is close to 1500 km<sup>3</sup> (Piper et al., 1997). MTDs are usually associated with spoon-shaped failure scars (slump scars) and limited by frontal and side scarps; they lie over a basal scour (Frey-Martinez et al., 2005; Gee et al., 2005; 2006). The seismic facies of MTDs is usually chaotic and/or discontinuous with low amplitude (Collot et al., 2001; Garziglia et al., 2008). Most of MTDs move over a short distance (a few metres to a few kilometres) with exceptions for the largest ones, which can move over hundreds of kilometres (Mulder, 2011).

The initiation of MTDs is still under debate and depends on their position in the stratigraphic column (Mulder, 2011). If they are more frequent and larger during sea-level fall and low stand than during sea-level rise (Rouillard, 2010), they could be related to a combination of processes including over steepening, overloading (intensified by high sedimentation and progradation rates during pluvial phases) and earthquakes (Mulder, 2011). The role of upward moving fluids can also be very important, particularly the global destabilization of gas hydrates (Mulder, 2011). As an example, fluid-escape structures, including gas chimneys, mud volcanoes (Sharp and Samuel, 2004) and free gas, were evidenced close to the source of the MTDs in the Nile system (Bayon et al., 2009; Dupre´ et al., 2007; Huguen et al., 2009) and in the source area of Storegga (Mienert et al., 2005). Whatever their origin is, MTDs completely reshape the morphology of deep-sea turbidite systems and they are very good stratigraphic markers (Mulder, 2011).

### **1.3.3.6 Turbidites**

Turbidites are sea-bottom deposits formed by massive slope failures (USGS, 2018). When a river carrying sediment flows into the ocean it deposits these sediments on the continental shelf and slope. These slopes can fail due to the weight of the excessive sedimentation load and sometimes earthquake shaking, sending all the sediments sliding down to the ocean bottom to create a turbidite. These turbidity currents can carry variable amounts of mud, sand and gravel tens, hundreds and even over a thousand kilometres out onto the basin plain. The turbidites deposited can range in thickness from a few millimetres to tens of metres (Bogs, 2006). When the turbidite composition becomes denser it results in high-density turbidites that have different characteristics respect to the 'Bouma Sequences' seen in low and medium density turbidites (Fig. 1.25). Direct observation of turbidity currents on the ocean floor is very difficult but their effects have been monitored on a small number of occasions (Reading, 1994).

On passive margins and in back-arc basins, the deposits of these flows spread out from the mouths of the canyons onto the deep seafloor to form deep-sea fans, and they contribute in part to building of the continental rise. In the fore-arc region of active margins, submarine canyons discharge turbidites into fore-arc basins on the slope or into deep-sea trenches where they may spread out along the canyon axis. Turbidites may occur in the lower reaches of submarine canyons and farther seaward in deep-sea channels, but

most are deposited in broad, cone-shaped fans (Shanmugam, 2000). These turbidite fans, or submarine fans, spread outward on the seafloor from the mouths of canyons (Stow, 1996). Where submarine canyons are closely spaced along the slope, the fans at the base of the slope may coalesce to build a broad, gently sloping continental rise (Shanmugam, 2006).

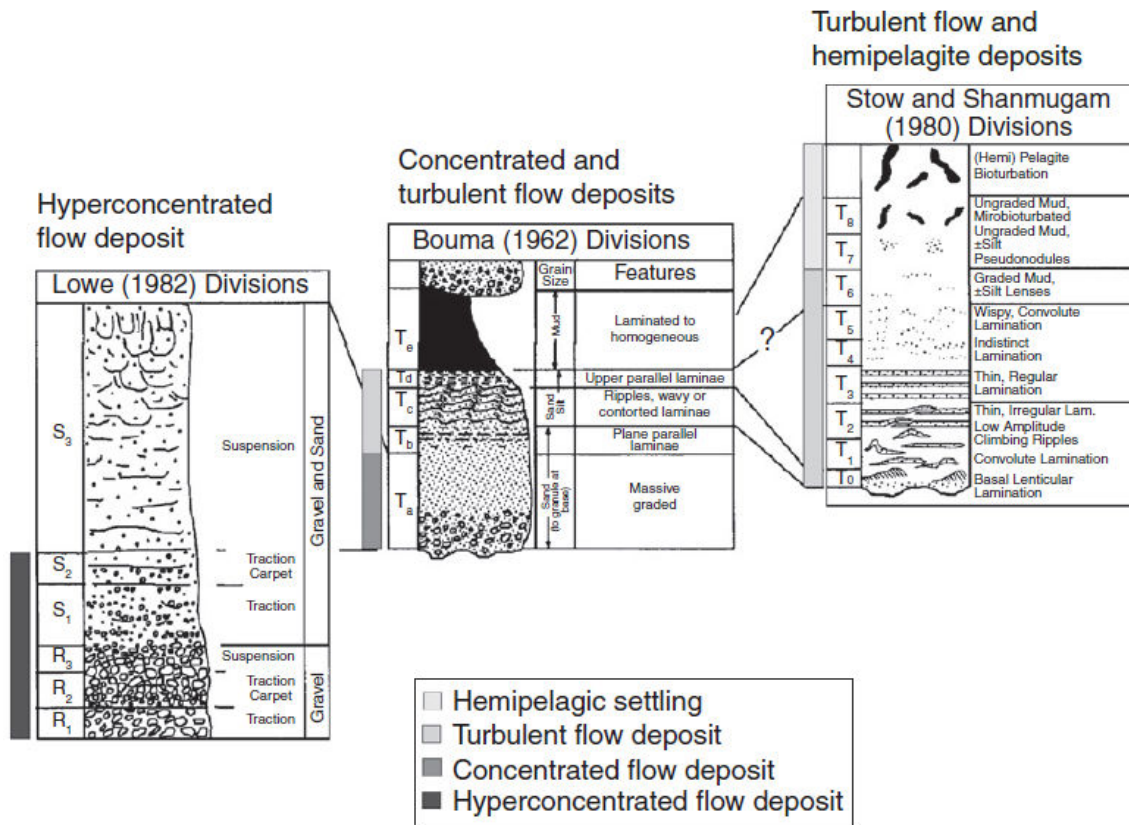


Fig. 1. 25 Diagram showing the continuity of deposits from a hyperconcentrated flow represented by the base of Lowe sequence (Lowe, 1982), a concentrated flow represented by the transition from the top of Lowe sequence to T<sub>a</sub> interval of Bouma sequence (Bouma, 1962) and finally a turbulent flow (turbidite) represented by the transition from T<sub>b</sub>-e intervals of Bouma sequence to Stow and Shanmugam sequence (Stow and Shanmugam, 1980), equivalence with terminology of Mulder and Alexander (2001a). Figure taken from Mulder, 2011 which is a modification from Shanmugam, 2000

On active margins where a trench is present, turbidites commonly occur on the trench floor throughout the length of the trench owing to deposition from turbidity currents flowing longitudinally through the trench. Most turbidites are composed of sands, silty sands or gravelly sands interbedded with pelagic clays. They are commonly characterized by normal size grading and may or may not display complete Bouma sequences. Many turbidites lack either the basal (A unit) or upper (D unit) part of the Bouma sequence, or both (Stow, 1996). Sole markings, such as flute clasts, groove clasts and load clasts are common on the base of many turbidite sequences (Bogs, 2006). In addition to sandy turbidites, mud turbidites occur in many parts of the modern ocean floor (Shanmugam, 2006). These turbidites are composed of normally graded silt and clay that may be either

laminated or massive and that commonly lack extensive bioturbation (Stow, 1996). Turbidites are widely distributed in the modern oceans on passive margins and in both the back-arc and the fore-arc regions of active margins. (Shanmugam, 2006)

## **1.4 Triggering Mechanisms**

Submarine landslides are triggered either by an increase in the driving stresses, a decrease in strength, or a combination of the two (Lee et al., 2007). The following possible triggers show the interplay of these factors. It has been noted that the relative importance of each of these triggers is not well understood. For example, in some environments one, or maybe more, of these triggers will dominate, whereas in others a different trigger will be most significant depending on their geological, structural or sedimentary characteristics (Lee et al., 2007).

### **1.4.1 Sediment Accumulation**

The rapid accumulation of sediments has a great influence to the failure of the slope-edge in many ways. When the sedimentation rate is high sediments accumulate fast and in large quantities, most of the weight of this new added material is due to the water inside pores of the sediments. Because of the progressive increase in the weight of the upper layers some water will be squeezed out even if the consolidation of these materials is low. However, it is clear that the shear stress that will act downslope increases more rapidly and eventually will cause the failure of the accumulated sediment.

### **1.4.2 Erosion**

Erosional processes, especially those very localized, due to water motion or sediment flows are quite common in those areas suitable for transporting clastic materials such as deep-sea channels, submarine canyons, gullies and other sediment transport systems. When the seafloor is cut by a sediment flow this produce a decreasing in the stability due to the increasing of shear stress and sometimes by decreasing the shear strength. There are many cases when these sedimentary flows obstruct the canyons and as a result the subsequent sedimentary flows are diverted, leading to further erosion and construction of second generation landslides. (Greene et al., 2002).

### **1.4.3 Earthquakes**

Very frequently earthquakes are considered as a cause for many unexplained submarine landslide features (Lee & Edwards, 1986; Hampton et al., 1996). One probably reason is that, under water, earthquake-induced shear stresses are quite large relative to shear strength (Lee et al., 2007). The shear stress produced by the earthquake is high because it has to accelerate all the sedimentary materials and that include the porous water inside the beds. The shear strength uses to be relatively low because it builds up proportionally to the submerged unit weight of the sedimentary material and may be even lower if there are excess pore pressures (Lee et al., 2007). Under water the ratio of driving stress to resisting strength is high comparing to what is usually found on land for the same event

(Lee et al., 2007). This phenomenon is due to, over the land, the water table is seldom at the surface in a continuous way, in that case the strength builds up with the total weight of sedimentary material above the water table (i.e. without presence of interstitial water or negligible). Earthquakes can also generate an excess in the pore pressures through an increasing in the weight due to an increase in the sedimentary load, which can decrease the strength much more and possibly induce a state of liquefaction. Landslides triggered by earthquakes, the resulting turbidity currents, and the turbidites generated by these events have been used to date major subduction-zone earthquakes in Cascadia for example (Goldfinger et al., 2003).

#### **1.4.4 Volcanoes**

The presence of enormous submarine landslides around the Hawaiian Islands has been debated for at least 50 yr (Normark et al., 1993). By the use of limited bathymetry data, Moore (1964) interpreted irregular blocky ridges extending downslope from large scars on the submarine north flanks of Molokai and Oahu as representing giant landslides. The origin of these deposits was confirmed when complete GLORIA sidescan-sonar data were acquired in the 1980s (Moore et al., 1989). In fact, the GLORIA surveys showed that the Hawaiian Islands were surrounded by many giant submarine landslides (Moore et al., 1989). Subsequent work (Holcombe & Searle, 1991) has shown that the Hawaiian Islands are not the only cases, and that most of the oceanic volcanoes fail catastrophically at certain moments of their existence. It has been noted that some components acting during oceanic volcanism are clearly a trigger for submarine landslides, but the origin and nature of that components has not been determined. Most of the larger, older landslides seem to have occurred late in the shield-building phase of the host volcano (Moore et al., 1989).

#### **1.4.5 Waves**

Slope failure can be also generated by storm waves. Storm wave induced failure involves several elements (Lee et al., 2007). The passage of a strong wave train subjects the seabed to alternating water pressure as the crests and troughs pass (Henkel, 1970). This non-uniform pressure field induces the greatest shear stresses between crest and trough. Henkel (1970) considered the situation to be one of a simple moment resulting from alternating zones of positive and negative pressure. Induced shear stresses may vary depending on the characteristics of the waves, the water depth and the depth below the seafloor (Lee et al., 2007). These shear stresses are very similar to earthquake loads in the fact that they add to pre-existing downslope gravitational stresses and they are cyclic in nature; therefore, they gradually induce increasing pore-water pressures in the sedimentary material (Lee et al., 2007). The sediment can fail after the passage of a wave train, or it can liquefy and flow if the pore pressures reach a high enough value (Van Kessel & Kranenburg, 1998).

#### **1.4.6 Gas and Gas Hydrates**

Gas charging of sediment is not so much a trigger, but a means by which shear strength may be altered (Lee et al., 2007). Presence of gas can affect sediment strength either by decreasing it through the development of excess pore pressures, or potentially increasing it by reducing the impact of cyclic loads (Lee et al., 2007). normally in cases where gas load reduces layers strength, the actual trigger causing failure is likely to be some other factor such as an earthquake (Hornbach, 2015). Dissociation of gas hydrates can be considered as a trigger because it results from environmental changes (Hornbach, 2015). Sea-level fall can also be considered as a means for generating landslides through destabilization at the base of the gas-hydrate zone (Lee et al., 2007).

#### **1.4.7 Groundwater seepage**

Sangrey (1977) speculated, based on his experience and previous works, that under consolidation and excess pore pressures, artesian reservoir sources are 'very common offshore and may be the most significant mechanism' for causing slope failure. Orange & Breen (1992) suggested that pore fluids percolating up from subducted sediment could induce slope failure and lead to the development of submarine canyons that are not linked to incised valleys on the shelf. Many others (Saffer & Bekins, 1999) have developed models trying to explain how the subducted fluids and the resulting excess pore pressures can influence the mechanics of subduction zones. Groundwater seepage from coastal aquifers also could serve as a trigger for landslides (Lee et al., 2007). Based on an examination of morphology, Robb (1984) suggested that erosion of sediment and rock by underwater springs may have occurred on the lower continental slope off New Jersey during periods of lowered sea level.

#### **1.4.8 Diapirism**

Tectonic activity always tends to alter the landscape, hence any tectonic or diapiric deformation of the marine terrain that results in steepened seabed surfaces will lead to a reduction in the stability and increased likelihood of slope failure. . Therefore, this element becomes one of a number of factors that ultimately determine whether or not a slope will fail (Lee et al., 2007). an area where diapiric deformation constitutes one of the major causes of failure on the continental slope is the northern Gulf of Mexico (Bouma, 1985). In their article of 1982 Martin & Bouma noted that large diapiric and non-diapiric masses of Jurassic salt and Tertiary shale underlie the northern Gulf of Mexico continental slope and adjacent outer continental shelf. According to their results all these masses show evidence of being structurally active at present and also in the very recent geological past. The vertical growth of these tectonic structures has causes local steepening of the seafloor and causes the creation of many knolls and ridges interspersed by topographic depressions and canyon systems (Jakob et al., 2005). Large overburden pressures that have been created by sediment accumulation from the late Jurassic to the present have caused the underlying salt sheet to flow and outcrop to the surface (Jakob et al., 2005). The movement of the salt sheet, or "halokinesis", is largely considered responsible for the surface morphology (Silva et al., 2004).

### 1.4.9 Human Activities

All the facilities developed by humans along the shoreline have the quite potential of causing submarine slope failures, especially those set on the seabed. Typically, these facilities increase the downslope stresses (Lee et al., 2007). This a subject intensely debated because the generation of landslide influenced by human activities has provoked damages, injuries and even death. Usually the most debated question tries to define whether a natural slope failure affected the human activities or whether the human activities caused the slope to fail (Lee et al., 2007). But there are cases where the role of human activities has been the main influence in the slope failure, such is the case of the quick-clay failure in Rissa, Norway, during 1978. The slope failure, and its subsequent landslide, occurred when 700 m<sup>3</sup> of earth fill was placed by the shore of Lake Bottnen to expand the area of a local farm. The fill had just been finished when 90 m of shore slid into the lake. . The slide then started to develop retrogressively with each new slide fully liquefying and flowing into the lake. After about 40 min, a very large slide removed an area of about 150 m × 200 m. The sliding took only about 5 min. A house was seen moving down the 'quick clay river' at 30–40 km/h (Gregersen, 1981).



## References

- Aleshire, P., 2007. Ocean ridges and trenches. New York. ISBN-10: 0-8160-5919-5
- Allen J.R.L. (1991) The Bouma Division A and the possible duration of turbidity currents. *J. sedim. Petrol.*, 61, 291-295.
- Anastasakis, G., 2006. The anatomy and provenance of thick volcanoclastic flows in the Cretan Basin, South Aegean Sea. *Mar. Geol.* 240, 113–135.
- Asquith S.M. (1979) Nature and origin of the lower continental rise hills, off the east coast of the United States. *Mar. Geol.*, 32, 165-190.
- Aubouin, J., Von Huene, R., Baltuck, M., Arnott, R., Bourgois, J., Filewicz, M., Kvenvolden, K., Leinert, B., McDougall, K., Ogawa, Y., Taylor, E. and Winsborough, B., 1982. Leg 84 of the Deep Sea Drilling Project. Subduction without accretion: Middle America Trench off Guatemala. *Nature*, 297:458-460.
- Aubouin, J., Bourgois, J. and Azema, J., 1984. A new type of active margin: the convergent-extensional margin as exemplified by the Middle America Trench off Guatemala. *Earth Planet. Sci. Lett.*, 87:111-126.
- Bagnold R.A. (1954) Experiments on a gravity-free dispersion of large solid spheres in a Newtonian fluid under shear. *Proc. R. Soc. Lond. Ser. A*, 225, 49-63.
- Bagnold R.A. (1962) Auto-suspension of transported sediment: turbidity currents. *Proc. R. Soc. Lond. Ser. A*, 265, 315-319.
- Bayon, G., Loncke, L., Dupre´, S., Caprais, J.-C., Ducassou, E., Duperron, S., et al., (2009). Multi-disciplinary investigation of fluid seepage on an unstable margin: the case of the Central Nile deep sea fan. *Mar. Geol.* 261 (1–4), 92–104.
- Bird, P., 2003. An updated digital model of plate boundaries, *Geochemistry Geophysics Geosystems*, 4(3), 1027, doi:10.1029/2001GC000252.
- Bogs, S., (2006). Principles of Sedimentology and Stratigraphy, fourth edition. Prentice Hall. ISBN 0-13-154728-3.
- Booth, J.S., O’Leary, D.W., Popenoe, P., Danforth, W.W., (1993). U.S. Atlantic continental slope landslides: Their distribution, general attributes, and implications. In: Schwab, W.C., Lee, H.J., Twichell, D.C. (Eds.), *Submarine Landslides: Selected Studies in the U.S. Exclusive Economic Zone*, U.S. Geological Survey Bulletin 2002, pp. 14–22.
- Bouma A.H. (1962) Sedimentology of Some Flysch Deposits: A Graphic Approach to Facies Interpretation, 168 pp. Elsevier, Amsterdam.

Bouma A.H., Normark W.R. & Barnes N.E. (Eds) (1985) *Submarine Fans and Related Turbidite Systems*, 351 pp. Springer-Verlag, New York.

Bourgeois, J., Azema, J., Baumgartner, P., Tournon, J., Desmet, A., Aubouin, J., 1984. The geologic history of the Caribbean-Cocos plate boundary with special reference to the Nicoya ophiolite complex (Costa Rica) and D.S.D.P. results (Legs 67 and 84 off Guatemala): a synthesis. *Tectonophysics*, 108: 1-32.

Bourgeois, J., 1993, La fosse d'Amérique Centrale, convergence, accretion, érosion tectonique Article in *Comptes rendus de l'Académie des sciences. La vie des sciences* · January 1993

Bourgeois, J., Lagabrielle, Y., De Wever, P., & Suess, E. (1993). Tectonic history of the northern Peru convergent margin during the past 400 ka. *Geology*, 21(6), 531-534.

Bromley R.G. & Ekdale A.A. (1987) Mass transport in European Cretaceous chalk: fabric criteria for its recognition. *Sedimentology*, 34,1079-1092.

Burk, C. A. and Drake, C. L., (1974). *The Geology of Continental Margins* (1009 p.). Springer, Berlin, Heidelberg.

Camerlenghi, A., Crise, A., Accerboni, E., Laterza, R., Pudsey, C.J., Rebesco, M., 1997b. Tenmonth observation of the bottom current regime across a sediment drift of the Pacific margin of the Antarctic Peninsula. *Antarctic Science* 9, 424–431.

Ceramicola, S., Rebesco, M., De Batist, M., Khlystov, O., 2001. Seismic evidence of smallscale lacustrine drifts in Lake Baikal (Russia). *Marine Geophysical Research* 22, 445–464.

Chan M.A. & Dort R.H. Jr (1983) Shelf and deep-sea sedimentation in Eocene forearc basin, western Oregon - fan or non-fan? *Bull. Am. Ass. petrol. Geol.*, 67, 2100-2116.

Chapron, E., 1999. Contrôle climatique et sismo-tectonique de la sédimentation lacustre dans l'Avant-Pays Alpin (Lac du Bourget, Le man) durant le Quaternaire récent. *Géologie Alpine. Mémoire Hors-Série no. 30*, 265pp.

Christiansen, E. H., & Hamblin, W. K. (2009). *Earth's Dynamic Systems Web*.

Cita M.B., Camerlenghi A., Kastens K.A. & McCoy EW. (1984) New findings of Bronze Age homogenites in the Ionian Sea: geodynamic implications for the Mediterranean. *Mar. Geol.*, 55, 47-62.

Cita, M.B., Beghi, C., Carmelenghi, A., Kastens, K.A., McKoy, F.W., Nosetto, A., et al., 1984. Turbidites and megaturbidites from the Herodotus Abyssal Plain (Eastern Mediterranean) unrelated to seismic events. *Mar. Geol.* 55, 79–101.

Cita, M.B., Carmelenghi, A., Rimoldi, B., 1996. Deep-sea tsunami deposits in the eastern Mediterranean: new evidence and depositional model. *Sediment. Geol.* 104, 155–173.

Clift, P. and Vannucchi, P., 2004. Controls on tectonic accretion versus erosion in subduction zones: Implications for the origin and recycling of the continental crust. *Reviews of Geophysics*, 42(2)

Clift, P. D., Schouten, H., and Vannucchi, P., 2009. Arc-continent collisions, sediment recycling and the maintenance of the continental crust. Geological Society, London, Special Publications, 318(1), 75-103.

Cloos, M., & Shreve, R. L. (1996). Shear-zone thickness and the seismicity of Chilean- and Marianas-type subduction zones. *Geology*, 24(2), 107-110.

Collot, J.-Y., Lewis, K., Lamarche, G., Lallemand, S., 2001. The giant Ruatoria debris avalanche on the northern Hikurangi margin, New Zealand: result of oblique seamount subduction. *J. Geophys. Res.* 106 (9), 19271–19297.

Coniglio M. & James N.P. (1990) Origin of fine-grained carbonate and siliciclastic sediments in an Early Palaeozoic slope sequence, Cow Head Group, western Newfoundland. *Sedimentology*, 37, 215-230.

Coste, M., 2014, Les processus sédimentaires, depuis la pente continentale jusqu'au bassin, en contexte de tectonique active : analyse comparée entre la Marge Calabro-lonienne et la Marge Ligure durant les derniers 5 Ma, Thèse Université de Nice.

Damuth, J.E., Embley, R.W., 1981. Mass-transport processes on the Amazon Cone: *Amer. Assoc. Petrol. Geol. Bull.* 65, 629–643.

Dingle, R.V., 1977. The anatomy of a large submarine slump on a sheared continental margin (SE Africa). *Journal of Geological Society of London*, 134, 293–310.

Ducassou, E., Migeon, S., Capotondi, L., Mascle, J., 2010. Les coulées de débris dans un système turbiditique profond. Environnement de dépôt, origine et mise en place. 23<sup>e</sup>me Réunion des Sciences de la Terre, Bordeaux, October 25-29th, Abstract Book, p. 103.

Dupré, S., Woodside, J., Foucher, J.-P., de Lange, G., Mascle, J., Boetius, A., et al., (2007). Seafloor geological studies above active gas chimneys off Egypt (Central Nile Deep Sea Fan). *Deep Sea Res.* 1 54 (7), 1146–1172.

Edwards D.A., Leeder M.R., Best J.L. & Pantin H.M. (1994) On experimental reflected density currents and the interpretation of certain turbidites. *Sedimentology*, 41, 437-461.

Einsele, G. (2013). *Sedimentary basins: evolution, facies, and sediment budget*. Springer Science & Business Media.

Embley R.W., Hooje P.J., Lonsdale P., Mayer L. & Tucholke B.E. (1980) Furrowed mud-waves on the western Bermuda rise. *Bull. geol. Soc. Am.*, 91, 731-740.

Faugeres J.C., Mezeraï M.L. & Stow D.A.V. (1993) Contourite drift types and their distribution in the North and South Atlantic Ocean basins. In: *Contourites and Bottom Currents* (Ed. by D.A.V. Stow and J.-C Faugeres), pp. 189-203. *Sedim. Geol.*, 82.

Faugeres J.C. & Stow D.A.V. (1993) Bottom-current-controlled sedimentation: a synthesis of the contourite problem. *Sedim. Geol.*, 82, 287-297.

Feldhausen P.H., Stanley D.J., Knight R.J. & Maldonado A. (1981) Homogenization of gravity-emplaced muds and unites: models from the Hellenic Trench. In: *Sedimentary Basins of Mediterranean Margins* (Ed. by F.C. Wezel), pp. 203-226. CNR Italian Project of Oceanography, Tecnoprint, Bologna.

Flood R.D. & Shor A.N. (1988) Mud waves in the Argentine Basin and their relationship to regional bottom circulation patterns. *Deep Sea Res.*, 35, 943-971.

Frey-Martinez, J., Cartwright, J., Hall, B., 2005. 3D seismic interpretation of slump complexes: examples from the continental margin of Israel. *Basin Res.* 17, 83–108.

Garziglia, S., Migeon, S., Ducassou, E., Loncke, L., Mascle, J., (2008). Mass-transport deposits on the Rosetta province (NW Nile deep-sea turbidite system, Egyptian margin): characteristics, distribution, and potential causal processes. *Mar. Geol.* 250 (3–4), 180–198.

Gee, M.J.R., Gawthorpe, R.L., Friedmann, J.S., 2005. Giant striations at the base of a submarine landslide. *Mar. Geol.* 214, 287–294.

Gee, M.J.R., Gawthorpe, R.L., Friedmann, J.S., 2006. Triggering and evolution of a giant submarine landslide, offshore Angola, revealed by 3D seismic stratigraphy and geomorphology. *J. Sediment. Res.* 76, 9–19.

Geersen, J., Völker, D., Behrmann, J. H., Reichert, C., & Krastel, S. (2011). Pleistocene giant slope failures offshore Arauco peninsula, southern Chile. *Journal of the Geological Society*, 168(6), 1237-1248.

Giorgetti, A., Crise, A., Laterza, R., Perini, L., Rebesco, M., Camerlenghi, A., 2003. Water masses and bottom boundary layer dynamics above a sediment drift of the Antarctic Peninsula Pacific margin. *Antarctic Science* 15, 537–546.

Glaçon, G. and Bourgois, J., 1985. Upper Oligocene to Recent planktonic foraminiferal remains in sediments of the inner wall of the Middle America Trench with special emphasis on Globorotalia. In: R. von Huene, J. Aubouin et al. (Editors), *Init. Rep. DSDP*, 84: 473-513.

Gorsline D.S. (1978) Anatomy of margin basins. *J. Sedim. Petrol.*, 48,1055-1068.

Gorsline D.S. & Emery K.O. (1959) Turbidity-current deposits in San Pedro and Santa Monica basins off southern California. *Bull. geol. Soc. Am.*, 70, 279-290.

Hampton, M.A., Lee, H.J., Locat, J., 1996. Submarine landslides. *Reviews of Geophysics*, 34, 33–59.

Heezen B.C. & Ewing M. (1952) Turbidity currents and submarine slumps, and the 1929 Grand Banks earthquake. *Am. J. Sci.*, 250, 849-873.

Heezen B.C. & Hollister C.D. (1971) *The Face of the Deep*, 659 pp. Oxford University Press, New York.

Heezen B.C., Hollister E.D. & Ruddiman W.E (1966) Shaping of the continental rise by deep geostrophic contour currents. *Science*, 152,502-508.

Heller P.L. & Dickinson W.R. (1985) Submarine ramp facies model for delta-fed, sand-rich turbidite systems. *Bull. Am. Ass. petrol. Geol.*, 69, 960-976.

Henkel, D.J. (1970) The role of waves causing submarine landslides. *Géotechnique*, 20, 75–80.

Hernández-Molina, F.J., Llave, E., Somoza, L., Fernández-Puga, M.C., Maestro, A., León, R., Barnolas, A., Medialdea, T., García, M., Vázquez, J.T., Díaz del Río, V., Fernández-Salas, L.M., Lobo, F., Alveirinho Dias, J.M., Rodero, J., Gardner, J., 2003. Looking for clues to paleoceanographic imprints: a diagnosis of the gulf of Cadiz contourite depositional systems. *Geology* 31, 19–22

Hernández-Molina, F.J., Larter, R.D., Rebesco, M., Maldonado, A., 2006b. Miocene reversal of bottom water flow along the Pacific Margin of the Antarctic Peninsula: stratigraphic evidence from a contourite sedimentary tail. *Marine Geology* 228, 93–116.

Hernández-Molina, F.J., Maldonado, A., Stow, D.A.V., 2008a. Abyssal plain contourites. In: Rebesco, M., Camerlenghi, A. (Eds.), *Contourites. Developments in Sedimentology*, 60. Elsevier, Amsterdam, pp. 345–378

Hernández-Molina, F.J., Paterlini, M., Violante, R., Marshall, P., de Isasi, M., Somoza, L., Rebesco, M., 2009. Contourite depositional system on the Argentine slope: an exceptional record of the influence of Antarctic water masses. *Geology* 37, 507–510.

Hillenbrand, C.-D., Camerlenghi, A., Cowan, E.A., Hernández-Molina, F.J., Lucchi, R.G., Rebesco, M., Uenzelmann-Neben, G., 2008. The present and past bottom-current flow regime around the sediment drifts on the continental rise west of the Antarctic Peninsula. *Marine Geology* 255, 50–63.

Holcomb, R.T. and Searle, R.C. (1991) Large landslides from oceanic volcanoes. *Mar. Geotech.*, 10, 19–32.

Hollister C.D., Flood R.D., Johnson D.A., Lonsdale P.E Southard J.B. (1974) Abyssal furrows and hyperbolic echo-traces on the Bahama Outer Ridge. *Geology*, 2, 395-400.

Hollister C.D. & Heezen B.C. (1967) Contour current evidence from abyssal sediments. *Trans. Am. Geophys. Union*, 48.

Hollister C.D. & Heezen B.C. (1972) Geological effects of ocean bottom currents: western North Atlantic. In: *Studies in Physical Oceanography*, vol. 2 (Ed. By A.L. Gordon), pp. 37-66. Gordon & Breach, London.

Hollister C.D. & McCave LN. (1984) Sedimentation under deep-sea storms. *Nature*, 309, 220-225.

Hornbach, M.J., DeShon, H.R., Ellsworth, W.L., Stump, B.W., Hayward, C., Frohlich, C., Oldham, H.R., Olson, J.E., Magnani, M.B., Brokaw, C., Luetgert, J.H., (2015). Causal factors for seismicity near Azle, Texas. *Nature communications*, 6, Article number 6728 (2015). <https://doi.org/10.1038/ncomms7728>.

Hughes Clarke J.E., Shor A.N., Piper D.J.W. & Mayer L.A. (1990) Large-scale current-induced erosion and deposition in the path of the 1929 Grand Banks turbidity current. *Sedimentology*, 37, 613-629.

Huguen, C., Foucher, J.-P., Mascle, J., Ondreas, H., Thouement, M., Gontharet, S., et al., 2009. Menes caldera, a highly active site of brine seepage in the Eastern Mediterranean sea: "in situ" observations from the NAUTINIL expedition (2003). *Mar. Geol.* 261 (1–4), 138–152.

Huyghe, P., Foata, M., Deville, E., Mascle, G. and Grp, C.W., 2004. Channel profiles through the active thrust front of the southern Barbados prism. *Geology*, 32(5): 429-432.

Jacka A.D., Beck R.H., St. Germain L.C & Harrison S.G. (1968) Permian deep-sea fans of the Delaware Mountain Group (Guadalupian), Delaware Basin. In: *Guadalupian Facies, Apache Mountain Area, West Texas* (Ed. by B.A. Silver), pp. 49-90. *Soc. econ. Paleont. Miner. Permian Basin Section Publication*, 68-11, 49-90.

Jakob, M., Hungr, O., (2005). *Debris Flow Hazards and Related Phenomena*. Springer-Praxis Books in Geophysical Sciences. ISBN 3-540-20726-0

Johnson A.M. (1970) *Physical Processes in Geology*, 577 pp. Freeman, Cooper & Co., San Francisco.

Johnson, A.M., 1984. Debris flow. In: Brunden, D., Prior, D.B. (Eds.), *Slope Instability*. Wiley, Toronto, pp. 257–362.

Kelts K. & Arthur M.A. (1981) Turbidites after ten years of deep-sea drilling - wringing out the mop? In: *The Deep-Sea Drilling Project: it Decade of Progress* (Ed. by J.E. Warme, R.G. Douglas and E.L. Winterer), pp. 91-127. Spec. Publ. Soc. econ. Paleont. Miner., 32, Tulsa.

Kidd, R.B., Hill, P.R., 1986. Sedimentation on mid-ocean sediment drifts. In: *North Atlantic Palaeoceanography* (Edited by C.P. Summerhayes and N.J. Shackleton), pp. 87-102. Spec. Publ. Geol. Soc. Lond., 21.

Kidd R.B., Ruddiman W.E, et al. (1986) *Init. Repts DSDP 94*. US Government Printing Office, Washington, DC.

Kneller B.C., Edwards D.A., McCaffrey W.D. & Moore R. (1991) Oblique reflection of turbidity currents. *Geology*, 19, 250-252

Kneller B.C. & Branney M.J. (1995) Sustained high-density turbidity currents and the deposition of thick, massive beds. *Sedimentology*, 42,607-616

Kolla V., Eitrem S., Sullivan L., Kosteki J.A. & Burckle L.H. (1980) Current-controlled, abyssal microtopography and sedimentation in Mozambique basin, Southwest Indian Ocean. *Mar. Geol.*, 34, 171-206.

Komar P.D. (1985) The hydraulic interpretation of turbidites from their grain sizes and sedimentary structures. *Sedimentology*, 32, 395-407.

Kuenen, Ph.H., 1937. Experiments in connection with Daly's hypothesis on the formation of submarine canyons. *Leids geol. Meded.*, 8, 327-335.

Kuenen, Ph.H., Migliorini, C.I., 1950. Turbidity currents as a cause of graded bedding. *J. Geol.*, 58, 91-127.

Lamb and Davis, 2003, *Cenozoic climate change as a possible cause for the rise of the Andes* *Nature* 425, 792–797 (23 October 2003)

Laberg, J.S., Dahlgren, T., Vorren, T.O., Hafliason, H., Bryn, P., 2001. Seismic analyses of Cenozoic contourite drift development in the Northern Norwegian Sea. *Marine Geophysical Research* 22, 401–416.

Lee, H.J., Schwab, W.C., Booth, J.S., (1993). Submarine landslides: an introduction. In: Schwab, W.C., Lee, H.J., Twichell, D.C. (Eds.), *Submarine Landslides: Selected Studies in the U.S. Exclusive Economic Zone*, U.S. Geological Survey Bulletin 2002, pp. 1–13.

Lee, H.J., Locat, J., Desgagnés, P., Parsons, J.D., McAdoo, B.G., Orange, D.L., Puig, P., Wong, F.L., Dartnell, P. and Boulanger, E., (2007). Submarine mass movements on continental margins. In *Continental Margin Sedimentation, from sediment transport to sequence stratigraphy*. Nittrouer, C.A., Austin, J.A., Field, M.E., Kravitz, J.H., Syvitski, J.P.M., and Wiberg, P.L. (Eds). Special Publication, number 37, International Association of Sedimentologists.

Llave, E., Hernández-Molina, F.J., Somoza, L., Stow, D.A.V., Díaz del Río, V., 2007. Quaternary evolution of the contourite depositional system in the Gulf of Cadiz. In: Viana, A.R., Rebesco, M. (Eds.), *Economic and Palaeoceanographic Significance of Contourite Deposits*. Geological Society, London, Special Publication, 276, pp. 49–79.

Lowe D.R. (1975) Water escape structures in coarse-grained sediments. *Sedimentology*, 22, 157-204.

Lowe D.R. (1982) Sediment gravity flows: II. Depositional models with special reference to the deposits of high-density turbidity currents. *J. Sedim. Petrol.*, 52, 279-297.

Lowe D.R. & LoPiccolo R.D. (1974) The characteristics and origins of dish and pillar structures.]. *sedim. Petrol.*, 44, 484-501.

Marani 11,1., Argnani A., Roveri M. & Trincardi E (1993) Sediment drifts and erosional surfaces in the central Mediterranean: seismic evidence of bottom-current activity. *Sedim. Geol.*, 82, 207-220.

Martin, R.G. and Bouma, A.H. (1982) Active diapirism and slope steepening, northern Gulf of Mexico continental slope. *Mar. Geotech.*, 5, 63–91

Martinsen O.J. & Bakken B., 1990. Extensional and compressional zones in slumps and slides in the Namurian of County Clare, Ireland. *J. geol. Soc. Lond.*, 147, 153-164.

Maslin, M., Vilela, C., Mikkelsen, N., Grootes, P., 2005. Causes of catastrophic sediment failures of the Amazon Fan. *Quatern. Sci. Rev.* 24, 2180–2193.

Masson, D.G., 1996. Catastrophic collapse of the volcanic island of Hierro 15 ka ago and the history of landslides in Canary Islands. *Geology* 24 (3), 231–234.

McAdoo, B.G., Pratson, L.F. and Orange, D.L., 2000. Submarine landslide geomorphology, US continental slope. *Marine Geology*, 169(1-2): 103-136.

McCave LN. & Jones P.N. (1988) Deposition of ungraded muds from high-density non-turbulent turbidity currents. *Nature*, 333, 250-252.

McCave LN. & Tucholke B.E. (1986) Deep current-controlled sedimentation in the western North Atlantic. In: *The Geology of North America*, vol. M. The Western North



Atlantic Region, Decade of North America Geology (Ed. by P.R. Vogt and B.E. Tucholke), pp. 451-468. Geol. Soc. Am., Boulder; CO.

McLean, T., 2011. Ocean Morphology. Power point presentation. Old Dominion University in Norfolk, Virginia. <https://www.slideshare.net/expattam/ocean-morphology>

Mercier de Lépinay, B, F. Michaud, T. Calmus, J. Bourgois, G. Poupeau, P. Saint Marc and The NAUTIMATE team, 1997, *Large Neogene subsidence event along the Middle America Trench off Mexico (18°N–19°N): Evidence from submersible observations*, *Geology*, 25; p. 387-390

Michaud F., Mercier de Lépinay B., Saint-Marc P., Sosson M., Villeneuve M., Bourgois J. and Calmus T. (1995). Neogene Subsidence Event Along the Acapulco Trench off Manzanillo (Mexico, 18°-19°N): Evidences from Deep sea Submersible Observations: *Eos*, Transactions, American Geophysical Union, 1995 Fall meeting, p. 535

Mienert, J., Buenz, S., Guidard, S., Vanneste, M., Berndt, C., 2005. Ocean bottom seismometer investigations in the Ormen Lange area offshore mid-Norway provide evidence for shallow gas layers in subsurface sediments. *Mar. Pet. Geol.* 22 (1–2), 11–19.

Moore, J.G. (1964) Giant submarine landslides on the Hawaiian Ridge. U.S. Geol. Surv. Prof. Pap., 501-D, D95–D98.

Moore, J.G., Clague, D.A., Holcomb, R.T., et al. (1989) Prodigious submarine slides on the Hawaiian Ridge. *J. Geophys. Res.*, 94, 17,465–17,484.

Moore, J. C., & Saffer, D. (2001). Updip limit of the seismogenic zone beneath the accretionary prism of southwest Japan: An effect of diagenetic to low-grade metamorphic processes and increasing effective stress. *Geology*, 29(2), 183-186.

Mulder T. & Syvitski J.P.M. (1995) Turbidity currents generated at river mouths during exceptional discharges to the World Oceans. *J. Geol.*, 103, 285-299.

Mulder, T., Zaragosi, S., Razin, P., Grelaud, K., Lanfumey, V., Bavoil, F., 2009b. A new conceptual model for the deposition process of homogenite: application to a cretaceous megaturbidite of the western Pyrenees (Basque region, SW France). *Sediment. Geol.* 222, 263–273.

Mulder, T., (2011). Gravity Processes and Deposits on Continental Slope, Rise and Abyssal Plains. In Heiko Hüneke and Thierry Mulder, editors: *Developments in Sedimentology*, Vol. 63, Amsterdam: The Netherlands, 2011, pp. 25-148. ISBN: 978-0-444-53000-4

Mulder, T., Hassan, R., Ducassou, E., Zaragosi, S., Gonthier, E., Hanquiez, V., Marchès, E., Toucanne, S., (2013). Contourites in the Gulf of Cadiz: a cautionary note on potentially

ambiguous indicators of bottom current velocity. *Geo-Mar Lett* (2013) 33:357-367. DOI 10.1007/s00367-013-0332-4

Mutti E. & Ricci Lucchi E (1972) Le torbiditi dell' Appennino Settentrionale: introduzione all'analisi di facies. *Mem. Soc. geo/. Ital.*, 11, 161-199.

Nemec W. & Steel R.J. (1984) Alluvial and coastal conglomerates: Their significant features and some comments on gravelly mass flow deposits. In: *Sedimentology of Gravels and Conglomerates* (Ed. by E.H. Koster and R.J. Steel), pp. 1-31. *Mem. Can. Soc. petrol. Geol.*, 10, Calgary.

Normark W.R. (1970) Growth patterns of deep sea fans. *Bull. Am. Ass. petrol. Geol.*, 54, 2170-2195.

Normark W.R. & Piper D.J.W. (1985) Navy Fan, Pacific Ocean. In: *Submarine Fans and Related Turbidite Systems* (Ed. by A.H. Bouma, W.R. Normark and N.E. Barnes), pp. 87-94. SpringerVerlag, New York.

Normark W.R. & Piper D.J.W. (1991) Initiation processes and flow evolution of turbidity currents: implications for the depositional record. In: *From Shoreline to Abyss; Contributions in Marine Geology in Honor of Francis Parker Shepard* (Ed. by R.H. Osborne), pp. 207-230. *Spec. Publ. econ. Paleont. Miner.*, 46, Tulsa.

Normark, W.R., Moore, J.G. and Torresan, M.E. (1993). Giant volcano-related landslides and the development of the Hawaiian Islands. In: *Submarine Landslides: Selected Studies in the U.S. EEZ* (Eds W.C. Schwab, H.J. Lee and D.C. Twichell). *U.S. Geol. Surv. Bull.*, 2002, 184–196.

Nowell A.R.M. & Hollister CD. (Eds) (1985) *Deep Ocean Sediment Transport: Preliminary Results of the High Energy Benthic Boundary Layer Experiment*, 409 pp. *Mar. Geol.*, 66.

Nichols, G., (2009). *Sedimentology and Stratigraphy*, second edition. Wiley-Blackwell

Oncken, O., Hindle, D., Kley, J., Elger, K., Victor, P., & Schemmann, K. (2006). Deformation of the central Andean upper plate system—Facts, fiction, and constraints for plateau models. In *The Andes* (pp. 3-27). Springer Berlin Heidelberg.

Pantin H.M. (1979) Interaction between velocity and effective density in turbidity flow: phase-plane analysis, with criteria for autosuspension. *Mar. Geol.*, 31, 59-99.

Piper D.J.W. (1978) Turbidite muds and silts on deepsea fans and abyssal plains. In: *Sedimentation in Submarine Canyons, Fans and Trenches* (Ed. by D.] Stanley and G. Kelling), pp. 163-176. Dowden, Hutchinson & Ross, Stroudsburg, PA.

Piper D.J.W. & Normark W.R. (1983) Turbidite depositional patterns and flow characteristics, Navy Submarine Fan, California Borderland. *Sedimentology*, 30, 681-694.

Piper D.J.W., Shor A.N. & Hughes Clarke J.E. (1988) The 1929 Grand Banks earthquake, slump and turbidity current. *Spec. Pap. geol. Soc. Am.*, 229, 77-92.

Piper D.J.W. & Stow D.A.V. (1991) Fine-grained turbidites. In: *Cycles and Events in Stratigraphy* (Ed. by G. Einsele, W. Rieken and A. Seilacher), pp. 360-376. Springer-Verlag, Berlin.

Piper, D.J.W., Deptuck, M., 1997. Fine-grained turbidites of the Amazon Fan: facies characterization and interpretation. In: Flood, R.D., Piper, D.J.W., Klaus, A., Peterson, L.C. (Eds.), *Proc. ODP, Sci. Results*, 155, 79–108 College Station, TX.

Porebski S.J., Meischner D. & Gorlich K. (1991) Quaternary mud turbidites from the South Shetland Trench (West Antarctica): recognition and implications for turbidite facies modelling. *Sedimentology*, 38, 691-715.

Prave, A.R., Duke, W.L., 1990. Small-scale hummocky cross-stratification in turbidites: a form of antidune stratification. *Sedimentology* 37 (3), 531–539.

Ranero, C.R. and von Huene, R., 2000. Subduction erosion along the Middle America convergent margin. *Nature*, 404.

Reading H.G. & Richards M. (1994) Turbidite systems in deepwater basin margins classified by grain size and feeder system. *Bull. Am. Ass. petrol. Geol.*, 78, 792-822.

Rebesco, M., 2005. Contourites. In: Selley, R.C., Cocks, L.R.M., Plimer, I.R. (Eds.), *Encyclopedia of Geology*. Elsevier, Oxford, pp. 513–527.

Rebesco M., Hernandez-Molina F.J., Van Rooij D. & Wåhlin A., 2014. Contourites and associated sediments controlled by deep-water circulation processes: State-of-the-art and future considerations. *Marine Geology*, 352, 111-154.

Robb, J.M. (1984) Spring sapping on the lower continental slope, offshore New Jersey. *Geology*, 12, 278–282.

Rothery, D., 2015. *Geology, A Complete Introduction*. The Open University. Paperback ISBN 978 1 473 60155 0. eBook ISBNs 978 1 473 60157 4, 978 1 473 60156 7

Rothwell R.G., Weaver P.P.E. et al. (1994) Clayey nanofossil ooze turbidites and hemipelagites at Sites 834 and 835 (Lau Basin, SW Pacific). In: *Proc. ODP Sci. Results*, 135 (Ed. by]. Hawkins, L. Parsons et al.) pp. 101-130.

Rouillard, P., 2010. Mode`le architectural et lithologique du syste`me de Rosetta (Delta du Nil, Me´diterrane´e Orientale): implications pour un analogue actuel de re´servoir pe´trotlier. Unpubl. Ph.D. thesis, Universite´ de Nice Sophia-Antipolis, 375pp.

Sage, F., Collot, J.Y. and Ranero, C.R., 2006. Interplate patchiness and subduction-erosion mechanisms: Evidence from depth-migrated seismic images at the central Ecuador convergent margin. *Geology*, 34(12): 997-1000.

Sangrey, D. (1977) Marine geotechnology – state of the art. *Mar. Geotech.*, 2, 45–80.

Scholl, D. W. (1974). Sedimentary sequences in the north Pacific trenches. In *The geology of continental margins* (pp. 493-504). Springer, Berlin, Heidelberg.

Scholl, D.W. , R. Von Huene, T.L. Vallier, D.G. Howell Sedimentary masses and concepts about tectonic processes at underthrust ocean margins *Geology*, 8 (1980), pp. 564-568

Seely, D.R., Vail, P.R. and Wailton, G.G., 1974. Trench slope model. In: C.A. Burk and C.L. Drake (Editors), *The Geology of the Continental Margins*. Springer, New York, pp.249-260.

Shanmugam G. & Moiola R.J. (1988) Submarine fans: characteristics, models, classification, and reservoir potential. *Earth Sci. Rev.*, 24,383-428.

Shanmugam G., Spalding T.D. & Rofheart D.H. (1993) Process sedimentology and reservoir quality of deep-marine bottom current reworked sands (sandy contourites): an example from the Gulf of Mexico. *Bull. Am. Ass. petrol. Geol.*, 77,1241-1259.

Shanmugam, G., Lehtonen, L.R., Straume, T., Syversten, S.E., Hodgkinson, R.J., Skibeli, M., (1994). Slump and debris flow dominated upper slope facies in the Cretaceous of the Norwegian and Northern North Seas (61–67 N): implications for sand distribution. *AAPG Bulletin*, 78, 910–937.

Shanmugam, G., (2000). 50 years of the turbidite paradigm (1950s-1990s) deep-water processes and facies models, a critical perspective. *Marine and Petroleum Geology*, 17 (2000), p. 285-342

Shanmugam G., (2006). *Handbook of Petroleum Exploration and Production: Chapter 4 Deep-water bottom currents*. Volume 5, p. 85-139. Elsevier. [https://doi.org/10.1016/S1567-8032\(06\)80023-6](https://doi.org/10.1016/S1567-8032(06)80023-6)

Shanmugam, G., (2015). The Landslide Problem. *Journal of Palaeogeography*. 4(2): 109-166. DOI: 10.3724/SP.J.1261.2015.00071

Sharp, A., Samuel, A., 2004. An example study using conventional 3D seismic data to delineate shallow gas drilling hazards from West Delta Deep Marine concession, offshore Nile Delta, Egypt. *Pet. Geosci.* 10, 121–129.

Shreve, R. L., & Cloos, M. (1986). Dynamics of sediment subduction, melange formation, and prism accretion. *Journal of Geophysical Research: Solid Earth*, 91(B10), 10229-10245.

Sparks R.S.J., Bonnacaze R.T., Huppert H.E., Lister J.R., Hallworth M.A., Mader H. & Phillips J. (1993) Sediment-laden gravity currents with reversing buoyancy. *Earth Planet Sci. Lett.*, 114, 243-257.

Stanley, D.J., 1993. Model for turbidite-to-contourite continuum and multiple process transport in deep marine settings: examples in the rock record. In: *Contourites and Bottom Currents* (Edited by D.A.V. Stow and J.-C. Faugeres), pp 241-255. *Sedim. Geol.*, 82.

Sosson, M., Bourgois, J., & de Lépinay, B. M. (1994). SeaBeam and deep-sea submersible Nautilie surveys in the Chiclayo canyon off Peru (7 S): subsidence and subduction-erosion of an Andean-type convergent margin since Pliocene times. *Marine Geology*, 118(3-4), 237-256.

Southard J.B. & Mackintosh M.E. (1981) Experimental test of autosuspension. *Earth Surf. Proc. Landf.*, 6, 103-111.

Stow D.A.V. (1979) Distinguishing between fine-grained turbidites and contourites on the Nova Scotian deep water margin. *Sedimentology*, 26,371-387.

Stow D.A.V. (1985) Deep-sea clastics: where are we and where are we going? In: *Sedimentology: Recent Developments and Applied Aspects* (Ed. by P.J. Brenchley and B.P.J. Williams), pp. 67-93. *Spec. Publ. geol. Soc. Land.*, 18.

Stow D.A.V. (1986) Deep clastic seas. In: *Sedimentary Environments and Facies* (Ed. by H.G. Reading), pp. 399-444. Blackwell Scientific Publications, Oxford.

Stow D.A.V. & Bowen A.J. (1980) A physical model for the transport and sorting of fine-grained sediments by turbidity currents. *Sedimentology*, 27, 31-46.

Stow D.A.V. (1982) Bottom currents and contourites in the North Atlantic. *Bull. Inst. Geol. Bassin d'Aquitaine*, 31.

Stow, D.A.V., Holbrook, J.A., 1984. North Atlantic contourites: an overview. In: *Fine-grained Sediments: Deep-Water Processes and Facies* (Edited by D.A.V. Stow and D.J.W. Piper), pp. 245-256. *Spec. Publ. Geol. Soc. Lond.*

Stow, D., Faugeres, J., Gonthier, E., 1986. Facies distribution and textural variation in Faro Drift contourites: velocity fluctuation and drift growth. *Marine Geology*, 72, 71-100.

Stow D.A.V. (1994) Deep sea processes of sediment transport and deposition. In: Sediment Transport and Depositional Processes (Ed. by K. Pye), pp. 257-291. Blackwell Scientific Publications, Oxford.

Stow D.A.V. & Lovell J.P.B. (1979) Contourites; their recognition in modern and ancient sediments. *Earth Sci. Rev.*, 14, 251-291.

Stow D.A.V. & Shanmugam G. (1980) Sequence of structures in fine-grained turbidites; comparison of recent deep-sea and ancient flysch sediments. *Sedim. Geol.*, 25.

Stow D.A.V. & Wetzel A. (1990) Hemiturbidite: a new type of deep water sediment. In: Proc. ODP Sci. Results, 116 (Ed. by J.R. Cochran, D.A.V. Stow et al.), 25-34.

Stow D.A.V., Reading H.G. and Collinson J.D., (1996). Deep seas. Chapter 10 in *Sedimentary Environments: Processes, Facies and Stratigraphy*, Edited by H.G. Reading, Third edition. Blackwell Publishing. Pag. 395 – 451.

Twenhofel, W.H., (1932). *Treatise on Sedimentation*, 2nd Edition, Completely Revised. The Williams & Wilkins Company, Baltimore, p. 926.

Underwood M.B. & Moore G.F. (1995) Trenches and trench-slope basins. In: *Tectonics of Sedimentary Basins* (Ed. by e./ Busby and R.V. Ingersoll), pp. Blackwell Science Inc., Boston.

United States Geological Survey (USGS), (2018). <https://earthquake.usgs.gov/learn/glossary/?term=turbidites>

Urgeles, R., Masson, D. G., Canals, M., Watts, A. B., & Le Bas, T. (1999). Recurrent large-scale landsliding on the west flank of La Palma, Canary Islands. *Journal of Geophysical Research: Solid Earth*, 104(B11), 25331-25348.

Van Rooij, D., Iglesia, J., Hernández-Molina, F.J., Ercilla, G., Gomez-Ballesteros, M., Casas, D., Llave, E., De Hauwere, A., Garcia-Gil, S., Acosta, J., Henriot, J.-P., 2010. The Le Danois Contourite Depositional System: Interactions between the Mediterranean Outflow Water and the upper Cantabrian slope (North Iberian margin). *Marine Geology* 274, 1–20.

Varnes, D.J., (1958). Landslide types and processes. In: Eckel, E.D. (Ed.), *Landslide and Engineering Practice*, Highway Research Board Special Report 29, pp. 20–47.

Völker, D., Wiedicke, M., Ladage, S., Gaedicke, C., Reichert, C., Rauch, K., ... & Heubeck, C. (2006). Latitudinal variation in sedimentary processes in the Peru-Chile Trench off Central Chile. *The Andes*, 193-216.

Völker, D., Geersen, J., Contreras-Reyes, E., & Reichert, C. (2013). Sedimentary fill of the Chile Trench (32–46° S): volumetric distribution and causal factors. *Journal of the Geological Society*, 170(5), 723-736.

Von Huene, R. and Scholl, D.W., 1991. Observations at convergent margins concerning sediment subduction, subduction erosion, and the growth of continental crust. *Reviews of Geophysics*, 29: 279-316.

Von Huene, 1974, Modern trench sediment, in Burk, C. A. and Drake, eds, *The Geology of Continental Margins*, Springer, Berlin, Heidelberg, p. 207-211.

Von Huene, R.E., Aubouin, J., Azema, J., Blackinton, G., Carter, J.A., Coulbourn, W.T., Cowan, D.S., Curiale, J.A., Dengo, C.A., Faas, R.W., Harrison, W., Hesse, R., Hussong, D.M., Ladd, J.N. and Muzylov, 1980. Mid-America Trench transect off Guatemala. *Geol. Soc. Am. Bull.*, 91: 421-422.

Walker R.G. (1965) The origin and significance of the internal sedimentary structures of turbidites. *Proc. Yorks. geol. Soc.*, 35.

Walker R.G. (1966a) Shale Grit and Grindslow Shales: transition from turbidite to shallow water sediments in the Upper Carboniferous of northern England. *J. sedim. Petrol.*, 36, 90-114.

Walker R.G. (1967) Turbidite sedimentary structures and their relationship to proximal and distal depositional environments. *J. sedim. Petrol.*, 37, 25-43.

Walker R.G. (1978) Deep-water sandstone facies and ancient submarine fans: models for exploration for stratigraphic traps. *Bull. Am. Ass. petrol. Geol.*, 62,932-966.

Wang, K., Hu, Y., Von Huene, R., and Kukowski, N., 2010. Interplate earthquakes as a driver of shallow subduction erosion. *Geology*, 38(5), 431-434.

Ward, W.H., 1945. The stability of natural slopes. *The Geographical Journal*, 105, 170–191.

Weimer, P., 1989. Sequence stratigraphy of the Mississippi Fan (Plio–Pleistocene), Gulf of Mexico. *Geo-Mar. Lett.* 9, 185–272.

Weimer, P., 1990. Sequence stratigraphy, facies geometries, and depositional history of the Mississippi Fan, Gulf of Mexico. *Am. Assoc. Pet. Geol. Bull.* 74 (4), 425–453.

Wetzel A. (1993) The transfer of river load to deep-sea fans: a quantitative approach. *Bull. Am. Ass. petrol. Geol.*, 77, 1679-1692.

Wezel EC., Savelli D., Bellagamba M., Tramontana M. & Bartole R. (1981) Plio-Quaternary depositional style of sedimentary basins along insular Tyrrhenian margins.

In: Sedimentary Basins of Mediterranean Margins (Ed. by Ee. Wezel), pp. 239-269. CNR Italian Project of Oceanography.`

Zhong, S., & Gurnis, M. (1994). Controls on trench topography from dynamic models of subducted slabs. *Journal of Geophysical Research: Solid Earth*, 99(B8), 15683-15695.



# Chapter 2

## Geological setting of the Ecuadorian margin

### 2.1 Geodynamic context of the Ecuadorian active margin

The Nazca plate underthrusts eastward the Ecuadorian margin, at a rate ranging 5.6–5.8 cm/year relative to the South American plate (Trenkamp et al. 2002; Nocquet et al., 2009, 2014) in a N83°E direction, along the Ecuadorian margin. The basement of the coastal area of Ecuador consists of accreted oceanic terranes (Jaillard et al. 1997). The subduction of the Carnegie ridge (Gutscher et al. 1999; Michaud et al. 2009; Collot et al. 2009) and the northward escape of the North Andean block with respect to the South American plate, (Witt et al. 2006; Trenkamp et al. 2002; Nocquet et al. 2009) (Fig. 2.1) control the geologic evolution of the Ecuadorian margin.

The age of the subduction of the Carnegie Ridge is debated in the literature (Michaud et al., 2009). Based in the crustal structure of the Nazca plate, Graindorge et al., (2004) indicates that the subduction has been working at least since the last 1.3 Ma. The subduction of the Carnegie ridge or the collision of along-strike positive relief (Witt et al., 2006) is synchronous with the acceleration of the subsidence in the Gulf of Guayaquil (Deniaud et al., 1999) since 1.6–1.8 Ma ago, which in turn has been attributed to an increase of the escape velocity of the North Andean block (Witt et al., 2006). Based on a kinematic reconstruction and a morphologic analysis of the margin outer-wedge, Collot et al. (2009) suggested that the Carnegie Ridge subduction initiated 4–5 Ma ago and was fully established about 2 Ma ago.

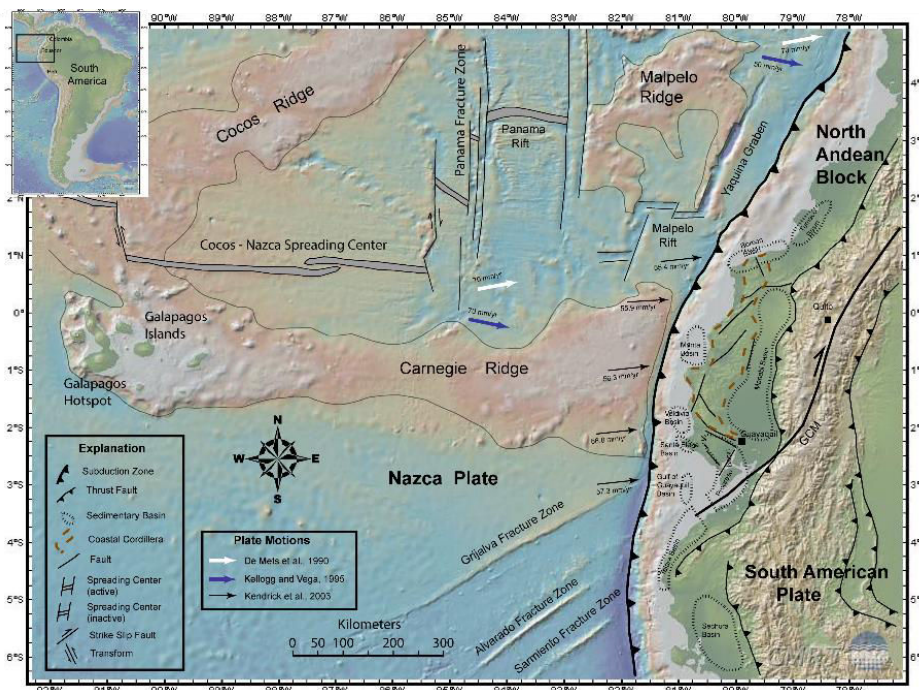


Fig. 2.1 Geodynamic context of the Ecuadorian margin. This area is characterized by the subduction of the Carnegie ridge and the northward motion, respect to the South American plate, of the North Andean block. (Base map from Ryan et al, 2009; boundaries of the forearc basins from Deniaud, 2000; Jaillard et al., 2009 and Witt et al., 2017)

## 2.2 Main controls of the regional detrital trench sedimentary supply

Along the Ecuadorian margin, the principal sources of detrital material transported to the trench are the western cordillera of the Andes and the coastal plains (Fig. 2.2). One characteristic of the Ecuadorian margin is the presence of a Coastal Cordillera (Reyes, 2013). Across the forearc, the uplift of the coastal cordillera diverts the sediments supply from the Andes to the north and to the south (Collot et al. 2009). Hence the drainage from the Andes is diverted in both directions: (a) towards the Esmeraldas river in the North, which transfers sediments into the trench through the Esmeraldas canyon; and (b) towards the Guayas river in the south, which transfers sediments to the Gulf of Guayaquil and the trench through the canyon of Guayaquil (Fig. 2.2). The coastal uplift (Pedoja et al. 2006a, b) is inferred to be related to the subduction of the Carnegie Ridge. The age of the uplift of the Coastal cordillera is still debated, but recent preliminary results from thermochronological studies (Vacherat et al. 2016) suggest that this uplift began around 5 Ma ago. Consequently, the Coastal Cordillera controls the distribution of sedimentary supply into the trench.

Sediment transfer from the onland sources to the trench is carried out through the Guayaquil canyon and the Esmeraldas canyon. Northward the detrital sediment supply is transferred through the Esmeraldas canyon directly to the trench, where the sedimentary infill reaches 3.5 to 4.8 km thick (Collot et al., 2009). Southward, in front of the Gulf of Guayaquil, the thickness is less than 0.8 km (Collot et al., 2009); in this area the material is partially trapped on the continental shelf (Witt et al., 2006; Loayza et al., 2014); the material reaches the trench through the Guayaquil canyon during global lowstand eustatic stages.

In contrast, in front of the Carnegie ridge, very few terrestrial sediments have been deposited in the shallow trench of this segment of the margin. Indeed, in this area, the detrital material mainly comes from the coastal cordillera; as the relief of the coastal cordillera is less steep than the Andes, the quantity of material transferred from these areas to the trench is less than the material transferred northward and southward from the Andes. Moreover, this material is partially trapped and accumulated on the continental shelf (Martillo, 2016) and the slope basins. Consequently, in front of the Carnegie ridge, the amount of material which reaches the trench is less important and in many places, is absent (Collot et al., 2009).

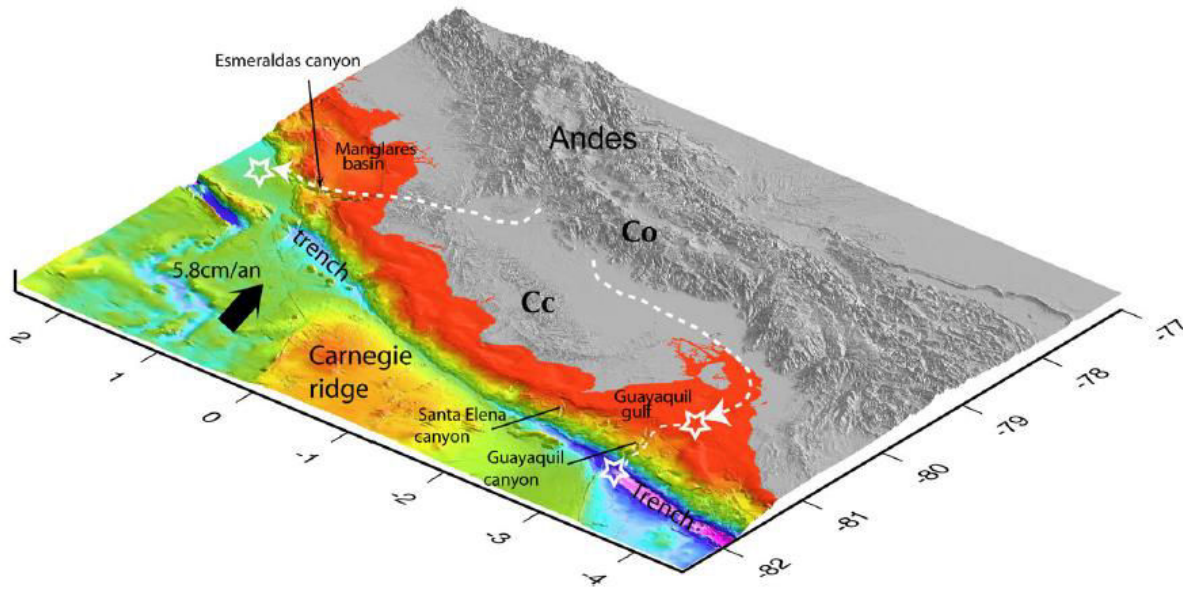


Fig. 2.2 The western cordillera of the Andes is considered the main source of detrital material transported to the trench. The Coastal cordillera acts like a natural barrier for all drainage coming from the Andes, thus this is diverted i) to the Esmeraldas river in the north which transfer the sediments through the Esmeraldas canyon, and ii) to the Guayas river in the south which transfer the sediments through the Guayaquil canyon. White dashed lines show sediment pathways; white stars represent sites of sediment accumulation. Convergence velocity after Trenkamp et al., 2002. Bathymetry from Michaud et al., 2006. Image from Michaud et al., 2015.

### 2.3 Morphologic segmentation of the slope

Based on a compilation of swath bathymetric data Collot et al., (2009) have described, at regional scale, the morphology of the trench, the slope and the continental shelf (Fig. 2.3), in order to evaluate the modes of mass transfer along the margin. In fact, along the slope there are strong variabilities in the morphology which can be related to instability. These authors have distinguished three segments. The first order segmentation of the Nazca plate due to the Carnegie ridge and Grijalva fracture zone (GFZ) (Fig. 2.3) has a strong influence in the geomorphology of the trench and the slope, therefore delimiting these areas in three geomorphological segments: southern, central and northern segments. The identification of three first-order segments along the Ecuadorian margin (Collot et al., 2009) is based on i) internal velocity structures (Gailler et al., 2007), ii) the variations in the trench-shoreline distances and iv) the changes in the morpho-structure along the margin (Fig. 2.3).

The boundaries of two of the first-order segments are delineated by important changes in the platform width, associated with structural changes along the margin slope. The boundary of the first segment separates the southern segment, associated with the Gulf of Guayaquil (Calahorrano, 2005), from the central segment that characterizes most of the Ecuadorian margin and extends from Punta de Salinas to the Esmeraldas platform northward of Punta Galera (Fig. 2.3). The boundary of the second segment is marked by a protrusion on the lower slope of the margin near latitude 1°20'N and the upper part of



the Esmeraldas canyon. Northward of the Esmeraldas platform three smaller margin segments were recognized (Fig. 2.3), based on the morpho-structural changes of the margin.

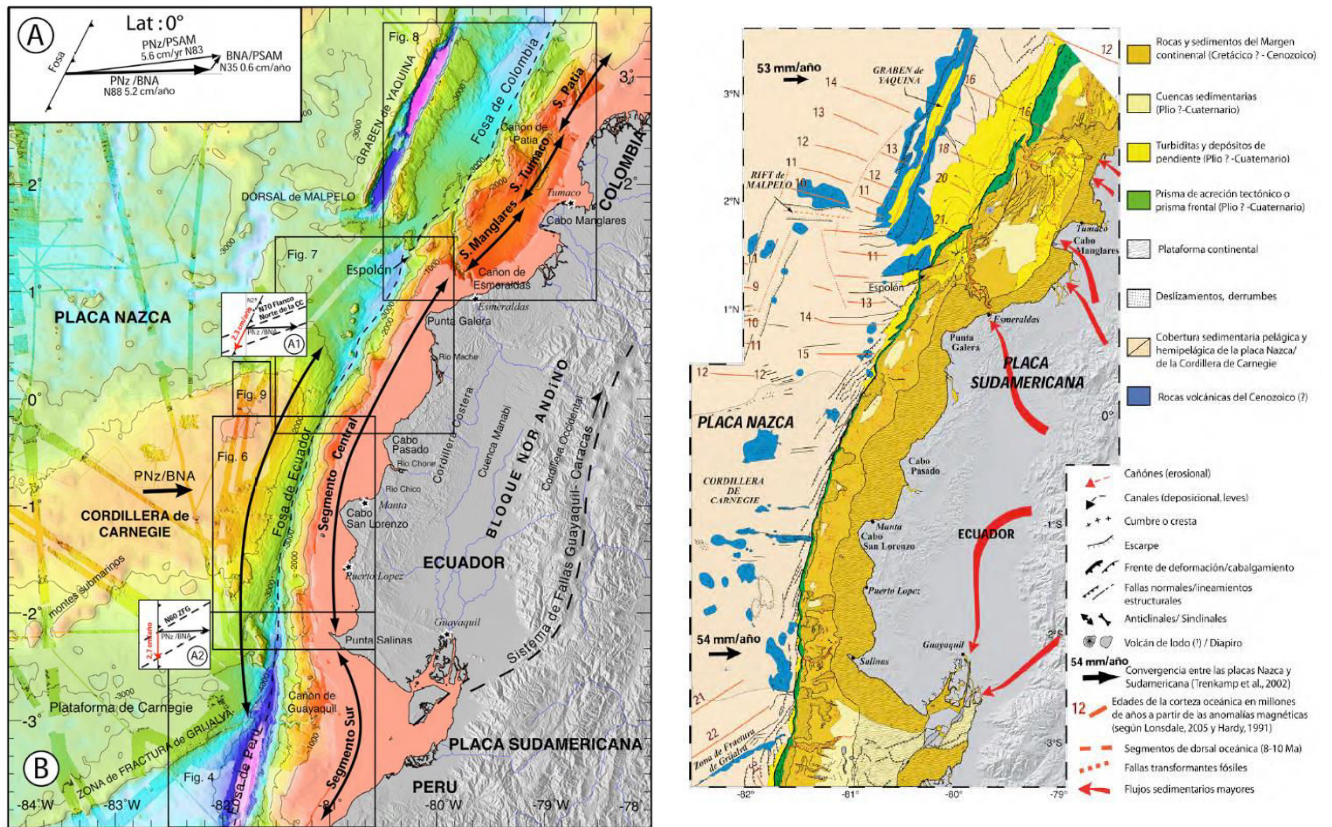


Fig. 2. 3 from (Collot et al., 2009): Left = Map of the different morphologic segments along the margin. Right = Geological and structural interpretation showing the variabilities of the trench infill along the margin.

### 2.3.1 Southern segment of the margin

The morphology of the middle and lower slopes differs to some extent at north and south of the Guayaquil canyon. The Santa Elena and Guayaquil canyons cut deeply (up to 600-1000 m) the middle slope at about 1000 to ~ 2500 m deep. Between the canyons, the middle slope is in average steeper (3.5°-3.8°) and generally rougher than the upper slope, revealing an area of 50 km long by 40 km width of an extremely disturbed marine floor, indicating an extensive destabilization of the slope (S, in Fig. 2.4 and Fig. 2.5). To the south of the Guayaquil canyon, processes of destabilization affect less the middle slope than in the north. In conclusion, the Guayaquil canyon is an important morphological boundary, transverse to the internal slope of the trench. This boundary separates to the south a relatively smooth slope controlled by faults, and the presence of an accretionary prism at the foot of the margin of a heavily disturbed slope, from the presence of a poorly developed frontal prism north of the canyon. Although the Guayaquil and Santa Elena canyons locally cut the frontal prism, elongated seamounts with a seaward orientation, crosses the mouth of the Santa Elena canyon right in the trench indicating that the

tectonics of the frontal deformation overcome the erosion due to the transportation of sediments along the canyons, suggesting a current low canyon activity (Loayza et al, 2013, Martillo, 2016).

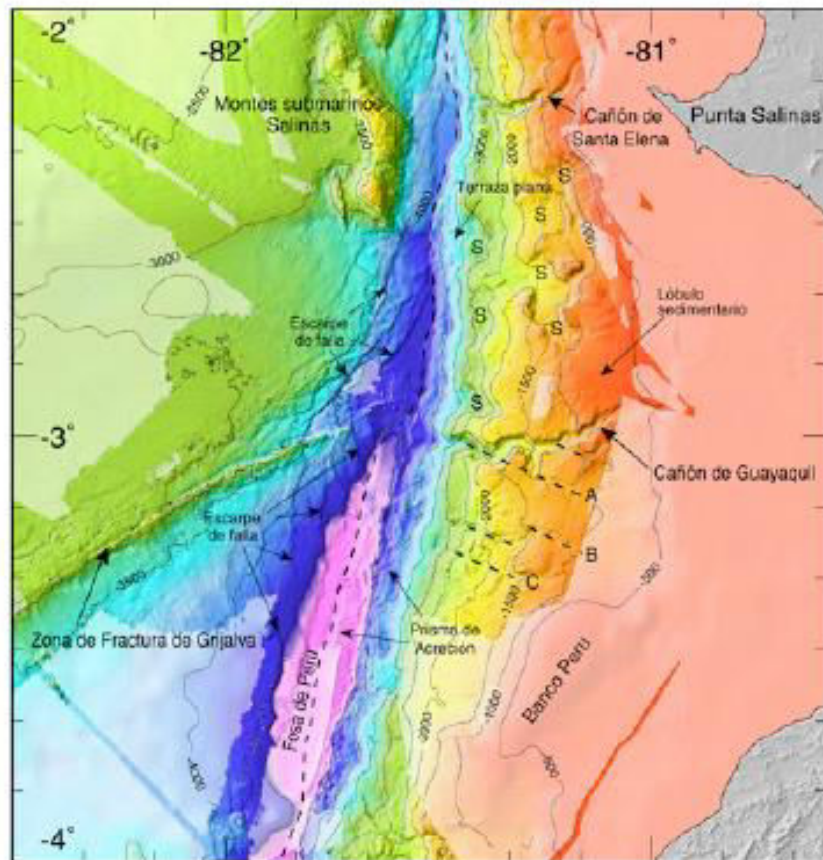


Fig. 2. 4 Bathymetry map, with contour lines each 50 m, of the southern segment of the Ecuadorian margin. In this map, we can note the northern end of the Peruvian trench, the Grijalva fracture zone, the Salinas seamounts and the Guayaquil and Santa Elena canyons. S = scars of landslide surfaces; A, B and C represent fault-controlled canyons (Collot et al., 2009)

### 2.3.2 Central segment of the margin

The slope varies in direction from an orientation N-S to an orientation progressively more N-E north of latitude 1°35'S. The N-S margin segment shows a very rough morphology (Sage et al., 2006) with a large re-entrant, 15 km wide and 35 km long, which cuts the margin until the upper slope (Fig. 2.6), named the Ayampe slope basin (Martillo, 2016; Dufeu et al., 2016). Escarpments hundreds of meters high with slopes > 20°, isolated mounds and wavy forms make up much of the middle and lower slope (Fig. 2.5 and 2.6). A short NS-oriented mountain range (R range in fig 6) of about 150 m high respect to the surrounding ocean floor, deforms the upper slope and is separated from a chaotic terrace on the lower slope by a concave middle slope of 14° and 2200 m high. South of the R mountain range, several 100-200 m high escarpments reveal normal faults affecting the



middle and upper slope (Villamar, 2001; Martillo, 2016). Locally, the margin foot is abruptly truncated by a 500-m high and 23° dip escarpment associated with a rough topography in the trench suggesting a catastrophic mass transport. Taken together, these morphological features indicate that the margin is very unstable and has been affected by deep tectonic and erosional disturbances.

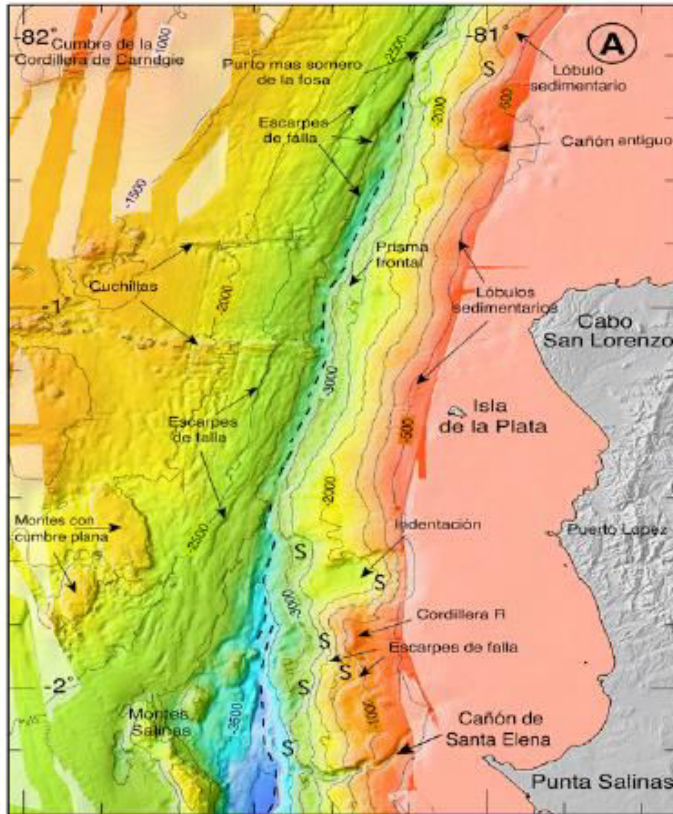


Fig. 2. 5 The southern part of the central segment. Bathymetry map with contour lines each 50 m of the central segment of the Ecuadorian margin offshore between Punta Salinas and Cabo San Lorenzo (from Collot et al., 2009). South of the latitude 1°35'S the slope morphology is highly irregular, meanwhile northward the slope morphology tends to be smoother. There are also E-W oriented seamounts subducting the South American plate. S = main scars of landslide surfaces.

Between latitudes 1°35'S and 0° (Figs. 2.5) the slope of the margin is noticeably smoother than towards the south, hence latitude 1°35'S can be considered as a remarkable transverse limit in the slope morphology. The upper slope shows flat topographies dipping seaward with slopes of ~ 6° alternating with wide and smooth depressions where the networks of channels are concentrated (Fig. 2.5). The middle slope exhibits bank structures with slopes of 2° and sediments collected from the channels, between 1500 and 2200 m depth (Fig. 2.5). The lower slope is irregular with flat zones, chaotic topographies and steep slopes up to 8° in the deformation front, thus revealing some degree of instability of the slope.

### 2.3.3 Northern segment of the margin

Between Cabo Pasado and Punta Galera (Fig. 2.6), there are two re-entrants of 25 to 40 km wide with slopes ranging from 4° to 6° respectively located on the upper slope and separated by a superficial promontory (P in Fig. 2.6). However, the lower slope of the promontory P is severely cut by a series of 5 km wide small re-entrants, with slopes up to

22°, forming together a 20-km wide re-entrant (Ratzov et al., 2010) which looks more recent than the larger re-entrant of the upper slope (S in Fig. 6). The ending of the N-S lineament of the Atacames seamounts, immediately to the west of the slope scar, together with evidence from seismic reflection lead to the determination that exist a buried seamount beneath the promontory P (d'Acremont et al., 2005; Marcaillou et al., 2016), this support the interpretation that the small re-entrants on the lower-slope resulted from the subduction of seamounts (Figs. 2.5 and 2.6) (Collot et al., 2004; Martillo, 2016; Marcaillou et al., 2016). In this area, mass transport deposits were evidenced and dated by Ratzov et al., (2010).

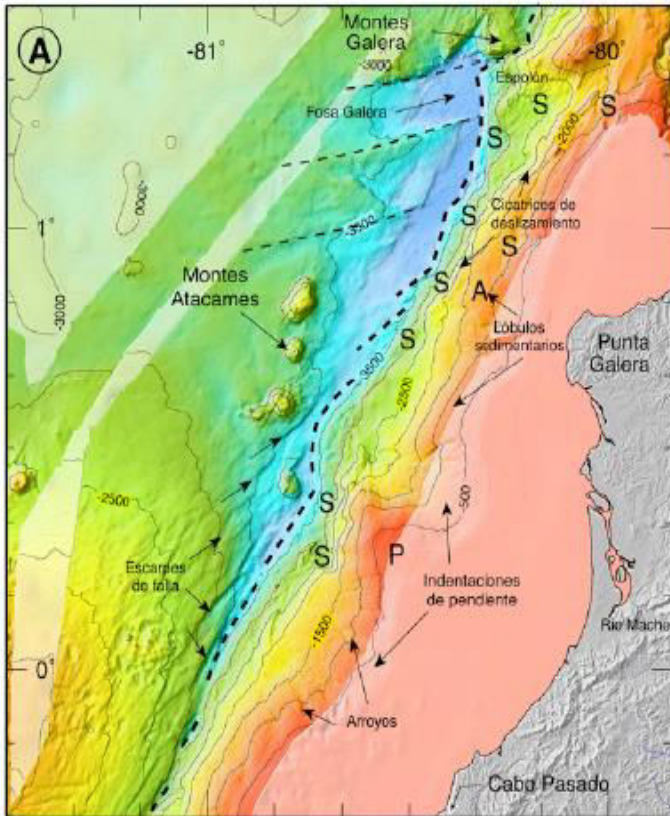


Fig. 2. 6 The northern part of the central segment. Bathymetry map with contour lines each 50 m offshore between Cabo Pasado and Punta Galera, (from Collot et al., 2009). where we can see the northeast extreme of the Carnegie ridge and the Atacames and Galera seamounts. The trench axis shows a "en-échelon" disposition (black dotted line), and numerous plate bending-related normal faults, associated to subduction, are affecting the outer wall of the trench. Note that offshore Punta Galera the continental shelf is very narrow and affected by large re-entrants, and also the lower slope is dominated by irregular steep scarps (S) forming a spur-like topographic feature in the north where the Galeras seamounts collide with the slope. A=smooth morphology, P represents a promontory overlie by a seamount (D'Acremont et al., 2005).

West of Punta Galera, the upper slope slightly dips seaward at ~ 5° and the middle slope shows a smooth morphology (A in Fig. 2.6) extending downhill to 1000-2000 m deep, where is abruptly truncated by a very steep escarpment (23°) parallel to the trench. The lower slope is rough and generally steep. North of Punta Galera, the average of the margin slope since the end of the continental shelf to the foot of the margin is about 8°, and locally the middle and upper slopes can reach more than 12°. In this region, the lower slope, which is deeper than 2500 m, tends to widen to the north, following the contour line in the direction of the trench from an orientation N-E to N-S, until the latitude 1°30'N.

In conclusion, the slope of the central and northern segments of the margin is divided into a relatively simple and undisturbed morphology (between latitudes 1°35'S and ~ 0°) bounded both southward (between Punta Salinas and latitude 1 ° 35'S) and northward

(between 0° and Galera seamounts) by areas of deeply disturbed morphology, which probably reflect the history of recent subduction of a rugged oceanic plate.

## 2.4 The trench: morphology and sediments distribution

The Ecuadorian trench has been first described incidentally by Hayes, 1966; Van Andel et al., 1971 and Lonsdale and Klitgard, 1978). But the first study focused on the Ecuadorian trench (Fig. 7) was conducted by Lonsdale, (1978). Based on single beam bathymetry, this last author described the morphology of the trench revealing a shallow area (with a minimum depth of 2920m) in front of the Carnegie ridge. One of the first attempts to represent the lateral variation of the sedimentary infill into the trench was proposed by Gustcher et al. (1999), at regional scale (Fig. 2.7).

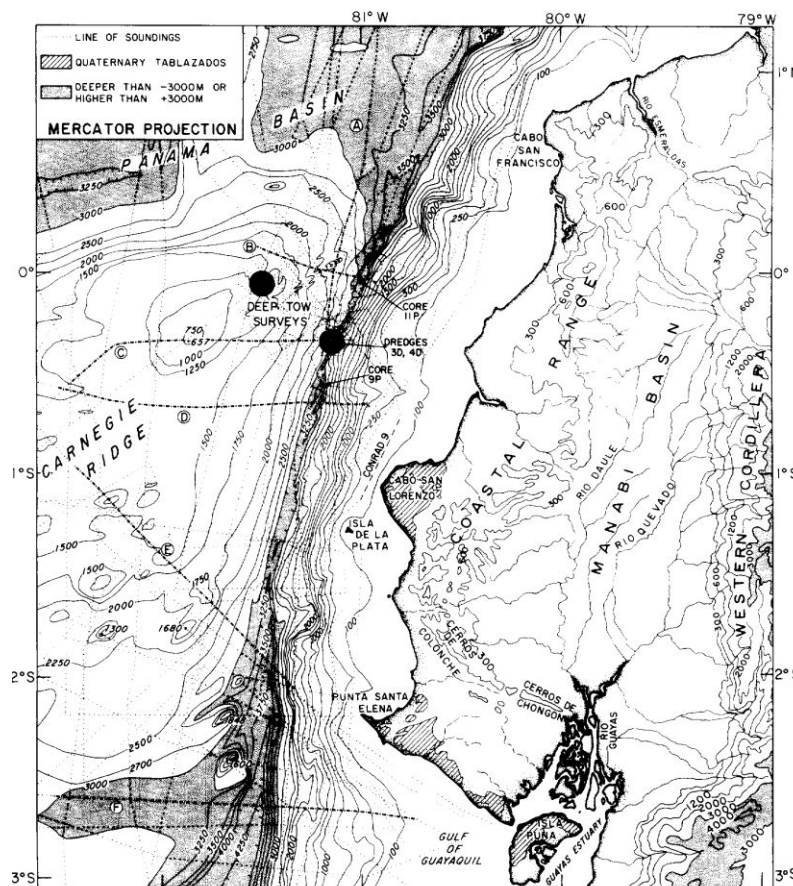
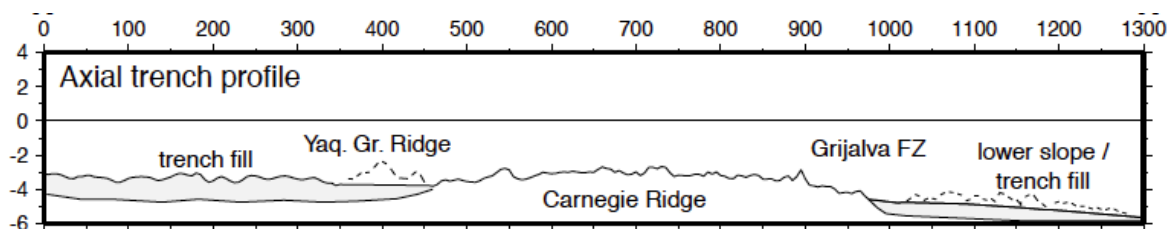


Fig. 2.7 Left : First representation of the Ecuadorian trench bathymetry as it is shown by Lonsdale (1978)

Down: first section along the trench showing the variation of the sedimentary fill on the both sides of the Carnegie ridge (Gustcher et al., 1999).





The first regional description of the trench morphology from multibeam data was proposed by Collot et al., (2009). South of the Grijalva fracture zone (GFZ) the Peruvian trench is oriented N14E and reaches 4700 m in depth (Fig. 4). This has a horizontal sea floor underlay by ~ 0.8 km of turbiditic deposits (Fig. 2.8) according to seismic reflection data (Lonsdale, 1978; Calahorrano, 2005; Calahorrano et al., 2008). Near the trench-GFZ intersection, the trench shows an undulated topography suggesting deposits of transported material. Towards the North from the trench-GFZ intersection, the trench changes to an approximately N-S direction and rises successively through discrete steps, forming a series of narrow, closed flat-floor basins that are displaced laterally to the latitude 0°20'S, where the trench is shallower (2880 m) (Fig. 2.5 and 2.8).

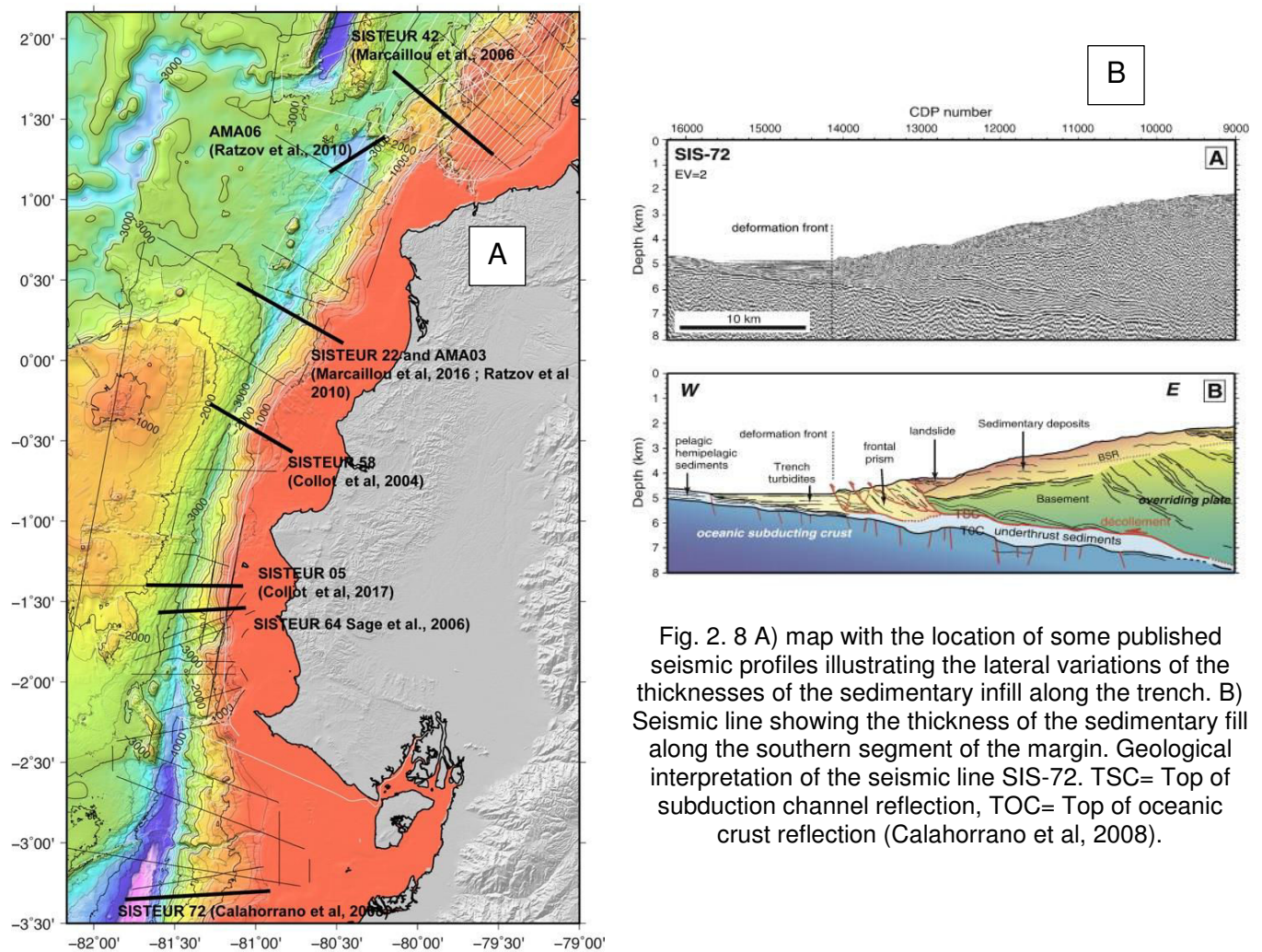


Fig. 2. 8 A) map with the location of some published seismic profiles illustrating the lateral variations of the thicknesses of the sedimentary infill along the trench. B) Seismic line showing the thickness of the sedimentary fill along the southern segment of the margin. Geological interpretation of the seismic line SIS-72. TSC= Top of subduction channel reflection, TOC= Top of oceanic crust reflection (Calahorrano et al, 2008).

A sedimentary core into the ~ 75 m of laminated sedimentary fill, on the eastern side of one of the small closed basins, reveals 4 m of a hemipelagic dark-green mud overlying 1 m of Holocene turbidites (Lonsdale, 1978). Along this area, the trench sedimentary fill is very weak (Fig. 2.8 and 2.9) as we can see along several published seismic profiles in Collot et al., (2004), Sage et al., (2006), Sanclemente, (2014) and Collot et al., (2017).

Further to the north around 0° latitude, the trench has a N27E orientation (Fig. 2.6 and 2.8).

Escarpmnts related to the flexure of the oceanic plate, together with the deformation front, define tiny trench-basins that are displaced laterally while the trench is deepened to the north until the 3900 m of Galera depression (Fig. 2.6). Seismic reflection data (Fig. 2.10) indicate that the trench contains ~ 0.5-0.6 km of sub-horizontal stratified sediments (d'Acremont et al., 2005; Marcaillou et al., 2016). Sedimentary core obtained by Lonsdale, (1978) was taken from a raised faulted block that entered the trench, 36 km north of the shallowest trench area. The core reveals Pleistocene calcareous lime of pale-green to olive-green color, with volcanic ash. In this part of the trench, sediments are interpreted as eroded by rapid, thermohaline bottom currents flowing to the north (Lonsdale, 1978).

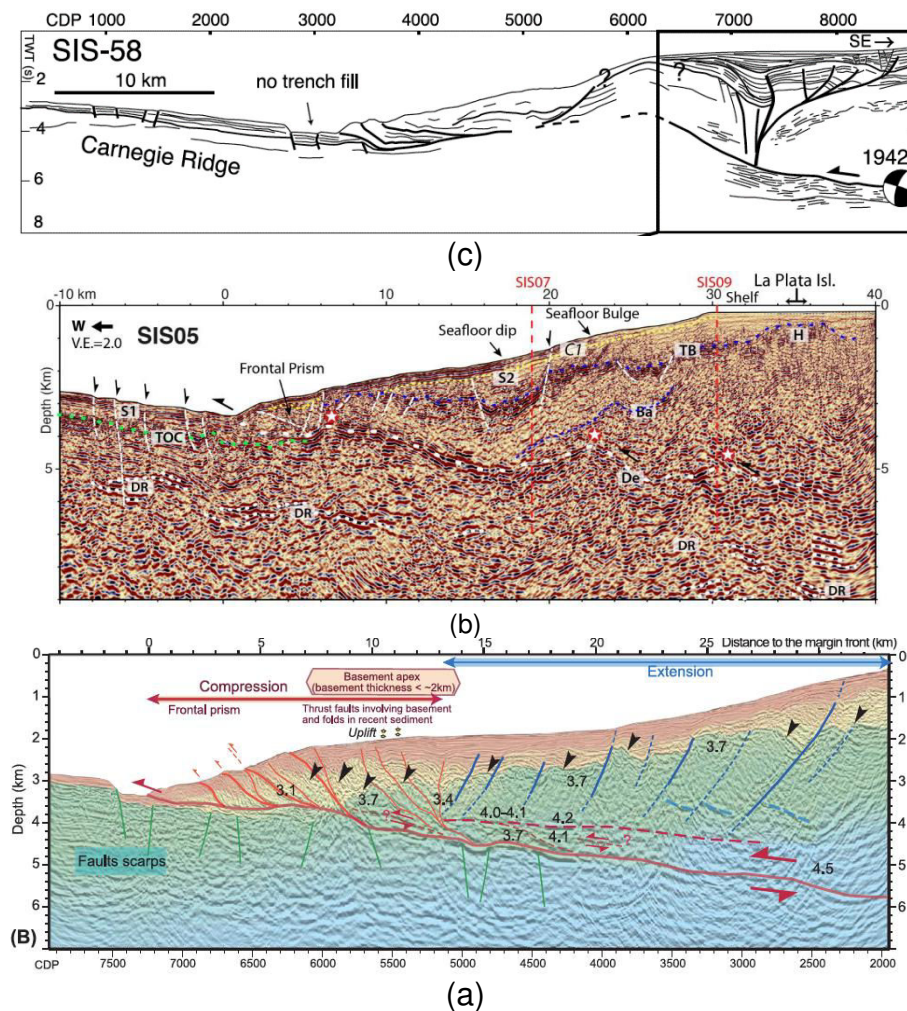


Fig. 2. 9 Illustration of the thickness of the trench sedimentary infill along the central segment of the Ecuadorian margin front of the Carnegie ridge (location of the profiles on Figure 2.8). From south to North, (a) Sisteur cruise seismic profile from Sage et al., 2006; (b) Sisteur cruise seismic profile from Collot et al., 2017 and (c) Sisteur cruise seismic profile from Collot et al., 2004. With this seismic resolution profiles, the trench is empty.



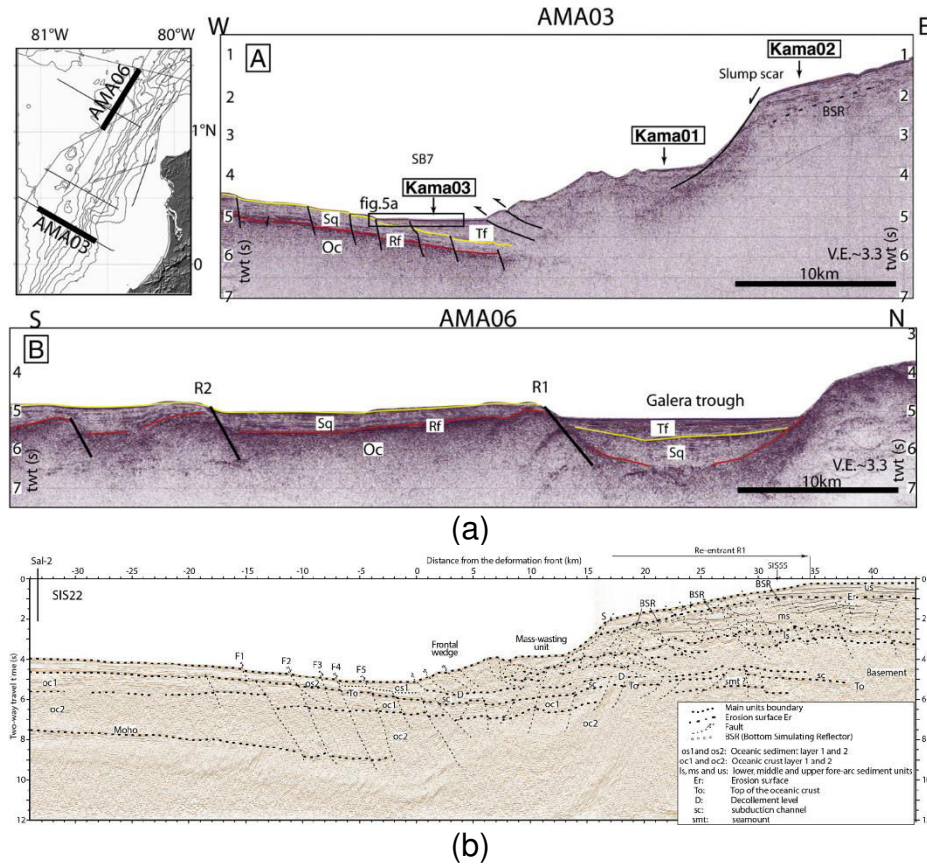


Fig. 2. 10 Illustration of the thickness of the trench sedimentary fill north of latitude 0° of the Ecuadorian margin (location of the profiles on Figure 8.). The thickness is less than 1 stwtt.  
 (a) Amadeus cruise = from Ratzov et al., 2010; (b) Sisteur cruise from Marcaillou et al., 2016.

Where the trench is deeper, in front of Punta Galera, a 25-km long segment of the plate boundary abruptly turns to a N-S direction (Fig 2.6 and 2.8). At latitude 1°25'N, the trench is dammed by the Galera seamount (Fig. 2.3 and 2.6), causing an elevation of 600 m high through the floor of the trench. To the north of the Galera seamounts, the trench is oriented N30E and its sea floor forms a bulge at ~ 3000 m deep, elongated, parallel to the trench and associated with the Esmeraldas deep submarine (Collot et al., 2004; Ratzov et al., 2010).

The bathymetric map shows a fan radiating asymmetrically from the mouth of the Esmeraldas canyon to the north, along the winding Esmeraldas canal; the sediment flow is blocked to the south by the Galera seamount and diverted to the north by the elevated topography of the eastern edge of the Yaquina graben (Fig. 2.3). The bathymetry of the Colombian trench deepens slightly northward to ~ 3900 m, near latitude 3°30'N, far from

the top of the fan. Seismic reflection data (Fig. 2.11) show that the deep undersea fan consists of 3.5- 4.8 km of well-stratified sediments that decline northward to ~ 2 km near latitude 3°20'N (Marcaillou et al., 2008).

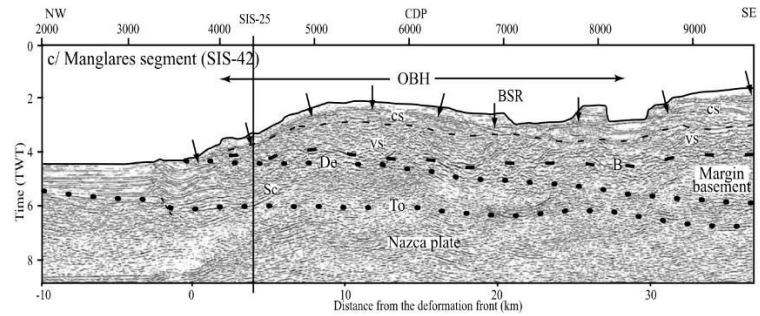
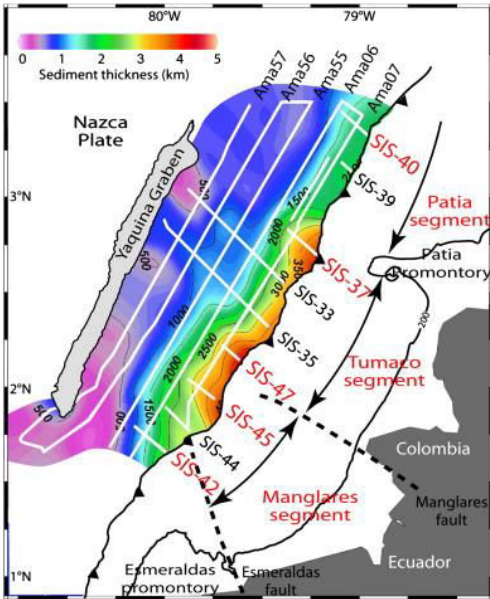


Fig. 2. 11 Left: isopach map of the sediment thickness into the trench, close to the foot of the margin, where the deep-sea fan of the Esmeraldas canyon forms the thickness reaches more than 4 kms (Marcaillou et al., 2008). Right: seismic profile 42 of the Sisteur cruise showing the trench fill thickness (up to 2stwt) (Marcaillou et al., 2006), location on Figure 8.

## 2.5 Seismological segmentation of the Ecuadorian active margin

The Ecuador–Colombia subduction zone has experienced five large megathrust earthquakes during the 20th century (Beck and Ruff, 1984; Kanamori and McNally, 1982; Swenson and Beck, 1996). From central Ecuador to north Colombia, megathrust earthquakes occurred in 1942 (Mw=7.8), 1958 (Mw=7.7), 1979 (Mw=8.2) and 1998 (Mw=7.1) within the 500-km long rupture area of the great 1906 (Mw=8.8) Colombia–Ecuador earthquake (Fig. 2.12). On April 16th, 2016, a 7.8 magnitude earthquake hit the Ecuadorian coast at the same location than the 1942 earthquake, possibly starting a new seismic supercycle similar to the one observed during the 20th century (Nocquet et al., 2016).

Spatial distribution of interseismic coupling along the subduction plate interface shows that the southern Ecuador northern Peru subduction zone exhibits a fundamentally different mode of stress accumulation and release compared with its neighboring segments (Chlieh, et al., 2014; Nocquet et al., 2014). These Interseismic models indicate that the coupling is weak and very shallow (0–15km) in south Ecuador and increases northward, with the maximum rupture zone found for a large (Mw>7.0) megathrust earthquake occurred during the 20th century (Fig. 2.12). Indeed, along the southern segment of the margin there have not been recorded great earthquakes triggered deposits meanwhile in the northern segment of the margin five large megathrust earthquakes triggered deposits have been recorded during the 20th century.

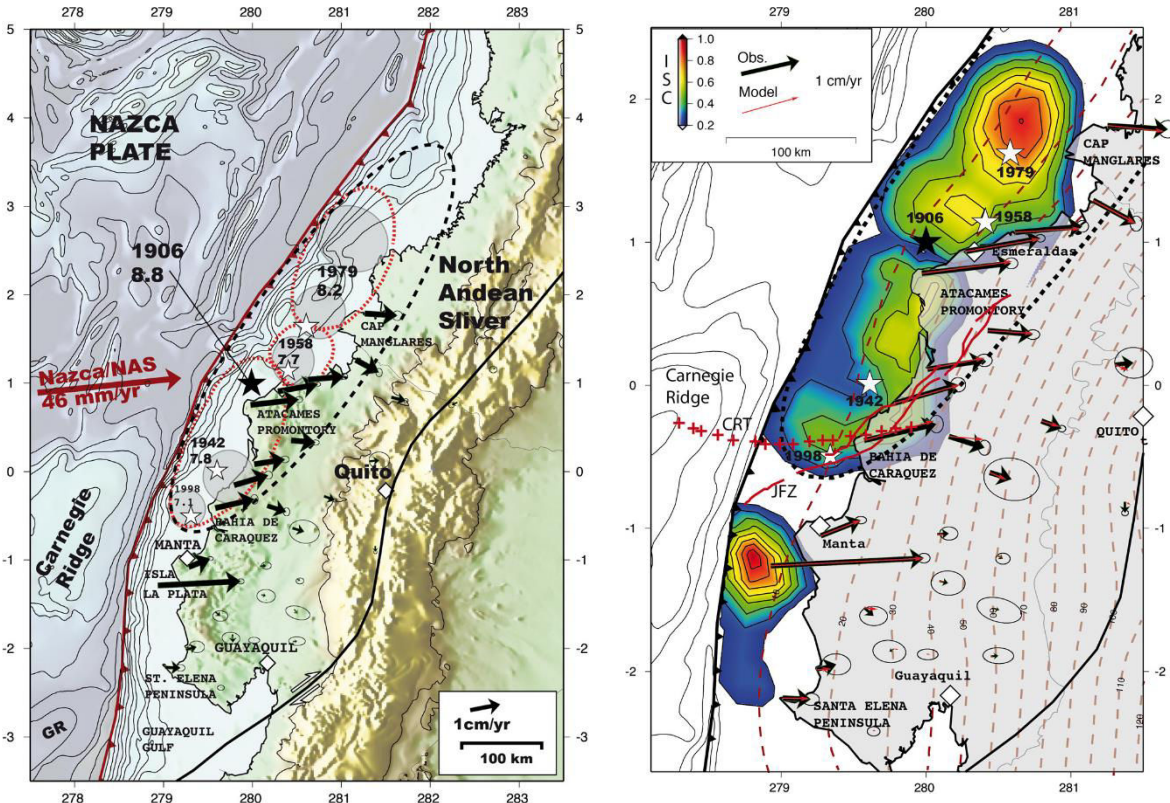


Fig. 2. 12 Great earthquakes and coupling areas along the Ecuadorian trench. Left: location of the great earthquakes along the Ecuadorian margin (from Chlieh et al., 2014) (black star = the epicenter of the great 1906 event; white stars = the epicenters of the Mw>7.0 1942–1998 seismic sequence). Grey shaded ellipses = high slip region of the 1942, 1958, 1979 and 1998 seismic sources. Red dashed contours = relocated aftershocks areas of the 1942, 1958 and 1979 events. Right: Distribution of the inter-seismic coupling (ISC) along the Ecuadorian subduction zone derived from the inversion of the inter-seismic GPS velocities (from Chlieh et al., 2014). Red–yellow patches = highly locked asperities and white–blue patches = highly creeping regions of the megathrust interface. Arrows represent respectively the inter-seismic GPS data (black) and synthetic (red). Red dotted lines are the 10-km iso-depth contours of the slab interface (Font et al., 2013). In the rupture area of the great 1906 earthquakes (black dashed line), the coupling is confined within the first 35km depth of the slab interface. A large creeping corridor lies immediately south of the shallow axis of the Carnegie Ridge Track (CRT). Southwest of Manta, the permanent GPS station of La Plata Island (ISPT) suggests a highly-coupled patch confined between the trench axis and 15-km depth. In south Ecuador, the ISC is weak and shallow.

## 2.6 Paleo-seismological studies and time recurrence of the mega-earthquakes

The paleoseismic approach consists in identifying in the sedimentary archives characteristics of co-seismic destabilization of the continental slopes. This makes possible to build time series of paleo-earthquakes over thousands to tens of thousands of years (Goldfinger et al., 2003, Gracia et al., 2010, Polonia et al., 2013, Poudoux et al., 2014, Ratzov et al., 2015, Patton et al., 2015). Paleo-seismological studies are poor along the Ecuadorian margin and are concentrated exclusively along the northern part of the margin where the greatest historical earthquakes were recorded. A first attempt was performed by Ratzov et al., (2010) which have investigated Mass-Transport Deposits



(MTDs) and turbidite deposition in the North Ecuador subduction trench (Fig. 2.13). The studied trench segment has been the site of four great subduction earthquakes ( $7.7 \leq M_w \leq 8.8$ ) during the 20th century. Swath bathymetry, seismic reflection and Chirp data, together with sedimentary cores and  $^{14}\text{C}$  dating revealed that seven MTDs were emplaced since  $\sim 23$  kyr, and 27 turbidites deposited in the southernmost trench sub-basin, of this northern segment, since  $\sim 4.9$  kyr. Temporal correlations between MTDs emplaced within trench sub-basins indicate that the seven MTDs were emplaced during five main events. Three were triggered locally and tentatively dated 5.8, 1.6 kyr and Recent, whereas four were emplaced in distinct trench sub-basins as a result of two regional events at 22.6 and 15.4 kyr (Fig. 2.14). The large 1.5–13.5 kyr return time of the MTDs contrasts with that of 189 yr of the turbidites. The latter is consistent with the 73 yr return time of two local  $M_w \geq 8.2$  earthquakes, implying that turbidites might have been triggered by large earthquakes.

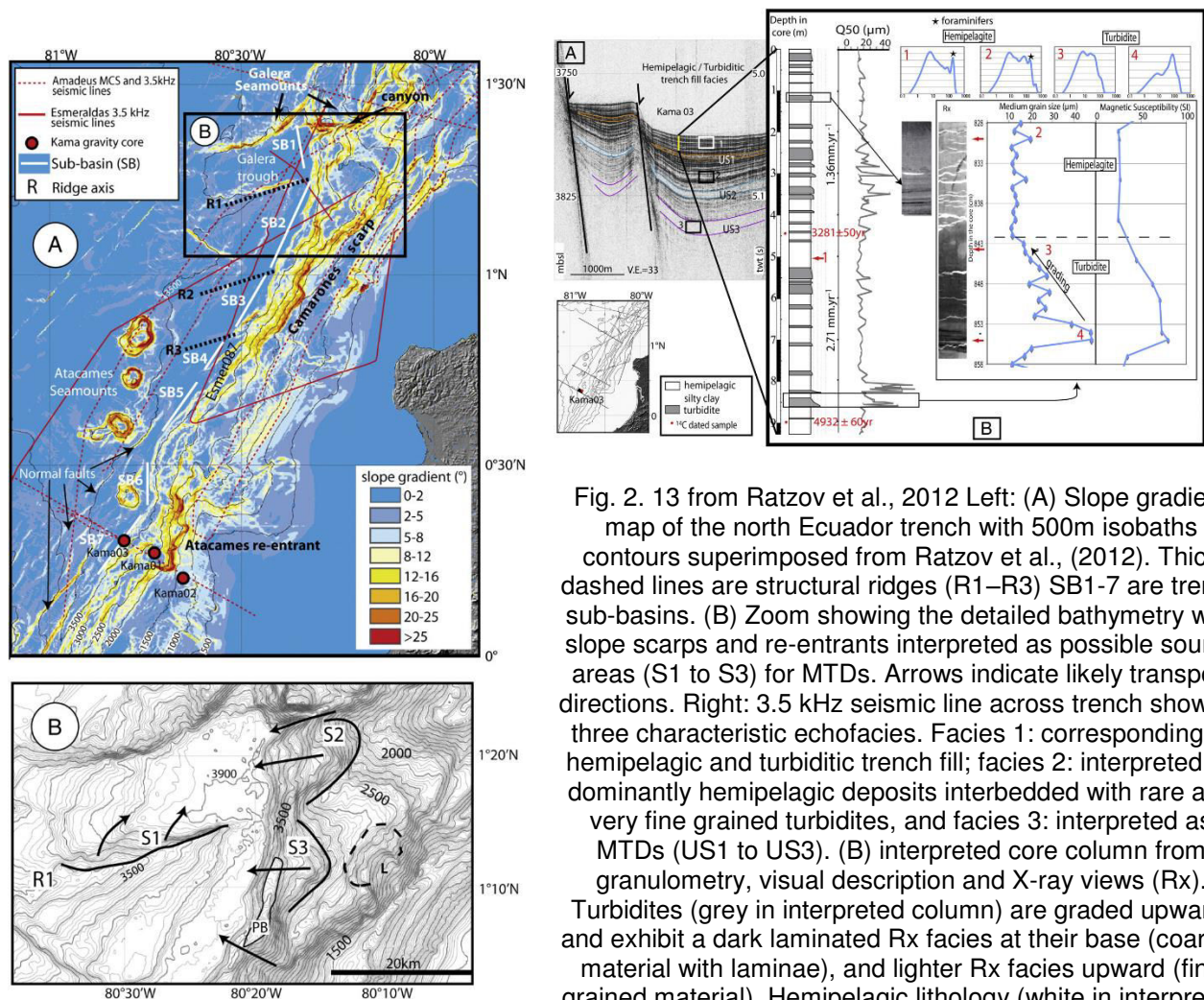


Fig. 2. 13 from Ratzov et al., 2012 Left: (A) Slope gradient map of the north Ecuador trench with 500m isobaths contours superimposed from Ratzov et al., (2012). Thick dashed lines are structural ridges (R1–R3) SB1–7 are trench sub-basins. (B) Zoom showing the detailed bathymetry with slope scarps and re-entrants interpreted as possible source areas (S1 to S3) for MTDs. Arrows indicate likely transport directions. Right: 3.5 kHz seismic line across trench showing three characteristic echofacies. Facies 1: corresponding to hemipelagic and turbiditic trench fill; facies 2: interpreted as dominantly hemipelagic deposits interbedded with rare and very fine grained turbidites, and facies 3: interpreted as MTDs (US1 to US3). (B) interpreted core column from granulometry, visual description and X-ray views (Rx). Turbidites (grey in interpreted column) are graded upward, and exhibit a dark laminated Rx facies at their base (coarser material with laminae), and lighter Rx facies upward (fine grained material). Hemipelagic lithology (white in interpreted column) is outlined by a poorly sorted grain size distribution (1–2), whilst turbidite lithology (3–4) shows well sorted grain size distribution.

More recently, in a paleo-seismological study Migeon et al. (2016) have identified and dated earthquake-induced turbidites related to 4 historical greatest earthquakes recorded along the northern Ecuadorian margin; they propose a recurrence time for these earthquakes. The bathymetry (Fig. 2.15) shows that the Esmeraldas canyon, which deeply incises the continental slope, is at the origin, into the trench, to the construction of a large deep-sea fan named the Esmeraldas Turbidite System (Ratzov et al., 2010; Migeon et al., 2016).

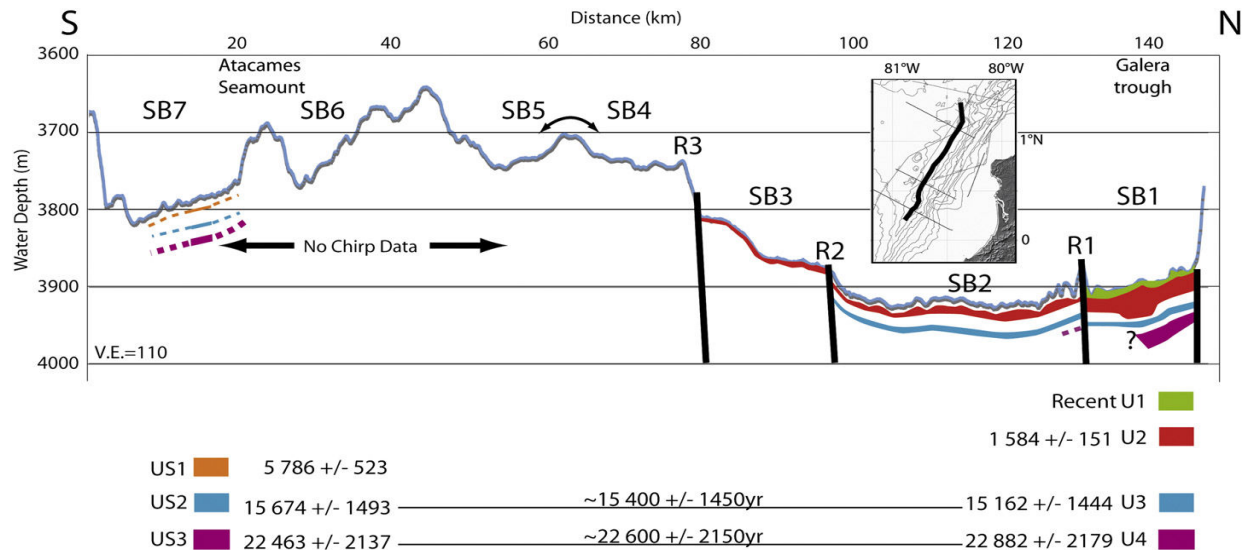


Fig. 2. 14 Synthetic bathymetric cross section along the north Ecuadorian trench showing the seven identified MTDs. SB1 to SB7=trench sub-basins 1 to 7, R1 to R3=structural ridges. Depot centers of Sub-basins 1 to 3 and 7 are unconnected because of the structurally uplifted sediment in the trench saddle (SB4–SB5). Dated MTDs suggest that U1, U2 and US1 were triggered locally, whereas the paired units US2–U3, and US3–U4 possibly resulted from two regional events, likely earthquakes, at ~15.4 kyr and ~22.6 kyr. (Ratzov et al., 201)

Based on the analysis of sedimentary cores collected in the Esmeraldas Turbidite System Migeon et al., (2016) have discriminated two types of coarse-grained deposits: (1) “classical” flood generated turbidites which are normally graded beds with structureless, laminated and cross laminated intervals and high organic-matter content, (2) earthquake-induced deposits which consist of amalgamated normally-graded laminated/cross-laminated intervals separated by erosive surfaces. These latter are interpreted to be deposited by quasi-synchronous flows generated during a single earthquake. In this work, a temporal relationship is established between the 1906, 1942, and 1979 earthquakes (Fig. 2.15), and three coarse-grained beds showing features of earthquake-induced turbidites, suggesting the Esmeraldas Canyon was the main source for sediments to be remobilized during these earthquakes. At least ten earthquakes with the highest magnitudes were recorded within the last 800 years with a recurrence time ranging from about 280 yrs to 40-70 yrs, or less for the 20th Century earthquakes. The comparison of the main features of the 1906 turbidite with older earthquake-triggered turbidites identified in a core collected in the trench suggests that one or two earthquakes similar to the 1906 event might have occurred ~600 yrs ago.

This recurrence time for the greatest earthquake identified by this palaeoseismological studies (Migeon et al., 2016) is coherent with the recent study published by Nocquet et al., (2016). This latter author combines historical seismology results, present-day geodesy data, and dense local observations of the recent Mw 7.8 2016 Pedernales earthquake to reconstruct the strain budget at the Ecuador subduction zone since the great 1906 earthquake. They consider that the Ecuador Colombia subduction zone illustrates in the present time a fault behavior predicted by physical models that include spatial variation of fault friction showing temporally clustered earthquakes separated by periods of seismic quiescence. This supports the view as earthquake-triggered deposits show 1906-like turbidites 600 years ago, followed by a cluster of events with recurrence time of 40-70 years and then a 300 years of quiescence period preceding the twentieth-century sequence.

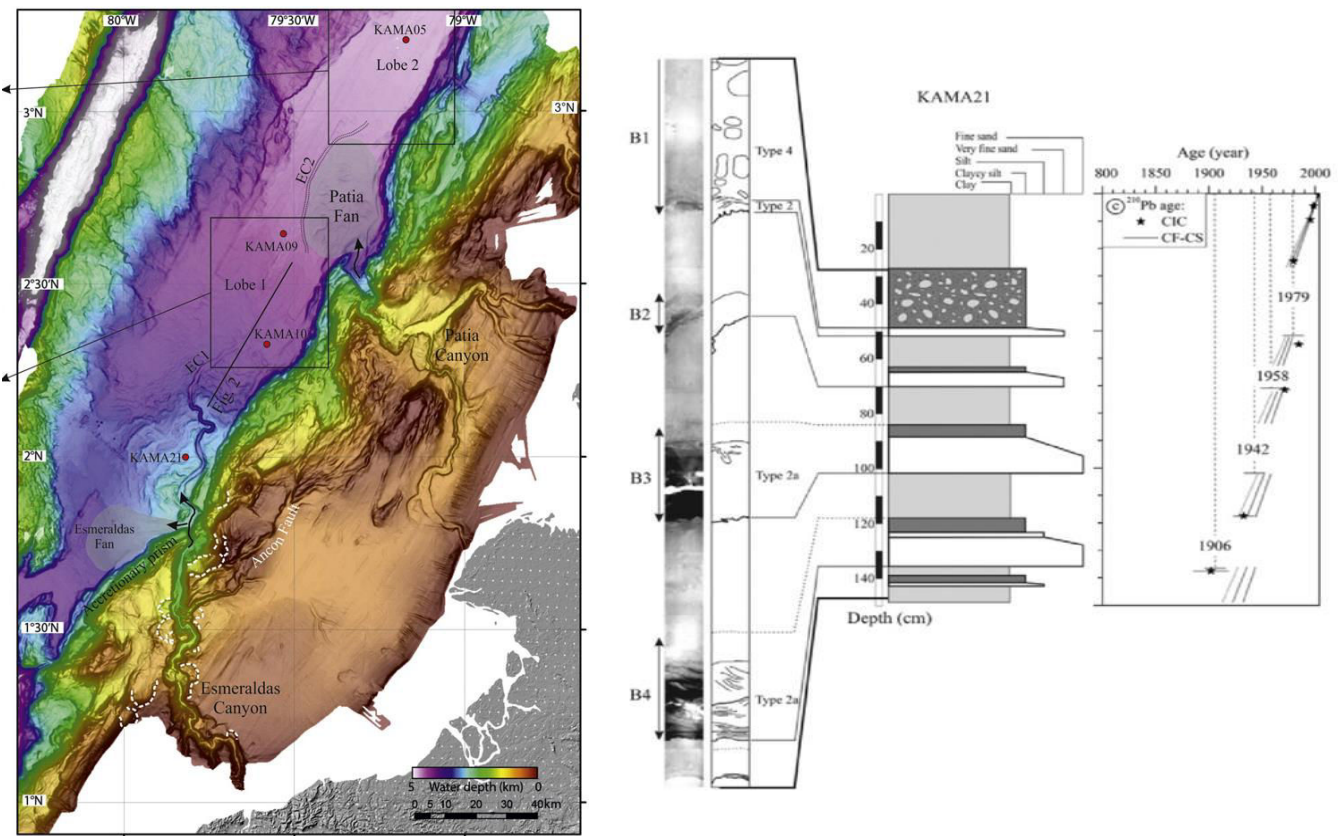


Fig. 2. 15 Left: location of the core KAMA 21 along which 4 sedimentary records of the mega-earthquake were identified. Right: Graphic-core log of the first (top) 150 cm of core KAMA21 into the Esmeraldas Turbidites System (Migeon et al., 2016). The X-ray image and its interpretative drawing reveal the presence of four main coarse-grained layers (B1 to B4) interpreted as earthquake-triggered deposits. The age model is based on  $^{210}\text{Pb}$  excess. The four main earthquakes that affected the north Ecuador/south Colombia margin during the 20th Century are located on the age model.

## 2.7 Partial conclusions: objectives and organization of this work

The Ecuadorian margin thus appears as a very segmented margin (Fig. 2.16) both 1) from the morphological point of view (Collot et al., 2009), 2) and from the point of view of the source and quantity of sedimentary inputs to the trench (Calahorrano et al., 2008) 3)



and from the point of view of the distribution of seismology, especially of large earthquakes (Collot et al., 2004, Font et al., 2013, Chlieh et al., 2004, Nocquet et al., 2014). Sediment deposits along the trench should therefore be expected to be non-homogeneous and show significant lateral variability (Gonzalez et al. 2016). And that in particular the sedimentary record in response to a large earthquake is not identical and uniform throughout the trench. Indeed, both stratigraphic and tectonic heterogeneities of the continental slope, will produce areas of localized weaknesses, which stimulated by an earthquake will promote and guide the destabilizations. The nature of sediments, their content of fluids, and their style of deformation are important parameters that will, in terms of slip (frequency, volume, distribution, nature), result in a heterogeneous response (Harders et al., 2011) along the continental slope.

Finally, the work carried out on the KAMA21 sedimentary core (localization Fig. 2.15 and 2.16) of the AMADEUS campaign (2005) has made it possible, thanks to new sedimentological criteria to distinguish seismo-turbidites from climatic turbidites, to identify at the outlet from the Esmeraldas Canyon the complete sequence of the great earthquakes of the 20th century (Fig. 2.16) (Migeon et al., 2017). Conversely, in the trench segment located at the right of the rupture zone of the 1942 and 2016 earthquakes, the sequence of the 20th century was not recognized. On the other hand, many turbidites whose frequency is compatible with that of  $M_w > \sim 8$  earthquakes in the zone, and several recent "Mass Transports Deposit" (MTD) at 22 kyr are identified (Ratzov et al., 2010).

How will the variability and segmentation of the margin be translated into the sedimentary filling of the trench? How are the factors that vary along the margin (fracturing, circulation of fluids, rock nature, instabilities) will translate into landslides (in terms of frequency, volume, distribution, nature)? In areas of unstable slopes north and south of the impact of the Carnegie Ridge, what are the modalities of mass transfers along the slope? Are these shifts polyphase? Can we date them? What is the influence of the asperities (reliefs) carried by the plunging plate on the distribution of the landslides? Are the major earthquakes recorded at the mouth of the Esmeraldas Canyon also recorded in the northern segment of the trench? If so, how were they recorded in the sedimentation in this open margin area, which will tend to disperse the slipped material, while the Esmeraldas Canyon will tend to concentrate it?

It is to try to answer these questions, that the new data of multibeam, Chirp and coring were acquired all along the trench of Ecuador during the Atacames campaign. In my study, these high resolution and superficial data were supplemented by the use of oil seismic data, which pass transversely over the trench every 4 kilometers. In the following chapters, we propose from the analysis of these data:

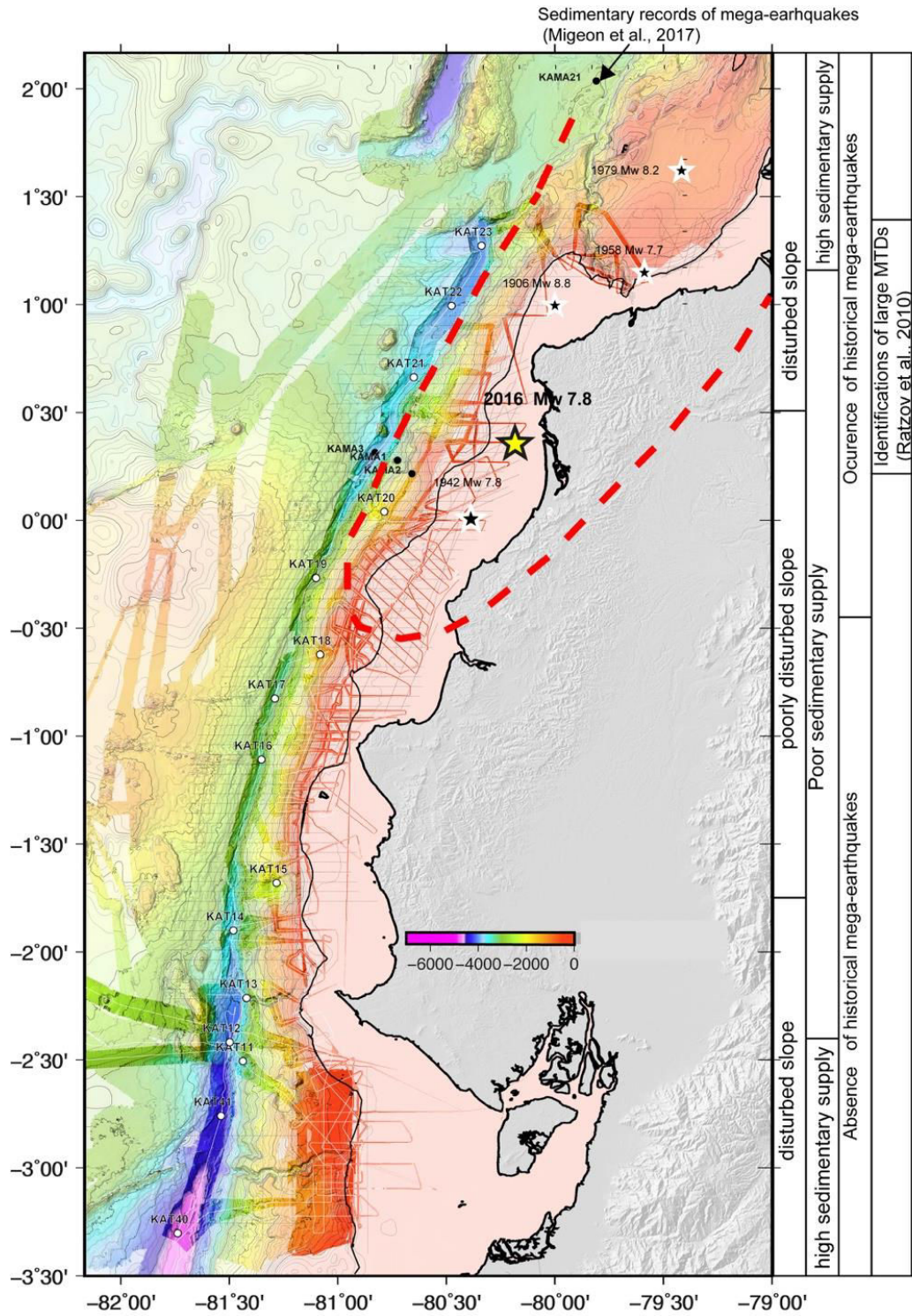


Fig. 2. 16 Illustration which resumes the segmentation of the Ecuadorian margin. In this figure, we have located the new data of Atacames (dark colors and white lines). The new cores are white circles. The thin black lines correspond to SHE seismic lines. The locations of the mega-earthquakes epicenters correspond to the stars (from Nocquet et al., 2014). The thick red dotted-line corresponds to the rupture zone of 1906 earthquake.

To specify the nature and distribution of the sediment filling of the trench. It will mainly be based on data from the Chirp and cores to describe the facies and their distribution in the trench. This is the purpose of Chapter 4 which, in the form of a draft article, deals with sedimentation at the regional scale in the trench.

To study in detail the setting up and the chronology of the destabilization of the margin and associated massive gravitational slumps, in the framework of the successive subduction of seamounts. This will be based on the interpretation of bathymetry, seismic (Chirp, THR and oil) and core data, to clarify the role of the impact of seamount subduction on the sedimentation of the sea. subduction margin of Ecuador. This is the subject of Chapter 5 in the form of a draft article, dealing with the filling of the Ayampe slope basin (Fig. 2.3 and 2.5).

To determine in the northern segment of the trench, where large historical earthquakes are listed, what are the paleo-seismological indicators in the trench? The earthquakes of the 20th century have been recognized further north at the mouth of the Esmeraldas Canyon, which can be explained by the fact that the canyon drains sedimentary transfers from the ground almost permanently and concentrates them at the mouth of the canyon. Conversely, at the rupture zone of 1942 and 2016, no canyon or major river supplies sediment to the slope and the trench so that the continental slope, main source of clastic material, may not be sufficiently recharged with sediment between two earthquakes, resulting in an incomplete paleo-seismic archive.

The first step is to analyze the new data to clarify the distribution and age of the various slipped masses highlighted by Ratzov et al., in 2010. The analysis of the oil seismic profiles will allow to extend in the time the analysis and the source of the masses slipped older in the sedimentary filling of the trench. In a second step it is a question of looking in the cores for clues allowing to associate the slipped material with seismological events and to recognize the sequence of mega-earthquakes. This is the purpose of chapter 6, which in the form of a draft article analyzes the modalities of sedimentary transfers in the northern sector of the trench.

## References

- Beck, S.L. and Ruff, L.J. (1984). The rupture process of the great 1979 Colombia Earthquake: Evidence for the asperity model. *Journal of Geophysical Research* 89: doi: 10.1029/JB080i011p09281. issn: 0148-0227.
- Calahorrano, A. (2005). Structure de la marge du golfe de Guayaquil (Equateur) et propriétés physiques du chenal de subduction, à partir de données de sismique marine réflexion et réfraction. PhD's thesis from University Pierre et Marie Curie Paris VI.
- Calahorrano, A., Sallarès, V., Collot, J. Y., Sage, F., & Ranero, C. R. (2008). Nonlinear variations of the physical properties along the southern Ecuador subduction channel: Results from depth-migrated seismic data. *Earth and Planetary Science Letters*, 267(3), 453-467.
- Chlieh, M., de Chabalière, J.B., Ruegg, J.C., Armijo, R., Dmowska, R., Campos, J., and Feigl, K.L., (2004), Crustal deformation and fault slip during the seismic cycle in the north Chile subduction zone, from GPS and InSAR observations, *Geophys. J. Int.*, 158, 695 – 711, doi:10.1111/j.1365-246X.2004.02326.x
- Chlieh M., Mothes P.A., Nocquet J.-M., Jarrin P., Charvis P., Cisneros D., Font Y., Collot J.-Y., Villegas-Lanzad J.-C., Rolandone F., Vallée M., Regnier M., Segovia M., Martin X., Yepes H., (2014) Distribution of discrete seismic asperities and aseismic slip along the Ecuadorian megathrust, *Earth and Planetary Science Letters* 400 (2014) 292–301
- Collot, J. Y., Marcaillou, B., Sage, F., Michaud, F., Agudelo, W., Charvis, P., ... & Spence, G. (2004). Are rupture zone limits of great subduction earthquakes controlled by upper plate structures? Evidence from multichannel seismic reflection data acquired across the northern Ecuador–southwest Colombia margin. *Journal of Geophysical Research: Solid Earth*, 109(B11).
- Collot J.Y., Michaud F., Alvarado A., Marcaillou B., Sosson M., Ratzov G., Migeon S., Calahorrano A., Pazmiño A., (2009): Visión general de la morfología submarina del margen convergente de Ecuador- Sur de Colombia: implicaciones sobre la transferencia de masa y la edad de la subducción de la Cordillera de Carnegie. In Collot JY, Sallares V, Pazmiño A (ed) *Geología y Geofísica Marina y Terrestre del Ecuador*. Publicación CNDM-INOCAR-IRD, PSE001-09, Guayaquil, Ecuador, pp. 47–74
- Collot J.-Y., Sanclemente E., Nocquet J.-M., Leprêtre A., Ribodetti A., Jarrin P., Chlieh M., Graindorge D. et Charvis P., (2017) Subducted oceanic relief locks the shallow megathrust in central Ecuador, *Journal of Geophysical Research: Solid Earth*, pp. online first, 2017.
- D'Acremont E., Leroy S., Beslier M-O., Bellahsen N., Fournier M., Robin C., Maia M., Gente P., (2005) Structure and evolution of the eastern Gulf of Aden conjugate margins

from seismic reflection data, *Geophys. J. Int.*, 160, 869-890, doi: 10.1111/j.1365-246X.2005.02524.x

Deniaud, Y., (2000) : Enregistrements sédimentaire et structural de l'évolution géodynamique des Andes Equatoriennes au cours du Néogène: Etude des bassins d'avant arc et bilan de masse. Thèse de l'Université de Grenoble (France), Géologie Alpine, Mémoire HS (32), 159p.

Deniaud Y., Baby P., Basile C., Ordoñez M., Montenegro G., Mascle G., (1999): Opening and tectonic and sedimentary evolution of the gulf of Guayaquil: neogene and Quaternary fore-arc basin of the south Ecuadorian Andes. *Comptes Rendus à l'Académie des Sciences, Paris* 328:181–187

Dufeu C., Proust J.-N., Gonzalez M., Pouderoux H. et Michaud F., (2016) Impact de la subduction de monts sous-marins sur l'érosion tectonique et la sédimentation des marges actives. Exemple de la marge en subduction d'Equateur, 25ème Réunion des Sciences de la Terre (RST 2016), vol. Livre des résumés, pp. 106, Caen (France), Octobre, 2016.

Font Y., Segovia M., Vaca S. and Theunissen T., (2013) Seismicity patterns along the Ecuadorian subduction zone: new constraints from earthquake location in a 3-D a priori velocity model, *Geophysical Journal International* (2013) 193, 263-286, doi: 10.1093/gji/ggs083

Gailler, A., Charvis, P., Flueh, E. R., 2007. Segmentation of the Nazca and South American plates along the Ecuador subduction zone from wide angle seismic profiles. *Earth and Planetary Science Letters*, 260, 3-4, 444–464

Graindorge D., Calahorrano A., Charvis P., Collot J.Y., Bethoux N., (2004): Deep structures of the margin and the Carnegie Ridge, possible consequence on great earthquake recurrence interval. *Geoph Res Lett* 31. doi:10.1029/2003GL018803

Goldfinger, C., Nelson, C.H., Johnson, J.E., et al. , 2003. Deep-water turbidites as Holocene earthquake proxies: the Cascadia subduction zone and Northern San Andreas Fault systems. *Annals of Geophysics* 46, 1169-1194.

Gonzalez M., Proust J.-N., Michaud F., Ratzov G. et Dufeu C., *Nature and distribution of recent sediments in the trench of the subduction margin of Ecuador*, 25ème Réunion des Sciences de la Terre (RST 2016), vol. Livre des résumés, pp. 144, Caen (France), Octobre, 2016.

Gutscher, M. A., Malavieille, J., Lallemand, S., & Collot, J. Y. (1999) : Tectonic segmentation of the North Andean margin: impact of the Carnegie Ridge collision. *Earth and Planetary Science Letters*, 168(3), 255-270.

Harders, R., Ranero, C. R., Weinrebe, W., & Behrmann, J. H. (2011). Submarine slope failures along the convergent continental margin of the Middle America Trench. *Geochemistry, Geophysics, Geosystems*, 12(6).

Jaillard E., Benitez S., Mascle G., (1997): Les déformations paleogènes de la zone d'avant arc sud-équatorienne en relation avec l'évolution géodynamique. *Bull Soc Géol France* 168:403–412

Jaillard, E. Lapiere, H., Ordoñez, M., Toro, J., Amortegui, A., Vanmelle, J., (2009): Accreted oceanic terranes in Ecuador: Southern Edge of the Caribbean plate?. *Geological Society Special Publication*, Geological Society, London, Special Publications (328), pp.469-485.

Kanamori, H. and McNally, K.C., (1982), *Variable rupture mode of the subduction zone along the Ecuador-Colombia coast*. *Bulletin of the Seismological Society of America*, 72 (4). pp. 1241-1253. ISSN 0037-1106. <http://resolver.caltech.edu/CaltechAUTHORS:20140814-084203152>

Loayza G., Proust JN, Michaud F, Collot JY, (2013). Evolution pléistocène du système de canyons du Golfe de Guayaquil (Equateur). Contrôles paléo-climatique et tectonique. 14e Congrès ASF, 5-7 Novembre, Paris.

Lonsdale, P., & Klitgord, K. D. (1978). Structure and tectonic history of the eastern Panama Basin. *Geological Society of America Bulletin*, 89(7), 981-999.

Marcaillou, B., Spence, G., Collot, J. Y., & Wang, K. (2006). Thermal regime from bottom simulating reflectors along the north Ecuador–south Colombia margin: Relation to margin segmentation and great subduction earthquakes. *Journal of Geophysical Research: Solid Earth*, 111(B12).

Marcaillou, B., Spence, G., Wang, K., Collot, J. Y., & Ribodetti, A. (2008). Thermal segmentation along the N. Ecuador–S. Colombia margin (1–4 N): Prominent influence of sedimentation rate in the trench. *Earth and Planetary Science Letters*, 272(1), 296-308.

Marcaillou, B., Collot, J. Y., Ribodetti, A., d'Acremont, E., Mahamat, A. A., & Alvarado, A. (2016). Seamount subduction at the North-Ecuadorian convergent margin: Effects on structures, inter-seismic coupling and seismogenesis. *Earth and Planetary Science Letters*, 433, 146-158.

Martillo, C., 2016. Enregistrements stratigraphiques des cycles glacio-eustatiques et de la déformation durant le pléistocène le long la marge centrale d'équateur (exploitation des données de la campagne atacames). Unpublished PhD thesis, Nice University.

Michaud F, Collot J-Y, Alvarado A, Lopez E y el personal científico y técnico del INOCAR, (2006) República del Ecuador, Batimetría y Relieve Continental, publicación IOA-CVM-02- Post. INOCAR, Guayaquil.

Michaud F., Witt C., Royer J.Y., (2009): Influence of the Carnegie ridge subduction on Ecuadorian geology: reality and fiction: In Kay S, Ramos V, and Dickinson WR (eds) Backbone of the Americas: Shallow Subduction, Plateau Uplift and Ridge and terrane Collision. Geol Soc Am Memoir 204:217–228 doi:10.1130/2009.1204.10

Michaud, F., Proust, J. N., Collot, J. Y., Lebrun, J. F., Witt, C., Ratzov, G., ... & Penafiel, L. (2015). Quaternary sedimentation and active faulting along the Ecuadorian shelf: preliminary results of the ATACAMES Cruise (2012). *Marine Geophysical Research*, 36(1), 81-98.

Nocquet J.M., Mothes P., Alvarado A., (2009): Geodesy, geodynamics and earthquake cycle in Ecuador. *Geology and marine and onland Geophysics of Ecuador: from the continental coast to the Galapagos Islands*. In Collot JY, Sallares V, Pazmiño A (eds) *Geología y Geofísica Marina y Terrestre del Ecuador*. Publicación CNDM-INOCAR-IRD, PSE001-09, Guayaquil, Ecuador pp 83–94

Nocquet J.-M., Villegas Lanza J.-C., Chlieh M., Mothes P. A., Rolandone F., Jarrin P., Cisneros D., Alvarado A., Audin L., Bondoux F., Martin X., Font Y., Régnier M., Vallée M., Tran T., Beauval C., Maguiña Mendoza J.-M., Martinez W., Tavera H. et Yepes H., (2014): Motion of continental slivers and creeping subduction in the northern Andes, *Nature Geoscience*, vol. 7, n°4, pp. 287-291.

Nocquet J.-M., Jarrin P., Vallée M., Mothes P. A., Grandin R., Rolandone F., Delouis B., Yepes H., Font Y., Fuentes D., Régnier M., Laurendeau A., Cisneros D., Hernandez S., Sladen A., Singaicho J.-C., Mora H., Gomez J., Montes L. and Charvis P., (2016) Supercycle at the Ecuadorian subduction zone revealed after the 2016 Pedernales earthquake, *Nature geoscience*, DOI: 10.1038/NGEO2864

Patton, J.R., Goldfinger, C., Morey, A.E., Ikehara, K., Romsos, C., Stoner, J., Djadjadihardja, Y., Udrek, Ardhyastuti, S., Gaffar, E.Z., and Vizcaino, A., (2015), A 6600-year earthquake history in the region of the 2004 Sumatra-Andaman subduction zone earthquake: *Geosphere*, v. 11, no. 6, p. 1–63, doi:10.1130/GES01066.1.

Pedoja K, Ortlieb L, Dumont JF, Lamothe M, Ghaleb B, Auclair M, Labrousse B (2006) Quaternary coastal uplift along the Talara Arc (Ecuador, Northern Peru) from new marine terrace data. *Mar Geol* 228:73–91

Pedoja K., Dumont J.F., Lamothe M., Ortlieb L., Collot J.-Y., Ghaleb B., Auclair M., Alvarez V., Labrousse B., (2006b). Plio-Quaternary uplift of the Manta Peninsula and La Plata Island and the subduction of the Carnegie Ridge, central coast of Ecuador, *Journal of South American Earth Sciences* 22 (2006) 1–21, doi:10.1016/j.jsames.2006.08.003

Pouderoux H., Proust J.-N., Lamarche G., (2014). Submarine paleoseismology of the northern Hikurangi subduction margin of New Zealand as deduced from Turbidite record

since 16 ka, *Quaternary Science Reviews* 84 (2014), 116-131.  
<http://dx.doi.org/10.1016/j.quascirev.2013.11.015>

Ratzov, G., Collot, J. Y., Sosson, M., & Migeon, S. (2010). Mass-transport deposits in the northern Ecuador subduction trench: Result of frontal erosion over multiple seismic cycles. *Earth and Planetary Science Letters*, 296(1), 89-102.

Ratzov, G., Cattaneo, A., Babonneau, N., Déverchère, J., Yelles, K., Bracène, R., Courboux, F., (2015). Holocene turbidites record earthquake supercycles at a slow-rate plate boundary. *Geology* 43, 331-334.

Reyes P., (2013): Evolution du relief le long des marges actives : étude de la déformation Plio- Quaternaire de la cordillère côtière d'Équateur. *Sciences de la Terre*. Université Nice Sophia Antipolis, 2013. Français. NNT : 2013NICE4006.

Ryan, W.B.F, Carbotte, S.M., Coplan, J.O., O'Hara, S., Melkonian, A., Arko, R., Weissel, R.A., Ferrini V., Goodwillie A., Nitsche, F., Bonczkowski, J., and Zemsky, R., (2009): Global Multi-Resolution Topography synthesis, *Geochem. Geophys. Geosyst.*, 10, Q03014, doi: 10.1029/2008GC002332

Sage, F., Collot, J. Y., & Ranero, C. R. (2006). Interplate patchiness and subduction-erosion mechanisms: Evidence from depth-migrated seismic images at the central Ecuador convergent margin. *Geology*, 34(12), 997-1000.

Swenson J.L., Beck S.L., (1996) Historical 1942 Ecuador and 1942 Peru subduction earthquakes, and earthquake cycles along Colombia–Ecuador and Peru subduction segments, *Pure Appl. Geophys.* 146, 67–101.

Trenkamp R., Kellogg J.N., Freymueller J.T., Mora P., (2002): Wide plate margin deformation, southern Central America and northwestern South America, CASA GPS observations. *J S Am Earth Sci* 15:157–171

Vacherat A., Brichau S., Reyes P., Michaud F., Proust J-N, and Hernandez M., (2017). First constraints on the timing of the Ecuadorian Coastal Cordillera uplift and geodynamic implications. *Geophysical Research Abstracts* Vol. 19, EGU2017-14542, 2017 EGU General Assembly 2017

Van Andel et al., Ross Heath G., Malfait B.T., Heinrichs D., Ewing J.I., (1971) Tectonics of the Panama Basin, Eastern Equatorial Pacific, *GSA Bulletin* (1971) 82 (6): 1489-1508, doi.org/10.1130/0016-7606(1971)82[1489:TOTPBE]2.0.CO;2

Villamar, R., (2001). Subduction de la ride de Carnegie sous la marge d'Équateur : structure et déformation à partir des données de sismique multitrace. *Géologie Alpine*, t. 77



Witt C., Bourgois J., Michaud F., Ordoñez M., Jiménez N., Sosson M., (2006): Development of the Gulf of Guayaquil (Ecuador) as an effect of the North Andean Block tectonic escape since the lower Pleistocene. *Tectonics* 25. doi:10.1029/2004TC001723

Witt, C., Rivadeneira, M., Poujol, M., Barba, D., Beida, D., Beseme, G., & Montenegro, G. (2017): Tracking ancient magmatism and Cenozoic topographic growth within the Northern Andes forearc: Constraints from detrital U-Pb zircon ages. *Geological Society of America Bulletin*, 129(3-4), 415-428.

# Chapter 3

## Materials and Methods

### 3.1 Introduction

Most of the data used in the elaboration of this work was collected during the ATACAMES scientific cruise which took place from January 14<sup>th</sup> to February 21<sup>st</sup> of 2012. The word ATACAMES is an acronym for “Archivage de la Tectonique Active et du Climat le long de la Marge d’Équateur en Subduction”. This cruise was conducted by the French national scientific consortium “Geoazur” (Institut de Recherche pour le Développement, Centre National de la Recherche Scientifique, Université Pierre et Marie Curie, Université de Nice Sophia Antipolis) and Geosciences Rennes (Centre National de la Recherche Scientifique, Université de Rennes 1) in collaboration with the Universities of Guyane-Antilles and Lille (France), INOCAR (Ecuador), Escuela Politecnica Nacional (Ecuador) and the Exploration and Production Department of PetroEcuador (a branch of the National Petroleum Company of Ecuador).

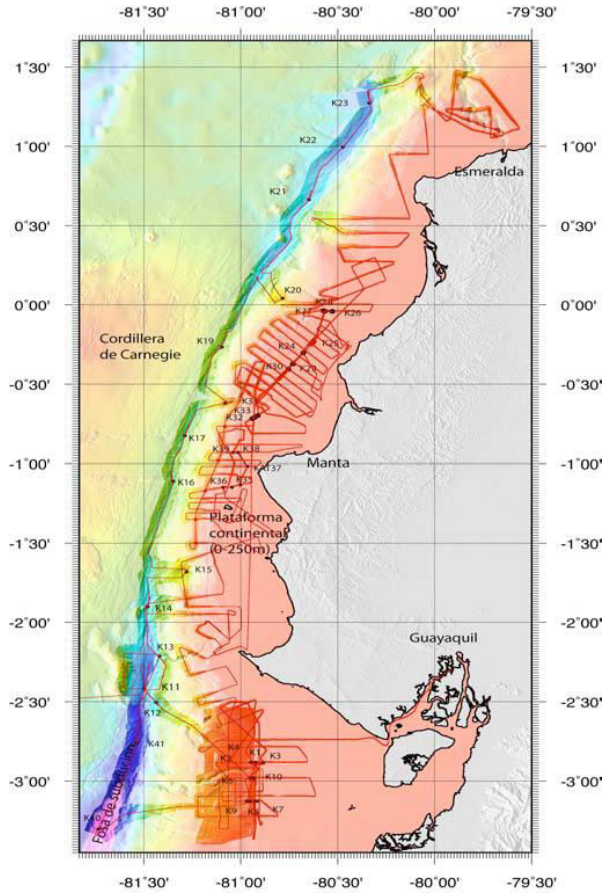


Fig. 3. 1 Location of the ATACAMES navigation track. In dark shade, multibeam from the Atacames cruise (grid spacing 50m). In the Gulf of Guayaquil Gemac campaign data, collected by INOCAR in 2009, are added. Numbers corresponds to the location of core.

The ATACAMES Expedition (Fig. 3.1) was carried out onboard of the research vessel L’Atalante belonging to the “Institut Français de Recherche pour l’Exploitation de la Mer” (Ifremer) with the technical support of the French Maritime Navigation Company “Genavir”, the “Institut National des Sciences d l’Univers” (INSU) and the “Centre National de la Recherche Scientifique” (CNRS) (Michaud et al, 2012).

During this scientific cruise, an area of about 20000 km<sup>2</sup> of the trench, the margin slope, the southern flank of the Carnegie ridge and the Ecuadorian continental shelf were mapped between latitudes 2°00’N and 3°00’S. This data was collected by using

multibeam bathymetry, back scatter imagery, 3.5 Kilo-Hertz mud penetrator, seismic reflection (~ 4500 km of profiles), and magnetic measurements. Additionally, 44 sedimentary cores (with a total length of ~168.3 m), taken both in deep and shallow sites, were collected for sediment analysis. These sedimentary materials were collected from surface layers of the sea floor along the continental shelf (26), the Carnegie ridge (3) and the subduction trench (15).

One of the purposes of the ATACAMES Expedition is to analyze the evolution of the Quaternary emerged and submerged reliefs along the active erosional subduction margin of Ecuador, with a special focus on the upper slope, between 100 m and 1000 m depth (Michaud et al, 2012).

## 3.2 Materials

### 3.2.1 Bathymetry

The main bathymetric dataset was collected during the Atacames campaign through the multibeam systems mounted on the research vessel L'Atalante, which comprise the EM710D and EM122 systems (Kongsberg Simrad). The EM710D system can be used to make measurements in shallow waters until about 1000 m depth, and the EM122 system can be used to scan the seafloor at greater depths until a limit of about 10000 m depth (Fig. 3.2). Each system is comprised by two rectangular arrays of transducers: one for the emission in the along-track direction and one for the reception in the transverse direction.

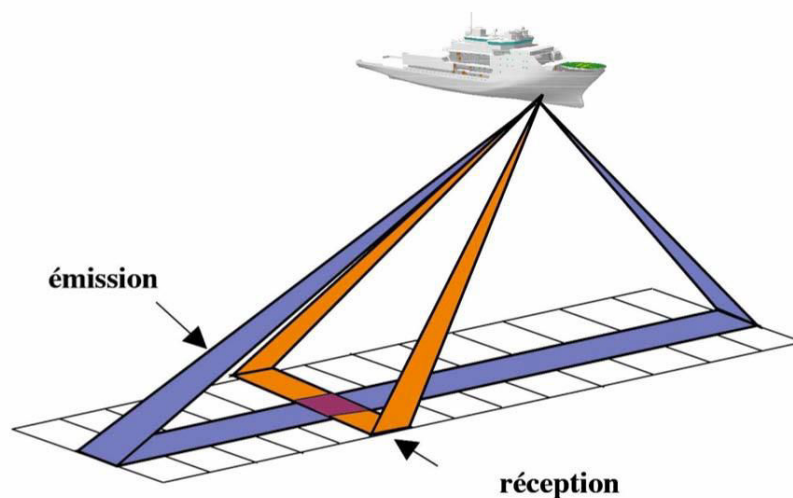


Fig. 3. 2 This diagram shows the emission and reception basics of the EM122 and EM710 systems. The acoustic wave is reflected by the seabed back to the antennas, which measure the signal in the form of a narrow fan shape in the transverse direction (Michaud et al, 2012).

The frequency of the emission acoustic signal for the EM122 system range between 11 - 13 kHz which allows mapping of the seafloor from 100m to 10000m depth. The EM710D

system has a range of frequency between 73 - 97 kHz. This frequency range allows mapping of the seafloor from 2m to 1000m. Practically the two devices work at the same time until 1000 m depth, then the EM710 stops. This dataset allows the construction of a digital elevation model with 25 m of spatial resolution for depth <-1000m and with 50m spatial resolution for depth > -1000m.

The Atacames bathymetry data were complemented with other datasets: a bathymetry grid from the Pugu-Salieri-Amadeus campaigns (2005), multibeam bathymetry data from Gemac campaign, collected by INOCAR in 2009, and single beam bathymetry data from I.O.A. 1:100000 nautical charts, collected by INOCAR in different years. (Martillo, 2016).

### 3.2.2 Seismic data

The seismic data (Fig. 3.3) used in this work consists of two datasets: i) the seismic reflection data acquired during the SCAN campaign (2009), and ii) the high-resolution seismic profiles (Chirp 3.5 Khz) acquired during the ATACAMES campaign (2012).

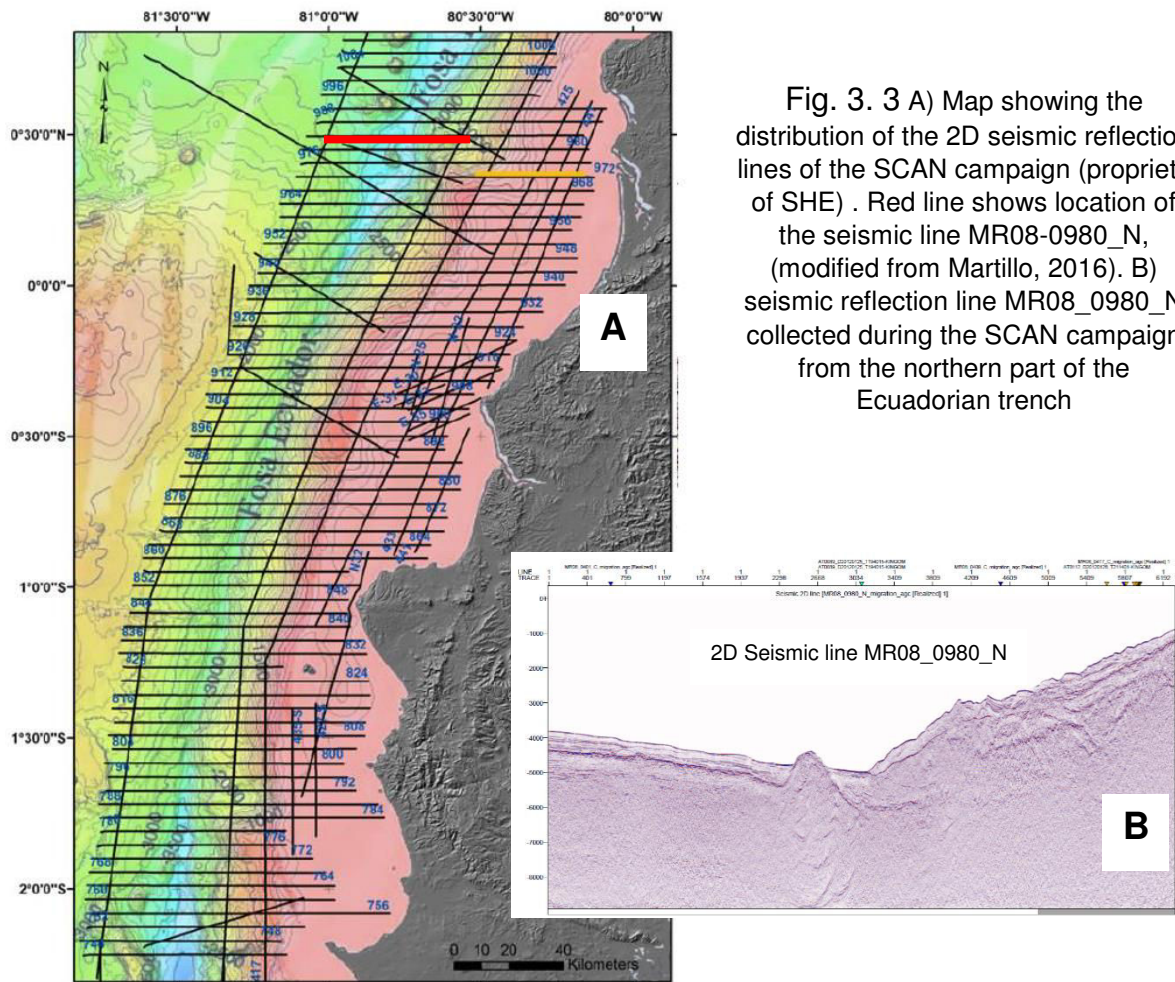


Fig. 3. 3 A) Map showing the distribution of the 2D seismic reflection lines of the SCAN campaign (propriety of SHE) . Red line shows location of the seismic line MR08-0980\_N, (modified from Martillo, 2016). B) seismic reflection line MR08\_0980\_N collected during the SCAN campaign from the northern part of the Ecuadorian trench

The 2D multichannel seismic reflection data, collected during the SCAN campaign, was shared by the “Secretaria de Hidrocarburos del Ecuador” (S.H.E. in Spanish) to GeaAzur. It consists of 78 multichannel profiles in E-W direction and 12 profiles with N-S direction. The acquisition parameters were: compressed air guns at 400 in<sup>3</sup> as source, distance source-receptor 183 m, shooting interval between points of 25 m. Flute length streamer 8000 m, streamer depth 8 m, number of traces 640, record time 9 s, sampling rate 2 ms. (Hernández, 2014). This data where used to precise the structures at large scale along the margin and to follow the trench sedimentary fill all along the trench.

The high-resolution seismic data was acquired with the sub-bottom profiler (SUBOP) mounted onboard of the research vessel L’Atalante during the ATACAMES campaign. With this device high-resolution seismic profiles of the surface layers along the trench, the slope and some areas of the continental shelf were collected. This device is an IXSEA type system controlled by the computer system SUBOP. Usually this sub-bottom profiler is referred as “Chirp 3.5 KHz” due to the frequency range of its emission signal. The SUBOP computer system configuration selected for data-acquisition during the ATACAMES scientific cruise is the following:

Chirp signal length:	80 ms (deep water) / 50 ms (shallow water)
Signal frequency swath:	1.8 KHz – 5.3 KHz
Imbrication of shots:	800 ms (or 1.1 ms)
Power (Deep water > 1000 m) (Shallow water < 1000 m)	80% of the maximun SBP power 50% of the maximun SBP power

All the Chirp data acquired by the SUBOP system is stored under the SEG-Y format which is a standard easily readable by the free software “Seismic Unix” (Colorado School of Mines <http://www.cwp.mines.edu/cwpcodes/>). The seismic files have a maximum size of 100 Megabytes. The files are automatically designated with the date and time at which they were created. The file names have a prefix that identifies the expedition name (AT), the line number (0000), the date when this line was taken and the time in the Universal Time (UT) format. A suffix “.seg” (standing for SEG-Y) is also added. File name examples are as follows:

AT0089_D20120125_T205757.seg	Expedition name ATACAMES (AT), seismic line number 0089, taken in January 25 <sup>th</sup> of 2012 starting at 20h57’57” UT
AT0090_D20120126_T013113.seg	When a change of profile occurs immediately a new file is opened: expedition name ATACAMES (AT), seismic line number 0090, taken in January 26 <sup>th</sup> of 2012 starting at 01h31’13” UT

This data was used to characterized in detail the most recent sedimentary deposits along the trench and to identify the units sampled by cores. The Atacames chirp were analyzed



all along the trench; along the northern trench segment the Amadeus cruise Chirp data were used as a complement of Atacames cruise Chirp data.

During the Atacames cruise we have also recorded reflexion seismic data (for detail of the data acquisition, see Martillo, 2016). These data were located mainly on the platform which is out of the scope of this study. Nevertheless, in some locations along the trench, reflexion seismic were acquired and these data were used in this study (Fig. 3.4).

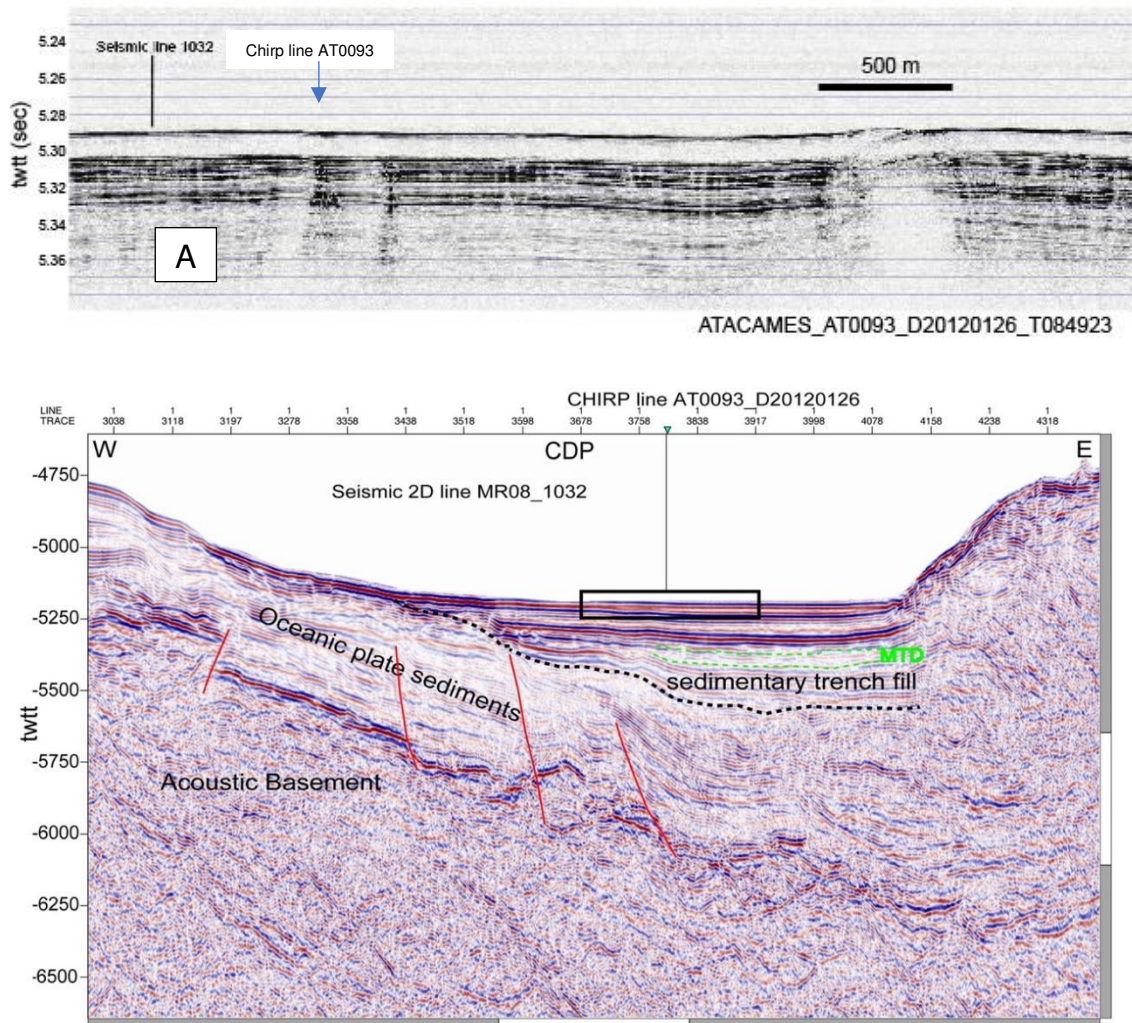


Fig. 3. 4 Illustration of the difference of resolution between Chirp and seismic data crossing the Ecuadorian trench. A) Example of the chirp line 0093 acquired along the northern part of the Ecuadorian trench, B) Example of seismic reflection line 1032 (propriety of the SHE) crossing the chirp line AT0093. The black rectangle corresponds to the vertical penetration of the Chirp image. This illustration shows that the Chirp data allows us to study the more recent sedimentary trench fill with high resolution; meanwhile the seismic data allows us to study the entire trench fill but with low resolution.

### 3.2.3 Deep Sea Sedimentary Cores

The 44 sediment cores collected during the ATACAMES campaign were acquired using a Kulleberg corer (Fig. 3.5). The principle of this device is based on the free fall of a steel core barrel into the soft sediment. After being lowered on a wire from the side of a ship, the piston corer approaches the seafloor preceded by the small gravity corer. Upon contact, the tripping arm "opens," sending the piston corer on a fast fall to the bottom. As the piston corer penetrates the seafloor, the piston inside stops at the sediment surface. The action of the piston creates a pressure differential at the top of the sediment column. This allows the soft material to enter the core liner without disruption. Within seconds, the process is complete. Crew on the ship then haul the wire in until the corer is free of the seafloor.

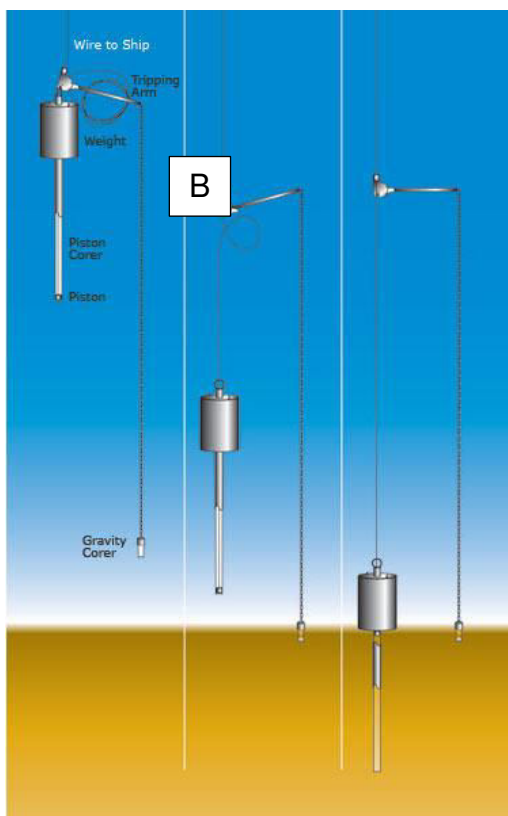


Fig. 3. 5 This diagram shows the main characteristics of the Kulleberg corer and it works. (Illustration by Fritz Heide, WHOI <http://www.whoi.edu/instruments/gallery.do?mainid=17288&iid=8087>)

## 3.3 Methods

### 3.3.1 Bathymetric analysis

The high-resolution bathymetry data collected during the ATACAMES scientific cruise was processed onboard L'Atalante using the software CARAIBES v3.8, developed by IFREMER. The ATACAMES bathymetry data was mainly focused in logging the geomorphological features of the trench, hence it did not cover the totality of the slope and the continental shelf. Nevertheless, we have used in this work a 50m spatial

resolution all along the trench which allow us to distinct some morphology with more details (Fig. 3.6).

At the margin scale, it is necessary to generate a general bathymetric map which allow us to make geomorphological analysis of all these areas. Consequently, the ATACAMES bathymetry data was complemented with multibeam bathymetry data from previous seismic campaigns such as: Pugu campaign, (2009); Amadeus campaign (2005) of the R/V L'Atalante (EM12 dual) compiled by Michaud et al (2006), Salieri cruise 2001 (EM122); GEMAC campaign (INOCAR, 2009) and single beam bathymetry data from I.O.A. 1:100.000 nautical charts from INOCAR (different years).

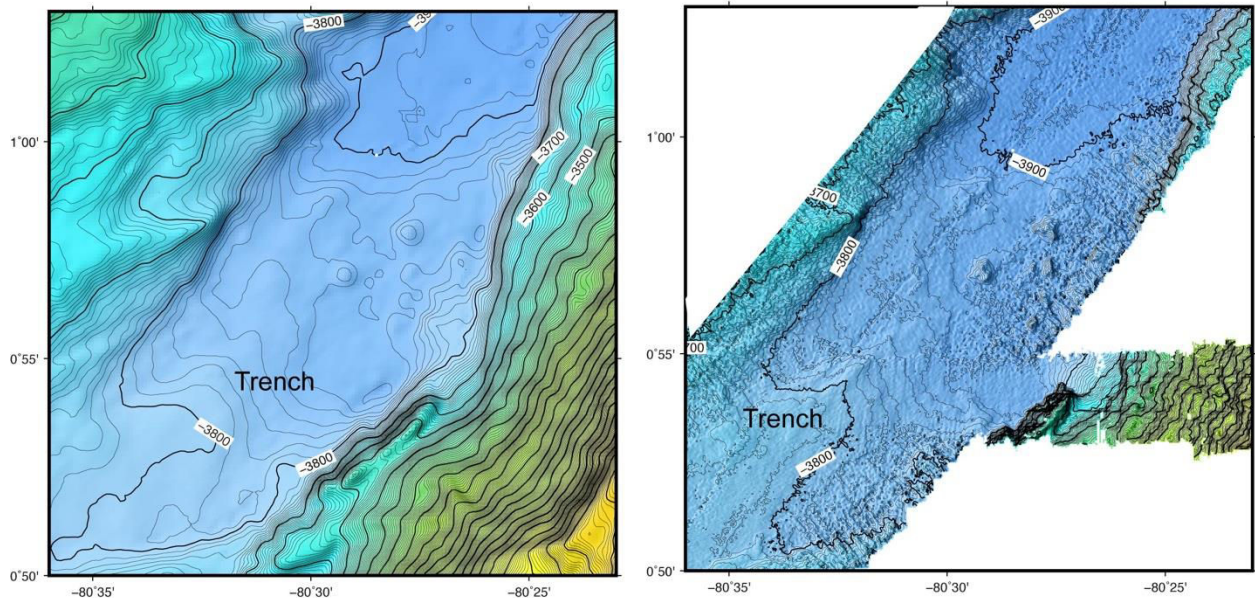


Fig. 3. 6 Comparison along a trench segment of the multibeam bathymetry before Atacames and after Atacames : to the left multibeam data before 2012 (150m grid Pugu-Salieri-Amadeus) ; to the right, multibeam data after 2012 (50m grid Atacames). The highest resolution allows us to distinguish some kilometer-size block on the trench seafloor (see following paragraph about the results).

We used in this work the grid realized by Martillo (2016). To generate this grid, all the bathymetry grids were homogenized to a 30m-resolution grid, and they were integrated using the Global Mapper G.I.S. application. The Pugu, Salieri and Amadeus multibeam bathymetry mainly covers the slope and trench of the Ecuadorian margin, and the front side of the Carnegie subduction (Fig. 3.7A). The INOCAR grid (from conventional data) includes data from the coastline to the edge of the continental shelf (Fig. 3.7B); The INOCAR grid from multibeam of Gemac cruise are located into the upper slope and the shelf of the Gulf of Guayaquil; and the ATACAMES data comprises the trench and some areas of the slope and the continental shelf (Figure 3.7C).

After merging the data from PUGU-SALIERI-AMADEUS, INOCAR and ATACAMES the resulting bathymetric map showed some gaps along the edge of the continental shelf (Fig. 3.7D). To avoid this the Inverse Distance Weighting (IDW) interpolation method, from the



Spatial Analyst Application of the ArcGis software, was used by Martillo (2016) to fill those gaps. As a result, it was possible to generate a homogenous bathymetric map with spatial resolution of 30 m, which allow us to have a general morphological context of the margin.

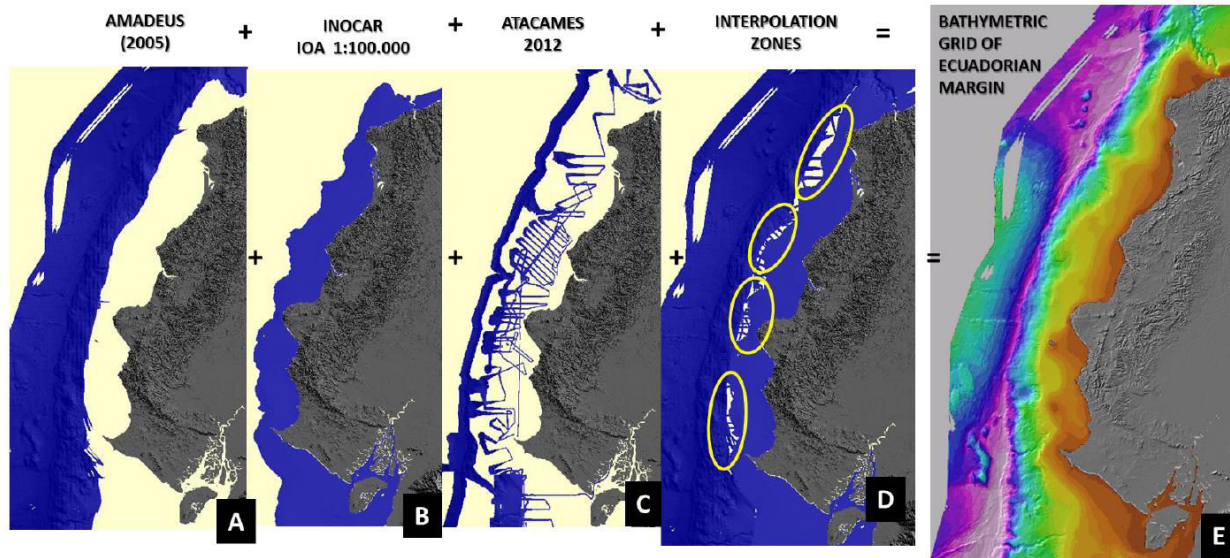


Fig. 3. 7 Bathymetry data from previous campaigns was used to build the 30-m bathymetric grid of the Ecuadorian margin. (Martillo, 2016). The different steps of construction of the grid used in this study

### 3.3.2 Core Description

#### 3.3.2.1 Split cores Observations

Along the Ecuadorian trench the 15 sedimentary cores were collected at depths between 1606 and 4698 m, and their lengths range from 2.92 to 9.47 m. The cores retrieved were divided into 1 m long sections and horizontally stored until their analysis in the laboratory. At the laboratory, the core sections were split in two halves, one for work and the another for the archive. All the cores were photographed with a digital camera and compiled with the Adobe illustrator CS6 software. The cores were described in terms of color, visually estimated grain-size, sedimentary structures, organic material and bioturbation. Based on these descriptions different lithofacies were identified. These visual descriptions were also used to determine locations for microfossil sampling for age dating using  $^{14}\text{C}$  radiometric method.

#### 3.3.2.2 Petrophysical parameters and High-resolution Photography

After visual description, non-destructive measurements of petrophysical parameters were carried out. Measurements of magnetic susceptibility, density, gamma ray, P-wave velocity and resistivity were performed using a GEOTEK multi sensor core logger. Besides high-resolution color photography of all cores was also taken.

### 3.3.2.3 X-ray Images

X-ray radiograph is a non-destructive method that allow us to determine the physical, biological and sedimentary structures inside a sediment core. The X-ray images are obtained by exposing the core to an X-ray source (160 kV, 19 mA). After X-rays pass through the sample, the high-energy brightness amplifier improves the contrast and a high-resolution camera, with a resolution of 756x581 pixels, detects the X-rays and supplies images to the computer.

In this work X-ray images came from two institutions. Images of cores 12, 14, 15, 16, 18, 20, 21, 40 and 41 were acquired with the SCOPIX system developed at the University of Bordeaux (Migeon et al, 1999). Images of cores 13, 17, 22 and 23 were acquired from the IFREMER – Centre de Brest (Plouzan).

### 3.3.2.4 Geochemical Analysis

For selected segments of some cores, along-core element relative abundance was performed using an X-ray fluorescence (XRF) core scanner AVAATEC. The analysis of major and trace elements in geological materials by x-ray fluorescence is made possible by the behavior of atoms when they interact with radiation. When materials are excited with high-energy, short wavelength radiation (e.g., X-rays), they can become ionized. If the energy of the radiation is sufficient to dislodge a tightly-held inner electron, the atom becomes unstable and an outer electron replaces the missing inner electron. When this happens, energy is released due to the decreased binding energy of the inner electron orbital compared with an outer one. The emitted radiation is of lower energy than the primary incident X-rays and is termed fluorescent radiation. Because the energy of the emitted photon is characteristic of a transition between specific electron orbitals in a particular element, the resulting fluorescent X-rays can be used to detect the abundances of elements that are present in the sample ([https://serc.carleton.edu/research\\_education/geochemsheets/techniques/XRF.html](https://serc.carleton.edu/research_education/geochemsheets/techniques/XRF.html)).

The core sections were measured every 5 or 1 mm, with energies of fluorescence radiation of 10 keV and 30 keV to reach a large spectrum of elements from Al to U. The elemental distributions are expressed in counts per second (cps), which is proportional to the chemical concentration (Tjallingii et al., 2007).

### 3.3.2.5 Age Dating

Chronological control of the sedimentary sequences analyzed in this work was obtained through  $^{14}\text{C}$  age dating. The measurements were performed through CNRS-INSU ARTEMIS program at Saclay CEA Laboratory. This technique involves dating of shells of planktonic foraminifera. In dating turbidites samples were taken below each turbidite because the boundary between the top of the turbidite tail and the hemipelagic sediment is difficult to identify reliably and bioturbation is concentrated at this boundary (Goldfinger et al, 2009).

Foraminiferal samples are dated using accelerator mass spectrometry (AMS) methods which can make use of as little as a ~1 mg carbon sample, which required the collection of about 10 mg of microfossil shells for each sample. Because the samples were taken in sub-aquatic environments the values were calibrated according to the Marine13 dataset (Stuiver and Reimer, 1993) with a local reservoir mean age of 434 years and  $\Delta R=29$ , using the CALIB Rev 7.0.2 software.

## References

- Hernández, M.J., 2014. Structures de la plateforme continentale de la marge d'Equateur à partir de l'interprétation de sismique pétrolière. Interaction plaque plongeante/plaque chevauchante et segmentation de la marge. Université de Nice Sophia-Antipolis. Master Pro2 AGI Sciences de la Terre et Environnement.
- Goldfinger, C., 2009. Sub-Aqueous Paleoseismology. Chapter 2B from book Paleoseismology edited by James P. McCalpin. International Geophysics Series. Vol. 95, second edition. 119-170.
- Martillo, C, 2016. Stratigraphic Record of the Glacio-eustatic Cycles and the Deformation during the Pleistocene along the Central Ecuadorian Margin (Using the ATACAMES Data Campaign). PhD Thesis. Université de Nice-Sophia Antipolis – UFR Sciences.
- Michaud, F., Proust, J.N., Collot, J.Y., Lebrun, J.F., Witt, C., Ratzov, G., Pouderoux, H., Martillo, C., Hernández, M.J., Loayza, G., Peñafiel, L., Schenini, L., Dano, A., González, M., Barba, D., De Min, L., Ponce, G., Urresta, A., Calderón, M., Depretz de Gesincourt, O., 2012. The ATACAMES Expedition.
- Migeon, S., Weber, O., Faugeres, J.C., Saint-Paul, J., 1999. SCOPIX: A new X-ray imaging system for core analysis. *Geo-Marine Letters* 18, p. 251-255.
- Stuiver, M., and Reimer, P.J., 1993. Extended  $^{14}\text{C}$  data base and revised CALIB 3.0  $^{14}\text{C}$  age calibration program. *Radiocarbon*, Vol. 35, No. 1, p. 215-230.
- Tjallingii, R., Rohl, U., Kolling, M., Bickert, T., (2007). Influence of the water content on X-ray fluorescence core-scanning measurements in soft marine sediments. Published by the American Geophysical Union and the Geochemical Society, *Geochemistry, Geophysics, Geosystems*, Volume 8, Number 2, Q02004, doi:10.1029/2006GC001393, ISSN: 1525-2027

## Chapter 4

### Sedimentary filling of the Ecuadorian subduction trench: An overview

#### 4.1 Introduction

Deep-marine subduction trench sediments have several sources. The first source is the oceanic plates sediments, which passively are conveyed by plate motions into the trench during subduction. The second source is the lateral input from the forearc with axial transport of sediments along the trench from distant areas. The last source results from the development of a sedimentary wedge along the foot of the outer-wall of the trench. This wedge is developed by the lateral input from the fore-arc which produce two principal contrasting trench deposits: blocky and debris flow deposits locally derived from the lower and middle slope of the inner-wall of the trench, or from more distant source as the upper slope and shelf break; and relatively fine grained deposits supplied to the trench and lower slope by turbidity currents. This sediments infill and drape the uneven topography of the oceanic plate with a sheet-like geometry onlapping the peripheral outer-wall slope.

Part of these sediments accumulated in the trenches is commonly dragged with the down going plate beneath the upper plate margin. This down going sediments form the so-called subduction channel (Calahorrano et al., 2008), which is structurally squeezed between upper and lower plates. The physical properties of the subduction channel material deeply rely on sediment supply and nature, water content and fluid pressure variations, which are believed to play a major role in controlling deformation processes and fault dynamics along subduction zone megathrusts. The nature and amount of sediment into the trench are known to control the subduction processes (erosion/accretion) and the earthquake occurrence. Some authors consider that the sediments lubricate the interplate contact (Shreve and Cloos 1986) while others think that they increase the coupling (Ruff, 1989). Among these, one of the major remaining questions is whether the segmentation of active margin controls the sediment supply, in terms of slide and slump frequency and size, and consequently the subduction channel and the occurrence of large earthquakes.

One characteristic of the Ecuadorian margin is, across the forearc, the presence of a coastal cordillera, which diverts the sediments supply from the Andes to the north and to the south: (a) towards the Esmeraldas river in the North, which transfers sediments into the trench through the Esmeraldas canyon; and (b) towards the Guayas river in the south, which transfers sediments to the Gulf of Guayaquil and the trench through the canyon of Guayaquil. Therefore, the Coastal Cordillera uplift, inferred to be related to the subduction of the Carnegie Ridge controls the distribution of sedimentary supply into the trench. Consequently, in contrast, in front of the Carnegie ridge, very few terrestrial sediments have been deposited in the trench. Indeed, in this area, the detrital material mainly comes from the costal cordillera; as the relief of the coastal cordillera is less steep that the Andes, the quantity of material transferred from these areas to the trench is less than the material transferred northward and southward from the Andes. Moreover, this material is partially trapped and accumulated on the continental shelf and the slope basins. Consequently, in front of the Carnegie ridge,

the amount of material, which reaches the trench, is less important and lacks in many places. Another characteristic of the Ecuadorian margin is that the margin is seismically segmented. To the North large earthquakes have occurred meanwhile, southward large earthquakes are not reported (Chieh et al., 2014; Nocquet et al., 2016). Until now the distribution and nature of the trench fill of the Ecuadorian margin is poorly known (Calaharano et al., 2008; Collot et al., 2009). New Chirp and core data together with low-resolution seismic data allow us to precise at different scales the distribution and the nature of the sedimentary infill of the trench all along the Ecuadorian margin. This distribution will be related to the destabilization features revealed by the available multibeam bathymetry and later tentatively compared to the mega earthquakes sequence repartition along the margin.

## 4.2 Geologic and Tectonic Settings

In Ecuador, the Nazca Plate is subducting at a velocity of c. 4.7 cm/y with respect to the South American Plate (Trenkamp et al., 2002, Kendrick et al., 2003) (Figure 4.1). The evolution of the margin is strongly influenced by the subduction of the Carnegie aseismic Ridge, which corresponds to the track on the Nazca plate of the Galapagos Hot Spot (Lonsdale, 1978, 2005; Sallarès and Charvis, 2003). The subduction of the Carnegie Ridge (CR) and the obliquity of the subduction influence the motion toward the North of the North Andean Block (NAB) (Ego et al., 1996; Dumont et al., 2005; Nocquet et al., 2009), the Nazca Plate subducting at only 4.7 cm/y below the NAB. The northern Ecuadorian margin has experienced a Mw 8.8 mega-earthquake in 1906 (Kanamori & Given, 1981), the 7th world largest earthquake ever recorded by seismometers. This major event has been followed by three 7.6-8.2 earthquakes in 1942, 1958, 1979 that are considered to have ruptured consecutively, from South to North, part of the 1906 rupture zone. On April 16th, 2016, a 7.8 magnitude earthquake hit the Ecuadorian coast at the same location than the 1942 earthquake (Nocquet et al., 2016).

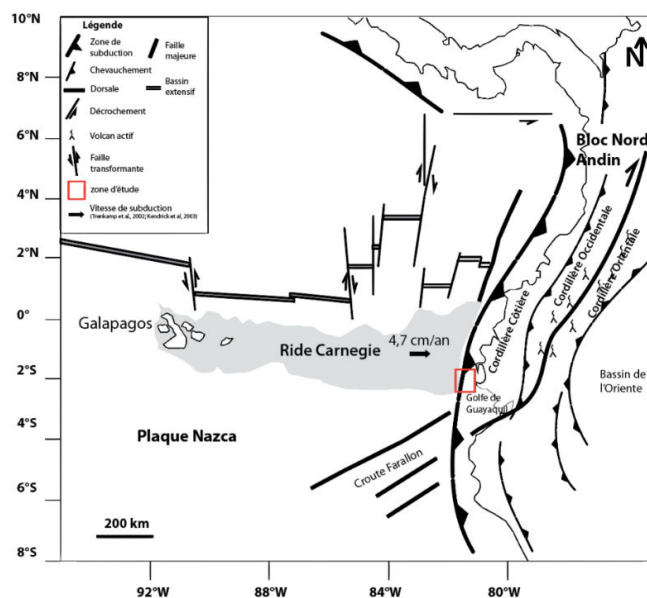


Fig. 4. 1 Geodynamic setting of the north andean margin (modified from Gutscher et al., 1999)

The subduction of the CR is supposed to generate an excess of coastal uplift of 0.2-0.3 mm yr<sup>-1</sup> of the northern part of the Talara Arc - a 1000-km-long stretch of the coast of Ecuador and northern Peru, characterized by subduction with a concave landward plane-view (Pedoja et al., 2006b) and the segmentation of the Ecuadorian margin into three morphological zones, *i.e.* northern, central and southern segments (Gailler et al., 2007; Collot et al., 2009). The northern segment, at Punta Galera point, and the southern segment, at Salinas Cape, are located respectively to the north and south of the CR whereas the central segment, in the middle, faces the top of the CR (Figure 2).

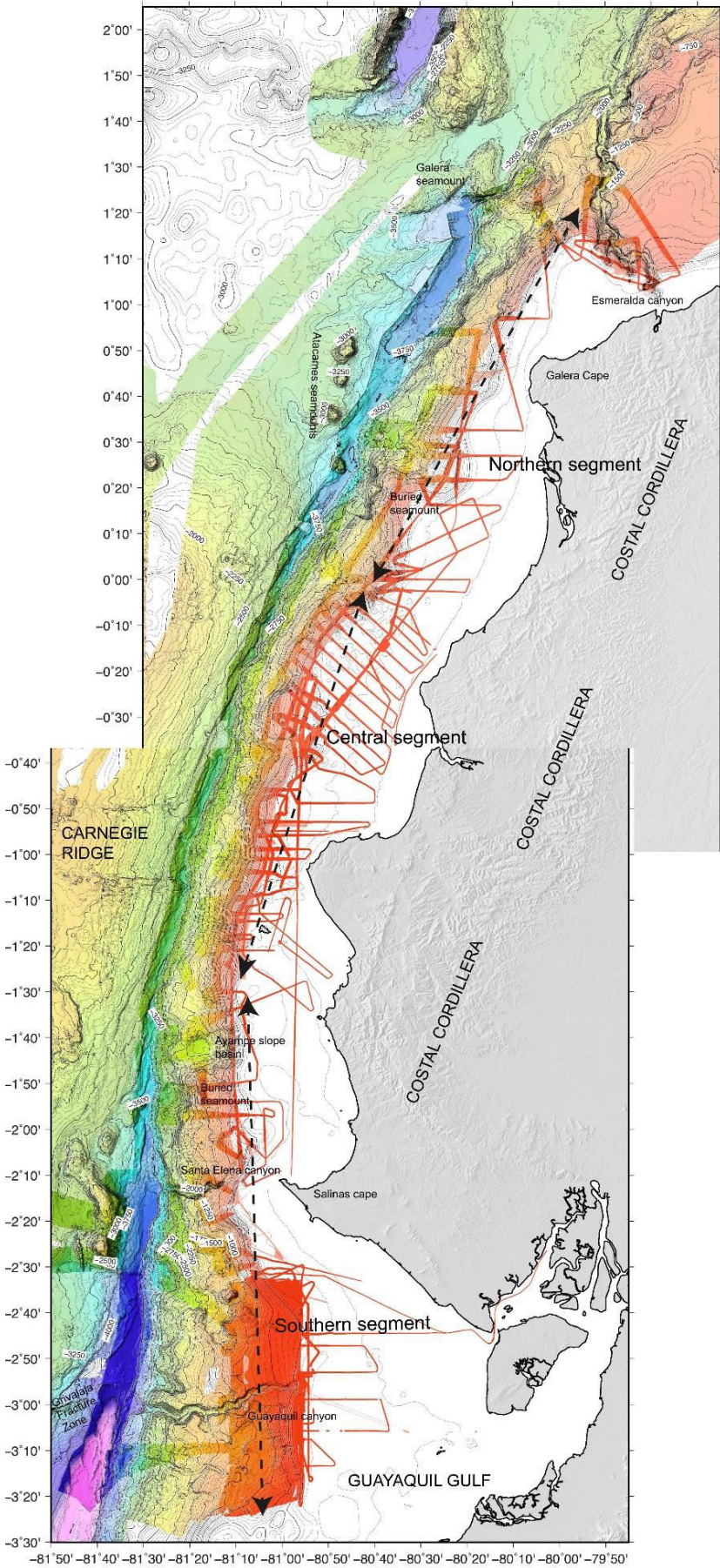
The oceanic Nazca plate shows a wrinkled morphology with blade reliefs (5000 m large and 400 m high), scarps of SW-NE-oriented normal faults and seamounts (Figure 4.2), (Collot et al., 2009). The outer-wall of the trench exhibits escarpments related to the flexure of the oceanic plate corresponding to SW-NE trending normal faults. This roughness participates in the destabilization of the slope of the continental margin (Sage et al., 2006) which is characterized by a poorly developed accretionary prism, *e.g.* presence of 5km-large fans of recent sediments, landslides, scarps and rubbles, gullies, promontories and canyons (Figure 4.2) with consequences on the seismicity in this zone (Bethoux et al., 2011; Font et al., 2013; Vallée et al., 2013).

Little is known of the geology of the continental shelf, the slope and the trench. Onshore, the coast shows Cretaceous age basalts (Piñon Formation) overlapped by marine volcanoclastics (Cayo Formation) and Mio-Pleistocene sediments filling the Borbón, Manabí and Progreso forearc basins (Benitez, 1995; Jaillard et al., 1996; Deniaud et al., 1999). Some large NE-SW and EW regional faults can be observed on land but only a few of them show a well-established offshore extension (*e.g.* Jama fault, Montecristi fault). The Pleistocene marine deposits of the Canoa and Tablazos formations, which drape most of the shelf, are well exposed along extensive cliff exposures at the coast (Di Celma et al., 2005; Reyes, 2013).

The marine terraces of the Tablazos formation crop out along the Talara Arc and record the vertical ground motion superimposed on Quaternary global sea level oscillations (Pedoja et al., 2006b, 2014; Proust et al., 2016). The slope shows strong lateral variabilities on swath bathymetry data that led to distinguish several segments along the margin based on internal velocity structures (Gailler et al., 2007), variations in the trench-shoreline distances and the changes in the structural pattern along the margin (Collot et al., 2009). The trench is oriented N14E and reaches 4700 m in depth South of the Grijalva fracture zone (GFZ). The trench has a horizontal seafloor underlain by an estimated ~ 0.8 km of trench sediments deposits (Calahorrano et al., 2008). Towards the North, from the trench-GFZ intersection until 1°35'S, the trench changes to an approximately N-S direction and the sediment fill thins out. Northward, the trench rises successively through discrete steps, forming a series of narrows and closed flat-floor basins including the point where the trench is shallowest (2880 m) at the latitude 0°20'S. Further to the north around 0° latitude, the trench has a N27E orientation; escarpments related to the flexure of the oceanic plate, together with the deformation front, define small trench-basins (Ratzov et al., 2010) while the trench is deepened to the north until the 3900 m.



Fig. 4.2 Bathymetric map of the active subduction margin of Ecuador showing the main morpho-tectonic elements particularly the three different segments.





The interplay of the Galapagos hotspot with the Galapagos spreading centre during the Neogene led to the formation of two hotspot tracks, the Cocos and Carnegie Ridges (Lonsdale and Klitgord, 1978; Sallares and Charvis, 2003). The Carnegie Ridge is composed of two segments separated by a topographic low (saddle) at 2400-m depth. The western segment, including the Galapagos Islands and the Galapagos platform, is less than 1000 m deep. The eastern segment rises up to 700 m depth near its intersection with the subduction trench.

### 4.3 Data and Methods

The study is based on the analysis of low and very high-resolution seismic data, bathymetric data and core data collected along the Ecuadorian trench (Michaud et al., 2014, 2015), (Figure 4.3).

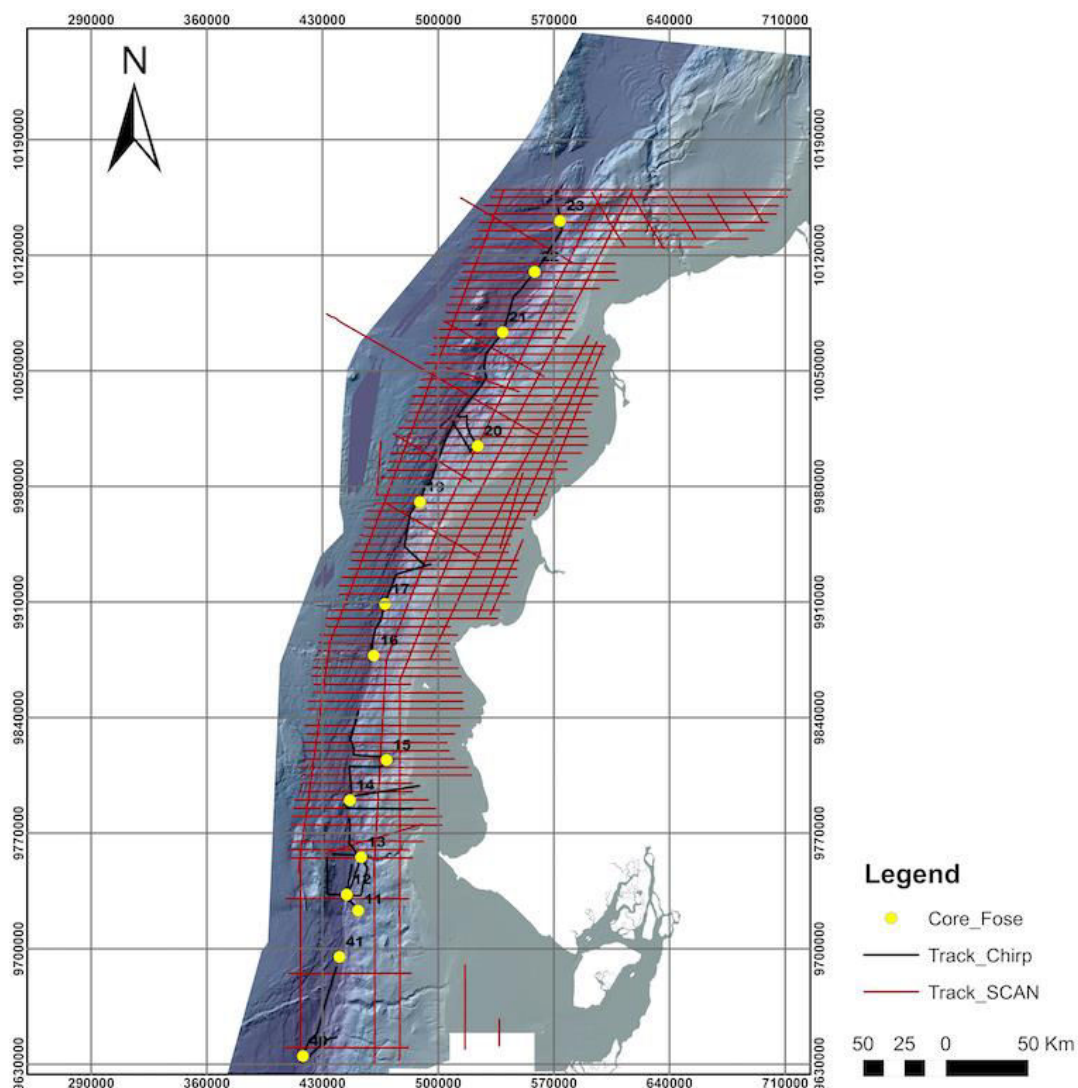


Fig. 4. 3 Bathymetric map of the Ecuadorian trench showing the location of the cores, the high-resolution CHIRP seismic lines and the low-resolution SCAN lines.

Deep penetration multichannel seismic reflection (MCS) data were obtained across the Ecuador margin during the SCAN cruise (Figure 4.3). MCS data were recorded

using a 4000 in3 air gun seismic source, and a 640 -channel, 8-km-long 8m-depth streamer. Shots were fired every 25 m providing 160 folds coverage with a distance of 183m between the source and the first channel. Very high-resolution seismic data, bathymetry and core data were collected in the trench during the ATACAMES Expedition in the L'Atalante research vessel (Michaud et al, 2014; 2015) (Figure 4.4). The very high-resolution seismic data are comprised of c. 500 km of sub-bottom profiler (1.8 kHz to 5.3 kHz) acquired in a direction subparallel to the trench axis. The bathymetric data were acquired along the sub bottom profiler lines by using Kongsberg-Simrad EM710D and EM122. These data, completed by older multibeam of 50 m resolution (Michaud et al., 2006; 2009), provided a bathymetric grid with a 25 m large cell-grid size. 15 piston cores, 3 to 10 m-long, collected a few tens of km apart, in 4700-3500 m of water depth all along the trench axis, complete the dataset.

The seismic profiles were interpreted applying the criteria of seismic stratigraphy as originally defined by Mitchum et al. (1977) *i.e.* configuration, amplitude, continuity and frequency to identify seismic facies and the stratal termination patterns *i.e.* onlap, toplap, downlap, truncation and offlap, to discriminate the main surfaces bounding genetically related packages of seismic facies.

We use Caraibes (©Ifremer), ArcGis (©ESRI), Seismic Unix (©Colorado School of Mines) software to process respectively the bathymetric, the D-GPS and the seismic data and Kingdom Suite (©IHS) and Petrel (©Schlumberger) to interpret the seismic data. The depth conversion of the seismic data recorded in time was run by using a velocity of 1600 to 1900 m.s<sup>-1</sup> of sound in the sediment (*i.e.*, a velocity range used for seismic data processing) depending on the depth in the sedimentary record.

The cores were cut in 1m-long sections, then split for visual descriptions, photographed and sampled for <sup>14</sup>C age dating. The radiocarbon dates were calibrated to calendar years with a 399 ±30 yr marine reservoir age (Etayo-Cadauid et al, 2013) using CALIB Rev 7.0.2/Marine13 dataset (Stuiver and Reimer, 1993).

## 4.4 Results

This section shows the results obtained from the analysis of bathymetry, seismic and core data collected during the ATACAMES campaign in 2012 (Michaud et al., 2014; 2015) between the Esmeraldas canyon in the north and the Guayaquil canyon in the south (Figure 4.2).

### 4.4.1 Bathymetry data

Along the margin, the bathymetry allows us to define three distinct segments. The southern segment, including the slope front of the Gulf of Guayaquil, extends until 1°35'S. The central segment that characterizes most of the Ecuadorian margin extends from 1°35'S until 0° of latitude. The northern segment extends until 1°35'N latitude, north of Galera cape (Fig. 4.2).

**The southern segment of the margin** — This NS trending segment is characterized by two main canyons and by a rough morphology of the middle and lower slopes. This segment is shown on Fig. 2.4 from chapter 2. The Guayaquil canyon cuts deeply (up to 600-1000 m) the middle slope at about 1000 to ~ 2500 m in water depth. This

canyon is an important morphological boundary, transverse to the inner slope of the trench. It separates to the south a relatively smooth slope with the presence of an accretionary prism at the foot of the margin from a heavily disturbed slope with the presence of a poorly developed frontal prism to the north. Along the lower slope, the Guayaquil canyon does not cut the frontal prism. North of the Guayaquil canyon and until the Santa Elena canyon, the middle slope is in average steeper ( $3.5^{\circ}$ - $3.8^{\circ}$ ) and generally rougher than the upper slope, revealing a disturbed seafloor with reentrants, indicative of an extensive destabilization of the middle slope. North of the Santa Elena canyon and until of latitude  $1^{\circ}35'S$  the margin segment shows also a rough morphology (Sage et al., 2006) with a large re-entrant, 15 km wide and 35 km long, which breaches the margin until the upper slope, named the Ayampe slope basin (Martillo, 2016; Dufeu et al., 2016; see chapter 5). The Ayampe slope basin reveals escarpments of hundreds of meters high with slopes  $> 20^{\circ}$ .

The Ayampe slope basin is bounded to the South by a 150m-high, NS-oriented relief. This relief overlies a buried subducted oceanic seamount (Sage et al., 2006; Sanclemente, 2014). At the same latitude in a seaward direction, the foot of the margin is abruptly truncated by a 500-m high and  $23^{\circ}$  dip escarpment facing a rough topography into the trench suggesting mass transport deposits. South of this relief, several N-S trending 100-200m-high escarpments underline elongate steps, which are controlled by normal faults (Sage et al., 2006) affecting the middle and upper slope. Taken together, these morphological features along the slope indicate that this margin segment is very unstable and has been affected by the subduction of oceanic plate rough topographies. Consequently, along this segment, the sediment supply to the trench is controlled both by the destabilization of the slope at various scales and by the canyon activity which deeply cut the slope.

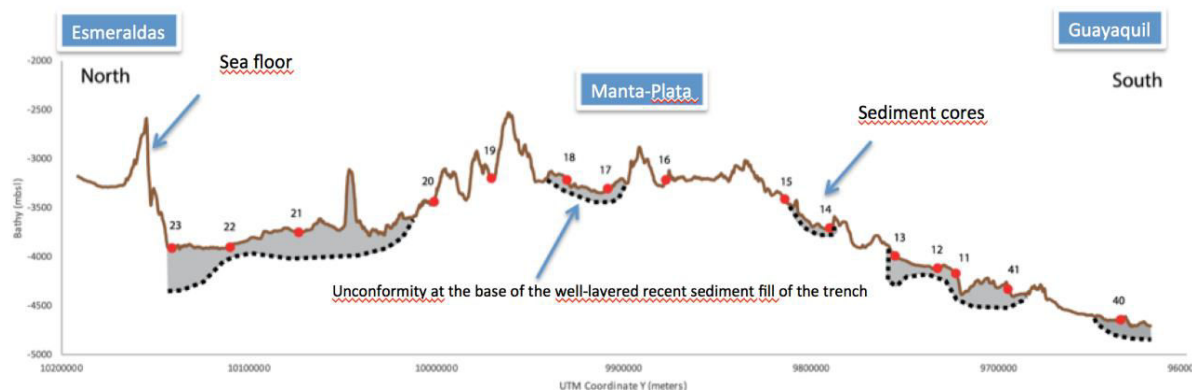


Fig. 4. 4 Topographic profile of the trench floor passing through the core sites. The core sites in slope basins are projected to the main line.

**The central segment of the margin** — The slope varies in direction from an orientation N-S to an orientation progressively more SSW-NNE north of latitude  $1^{\circ}35'S$ . This segment is shown in Fig. 2.5 from chapter 2. The trench direction changes to an approximately SSW-NNE direction and raises successively through discrete steps, forming a series of narrow, closed flat-floor basins that are displaced progressively laterally to the East. At the latitude  $0^{\circ}20'S$ , the trench reaches its shallowest point (2880 m in depth), (Figure 4.4).

Along this segment, the platform is relatively narrow, 40-50 km wide in average with a shelf break, which varies in water depth from 140 to 500 m. The platform edge shows by places, offshore La Plata Island, between 1°25'S and 1°05'S, landward curved re-entrances associated with concave lower slope interpreted as the trace of subducting seamounts (e.g. Sanclemente, 2014; Michaud et al., 2015), which landward displacement can be traced back from the analysis of the platform sediment fill (Proust et al., 2016).

In this area, between latitudes 1°35'S and 0° the slope of the margin is noticeably smoother than along the southern and northern segments. The upper slope shows flat topographies dipping seaward with slopes of ~ 6° alternating with wide and smooth depressions that concentrate networks of gullies. The middle slope exhibits small terraces structures with slopes of 2° between 1500 and 2200 m depth. The lower slope is irregular with flat zones, chaotic topographies and locally steep slopes up to 8° the deformation front, thus revealing some degree of instability.

**The northern segment of the margin** — Along this segment, the slope is more complicated and irregular than in the central segment. The trench axis shows an “en-échelon” geometry, and numerous plate bending-related normal faults affect the outer wall of the trench. This segment is shown in Fig. 2.6 from chapter 2.

The upper slope ranges from 200 to 1500 m in water depth. It exhibits a gentle slope gradient (3–5°) south of latitude 0°50'N, while north of this latitude, the slope is steeper (>7°). A 22 km-wide re-entrant located between 0°20'N and 0°35'N breaches the shelf break, and bounds a 25 km-wide, shallow promontory forming a spur on its southern flank. No other large scarps of slope failure affect the upper slope and the shelf break. The lower slope extends from 1500 to 3900 m in water depth and is characterized by steep scarps. Between 0°10'N to 0°25'N in latitude three interconnected, semi-circular, 5–6 km-wide scarps form a re-entrant up to 1500 m-high with slope gradients up to 30° in dip. These semi-circular scarps are surmounted by the shallow promontory describe above, which faces the N-S trending chains of Atacames seamounts.

Additional evidences from seismic reflection lead to assume the presence of a buried seamount beneath the shallow promontory (Marcaillou et al., 2016). From 0°25'N to 0°35'N latitude, the lower slope is convex upwards and exhibits a gentle slope gradient. This area is bounded upward by the wide re-entrant breaching the shelf break describes above, and downslope, by an arcuate body, which covers the trench floor. This morphological succession from the upper slope to the trench suggests that an old huge mass wasting occurs at this place. From 0°40'N to 1°30'N the lower slope exhibits a trench-parallel linear scarp. This up to 1000 m-high steep linear slope failure scarp is located in the prolongation of active faults system known northward (Collot et al., 2009). Between 1°10'N and 1°30'N the lower slope exhibits a 30 km-wide, triangular shape, 2000–2600 m-deep terrace. Seaward of the triangular terrace, the slope is affected by two semi-circular slope re-entrants 10–12 km-wide and 800 to 1000 m-high that are inferred to be recent, moderate-sized, failure scarps.

In summary, the slope of the central and northern segments of the margin is characterized by a relatively simple and undisturbed morphology (between latitudes 1°35'S and ~ 0°) bounded both southward (between 1°35'S and latitude 3 °30'S) and

northward (between 0° and Galera cape) by areas of deeply disturbed morphology, which reflect the history of recent subduction of a rough oceanic plate topography.

#### **4.4.2 Low resolution seismic data**

The analysis of the SCAN seismic lines confirms that small volumes of sediments fill the Ecuadorian trench (Figure 4.5). The maximum thickness is reached in the North (c. 400m) and in the South (c.300m). At the front of the Carnegie Ridge, the trench-fill is commonly lacunar with locally a maximum thickness of 100m. The basement of the trench fill is highly irregular (Figure 4.4). It is as deep as 4300 mbsl in the North (approx. at location of core 23, c.1°15'N) and 4800 mbsl in the South (approx. at location of core 40, c.3°0'S). At the front of the Carnegie Ridge, the basement is shallower with a succession of peaks (e.g. 2800 mbsl, approx. at location of core 19, 0°20'S) and lows (e.g. 3700 mbsl, approx. at location of core 17, 0°40'S).

On the westward side of the trench (Fig. 4.5), the basement is comprised of two seismic units bounded by a set of high amplitude reflectors. The lower unit shows a homogeneous chaotic facies when the upper unit exhibits a well-layered facies with regular, medium to high amplitude, high frequency and continuous parallel reflections. On the eastward side of the trench, the basement of the upper plate is comprised of a single unit of discontinuous to chaotic, high amplitude reflections.

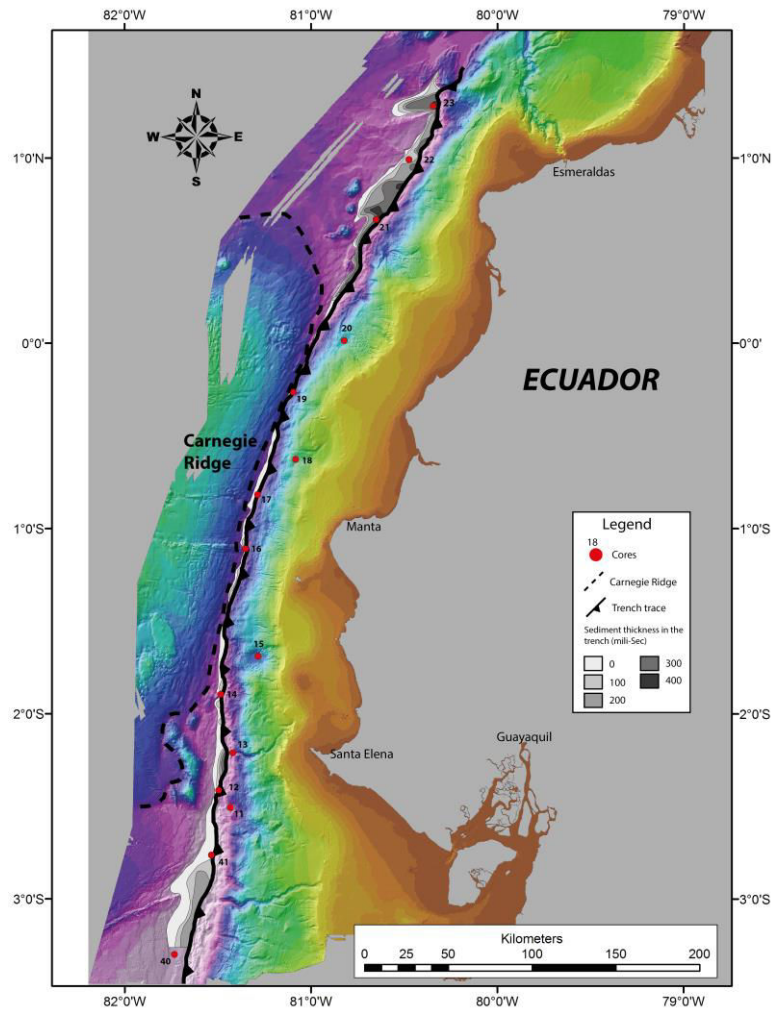


Fig. 4. 5 Thickness and distribution of the sediment in the Ecuadorian trench from the analysis of the low-resolution seismic data (SCAN).

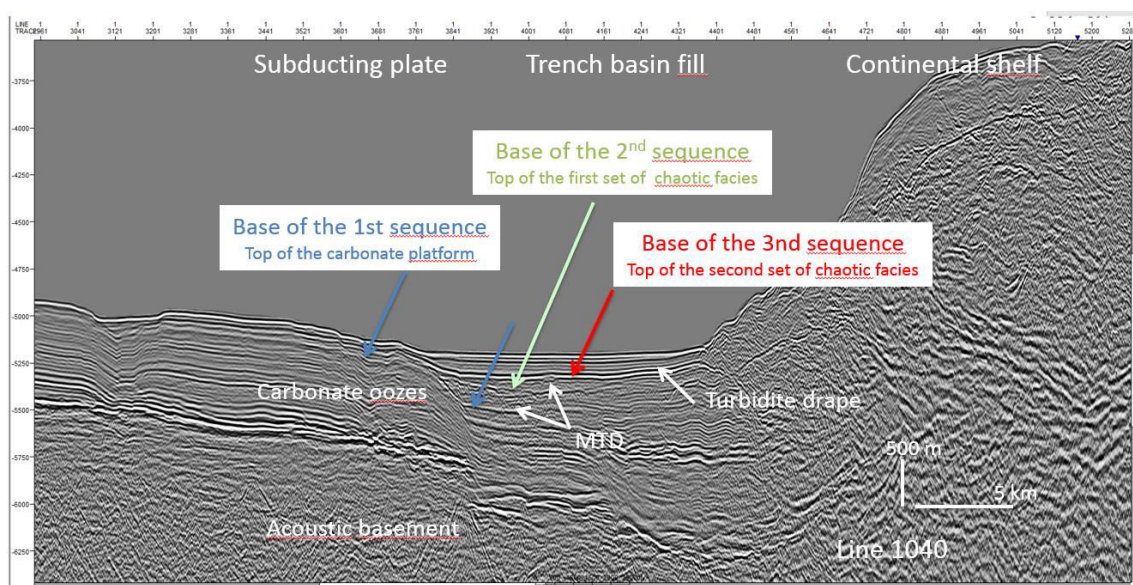
The trench-fill overlies the lower (Pacific) plate basement in the west and is overthrust by the North Andean terranes to the East. The thickest sections of the trench fill, in the North and in the South, are comprised of three seismic sequences bounded by unconformities (Figure 4.6A and C). The lower two units are a few tens to two hundred m-thick when the upper one can reach 300 m-thick. The depocenter of each unit progressively steps in an eastward direction. The lower two units are wedge- to lens-shape and exhibit a chaotic to reflection-free facies. The upper unit shows a sheet drape shape with a well layered, parallel reflector configuration and reflections of continuous, moderate to high amplitude and frequency. In front of the Carnegie Ridge, the trench fill is lacunar (Figure 4.6). The surfaces at the base and the top of the trench fill show irregular erosion surfaces with channeling (e.g. Figure 4.6). By places, where the trench is empty, channel features re-incise the footwall of faulted basement blocks (e.g. Figure 4.6).

*Interpretation* — According to ODP 202 studies at sites 1238 and 1239 (Mix et al., 2003), drilled a hundred to 150km east of the trench axis, the Carnegie Ridge are comprised of a 400 to 500 m thick sedimentary blanket over a volcanic basement. They likely respectively correspond to the lower and upper units observed on the

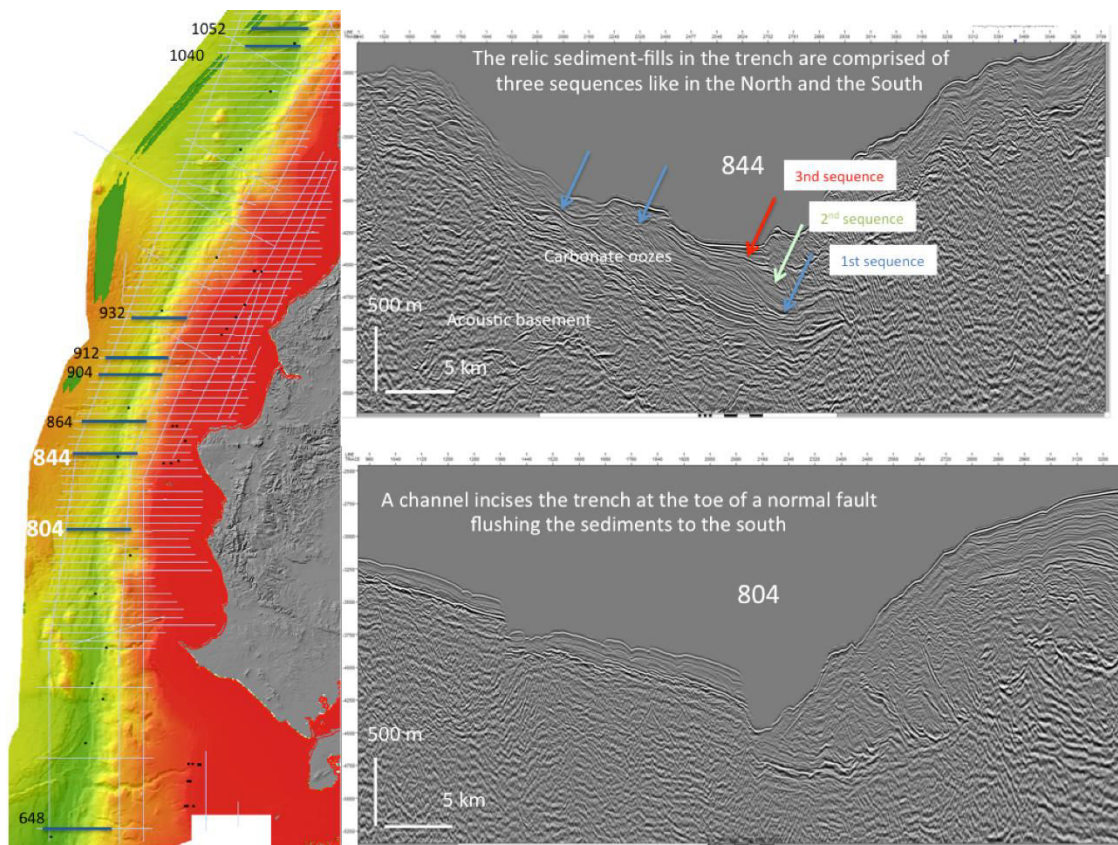


seismic sections in the basement underlying the sediment fill of the trench. The 400 to 500 m thick sedimentary blanket is Miocene to Pleistocene in age and wholly build of carbonate sediments. Two lithologic units were defined at site 157 and 1238: a ~300m upper unit consists of diatom nannofossil and chalk ooze; and a ~100m or less, basal unit is characterized by increased lithification and diagenesis with chalk and occasional chert horizons of mid to late Miocene age. The latter might correspond to the high amplitude reflections observed at the base of the well-layered seismic unit of carbonate ooze. The Carnegie Ridge is known to exhibit large-scale erosion, downslope transport from the ridge top and redeposition of pelagic sediments (Lonsdale and Malfait, 1974; Malfait and Van Andel, 1980) and extensive areas on top of the Carnegie Ridge were found to be clean of sediments (Brooks et al., 2011). The seismic profiles show that inner wall of the trench is draped by a 500m-thick layer of carbonate oozes that thins out southward and northward in a trench parallel direction, towards the top of the Carnegie Ridge. Erosion surfaces along channels are observed locally on the eastward slope of the Carnegie Ridge as well an extensive erosion areas and incisions along and in the thalweg of the trench. These incisions lack to the South and to the North of the Carnegie Ridge where the Pleistocene carbonate oozes and the recent sedimentary cover of the trench fill thicken and the sea floor flatten.

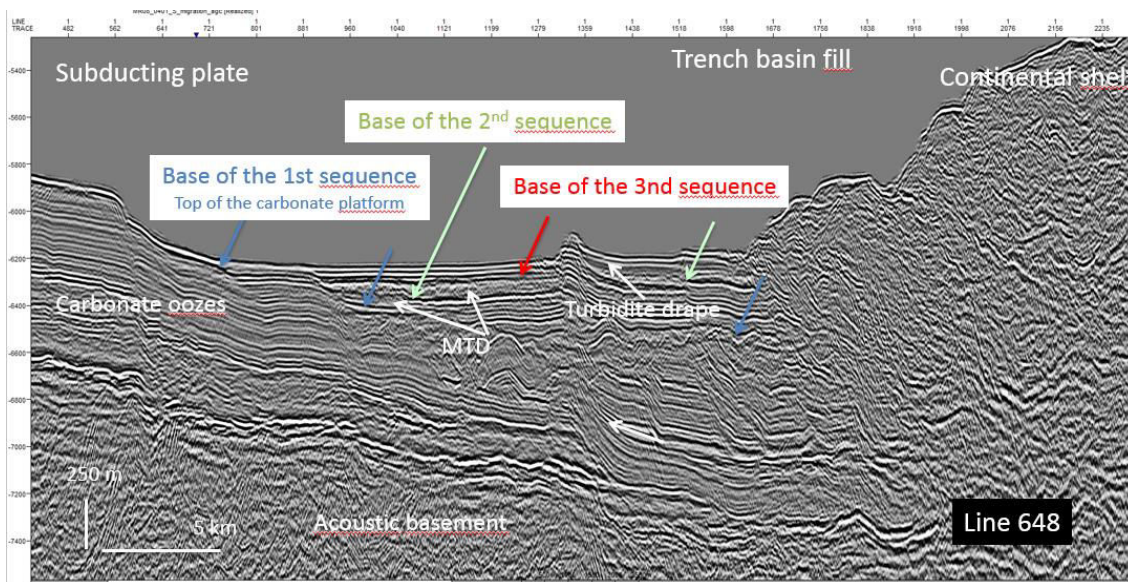
The strongly chaotic pattern of the seismic reflections in the lower two units of the trench fill is interpreted as the image of intensely deformed sedimentary strata as usually observed in mass transport deposits (MTDs). These two units step eastward and wedge out westward onlapping the basement of the downwarping faulted Pacific Plate (Fig. 4.6). This suggests an eastward source of sediment at the origin of the MTDs preserved at the base of the trench fill. These MTDs are exceptionally large in the northern (Esmeraldas) and southern (Guayaquil) areas where they can reach a few tens to 200m-thick and 5-10km-large in a section perpendicular to the trench axis. The upper unit of the trench-fill seals these MTDs almost everywhere. The upper unit is well layered with high and moderate amplitude reflectors indicative of well stratified but contrasted lithologies interpreted as turbidite deposits interbedded with some tephra layers (see below).



(A)



(B)



(C)

Fig. 4. 6 Examples of low-resolution seismic profiles shot across the trench in the northern (A), the central (B) and southern (C) segments of the margin. The profiles show the acoustic basement, the carbonate oozes covering of the oceanic crust and the trench fill. The trench fill is composed of three main unconformity—bounded seismic units or “sequences” onlapping the acoustic basement and the carbonate ooze. We can follow up the three sequences in all depocenters along the margin.



#### 4.4.3 High resolution CHIRP seismic data

The top of the upper unit imaged with the low-resolution seismic SCAN data was explored with more details with the high-resolution CHIRP seismic tool during the ATACAMES campaign. The CHIRP tool can penetrate about 100 m of sediment but a correct image is obtained in the first 10 meters. The seismic facies are of three types: transparent, layered and chaotic with diffractions.

**The transparent facies** occur in the North (cores 22 and 23) and the South (cores 14 and 12) of the Carnegie Ridge as well in the offshore of the Gulf of Guayaquil, at the base of core 40. They form extensive, fan shape, c.45 m-thick greyish/whitish bodies wedging out after 1 to 10's km in a direction parallel to the trench (Fig. 4.7a). These sediment bodies repose either on an older one or on a well-layered seismic facies, without any significant erosion surface. The base of the transparent facies bodies is flat while their top is irregular, with bumps underlined by low amplitude seismic diffractions. The sediment body is capped by few continuous, moderate amplitude reflections.

**The layered facies** is exposed in the trench, facing the central part of the subducting Carnegie Ridge (cores 16, 17, 18) and in the offshore of the Gulf of Guayaquil, in core 41 and top of core 40. The layered facies drapes the underlying irregularities of the substrate (Fig. 4.7b). It shows high to moderate amplitude, high to moderate continuity and parallel reflection configuration with a lateral frequency change from thinly- to thickly-layered characters *i.e.* the thickness of the transparent facies between to high amplitude reflectors varies and wedges out laterally.

**The chaotic facies with diffractions** is exposed in intermediate areas between the central part of the trench facing the Carnegie Ridge and the northern and southern sections of the trench (cores 11, 12, 13 and 19 respectively). The facies shows incoherent reflections showing either a blurred mix of high and low amplitudes (cores 13) or very low amplitude (core 11) with abundant diffractions (Fig. 4.7c).

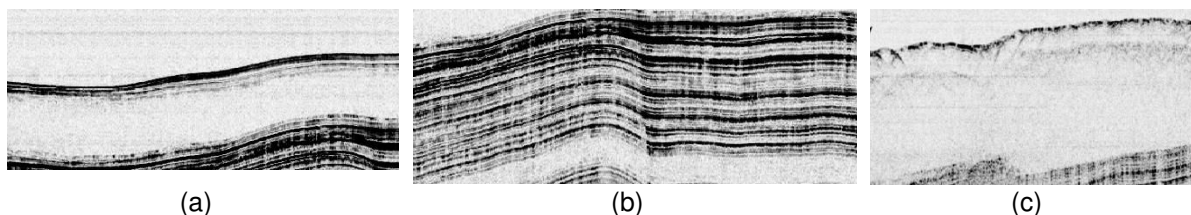


Fig. 4. 7 High-resolution CHIRP seismic facies, (a) transparent facies at northern segment of the trench, (b) layered facies at northern segment of the trench, and (c) chaotic facies with diffractions at northern segment of the trench

#### 4.4.4 Piston core data

We collected 15 piston cores: 10 cores in the trench (41, 40, 12, 14, 16, 17, 19, 21, 22, 23) and 5 piston cores in toe of slope basins (11, 13, 15, 18, 20). This section describes and interprets the depositional processes from the sedimentary facies observed in the cores (annex 1). We identified 11 sedimentary facies end-members (facies 1 to 11, annex 2) in the ATACAMES cores.

**Facies 1 — Hemipelagites**— Facies 1 is the finest of all facies and widely scattered in all cores. It is olive-grey homogenous clay to silt-size planktonic and benthic foraminifers and diatoms with a low magnetic susceptibility (27 SI) and average density (2.49). This facies is typically moderately to highly, but thoroughly, bioturbated.

*Interpretation* — Facies 1 is the finest facies observed in the core data. Facies 1, shows a mix of clay and biogenic silt size sediment but lacks detrital terrigenous material as indicated by the low magnetic susceptibility, which is characteristic of hemipelagic sedimentation.

**Facies 2 to 6 — mud turbidites** — Among the 11 sedimentary facies end-members, facies 2 to 6 are stacked in incomplete fining upward sequences representing either a base- or top-cut-out sequence. — None of them show the complete fining up succession from facies 6 to 2. The coarsest facies 6 is a fining upward, darkish olive-grey sand to silt material with a high magnetic susceptibility (c.80 SI) and density (c.2.66), a massive basal part and horizontal to lenticular, ripple-laminated top part. This facies is rich in foraminifers. The intermediate facies 5 and 4 are olive greyish, silty clay to silt-size sediment with rare foraminifers, a medium but peaky magnetic susceptibility (35-37 SI) and average density (2.5). Facies 5 shows low angle planar- or rippled cross-laminations with low angle truncations while facies 4 exhibits remnant of silt laminations, flame, convolute and synsedimentary microfolds. The overlying facies 3 and 2 are olive greyish, clay to silty clay with rare foraminifers, a moderate magnetic susceptibility (c.20-25) with a flat-shaped curve and a low density (2.2-2.4). Facies 3 shows thin wispy silt lamination when facies 2 is a massive clay typically bioturbated at the top. The mud-turbidites show the complete stack of facies in only few examples (core 21, 18, 12). Basically, any fining upward combination of facies is possible but facies 6 as well as facies 4 are frequently missing in the facies successions.

*Interpretation* — Facies 2 to 6 are typically stacked in incomplete but strictly fining upward muddy successions that show an overall decreasing and smoothing upward trend in magnetic susceptibility. The lower part of the individual successions (facies 6, 5) displays low angle lamination and erosion surfaces due to current activity on the seafloor while the middle part (facies 4) shows dewatering structures like flames and convolutes indicative of dewatering of rapidly deposited sediment, which is overlain by massive muds (facies 5-6) indicative of the passive settling of mud in the water column capped by an intensely bioturbated horizon. This kind of successions, although usually incomplete here, is interpreted as the result of the rapid transport of a mix of sandy mud and water by waning turbulent flows traveling down the slope of the margin to the trench i.e. turbidites (e.g. Bouma, 1962). The lack of coarse-grained material makes them close to the mud-turbidites of Stow and Piper (1984), (see the correspondence with the Stow and Piper subdivisions of turbidites in Fig. 1.25 from chapter 1). The origin of the truncated facies successions in the turbidites is a matter of debate (Stow and Piper, 1984). The top-cut-out sequences are very likely caused by the erosion at the base of the subsequent turbidite; the base-cut-out sequences might reflect the distance to the source with the freezing of the coarse grain fraction in the upslope direction, when the lack of a certain grain fraction, like for example the silt fraction, in the sediment could be at the origin of the lack of the intermediate facies 4 or 3 in the succession.

**Facies 8 and 7 — Volcanoclastic turbidites** — These facies are light brownish and usually superposed in cores in fining upward successions. Facies 8 is fine-grained bioclastic quartz and ferromagnesian sand with benthic and planktonic foraminifers and radiolarian. The magnetic susceptibility is very high (c.200 SI) and peaky but density is quite low (2.15). Sedimentary structures are planar to low angle lamination underlined by ferromagnesian mineral layers. Bioturbation is scarce but can be abundant. The overlying facies 7 is a structureless quartz and ferromagnesian silt with no foraminifers and no bioturbation. The magnetic susceptibility is very high (180 SI) but decreasing up section and the density average (2.5).

*Interpretation* — Facies 7 and 8 share the main characters of facies 2 to 6 with a fining up trend with a decreasing upward magnetic susceptibility and low angle laminations indicative of current traction at base overlain by massive muds indicative of decantation that leads to interpret them as turbidite deposits. However, their extremely high magnetic susceptibility together with the high content of ferromagnesian material points to their volcanoclastic origin. However, this event corresponds to a two parts bed with a true turbidite at base (facies 7) with abundant biogenic material, probably reworked during the downslope travelling of the turbulent flow and thoroughly bioturbated at top, overlain by facies 8 resulting from the passive settling of structureless mud (facies 8) with no fauna and no bioturbation, probably resulting from aerial settling of volcanic ashes (Schneider et al., 2001).

**Facies 9 and 10 — Mass transport deposits** — These facies appear usually scattered in the core sections. They show an olive grey to yellowish or whitish color and a very low, flat-curved, magnetic susceptibility (10-13 SI) and density (2.2-2.4). Facies 9 is a massive silty clay to quartz silt with cm to dm-scale yellowish-brown subangular clasts of the same material and with traces of anhydrite. The fauna is abundant and diversified with benthic and planktonic foraminifers, diatoms and radiolarian. Bioturbation is scarce to absent. Facies 10 is similar to facies 9 but shows soft deformation folds instead of large clasts.

*Interpretation* — Facies 9 and 10 are massive, with a low magnetic susceptibility, diversified and mixed faunas, and no grading. They show either subangular clasts of the same material of the matrix or soft deformation structures indicative of the downslope transport of a mass of plastic sediment. The presence of anhydrite in facies 9 might indicate a close relationship with hydrothermal fluid vents at the up dip source of the debris flow.

**Facies 11 — Carbonate oozes** — This facies occurs solely at the very top of core 19. Facies 11 is a yellowish massive fine-grained foraminiferal and radiolarian sand or ooze with no bioturbation. Magnetic susceptibility is very low (10 SI) and density is average (2.55). Sedimentary structures are scarce with some low angle planar lamination with low angle erosion surfaces.

*Interpretation* — Facies 11 is a laminated clean ooze that characterizes the passive setting of planktonic foraminifers on a current swept floor in clear waters located at some distance from sediment gravity flows and above the carbonate compensation depth.

#### 4.4.5 Correlation of the core data with the seismic data: sedimentary facies distribution

The migration in depth of the CHIRP seismic data was run by using a velocity of sound of 1600m/s in the upper 10 m of sediments. This migration allows a direct comparison of the seismic data with the core data (Annexe 1 and 3) that helps to describe the main characters of the sedimentation distribution in the trench.

***Sedimentary facies stacking patterns*** — The diversity of the facies stacks in cores is very high. They subdivide in “mega-beds” that are n x m-scale acoustically transparent or chaotic sediment bodies and thin beds that are of dm to 1 m-scale facies packages acoustically layered.

***The mega-beds*** are either simple or composite. The simple mega-beds are thick, 6 to 8.60 m-thick with a transparent seismic facies (cores 14, 22 and 23), or thinner, 2 or 3 m-thick, with a chaotic seismic facies (cores 11 and 19). The thick ones are fining upward and show either (1) a debris flow overlain by a thin planar laminated and convoluted sandy silt and massive muds (core 23) or (2) an alternation of laminated and slumped sandy silts overlain by a 6 m-thick slump in silty clays (core 14) or (3) planar laminated sands overlain by laminated silts and massive mud bioturbated at top (core 22). The thin ones are exclusively composed of sandy mud debris flow (core 11) or carbonate ooze granular flow facies (core 19). The composite mega-beds are 4 to 5 m-thick in cores 40 and 12 respectively in the transparent and chaotic seismic facies. They show a stack of dm to m-scale, thickening upward, muddy turbidites with basal laminated sand overlain by slumped silty muds, giving rise up section to m-scale debris flows cap by a thick turbidite (core 12) or an hemipelagite (core 40).

***Interpretation*** — The simple-thick mega-beds show a fining upward trend and complete suite of sedimentary structures indicative of a progressive decrease in the energy of transport (planar to wispy and convolute lamination) in a single mass flow event. These events are largely laid down by turbulent flows typical of turbidite deposition and can be referred to as “mega-turbidites” according to Bouma (1987), Mulder et al. (2009) among others. The simple-thin mega-beds lie on and are sealed by thin mud-turbidites (core 11) or laminated carbonate oozes (core 19). They are interpreted as single gravity flow events; respectively matrix- and grain-supported flows. The composite mega-beds show a thickening and coarsening upward trend with slumped muddy beds in water-supported flow at base to massive matrix-supported debris flow at the top. These trends are interpreted as the result of a progressive increase of the energy of transport of sediment in an overall large-scale gravitational event like the transition from the sole to the core of a mass transport deposit.

***The thin beds*** show either a thinly or a thickly layered seismic facies. The thinly layered seismic facies corresponds in cores to 3-4m-thick stacks of 0.2 to 0.5m-thick mud-turbidites and volcanoclastic turbidites. These stacks appear in most cores like cores 40, 12, 14, 15, 16, 18, 20, 21 and 22. However, thinner packages of 0.2 to 0.5m-thick turbidites interlayered with other facies, which do not appear in seismic data are present in the muddy sections of almost every cores except core 19 (carbonate ooze). The thickly layered seismic facies corresponds in cores to 5 to 7 m-thick stacks of c.2m-thick fining upward turbidites successions. They appear in cores 41, 16 and 17. In core 41 and 16, they show the simple but thick successions of the mud-turbidites

with from base to top, laminated sandy silts (facies 5), convoluted wispy silts (facies 4 and 3) and massive mud (facies 2). In core 17, by places, 0.5 to 0.8m-thick debris flows underlie the base of the thick mud-turbidites.

*Interpretation*— The thin beds show the regular structures of mud turbidites laid down by turbulent flows (see above). Some of the thickest ones could be referred to as mega turbidites with regards to their large thickness, and certainly a continuum exists between mega turbidites and thick turbidites, but the well-layered seismic facies differ definitively from the transparent one of the mega-beds.

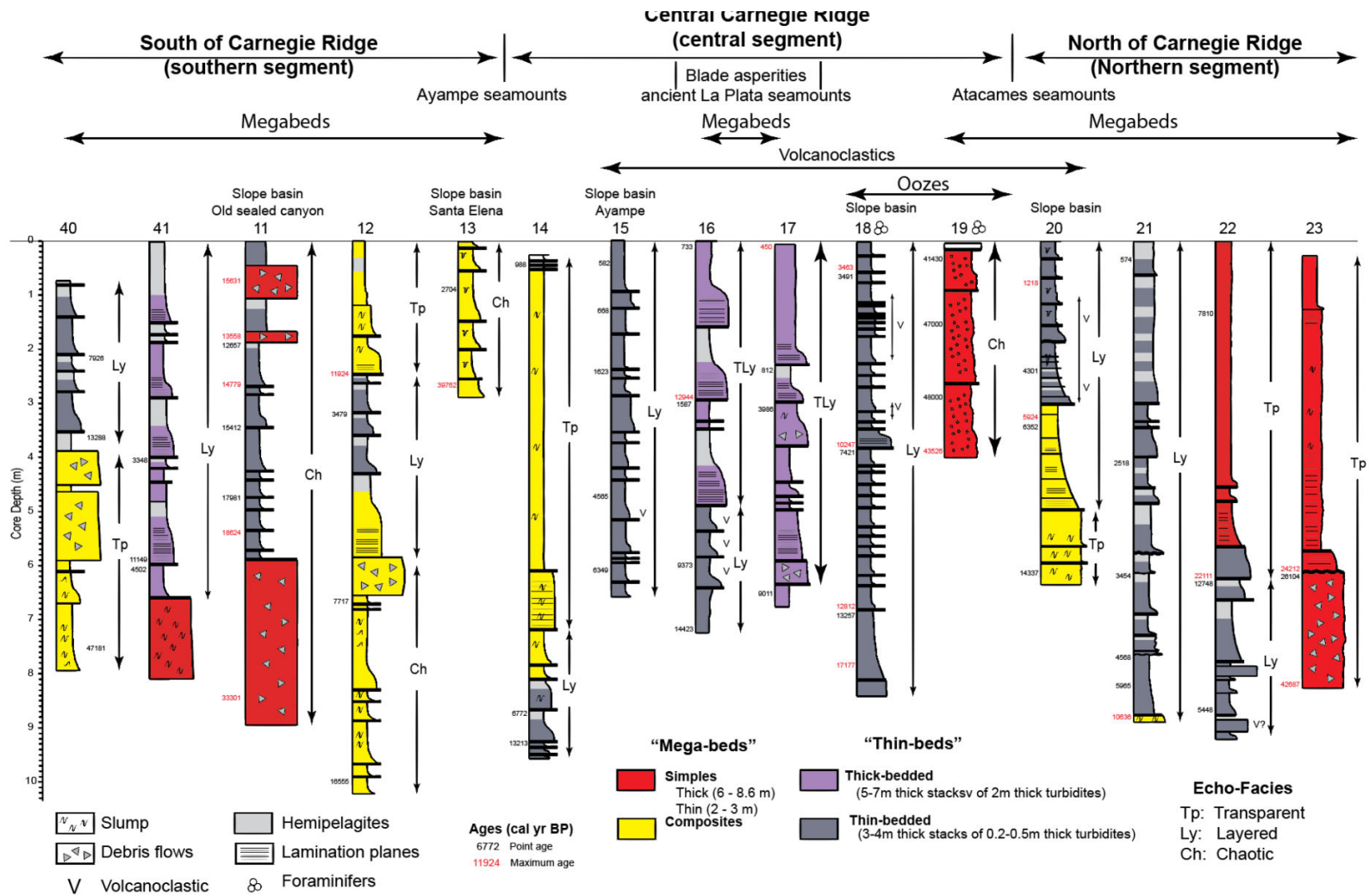


Fig. 4. 8 Oversimplified representation of the sedimentary facies observed in the cores collected in the trench and in the lower slope basins together with their seismic facies and approximate ages. See the full dataset in annexes 1, 2, 3 and 4 and a blowout of this figure in annex 3



*Lateral distribution of the sediment in the trench and lower slope basins* — If the sediments in cores are largely muddy with mud-turbidites widely distributed in all cores, the hemipelagites are scarce and the volume of thin-bedded turbidite is reduced meaning that the number of gravity event is limited: most of the sedimentary record being composed of mega-beds and thick-bedded turbidites sequences (Fig. 4.8).

The mega-beds are located geographically to the south and to the north of the Carnegie Ridge. The thin and simple mega-beds with the chaotic seismic facies and scattered debris flows are located in lower slope basins of the inner (cores 11 and 13) or outer walls (core 19 with oozes) of the trench. The thick and simple mega-beds with the transparent seismic facies and mega-turbidites are located at places where we have evidences of major destabilizations of the inner trench slope in the north (cores 22, 23, see chapter 6) and in the south (core 14, see chapter 5). The composite mega-beds, either transparent or chaotic that correspond to enhanced sequences of slumps and debris flows, are located in the trench, in the south at some distance from the Carnegie Ridge. The thick-bedded turbidites are well represented in the shallow part of the trench at the apex of the subducting Carnegie Ridge (Fig. 4.8) facing Manta Peninsula (cores 16 and 17) together with the volcanoclastic turbidites solely observed in cores 16, 17, 18 and 20.

Remarkably, we found sediment gravity events exceptionally rich with foraminifera in both the inner wall cores 18 and the outer wall core 19 and thoroughly bioturbated by *Scolicia* top part of the cores 13 at the outlet of the Santa Elena canyon and core 29 at the toe of a gully water shed basin.

#### **4.4.6 Age dating of the sediments in cores**

66 samples were analysed for  $^{14}\text{C}$  age dating (table 1, annex 4). 45 samples are planktonic foraminifera shells (species) collected in the Hemipelagite facies (facies 1). 25 samples were taken at the base of turbidites (facies 6 or 5). The former provides a direct age dating of the sediment while the latter provide only a maximum age for the deposit. Unfortunately, the small volumes of hemipelagite sediments and the loose distribution of the samples prevent the construction of an age model that would provide an age for each gravity events. However, the age dating offers an estimate of the approximate age of the main sedimentary events (Fig. 4.8).

The results show that the oldest deposits are provided by the debris flows sourced by the Carnegie Ridge sediments (c. 48000 yrs BP, core 19) and the sediments sourced by the coastal cordillera, sampled at the outlet of the Santa Elena canyon (c.39000yrs BP, core 13). The youngest sediments in our record are c.574yrsBP in core 21 as well as 576yrs BP in core 15. We got as well 730yrs BP in core 16, and 988yrs BP in core 14.

The point sampling for age dating of the sediments in the cores collected in the trench shows that the mega-beds, which compose the lower part of most cores in the northern and southern parts of the trench, are the oldest. The northernmost and oldest mega-turbidite of our record, in core 23, dates back to c.23000yrs. This event is followed a large composite sequence of debris flows sealed by a c.13000yrs-old hemipelagite settled in

the southernmost part of the Ecuadorian trench in core 40. The latter predates shortly the deposition of another large mega-turbidite but with no coarse debris flow at its base, at the northern end of the trench (core 22) close and to the south of the former one at c.12000yrs. The youngest mega-beds are deposited in the South, close to Ayampe seamounts (cores 12, 14). They comprise a sole made up of a succession of slumps overlain by a mega-turbidite event with a basal debris flow. These events date back respectively at c.7800yrs BP and 6500yrsBP.

The thick-bedded turbidites preserved at the apex of the central segment of the trench (cores 16-17) show a broad age range bracketed between 9300 yrs BP and 730 yrs BP. They comprise or overly volcanogenic sediments. The volcanoclastic turbidites in core 20 are bracketed between 6300 and 4300yrs BP. The age dating of the volcanogenic sediments in the other cores (cores 15, 16, 17 and 18), which include the thick-bedded turbidites, is less precise but fits well in this bracket. It comes then that the thick-bedded turbidites could be as young as 6300 yrs BP post dating most of the mega-bed deposition in the southern and northern segments.

The thin-bedded turbidites tend to seal the mega-beds. They are ubiquitous but they are really predominant in the transitional zones between the different segments as a lateral equivalent to the thick-bedded turbidites. Our core sampling shows that they can be as old as 13000 yrs BP in the South (core 40) or 14000yrs BP in the central segment (core 16), but in the best records they appear younger than 4500yrs BP (core 41), or 5600yrs BP in core 21 in the North.

In the slope basins, the diversity of ages is very large and can hardly be correlated due to the conditions of sedimentation particular of each site.

#### **4.5 Conclusion**

Improving the knowledge of the nature and volumes of sediments deposited in subduction trenches is a major challenge that will help to understand the mechanic of interplate coupling and earthquake triggering. Advances have been made in the recent years in sediment-rich accretion margin (*e.g.* Hüper et al., 2017) but we know less about sediment-starved margins in tectonic erosion partly because the sedimentary archives of tectonic events and earthquakes record are lacunar.

Comprehensive datasets recently acquired along the subduction margin of Ecuador like the ATACAMES campaign (2012) — building on previous campaigns AMADEUS (2005) and SYSTER (2000) — and SCAN campaigns in particular, shed a new light on the sedimentary record in the trench of a subduction margin in tectonic erosion.

This record shows an oceanic plate overlain by 400-500m-thick carbonate ooze with a basal cherty cementation that subducts beneath an overriding plate composed of a complex set of accreted terranes. The subducting plate shows a highly irregular topography with an EW-oriented, 2000m-high Carnegie Ridge that exerts a strong control on the overall morpho-dynamic and sediment fluxes of the margin. The bathymetry data

shows that the inner wall of the trench of the central segment facing the Carnegie Ridge is significantly smoother than the slope of northern and southern segments, which is particularly highly destabilized at the edges of the Carnegie Ridge (Atacames and Ayampe areas) where spotted seamounts hit the lower slope.

The topography of the trench characteristically mimics the topography of the subducting plate. It is 4800m-deep in the South, 4300m-deep in the North and c.3700m-deep in front of the Carnegie Ridge where it appears very rough, with a few hundreds m-high to 600m-high local relief overhanging the surrounding seafloor. The relatively thin trench fill draping this topography is then highly lacunar. The thickest depocenters are located in the northern (c.400m) and southern (c.300m) segments of the margin when, in front of the Carnegie Ridge, the trench shows scattered c. 100m depocenters between the reliefs. Large parts of the trench that lack any sediment shows sharp erosion features caused by bottom currents channelled by the trench walls.

The sediment fill is comprised of three major depositional sequences of Pleistocene age. The lower two are chaotic to layered, eastward stepping sequences of exceptionally large (200m-thick and 5-10km-large) mass transport deposits while the upper one drapes the trench floor with well-layered thin-bedded turbidite and hemipelagic deposits.

The detailed seismic imaging and the analysis and age-dating of c.10m-long cores of sediment sampling the upper portion of the trench fill show that the well-layered reflectors in low-resolution seismic data draping of the trench floor is quite complex. The oldest sediments sampled in our cores are large sediment debris flows provided by the outer trench wall of the Carnegie Ridge at c.48kyrs and by the Santa Elena canyon cutting through its inner wall at c.39kyrs. The bulk of the trench fill shows c.23 and c.12kyrs-old BP mega-beds (scattered debris flows, mega-turbidites, stacked slumps and debris flows) deposited in the northernmost and southernmost segments of the trench and younger ones at c.7.8 and 6.5kyrs BP in Ayampe area, at the southern edge of Carnegie Ridge. These events are post-dated by the deposition of a set of three thick-bedded and volcanoclastic turbidites, possibly as old as c.6.3 to c.4.3kyrs BP, in the central segment, nearby the blade asperities that face the Manta Peninsula. In both the southern and the northern segments mainly — the thin turbidites are widespread in the trench at any time — the trench fill is completed by the deposition of thin-bedded turbidites from c.4.5kyrs BP in the south and c.5.6kyrs in the North onward. This record is completed in the North, as well as in the South in Ayampe area, by recent slides and km-scale rockfalls that testify of the permanent destabilization of the inner trench-wall.

The trench fill represents a lacunar but important record of the history of the subduction margin. The large eastward stepping debris flows in the lower two sequences are probably the results of slope failures along large normal faults due to the downward bending of the subducting oceanic plate. The correlation with the distant ODP holes show that these events could be Pleistocene in age. The Carnegie Ridge sources as well the oldest debris flows sampled in our record. These deposits are very small and limited to a single place the footwall of a normal fault affecting the outer wall of the trench — there is no trace of any outward source of large debris flows in the well-layered seismic facies

draping the trench floor. Nonetheless, these small debris flows, which are as young as c.48kyrs BP, point to a steady and remote contribution of the Carnegie Ridge to the trench fill. From 23kyrs BP onward, but probably much earlier, since the beginning of the deposition of the well-layered seismic facies in the early to mid-Pleistocene, the source of sediment switch to the inner wall of the trench. Large c.23 and 12kyrs-old BP mega-beds settle in the North triggered by large regional fault scarps (see chapter 6) and in the South enhanced by the activity of sets of splay faults at the toe of the slope overhanging the seafloor. A new set of mega-beds followed, deposited in the South at c.7.8 and 6.5kyrs BP in Ayampe area. They compare to mega-beds described in the North in Atacames region (SB7, Kama 03, see chapter 6). Both are small-size, fluid rich (slump) events triggered by the subduction of isolated seamounts at the edges of the Carnegie Ridge.

They give rise to frequent but small destabilizations of an inner trench wall “preconditioned” by the repeated impacts of the successive seamounts (see chapter 6). The very thick turbidite events were deposited at c.6.3 to c.4.3kyrs BP in the central part of the margin, and apex of the trench floor facing the Carnegie Ridge, close to the intersection of the so-called “blade asperities” with the sub-meridian faults of the outer wall. This part of the central segment was the location of strong coastal and continental slope uplift (Pedoja et al., 2006a) in relation with the subduction of seamounts (Sanclemente, 2014; Proust et al., 2016; Collot et al., 2017) that might have also preconditioned the inner trench wall for future destabilization by earthquake shakings at the origin of the turbidites. Some of these turbidites comprise volcanoclastics elements indicating a possible influence of the first of last two and largest volcanic eruptions in the western cordillera (SW Quito), which produces huge plinian and pyroclastic flow deposits at around  $4400 \pm 35$  yr BP and  $2270 \pm 15$  yr BP (Hidalgo et al., 2008). Thin-bedded turbidites constitutes the final drape the trench floor showing a relative quiescence of the inner trench wall and the return to “normal” turbulent transport of sediment from more distant sources despite some rock fall may occur from place to place in the North (see chapter 6).

These results show the complexity of the sedimentation in the trench of a subduction margin in tectonic erosion. The sedimentary record exhibits a large volumetric dominance of rare but large gravity events (laminar flows i.e. matrix-, grain- and water-supported) over the thin turbidite events (turbulent flows). This points to the importance of the proximity of the sources and the tectonic reactivation of the outer and inner trench walls along regional or local faults at the origin of the gravity events. They dominate the transport of sediment by turbulent flow sourced by the continental platform or the upper slope, which was certainly largely starved of sediments — sediment pathways being cut off by the rise of the coastal cordillera.

## **Acknowledgments**

Data were acquired in 2012 during the IRD-CNRS oceanographic campaign ATACAMES on board the IFREMER research vessel *L'Atalante*. This work was carried out in the framework of the Joint French-Ecuador Laboratory LMI “Séismes et Volcans dans les Andes du Nord” with the financial support of the CNRS-INSU, IRD, Rennes 1 and Nice

Universities and IFREMER. We thank SENESCYT (Secretaría Nacional de Ciencia y Tecnología del Ecuador) for the student scholarships; ESPOL and INOCAR for their support and also *Schlumberger* and *IHS* for making available respectively *Petrel* and *Kingdom Suite* seismic interpretation software. Age datings were run at the LMC14 (Saclay) with the accelerator mass spectrometer ARTEMIS and funded by INSU CNRS. We thank Hugo Poudroux, Gueorgui Ratzov and the ATACAMES Science Party for their help in gathering and processing the data during the campaign and for the fruitful scientific discussions at different stages afterwards.

## References

- Benitez, S., 1995. Évolution géodynamique de la province cotiere sud-équatorienne au Crétacé supérieur-Tertiaire. *Géologie alpine*, 71, 3-163.
- Bethoux, N., Segovia, M., Alvarez, V., Collot, J.Y., Charvis, P., Gailler, A., Monfret, T., 2011. Seismological study of the central Ecuadorian margin: Evidence of upper plate deformation. *Journal of South American Earth Sciences*, 31, 1, 139–152.
- Bouma, A.H., 1962. *Sedimentology of Some Flysch Deposits. A Graphic Approach to Facies Interpretation*, Elsevier. 168 pp.
- Bouma, A.H., 1987. Megaturbidite: an acceptable term? *Geo Mar. Lett.* 7, 63–67.
- Brooks, C.K., Lyle, M.W., Marcantonio, F., Lewis, D.M., and Paul, C., 2011, Pelagic erosion and sedimentation north of Carnegie Ridge, eastern equatorial Pacific: American Geophysical Union, Fall Meeting 2011, 13A1512B.
- Calahorrano, A., Sallarès, V., Collot, J. Y., Sage, F., & Ranero, C. R. (2008). Nonlinear variations of the physical properties along the southern Ecuador subduction channel: Results from depth-migrated seismic data. *Earth and Planetary Science Letters*, 267(3-4), 453-467.
- Cantalamessa, G., Di Celma, C., 2004. Origin and chronology of Pleistocene marine terraces of Isla de la Plata. *Journal of South American Earth Sciences*, 16, 8, 633–648.
- Collot, J.Y., Agudelo, W., Ribodetti, A., Marcaillou, B., 2008. Origin of a crustal splay fault and its relation to the seismogenic zone and underplating at the erosional north Ecuador-South Colombia oceanic margin. *Journal of Geophysical Research*, 113, B12102.
- Collot, J.Y., Charvis, P., Gutscher, M. A., Operto, S., 2002. Exploring the Ecuador-Colombia active margin and inter-plate seismogenic zone. *EOS Transactions American Geophysical Union*, 83, 17, 189-190.
- Collot, J.Y., Michaud, F., Alvarado, A., Marcaillou, B., Sosson, M., Ratzov, G., Migeon, S., Calahorrano, A., Pazmino, A., 2009. Visión general de la morfología submarina del margen convergente de Ecuador-Sur de Colombia: implicaciones sobre la transferencia de masa y la edad de la subducción de la Cordillera de Carnegie: *Geología y Geofísica Marina y Terrestre del Ecuador*, p. 47–74.
- Collot J.-Y., Sanclemente E., Nocquet J.-M., Leprêtre A., Ribodetti A., Jarrin P., Chlieh M., Graindorge D. et Charvis P., Subducted oceanic relief locks the shallow megathrust in central Ecuador, *Journal of Geophysical Research: Solid Earth*, vol. 122, n°5, pp. 3286–3305, 2017.



Deniaud, Y., Baby, P., Basile, C., Ordoñez, M., Montenegro, G., Mascle, G. , 1999. Opening and tectonic and sedimentary evolution of the Gulf of Guayaquil Neogene and Quaternary fore-arc basin of the south Ecuadorian Andes. *Comptes Rendus de l'Académie des Sciences, Paris*, 328, 181–187.

Di Celma, C., Ragaini, L., Cantalamessa, G., Landini, W., 2005. Basin physiography and tectonic influence on sequence architecture and stacking pattern: Pleistocene succession of the Canoa Basin (central Ecuador). *Geological Society of America Bulletin*, 117, 9, 12-26.

Dumont, J. F., Santana, E., Vilema, W., Pedoja, K., Ordóñez, M., Cruz, M., Jiménez, N., Zambrano, I., 2005. Morphological and microtectonic analysis of Quaternary deformation from Puná and Santa Clara Islands, Gulf of Guayaquil, Ecuador (South America). *Tectonophysics*, 399, 1-4, 331–350

Ego, F., Sébrier, M., Lavenu, A., Yepes, H., Egues, A., 1996. Quaternary state of stress in the Northern Andes and the restraining bend model for the Ecuadorian Andes. *Tectonophysics*, 259, 1-3, 101–116.

Etayo-Cadavid, M.F., Andrus, C.F.T., Hodgins, G.W.H., Jones, K.B, Quilter, F., Sandweiss, D.H., Uceda-Castillo, S., 2013. Marine radiocarbon reservoir age variation in *Donax obesulus* shells from northern Peru: Late Holocene evidence for extended El Niño. *Geology*, 41, 599-602.

Font, Y., Segovia, M., Vaca, S., Theunissen, T., 2013. Seismicity patterns along the Ecuadorian subduction zone: new constraints from earthquake location in a 3-D a priori velocity model. *Geophysical Journal International*, 193, 1, 263–286.

Gailler, A., Charvis, P., Flueh, E. R., 2007. Segmentation of the Nazca and South American plates along the Ecuador subduction zone from wide angle seismic profiles. *Earth and Planetary Science Letters*, 260, 3-4, 444–464.

Gutscher, M.A., Malavieille, J., Lallemand, S., Collot, J.Y., 1999. Tectonic segmentation of the Northern Andean margin : impact of the Carnegie Ridge collision. *Earth and Planetary Science Letters*, 168, 255-270.

Hidalgo, S., Monzier, M., Chazot, G., Eissen, J.P., Van Der Plicht, J., et al., 2008. Late Pleistocene and Holocene activity of the Atacazo–Ninahuilca Volcanic Complex (Ecuador). *Journal of Volcanology and Geothermal Research*, 176 (1), pp.16-26.

Hüpers, A., Torres, M.E., Owari, S., McNeill, L.C., Dugan, B., Henstock, T.J., Milliken, K.L., Petronotis, K.E., Backman, J., Bourlange, S. and Chemale, F., 2017. Release of mineral-bound water prior to subduction tied to shallow seismogenic slip off Sumatra. *Science*, 356 (6340), pp.841-844.

- Jaillard, E., Ordóñez, M., Berrones, G., Bengtson, P., Bonhomme, M., N. Jiménez, Zambrano, I., 1996. Sedimentary and tectonic evolution of the arc zone of Southwestern Ecuador during Late Cretaceous and Early Tertiary times, *Journal of South American Earth Sciences*, 9, 131–140.
- Kendrick, E., Bevis, M., Smalley, J.R., Brooks, B., Vargas, R.B., Lauria, E., Souto Fortes, L.P., 2003. The Nazca–South America Euler vector and its rate of change. *Journal of South America Earth Science*, 16, 2, 125–131.
- Lonsdale, P., Malfait, 1978. Abyssal dunes of foraminiferal sands on the Carnegie Ridge. *Geol. Soc. Amer. Bull.*, 65, 1697- 1712
- Lonsdale, P., 1978. Ecuadorian subduction system. *American Association of Petroleum Geologists Bulletin*, 62, 12, 2454-2477.
- Lonsdale, P., and Klitgord A.D., 1978. Structure and tectonic history of the eastern Panama Basin. *Geol. Soc. Amer. Bull.*, 89, 1-9.
- Lonsdale, P., 2005. Creation of the Cocos and Nazca plates by fission of the Farallon plate. *Tectonophysics*, 404, 237-264.
- Malfait, B. T., and Van Andel, T.H., 1980, A modern oceanic hardground on the Carnegie Ridge in the eastern Equatorial Pacific: *Sedimentology*, v. 27, p. 467-496.
- Marcaillou, B, Collot, J.Y., Ribodetti A., d’Acremont E., Mahamat, A., Alvarado A., 2016. Seamount subduction at the North-Ecuadorian convergent margin: Effects on structures, inter-seismic coupling and seismogenesis. *Earth and Planetary Science Letters*, 433, 146–158
- Martillo, C., 2016. Enregistrements stratigraphiques des cycles glacio-eustatiques et de la deformation durant le pleistocene le long la marge centrale d’equateur (exploitation des donnees de la campagne atacames). Unpublished PhD thesis, Nice University.
- Michaud F, Collot J-Y, Alvarado A, Lopez E y el personal científico y técnico del INOCAR, (2006) Republica del Ecuador, Batimetría y Relieve Continental, publicacion IOA-CVM-02- Post. INOCAR, Guayaquil
- Michaud F, Proust JN and ship board party (2014). The ATACAMES Expedition CNRS-IRD, Univ Rennes1 and Nice, Ecuador 15 January-19 February 2012 RV L’Atalante (Ifremer). 188p
- Michaud, F., Proust, J.N., Collot, J.Y., Lebrun, J.F., Witt, C., Ratzov, G., Pouderoux, H., Martillo, C., Hernandez, M.J., Loayza, G., Penafiel, L., Schenini, L., Dano, A., Gonzalez, M., Barba, D., De Min, L., Ponce, G., Urresta, A., Calderon, M., 2015. Quaternary sedimentation and active faulting along the Ecuadorian shelf: preliminary results of the ATACAMES Cruise (2012). *Marine Geophysical Research*, 36, 1, 81-98.

Michaud, F., Witt, C., Royer, J.Y., 2009. Influence of the Carnegie ridge subduction on Ecuadorian geology: reality and fiction. In: Kay, S., Ramos, V., Dickinson, W.R. (Eds), Backbone of the Americas : Shallow Subduction, Plateau Uplift and Ridge and terrane Collision, Geological Society of America Memoir, 204, 12 p.

Mitchum Jr., R.M., Vail, P.R., 1977. Seismic stratigraphy and global changes of sea-level, part 7: stratigraphic interpretation of seismic reflection patterns in depositional sequences. In: Payton, C.E. (Ed.), Seismic Stratigraphy — Applications to Hydrocarbon Exploration. Memoir 26. American Association of Petroleum Geologists, 135–144.

Mulder, Th., Zaragosi, S., Razin P., Grelaud C., Lanfumey V., Bavoil F. (2009). A new conceptual model for the deposition process of homogenite: Application to a cretaceous megaturbidite of the western Pyrenees (Basque region, SW France). *Sedimentary Geology*, 222, 263–273

Nocquet, J. M., Mothes, P., Alvarado, A., 2009. Geodésia , geodinámica y ciclo sísmico en Ecuador. *Geología y Geofísica Marina y Terrestre del Ecuador Special Publication INOCAR-IRD*, 83–95.

Nocquet, J.-M., Villegas-Lanza, J.C., Chlieh, M., Mothes, P.A., Rolandone, F., Jarrin, P., Cisneros, D., Alvarado, A., Audin, L., Bondoux, F., Martin, X., Font, Y., Regnier, M., Vallee, M., Tran, T., Beauval, C., Maguina Mendoza, J.M., Martinez, W., Tavera, H., Yepes, H., 2014. Motion of continental slivers and creeping subduction in the northern Andes. *Nat. Geosci* 7, 287–291.

Nocquet J.-M., Jarrin P., Vallée M., Mothes P. A., Grandin R., Rolandone F., Delouis B., Yepes H., Font Y., Fuentes D., Régnier M., Laurendeau A., Cisneros D., Hernandez S., Sladen A., Singaicho J.-C., Mora H., Gomez J., Montes L. and Charvis P., 2016. Supercycle at the Ecuadorian subduction zone revealed after the 2016 Pedernales earthquake. *Nature Geoscience*, DOI: 10.1038/NGEO2864

Pedoja, K., Dumont, J. F., Lamothe, M., Ortlieb, L., Collot, J.Y., Ghaleb, B., Auclair, M., Alvarez, V., Labrousse, B., 2006a. Plio-Quaternary uplift of the Manta Peninsula and La Plata Island and the subduction of the Carnegie Ridge, central coast of Ecuador. *Journal of South American Earth Sciences*, 22, 1-2, 1–21.

Pedoja, K., Ortlieb, L., Dumont, J. F., Lamothe, M., Ghaleb, B., Auclair, M., Labrousse, B., 2006b. Quaternary coastal uplift along the Talara Arc (Ecuador, Northern Peru) from new marine terrace data. *Marine Geology*, 228, 1-4, 73–91.

Proust, J.-N., Martillo, C., Michaud, F., Collot J.-Y., Dauteuil, O., 2016. Subduction of seafloor asperities revealed by a detailed stratigraphic analysis of the margin shelf sediments of Central Ecuador. *Marine Geology*, doi:10.1016/j.margeo.2016.03.014

Ratzov, G., Collot, J.Y., Sosson, M., Migeon, S., 2010. Mass-transport deposits in the northern Ecuador subduction trench: Result of frontal over multiple seismic cycles. *Earth and Planetary Science Letters*, 296, 89–102

Ratzov, G., Sosson, M., Collot, J.Y., Migeon, S., 2012. Late Quaternary geomorphologic evolution of submarine canyons as a marker of active deformation on convergent margins: The example of the South Colombian margin. *Marine Geology*, 315–318, 77–97.

Reyes, P., 2013. Thèse de doctorat de l'université de Nice Sophia Antipolis. Thèse de Doctorat de l'Université de Nice Sophia Antipolis.

Sage, F., Collot, J.Y., Ranero, C. R., 2006. Interplate patchiness and subduction-erosion mechanisms: Evidence from depth-migrated seismic images at the central Ecuador convergent margin. *Geology*, 34, 12, 997-1000.

Sallarès, V., Charvis, P., 2003. Crustal thickness constraints on the geodynamic evolution of the Galapagos Volcanic Province. *Earth and Planetary Science Letters*, 214, 3-4, 545–559.

Sanclemente, E., 2014. Seismic imaging of the structure of the central Ecuador convergent margin: relationship with the inter-seismic coupling variations. *Earth Sciences, Université de Nice Sophia Antipolis*, 273p.

Schneider, J.L., Le Ruyet, A., Buret, C., Chanier, F., Ferrière, J., Proust, J.N., Rosseel J.B. (2001). Primary or secondary ash turbidites : how to make the distinction ? An example from the Miocene of New Zealand (Mahia Peninsula, North Island). *Sedim. Geol.* 145, 1-2, 1-22

Scholz, C.H., Small, C., 1997. The effect of seamount subduction on seismic coupling. *Geology*, 25, 487-490.

Stow, D.A.V. , and Piper, D.J.W. , (1984). Deep-water fine-grained sediments: facies models. Lyell collection

Stuiver, M., Reimer, P.J., 1993. Extended C-14 data-base and revised calib 3.0 C-14 age calibration program. *Radiocarbon* 35, 215–230.

Trenkamp, R, Kellogg, J.N., Freymueller, J.T., Mora P., 2002. Wide plate margin deformation, southern Central America and northwestern South America, CASA GPS observations. *Journal of South American Earth Science*, 15, 157–171.

Vallée, M., Nocquet, J.M., Battaglia, J., Font, Y., Segovia, M., Régnier, M., Mothes, P., Jarrin, P., -Cisneros, D., Vaca, S., Yepes, H., Martin, X., Béthoux, N., Chlieh, M.,. 2013. Intense interface seismicity triggered by a shallow slow slip event in the Central Ecuador subduction zone. *Journal of Geophysical Research Solid Earth*, 118, 6, 2965-2981.

## Chapter 5

### Nature and controls on the frontal erosion of the subduction margin of Ecuador: The example of the Ayampe area

#### 5.1 Introduction

The sediment supply to the oceanic trench is an important player in the overall stability of the active margins. First, the trench fill is a key parameter affecting the accretion or erosion states of an active margin (Lallemand et al., 1994). On average, circum-Pacific convergent margins switch from subduction erosion to subduction accretion, with development of an accretionary wedge, when trench fill thickness exceeds ca 1000 m (Clift and Vannucchi 2004). Decreasing sediment thickness should therefore promote subduction erosion. Second, the subduction of hydrated sediments dropping down the interplate coupling modifying the overall strain state of the margin, some authors considering that the sediments lubricate the interplate contact (Shreve and Cloos 1986) while others think that they increase the coupling (Ruff, 1989). The subducting material contains pore-filling fluids in variable amounts depending on the nature and thickness of the underthrust sediment deposit (Cloos and Shreve, 1996) and as the interplay between amount of sediments and the asperities of the oceanic plate (Cloos and Shreve, 1996), fluid pressure variations are believed to play a major role in controlling deformation processes and fault dynamics along subduction zone megathrusts (Moore and Saffer, 2001; Sage et al., 2006; Calahorrano et al., 2008).

Sediment supply depends on climatic changes (rainfall) while tectonic deformation controls the place where sediments accumulate. At erosive margins, like in Ecuador, the relatively limited volumes of sediments in the trench reduce the penetration of water-soaked sediment between the two plates increasing the plate coupling (Sage et al., 2006) and tectonic erosion at the base of the upper plate. But the sedimentary supply in the trench can be increased by destabilization along the inner-wall of the trench and mass wasting. First, in association with long-term erosive margin seafloor subsidence (Scholl et al., 1980; von Huene et al., 1988, Sosson et al., 1994; Mercier de Lepinay et al., 1997; Sage et al., 2006), extensional tectonic features can occur and control massive gravity failure (Bourgeois et al., 1993). Second, the roughness of the subducting plate (seamount subduction) increases locally the instability of the continental slope with important gravitational collapses of unlithified sediments and large blocks. The sediments are transported mainly by gravitational processes giving rise to Mass Transport Deposits (MTD) by slumping, sliding and creeping and to gravitational flows either laminar (e.g. debris flows) or turbulent (turbidity currents) (Mulder and Cochonat, 1996; Mulder and Alexander, 2001).

Consequently, along the erosive margins, the amount of sediment supply along the slope and into the trench can be increased by mass wasting, especially during seamount subduction. Seamounts uplift the seafloor, fracture the upper plate and, as a consequence, generate large erosional scars and mass wasting. These latter constitute an excellent record of the history of the erosion, the sedimentation and the geodynamic of the margin. Indeed, the age and the location of gravitational events can help to locate the seamounts at the origin of the sequence of deformation in the upper plate. Moreover, along erosive margins the slope indentations due to seamount

impacts, remain for a long time after the seamount subduction (Dominguez et al., 1998; Laursen et al., 2002; Hampel, et al., 2004; Hampel and Kukowski, 2004a), while in the accretionary margin the re-entrant are swiftly filled by sediments, allowing to constrain the deformation and the sedimentary transfers evolution during a long period of time. While seamount subduction has a potentially significant impact on structures and processes along the subduction thrust, little is still known about the evolution over time of the triggering slope failure and mass wasting in the trench as they are subducted.

The goal of this chapter is to describe and to date the deformation and sedimentary structures formed by frontal erosion of an active subduction margin in tectonic erosion in a place where seamounts are actively and successively subducting. The study concentrates on the frontal erosion of the Ecuadorian margin in Ayampe area, where a large slope indentation was observed (Collot et al., 2009) and subducting seamounts highlighted (Sage et al., 2006). From new bathymetric data, HR seismic and Chirp lines and gravity cores, we successively describe and interpret the morphology of the seafloor, the margin-scale deformation structures and the large and small-scale sedimentary architectures. The results show how different tectonic processes related to the subduction of lower plate asperities interact in time and space to trigger slope failures, large mass wasting (and then trench sediment supply) and possibly tsunamis — detailed analysis pointing to a quasi-permanent stress state building up slope instabilities in the area.

## **5.2 Geological setting**

The active margin of Ecuador, part of the northern Andes orogenic system, is located on the NW border of South America between the latitudes of 1°N and 4°S (Fig. 5.1). The geodynamic history of the northern Andes is intimately linked to the eastward subduction of the Nazca Plate, which results from the dislocation of the Farallon Plate 25 Ma ago (Lonsdale, 2005), below the North Andean block (Fig. 5.1). The slab dips 25° at a rate of 47mm/year (Trenkamp et al., 2002; Kendrick et al., 2003; Nocquet et al., 2014).

The Ecuadorian subduction margin is one of narrowest of South America, with a 20 to 50km-large continental shelf and a 25-40km-large and 4-5° continental slope (Collot et al. 2009). It is characterized by large changes in seismicity, uplift, deformation and sediment delivery (Collot et al., 2004; Collot et al. 2009). The uplift of the central segment of the margin is closely related to the subduction of the Carnegie ridge (Collot et al., 2009). This 280km-wide oceanic plateau originating in the Galapagos Islands raises 2km above the surrounding abyssal plains. The Carnegie ridge separates the northern and the southern segments of the margin, which show a deep trench (Ratzov et al., 2010; Marcaillou, 2016). The uplift of the coastal cordillera caused the separation of the drainage system of the Andes to the west on both sides of the central zone. Sediment fluxes are now directed to the north and the south in the submarine canyons of Esmeraldas and Guayaquil (Collot et al., 2002; Ratzov et al., 2010). The central segment is starved of sediments (Collot et al., 2002; Sage et al., 2006; Collot et al., 2009) functioning in subduction-erosion (Gutscher et al., 1999; Sage et al., 2006). The continental slope is straight and smooth in the central zone and rougher at the northern and southern boundaries of the Carnegie ridge (Collot et al., 2009). The latter are structured by a set of large seaward-deeping normal faults rooted at the plate interface (Sage et al., 2006) and related to the subduction erosion processes. This process is



locally affected by the subduction of seamounts and characterized by coupling heterogeneities, steep continental slope, deep reentrants, km-thick subduction channel acting like lubricant and allowing local decoupling (Sanclemente, 2014). In the south of the Carnegie ridge, the Ayampe basin (Figs. 5.1 and 5.2) constitutes a deep reentrant forming a slope basin. The Pleistocene basin fill is more than a thousand m-thick and probably older than 1.45Ma by considering an average sedimentation rate of 0.83mm/an (Ratzov et al., 2010). According to Sanclemente (2014), the Ayampe basin originates by the subduction of a conical shape seamount with very steep slopes. Considering a constant subduction velocity of the oceanic plate of 47mm/year, the seamount should localize 70km of the trench in a landward direction. Several other seamounts (SMT5, SMT6 and SMT7, Fig. 5.1b) are mapped at the plates interface by Sanclemente 2014.

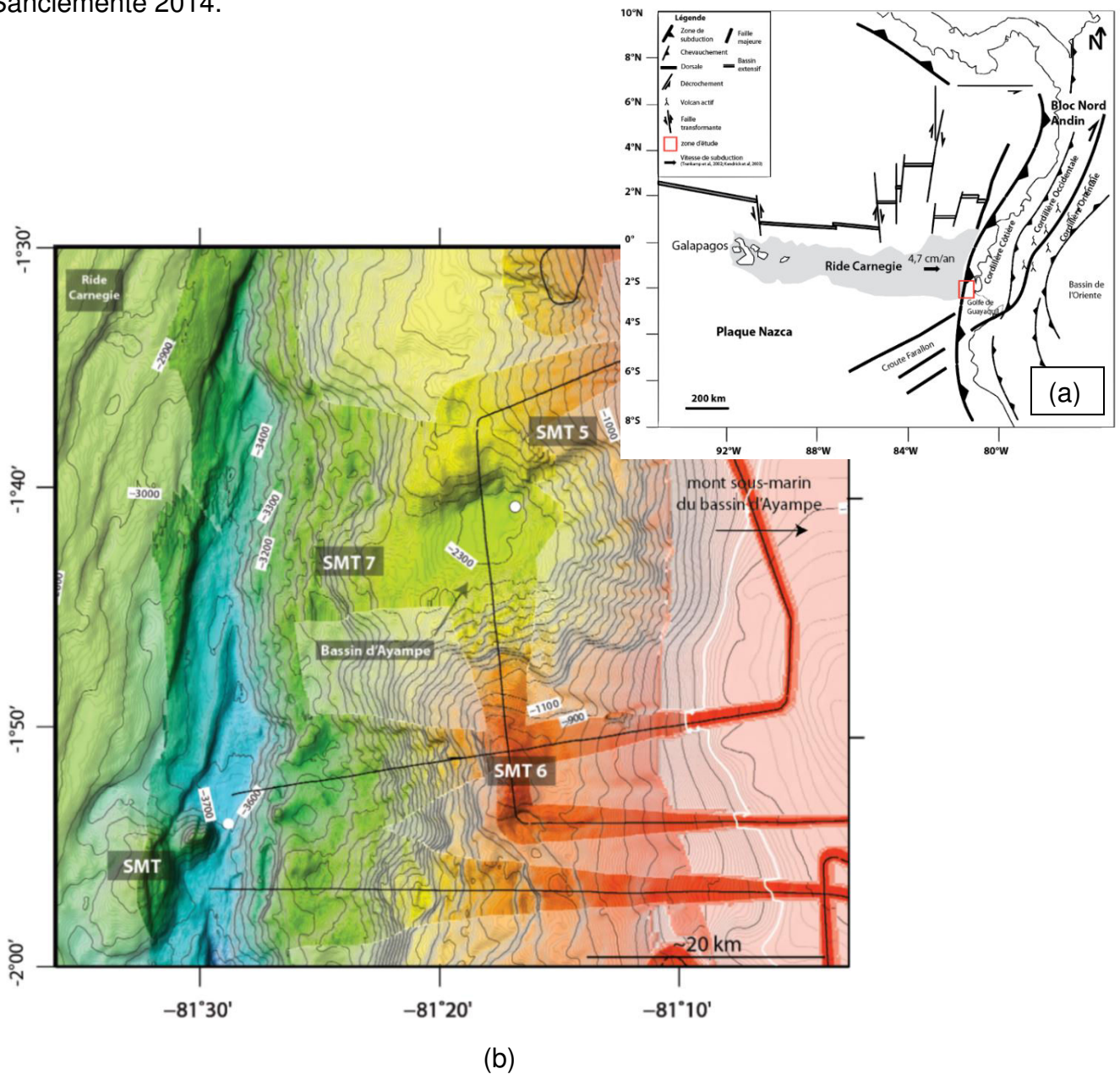


Fig. 5. 1 (a) Geodynamic setting of the north andean margin (modified from Gutscher et al., 1999), and (b) map of the study area with the location of the seismic lines used in this study .and the subducting seamounts (=smt) numbering is from Sanclemente (2014) Figure 7.3.

The subducting seamount (=smt6), focuses upward fluid migration corresponding to several flare-shaped acoustic anomalies in the water column (Michaud et al., 2015). Others (= Smt, Fig. 5.1) are actually entering in subduction close to the Ayampe basin (Sage, 2006), and the area above the subducting seamount (=smt6), focuses the upward fluid migration corresponding to several flare-shaped acoustic anomalies in the water column (Michaud et al., 2015).

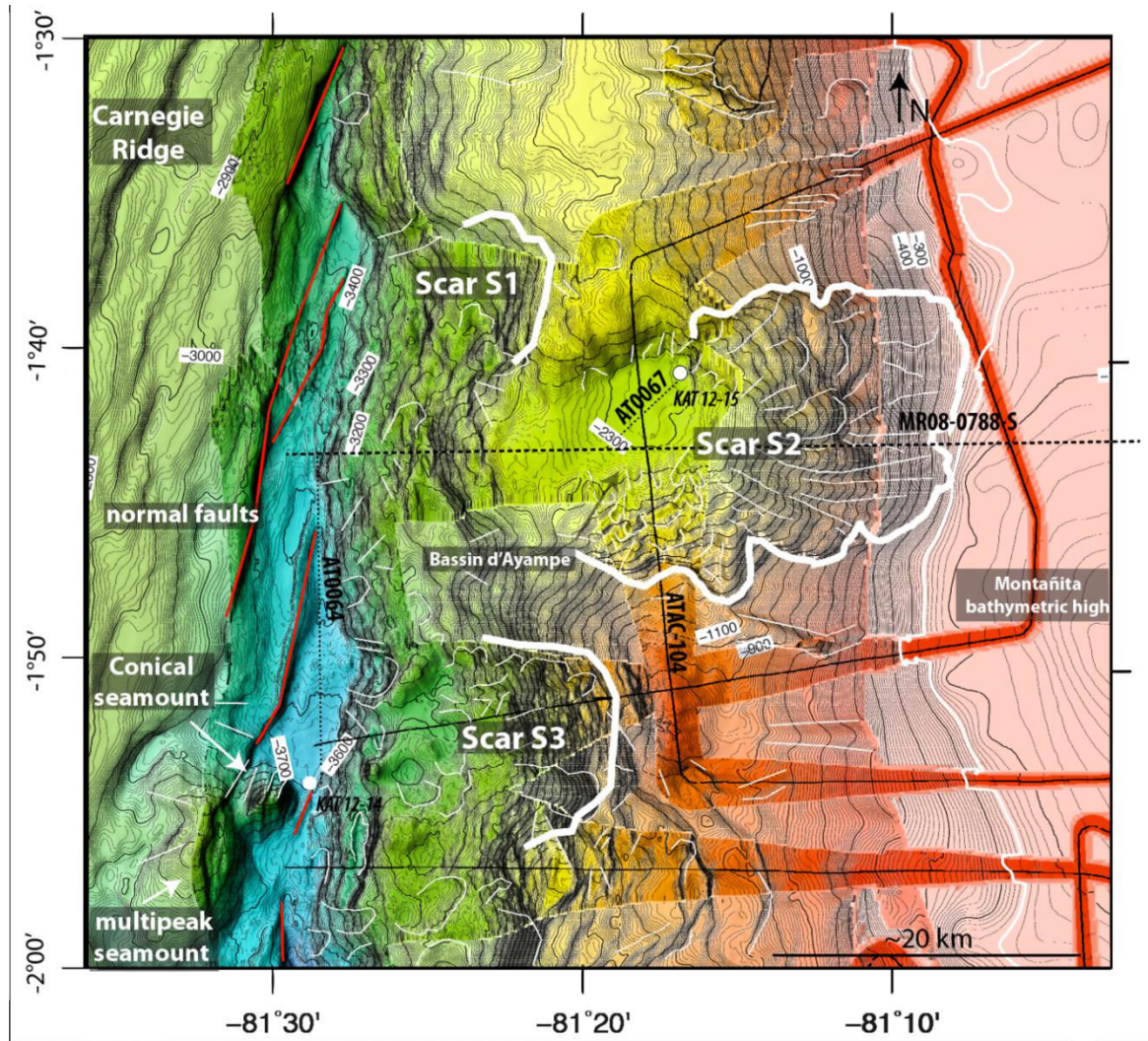


Fig. 5. 2 Bathymetric map of the study area showing the main morphostructural elements at the seafloor

The Ecuadorian margin shows a high lateral variability of seismicity and coupling. The historical records show that the seismicity of the northern segment is very high. In 1906 occurred one of the largest subduction earthquake (Mw8.8) of the 20<sup>th</sup> century, which ruptured the plate boundary on 500km (Kelleher, 1972). In 1942 and 1958, two major earthquakes in Ecuador (respectively Mw7.8 and 7.7) and an earthquake in Colombia (Mw8.2) reactivated the subduction fault. Again, in April and May 2016, two subduction earthquakes MW 7.8 and 6.7 affected the same area at the northern boundary of the central segment. On the other hand, the historical record since 1700 shows no subduction mega-earthquake in the southern as well as in the central segments. The



coupling is very high in the central segment where slow slip events (Chlieh et al., 2014) drop down the accumulated stress along the subduction fault, and low in the south, in the Ayampe area.

The continental shelf is made up of 1000 to 4000m of sediments lying above a lower cretaceous basaltic and doleritic basement. The basement shows two main parts (Hernandez et al., 2015). A northern area (0°45'S-0°40'N) characterized by a low acoustic basement (2-3 twtt) and regional sedimentary basins. A southern area (2°S-0°45'S) characterized by a high acoustic basement (0.8-1 stwtt) with localized sedimentary basins and by N320°-340° trending normal faults dipping to the north. The sedimentary record is comprised of Upper Cretaceous to Lower Eocene small inter-arc basins (Lebrat et al., 1987; Jaillard et al., 1995; 1997, Deniaud, 2000) and Paleogene to Neogene fore-arc basins (Marksteiner et Aleman, 1991; Jaillard et al., 1995; Benitez, 1995). According to Hernandez et al. (in prep.), the Neogene sedimentary basins were initiated along N80°-90° trending normal faults in a regional N30°-50° trending strike slip system. Uplift and local subsidence of the shelf edge with reactivation of a strike slip fault system occurred from Pliocene (?) to Present. The arrival of the Carnegie ridge and associated seamounts to the trench axis is proposed at the origin of this last stage.

The Pleistocene sedimentary record shows well-defined shallow marine sedimentary sequences tied to the climato-eustatic curve of Lisiecki and Raymo (2005), (Martillo, 2016; Proust et al., 2016). These transgressive-regressive (TR) depositional sequences group in megasequences bounded by regional angular unconformities. From base to top: LTR 1.53-1.06Ma (12 TR sequences), MTR 1.03-0.8Ma (6 TR sequences), UTR 0.79-actual (10 TR sequences). This high-resolution record shows that the differential subsidence on the shelf is controlled in some area, like in Manta-Isla de la Plata area, by the subduction of asperities (Proust et al., 2016).

### **5.3 Data and methods**

This work relies on bathymetry, cores and seismic data. Bathymetric data were analyzed to describe the morphology of the seafloor in and around the Ayampe basin. The seismic data helped to characterize the sedimentary and structural geometries, the chronology of sedimentary events and of the deformation sequences and the source of the mass transport deposits.

#### **5.3.1 Bathymetric data**

The bathymetric map on Fig. 5.2 is a synthesis of the multibeam data acquired during successive oceanographic campaigns, and the last campaign is the ATACAMES 2012 cruise (Michaud et al., 2015). The multibeam data are completed on the platform by single beam data from INOCAR (Michaud et al., 2006). The data were processed with the seafloor mapping software CARAIBES (@IFREMER) and set to 150 m grid size cells (50m grid cells for Atacames data).

#### **5.3.2 Seismic data**

The seismic data are comprised of low resolution seismic data (SCAN 2009) provided by the SHE (Secretaria de Hidrocarburos del Ecuador) and high resolution seismic

data acquired during the ATACAMES campaign (2012) on board RV L'Atalante. For this study, we used the SCAN-2009 seismic line MR08-0788S and ATACAMES seismic line ATAC\_104 oriented respectively dip (EW) and strike (NS) across the slope and the Ayampe basin (Fig. 5.3). These data are complemented by CHIRP profiles AT0064 and AT0067 acquired respectively in the trench and in the Ayampe basin during the ATACAMES 2012 campaign.

The low resolution, deep penetration, multichannel seismic reflection (MCS) were recorded using a 4000 in3 air gun seismic source, and a 640 -channel, 8-km-long 8m-depth streamer. Shots were fired every 25 m, providing 160-fold coverage with a distance of 183m between the source and the first channel.

The high-resolution seismic reflection data were recorded using a 72-channels digital streamer towed at 2 m of water depth (channel length 6.25 m). The source array towed at 2.1m of water depth consisted of two ramps mounted with three 13/13Ci plus three 24/24Ci mini GI gun. Shots was fired at 140 bars every 25 m. Given this shot rate and the streamer configuration this seismic reflection system ensures a 9-fold stack. The seismic lines were processed on board with the Seismic Unix (SU) software (Center of Wave Phenomena, Colorado School of Mines) for Band Pass Filtering, spherical divergence correction (water velocity) - NMO velocity analysis and correction, 9-fold stack and constant velocity time migration (1490 m/s).

The CHIRP sub-bottom profiles were acquired with a hull-mounted Chirp system (1.8–5.3 kHz). Vertical resolution is dm-scale. These data were used to correlate seismic data with core data.

The seismic profiles were interpreted applying the criteria of the seismic stratigraphy (Mitchum et al. 1977): configuration, amplitude, continuity and frequency for identifying the seismic facies (Damuth, 1980; Proust et al., 2016), and the stratal terminations (Vail et al., 1977) for definition of seismic unit. The velocities used to interpret the depth of reflectors in the Pleistocene part of the sections are the followings: 1900m/s in LTR, 1800m/s in MTR, 1700m/s in UTR and 1600m/s at the seafloor (Martillo, 2016). For the deep seismic data, we used the following velocities (Sanclemente, 2014).

### **5.3.3 Core data**

Two cores issued from the ATACAMES campaign were selected for this study: core KAT12-15 in the Ayampe basin and core KAT12-14 at the toe of the slope, in the trench. We ran a series of analysis to identify the sedimentary facies and to date them. These analyses include the followings.

The high-resolution photography of the full length of the cores, petrophysical measurements (magnetic susceptibility, density) acquired with a Geotek multisensor core logger of the University of Rennes1 (Geosciences Lab); X-Ray imaging and XRay fluorescence of the full core length acquired respectively with a Scopix core scanner (Migeon et al., 1999) and the Avaatech XRF core scanner 10-50kV (Richter et al., 2006) of the University of Bordeaux 1 (EPOC lab); The XRF sampling was realized every cm at 10 and 30kV to trace changes in Ca, Fe, Si, Ti, Sr, Cu, Zn, Mn, V, Rb, Cr, Al, Al, S, Cl, K, Br and Zr contents. The ratio Ti/Ca proved to be very useful to trace terrigenous fluxes since Ti is more of continental affinity while Ca is more marine (Saint

Onge et al., 2007). 14C age dating performed with the ARTEMIS platform in Saclay on planktonic foraminifera from hemipelagites.

## 5.4 Results

This section presents the results of the analysis of the bathymetric data, the seismic data and the core data acquired in Ayampe basin area. The seismic data are at different resolutions, low (MR08-788S), high (ATAC 104) and very high (AT00067 in the Ayampe basin and AT00064 in the trench) resolutions. The core data are core KAT12-15 in the basin and core KAT12-14 in the trench.

### 5.4.1 Seafloor morphology

The compilation of the bathymetric data in the Ayampe basin area allows to better understand the morphology of the subduction margin where seamounts are still actively subducting (Fig. 5.2).

The Ayampe basin is facing the southern end of Carnegie ridge, a place where the ridge is spotted with 100 m-high and 10-15 km large seamounts. Here, the trench is 10 km large, comprises few seamounts including one conical-shape and one multipeak (Fig. 5.2) and is dissected by NNE-SSW oriented faults that dip southward at a regional scale. The trench floor dips regionally to the south like. The bathymetry of the trench varies from 3250mbsl in the north where its faces the top of the Carnegie ridge, to 4500mbsl, in the south (Fig. 5.2).

To the east of the trench, the continental slope and the continental shelf are very narrow, respectively 25-40 km and 20-50km-wide. The continental slope varies in depth from 100-150 mbsl to 3700mbsl and shows a drastic change from a smooth and linear morphology to the north to a rough and indented morphology to the south. In the later, the material could have been removed by tunneling and underthrusting of seamounts (Sage et al., 2006; Collot et al., 2009; San Clemente, 2014; Ranero and von Huene, 2000; von Huene et al., 2000).

The continental middle slope in Ayampe area is affected by numerous 100m to km-scale scars but three large ones are more than 10 km-large (1 to 3, white lines on Fig. 5.2). The large scars are quite regularly offset along the slope. They sit 5-10km apart along strike, c.700 m apart in water depth (headward limits of scar 1, 2000 mbsl; scar 3, 1200 mbsl; scar 2, 500 mbsl; Fig. 5.2) and 10 km apart in dip section — scar 1 is located at 8km from the trench, scar 3 at 16km and scar 2 at 32km. Scar 2 is the largest (20km-large) and deepest (2250m below the shelf edge) which sharply incises the frontal outer wedge and breaches the continental shelf edge. A deep subcircular reentrant characterizes scar S2 it with a flat at 2000 m in water depth and headward, on the shelf. It is bordered to the southeast by a bathymetric high (Montanita high). The southern flank of scar 2 is irregular, undulated with 100-m high EW trending steps. The northern flank of scar 2 is more regular and straighter. The eastern flank of the scar 2 exhibits two different morphologies; one to the south with E-W gullies and one to the north with NS steps. The scarp 3 is characterized by numerous N-S narrow steps. East of the scar 3, the middle slope exhibits a N-S elongated bulge which overhangs the scar; this area of reverse slope corresponds to the location on the inter-plate of a subducting seamount down along the slab (SMT on the Figure 2 of Sage et

al, 2006) and related to the formation of the scar 3. South of this N-S elongated bulge, several linear to slightly arcuate 100m-high scarps cut the slope.

#### **5.4.2 Tectonic structures**

The seismic line MR0788S oriented in EW dip direction provides a general view of the subduction margin and Ayampe basin (Fig. 5.3).

To the west, the seismic profile shows the Nazca oceanic plate with the Carnegie ridge subducting below the North Andean Plate. The subducting plate shows the oceanic basement overlain by well-stratified reflectors corresponding to 500m-thick carbonate oozes (Mix et al., 2003). The oceanic plate and its sedimentary cover are cut by east dipping normal faults, the offset of some of them overhanging the trench floor by 100m-high reliefs.

The interplate boundary is characterized by an irregular, highly reflective horizon, with reverse polarity, dipping 4-5° (Sage et al., 2006) to 6-7° (Sanclemente, 2014) to the east and emerging at the trench floor. It shows a 600m-high mound sited below the uplifted apex of the basement. A 7km-wide, 200m-high lens of highly reflective and chaotic reflectors lies on the eastern flank of the mound when a 12km wide, 600m-high set of seaward deeping reflectors lies to the west.

Eastward, the overlying plate, which includes the Ayampe basin, shows a complex structure. The top of the basement is a very irregular and reflective horizon at the boundary between the massive, structureless to chaotic unit below and the well-stratified unit of the sedimentary cover above. These units correspond respectively to accreted, ancient oceanic terranes (Reynaud et al., 1999; Graindorge et al., 2004), Tertiary rocks (Hernandez et al., 2015) and Quaternary sediment (Martillo, 2016) cover. The basement rocks form a thick wedge, which pinches out sharply to the west, 8km from the trench axis. To the east, the top of the basement and its sedimentary cover are affected by west dipping normal faults delimiting 3-5km-large tilted blocks (Fig. 5.3). To the west, the apex of the basement is cut by numerous low angles, reverse faults. Beyond, the mound, the reverse faults propagate in the small (4-5km-wide) sediment accretion prism.



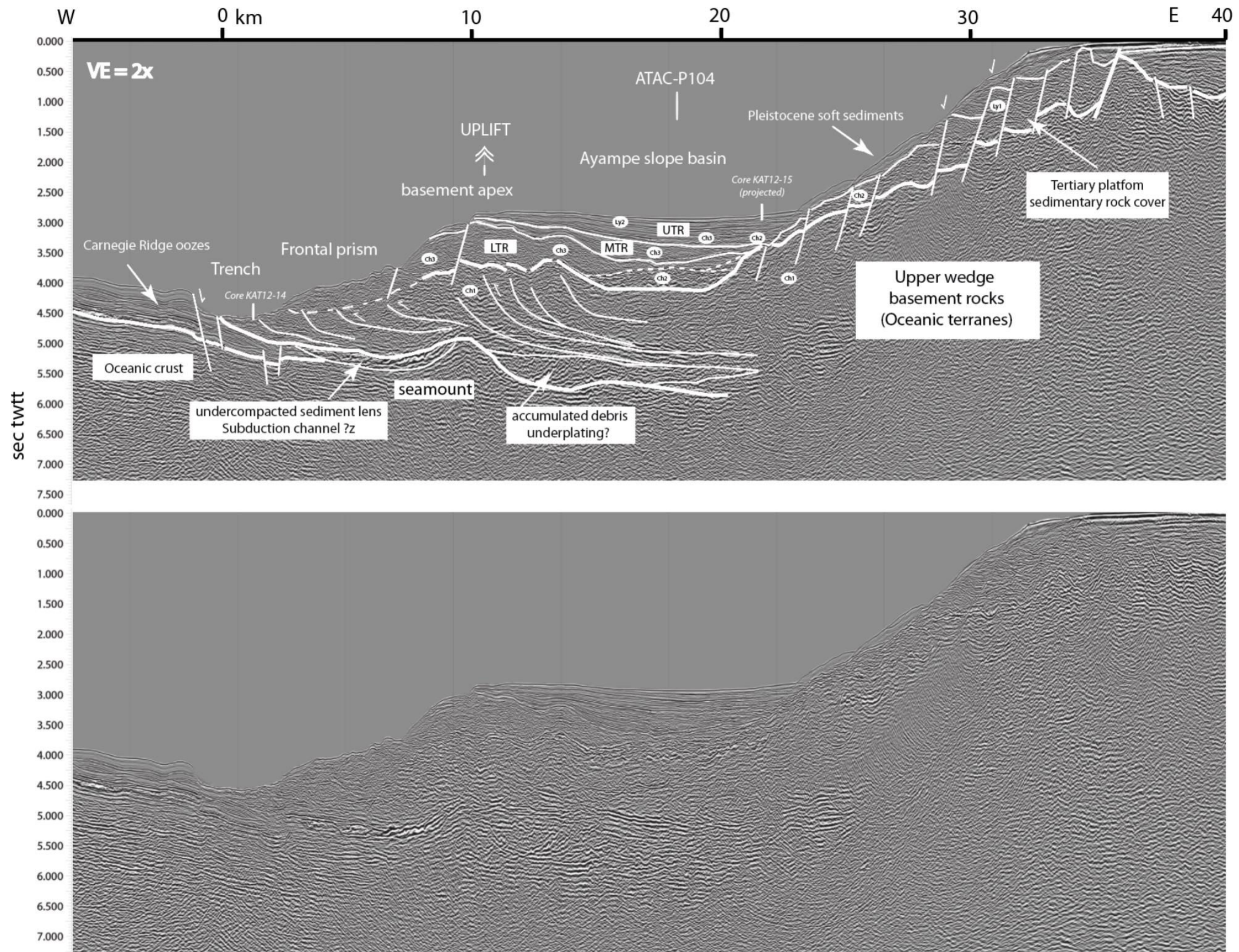


Fig. 5. 3 Line drawing of the low resolution seismic line MR08-788-S (see location on figure 5.2)



The margin basement is fronted by chaotic reflections to the east in a small accretion prism and overlain by 1250m of chaotic and well-stratified reflectors in the Ayampe slope basin, the upper slope and the platform. The sedimentary cover is comprised of three unconformity-bounded units: an entirely chaotic unit (LTR), and two chaotic and well-stratified units (MTR and UTR). The seafloor truncates the reflectors of the three units on the high above the set of reverse faults at the apex of the basement. On the north-south, high-resolution ATAC-104 seismic line (Fig. 5.4), the unconformities at the base of the three units merge along large km-scale glide planes overlain by tilted and rafted blocks (Fig. 5.4). These narrow-tilted blocks correspond to the narrow steps described above on the bathymetry along the southern flank of the scar 2. Along the northern flank of the scar 2 the tilted blocks are wider.

*Interpretation* — The conical shape mound at the interplate boundary is interpreted as the relic of an seamount now subducting. The highly reflective reflectors at the back of the mound present a facies similar to the one observed in the under compacted, high porosity (15-18%), water-charged sediment commonly observed in patches along subducting plate interfaces (Sage et al., 2006; Ranero and Von Huene, 2000). These water-saturated sediments are provided by rapid mass wasting in the trench by repeated instabilities of the slope (Collot et al., 2001). The seaward dipping reflectors at the front of the seamount might be tentatively interpreted as underplated material, a package of both drafted debris dragged from the trench and probably eroded from the base of the upper plate. This high basal friction and basal erosion is attested by the rapid seaward wedging out of the basement rocks together with the low angle reflectors and reverse faults at the apex of the basement. This area that superposes to the relief of the seamount appears uplifted by c.500m as attested by the high density of reverse faults in the apex of the basement, the topographic high at the seafloor of the same range as the underlying relief of the seamount, and the truncated reflectors of the sedimentary cover at the seafloor. The compression at the apex of the basement is contrasted by extension and faulting and block tilting along series of listric, normal faults which are rooted at the plate interface according to Sage et al. (2006) in the mid to upper slope. This extension probably promotes the formation of large gliding planes at the base of the sediment slides LTR, MTR and UTR. Southward of the Ayampe basin, the N-S seaward deepening scarps correspond to normal faults; these faults which are related to the regional subduction erosion process and were probably present northward, all along the area, before the arrival of the seamounts. Indeed, Sage et al., (2006) show that the middle slope of the margin is structured by normal faults rooted close to the plate interface.

### **5.4.3 Seismic Facies**

This section describes and interprets the seismic facies observed in the Ayampe area and provides an interpretation for their main characteristics in term of lithologies and depositional environments according to principles outlined in Mitchum et al. (1977) and Sangree and Widmier (1977). We recognized three main seismic facies at different scales on low (MR08-788S, Fig. 5.3), high (ATAC-104, Fig.4) and very high (AT0067, Fig. 5.6; AT0064, Fig. 5.7) resolutions seismic lines. The seismic facies are of three types: layered, chaotic with diffractions and semi-transparent facies, which give rise laterally to each other.

S

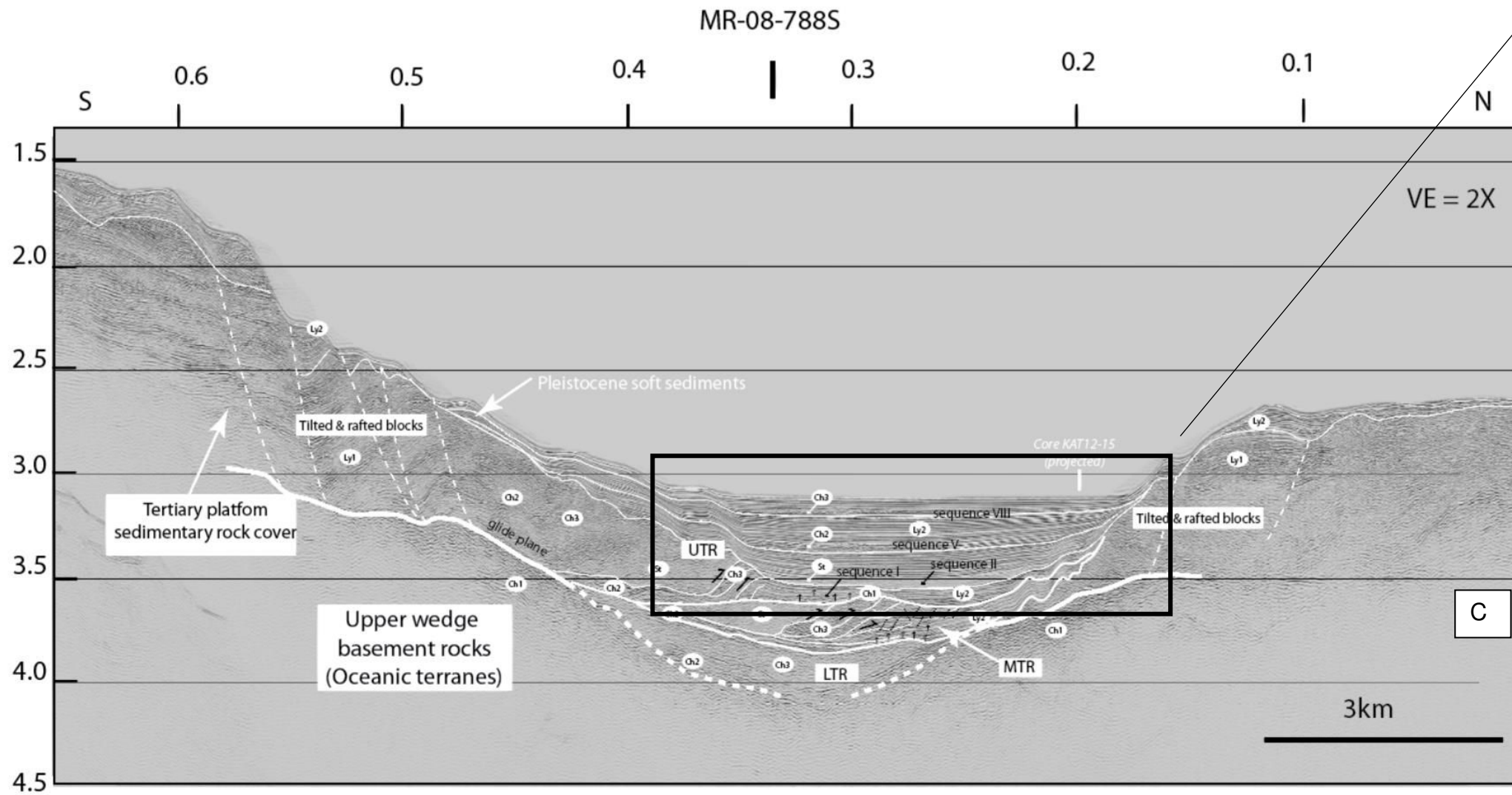
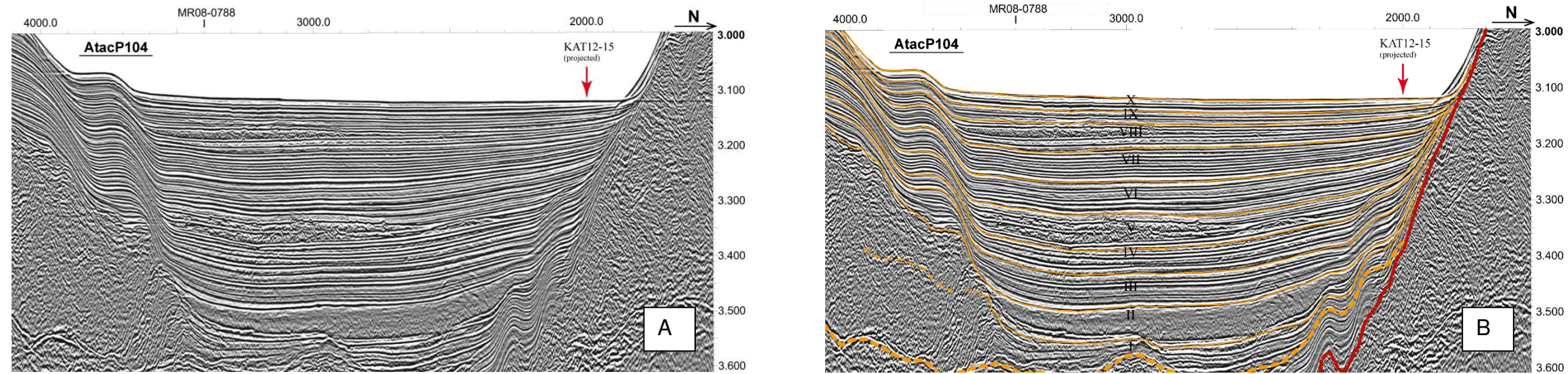


Fig. 5. 4 A) Chirp line AtacP104, without interpretation, showing details of the sedimentary basin (modified from Martillo, 2016), B) Interpretation of the sedimentary basin showed in (A) (Martillo, 2016), and C) Interpretation along hole seismic line ATAC-104 (see location on figure 5.2)

#### 5.4.3.1 The chaotic facies (Ch)

They are of three types. The *first type* (Ch1) is a high amplitude chaotic facies with abundant high angle diffractions. Its lower part is masked by sea floor multiples. A high amplitude reflector underlines its top. It is exposed at the base of the seismic sections where it forms the acoustic basement. The *second type* (Ch2) is a set of large scales, wavy, lens shape and chaotic reflections with high impedance contrasts. The *third type* (Ch3) is a blurred mix of small incoherent moderate and low amplitude reflections (Fig. 5.3, Fig. 5.4). By places, it shows km-scale folds of N00 axis draping the basement irregularities. This facies is exposed at the base of the Ayampe basin fill, along and at the toes of the detachment fault glide planes and in thin lenses interbedded in the layered facies of the basin fill (Fig. 5.3 and 5.4).

*Interpretation* — The first type (Ch1) chaotic configuration with highly inclined, disrupted reflections and high angle diffractions is indicative of the presence of thinly layered but deformed and dissected rock elements while the underlying transparent facies might be interpreted as massive rock bodies. This unit that constitutes our acoustic basement likely corresponds to the substratum of the platform. This substratum is largely composed of Cretaceous volcanics and volcanoclastic sediments as shown by the correlations with land exposures (Reynaud et al., 1999). The high impedance contrasts in the second type (Ch2) points to the accumulation of blocks and debris where the mix of rough and contorted bedding and glide planes suggests a partial dismembering of strata and blocks by places transformed in rock avalanches. The third type (Ch3) shows incoherent reflections of moderate amplitudes with almost no (or small) diffractions, which can hardly be distinguished from each others. It might correspond to highly disrupted, small-scale but well-lithified stratal elements (moderate amplitude reflections) mixed with soft incoherent and contorted lithologies (low amplitude reflections) arranged at random in large debris flows. The common lateral transition from facies Ch2 to Ch3 suggests a progressive evolution of the flow along slope.

#### 5.4.3.2 The layered facies (Ly)

They are also of two types. The *first type* “poorly layered (Ly1)” shows the interlayering of packages of low and high amplitude subparallel reflections with moderate to low continuity and frequency. It is exposed on the platform and at top of the surrounding reliefs (Fig. 5.4) where it is dissected by numerous normal faults. The *second type* “well-layered (Ly2)” shows high to moderate amplitude, high continuity and parallel reflection configuration with, by places, a lateral frequency change from thinly- to thickly-layered characters *i.e.* the thickness of the transparent facies between to high amplitude reflectors varies and wedges out laterally. It is well exposed in the trench and constitutes most of the Ayampe basin fill. The layered facies drapes the underlying irregularities of the substrate. By places, *i.e.* at the rim of the basin and at top of surrounding relief, it shows some km-scale S-type wavy-bedding, trough-shape and cross-bedded infills of erosive depressions (Fig. 5.4). Characteristically the troughs of the S-type wavy bedding and the trough shaped in fills superpose to the tip of the normal faults. Those in-fills are most pronounced, thicker and deformed, in an up dip direction where they are progressively onlapped by younger strata.



*Interpretation* — The first type of layered configuration (Ly1) shows, in area not disrupted by faults, a well-bedded configuration with regular alternations of low and high amplitude packages of strata. This configuration is common for sediments preserved in small depositional sequences or parasequences in the outer shelf parts of most continental platforms. This well lithified facies can be attributed here to the Tertiary sedimentary cover of the platform. The well-layered character of the second type (Ly2) draping the underlying irregularities of the substrate, points to thin- to medium-bedded sedimentary strata of different densities settled in the Ayampe basin. These strata correspond to the alternations of Pleistocene age sands and silty clays of turbidite origin recognized and groundtruthed elsewhere in Manta-Plata area (Proust et al., 2016; Martillo, 2016). At the rim of the Ayampe basin and the top of some large faulted blocks, the S-type wavy, trough and high angle cross-bedded are indicative of active hydrodynamic transport. Such processes at great depth (over 2000mbsl) and away of any recognized channel feeder resemble contourite drifts and/or sediment and water laid overflows (hyperpicnites?) beyond the edge of the platform. However, the thicker and increasingly deformed channel fills, which are set at the tip and along normal fault glide planes in an up-dip direction, indicates that these faults have been operating for a longer period of time at the top of the slope than at its base.

#### **5.4.3.3 The semi-transparent facies (St)**

It is almost devoid of any coherent reflections except some sparse remnant and contorted low amplitude and discontinuous reflections. This facies occurs in lenses at the base of the Ayampe basin fill in between the chaotic and the layered facies (Fig. 5.4) and forms extensive, fan shape, c.45 m-thick greyish/whitish bodies in the trench, wedging out after 1 to 10's km in a direction parallel to the trench (Fig. 5.7). These latter sediment bodies repose either on an older one or on a well-layered seismic facies, without any significant erosion surface (Fig. 5.4, Fig. 5.7) but disrupted by numerous fluid escape pipes. The base of the transparent facies bodies is flat while their top is irregular, with bumps underlined by low amplitude seismic diffractions. The sediment body is capped by few continuous, moderate amplitude reflections.

*Interpretation* — The homogenous character of this facies with the lack of coherent reflection is interpreted as a homogenous sediment body with rare but disrupted pieces of strata. Their fan shapes together with their flat base and their irregular top are indicative of their emplacement during single events along a non-erosional sole or glide plane. The presence of abundant fluid pipes below these bodies might explain either the basal buoyancy of the sliding mass and the overall transparent character of a sediment body deeply impregnated with fluids. This facies is interpreted as water saturated mass transport deposits or slump.

#### **5.4.4 Seismic facies architecture**

Martillo (2016) correlates the sequence stratigraphic framework established in Manta-Plata area for the Pleistocene sediments (Proust et al., 2016) along the ATACAMES and SCAN seismic grids to the Ayampe basin. This work provides a detailed and reliable time stratigraphy in the area. The individual sequences that compose the megasequences LTR and MTR are hardly distinguishable on the Ayampe seismic profiles but the UTR mega-sequence shows the full set of 100 kyrs- sequences. In the Ayampe basin, LTR, MTR and UTR lay on erosional, locally angular unconformities

that merge upslope with a large regional glide plane parallel to scar 2 and rooted in the normal faults at the base of the westward tilted blocks.

#### 5.4.4.1 The LTR mega-sequence

It is very thick (c.850 m in its thickest part), typically lens shape. LTR rests unconformably on the acoustic basement (Ch1) and on the sediments of the accretion prism beyond the basement edge apex, where it progressively wedges out in a seaward direction (Fig. 5.3). To the west, 1500m offset normal faults dissect LTR at the outer edge of the Ayampe slope basin (Fig. 5.3). Km-scale folds, parallel at the base and top of LTR, superpose to large-scale reverse basement faults. In a downslope and seaward direction, LTR shows the lateral transition from of the chaotic facies with high and low impedances Ch2 and Ch3. It is overlain on its landward side by a thin slice of semi-transparent facies St.

*Interpretation* — The LTR mega-sequence shows the lateral change from chaotic debris avalanche (Ch2) and more mature debris flows (Ch3) capped by slumped water saturated sediment (St). Such an evolution is usually observed in the proximal part of gravitational sequences, at the toe of slopes, where the transition between mass wasting (avalanche, slump) and gravitational laminar flows (debris flows) occurs (Fig. 5.5). Indeed, LTR basal unconformity onlaps (at the seismic data scale) the glide plane between the deformed tertiary sedimentary rocks and the basement indicating that it might results from a large sediment pile sliding down the slope in a WNW direction — most of it being eroded out now.

LTR is offset by large normal faults above the apex of the basement, giving rise to a massive accumulation of sediment at the toe of the slope. This wedge is thicker on the hanging wall of the faults, which confirms the uplift of the Ayampe basin outer edge relatively to its depocenter. Post depositional folding at the tip of the underlying reverse faults as well as the truncation of strata by the seafloor support this hypothesis.

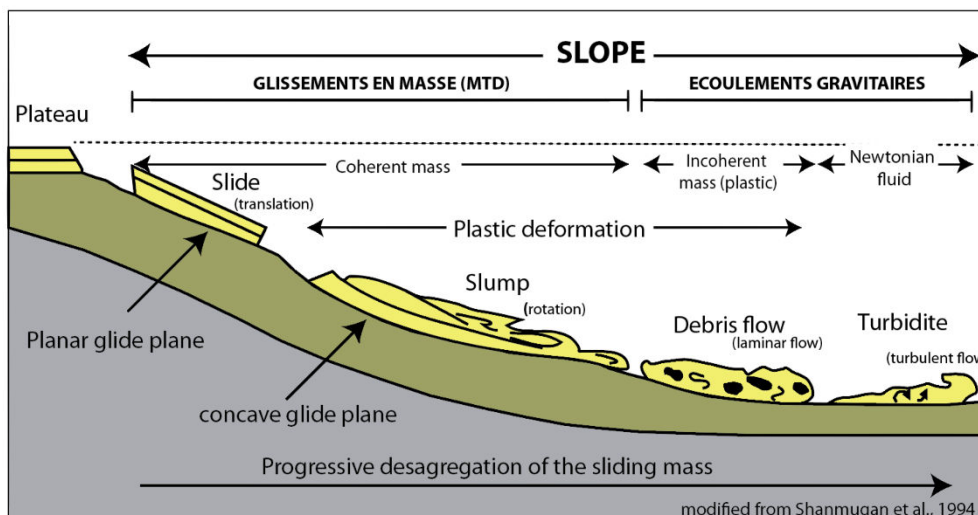


Fig. 5. 5 Oversimplified drawing showing the lateral distribution of the gravitational sedimentary events along a virtual continental slope. Modified from Shanmugan et al, 1994.



#### **5.4.4.2 The MTR mega-sequence**

It is c.250m in its thickest part. It largely rests unconformably on LTR but as well, on the Tertiary sediments, to the south of Scar 2 (Fig. 5.4). On the dip section (EW), it wedges out seaward onlapping LTR and thicken in a landward direction, lapping out on the basin edge (Fig. 5.3). It is comprised of a set of well-layered sequences (Ly2), which give rise in a landward direction, to the chaotic facies Ch3. The latter deeply incises into the layered facies Ly2 for 200m.

On a strike section, the sediment wedge shows a facies change to the north from semi-transparent (St), to chaotic with no diffraction (Ch3) interlayering with the well-layered facies (Ly2) (Fig. 5.4). The two facies St and Ch3 laying on a lens of facies chaotic Ch2. Facies Ch3 and Ly2 at the northward end of the wedge are cut by small high angle reverse faults dipping to the south, and fluid escape structures.

*Interpretation* — On the dip section, the MTR mega-sequence shows a divergent pattern to the east and wedges out to the west, where it onlaps the LTR high and is truncated by the seafloor. This suggests a differential subsidence with an active uplift to the west and a sharp drowning to the east. The chaotic debris flows Ch3 accumulate to the east, in the upper part of the well-layered deep marine turbidites, next to the basin margin. The debris flows down cut sharply into the underlying well-layered sediments to the east and less to the west. This suggests that the debris flow was not provided from the uplifting high to the west and that sediments were very effectively transported from the east or partly sidewise, along the continental slope.

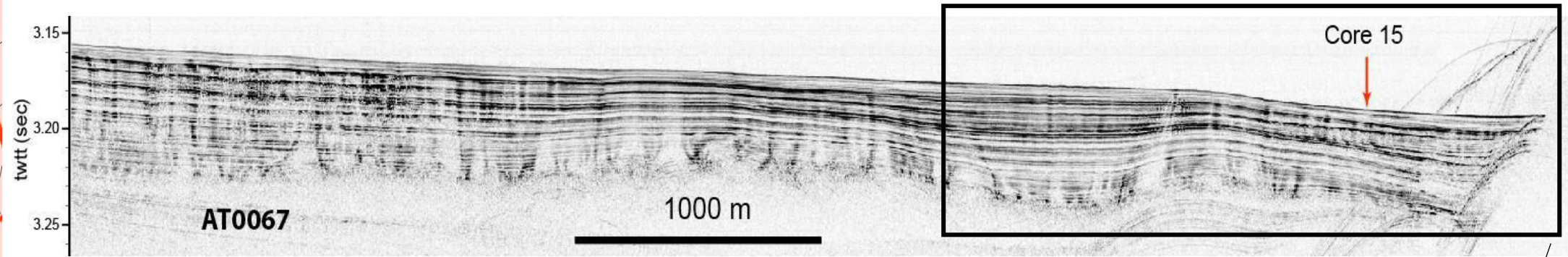
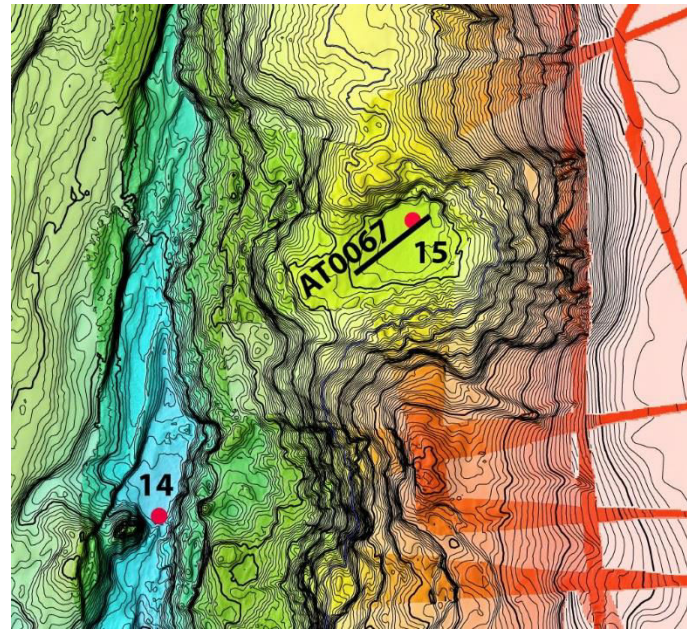
On the strike section, the MTR mega-sequence shows a complex suite of facies indicative of the lateral evolution of a succession of northward flowing large gravitational events. The suite comprises homogenized slump blocks (facies St), a series of debris flows (facies Ch3) crosscuts by imbricated reverse faults interlayering with turbidites deposits (facies Ly2). This suite of facies lays on a sole of highly reflective debris (facies Ch2). Like LTR, this suite of facies is typical of a toe of slope sequence of a large gravitational event. The sequence is more complete showing (1) the transition from plastic deformation (slump and debris flows) to fluid and turbulent transportation (turbidites) a little bit farther downslope and (2) a sole of coarse debris along the basal highly frictional plane.

#### **5.4.4.3 The UTR mega-sequence**

It is c.450m-thick in its thickest part. On the dip section, like MTR, it wedges out in a seaward direction and thickens in a landward direction, reflectors lapping out the base of the slope of the eastern basin edge and onlapping the high to the west (Fig. 5.3). UTR is comprised of set of unconformity-bounded depositional sequences in the well-layered facies (Ly2), which give rise to the east, to lenses of the chaotic facies (Ch3), next to the basin edge (Fig. 5.3). The chaotic facies are cast in sequences I, II, V and VIII. There are usually thin, less than 50m-thick, but reach 200m-thick in sequence II, where the chaotic facies shows many incised channel features.

On the strike section, UTR thins out to the South (Fig. 5.4). At the base, sequence I shows the lateral transition, from north to south, from (1) a c.950m-thick, progressively

tilted, poorly layered facies (Ly1) truncated by large normal listric faults dipping and decreasing in dip to the north to (2) a semi-transparent facies (St), (3) a chaotic facies without diffractions (Ch3) and (4) a well layered facies (Ly2) truncated by small reverse faults dipping to the South, and fluid escape pipes (Fig. 5.6). Channel fills and S-type wavy bedding preserved in small grabens at the top of the poorly layered facies cap this succession. The graben fills are most pronounced, thicker and deformed in an up-dip direction where they are progressively overlapped by the younger sequences of UTR. UTR comprises some chaotic (Ch2, Ch3) and thin semi-transparent (St) facies in sequences II, V and VIII.



Low angle erosion surfaces overlain by downlapping patterns in Ly2 strata

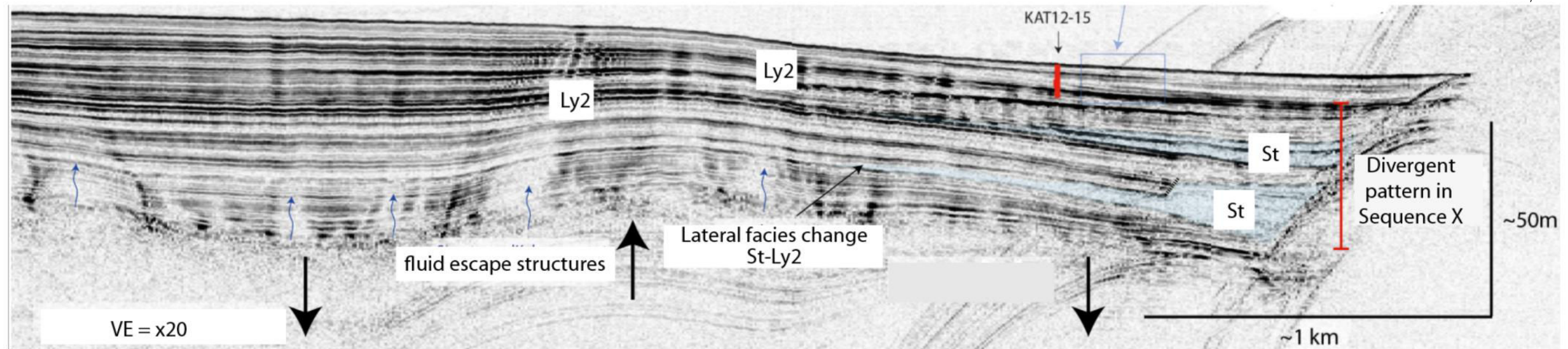


Fig. 5. 6 High resolution CHIRP seismic line AT0067 in the Ayampe basin (see location on figure 2)



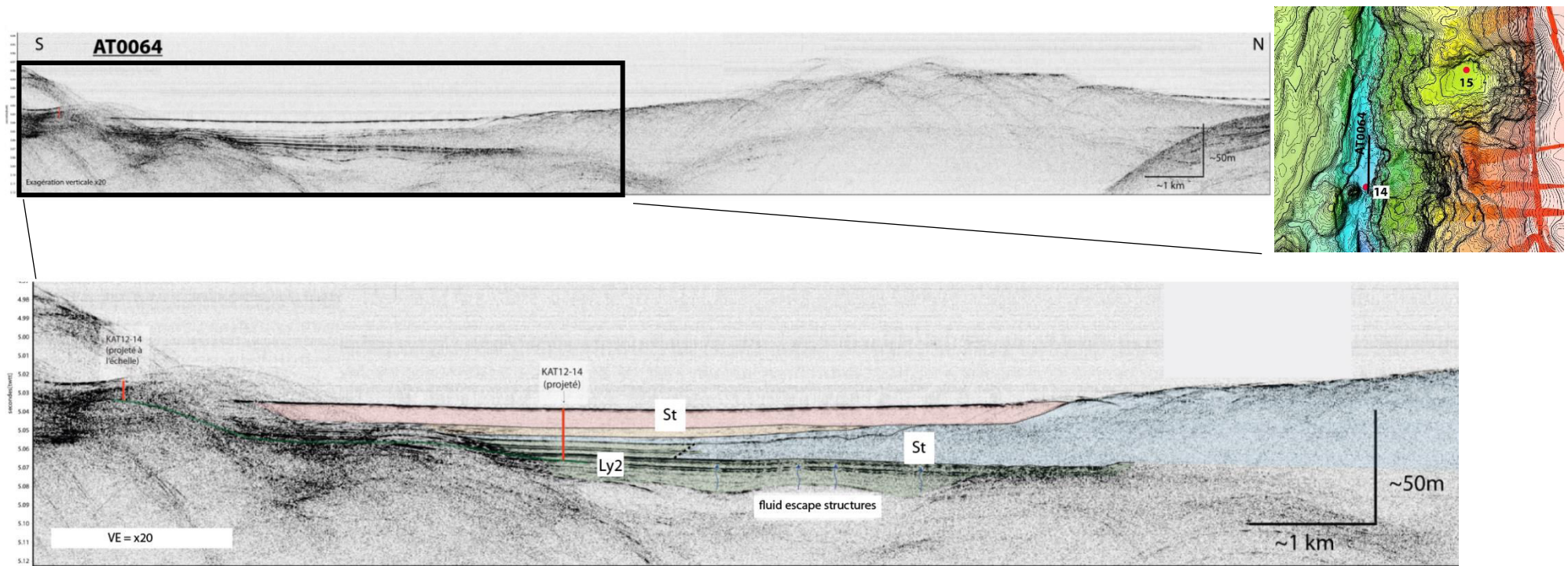


Fig. 5. 7 High resolution CHIRP seismic line AT0064 in the trench (see location on figure 2)

*Interpretation* — On the dip section, UTR shows a divergent pattern to the east. The well-layered reflectors onlap the high to the west and individual sequences shows erosional truncations indicative of a permanent uplift of the high to present day times. The chaotic facies concentrate in few sequences and to the east along the slope of the basin showing that the debris flows were not provided by the high to the west but more probably sporadically by the basin slope to the east at certain times. On the strike section, from south to north, the presence of a 250m-high scarp, the progressively tilted strata along decreasing dip listric normal faults (facies Ly1) rooted in a concave upward gliding plan and encased into slumped (facies St) and debris flow (facies Ch3) material interlayered with well bedded sediment (facies Ly2) is interpreted as the downward and outward movement of a mass on top of a concave upward failure surface (Abbott 2004) or rotational landslide (Hampton et al., 1996). The rotational displacement is confirmed by the presence of small reverse faults in the chaotic facies, which form the headward transverse ridges and cracks in the well-layered facies along with fluid escape features likely fed by water flows along a gliding surface underlined by large debris (facies Ch2).

The toe of the landslide is encased in the sequence I of the well-layered turbidite facies (Ly2). The other sequences from II to X progressively onlap the landslide in a well-layered sedimentary pattern. Sediment gravity flows are scarce and represented by a 70m-thick slump (facies St) in sequence II and m- to 10m-thick more or less mature debris flow in sequence V (mass transport facies Ch2) and VIII (debris flow facies Ch3). It is not clear how to correlate the infilling of the small grabens with the details of the UTR stratigraphy. However, the graben hyperpicnites and contourite infills at the top of the large normal faults seem thicker at the top than at the base of the slope suggesting that the faults worked or simply remained uncovered for a larger amount of time.

Mega-sequences LTR and MTR show facies successions that resemble the facies succession observed at the toe of UTR. They might represent two former rotational landslides which upper part had been removed by erosion.

### **5.4.5 Sedimentary Facies**

The sedimentary facies were sampled by coring the upper sedimentary sequence (sequence X in UTR) in the Ayampe basin (KAT12-15, Fig. 5.6, Fig. 5.8) and at the toe of the slope (KAT12-14, Fig. 5.7, Fig. 5.9). The cores were tied to the seismic interpretation by correlation with the 3.5kHz data in the basin (AT0067, Fig. 5.6) and the trench (AT0064, Fig. 5.7), which show a complex interlayering of the semi-transparent (St) and well-layered facies (Ly2).

#### **5.4.5.1 Core KAT12-15**

On the coring site, in Ayampe basin, reflectors on line AT0067 show a km-scale wavy configuration with a divergent pattern towards the toe of the slope (Fig. 5.6). At this later place, they show low angle erosion surfaces overlain either by sets of reflectors that downlap toward the trough at the base of the slope or lenses of facies St thickening at the approach of the slope. Fluid escape structures underline the erosion surface at the base of sequence X.

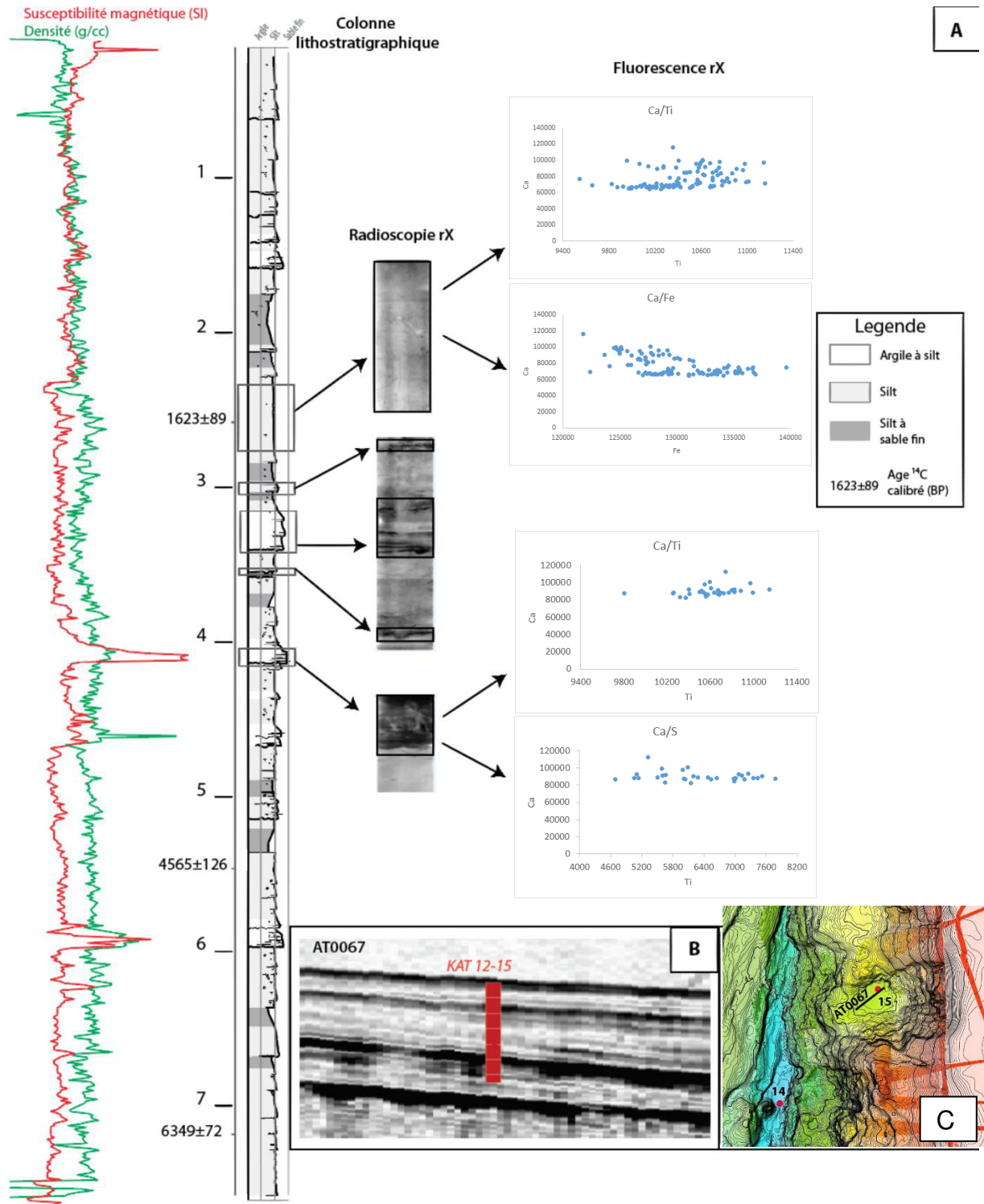


Fig. 5. 8 A) Synthetic lithostratigraphic column of core KAT-12-15 (Ayampe basin) with petrophysical parameters (density and magnetic susceptibility), x-ray fluoroscopy and X-ray fluorescence of two lithofacies. B) core projected on the seismic profile AT0067. C) location of the core on the map (fig.4).

The collected core is 7.5m-long (Fig. 5.8). It shows the superposition of cm to dm-scale fining upward successions of fine sands, silts and muds lying on discrete erosion



surfaces. The sand is fine-grained, quartz and lithic arenite, yellowish and fining upward with planar to low angle laminations. XRF data show that the sand is rich in terrigenous elements and, when present, Ca correlates with S and Ti pointing to its detrital origin. The silts are greenish-grey, fining upward with remnants of ripple and convolute laminations in the basal sandier horizons and planar laminated and bioturbated in the pure silty parts. The muds are greyish green, structureless but largely bioturbated and enriched with benthic and planktonic foraminifera. Ca does not correlate with Ti and S that is indicative of in situ marine origin of the Ca in the muds. Magnetic susceptibility (S) and density (D) logs show three peaks at 3.5, 4.0 and 5.2m and a low at 2.0m. The latter shows a sharp change in the log pattern from amalgamated and low D/S ratio, above, and separated and low D/S ratio, below. Three <sup>14</sup>C age dating were measured on planktonic foraminifera collected in the homogenous mud (hemipelagites): 6339±68 cal yr BP (@6.45m), 4541±114 cal yr BP (@4.72m) and 1614±85 cal yr BP (@2.12m)

*Interpretation* — The fining upward sand, silt and clay facies successions with low-angle planar, rippled and convoluted laminations capped by a bioturbated horizon resemble respectively the Tb (sands), Tc,d (silts) and Te (muds) divisions of an incomplete Bouma sequence (Bouma, 1962). In the marine environment, this sequence is classically interpreted as the consequence of waning flow as turbidity currents move downslope or move from a confined channel to unconfined fan environment. The lack of the massive sand of the Ta horizon shows that the flow traveled some distance before settling down the lighter fraction of the sediments.

The peaks of high density and susceptibility usually correspond to high impedance contrasts at constant velocity. This is especially true for tephra layers. The peaks at 3.5m, 4.0m and 5.2m correlate fairly well in depth to the high amplitude reflectors on the seismic line. The correlation shows that the tephra horizon (5.2m) underlines an unconformity overlain by a set of low angle reflectors (two of them at 3.5 and 4.0m) prograding in the trough, towards the slope (Fig. 5.7). This turbidite fan is capped by a low impedance horizon at 2.0m comprised of homogeneous fine-grained material (Fig. 5.7).

#### **5.4.5.2 Core KAT12-14**

On this coring site, at the toe of the continental slope, in the trench, reflectors on line AT0064 show a km-scale and more than 50m-thick lens of the semi-transparent facies (St) wedging out and progressively interfingering with the well-layered facies (Ly2) (Fig. 5.7). A homogeneous transparent layer seals these facies. Smooth diffractions at the top of the semi-transparent wedge away from the sidewalls of the trench indicate an irregular topography.

The collected core is 9.6m-thick (Fig. 5.9). It shows the superposition of a heterolithic section (U1, 8.7m-9.6m) and a massive sandy (U2, 6.1m-8.7m) and muddy (U3, 0.5m-6.1m) homolithic sections and a heterolithic section (U4, 0m-0.5m) (Fig. 5.10). The heterolithic sections U1 and U4 show cm to dm-thick, erosive base, fining upward successions of well planar-laminated sands, faintly planar, ripple-laminated silts and structureless muds with some bioturbation at the top. Some of these successions show a basal coarsening upward trend. The homolithic sandy section U2 shows the interbedding of (1) massive, fine-grained sands with clay clasts, wood and

volcanoclastic debris, (2) planar to low angle laminated sands and (3) blocky to chaotic fine sands giving rise up section to (4) silts with the same structures. This section is capped by mud with contorted faint laminations overlain by structureless, massive mud with rare bioturbation. The homolithic muddy section U3 is comprised of successions of massive greenish-grey, silt with contorted lamination overlain by contorted muds with faint lamination and massive structureless greenish clays. The contorted muds with faint laminations show a correlation in XRF between Ca, Si, Ti and Fe indicative of the presence of terrigenous and carbonate detrital material. The log pattern shows distinctive signatures in the different sections with a peaky shape in the heterolithic sections U1 and U4, a streaky shape with high average density and susceptibility in homolithic sandy U2, and a smooth shape with low D and S values in average in the homolithic muddy section U3. One  $^{14}\text{C}$  age dating was measured on planktonic foraminifera collected in the homogenous mud (hemipelagites):  $988 \pm 75$  cal yr BP (@0.6m) and two in resedimented sediment  $13204 \pm 109$  cal yr BP (@9.2m),  $6757 \pm 94$  cal yr BP (@8.35m).

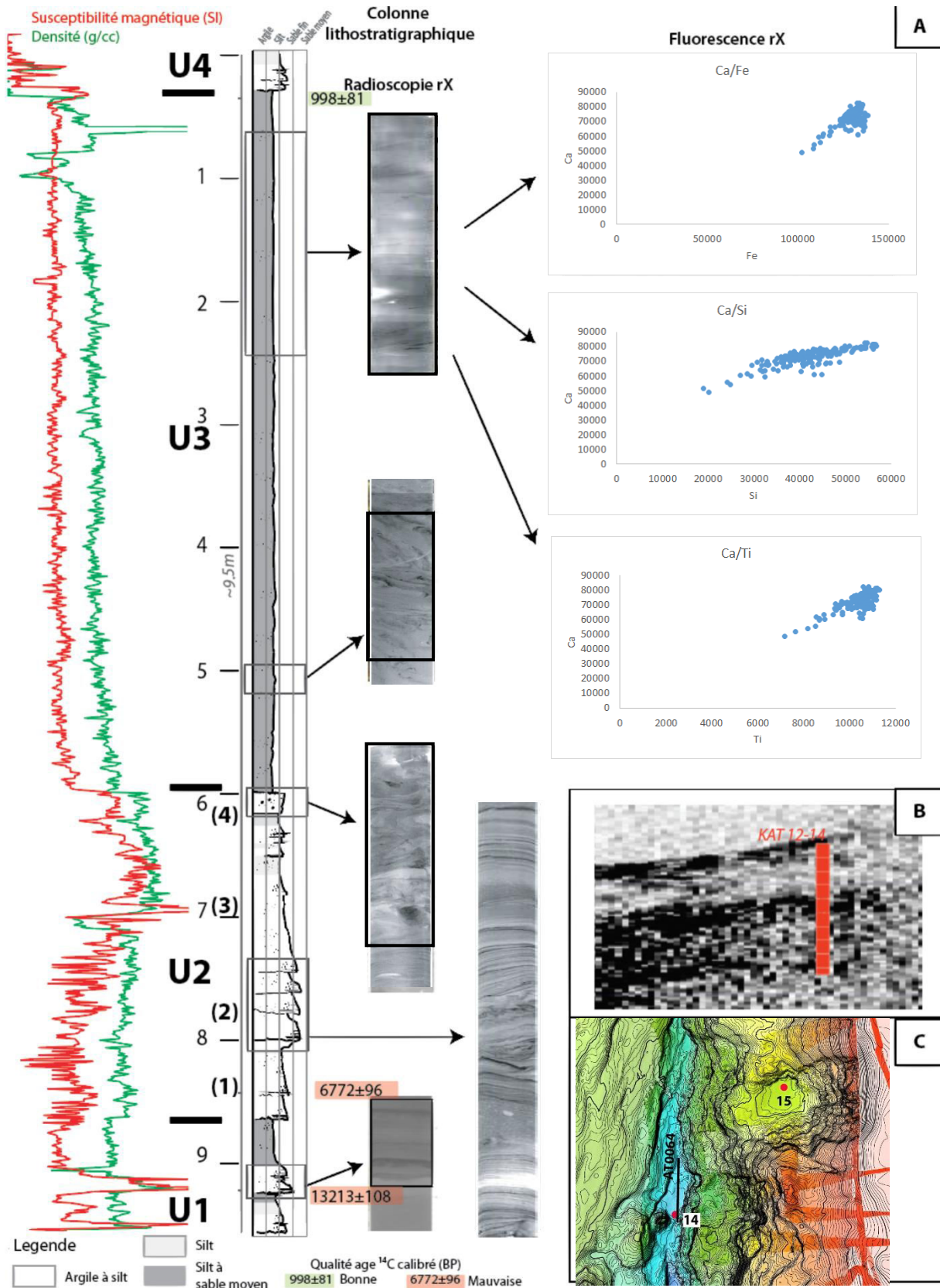


Fig. 5. 9 KAT-12-14, A) synthetic lithostratigraphic column of KAT-12-14 core (trench) with physical parameters (density and magnetic susceptibility), x-ray radiography and XR fluorescence of two lithofacies. B) core projected on the AT0064 seismic profile, and C) location of the carrot on the map

*Interpretation* — As said above, in core KAT12-15, the fining upward sand, silt and mud successions of the heterolithic facies U1 and U4 of core KAT12-14 resemble the incomplete Bouma turbidite sequences (Bouma, 1962). However, some show a basal a reverse grading as observed in turbidites emplaced during the waxing part of hyperpycnal flows (Mulder, 2003). The complex interbedding of sequences of massive, planar laminated by place over steepened and contorted sands in U2 is interpreted as a suite of overcharged turbulent flows rapidly settling down at the toe of a slope. The rapid settling is attested by the abundance of contorted sediment destabilized and slumped probably by dewatering along a nearby slope. U3 shows the alternation of contorted muds with a detrital terrigenous signature and massive structureless muds, which correspond to the same process of slumped mud overlain by passively settling massive muds from the standing water column.

The core correlates fairly well in depth with the seismic line. The tephra layer fits with the high amplitude reflector that underlines the base of the large semi-transparent massive lens (Fig. 5.9). The line shows that the sandy homolithic U2 is a lateral equivalent to the semi-transparent slumped facies when muddy homolithic U3 seals the lens. These two units are probably parts of the same large-scale gravitational event characterized in the trench by a large slump giving rise laterally to a complex multipart mega-turbidite event. This event is fed by continental sources as attested by the presence of wood debris. This material may have been flushed down the upper slope as a consequence for example a tsunami event following downslope mass wasting by earthquake shaking.

## **5.5 Discussion**

### **5.5.1 The frontal erosion in Ayampe Basin area**

The continental margin in Ecuador is linear and smooth in front of the Carnegie ridge and intensely indented at its northern and southern boundaries *i.e.* in Atacames (c.0.4°N) and Ayampe (c.1.4°S) areas (Collot et al., 2009). Numerous seamounts spot the oceanic plate in these areas, are tunneling and underthrusting below the upper plate, eroding both the front and the base of the continental margin (Sage et al., 2006; Marcaillou et al., 2016). The first indication of a subducting seamount is an anomaly of the overriding plate: a reentrant, an uplifted bulge, a scarp (Dominguez et al., 1998; Watts et al., 2010) or a landslide.

#### **5.5.1.1 Scars**

In Ayampe, the oceanic plate is spotted by nx100m-high, 3-4km-large conical and 10-15km-large multipeak seamounts (Fig. 5.10). The slope is affected by numerous small scars (nx100m to km-wide) in its lower part and three large ones (scars S1, S2, S3; nx10-km-wide) in its middle to upper part staggered in quincunx.

According to observations of Von Huene et al. (2000) along the Costa Rica margin, the headwall of the scars superposes to the summits of subducting seamounts. The seamount weakened and fractured the margin that lost support as the seamount passes beneath it and the dip steepens. Steepening of the slope results in failures and upward fluid migrations sending avalanches down the seafloor over the trailing edge of the seamount. The weakening of the margin by seamount underplating occurs

particularly passed the soft accretion prism, at the contact between the seamount and the apex of the hard basement.

The headwalls of scar S1, S2, S3 are located respectively at c.8km, 32km and 16km from the trench axis. The apex of the basement in Ayampe is located 8km from the trench axis, which is underlain by a c.500m-high seamount Smt7. It is the place of a large uplift, of about of the same height as the seamount's, which superposes to a set of reverse faults rooted at the plate interface. The presence of a subduction channel enriched in fluid on the seaward slope of the seamount shows that fluids might have percolated from the plate interface to the surface through the set of reverse faults to weaken the surficial cover of the continental slope. Seamount subduction, thrust faulting, local uplift and upward fluid migration altogether might have promoted the formation of a large scar like S1.

However, a seamount entering at the contact with the apex of the basement cannot explain the origin of scars S2 and S3 that are located farther east where the basement is thicker. The occurrence of debris at the front of the seamount 7, probably partly ripped off from the base of the upper plate, indicates that the upper plate undergo a severe erosion as confirmed by the rapid wedging out of the basement rocks to the west. The presence of a well-preserved accretion prism, not removed by frontal erosion, and the presence of large normal faults to the east, rooted at the plate interface, show that the trench is probably retreating and the upper plate experiences a gravitational (Rey et al., 2001) or down-drag collapse (Stern et al. 1989; 1991). Indeed, scars 2 and 3 formed along glide planes west of sets of large normal faults. Some of the faults, rooted at the plate interface (Sage et al., 2006), might be reactivated by the irregularities of the plate interface enhancing surficial failures and downslope mass wasting.

These seamounts represent considerable volumes of sediments removed from the upper plate and sent to the trench where they are rapidly subducted.



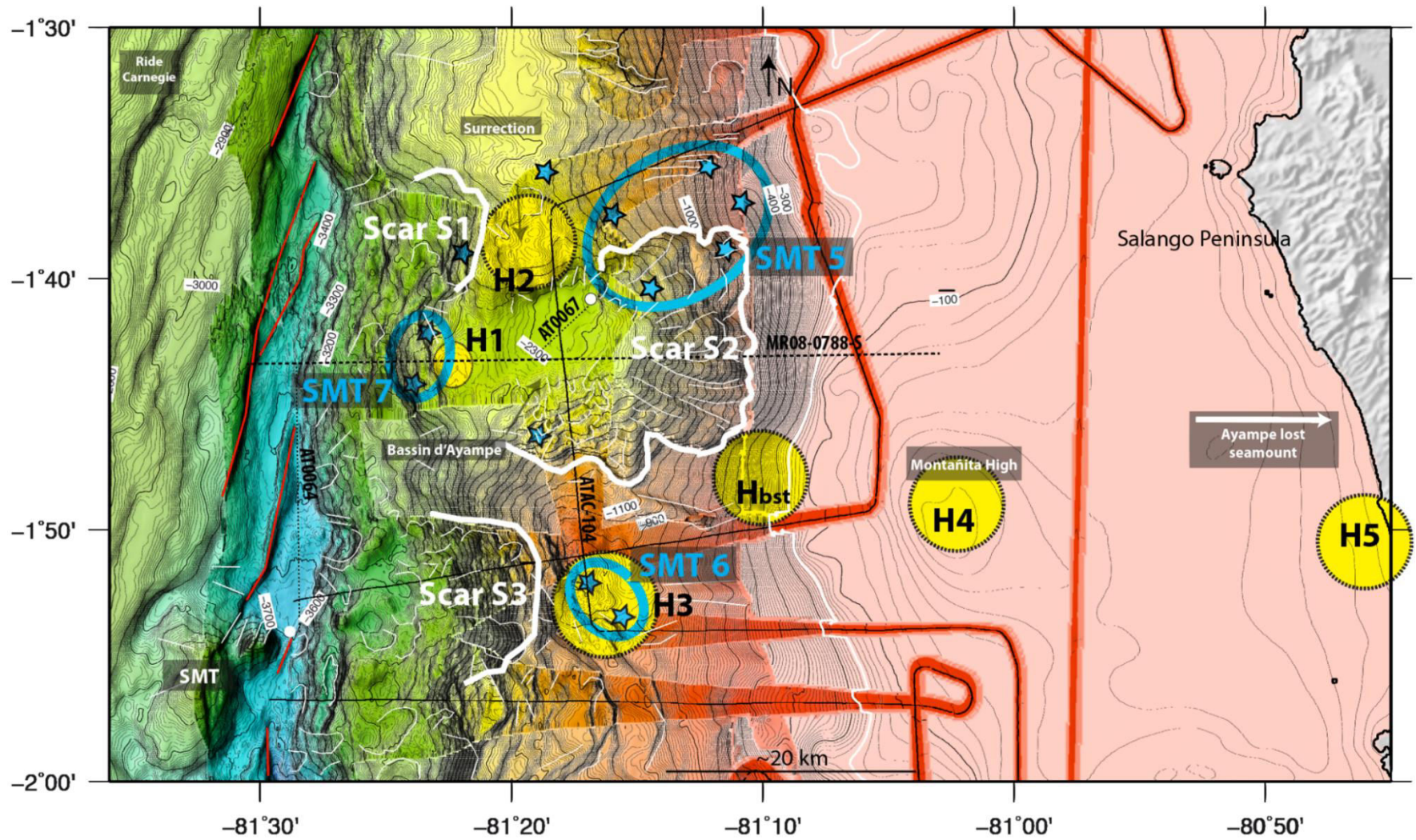


Fig. 5. 10 Map view of the lateral distribution of the scars, seamounts and highs in Ayampe area.



### **5.5.1.2 Landslides**

The detailed analysis of the sedimentary cover of the upper plate in S2 area shows that it is comprised of three rotational landslides. These landslides are 850m (LTR), 250m (MTR) and 950m-thick (Seq.1 UTR). The former one, of LTR age, slid downslope for more than 30km. The lower two landslides are sharply truncated by the last one (seq.I UTR). The feet of the landslides are sealed by recent turbidite sedimentation in UTR (seq.II to X) interlayered with lens-shape mass transport deposits in sequences II, V and VIII. Hyperpycnites and contourites drifts over spilled from the platform edge cap the top of the uppermost landslide filling the head of the tilted blocks, during faults offset. The landslides show facies successions typical of break-in-slope at the base of a slope. They are poorly mature with well-preserved facies successions but show a rapid evolution in 2km in well-layered turbidites, which can be deformed by the lateral displacement of the toe of the landslide. The formation of these landslides carved the scar S2 by the successive ablation of the slope partly related to the large listric normal faults probably rooted at the plate interface (Sage et al., 2006). By places and lately, they are cut by normal faults formed in response to the uplift above the seamount Smt7.

The formation of landslides is an instantaneous phenomenon at geological time scales. However, the age of the landslides can be approached by the age dating of the megasequences LTR, MTR and UTR and their internal sequences. The landslide in LTR is bracketed between 1031 and 1530ka, the landslide in MTR between 1031 and 790ka, the landslide in sequence 1 of UTR between 790 and 712ka (table 1). Smaller scale gravitational events in UTR are 712-621ka (sequence II), 424-337ka (sequence V), 130-57ka (sequence VIII).

### **5.5.1.3 Repetitive surficial erosion and sedimentation**

The detailed study of the surficial sediments deposited in the Ayampe basin and the trench with cores and 3.5kHz seismic sections shows that nxkm wavelength folding in the Ayampe slope basin could be simultaneous to large-scale mass transport deposits in the trench in the last 5000 yr. Large thrust faults rooted at the plate interface and formed right above seamount Smt7 close to the apex of basement, by promoting the rise of a high on the western side of the basin are at the origin of the folding. It is fairly likely that incremental displacements along the reverse faults, promoted by the roughness of the interplate boundary, produce simultaneously a reactivation of the seafloor topography in the Ayampe Basin and of the surrounding slope provoking slope failures and mass wasting from the upper slope to the trench. Likewise, the arrival of the seamount 6, contributes to destabilizing the slope of the southern flank of scar S2 of the Ayampe basin.

### **5.5.2 Frontal erosion triggers in Ayampe area**

The underthrusting of seamounts along active subduction margin can produce severe erosion of the continental slope of the upper plate (Von Huene et al. 2000, 2004, Dominguez et al., 1998; Watts et al., 2010; Collot et al., 2001; among others). The seamount generates the uplift of the seafloor and the fracturation of the upper plate and,

as a consequence, large erosional scars and mass wasting. The latter constitute an excellent record of the history of the erosion, the sedimentation and the geodynamic of the margin. Indeed, the age and the location of gravitational events can help to locate the seamounts at the origin of the sequence of deformation in the upper plate.

Table 5.1 Summary of the ages of the main morphostructural elements (scars, seamounts, highs) and sedimentary events (landslides, slump, debris flows) observed in Ayampe area

Groupes de séquences TR	Séquences TR	Ages (ka)	Age/Epoque
UTR	X	14	Holocène
	IX	14-57	Pléistocène sup.
	VIII	57-130	
	VII	130-243	Pléistocène moy.
	VI	243-337	
	V	337-424	
	IV	424-533	
	III	533-621	
	III	621-712	
I	712-790		
MTR	A à E (non détaillé ici)	790-1031	Pléistocène Calabrien
LTR	F à Q (non détaillé ici)	1031-1530	

Seamounts	distance from the trench axis			Calculated âge at 47mm/yr	Corresponding depositional sequence
	seaward boundary	landward boundary	peak		
Smt7	4km	10km	7km	149ka (85-212)	(IX) seq.VIII (VII)
Smt5	20km	32km	26km	553ka (425-680)	seq.II (I)
Smt6	16km	23km	19,5km	425ka (340-490)	seq.V (IV)

Scars	distance from the trench axis	Calculated âge at 47mm/yr
S1	8km+/-2	170ka+/-42
S2	32km+/-2	680ka+/-42
S3	16km+/-2	340ka+/-42

Highs	distance from the trench axis	Calculated âge at 47mm/yr
H1	12km	255ka
H2	14km	300ka
H3 (Smt6)	20km	425ka
Hbst (basement)	35km	744ka
H4 (Montañita)	48km	1021ka
H5 (Salango)	72km	1530ka

Gravitational events	Age dating (Martillo, 2016)	Theoretical location of a postulated seamount at 47mm/yr		Possible corresponding seamount or high	Possible corresponding Scar
UTR sequence VIII	57-130ka	2,7km (57ka)	6,1km (130ka)	Smt7 located at 4-10km	Scar S1
UTR sequence V	337-424ka	15,8km (337ka)	20km (424ka)	Smt6 at 16-23km	Scar S3
UTR sequence II	621-712ka	29,2km (621ka)	33,5km (712ka)	Smt5 at 20-32km	Scar S2
UTR sequence I	712-790ka	33,5km (712ka)	37,1km (790ka)	? Basement high 1200m b	Scar S2
MTR	790-1031ka	37,1km (790ka)	48,5km (1031ka)	Montanita high H4 at 48k	Scar S2
LTR	1031-1530ka	48,5km (1031ka)	72km (1530ka)	? Coastal uplift	

Thus, the large debris flow in sequence VIII (UTR) — a sequence that was deposited between 57 and 130ka (Proust et al., 2016; Martillo, 2016) — could have been triggered by a seamount located now between 2.7 and 6.1 km from the trench, considering an oceanic plate converging at a constant rate of 47mm/yr. (Nocquet et al, 2014) (Table 5.1, Fig. 5.9). Seamount Smt7, located between 4 and 10km from the trench could be at the origin of the deposition of this gravitational event and possibly the erosion of scar S1; although S1 is a little bit sideward of the mound (Fig. 5.9). H2 would be a good trigger for the formation of scar S1 but there no record of any seamount below H2 high. Uncertainties arise from the size of the accretion prism, which was anyway very small or inexistent, the deformations being supposedly enhanced when the seamount meets the apex of the basement. By repeating this reasoning, for the other gravitational events we can tentatively attribute the debris flow in sequence V (UTR) and sequence II (UTR) to the onset of seamounts Smt6 and Smt5 and respectively scars S3 and S2 (Table 5.1, Fig. 5.10).

The origin of the release of the landslides is more conjectural. Indeed, the well-preserved landslide contemporaneous of the deposition of sequence I (UTR) would correspond to the onset of a seamount located today between 33.5 and 37.1 km from the trench (Table 1, Fig.5.10). No seamount can be clearly identified at this location in our dataset because of the poor imaging at depth. However, at 35km the basement shows a prominent structural high overhanging the sedimentary slope by a distance of 1200m (Hbst, Fig.5.9). This basement high could be underlain by a seamount invisible because of the lack of resolution of the seismic data (Profiles P078 and MR756 in Martillo, 2016). In the same way, the landslide emplaced during the time of deposition of the megasequence MTR (790-1031ka) could correspond to the onset of a seamount located between 37.1 and 48.5km from the trench that matches the location the Montanita high at 48km (Table 5.1, Fig. 5.9). Finally, the first landslide, of LTR age (1031-1530ka), could be linked to the travelling through the upper wedge of a seamount located today between 48.5 and 72 km from the trench, which means under the present day coastline (H5, Fig. 5.9).

From the oldest to the youngest, the landslides slipped down the slope from headwalls located to the east and then to the southeast of scar 2. This can be due to the northward drift of the upper plate with respect to the oceanic plate (Collot et al., 2009; Nocquet et al., 2009). The deformation caused by the chain of seamounts on scar S2 being increasingly offsets to the south as the upper plate move northward. The offset vector oriented to the north was evaluated to 0.6cm/yr (Collot et al., 2009; Nocquet et al., 2009).

The present day position of the LTR-age seamount at the origin of scar S2 is offset by 9km southward of the headwall of scar 2 (Fig. 5.9).

However, a set of landslides can be as well simply produced by over steepening along detachment faults and rollover deformation triggered by earthquake shaking of a margin previously weakened by the subduction of a single seamount like in Peru (Duperret et al., 1995). In that case, there is no one to one relationship between a landslide and the subduction of a seamount. This hypothesis is supported by the presence of a large normal fault along the headward scarp S2 mapped by Hernandez (2015).

### **5.5.3 A permanent landslide triggering**

The two cores Kat12-14 and Kat12-15 show an unconformity underlines by a prominent tephra horizon at 6.1m and 5.2m respectively. The tephra layer is overlain by a turbidite fan migrating eastward in the trough towards the slope, in Ayampe Basin, and by a large gravitational multipart event, in the trench. The age of the turbidite fan is bracketed between 4565 $\pm$ 126  $^{14}\text{C}$  cal yr BP and 1623 $\pm$ 89  $^{14}\text{C}$  cal yr BP. The age of the gravitational event in the trench is older than 998 $\pm$ 81  $^{14}\text{C}$  cal yr BP and younger than 6772 $\pm$ 96  $^{14}\text{C}$  cal yr BP (resedimented). These two events that are particularly exceptional and sited above the same tephra horizon, are probably coincident.

The km-scale smooth folds in the Ayampe Basin are contemporaneous to the rise of the western high of the Ayampe Basin as shown by the numerous and prominent unconformities at the top of the high. These folds are a remote consequence of the regional compression at the origin of the uplift of the high to the west, itself related to the underlying thrust faulting and to the underthrusting of the seamount. Such a deformation can foster a change in the topography in the Ayampe Basin, compensated by the lateral migration of a turbidite fan, and a large-scale gravitational collapse of the slope. This tectonic event is probably of quite a large scale as the resedimented material is coming from the upper slope with regards to the presence of clay chips — reworking recently deposited muds — and wood debris of continental origin that can be rapidly deposited from hyperpycnal flows beyond the shelf edge.

These correlations show that the active deformation at the plate interface, dues to the subduction of lower plate asperities, can change the topography of the slope and trigger slope failure and mass wasting in the trench. These change in the topography of the slope occur at a frequency higher that the 40 and 100ka recurrence intervals of the UTR depositional sequences. Three internal unconformities are clearly seen of the Chirp profiles since 14kyrs in sequence X, showing that these changes can occur at the 1kyr-scale pointing to a quasi-permanent danger of landsliding in the area.

## **5.6 Conclusion**

In Ayampe area, at the southern edge of the subducting Carnegie Ridge, the oceanic plate is spotted by nx100m-high, 3-4km-large conical and 10-15km-large multipeak seamounts. In this area the trench is actively retreating and the slope experiences an

overall gravitational collapse as shown by the small accretion prism at the toe of the slope seated along a thrust faulted frontal bulge at the apex of the basement rocks, the mass transport deposits in the Ayampe slope basin and the large normal faults merging at the platform edge and rooted at the plate interface. The frontal erosion is very active. Numerous small scars (nx100m to km-wide) affect the slope in its lower part and three large ones (scars S1, S2, S3; nx10-km-wide) in its middle to upper part staggered in quincunx at 8, 16 and 32km from the trench. Three large landslides compose the sediment fill of the largest scar S2. The landslides are from base to top LTR 850m-, MTR 250m- and UTR 950m-thick. LTR landslide slides down the slope for 30km in a seaward while UTR truncates the other two landslides. Turbidites and mass transport deposits seals the foot of the landslides while contourite drifts and hyperpicnites fill the tilted block basins just beyond the platform edge, at their top. The three landslides are dated back to 1031-1530, 1031-790 and 790-712ka. The landslides carved scar S2 by the successive rotational ablation of the slope along large listric faults rooted at the plate interface.

By comparing the distance of the scars from the trench, the lateral offset due to the northward drift of the upper plate, the age of the gravitational events and the location of recognized seamounts on the plate interface we propose that the large scars observed today on the slope might have been carved or re-activated by the subduction of seamounts at 57-130ka (S1, Smt7), 337-424ka (S3, Smt6) and 620-712ka (S2, Smt5). Landslides are much older and no trace of seamounts of these ages can be depicted anymore on the deep plate interface. Nonetheless, three well defined topographic highs on the platform at 35, 48 and 72km from the trench axis fit with the age of eventual seamounts travelling from the trench to the highs in the age windows of the three landslides meaning that they might be responsible for the landsliding. However, oversteepening along detachment faults triggered by earthquake shaking of a margin previously weakened by the subduction of a seamount can as well produce a set of landslides with no one-to-one relationship between a landslide and the subduction of a single seamount. Such a permanent destabilization of the margin by the overall tectonic stresses is demonstrated by core sampling of the surficial sediment of the margin, which shows that compression at the toe of the slope modifies the slope topography producing mass transport deposits on the slope and turbidite fan in the trench fed by the platform edge sediments. These events occur at ka-scale and point out the important and multifactorial geological hazards in these areas.

## **Acknowledgments**

Data were acquired in 2012 during the IRD-CNRS oceanographic campaign ATACAMES on board the IFREMER research vessel L'Atalante. This work was carried out in the framework of the Joint French-Ecuador Laboratory LMI "Séismes et Volcans dans les Andes du Nord" with the financial support of the CNRS-INSU (INSU-SYSTER project and post campaign support), the IRD (BQR Sud funding), The Ministère français de l'Enseignement supérieur et de la Recherche (ANR research project REMAKE), the Universities of Rennes and Nice and the IFREMER. We thank SENESCYT (Secretaría Nacional de Ciencia y Tecnología del Ecuador) for the student scholarships; ESPOL (Escuela Superior Politecnica del Littoral de Guayaquil) and INOCAR (Instituto

Oceanografico de la Armada) for their support; The SHE (Society of Hydrocarburos of Ecuador) for the SCAN seismic data and also Schlumberger and IHS for making available, respectively, Petrel and Kingdom Suite seismic interpretation software. We thank Camille Dufeu, Matthieu Durand, Hugo Pouderoux and the ATACAMES Science Party for their help in gathering and processing the data during the campaign and for the fruitful scientific discussions and analysis at different stages afterwards.



## References

- Benítez, S., (1995). Évolution géodynamique de la province côtière sud-équatorienne au Crétacé supérieur Tertiaire : Géologie Alpine, v. 71, p. 5-163.
- Bouma, A H. (1962). Sedimentology of some Flysch deposits: A graphic approach to facies interpretation. Elsevier. p. 168 p.
- Bourgeois, J., Lagabriele, Y., de Wever, P., Suess, E., (1993). Tectonic history of the northern Peru convergent margin during the past 400 ka. *Geology*, v. 21, p. 531-534.
- Calahorrano, A., Sallarès, V., Collot, J. Y., Sage, F., & Ranero, C. R. (2008). Nonlinear variations of the physical properties along the southern Ecuador subduction channel: Results from depth-migrated seismic data. *Earth and Planetary Science Letters*, 267(3), 453-467.
- Chlieh, M., Mothes, P. A., Nocquet, J. M., Jarrin, P., Charvis, P., Cisneros, D., ... & Vallée, M. (2014). Distribution of discrete seismic asperities and aseismic slip along the Ecuadorian megathrust. *Earth and Planetary Science Letters*, 400, 292-301.
- Clift, P., Vannucchi, P., (2004). Controls on tectonic accretion versus erosion in subduction zones : Implications for the origin and recycling of the continental crust. *Reviews of Geophysics*, 42(2), 1-31.
- Collot, J. Y., Michaud, F., Alvarado, A., Marcaillou, B., Sosson, M., Ratzov, and Pazmino, A. (2009). Visión general de la morfología submarina del margen convergente de Ecuador-Sur de Colombia: implicaciones sobre la transferencia de masa y la edad de la subducción de la Cordillera de Carnegie. *Geología y Geofísica Marina y Terrestre del Ecuador*. Publicacion CNDM-INOCAR-IRD, PSE001-09, Guayaquil, Ecuador, 47-74.
- Collot, J. Y., Marcaillou, B., Sage, F., Michaud, F., Agudelo, W., Charvis, P., Spence, G., (2004). Are rupture zone limits of great subduction earthquakes controlled by upper plate structures? Evidence from multichannel seismic reflection data acquired across the northern Ecuador–southwest Colombia margin. *Journal of Geophysical Research : Solid Earth*, 109(B11), 1-14.
- Collot, J. Y., Charvis, P., Gutscher, M. A., Operto, S., (2002). Exploring the Ecuador-Colombia active margin and interplate seismogenic zone. *EOS, Transactions American Geophysical Union*, 83(17), 185-190.
- Collot, J.Y., Lewis, K., Lamarche, G. and Lallemand, S., (2001). The giant Ruatoria debris avalanche on the northern Hikurangi margin, New Zealand: Result of oblique seamount subduction. *Journal of Geophysical Research: Solid Earth*, 106(B9), pp.19271-19297.
- Cloos, M., & Shreve, R. L. (1996). Shear-zone thickness and the seismicity of Chilean- and Marianas-type subduction zones. *Geology*, 24(2), 107-110.

Damuth, J. E., (1980). Use of high-frequency (3.5–12 kHz) echograms in the study of near-bottom sedimentation processes in the deep-sea: a review. *Marine Geology*, 38(1), 51-75.

Deniaud, Y., (2000). Enregistrement sédimentaire et structural de l'évolution géodynamique des Andes équatoriennes au cours du Néogène: étude des bassins d'avant-arc et bilans de masse, Université Joseph Fourier—Grenoble I. Grenoble. 242 pp.

Dominguez, S., Lallemand, S. E., Malavieille, J., Von Huene, R., 1998. Upper plate deformation associated with seamount subduction. *Tectonophysics*, 293(3), 207-224.

Duperret, A., Bourgois, J., Lagabrielle Y., Suess E., (1995). Slope instabilities at an active continental margin: large-scale polyphase submarine slides along the northern Peruvian margin, between 5°S and 6°S. *Marine Geology*, 122, 303-328

Graindorge, D., Calahorrano, A., Charvis, P., Collot, J.-Y., and Bethoux, N., (2004). Deep structures of the margin and the Carnegie Ridge, possible consequence on great earthquake recurrence interval: *Geophysical Research Letters*, v. 31, doi:10.1029/2003GL018803

Gutscher, M.A., Malavieille, J., Lallemand, S. Collot, J.-Y., (1999). Tectonic segmentation of the North Andean margin : impact of the Carnegie Ridge collision. *Earth and Planetary Science Letters*, 168, 255-270.

Hampel, A., Adam, J., Kukowski, N., 2004a. Response of the tectonically erosive south Peruvian forearc to subduction of the Nazca Ridge: Analysis of three-dimensional analogue experiments *Tectonics*, 23, TC5003, doi:10.1029/2003TC001585

Hampel, A., Kukowski, N., 2004. Ridge subduction at an erosive margin: The collision zone of the Nazca Ridge in southern Peru. *Journal of Geophysical Research*, 109, B02101, doi:10.1029/2003JB002593, 2004

Hernández M.J., Michaud F., Collot J.Y., Proust J.N. Ortega R. and Aleman A. (2015). The Neogene forearc basins of the Ecuadorian Shelf (1°N-2°20'S): preliminary interpretation of a dense grid of MCS data. Poster AGU.

Jaillard, E., Ordoñez, M., Benitez, S., Berrones, G., Jiménez, N., Montenegro, G. and Zambrano, I., (1995). Basin development in an accretionary, oceanic-floored fore-arc setting: southern coastal Ecuador during late Cretaceous-late Eocene time. In : A. J. Tankard, R. Suarez Soruco, and H. J. Welsink, Eds, *Petroleum Basins of South America* , Memoir 62, American Association of Petroleum Geologists, pp.

Jaillard, E., Benitez, S. and Mascle, G.H., (1997). Les déformations paléogènes de la zone d'avant-arc sud-équatorienne en relation avec l'évolution géodynamique. *Bulletin de la Société géologique de France*, 168(4), pp.403-412.

Kelleher, J., 1972. Rupture zones of large South American earthquakes and some predictions. *Journal of Geophysical Research* 77, 2087–2103.

Kendrick, E., Bevis, M., Smalley, J.R., Brooks, B., Vargas, R.B., Lauria, E., Souto Fortes, L.P., (2003). The Nazca–South America Euler vector and its rate of change. *Journal of South America Earth Science*, 16(2), 125–131.

Lallemand, S. E., Schnürle, P., Malavieille, J., 1994. Coulomb theory applied to accretionary and nonaccretionary wedges : Possible causes for tectonic erosion and/or frontal accretion. *Journal of Geophysical Research: Solid Earth* (1978–2012), 99(B6), 12033-12055.

Lebrat, M., Mégard, F., Dupuy, C. and Dostal, J., (1987). Geochemistry of the Cretaceous volcanic rocks of Ecuador: geodynamic implications. *Bull. Geol. Soc. Am*, 22.

Laursen, J., Scholl, D.W. and von Huene, R., 2002. Neotectonic deformation of the central Chile margin: Deepwater forearc basin formation in response to hot spot ridge and seamount subduction. *Tectonics*, 21(5).

Lisiecki, L. E., Raymo, M. E., 2005. A Pliocene-Pleistocene stack of 57 globally distributed benthic  $\delta^{18}\text{O}$  records. *Paleoceanography*, 20(1), 1-17.

Lonsdale, P. (2005). Creation of the Cocos and Nazca plates by fission of the Farallon plate. *Tectonophysics*, 404(3), 237-264.

Marcaillou, B., Collot, J. Y., Ribodetti, A., d'Acremont, E., Mahamat, A. A., Alvarado, A., 2016. Seamount subduction at the North-Ecuadorian convergent margin: Effects on structures, inter-seismic coupling and seismogenesis. *Earth and Planetary Science Letters*, 433, 146-158.

Martillo C., (2016). Stratigraphic record of the glacio-eustatic cycles and the deformation during the Pleistocene along the central ecuadorian margin (using the atacames data campaign). Ph.D. Thesis, Université de Nice, 245 p.

Marksteiner, R, and Alemán, A., (1991). Coastal Ecuador technical evaluation agreement. -Amoco Prod. Co & Petroecuador, unpublished Report,, vol.1, 218p.

Mercier de Lepinay, B., Michaud, F., Calmus, T., Bourgois, J., Poupeau, G., Saint Marc, P., & NAUTIMATE team, T. (1997). Large Neogene subsidence event along the middle America Trench off Mexico (18 N–19 N): evidence from submersible observations. *Geology*, 25(5), 387-390.

Michaud, F., Proust, J. N., Collot, J. Y., Lebrun, J. F., Witt, C., Ratzov, G., Penafiel, L., (2015). Quaternary sedimentation and active faulting along the Ecuadorian shelf : preliminary results of the ATACAMES Cruise (2012). *Marine Geophysical Research*, 36(1), 81-98.

Michaud F, Collot J-Y, Alvarado A, Lopez E y el personal científico y técnico del INOCAR, (2006) República del Ecuador, Batimetría y Relieve Continental, publicación IOA-CVM-02- Post. INOCAR, Guayaquil.

Migeon, S., Weber, O., Faugères, J.-C., Saint-Paul, J., (1999). SCOPIX : a new X-ray imaging system for core analysis. *Geo-Marine Letters*, 18, 251–255.

Mitchum Jr., R.M., Vail, P.R., Sangree, J.B., (1977). Seismic stratigraphy and global changes of sea-level, part 6: stratigraphic interpretation of seismic reflection patterns in depositional sequences. In: Payton, C.E. (Ed.), *Seismic Stratigraphy — Applications to Hydrocarbon Exploration* Memoir 26. American Association of Petroleum Geologists.

Moore, J. C., & Saffer, D. (2001). Updip limit of the seismogenic zone beneath the accretionary prism of southwest Japan: An effect of diagenetic to low-grade metamorphic processes and increasing effective stress. *Geology*, 29(2), 183-186.

Mulder, T., Cochonat, P., 1996. Classification of offshore mass movements. *Journal of Sedimentary Research*, 66(1), 43-57.

Mulder, T., Alexander, J., 2001. The physical character of subaqueous sedimentary density flows and their deposits. *Sedimentology*, 48(2), 269-299.

Mulder, T., Syvitski, J., Migeon, S., Faugeres, J.C., Savoye, B., (2003). Marine hyperpycnal flows: initiation, behavior and related deposits. A review. *Marine and Petroleum Geology*, 20, p. 861-882.

Nocquet, J. M., Villegas-Lanza, J. C., Chlieh, M., Mothes, P. A., Rolandone, F., Jarrin, P. & Martin, X. (2014). Motion of continental slivers and creeping subduction in the northern Andes. *Nature Geoscience*, 7(4), 287-291.

Nocquet J-M, Mothes P, Alvarado A (2009) Geodesy, geodynamics and earthquake cycle in Ecuador. *Geology and marine and onland Geophysics of Ecuador: from the continental coast to the Galapagos Islands*. In Collot Jy, Sallares V, Pazmin~ O A (eds) *Geología y Geofísica Marina y Terrestre del Ecuador*. Publicación CNDM-INOCAR-IRD, PSE001-09, Guayaquil, Ecuador pp 83–94.

Proust, J.-N., Martillo, C., Michaud, F., Collot J.-Y., Dauteuil, O., (2016). Subduction of seafloor asperities revealed by a detailed stratigraphic analysis of the margin shelf sediments of Central Ecuador. *Marine Geology*.

Ranero Cr, Von Huene R (2000) Subduction erosion along the Middle America convergent margin: *Nature*, v. 404, p. 335–357.

Ratzov, G., Collot, J. Y., Sosson, M., Migeon, S., 2010. Mass-transport deposits in the northern Ecuador subduction trench: Result of frontal erosion over multiple seismic cycles. *Earth and Planetary Science Letters*, 296 (1), 89-102.

Rey, P.; Vanderhaeghe, O.; Teyssier, C., 2001. Gravitational collapse of the continental crust: definition, regimes and modes. *Tectonophysics*, Volume 342, Issue 3, p. 435-449

Reynaud, C., Jaillard, É., Lapierre, H., Mamberti, M. and Mascle, G.H., (1999). Oceanic plateau and island arcs of southwestern Ecuador: their place in the geodynamic evolution of northwestern South America. *Tectonophysics*, 307(3-4), pp.235-254.

Richter, T. O., van der Gaast, S., Koster, B., Vaars, A., Gieles, R., de Stigter, H. C., De Haas, H., van Weering, T. C. E., (2006). The Avaatech XRF Core Scanner: technical description and applications to NE Atlantic sediments: *Geological Society, London, Special Publications*, 267(1), 39-50.

Ruff, L. J. 1989. Do trench sediments affect great earthquake occurrence in subduction zones?. *Pure and Applied Geophysics*, 129(1), 263-282.

Sage, F., Collot, J. Y., Ranero, C. R., 2006. Interplate patchiness and subduction-erosion mechanisms : Evidence from depth-migrated seismic images at the central Ecuador convergent margin. *Geology*, 34(12), 997-1000.

Sanclémente, E., 2014. Seismic imaging of the structure of the central Ecuador convergent margin : relationship with the inter-seismic coupling variations. Ph.D. Thesis, Université de Nice, 273 p.

Sangree, J.B., and Widmier, J.M., (1977). Seismic interpretation of clastic depositional facies. In: C.E. Payton, Ed., *Seismic stratigraphy applications to hydrocarbon exploration*. AAPG Memoirs, 26, 165-184.

Shanmugam, G., Lehtonen, L. R., Straume, T., Syversten, S. E., Hodgkinson, R. J., and Skibeli, M., (1994). Slump and debris flow dominated upper slope facies in the Cretaceous of the Norwegian and Northern North Seas (61°–67° N): implications for sand distribution: *AAPG Bulletin*, v. 78, p. 910–937.

Scholl, D. W., von Huene, R., Vallier, T. L., & Howell, D. G. (1980). Sedimentary masses and concepts about tectonic processes at underthrust ocean margins. *Geology*, 8(12), 564-568.

Shreve, R. L., & Cloos, M. (1986). Dynamics of sediment subduction, melange formation, and prism accretion. *Journal of Geophysical Research: Solid Earth*, 91(B10), 10229-10245.

Sosson, M., Bourgois, J., & de Lépinay, B. M. (1994). SeaBeam and deep-sea submersible Nautilie surveys in the Chiclayo canyon off Peru (7 S): subsidence and subduction-erosion of an Andean-type convergent margin since Pliocene times. *Marine Geology*, 118(3-4), 237-256.

Saint-Onge, G., Mulder, T., Francus, P., Long, B., (2007). Continuous physical properties of cored marine sediments. *Proxies in Late Cenozoic Paleoceanography*. Elsevier, 63-98.

Stern, T.A. and ten Brink, U.S., (1989). Flexural uplift of the Transantarctic Mountains. *Journal of Geophysical Research: Solid Earth*, 94(B8), pp.10315-10330.

Trenkamp, R, Kellogg, J.N., Freymueller, J.T., Mora P., (2002). Wide plate margin deformation, southern Central America and northwestern South America, CASA GPS observations. *Journal of South American Earth Science*, 15, 157–171.

Vail, P.R., Mitchum, R.M., and Thompson, L.S., (1977). Seismic stratigraphy and global changes of sea level, part 4: Global cycles of relative changes of sea level. In: C.E. Payton, Ed., *Seismic stratigraphy applications to hydrocarbon exploration*. AAPG Memoirs, 26, 83-97.

von Huene, R., & Suess, E. (1988). Ocean Drilling Program Leg 112, Peru continental margin: part 1, tectonic history. *Geology*, 16(10), 934-938.

von Huene, R., C.R. Ranero, and Weinrebe, W. (2000). Quaternary convergent margin tectonics of Costa Rica, segmentation of the Cocos Plate, and central American volcanism. *Tectonics* 19:314–334.

von Huene, R., Ranero, C. R., Vannucchi, P., (2004). Generic model of subduction erosion. *Geology*, 32(10), 913-916.

Watts, A.B., Koppers, A.A.P., and Robin, D.P., 2010. Seamount subduction and earthquakes. *Oceanography*, 23, 1, 166-173.



## Chapter 6

### **Morpho-tectonic control and sedimentation modalities of mass transport deposits and mega-turbidites: example from the Ecuadorian northern trench**

#### **6.1 Introduction**

Subaqueous palaeoseismology emerged during the late 90's and has revealed as a powerful tool to reconstruct earthquake time series, especially where the seismogenic faults are not accessible in submarine or in coastal areas. Where a strong magnitude earthquake occurs below the continental slope or in adjacent areas, the acceleration on the seafloor can trigger slope failures, that run downslope and deposit in the subduction trench or in slope basins. They result in a wide range of types of deposits involving slumps, mass transport deposits (MTD) or turbidites, depending on the process of transport, the lithic or water content, or the distance between the source and deposit area (Middelton and Hampton, 1973; Shanmugam et al., 1994; Piper and Normark, 2009; Talling et al., 2012).

The greatest challenges while analyzing the deposit is to establish its trigger. Indeed, the most reliable way to do so is dating the deposits, and correlate them with an independent archive (historical record, paleoseismology onland, etc.) (Sumner et al., 2013). An alternate method, that also allows extending the time span beyond the historical record is based on dating and correlating turbidites across a wide area (hundreds of km), and across independent sedimentary systems. Such correlation supports synchronous slope failures that imply a regional trigger, most likely a large magnitude earthquake. Local triggers such as isolated slope failures caused by sediment overload can thus be discarded (Adams, 1990, Goldfinger et al., 2003; 2011). Especial attention has to be paid to storm waves and surges that, in some cases, can also be considered as regional triggers. This method has been successfully applied on numerous subduction zones (Goldfinger et al., 2003; Polonia et al., 2013; Pouderoux et al., 2014; Patton et al., 2015; San Pedro et al., 2017), but also on other active tectonics settings (Goldfinger et al., 2008; Gracia et al., 2010; Ratzov et al., 2015; Babonneau et al., 2017), as well as in mountain lakes (Chapron et al., 1999; Beck et al., 2009; Moernaut et al., 2007; Praet et al., 2017; van Daele et al., 2017).

In all these cases, defining distinctive sedimentary features to discriminate between different possible triggers is a must, but still a complicated task.

**Turbidites:** To date, most investigation have been conducted on turbidite deposits: pioneer work from Gorsline et al. (2000) dated historical turbidites in the Santa Monica basin, and showed that the thickness and volume of earthquake triggered deposits is an order of magnitude greater than those triggered by storms. Additionnaly, when seismically triggered, the sedimentary structure of turbidites can depart from the classical Bouma sequence (Bouma, 1962) and comprise amalgamated beds or multiple sandy or silty

pulses (Nakajima et al., 2000; Goldfinger et al., 1999; Guiterez-Pastor et al., 2013; Migeon et al., 2017; Van Daele et al., 2017) interpreted as resulting from the arrival of multiple turbidity currents reaching the coring site within a short period of time (hours to months). Finally, the mineral and biogenic content can help tracing the geographic source of the turbidity current: where the sources are in water deeper than the continental shelf and the storm wave base (<200m); storm and surge trigger could be discarded, Migeon et al., (2017) demonstrated that from deposits in the Esmeraldas channel-levée system (North Ecuador), climatic turbidites contain wood fragments, attesting a direct continental input whilst earthquake triggered turbidites do not contain any, because the sedimentary sources are deeper and the organic matter is oxidized.

**Megaturbidites:** Megaturbidites or Homogenites are widespread turbidites characterized by an extremely thick and homogeneous muddy term on top compared to sand or gravely basal deposits, the base may be erosive. They have been defined on Eocene outcrops (Mutti et al., 1984) but have since been retrieved in numerous modern Quaternary settings such as Eastern Mediterranean (Kastens and Cita, 1981; Hieke, 2000), western Mediterranean (Rothwell et al., 2000), Marmara sea (Beck et al., 2007), or mountain lakes (Beck, 2009 and references therein). Two distinctive sedimentary settings have been proposed: small and pounded basins where the homogenite is created by re-suspension of the seafloor hemipelagic deposits by tsunami waves (Cita and Aloisi, 2000). In the Mediterranean abyssal plains, the deposits show a more important sandy base and contain shelf fauna, supporting distal but widespread trigger, interpreted as a tsunami (Cita et al., 1982)

**Slumps / MTDS:** More massive and cohesive deposits such as slide/slumps or Mass Transport Deposits (MTDs) have only little been used for paleoseismic reconstructions although they can also be triggered by earthquakes. Because their transport process (debris flow) can evolve into turbidity current leading to turbidites when accelerating downslope and/or incorporating water (Piper and Normark, 2009; Talling et al., 2012), they are more likely to be deposited closer to their sources than turbidites. Such investigation has still proven successful especially in mountain lakes (Strasser et al., 2006; Beck et al., 2009; Waldmann et al., 2011; Moernaut et al., 2015; Van Daele et al., 2017) but only in few oceanic contexts. Based on Chirp data, Ratzov et al., (2010) showed that the North Ecuador trench contains multiple sedimentary units characterised by transparent acoustic facies and classically interpreted as Mass Transport Deposits (MTDs), and proposed their seismic trigger based on correlation in independent basins. Their recurrence is however greater than those of turbidites and Large subduction earthquakes in the area.

One other major question is whether the segmentation of active margin in terms of slope failure frequency and size may be a function of material properties and/or tectonic setting. Preconditioning factors for slope instability like sedimentation rate, changes in sediment type, and presence of gas hydrate are commonly considered to change along the strike of the margin, and explain the distribution and style of failure (Coleman and Prior, 1988). Links between mass movements and climate change have been considered (Owen et al., 2007), but long-term tectonic processes, which cause changes in slope morphology and

in the structure of the stratigraphic column (Ranero et al., 2008), create the most relevant preconditioning factors for slope instability (Harders et al., 2011). Additionally, the morphology of the margin is also an important factor: along a canyon, the material transferred from the destabilizations of the slopes canyon will be concentrated by the canyon itself, facilitating their record into the sediment of the trench, at the end of the canyon (Ratzov et al., 2012; Migeon et al., 2017); in contrast, in absence of well-developed canyons, the material resulting from the direct destabilization of submarine slopes is largely dispersed.

Along the northern segment of the Ecuadorian active margin, since the last century, several large historical earthquakes have occurred (Collot et al., 2004; Font et al., 2011; Vallée et al., 2013; Nocquet et al., 2014) (Fig. 6.1). Along this segment several mass transport deposits have been already identified (Ratzov et al., 2010) into the trench sediments, but these MTDs were not correlated to the historical earthquakes sequence. Meanwhile, northward, at the mouth of the Esmeraldas canyon (Fig. 6.1), a temporal relationship was established between gravity-flow deposits and the historical earthquakes, suggesting that the Esmeraldas canyon was the main source of sediments to be remobilized during these earthquakes. In the trench, at the end of the Esmeraldas canyon (Fig. 6.1B), the historical earthquake sequence has been recorded by coseismic turbidites (Migeon et al., 2017) with a recurrence of 600 years for the largest earthquakes.

New sediment cores and more continuous chirp profiles were collected during the Atacames cruise (Michaud et. 2015), along the northern segment of Ecuador trench to sample recent gravity-driven deposits (MTDs, Megaturbidites and turbidites) to tentatively date them and estimate their extent, volumes and sources. Additionally, we use deep seismic profiles (propriety of the Secretaria de Hidrocarburos del Ecuador) in order to refine the structural framework of the margin slope and identify older large (deep-seismic) MTD into the trench sedimentary fill. In this paper, we revisit the repartition, dating and number of MTDs and turbidites, and document the wide range of deposits associated to an earthquake. More specifically, we aim at understanding what parameters control the occurrence or not of each type of gravity driven deposit.

## **6.2 Geodynamic Setting of the Ecuador North Margin**

Along the Ecuadorian margin, the Nazca plate (Fig. 6.1A) subducts eastwards at a 6 cm/yr rate beneath the South America plate (Nocquet et al 2014). The evolution of the Ecuador margin is strongly influenced by the subduction of the Carnegie ridge (Michaud et al, 2009; Collot et al, 2009) and the northward tectonic escape of the North Andean block at a 0.95 cm/yr rate (Nocquet et al. 2014) (Fig. 6.1A). In the forearc, sediment supply from the Andes is deflected northwards and southwards by the uplift of the coastal cordillera (Collot et al . 2009). The thickness of trench sediments varies along the trench remarkably (Collot et al., 2009): In front of the Carnegie ridge, the trench exhibits almost no sediment infill; while on both sides of the Carnegie ridge, the infill is thicker, especially on the northern side, where the Esmeraldas canyon (Fig. 6.1B) significantly supplies the trench, providing over 4.8 km sediment trench fill.

The north Ecuador/south Colombia convergent margin is affected by recurrent subduction earthquakes with magnitudes greater than 7.5, like the 1906, 1942, 1958, 1979 and 2016 events. The largest historical earthquake (Mw 8.8) occurred in 1906 (Kanamori and Given, 1981) and had an estimated rupture zone of ~500 km long (Kelleher, 1972). The rupture zone was partially reactivated by large subduction earthquakes, which occurred from south to north, in 1942 (Mw 7.8), 2016 (Mw 7.8) (Nocquet et al., 2016), 1958 (Mw 7.7) and 1979 (Mw 8.2) (Beck and Ruff, 1984; Swenson and Beck, 1996) (Fig. 6.1B). Ground shaking related to these major events and their aftershock sequences may have caused submarine mass movements across the continental slope as suggested by Ratzov et al. (2009; 2010).

Ten earthquakes with the highest magnitudes were recorded on the turbidite levee within the last 800 years with a recurrence time ranging from about 280 yrs to 40-70 yrs, or less for the 20th Century earthquakes (Migeon et al. 2017). The comparison of the main features of the 1906 turbidite with older earthquake-triggered turbidites identified in a core collected in the trench suggests that one or two earthquakes similar to the 1906 event might have occurred ~600 yrs ago. This supports the recent study of Nocquet et al., (2016) proposing that the Ecuador Colombia subduction zone illustrates in the present time a fault behaviour predicted by physical models that include spatial variation of fault friction and identified by palaeoseismological studies, showing temporally clustered earthquakes separated by periods of seismic quiescence.

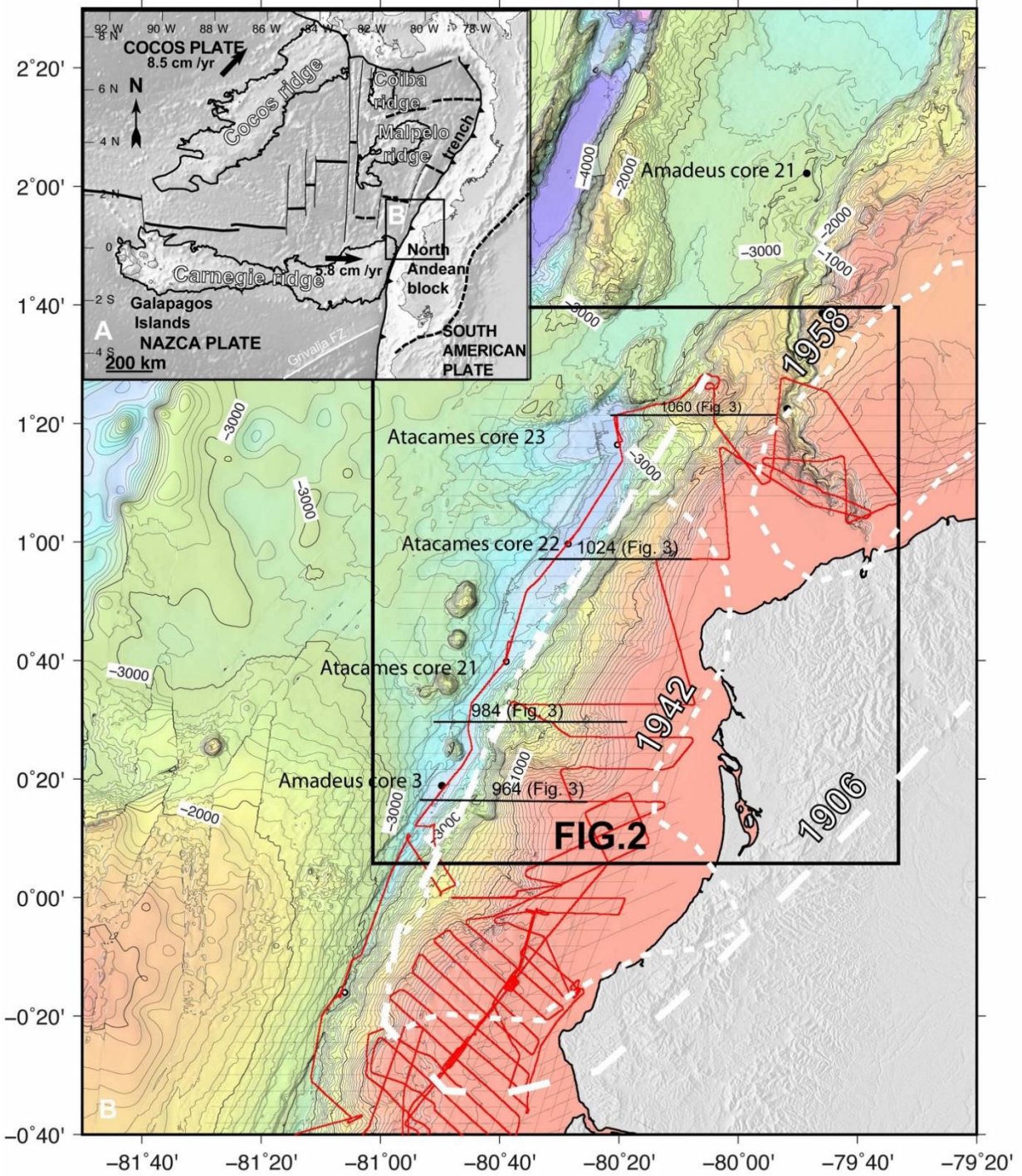


Fig. 6. 1 Bathymetric map of the northern segment of the Ecuadorian trench (from Michaud et al., 2009 including the new Atacames data). New high swath bathymetry was recorded along the Atacames cruise (red lines). A geodynamic framework from Michaud et al., 2015. B) study area; strong dotted white line = rupture zone of the main earthquakes from Font et al., 2013. Black rectangle = location of the Fig. 2.



Along the trench, seven sub-basins have been considered by Ratzov et al., (2010). The sub-basins are structurally separated by a trench structural saddle (Fig. 2). Both side of this saddle sub-basin1 sub-basin2 and sub-basins 6 and 7 form morphological sinks for the most recent deposit. Temporal correlations between interpreted MTDs emplaced within separated trench sub-basins indicate that the seven MTDs were emplaced during five main events. Three were triggered locally and tentatively dated 5.8, 1.6 kyr and recent, whereas four were emplaced in distinct trench sub-basins as a result of two regional events at 22.6 and 15.4 kyr (Ratzov et al., 2010).

### 6.3 Data Sets

Multibeam data were acquired during the Atacames cruise (Michaud et al., 2015) using a hull mounted Simrad EM710 and EM122 multibeam echosounder, yielding a Digital Terrain Models with a resolution of 50 m for bathymetry imagery. We also use swath bathymetry collected in 2005 during the Amadeus and Esmeraldas cruises onboard the R/V L'Atalante, using a Simrad EM12D multi-beam system (13 kHz, 162 beams) yielding a Digital Terrain Models with a resolution of 150 m for bathymetry imagery. The data were processed using the seafloor mapping software CARAIBES (developed by IFREMER). From this DTM we have also done slope DTM used to determine the slope basins.

New sub-bottom profiles were acquired with a hull-mounted Chirp system (1.8–5.3 kHz) using the IXSEA 3.5 kHz sub-bottom profiler with an observed vertical resolution of ~30 cm. Moreover, we have used some deep penetration multichannel seismic reflection (MCS) data were obtained across the Ecuador margin during the SCAN cruise (4000 in3 air gun seismic source; 640 -channel, 8-km-long 8m-depth streamer; shots every 25 m; 160 -fold coverage).

Cores were collected during the Atacames cruise using a Kullenberg corer (Fig. 6.2). They were cut in 1 m-long sections, then split for visual descriptions and photographed. Grain size measurements were performed locally, using a COULTER LS230 Laser granulometer. X-ray radiography of split core was made using the SCOPIX system (Migeon et al., 2000) in the University of Bordeaux I and using a CT core-scanner in IFREMER (Brest). The value of reflectivity was indirectly extracted: using the FIJI software, we read the level of gray along the central pixel along the core images; such value is proportional to the reflectivity, but depends on the contrast and brightness adjustment of the image on each core section; the value is therefore semi-quantitative (relative). These initial settings therefore account for the value jumps that may occur between sections.

X-Ray Fluorescence allows semi-quantitative measurement of Major elements, operated on a AVATECH XRF core-scanner performed in University of Bordeaux I. This measurement was performed only on core Kat22.

Finally,  $^{14}\text{C}$  dating was undertaken on foraminifer samples (*Neogloboquadrina dutertrei* and *Neogloboquadrina pachyderma*) using an accelerator mass spectrometer.



Radiocarbon dates were then corrected for marine age reservoir difference (405 yr) and calibrated to calendar years.

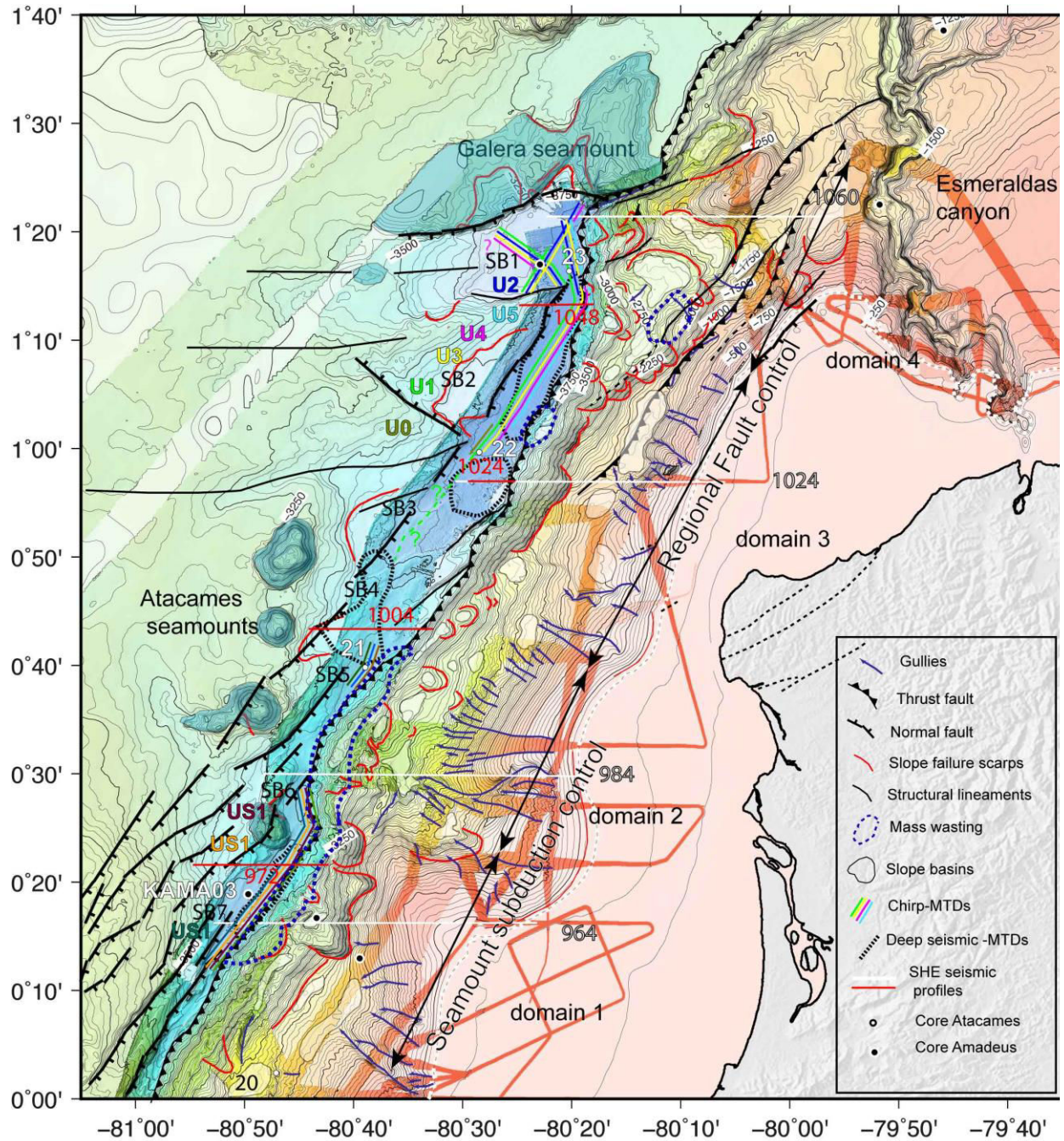


Fig. 6. 2 Morphostructural map of the study area (from Collot et al., 2009, modified). Strong white dotted line = isobath -150m.

## 6.4 Results

### 6.4.1 Morphologies and structures

#### 6.4.1.1 The slope

The upper slope ranges from 200 to 1500 mbsl and exhibits a gentle slope gradient (3–5°) south of latitude 0°50'N, while north of this latitude, the slope is steeper (>7°). A 22 km-wide re-entrant located between 0°20'N and 0°30'N breaches the shelf break, and bounds a 25 km-wide, shallow promontory forming a spur on its southern flank. Down, at the transition with the lower slope, and except at the latitude of this shallow promontory, the upper slope is bounded by terraces, corresponding probably to small slope basins and characterized by gentle slope gradient (Fig. 6.2). Many gullies cut the upper slope and end into these small slope basins. But no large slope failure scarps affect the upper slope and the shelf, excepted to the north (latitude 1°15') where km-scale slope failure scarp breaches the shelf break, close to trench-parallel thrust and normal faults (Profile 1060, Fig. 6.4).

The lower slope extends from 1500 to 3900 mbsl and is characterized by steep scarps. We considered from South to North four morphological domains along the lower slope (Fig. 6.2).

- Between 0°10' to 0°25' latitude (domain 1) three connected, semi-circular scarps form a re-entrant with scarps 5–6 km-wide, up to 1500 m-high, and exhibit slope gradients of up to 30° (Fig. 6.4, Profile 964). The deep seismic profile 964 (Fig. 6.4) exhibits slope failure scarp which is the sources for the MTDs identified in the trench. In this domain, up to the slope failure scarp, the topography is concave upwards and, above the acoustic basement, the sedimentary units are highly fractured (Profile 964, Fig. 6.3), related to the subduction of a seamount. Down to the slope, and close to the trench, chaotic seismic facies correspond to massive slope failure, bounded landward by a thrust fault.

- From 0°25' to 0°40' latitude (domain 2), the lower slope is convex upwards and shows a gentle slope gradient. This domain is bounded upward by a wide re-entrant that breaches the shelf break; and downward by downslope arcuate body, which covers the trench and where it is deformed by several thrust faults (Fig. 6.3, profile 984). This succession from the upper slope until the trench which is fronted by mass transport deposits reworked in frontal prisms, suggests that an old huge mass wasting occurs at this place.

- From 0°40' to 1°10' (domain 3) the lower slope exhibits a trench-parallel linear scarp. This up to 1000 m-high steep linear scarp is a slope failure scarp (Fig. 6.3, Profile 1024) and is located along an active thrust faults system. The sedimentary units are locally fractured along the faults contrasting which the domain 2 where the sedimentary unit are wholly fractured.

- Between 1°10' and 1°30' (domain 4) the lower slope exhibits a 30 km-wide, triangular shape, 2000–2600 m-deep terrace. Upward, this terrace is bounded by the fault-controlled linear scarp defined in the adjacent domain to the south, and some of these faults affect the seafloor. At this place, this scarp reveals several semicircular forming re-entrant with scarps 1-2 km-wide. Along this scarp and on the terrace a downslope lobate body suggests the presence of a mass-transport deposit. Seaward of the triangular terrace, the slope is affected by two semi-circular slope re-entrants 10–12 km-wide and 800 to 1000 m-high that are inferred to be recent, moderate-sized failure scarps.



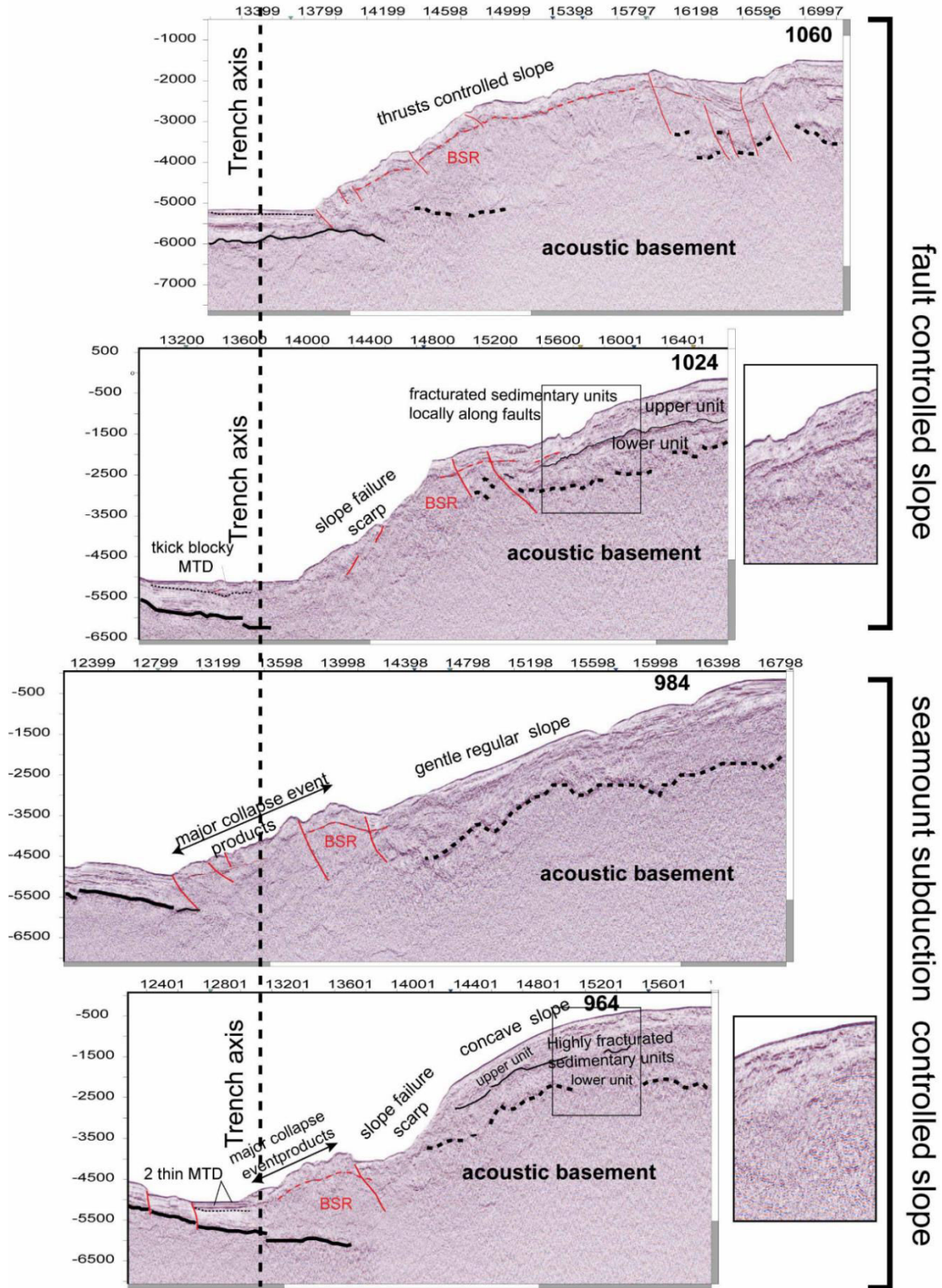


Fig. 6. 3 Deep seismic profiles across the margin (location on Figure 1B and Figure 2). Propriety of the SHE (Ecuador).

#### **6.4.1.2 The trench:**

The new high-resolution swath bathymetry (50-m grid size) allows us to precise the morphology of the sub-basins as described by Ratzov et al., 2010. As previously considered from 150-m size grid, the sub-basins SB-1, SB-2 and SB-5, SB-6 and SB7 are well defined by local bathymetric lows in the trench (Fig. 6.2). It is more difficult to define the SB-3 and SB-4 because they are located on steep terrain and both areas are gently dipping northward until the south limit of SB-2. Nevertheless, we conserve the denomination of Ratzov et al. (2010) in order to facilitate the comparison of the units' location along the trench. New bathymetry data confirms that the trench presents two main flat floor basins SB1-SB2 and SB6-SB7 separated by a saddle. This saddle is structurally controlled, at SB3 and SB4 latitude, by the NE-NW trending oceanic plate structures (Fig. 6.1B and 6.2), meanwhile, at SB5 latitude, the saddle corresponds to a large avalanche that have covered the trench axis (Fig. 6.4 and profile 984 on Fig. 6.3). These oceanic plate features are oblique to the inner wall of the trench. At the boundary between SB2 and SB3, the trench seafloor is rough and exhibit some kilometer-wide hummocks (Fig. 4).

#### **6.4.2 Trench stratigraphy and sedimentation**

MCS data in the trench reveals two main sequences as identified by Ratzov et al., (2010): an up to 0.5stwt -thick, highly reflective, subhorizontal trench fill (Fig. 3 and 4) on lapping a 0.3–0.4 stwt-thick, well-stratified sequence (Fig. 6.3 and 6.4). Sequence Sq dips gently landward and drapes the top of the oceanic crust characterized by a strong amplitude reflector (outlined in Fig. 6.3). Sequence Sq extends over the Carnegie Ridge, where IODP site 1239 recovered Pleistocene to Pliocene carbonate ooze with some ash layers (Blum et al., 2002).

The trench fill contains a series of transparent to chaotic units visible on both MCS and Chirp seismic data (where their thickness exceeds the resolution of MCS data). They were all interpreted by Ratzov et al., (2010) as Mass Transport Deposits in regard of their acoustic facies and the presence of semi-circular scarps on the seafloor of the continental slope. The new coverage provided by the SCAN MCS profiles and the ATACAMES Chirp lines allows better constraining the spatial distribution of the thick units (Deep seismic MTD) and the thinner units (Chirp MTD / Megaturbidites) respectively. Additionnaly, sedimentary cores allow sampling and providing groundtruth to the encountered facieses.



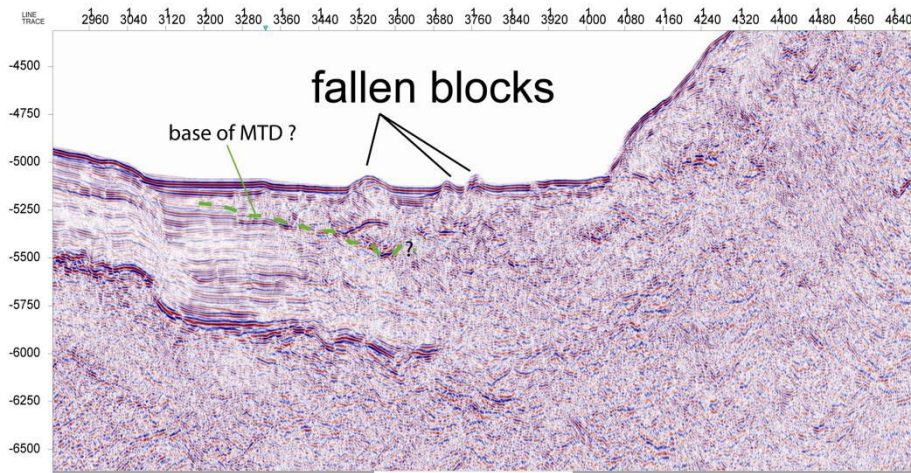
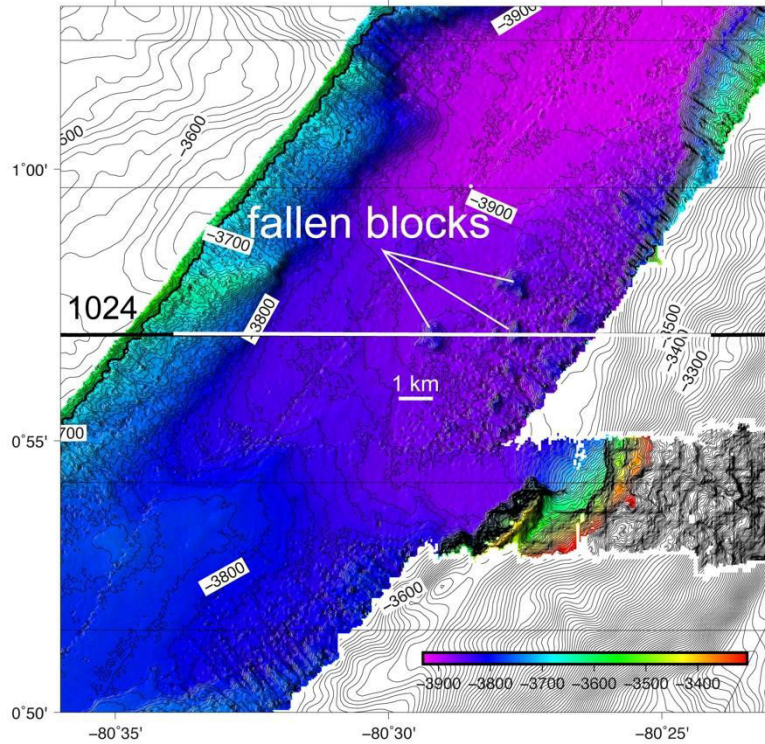


Fig. 6. 4 km-scale fallen blocks (bathymetry and deep seismic profile)

Based on colours, Xray reflectivity, sedimentary structures, Magnetic susceptibility, biotic and mineral content, and Ca/Ti and grain-size measurements where available, we identified seven distinctive facieses related to the five types of deposits described below. Moreover, based mainly on the sedimentary structures and the grainsize, we moreover identified the terms of the Stow and Shamungam (1980) turbidite sequence that is better suited for describing the deposition and waning processes in fine-grained (muddy) turbidites than the classical Bouma Sequence.



**Core: KAT-12-21**

Cruise: ATACAMES      Water depth: 3802 m  
 Date: 25-Jan-2012      Core length: 8.63 m  
 Latitude: 00° 39.819' N      Site: Ecuadorian trench,  
 Longitude: 80° 38.922' W      on the Atacames basin

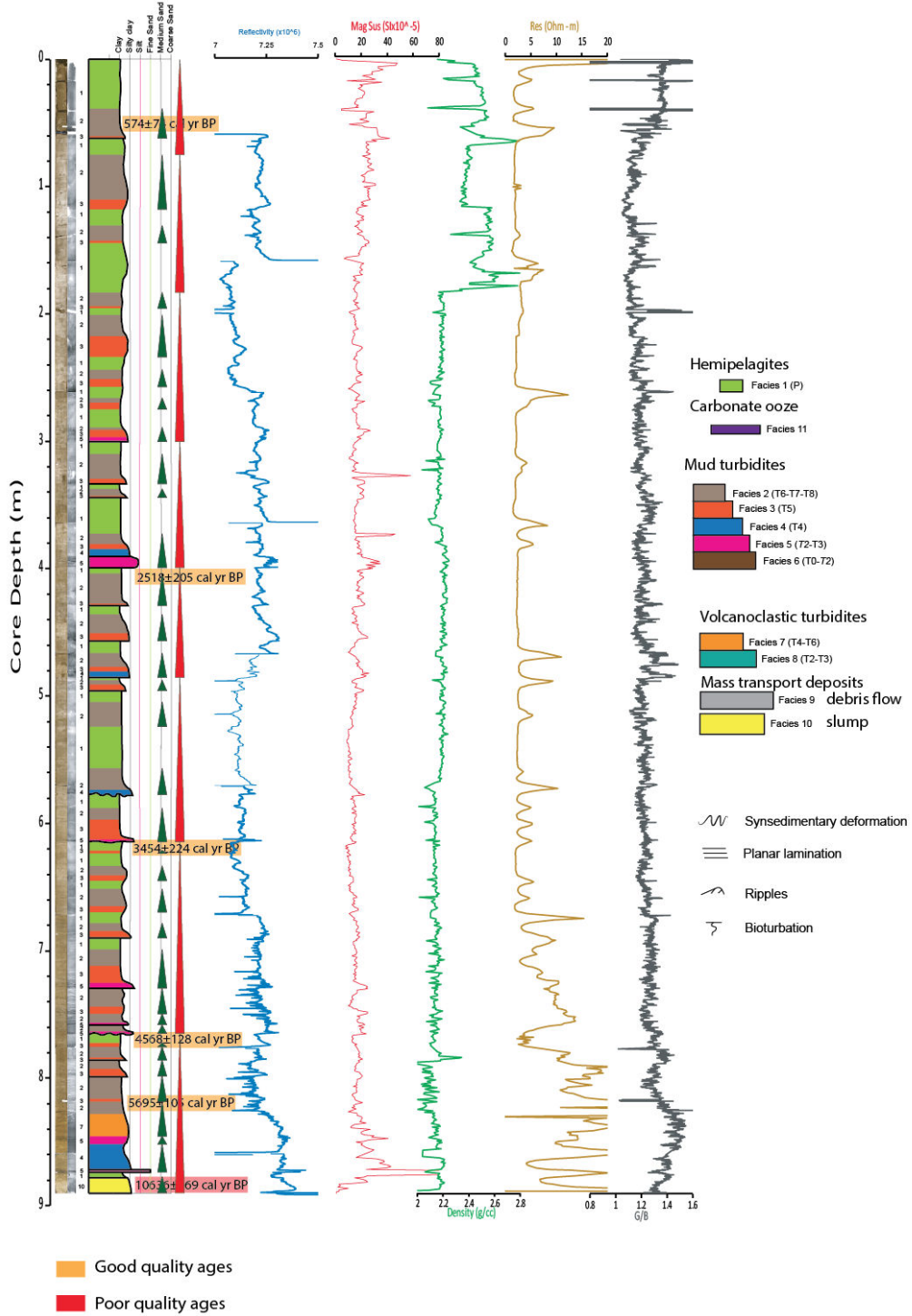


Fig. 6. 5 Stratigraphic log and deposits interpretation of core KAT-21

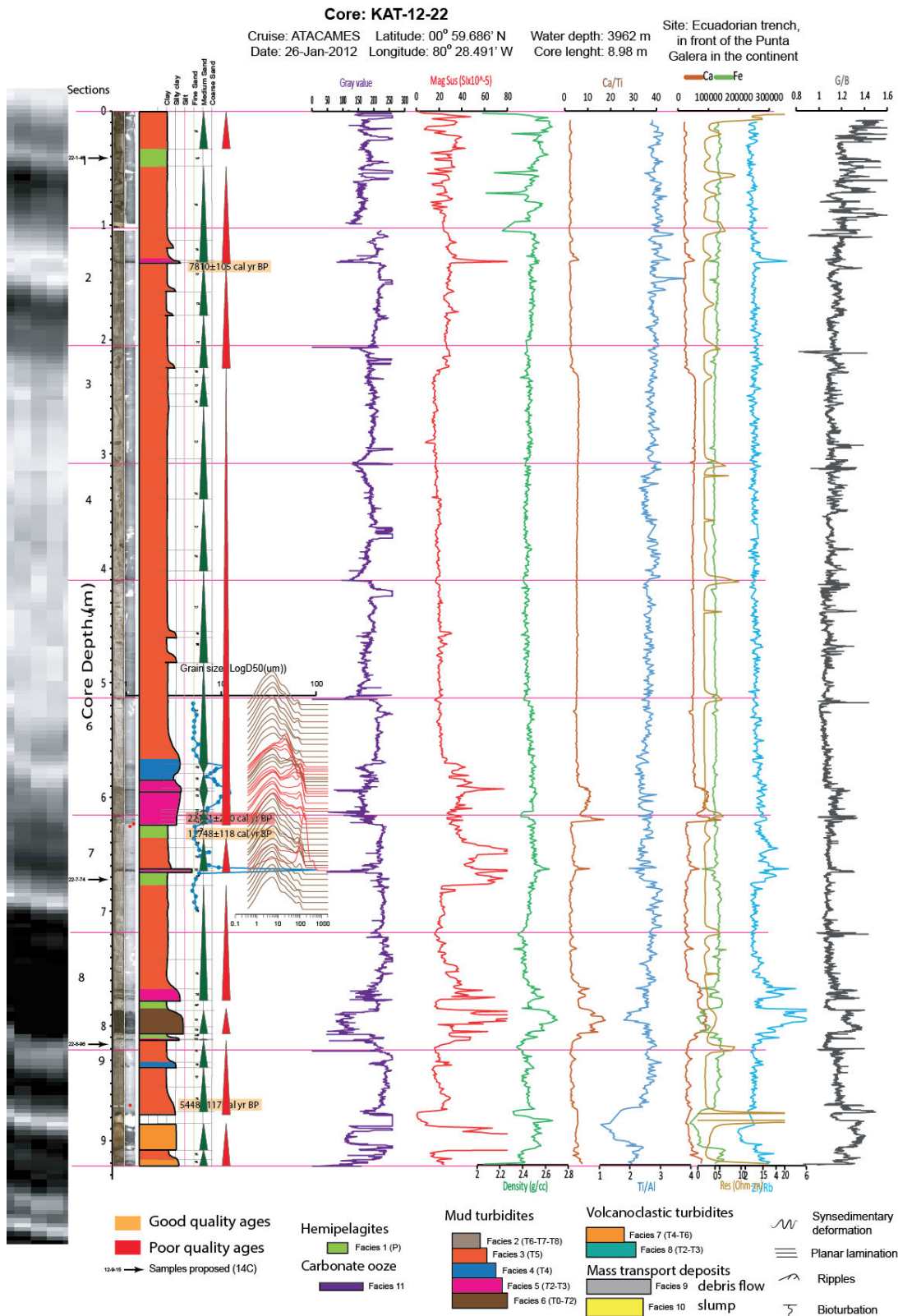


Fig. 6.6 Fig. 6.6: Stratigraphic log and deposits interpretation of core KAT22

**Core: KAT-12-23**

Cruise: ATACAMES  
 Date: 26-Jan-2012  
 Latitude: 01° 16.387' N  
 Longitude: 80° 20.206' W  
 Water depth: 3973 m  
 Core length: 8.18 m

Site: Ecuadorian trench,  
 about 10 km southward  
 of the Galeras seamounts

KAT-12-23

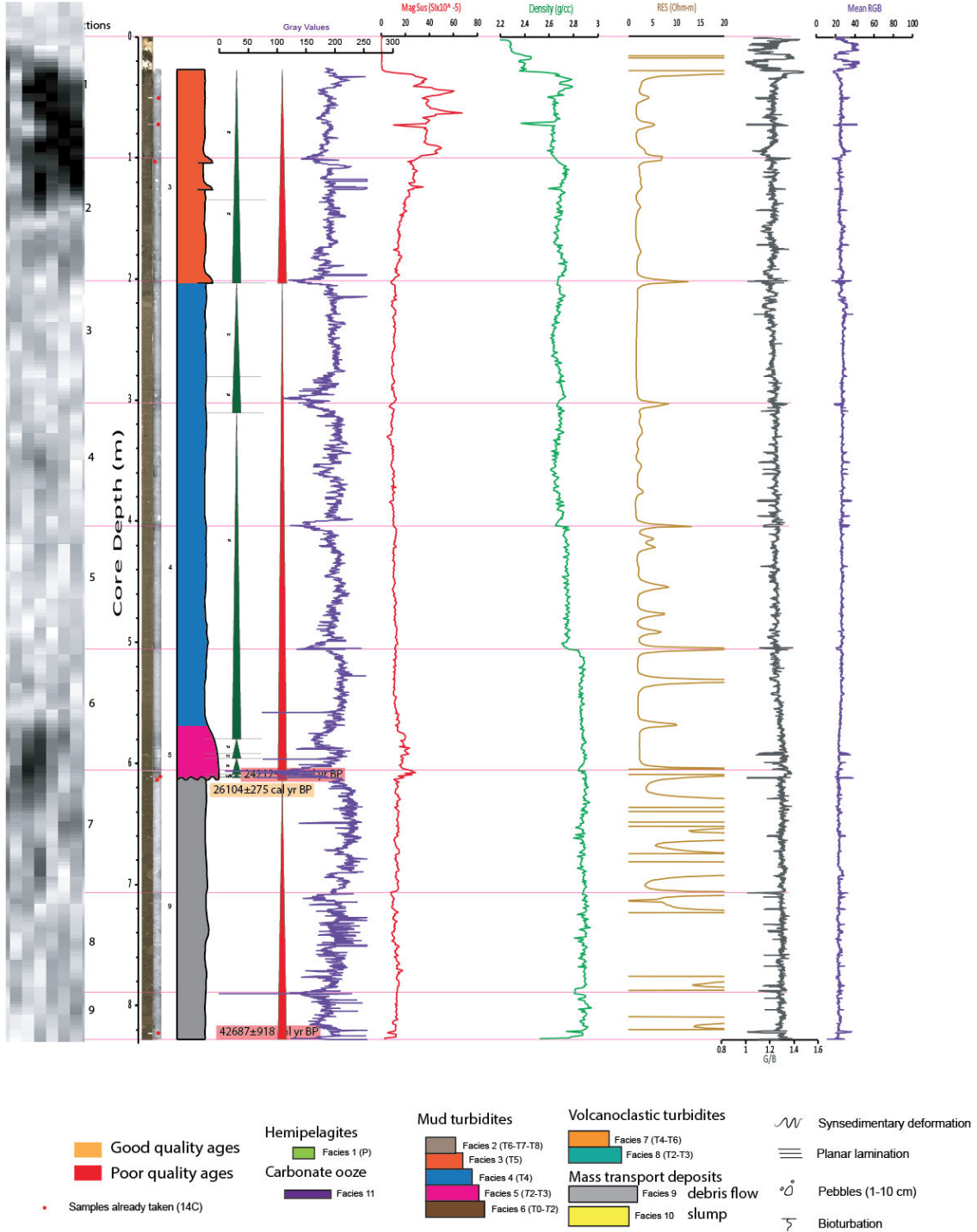


Fig. 6. 7 Stratigraphic log and deposits interpretation of core KAT23






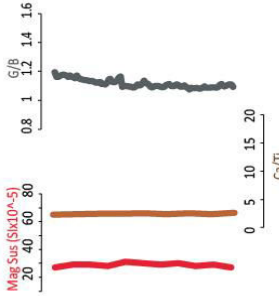




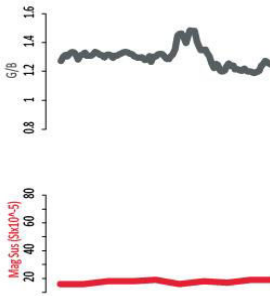

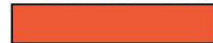

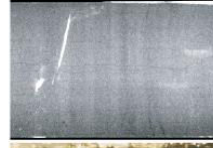
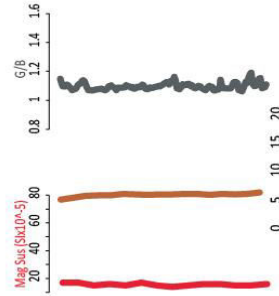

Color symbology	High-resolution photographs	X-ray images	Petrophysical parameters	Micro-facies photographs	Description
					<p>Average density 2.49 g/cc, average MS 27.38 SI  Olive grayish homogenous clay to silty clay  Moderately to highly bioturbated  Presence of foraminifers planctonics and benthics, diatoms  Degree of reflectivity: medium  No sedimentary structures except bioturbation  Minerals: few quartz and ferromagnesian grains</p>
					<p>Average density 2.2 g/cc, average MS 25 SI  Olive grayish homogenous clay  Moderately to highly bioturbated  Rare foraminifers  Degree of reflectivity: medium  No sedimentary structures except bioturbation  There is not evidence of minerals</p>
					<p>Average density 2.43 g/cc, average MS 19.86 SI,  with by places sharp increases to 30SI  Olive grayish clay to silty clay with no bioturbation and rare foraminifers  Degree of reflectivity: medium  Thin horizontal to low angle lamination  Similar to facies 1 except for the lamination and lack of bioturbation</p>

Fig. 6. 8 Detailed facies description





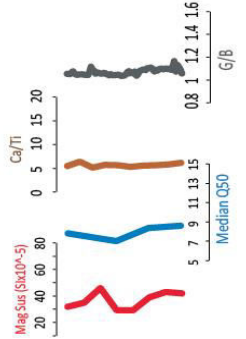




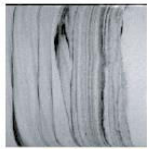
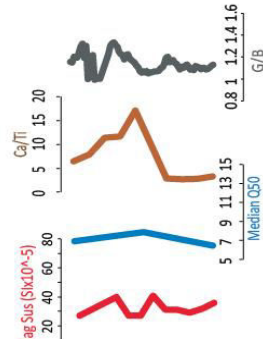



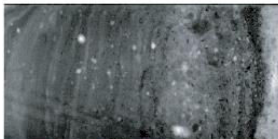
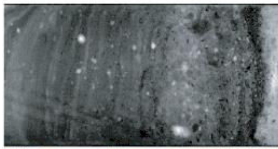
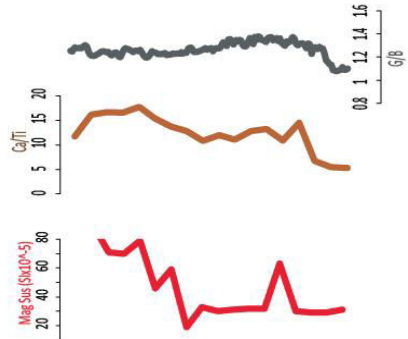

Color symbology	High-resolution photographs	X-ray images	Petrophysical parameters	Micro-facies photographs	Description
 <b>Facies 4 (T4)</b>	 			 Source: sample 22-6-65	<p>Average density 2.49 g/cc, average MS 35.40 SI Olive grayish clay to silty clay Rare foraminifers Degree of reflectivity: low to medium. low reflectivity is represented by the dark grayish silty laminations No or rare bioturbation Remnants of low angle laminations, flame and convolute structures and syndimentary microfolds Similar to facies 2 but more structured, showing intercalations of dark grayish silty clay laminations</p>
 <b>Facies 5 (T3)</b>	 			 Source: sample 22-7-48	<p>Average density 2.48 g/cc, average MS 37.70 SI Olive grayish silty clay to silt Rare foraminifers No bioturbation Degree of reflectivity: low to medium. Low reflectivity is represented by the dark grayish silty laminations Planar horizontal to low angle or rippled laminations with low angle erosion surfaces</p>
 <b>Facies 6 (T0-T2)</b>	 			 Source: sample 22-7-85	<p>Average density 2.66 g/cc, average MS 78.20 SI Darkish olive grey massive to laminated silt to silty sand Degree of reflectivity is Low representing dark grayish silty laminations Rich in foraminifers No bioturbation Fining up sand to silt, massive at base and then horizontal to low angle or ripple lamination Quartz, mica and shell bioclasts</p>

Fig. 6. 9 Fig. 6.9: Detailed facies description




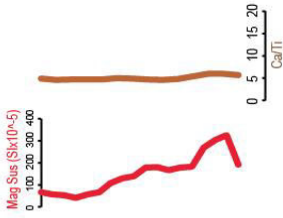




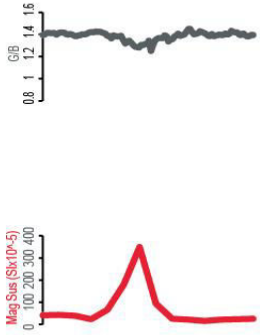




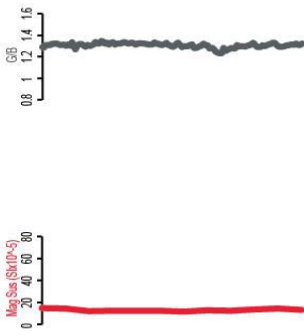

Color symbology	High-resolution photographs	X-ray images	Petrophysical parameters	Micro-facies photographs	Description
			 <p>Mag Sus (Sk10<sup>-5</sup>) scale: 0, 100, 200, 300, 400</p> <p>Car/Ti scale: 0, 5, 10, 15, 20</p> <p>GB scale: 0.8, 1, 1.2, 1.4, 1.6</p>	 <p>source: sample 22-9-72</p>	<p>Average density 2.51 g/cc, average very high MS 180 SI</p> <p>Brownish massive volcanogenic silt (tephra)</p> <p>No bioturbation, no foraminifers</p> <p>Degree of reflectivity is medium to high reflectivity</p> <p>Quartz, ferromagnesian minerals (biotite)</p> <p>Erosion surfaces at base and top</p> <p>T4-T6 (tephra) horizons of Stow</p>
			 <p>Mag Sus (Sk10<sup>-5</sup>) scale: 0, 100, 200, 300, 400</p> <p>Car/Ti scale: 0, 5, 10, 15, 20</p> <p>GB scale: 0.8, 1, 1.2, 1.4, 1.6</p>	 <p>Source: sample 21-10-12</p>	<p>Average density 2.15 g/cc, high average MS 200 SI</p> <p>Light brownish bioclastic sand with intercalations of black volcanogenic ferromagnesian sand laminae</p> <p>Shell hash of microfossils of benthic and planktonic forams, radiolarians</p> <p>Volcanic ash both base and top is characteristic in this facies</p> <p>Bioturbation</p> <p>Degree of reflectivity is medium</p> <p>Erosion surfaces at base and top</p> <p>Quartz and ferromagnesian minerals</p> <p>T2-T3 (bio-tephra) horizons of Stow</p>
			 <p>Mag Sus (Sk10<sup>-5</sup>) scale: 0, 20, 40, 60, 80</p> <p>Car/Ti scale: 0, 5, 10, 15, 20</p> <p>GB scale: 0.8, 1, 1.2, 1.4, 1.6</p>	 <p>Source: sample 23-7-50</p>	<p>Average density 2.43 g/cc, average MS 13.36 SI</p> <p>Olive grayish massive silty clay to silt with brown and yellow mottling, which represent relicts of centimetric to decimetric clasts</p> <p>No bioturbation</p> <p>Plenty of microfossils: benthic and planktonic forams, diatoms and radiolarians</p> <p>Medium to high reflectivity where high reflectivity is represented by the clear, transparent grayish silt</p> <p>Quartz</p>

Fig. 6. 10 Detailed facies description



### 6.4.2.1 Hemipelagites

Facies 1 is hardly visible on the seismic data (Fig. 6.5 and Fig. 6.8), since the deposits are only a few centimeters-thick and thus much below the theoretical resolution of the CHIRP data. The deposits consist mainly of grayish olive fine grained deposits (clay to silty clay) with moderate reflectivity. The deposits are homogeneous and show no specific sedimentary structures except moderate to high bioturbation depending on the cores (Fig 6.5 and 6.6). The magnetic susceptibility is moderate, ranging between 20 and 35, SI, and shows natural variability compared to other, sorted deposits. The minerals contained in the deposits are mainly quartz, few feldspar, chlorite, and few pale lithic fragments. Additionally, a limited amount of pumice is also visible. The biotic content shows both planktonic and benthic foraminifers (Fig. 6.8). Compared to other facies, most foraminifers are well preserved attesting of very low deposition energy. All these features are compatible with a slow and continuous hemipelagic deposition.

### 6.4.2.2 Muddy Turbidites

Turbidites are the most represented type of deposits in the trench. they may contain up to three facieses based mainly on their sedimentary structures, grain size, and in a lesser importance, their content. They are described from top to bottom as follows:

- Facies 2 (T7 and P terms of Stow sequence) (Fig. 6.5, 6.7, and 6.8): The uppermost deposits of turbidites are characterised by clayey turbidite tails: It shares numerous common features with hemipelagites and is very difficult to differentiate. As within hemipelagites, it also consists of Olive grayish fine-grained deposits (clay to silty clay) (Fig. 8B). The magnetic susceptibility is slightly lower (~18-25 SI), but shows in this case a little less variability. Bioturbation is still abundant affecting almost all deposits in core KAT 21 (Fig. 6.5, 6.8). The deposit is generally homogeneous. The major difference is the very poor mineral and biotic content compared to hemipelagites, with the presence of only few foraminifers (Fig. 6.8).

- Facies 3 (T5-T6 terms of Stow) also applies to turbidite tails: It is very similar to Facies 2. The first main difference with hemipelagites and Facies 2 is the limited amount of bioturbation (Fig. 6.8) especially in cores KAT 22 and KAT 23, but also the presence of slight millimetric planar lamination visible exclusively by very subtle variations of reflectivity on X-ray images (Fig. 6.8).

- Facies 4 (T4-T5 terms of Stow) is made of grayish Olive silty clays, slightly coarser than those of Facies 3 (Fig. 6.6 and 6.9). The major differences with Facies 3 are the greater Magnetic Susceptibility and the presence of more developed laminations. The magnetic susceptibility has irregular values depending on each laminae, but may reach up to ~40SI. The laminations are millimetric-thin, evidenced by relatively minor variation in X-ray reflectivity. They are particular because they are oblique but may also appear irregular, (i.e. undulated). Such feature is however uncommon in our dataset and could be interpreted either as convolute laminations (Fig. 9A): the Term T5 of the Stow sequence

This facies may represent up to 20cm-thick deposits in core KAT21 and 22 (Fig. 6.5 and 6.6).

- Facies 5 (T3-T4 terms of Stow sequence) is Usually observed at the base of turbidites (Fig. 6.5, and 6.9), it contains grayish olive to grayish silty clays to silts with a higher magnetic susceptibility than previously, oscillating from 25, up to 60 SI (Fig. 6.5 and 6.6), and an overall medium reflectivity, at least higher than on most other sedimentary facieses (Fig. 6.9). This facies is highly laminated, showing either oblique or planar laminations, overlying an erosive base. It is completely dominated by both planktonic and benthic foraminifers, although few quartz grains are also visible. The deposits are graded, where the amount and size of shells decreases upwards. This facies may represent up to ~40cm thick deposits (Fig. 6.5 and 6.6). Turbidites are fining upwards and get more clayey

#### **6.4.2.3 Megaturbidites**

The megaturbidites are a specific type of (very) muddy turbidites. They are clearly designable on the CHIRP data by their thick, acoustically transparent facies that overly more reflective deposits (Fig. 6.6 and 6.7). They have been cored on sites Kat22 and Kat 23, being respectively 3.98 and 4.1 m-thick. Sedimentologically, two main features depart muddy turbidites from Megaturbidites in our dataset: the first is the more complex basal part including multiple turbiditic pulses, while the second, and the most striking is the great thickness of the fine-grained part of the deposits, as identified on facies 3 and 4. To more accurately characterize these types of deposits, on core KAT 22, we additionally performed laser granulometry at a pitch of 5 cm and XRF geochemical analysis using an Avatech core scanner (Fig. 6.6).

#### **Multipulse turbidite base:**

On both coring sites, the base of Megaturbidites is erosive, characterized by the presence of silty deposits with numerous planar and oblique laminations (Facies 6.5 as identified previously).

#### **site KAT 22**

Based on the identification of the Stow turbidite sequence terms, where T0 and T8 are the basal and the uppermost terms respectively, we identify 5 pulses within the base of the turbidite (Fig. 6.6). We define each pulse as a succession from a low to higher term. Spikes of granulometry, but also of Magnetic susceptibility and Ca/Ti ratio, outline pulses. The two latter parameters are however not discriminating enough, since Magnetic Susceptibility shows too many variations, while Ca/Ti shows smoother patterns.

The most striking feature is a general reverse grading at the base within the three basal pulses: the median grainsize evolves from ~7 $\mu$ m to 11 $\mu$ m, a trend also visible on the Magnetic susceptibility evolving from 28 to 75 SI. Ca/Ti data however reveals a slightly more complex pattern, with a strong spike (value 17) at the first pulse, the general increase being mostly visible within the 2<sup>nd</sup> and 3<sup>rd</sup> pulse, the ratio evolving from values of 7 to 11. The fourth pulse is more classical for a turbidite, fining upwards (11 to 8  $\mu$ m),

the trend being similar in Ca/Ti and Magnetic susceptibility values. Finally, the fifth and last pulse of the megaturbidite base has a reverse grading (grainsize ranging from 7µm to 10µm), then fining upwards up to ~6µm. These two trends are both visible in Magnetic Susceptibility and Ca/Ti data, the contrast being however much less marked than previously (pulse 3), especially for the Ca/Ti values, ranging only from 5 to 6.

#### **site KAT 23**

In core Kat 23 the base of the Mega turbidites contains only three pulses (Fig. 6.7). We lack Grainsize and Ca /Ti data, but still observe the pulses in the Magnetic Susceptibility data. Compared to core Kat 22, the values and contrasts between spikes are much lower, values ranging only from ~11 to 28. The first pulse shows again a reverse grading (Mag. Sus: 11 to 28), while the two other show a normal one, the values in the second and third pulses respectively evolve from 28 to 18, and 21 to ~13.

#### **Complex Mega-turbidite tail.**

Alike the base of these deposits, the Mega-turbidite tails also aver complex, departing from a simple fining upwards trend.

#### **site KAT 22**

Both Magnetic susceptibility and Ca/Ti curves show a general decreasing trend up to the top of the deposits. The X-ray images however reveal seven pulses identified by the amalgamate successions of the Stow sequence terms. Since the deposits are very fine-grained, the sedimentary structures vary from very subtle and indistinct laminations (T4) to an almost ungraded mud (T7 and T8). Whispy convolute lamination (T5) are visible in only one of the pulses (Fig. 6.9) at 458-480cm depth, while isolated muddy intervals with few silty lenses are more present. They are visible because of a higher reflectivity on the Scopix images, and also slight spikes in Magnetic susceptibility (Fig. 6.6).

#### **site KAT 23**

The muddy fraction in core Kat23 (Fig. 6.7) is very similar to the one present in core KAT22 as it also presents amalgamate sequences. The main difference relies on the fact that the structures are more visible on the X-ray images.

### **6.4.2.4 Volcanoclastic deposits**

#### **a) Tephra**

Facies 7: This facies is visible only in core KAT 12-22 (Fig. 6.6). It is very different from all the others, since it has a gray to brownish colour, and the highest Magnetic suceptibility, reaching up to 400SI (Fig. 6.10). The Xray reflectivity is moderate to high. The deposits are generally massive silts to sands, with a sharp basal contact. The upper boundary is sharp, although the deposits are slightly fining upwards. This facies contains numerous biotites and quartz and no foraminifers, supporting a rhyolitic ash. Regarding all these features, this facies could correspond either to a tephra layer, or to a volcanoclastic turbidite.

## **b) Volcanoclastic Turbidites**

Facies 8: Only few turbidites are characterized by this facies (Fig. 6.6, 6m55): They are made of darkish olive fine-grained sand to silt. It departs from the previously described turbidite facieses because of its unusually high Magnetic Susceptibility, reaching up to 400 SI (Fig. 6.10), and its high X ray reflectivity, appearing almost black. The base, 2 to 10cm-thick is well laminated, fining upwards to facies 3. The deposits contain numerous Ferromagnesian minerals but also foraminifers, supporting a volcanoclastic turbidites that has incorporated hemipelagic deposits during its down going path.

### **6.4.2.5 Debrites / Mass Transport Deposits (MTDs)**

Facies 9. Debrites in our dataset are characterised by a muddy matrix supporting mud clasts that can reach up to ~10cm diameter (Fig. 6.7 and 6.10). The clasts are not systematically visible on the photographs and during the visual description, but appear doubtlessly on the X-ray images, usually with a higher reflectivity. The Magnetic susceptibility is moderate to high and appears homogeneous but more wiggling than compared to Megaturbidite tails (Fig. 6.7). Both matrix and clasts include reworked hemipelagites, shells, micas or quartz. Finally, the acoustic facies of debrites is chaotic (U2 in Fig. 6.13), but with a very low amplitude. The distinction with megaturbidites acoustic facies could not be well established by Ratzov et al. (2010), but the better quality of our Chirp Data allows identifying a slightly more reflective facies in the case of debrites (U2 in Fig. 6.13). The presence of sedimentary cores doubtlessly discriminate the two types of deposits.

### **6.4.3: Distribution of gravity flow deposits**

#### **6.4.3.1 Deep seismic MTD**

Using the deep seismic lines from SCAN cruise (propriety of the SHE), which cross the trench perpendicularly each four kilometers, we have identified, into the trench sedimentary fill, several seismically chaotic and/or transparent lenses that we interpret as old MTDs (Fig. 6.11) and called in this paper deep-seismic MTD. Along the foot of the margin, from N1°15' to N1°00' latitude (Fig. 6.2) the seismic profiles (profile 1048, Fig.11) show seismically semi-transparent to chaotic unit, interpreted as a deep-seismic MTD (thickness 0.11 twtt= 90 m; length 30km; width 5 km). This MTD is massive and extends in the sub-basin SB2, in front of the lower slope domains 3 and 4.

Southward, between latitude 1°02' and 0°55' (Fig. 6.2), a remobilized sedimentary mass (maximum thickness 0.25 twtt=180 m; length/width 11km) could be identified from the seafloor morphology and seismic facies. This MTD is composed by a chaotic weakly reflective seismically unit including a blocky sub-unit. This latter sub-unit consists (Fig. 6.3) of kilometer-wide hummocks on the seafloor (profile 1024, Fig. 6.11 and Fig. 6.3) which have high-amplitude well-stratified seismic characteristics. The largest blocks have reflectors tilted to the east, which indicates that the blocks area back-tilted to the east thus corroborating a failure mechanism of a slump. We interpreted these geometries as the result of a rock avalanche, cohesionless slump with deposits containing large fallen

blocks. Some blocks are more than 0.2 stwt thick (around 150 m) and more than 1000-m wide. Along the outer wall of the trench, the base of this MTD is erosive; toward the inner wall, into the trench it is more difficult to define the geometry of the base of this MTD.

On the outer wall of the trench (between latitude 0°40'-0°50', Fig. 6.2), chaotic to transparent 0.25 stwt thick facies extends until the middle of the trench. Finally, into the SB7 sub-basin (between latitude 0°15' and 0°25', latitude), thick transparent facies with no erosional base extends throughout the trench (profile 972, Fig. 6.11). Some other profiles (Profile 964, Fig. 6.3) show two similar MTDs.

### **6.4.3.2 Chirp MTD and Megaturbidites**

#### **6.4.3.2.1 General Stratigraphy**

The new continuous chirp profile (location on Figure 6.2) allows us to define two regional units (LR and UR Fig 6.12). We defined and follow some regional remarkable horizons in order to better constrains the stratigraphical position and continuity of these two units and of the Megaturbidites (Fig. 6.12).

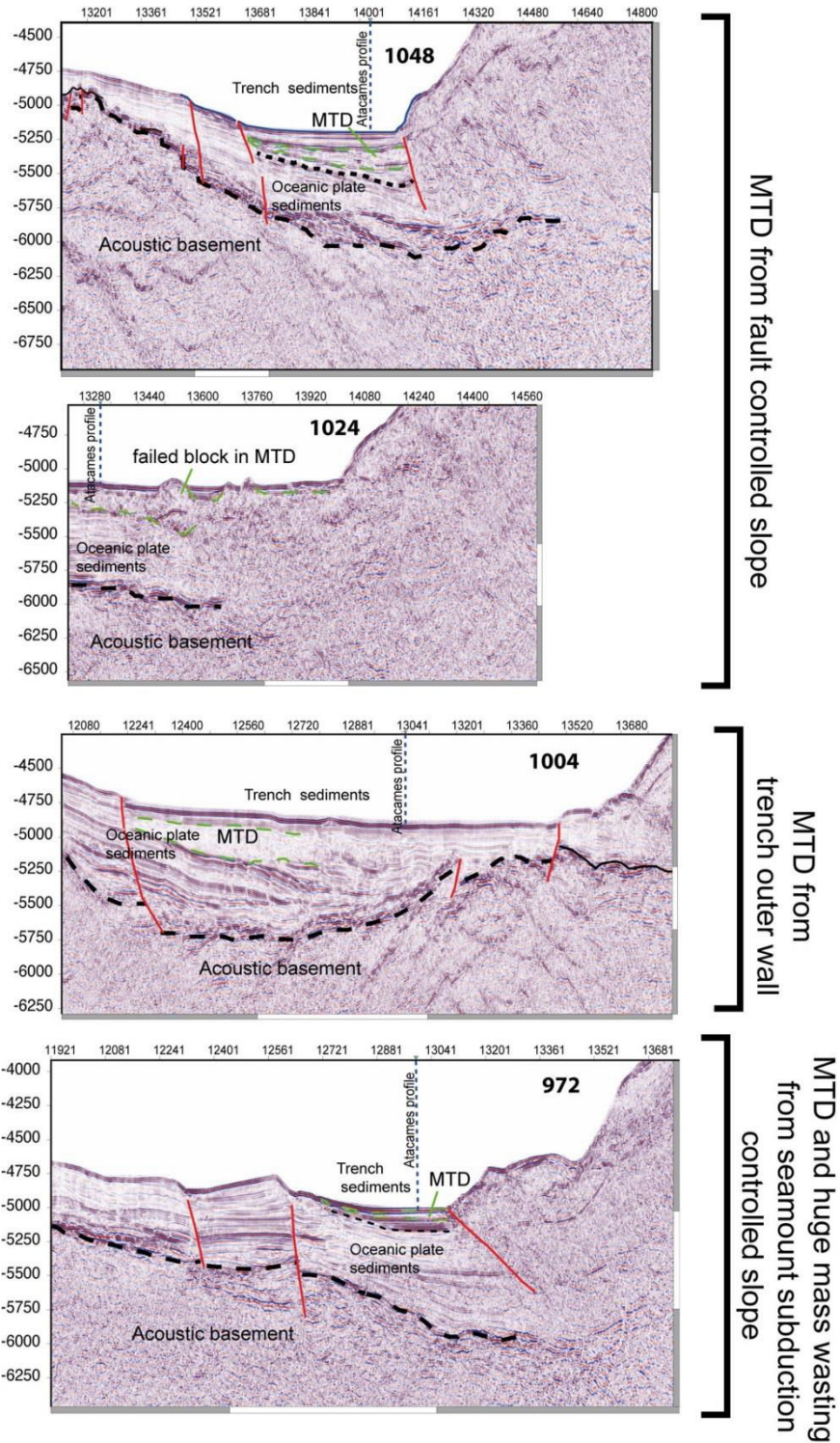


Fig. 6. 11 Deep seismic profiles (propriety of the SHE) crossing the trench (location on Figure 6.2).

All along the profile, including through the saddle area, well stratified succession of weak and strong reflectors is present. Nevertheless, from the top to the bottom we can distinguish two seismic units. An upper unit (UR, Fig. 6.12) with well stratified high



amplitude reflectors; below this upper unit, a lower unit which is also well stratified but lower in amplitude (LR, Fig. 6.12). This upper unit is well developed into the SB7 and SB6 but very thin on the saddle area excepted into the SB5. A similar upper unit is present into the SB1 and SB2 but at the boundary between SB2 and SB3 (northern limit of the saddle) no continuous reflector can be followed. The upper unit cannot be formally correlated between SB-1-SB2 and SB7-SB-6 areas. The lower unit is followed continuously from the SB7 until SB3, and through the saddle area where it is close to the seafloor. Again, there is no evident continuity with the similar unit present into SB1 and SB2. The well-stratified succession of weak and strong reflectors of these two seismic units, are interpreted as inter-bedded hemipelagic and turbiditic deposits common to all the sub-basins. The seismic units in the saddle area reveals in many areas, vertical transparent fluids escape pipes are present (Fig.6.12), and these features are more recurrent in the step terrains than the flat areas.

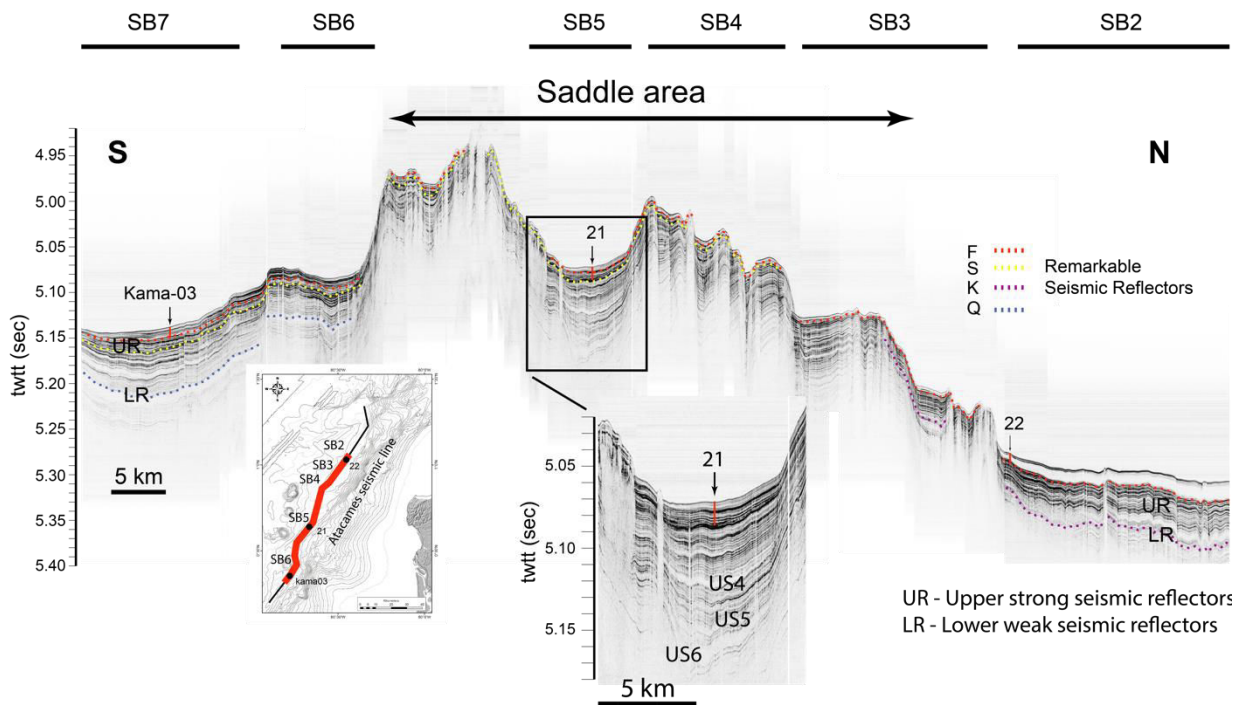


Fig. 6. 12 Atacames Chirp profile across the saddle area (location on Figure 2). Two regional units are distinguished. The dotted colored lines represent remarkable seismic reflectors (F, S, K, Q) used to refine the stratigraphical correlation between these two units and between the MTDs.

The continuity of some remarkable strong seismic reflectors was followed along the chirp profile (Fig. 6.12). Reflector F is strong amplitude and is tentatively identified in all the SBs. This reflector was sampled by 2 cores (Kat 21, 22) and corresponds to a sandy turbidite into hemipelagic sediment. This reflector is part an upper well-stratified, high-amplitude reflectors unit and the cores agree that this seismic unit is composed by inter-bedded hemipelagic and turbiditic deposits.

### 6.4.3.2.2 Chirp MTD and megaturbidites (MT) identification

Our new data shows that reveals that the transparent units most likely correspond to Megaturbidites (U1 in Fig. 6.13), whilst Chirp-MTDs show a more chaotic facies (U2 in Fig. 6.13). Although Ratzov et al., (2010) considered them all as MTDs, we decide to use the same nomenclature (U1, U2 etc...) in the sake of clarity and for easier correlation between the two datasets.

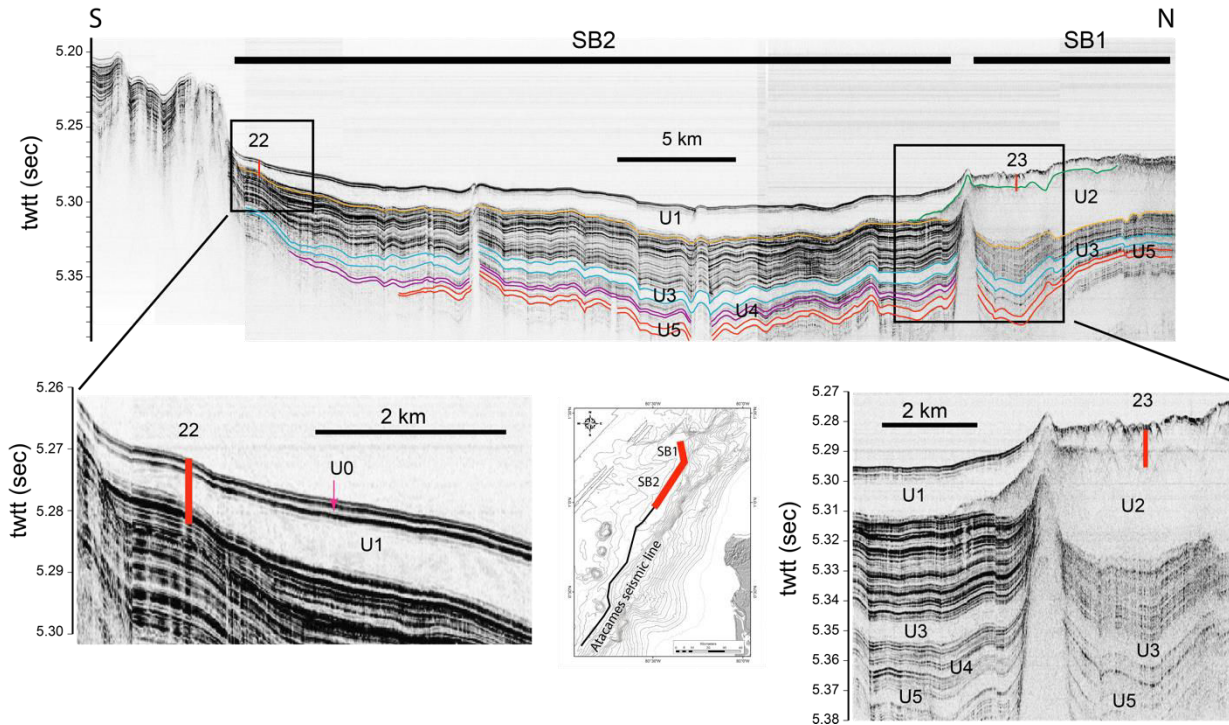


Fig. 6. 13 Atacames Chirp profile across the SB-1 and SB-2 area (location on Figure 2). We have identified more MTDs than Ratzov et al., 2010 and the thick MTD U2 is confined in the SB1.

Chirp data allows discrimination of shallow mass-transport deposits from hemipelagic and turbidite deposits on the basis of their acoustic facies (Table 1). MT and MTD in the SB1 and SB2 area, are found on top of the upper seismic unit (Fig. 13) and into the lower unit. In the SB6 and SB7, the MTDs are located into the two seismic units (Fig. 14), meanwhile into the SB5 the MTDs area identified into the lower unit (Fig. 14). We have identified 13 MTD deposits in total (Table 6.1).

Table 6.1. Characteristics of the seismic units observed along the trench.

Seismic units	Extension in latitude	Thickness	Base	Characteristics
U0	1°05'N to 1°00'N	Max: 0.001 sec, ~0.75 m, 1°00'N;	not erosive	Sub-horizontal, clear, transparent echo-layer located in the southern part of SB2. Its thickness remains almost

		Min: 0 sec, 1°05'N		constant except in the north border where it pinches. Thickness calculated using sound velocity in sediment = 1500m/s
U1	1°21'N to 1°00'N	Max: 0.017 sec, ~12.75 m, 1°04'N; Min: 0.004 sec, ~3 m, 1°15'N	not erosive	Horizontal, clear, transparent and chaotic echo-layer located in SB1 and SB2. Its thickness remains almost constant except in the borders. Thickness calculated using sound velocity in sediment = 1500m/s
U2	1°21'N to 1°14'N.	Max: 0.047 sec, ~35.25m, 1°16'N; Min: 0.002 sec, ~1.5m, 1°15'N.	erosive.	Sub-horizontal, clear, semitransparent, chaotic echo-layer located in SB1 and north part of SB2. Thickness calculated using sound velocity in sediment = 1500m/s
U3	1°21'N to 1°00'N.	Max: 0.008 sec, ~6m, 1°13'N; Min: 0.002 sec, ~1.5m, 1°00'N.	not erosive.	Sub-horizontal, clear, transparent, chaotic echo-layer located in SB1 and SB2. Thickness calculated using sound velocity in sediment = 1500m/s
U4	1°15'N to 1°01'N.	Max: 0.002 sec, ~1.5m, 1°14'N; Min: 0 sec, 1°02'N.	not erosive.	Sub-horizontal, clear, transparent, chaotic echo-layer located in SB2. Thickness calculated using sound velocity in sediment = 1500m/s
U5	1°21'N to 1°16'N, from 1°15'N to 1°02'N.	Max: 0.006 sec, ~4.5m, 1°15'N; Min: 0 sec, 1°03'N.	not erosive.	Sub-horizontal, clear, transparent, chaotic echo-layer located in SB1 and SB2. Thickness calculated using sound velocity in sediment = 1500m/s
US1	0°29'N to 0°12'N.	Max: 0.01 sec, ~7.5m, 0°17'N; Min: 0.006, ~4.5m, sec, 0°12'N.	not erosive.	Sub-horizontal, greyish, semitransparent, chaotic echo-layer located in SB6 and SB7. Thickness calculated using sound velocity in sediment = 1500m/s.
US1-1	0°29'N to 0°12'N.	Max: 0.005 sec,	not erosive.	Sub-horizontal, clear, transparent, chaotic echo-layer located in SB6 and SB7.

		~3.75m, 0°22'N; Min: 0.001 sec, ~0.75m, 0°24'N.		Thickness calculated using sound velocity in sediment = 1500m/s.
US2	0°29'N to 0°12'N.	Max: 0.01 sec, ~7.5m, 0°17'N; Min: 0.001 sec, ~0.75m, 0°27'N.	not erosive.	Sub-horizontal, clear, transparent, chaotic echo-layer located in SB6 and SB7. Thickness calculated using sound velocity in sediment = 1500m/s.
US3	0°29'N to 0°12'N.	Max: 0.015 sec, ~11.25m, 0°16'N; Min: 0.004 sec, ~3m, 0°25'N.	not erosive.	Sub-horizontal, clear, transparent, chaotic echo-layer located in SB6 and SB7. Thickness calculated using sound velocity in sediment = 1500m/s.
US4	0°42'N to 0°38'N.	Max: 0.005 sec, ~3.75m, 0°39'N; Min: 0 sec, 0°41'N.	not erosive.	Sub-horizontal, clear, transparent, chaotic echo-layer located in SB5. Thickness calculated using sound velocity in sediment = 1500m/s.
US5	0°42'N to 0°38'N.	Max: 0.006 sec, ~4.5m, 0°39'N, Min: 0 sec, 0°41'N	not erosive.	Sub-horizontal, clear, transparent, chaotic echo-layer located in SB5. Thickness calculated using sound velocity in sediment = 1500m/s.
US6	0°42'N to 0°38'N.	Max: 0.015 sec, ~11.25m, 0°39'N, Min: 0.003 sec, ~2.25m, 0°41'N	not erosive.	Sub-horizontal, clear, transparent, chaotic echo-layer located in SB5. Thickness calculated using sound velocity in sediment = 1500m/s.

#### 6.4.3.2.3 Spatial Distribution of MT and Chirp-MTDs

The interpretation does not allow us to correlate the MT continuously. Hence, we consider four sets of MTs: one set into the SB1 sub-basin, one set into SB2, one set into SB5 and one set into SB7 and SB6. (Fig. 6.2 and 6.12).

U0 is identified only in the southern part of the SB2. In the SB-1 and SB-2 area, the thicker U2 is confined into SB-1 and it is not deposited in the other sub-basins as it was previously claimed by Ratzov et al., 2010. This very 30 m-thick U2 stops just at the boundary between the two sub-basins. However, we cannot exclude that U2 may have been eroded by U1 inside SB-2, meanwhile the base of the U1 in SB2 is not erosive. U1 extends largely in the two sub-basins, with the largest thickness located in the middle of SB-2. We cannot exclude that this MT extends into the SB3 area meanwhile the facies is not typical as into SB2. U3 is present all along the SB-2. Southward, it becomes progressively thinner and finally disappearing before it reaches the SB-2 south boundary. Northward, the prolongation of the U3 into the SB-1 is problematic because the thickness of the upper seismic unit is not the same into the sub-basins SB1 and SB2. Nevertheless, the base of the U2 into the SB1 is strongly erosive (Fig. 6.13) which can probably explain the thickness difference of upper seismic unit between the two sub-basins; this supports the correlation of Ratzov et al. 2010 and the deposition of the U3 through the two sub-basins. U4 can be followed in the northern part of the SB2 and it becomes thinner and finally disappears close to south border of this sub-basin. As for the U3 the correlation with a similar Unit in the SB1 is questionable. Finally, the U5 is newly reported in the SB2 and extends from the SB1 to the middle of the SB2 basin where it disappears (Fig. 6.14).

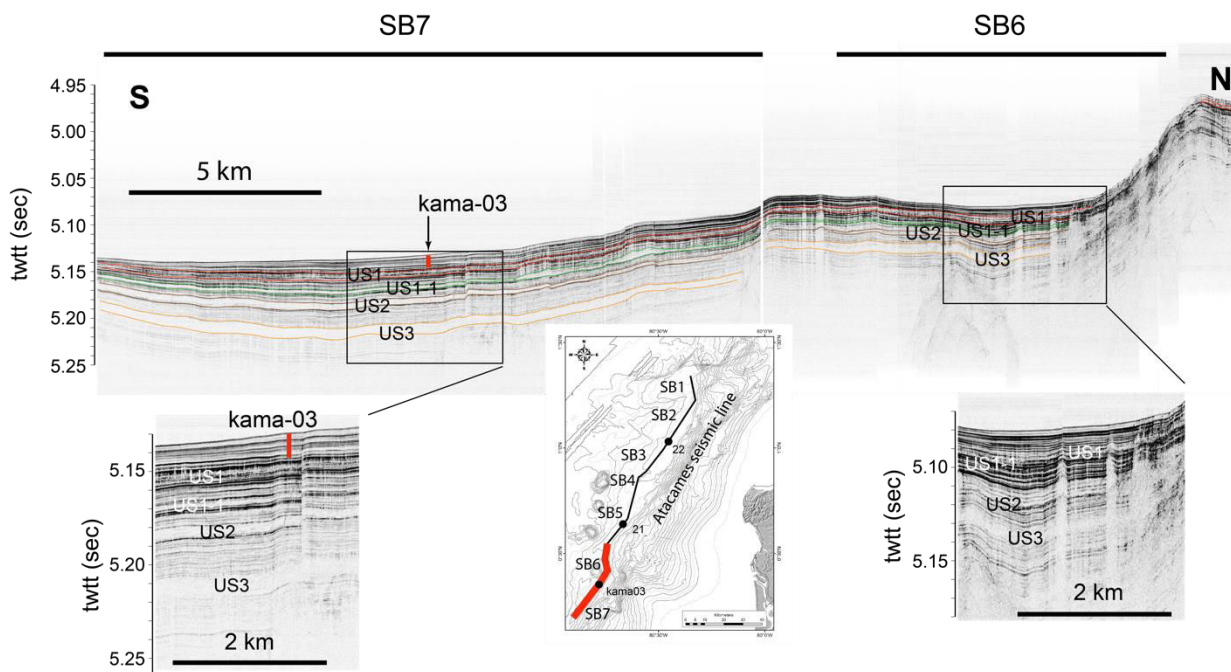


Fig. 6. 14 Atacames Chirp profile across the SB7and SB6 sub-basins area (location on Figure 2).

US-1, US-2 and US-3 extend into the SB-7 (Fig. 6.14). We can follow the US-1 northward, through the SB-6. Seismic units US2 and US3 extent all along SB7 but just before the northern boundary of this sub-basin those units become clearer and more transparent making difficult to appreciate their continuation northward. But they appear again in SB6, until the SB6 north boundary, where US2 is thinner and US3 keep the same thickness than in SB-7. US-1b is newly reported into the two sub-basins.

In the saddle area, only the SB5 can be characterized as a sub-basin where three new local MTD were identify.

In conclusion, U2 is confined to the SB1 and does not extend to the SB2 as previously described. U1 seems to be present is SB1 and SB2. U0, U5 and US1b are new MT identification. U3, U4 and U5 become thinner near the middle of the SB2. US1 extends in the SB7 and SB6 meanwhile the US2 and US3 extend only in the SB7. U1, U2, U3, U5 define the MT set of SB1. The MTs U0, U1, U3, U4 and U5, define the MTD set of SB2. The MTDs US4, US5 and US6 define the MTD set of the SB5. And finally, the MTDs US1, US1-1, US2 and US3 define the MTD set of SB7 and SB6.

#### **6.4.4 Sedimentation rate model and MT dating from Atacames cores**

After the identification based on acoustic facies of these four sets of MTs, we try to perform the age dating of the MTDs. We first realize measurement of MTs depth base and top in twtt in each sub-basin on the location of sedimentary cores. Secondly, we make the conversion of these twtt depths in meters using seismic waves velocity. In order to constrain error of depth based on seismic waves velocity, we use of 1500 and 1600 m/s velocity for the trench sediment. Moreover, to constrain error on the depth based on Chirp resolution, we applied +/- 20cm to each calculated depth (m). Thirty, we need to realize the conversion of the depth in age, by calculating a sedimentation rate. After the subtraction of MTs thickness from the total sedimentary column, based on sedimentary cores, we calculated mean sedimentation rates from the top to the deepest <sup>14</sup>C date. To constrain errors on sedimentation rates based on <sup>14</sup>C uncertainties, we calculated a minimum and maximum rate using the min/max age <sup>14</sup>C age (2sigma). Finally, ages were calculated applying min/max sedimentation rates to: min/max H/T thicknesses based on min/max Vp, and min/max depths according to CHIRP resolution errors. The proposed age is the median between the extreme values.

First using the dating of the Kama03 core (Ratzov et al. 2010), translate along the Atacames chirp profile we re-calculate the sedimentation rate for SB-7 and SB-6. Secondly, as explained above, we use the dating of core 21 for SB5. Unfortunately, along the core 22, the dating does not allow us to calculate a sedimentary rate. 3 dating were performed along this core. But two ages are into the MT U1 (Fig. 6.6) and indicated incoherent ages due to reworked material. Only one age, below the MTD U1 seems to be correct but it is located close to a turbidites tail; the calculation of sedimentation rate from this age gives us a very low sedimentation rate, about half of the sedimentation rate from Kama03.

We do not use this date along the core KAT22. For the same reasons, we do not use the dating performed along the core 23 into the SB1, because this core sampled the two MTD U1 and U2. Consequently, in the SB2 and SB1 we have used a sedimentation rate of 1.63 mm/y, which is median between the sedimentation rate calculated from core Kama03, and core 21 into the SB7 and SB5 respectively. The ages resulting for this method are reported in Table 2 and Fig. 6.15.



Table 6.2. Age estimations of MTD and MT units.

Seismic Unit	Mean thickness (m)	Mean hemipelagic/Turbiditic cover (m)	Sedimentation rate (mm/yr)	Mean age (cal yr BP)	Age error (cal yr BP)	Mean age (AD-BC)	Age error (AD-BC)
U0	0.5	1.15	1.63	720	50	1232 AD	22
U1	3.25	2	1.63	1253	157	699 AD	107
U2	30	1.8	1.63	1253	157	699 AD	107
U3	0.37	20.8	1.63	13001	852	11049 BC	637
U4	0.98	25.8	1.63	16187	1006	14235 BC	683
U5	2	27.8	1.63	17235	933	15283 BC	586
US1	5.32	12.45	1.81	6896	394	4944 BC	260
US1-1	3.73	19.8	1.81	10924	578	8972 BC	438
US2	5.47	26.5	1.81	14648	861	12696 BC	716
US3	9.3	43.25	1.81	23878	1446	21926 BC	910
US4	3.27	38.8	1.44	26979	1546	25027 BC	1023
US5	3.93	59	1.44	41067	2380	39115 BC	1181
US6	10.22	64.3	1.44	44627	2828	42675 BC	1489

We tentatively estimate a maximum age for the deep-seismic MTDs without considering the thickness of the chirp MTDs above the deep-seismic MTDs. The deep-seismic MTD along the profile 1048 (Fig. 6.11) is located below the seafloor at a depth of 0,0625 twtt= 106m with a velocity of 1700m/s (100 m for a velocity of 1600 m/s). Taking into account a sedimentation rate of 1.6 mm/y the maximum age is between 66250/62500 years. The deep-seismic MTD along the profile 1024 (Fig. 6.7) is located at depth 0,05 twtt = 85m with a velocity of 1700m/s (and 80m with a velocity of 1600 m/s). Taking into account a sedimentation rate of 1.6 mm/y = 50000/53125 years as maximum age. Along the profile 1004 (Fig. 6.11) the oceanic deep-seismic MTD more or less the same age than the deep-seismic MTD along the profile 1024. Finally, along the profile 972 (Fig. 6.11) we estimate the depth to 50 and 53 m and with a sedimentation rate of 1.8 mm/y the age is around 27000/24000 years.

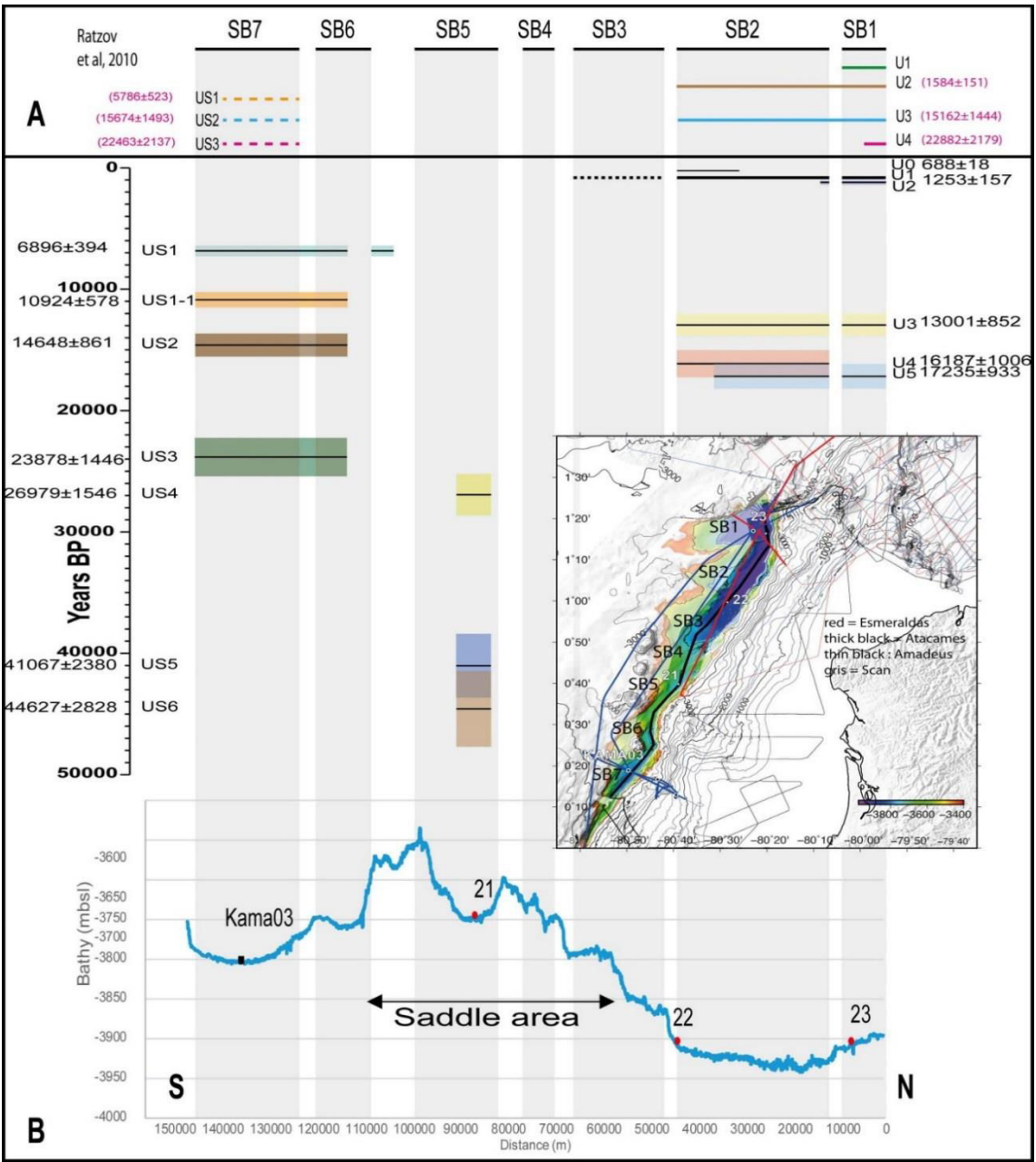


Fig. 6.15: Repartition of the MTDs along the northern Ecuadorian segment. Above from Ratzov et al., 2010; below this work. The bathymetric profile in blue is along the Atacames Chirp profile.

## 6.5 Discussion

### 6.5.1 Sources of gravity deposits (Turbidites, Megaturbidites and MTD)

The morphology analysis of the slope shows that there are no important slope failure scarps which have breached the upper slope in a recent past (Fig. 6.2). The upper slope is principally cut by downslope gullies which end into basins or terraces at the middle of

the slope. Important mass wasting related to upper slope re-entrant is observed along the domain 2 but it is ancient, meanwhile it affects always the trench morphology. Consequently, we assume that the upper slope is not actually the main source of the material which feed the trench. On the contrary, the lower slope exhibits many seaward concave scarps which are very steep into the domain 1, 3 and 4. The chirp-MTDs and deep seismic-MTDs are numerous into the trench segment facing these three domains.

#### **6.5.1.1 Spatial distribution**

The comparison of the spatial organization of Megaturbidites with the scar distribution along the slopes help constraining their possible source areas. Two areas are the main source of the MTDs; one front of the SB1 and SB2 (domain 3 and 4, Fig. 6.2); and another one front of SB6 and SB7 (domain 1, Fig. 6.2). Identified chirp-MTDs could have originated either from the outer or the inner trench slopes, as both are tectonically active. The top unit U0 is local and identified only into the southern part of the SB2. The unit U1 was identified all along the SB1 and SB2 (Fig. 6.2). Because it has its maximum thickness in SB2 we consider that its derived from the sub-linear adjacent margin lower slope of this sub-basin. The U2 was only identified within the SB1 sub-basin (Fig. 6.2) and Ratzov et al., (2010) used the asymmetry morphology of the basal erosive contact of this unit to derive a MDT origin from the continental slope. U2 could have derived from closer sources, such as the semi-circular lower slope re-entrants of the domain 4 (Fig. 6.2).

The US1, US1-1, US-2, US3 and US4 MTDs are present in SB7 and in the southern part of the SB6. These MTD are in front of the series of large slump scars in the adjacent Atacames re-entrant which indicate that these MTDs probably derived from this re-entrant. We agree with Ratzov et al., 2010, which have suggested that these MTDs result from secondary slope failures postdating a major collapse event, whose products form most of the ~10 km-wide frontal wedge that bridges the reentrant (Fig. 6.2; Profile 964, Fig. 6.3). Finally, the three MTDs into the SB5, in the saddle area, are too thin and very local and we assume that they come from the continental slope.

The deep-seismic MTDs distribution mimics the distribution of the recent chirp-MTDs and we assume that they come from the continental slope (Fig. 6.2). Into the SB2 the most extended and thick deep-seismic MTDs lies at the foot of the linear fault-controlled lower slope domain 3, as the thick blocky MTD (Fig. 6.3bis). Close to the Atacames seamount above the oceanic plate a thick MTD extending along the trench outer wall (profile 1004, Fig 6.8). Some landward circular scarps (Fig. 2) breach the seamounts themselves and the trench outer wall, both potential sources of this MTD. Front of the Atacames seamount reentrant, into the SB7 trench sedimentary the MTDs are relatively thin compared to the MTD of the SB2 sub-basin. Along the profile 964 (Fig. 6.3) two MTDs are present meanwhile one is present and only one along the profile 972 (Fig. 6.11). This suggests that the source of the MTD into the SB7 is recurrent but locals and with relatively small volume meanwhile MTDs identified in the SB2 are rare but very big.

### **6.5.1.2 Composition**

Finally, the composition of turbidites and megaturbidites does not make it possible to decide on the source areas of these deposits. The turbidites and the base of the megaturbidites show mainly an enrichment of the Ca/Ti ratio. This ratio is considered as a proxy for the biogenic/detrital component of the source deposits (Gracia et al., 2010, Polonia et al., 2013), low values involving detritism, while important values are related to stronger biogenic fractions. This trend may involve the destabilization of relatively carbonated sedimentary formations; it would therefore be incompatible with coastal sedimentary formations. Indeed, they are either sandstone (Angostura and Borbon formations), fine detrital (Tosagua and Onzole formations), or volcano-sedimentary formations composed by gabbros and basaltic flows (Piñon and Cayo formation) (Reyes and Michaud, 2012). Alternatively, the composition of gravitational deposits could imply the destabilization of the hemipelagic cover of the continental slope. In fact, the hemipelagic source material contains a biogenic part characterized, among other things, by planktonic and benthic foraminifers. During and after the turbiditic flows, all the contents are sorted and graded during the settling and deposition phases. These processes result in a concentration of coarse material at the base of the deposits, biogenic fractions in this case, as observed, for example, in eastern Taiwan (Lehu et al., 2015, 2016). Our observations agree with these phenomena: in addition to the mineral content, the turbidites and Megaturbidites bases have a high foraminiferal content, both benthic and planktonic

In order to try to identify with greater precision the source zones of each turbidite, and more particularly their depth, it would be necessary to carry out a systematic and quantified petrological and biostatigraphic characterization of each deposit.

### **6.5.2 Preconditioning factors for slope instability of the lower slope**

Slope instabilities are under the combined influence of various factors. The locations of slope failures are ultimately determined by the magnitudes of the forces that tend to drive sedimentary deposits downslope (gravity, seismic loading, and storm-wave loading) and the strength properties of the sediment that tend to resist such motion (Sultan et al., 2004; 2011). But long-term tectonic processes cause changes in slope morphology and in the structure of the stratigraphic column (Ranero et al., 2008) that create the most relevant preconditioning factors for slope instability (Harders et al., 2011).

#### **6.5.2.1 Stratigraphy**

Based on a regional study along the Ecuadorian margin from deep seismic profiles (Hernandez et al., 2013), identified several regional units above the acoustic basement. Additionally of the type of fracturation, the nature of the rocks outcropping along the lower slope is also a factor which controls the response of the scarps instability to an earthquake. The deep seismic profiles across the domain 1 (profile 964, Fig. 6.3) and across the domain 3 (profile 1024, Fig. 6.4) show a similar succession with two principal seismic facies. Above the acoustic basement, a basal unit shows high amplitude low

frequency semi-continuous reflectors unconformably overlying by a medium frequency continuous reflectors. Regionally we assume that the stratigraphy is the same along these two profiles. If it is true, the geology is not the principal factor which can explain the different styles of failure along the margin.

### **6.5.2.2 Tectonics**

Additionally of regional subduction erosion process, our results allow us to distinguish two different long-term tectonic process participating as preconditioning factors for slope instability which could explain the repartition and the frequency of the MTDs into the trench.

The first one corresponds to seamount subduction and related fracturation of the sediment. Where the Atacames seamounts intersect the trench, the lower slope re-entrant (domain 1) corresponds to the morphologic trace of the subduction of seamounts (Marcaillou et al. 2016). This topographic-high subduction leads to form this indentation, steepening the outer slope, and uplifting fore-arc corresponding to the spur-shaped shallow promontory. All these processes are associated by pervasive fracturing (Dominguez et al., 1998) as observed along the seismic profile 964 (Fig. 6.3). Indeed, subducting seamounts, fracture the entire overriding plate under the middle slope (~5–8 km thick). Fluids also ascent along seamount subduction induced fractures (Michaud et al., 2016), and fluid flow along fracture networks might also play a role in the weakening the strength properties of the sediment. The second one corresponds to the lower slope faults control of the domains 3 and 4. Active thrust faults are well defined along the domain 4 where they affect the seafloor (Fig. 6.2 and Fig. 6.3). In the domain 3 these faults prolong and affect locally the sedimentary unit. This implies that weakening of the strength properties of the sediment is not pervasive but limited to area close to the faults. The sedimentary units are locally fractured along the faults contrasting which the domain 2 where the sedimentary units are wholly fractured.

We assume that the strength properties of the sediment along the lower slope, sediment which are the source of deep seismic MTDs, change along the strike of the margin, and explain the distribution and style of failure.

### **6.5.3 Distribution and style of failure along the strike of the margin**

The sets of chirp-MTD and MT reveal a clear segmentation along the strike of the margin (Fig. 6.12). Into the SB-7-SB6 area the MTDs occur more and less regularly with a frequency between 6000 and 10 000 years. And the MTDs exhibit a medium thickness around 0.01 sttw. On the contrary, into the SB1-SB2 area, the frequency of the MTDs is more irregular than in the SB-7-SB6 (Fig. 6.15). They are distributed around two pulses separated by a long (around 10kyr) quiet episode (Fig. 6.15). In this area, the thickness of the MTDs vary four times from 0.01 sstw to 0.04 sttw. Moreover, the extension of the MTDs are much larger than in the SB7-SB6, corresponding to more important volume deposits related to larger reworked material. We suggest that the MTDs into the SB1-SB2, along the fault-controlled scarp, are greater and less frequent than along the

subduction seamount controlled scarp. We propose that these differences are directly related to the state of the slope scarps, that feed the trench, and which did not record the same tectonic history. In the area along the fault controlled scarps, some mass wasting deposits show that the fallen material have stood close to the failure scarps (Fig. 6.2) (along the middle slope at  $1^{\circ}10'$  in latitude and along the lower slope at  $1^{\circ}00'$  in latitude). This agrees with our hypothesis, because this imply that the source material along these scarps is still cohesive, poorly fractured and poorly drained by fluids.

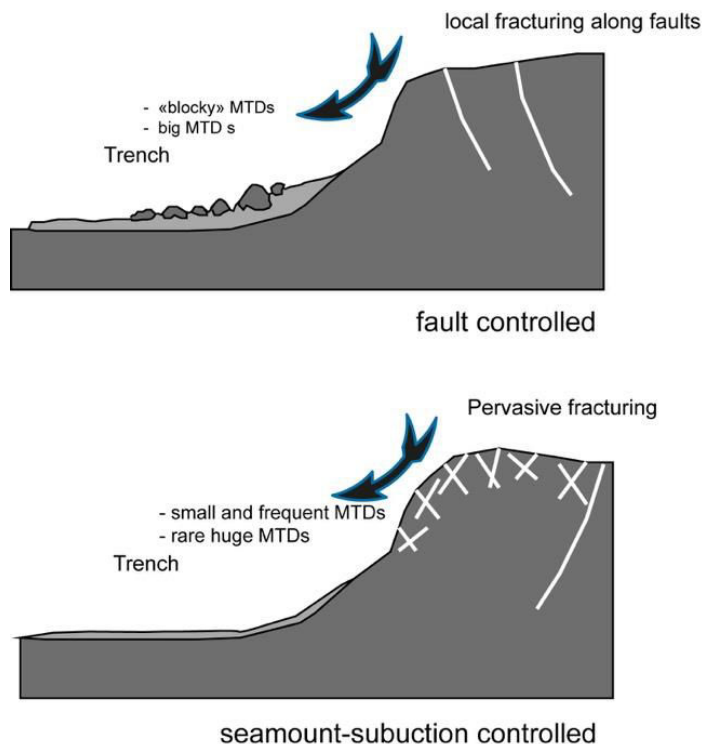


Fig. 6. 16 Conceptual cartoons of a cross section of submarine slope. Above fault control slope generating rock avalanche, cohesion less slump with deposits containing large blocks. Below seamount subduction controlled slope, with frequent thinner MTD or large huge slide.

Nevertheless, the larger mass wasting into the trench, is front of the domain 2, located north of the present impact of Atacames seamounts chain. This do not fit very well with our hypothesis defined above including thin and frequent mass wasting controlled by seamount subduction. Nevertheless, the morphology of the upper slope shows a large reentrant (Fig. 6.2) which could be correspond to the impact of an old large seamount. As for the Ruatoria giant avalanche in New Zealand (Collot et al., 2001; Lamarche et al., 2008) we proposed that this initial impact has weakened the slope, by pervasive fracturation and intense fluids circulations. Latter, the Atacames seamount chains subduction, beneath this pre-fractured area, probably facilitate this large mass wasting. This suggests that, the succession of seamounts subduction in the same segment of the slope is an important process to generate very large mass wasting.

As for the Chirp-MTDs, deep-seismic MTDs show several facies along the margin. One with the presence of blocks (Fig. 6.3bis) into the trench front of the domain 3; front of the domain 4 no blocks are identified but the deep-seismic MTDs are more chaotic than transparent, indicating that the reworked material has possibly conserved a cohesion from



the source material. These fallen blocks (Fig. 6.3) are stratified. Therefore, they consist of seismic sedimentary units, outcropping along the lower slope, more than from the acoustic basement. The strong sub-parallel reflectors (Fig. 6.11) into these fallen blocks are closer of those of the lower unit than the upper unit (Fig. 6.11). Indeed, the lower unit is probably more cohesive than the upper unit which is more recent and probably less compacted.

#### **6.5.4 Ages of MTs/MTDs and earthquake occurrence**

The proposals of ages for deposits U0 and U1/U2 at  $720 \pm 50$  yr BP and  $1250 \pm 160$  years BP respectively are compatible with mega-events of type 1906 (Mw8.8), but also with seismic supercycles of  $\sim 600$  years as proposed by Nocquet et al. (2016), who estimated it from the co-seismic slip deficit of the interplate contact accumulated since the 1906 earthquake. This recurrence has also been found in turbidite deposits at the outlet of the Esmeraldas canyon northward of the study area (Migeon et al., 2017). Nevertheless, the earthquake of 1906 did not initially give rise to a deposition of turbidites. However, because of the very low number of cores dating, and the impossibility of quantify the erosion at the base of the deposits, the ages of the events must be taken with great care. It should be noted, however, that this cyclicity is not found in older deposits.

In addition, there may be different sensitivity of the different terrains to co-seismic accelerations. Indeed, as previously proposed, depending on the state and the type of fracturing of the margin, as well as the slope gradient, the sedimentary cover is destabilized differently. Intuitively, we can assume that the most frequent destabilization would occur northward of the SB6-SB7 sub basins because the margin has undergone the passage of several seamounts, but it is actually fractured and shows the most important slope values. However, this observation seems to be not totally true since destabilization is not more frequent, and we do not find a priori traces of MT U0 and U1/U2.

#### **6.5.5 Hydrodynamic conditions for emplacement of megaturbidites**

Sedimentary analysis of megaturbidites shows a complex sequence that differs in part from that conventionally observed in the literature (Chapron et al., 1999, Beck et al., 2007, Polonia et al., 2017, San Pedro et al., 2017). Indeed, it is not possible to testify a “simple” implementation of a turbidity flow after decantation of the materials, but this necessarily implies several stages of implementation. At this stage of the study, we cannot propose a model that gathers all the observations, so we will present three hypotheses, with the arguments in favor, and the limits to the models.

##### **6.5.5.1 Triggering multiple sedimentary destabilizations ?**

Since the instrumental era, it has been shown that submarine or coastal earthquakes generate multiple and synchronous sedimentary destabilizations of the continental slope (Heezen and Ewing, 1952, Cattaneo et al., 2012). This characteristic also allows the regional use of these deposits for paleoseismic purposes as it was demonstrated in

subduction zones such as Cascades (Goldfinger et al., 2003), New Zealand (Pouderoux et al., 2014), Ecuador (Migeon et al., 2017), or areas with diffuse deformation (Gracia et al., 2010; Ratzov et al., 2015; Babonneau et al., 2017).

The first hypothesis to explain the presence of megaturbidites is thus the simultaneous triggering of multiple destabilizations. This hypothesis is supported by the observation of several turbiditic pulses, clearly visible at the base of megaturbidites in coarse fractions. These pulses, characterized by particle size variations, Magnetic Susceptibility, or chemical composition, would testify to deposits coming very close in time, and are characteristic of co-seismic deposits (Nakajima and Kanai, 2000, Migeon et al., 2017, Van Daele et al., 2017). The presence of an over-thickened clay fraction could in this case be due to the relatively confined morphology of the pit and the sub-basins present, which would thus prevent the dispersion of the turbidity current.

According to our interpretation (Fig. 6.17), the multipulse character would also be visible in the clay fraction of megaturbidites, through the amalgamated successions of the terms of the Stow sequence (Figs 6.6 and 6.7). The lamines that we interpreted would, in this case, be witnesses of an energy during the setting up. However, there are several limits to this model.

The main limit concerns the low sedimentation rate (settling) of the clay particles. Indeed, based on the Stokes law, and at an ambient temperature, the estimated fall velocity would be of the order of  $10^{-4}$  cm / s (Sutherland et al., 2015). Although laboratory measurements may show higher values in function of temperature, salinity, and clay concentration of the water, these values do not exceed  $10^{-2}$  cm / s (Sutherland et al., 2015), a few meters a day. This extremely slow speed potentially will involve several months for the clay fraction of a turbidity flow to settle: for example, two months after the Haiti's earthquake in 2010, the water column still showed a high turbidity over 600m above the bottom (McHugh et al., 2011).

Therefore, assuming several synchronous turbidity currents arriving slightly time-displaced in the trench (a few minutes to a few hours), it is difficult to conceive the recording of the pulses of the coarse fraction and then those of the clay fraction. Even if it is possible to record the silt-sandy fractions, due to a higher sedimentation rate, the clay fraction should be homogenized during the following months. Finally, the Ca/Ti curve of the clay fraction shows that there is no a punctual decay but homogeneous for the variations, which probably implies a lack of pulses in the fine fraction.

#### **6.5.5.2. Tsunami and / or Seiche effect?**

The preliminary age models show recurrences of megaturbidites of several thousands of years (this work and Ratzov et al., 2010) while the average frequency of turbidites in the south of the study area is about 73 years (Ratzov et al., 2010). According to previous proposals (Ratzov et al., 2010), the relative lack of occurrence of these deposits in the north could be the result of an extreme magnitude earthquake and its corresponding soil acceleration, or the result of a gradual weakening of the mechanical properties of the

sedimentary cover during several seismic cycles, which would lead to more voluminous destabilizations periodically (Ratzov et al., 2010). Moreover, as it is proposed in this work, the mechanical weakening can be directly related to the fracturing of the margin (seamounts, faults, fluids). Even if these hypotheses remain applicable, an alternative and compatible explanation could be the occurrence of a Tsunami as proposed before by many authors (Kastens and Cita, 1981, Cita et al., 1982, Polonia et al., 2017; San Pedro et al., 2017). Historically, only the 1906 earthquake generated a tsunami in the study area. Nowadays we do not have reliable dates to know if a particular repository is associated with this event.

In the case of a tsunami wave, the wavelength (up to several hundreds of km) is much greater than the thickness of the water body, the horizontal speed of displacement of the water particles is almost uniform over the entire water column contrary to "classical" waves of shorter wavelength. In particular, short-wave orbital velocities describe relatively flattened ellipses which decrease in amplitude with depth. In contrast, long waves describe very flattened ellipses, and more and more deeply: This results in a horizontal back and forth movement of the water column. For example, in the case of an initial wave of 1m the horizontal velocity of the particles at the bottom, at a trench's depth of ~ 3000 m as in our study case, would be of the order of 3cm / s (Mansour IOUALALEN Personal communication).

Based on Hjulstrom's empirical diagram, which shows the current velocities required for suspension, tensile transport, and deposition as a function of particle size, it seems that horizontal velocities induced by a tsunami allow the maintenance of transport of the fractions (<1mm) present in the megaturbidite by traction, but not the resuspension of the material already deposited on the bottom. This type of back-and-forth motion could also contribute to the creation of sedimentary lamines, and eventually of the "Multipulse" aspect of the deposit. However, this is a phenomenon different from the seiche effect conventionally used to explain certain deposits of homogenites with similar characteristics to those observed. This implies in fact a resuspension of the bottom sediment by the oscillation of the water column. In order to be effective this phenomenon requires a confined morphology and is particularly observed in mountain lake contexts (Siegenthaller et al., 1987, Chapron et al., 1999, Beck et al., 2009), or in practically enclosed seas like the Sea of Marmara (Beck et al., 2007). Although the trench is relatively confined, the height of the escarpments of the flexure faults from the dipping plate is probably insufficient to maintain a seiche effect.

Finally, in the case of a tsunami that would have flooded the coast and then retreated, a level containing littoral or continental elements may be found offshore in some cases, such as in the Calabrian subduction zone (Polonia et al. 2017). This level, called Tsunami Cap, was found by the authors on all of the cores taken from the Calabrais accretionary prism. A study based on the same subduction zone but on more distal sites identified the same co-seismic turbidites (SanPedro et al., 2017), but none was dominated by this characteristic level. The spatial expansion of this type of deposit is in fact variable. Currently we have not yet clearly identified such a deposit overlooking the Megaturbidite,

but further sedimentary analysis of the biostratigraphic association would provide more robust indications of the tsunami origin of megaturbidites.

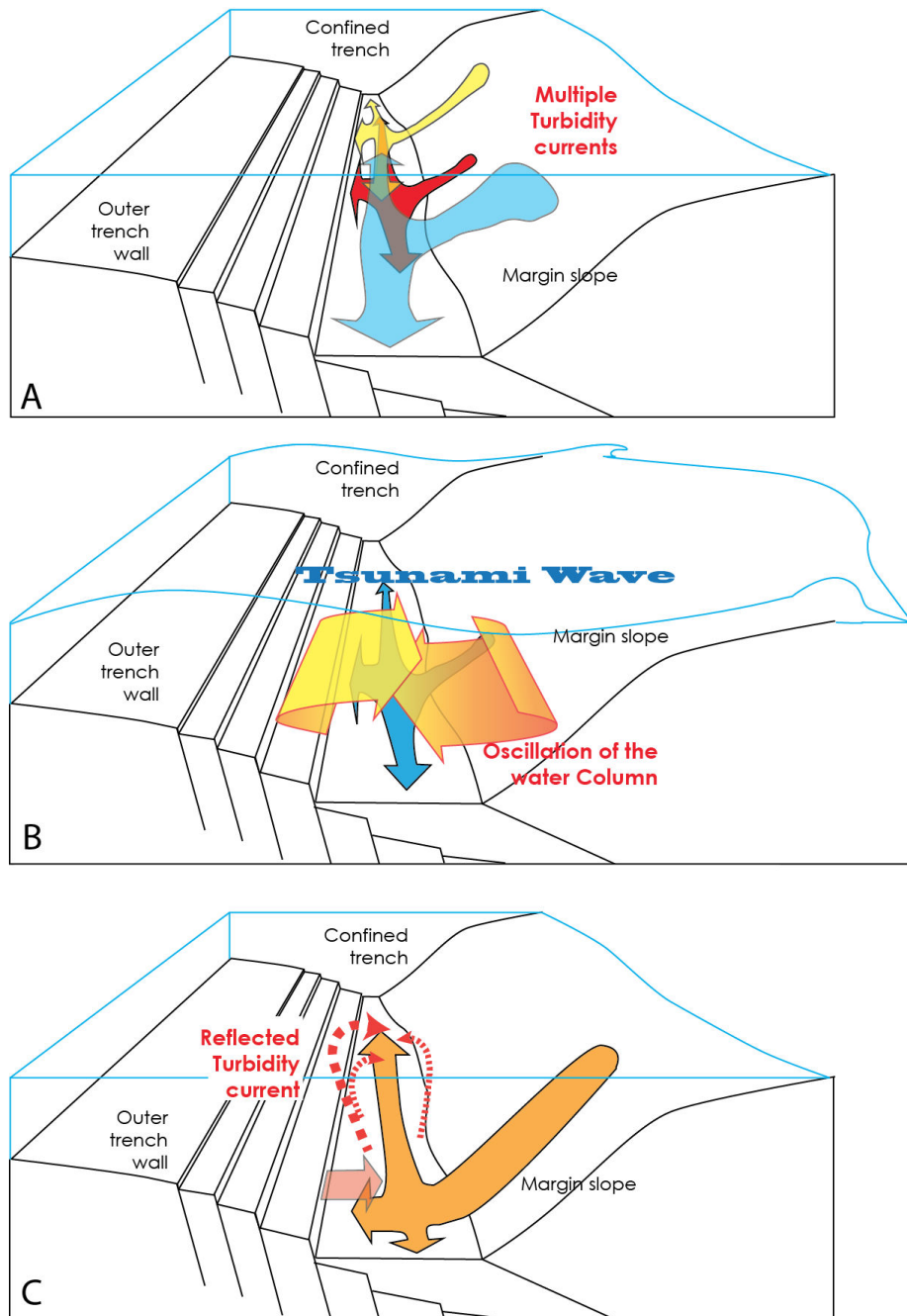


Fig. 6. 17 Models of hydrodynamic conditions for the settling of megaturbidites with amalgamated Stow sequences observed in a confined trench. A: Triggering multiple destabilizations. B: Oscillation of the water column following a tsunami, C: Reflection of turbidity currents along the escarpments and the slope.

### 6.5.5.3: Reflections of turbidity currents?

This hypothesis could involve the presence of a high-velocity turbidity current, which would have undergone several reflections along walls or escarpments of the trench. Such a phenomenon produces back-and-forth turbidity currents, manifested by a good segregation of the clay material, and currents patterns with opposite polarities (Pickering et al., 1985, Beck et al., 2007). In our case, the clay fraction is very well developed, and we can observe oblique laminations at the base of the Megaturbidites (Fig. 6.9B Kat22) which could testify alternating directions of transport. Despite escarpments of limited height on the outer trench, the presence of a counterslope (towards the trench) allows the currents to return, as demonstrated in the Nankai Trench (Pickering et al. 1992). This configuration would be particularly favorable in the case where there is a transport component along the axis of the trench; in this case, the current going up the outer trench would collapse and return towards the axis.

This scenario is possible in the study area due to the existence of a slope gradient northward and along the trench axis between sub-basins SB4 and SB1 (-3650 to -3925m), which could favor a lateral component of transport. Finally, this gradient of lateral slope could also favor the transportation of the finest fractions (the most "volatile") in the case of multiple destabilization triggers, and thus to explain the amalgamated character of the clay deposits, and the thickening of these units to the lower points of the SB2 basin (Fig. 6.17).

## 6.6 Conclusions

We observe however a wide variety of possibly earthquake triggered deposits. These include Slumps, blocs, Mass Transport Deposits, Megaturbidites, and Turbidites.

We propose that the distribution and the style of slope failure along the northern Ecuadorian margin is controlled principally by two tectonic process which both interact with the large earthquake occurrence. The northern segment of the Ecuadorian trench is clearly segmented in terms of slide and slump frequency and size. One process is driven by seamount subduction. In this case, the slope is affected by a pervasive fracturation and associated to fluids circulation. This weakens the slope as a whole and the collapse products are mainly characterized, on the one hand by numerous homogeneous, thin and local MTDs and on the other hand by rare but large collapse event which can buried entirely the trench. The other one is driven by regional fault which controls the linear geometry of the lower slope. In this case, the weakening of the slope is not pervasive but limited along the faults and the collapse products are characterized by thick non-homogenous MTDs including structured fallen blocks coming from the margin.

The dating of the MT and MTDs allow us to related the U0 to a possible great earthquake as U1/U2.

The Megaturbdites show a complex and amalgamate pattern observed both in the sandy/silty base, but also, more uncommonly in the overthickened and relatively

homogeneous mud tail. We discuss the specific hydrodynamic conditions observed in this confined trench that could account for the amalgamate pattern. These include A) multiple turbidity currents and a confined morphology preventing the dispersal of the fine-grained plume; B) Oscillation of the water column associated to a coseismic tsunami: the energy is apparently insufficient to resuspend seafloor deposits as proposed elsewhere, but sufficient to maintain an already initiated bedload transport; C) Multiple reflections of turbidity currents along the outer and inner trench walls.



## References

- Adams, J., 1990. Paleoseismicity of the Cascadia Subduction Zone - Evidence from Turbidites Off the Oregon-Washington Margin. *Tectonics*, 9(4): 569-583.
- Babonneau, N., Cattaneo, A., Ratzov, G., Déverchère, J., Yelles-Chaouche, A., Lateb, T., & Bachir, R. S. (2017). Turbidite chronostratigraphy off Algiers, central Algerian margin: A key for reconstructing Holocene paleo-earthquake cycles. *Marine Geology*, 384, 63-80.
- Beck, S. L., & Ruff, L. J. (1984). The rupture process of the great 1979 Colombia earthquake: Evidence for the asperity model. *Journal of Geophysical Research: Solid Earth*, 89(B11), 9281-9291.
- Beck C., Mercier de Lépinay, B., Schneider, J.-L., Cremer, M., Çağatay, N., Wendenbaum, E., Boutareaud, S., Ménot, G., Schmidt, S., Weber, O., Eris, K., Armijo, R., Meyer, B., Pondard, N., Gutscher, M.-A., and the MARMACORE Cruise Party, Turon, J.-L., Labeyrie, L., Cortijo, E., Gallet, Y., Bouquerel, H., Gorur, N., Gervais, A., Castera, M.-H., Londeix, L., de Ressaquièr, A., Jaouen, A. (2007). Late Quaternary co-seismic sedimentation in the Sea of Marmara's deep basins. *Sedimentary Geology*, 199, p. 65-89. doi:10.1016/j.sedgeo.2005.12.031.
- Beck, C. (2009). Late Quaternary lacustrine paleo-seismic archives in north-western Alps: Examples of earthquake-origin assessment of sedimentary disturbances. *Earth-Science Reviews*, 96(4), 327-344.
- Bouma, A.H., (1962). *Sedimentology of some flysch deposits: a graphic approach to facies interpretation*. Elsevier, Amsterdam.
- Cattaneo, A., Babonneau, N., Ratzov, G., Dan-Unterseh, G., Yelles, K., Bracène, R., & Déverchère, J. (2012). Searching for the seafloor signature of the 21 May 2003 Boumerdès earthquake offshore central Algeria. *Natural Hazards and Earth System Sciences*, 12(7), 2159-2172.
- Chapron, E., Beck, C., Pourchet, M., & Deconinck, J. F. (1999). 1822 earthquake-triggered homogenite in Lake Le Bourget (NW Alps). *Terra Nova*, 11(2-3), 86-92.
- Cita, M. B., Broglia, C., Malinverno, A., Spezzibottiani, G., Tomadin, L., & Violanti, D. (1982). Late Quaternary pelagic sedimentation on the southern Calabrian Ridge and western Mediterranean Ridge, eastern Mediterranean. *Marine Micropaleontology*, 7(2), 135-162.
- Cita, M. B., & Aloisi, G. (2000). Deep-sea tsunami deposits triggered by the explosion of Santorini (3500 y BP), eastern Mediterranean. *Sedimentary Geology*, 135(1-4), 181-203.

Coleman, J. M., & Prior, D. B. (1988). Mass wasting on continental margins. *Annual Review of Earth and Planetary Sciences*, 16(1), 101-119.

Collot, J. Y., Lewis, K., Lamarche, G., & Lallemand, S. (2001). The giant Ruatoria debris avalanche on the northern Hikurangi margin, New Zealand: Result of oblique seamount subduction. *Journal of Geophysical Research: Solid Earth*, 106(B9), 19271-19297.

Collot, J.-Y., Marcaillou, B., Sage, F., Michaud, F., Agudelo, W., Charvis, P., Graindorge, D., Gutscher, M.-A., Spence, G., (2004). Are rupture zone limits of great subduction earthquakes controlled by upper plate structures? Evidence from multichannel seismic reflection data acquired across the northern Ecuador-southwest Colombia margin. *Journal of Geophysical Research* 109.

Collot, J. Y., Michaud, F., Alvarado, A., Marcaillou, B., Sosson, M., Ratzov, G., ... & Pazmino, A. (2009). Visión general de la morfología submarina del margen convergente de Ecuador-Sur de Colombia: implicaciones sobre la transferencia de masa y la edad de la subducción de la Cordillera de Carnegie. *Geología y Geofísica Marina y Terrestre del Ecuador*. Publicacion CNDM-INOCAR-IRD, PSE001-09, Guayaquil, Ecuador, 47-74.

Dominguez, S., Lallemand, S. E., Malavieille, J., & von Huene, R. (1998). Upper plate deformation associated with seamount subduction. *Tectonophysics*, 293(3-4), 207-224.

Font, Y., Segovia, M., Vaca, S., Theunissen, T., (2013). Seismicity patterns along the Ecuadorian subduction zone: new constraints from earthquake location in a 3-D a priori velocity model. *Geophysical Journal International*, 193, p. 263-286. doi: 10.1093/gji/ggs083

Goldfinger, C., Nelson, C.H., Johnson, J.E., the Shipboard Scientific Party, (2003). Deep-water turbidites as Holocene earthquake proxies: the Cascadia subduction zone and Northern San Andreas Fault systems. *Annals of Geophysics* 46, 1169-1194.

Goldfinger, C., Grijalva, K., Burgmann, R., Morey, A.E., Johnson, J.E., Hans Nelson, C., Gutiérrez-Pastor, J., Ericsson, A., Karabanov, E., Chaytor, J.D., Patton, J.R., Gràcia, E., (2008). Late Holocene rupture of the Northern San Andreas Fault and possible stress linkage to the Cascadia Subduction Zone. *Bulletin of the Seismological Society of America* 98, 861-889.

Goldfinger, C., (2011). Submarine paleoseismology based on turbidite records. *Annual Review of Marine Science* 3, 36-66

Gorsline, D. S., De Diego, T., & Nava-Sanchez, E. H. (2000). Seismically triggered turbidites in small margin basins: Alfonso Basin, western Gulf of California and Santa Monica Basin, California borderland. *Sedimentary Geology*, 135(1-4), 21-35.

Gràcia, E., Vizcaino, A., Escutia, C., Asioli, A., Rodès, A., Pallàs, R., Garcia-Orellana, J., Lebreiro, S., Goldfinger, C., (2010). Holocene earthquake record offshore Portugal (SW

Iberia): testing turbidite paleoseismicity in a slow-convergence margin. *Quaternary Science Reviews* 29, 1156-1172.

Gutiérrez-Pastor, J., Nelson, C.H., Goldfinger, C., Escutia, C., (2013). Sedimentology of seismo-turbidites off the Cascadia and northern California active tectonic continental margins, northwest Pacific Ocean. *Marine Geology* 336, 99-119.

Harders, R., Ranero, C. R., Weinrebe, W., & Behrmann, J. H. (2011). Submarine slope failures along the convergent continental margin of the Middle America Trench. *Geochemistry, Geophysics, Geosystems*, 12(6).

Hieke, W. (2000). Transparent layers in seismic reflection records from the central Ionian Sea (Mediterranean)—evidence for repeated catastrophic turbidite sedimentation during the Quaternary. *Sedimentary Geology*, 135(1-4), 89-98.

Ioualalen, M., (2017). Personal communication

Kanamori, H., Given, J.W., (1981). Use of long-period surface waves for rapid determination of earthquake source parameters. *Physics of the Earth and Planetary Interiors* 27, 8-31.

Kastens, K. A., & Cita, M. B. (1981). Tsunami-induced sediment transport in the abyssal Mediterranean Sea. *Geological Society of America Bulletin*, 92(11), 845-857.

Kelleher, J., 1972. Rupture zones of large South American earthquakes and some predictions. *Journal of Geophysical Research* 77, 2087-2103.

Lamarche, G., Joanne, C., & Collot, J. Y. (2008). Successive, large mass-transport deposits in the south Kermadec fore-arc basin, New Zealand: The Matakaoa Submarine Instability Complex. *Geochemistry, Geophysics, Geosystems*, 9(4).

Lehu, R., Lallemand, S., Hsu, S. K., Babonneau, N., Ratzov, G., Lin, A. T., & Dezileau, L. (2015). Deep-sea sedimentation offshore eastern Taiwan: facies and processes characterization. *Marine Geology*, 369, 1-18.

Lehu, R., Lallemand, S., Ratzov, G., Babonneau, N., Hsu, S. K., Lin, A. T., & Dezileau, L. (2016). An attempt to reconstruct 2700 years of seismicity using deep-sea turbidites offshore eastern Taiwan. *Tectonophysics*, 692, 309-324.

Marcaillou, B., Collot, J. Y., Ribodetti, A., d'Acremont, E., Mahamat, A. A., & Alvarado, A. (2016). Seamount subduction at the North-Ecuadorian convergent margin: Effects on structures, inter-seismic coupling and seismogenesis. *Earth and Planetary Science Letters*, 433, 146-158.

McHugh, C. M., Seeber, L., Braudy, N., Cormier, M. H., Davis, M. B., Diebold, J. B., ... & Johnson III, H. E. (2011). Offshore sedimentary effects of the 12 January 2010 Haiti earthquake. *Geology*, 39(8), 723-726.

Michaud, F., Witt, C., & Royer, J. Y. (2009). Influence of the subduction of the Carnegie volcanic ridge on Ecuadorian geology: Reality and fiction. *Backbone of the Americas: Shallow Subduction, Plateau Uplift, and Ridge and Terrane Collision*, 204, 217.

Michaud F., Proust J.-N., Collot J.-Y., Lebrun J.-F., Witt C., Ratzov G., Pouderoux H., Martillo C., Hernández M.-J., Loayza G., Penafiel L., Schenini L., Dano A., Gonzalez M., Barba D. , De Min L., Ponce Adams G., Urresta A. et Calderon M., (2015) Quaternary sedimentation and active faulting along the Ecuadorian shelf: preliminary results of the ATACAMES Cruise (2012), *Marine Geophysical Research*, vol. 36, n°1, pp. 81-98.

Michaud, F., Proust, J. N., Dano, A., Collot, J. Y., Guiyeligou, G. D., Salazar, M. J. H., ... & Lebrun, J. F. (2016). Flare-Shaped Acoustic Anomalies in the Water Column Along the Ecuadorian Margin: Relationship with Active Tectonics and Gas Hydrates. *Pure and Applied Geophysics*, 173(10-11), 3291-3303.

Middleton, G.V. and Hampton, M.A., (1973). Sediment gravity flows: mechanics of flow and deposition. In: G.V. Middleton and A.H. Bouma (Editors), *Turbidite and deep water sedimentation - Pacific section*. Tulsa pp. 1-38.

Migeon, S., Savoye, B., Faugères, J.-C., (2000). Quaternary development of migrating sediment waves in the Var deep-sea fan: distribution, growth pattern, and implication for levee evolution. *Sediment. Geol.* 133, 265–293.

Migeon, S., Garibaldi, C., Ratzov, G., Schmidt, S., Collot, J. Y., Zaragosi, S., & Texier, L. (2017). Earthquake-triggered deposits in the subduction trench of the north Ecuador/south Colombia margin and their implication for paleoseismology. *Marine Geology*, 384, 47-62.

Moernaut, J., Van Daele, M., Strasser, M., Clare, M.A., Heirman, K., Viel, M., Cardenas, J., Kilian, R., Ladrón de Guevara, B., Pino, M., Urrutia, R., De Batist, M., (2015). Lacustrine turbidites produced by surficial slope sediment remobilization: a mechanism for continuous and sensitive turbidite paleoseismic records. *Marine Geology*. Doi: 10.1016/j.margeo.2015.10.009

Moernaut, J., De Batist, M., Charlet, F., Heirman, K., Chapron, E., Pino, M., ... & Urrutia, R. (2007). Giant earthquakes in South-Central Chile revealed by Holocene mass-wasting events in Lake Puyehue. *Sedimentary Geology*, 195(3-4), 239-256.

Mutti, E., Lucchi, F. R., Seguret, M., & Zanzucchi, G. (1984). Seismoturbidites: a new group of resedimented deposits. *Marine Geology*, 55(1-2), 103-116.

Nakajima, T., & Kanai, Y. (2000). Sedimentary features of seismoturbidites triggered by the 1983 and older historical earthquakes in the eastern margin of the Japan Sea. *Sedimentary Geology*, 135(1-4), 1-19.

Nocquet, J.-M., Villegas-Lanza, J.-C., Chlieh, M., Mothes, P.A., Rolandone, F., Jarrin, P., Cisneros, D., Alvarado, A., Audin, L., Bondoux, F., Martin, X., Font, Y., Regnier, M., Vallée, M., Tran, T., Beauval, C., Maguina Mendoza, J.M., Martinez, W., Tavera, H., Yepes, H., (2014). Motion of continental slivers and creeping subduction in the northern Andes. *Nature Geoscience* 7, 287-291.

Nocquet, J. M., Jarrin, P., Vallée, M., Mothes, P. A., Grandin, R., Rolandone, F., ... & Régnier, M. (2016). Supercycle at the Ecuadorian subduction zone revealed after the 2016 Pedernales earthquake. *Nature Geoscience*, 10(2), 145-149.

Owen M., Day S., Maslin M., 2007, Late Pleistocene submarine mass movements: occurrence and causes *Quaternary Science Reviews* 26 (2007) 958–978

Patton, J. R., Goldfinger, C., Morey, A. E., Ikehara, K., Romsos, C., Stoner, J., ... & Vizcaino, A. (2015). A 6600-year earthquake history in the region of the 2004 Sumatra-Andaman subduction zone earthquake. *Geosphere*, 11(6), 2067-2129.

Pickering, K. T., & Hiscott, R. N. (1985). Contained (reflected) turbidity currents from the Middle Ordovician Cloridorme Formation, Quebec, Canada: an alternative to the antidune hypothesis. *Sedimentology*, 32(3), 373-394.

Pickering, K. T., Underwood, M. B., & Taira, A. (1992). Open-ocean to trench turbidity-current flow in the Nankai Trough: Flow collapse and reflection. *Geology*, 20(12), 1099-1102.

Piper, D. J., & Normark, W. R. (2009). Processes that initiate turbidity currents and their influence on turbidites: a marine geology perspective. *Journal of Sedimentary Research*, 79(6), 347-362.

Polonia, A., Panieri, G., Gasperini, L., Gasparotto, G., Bellucci, L.G., Torelli, L., (2013). Turbidite paleoseismology in the Calabrian Arc Subduction Complex (Ionian Sea). *Geochemistry, Geophysics, Geosystems* 14, 112-140.

Polonia, A., Nelson, C. H., Romano, S., Vaiani, S. C., Colizza, E., Gasparotto, G., & Gasperini, L. (2017). A depositional model for seismo-turbidites in confined basins based on Ionian Sea deposits. *Marine Geology*, 384, 177-198.

Pouderoux, H., Proust, J.-N., Lamarche, G., (2014). Submarine paleoseismology of the northern Hikurangi subduction margin of New Zealand as deduced from turbidite record since 800 ka. *Quaternary Science Reviews* 84, 116-131.

Praet, N., Moernaut, J., Van Daele, M., Boes, E., Haeussler, P. J., Strupler, M., ... & De Batist, M. (2017). Paleoseismic potential of sublacustrine landslide records in a high-seismicity setting (south-central Alaska). *Marine Geology*, 384, 103-119.

Ranero, C. R., Grevemeyer, I., Sahling, H., Barckhausen, U., Hensen, C., Wallmann, K., ... & McIntosh, K. (2008). Hydrogeological system of erosional convergent margins and its influence on tectonics and interplate seismogenesis. *Geochemistry, Geophysics, Geosystems*, 9(3).

Ratzov, G., Cattaneo, A., Babonneau, N., Déverchère, J., Yelles, K., Bracène, R., Courboulès, F., (2015). Holocene turbidites record earthquake supercycles at a slow-rate plate boundary. *Geology* 43, 331-334.

Ratzov, G., Sosson, M., Collot, J.-Y., Migeon, S., (2012). Late Quaternary geomorphologic evolution of submarine canyons as a marker of active deformation on convergent margins: the example of the south Colombian margin. *Marine Geology* 315-318, 77-97.

Ratzov, G., Collot, J. Y., Sosson, M., & Migeon, S. (2010). Mass-transport deposits in the northern Ecuador subduction trench: Result of frontal erosion over multiple seismic cycles. *Earth and Planetary Science Letters*, 296(1), 89-102.

Reyes P. et Michaud F., (2012) Mapa Geologica de la margen costera ecuatoriana (1:500000), *EPPetroEcuador-IRD (Eds)*, Quito, Ecuador, 2012.

Rothwell, R. G., Reeder, M. S., Anastasakis, G., Stow, D. A. V., Thomson, J., & Kähler, G. (2000). Low sea-level stand emplacement of megaturbidites in the western and eastern Mediterranean Sea. *Sedimentary Geology*, 135(1-4), 75-88.

San Pedro, L., Babonneau, N., Gutscher, M. A., & Cattaneo, A. (2017). Origin and chronology of the Augias deposit in the Ionian sea (central Mediterranean sea), based on new regional sedimentological data. *Marine Geology*, 384, 199-213.

Shanmugam, G., Lehtonen, L.R., Straume, T., Syvertsen, S.E., Hodgkinson, R.J. and Skibeli, M., (1994). Slump and Debris-Flow Dominated Upper Slope Facies in the Cretaceous of the Norwegian and Northern North Seas (61-67-Degrees-N) - Implications for Sand Distribution. *Aapg Bulletin-American Association of Petroleum Geologists*, 78(6): 910-937.

Siegenthaller, C., Finger, W., Kelts, K., & Sumin, W. (1987). Earthquake and seiche deposits in Lake Lucerne, Switzerland. *Eclogae Geologicae Helvetiae*, 80(1), 241-260.

Stow, D. A., & Shanmugam, G. (1980). Sequence of structures in fine-grained turbidites: comparison of recent deep-sea and ancient flysch sediments. *Sedimentary Geology*, 25(1-2), 23-42.



Strasser, M., Anselmetti, F. S., Fäh, D., Giardini, D., & Schnellmann, M. (2006). Magnitudes and source areas of large prehistoric northern Alpine earthquakes revealed by slope failures in lakes. *Geology*, 34(12), 1005-1008.

Sultan, N., Cochonat, P., Canals, M., Cattaneo, A., Dennielou, B., Hafliðason, H., ... & Urgeles, R. (2004). Triggering mechanisms of slope instability processes and sediment failures on continental margins: a geotechnical approach. *Marine Geology*, 213(1), 291-321.

Sultan, N, Riboulot, V., Ker, S., Marsset, B., Géli, L., Tary, J.B., Klingelhoefer, F., Voisset, M., Lanfumey, V., Colliat, J.L., Adamy, J., Grimaud, S. (2011). Dynamics of fault–fluid–hydrate system around a shale-cored anticline in deepwater Nigeria *Journal of Geophysical Research*, 116 (2011) (B12110)

Sumner, E. J., Siti, M. I., McNeill, L. C., Talling, P. J., Henstock, T. J., Wynn, R. B., ... & Permana, H. (2013). Can turbidites be used to reconstruct a paleo earthquake record for the central Sumatran margin?. *Geology*, 41(7), 763-766.

Sutherland, B. R., Barrett, K. J., & Gingras, M. K. (2015). Clay settling in fresh and salt water. *Environmental Fluid Mechanics*, 15(1), 147-160.

Swenson, J.L., Beck, S.L., 1996. Historical 1942 Ecuador and 1942 Peru subduction earthquakes, and earthquake cycles along Colombia-Ecuador and Peru subduction segments. *Pure and applied geophysics*. 146, 67-101.

Talling, P. J., Masson, D. G., Sumner, E. J., & Malgesini, G. (2012). Subaqueous sediment density flows: Depositional processes and deposit types. *Sedimentology*, 59(7), 1937-2003.

Vallee, M., Nocquet, J. M., Battaglia, J., Font, Y., Segovia, M., Regnier, M., ... & Yepes, H. (2013). Intense interface seismicity triggered by a shallow slow slip event in the Central Ecuador subduction zone. *Journal of Geophysical Research: Solid Earth*, 118(6), 2965-2981.

Van Daele, M., Meyer, I., Moernaut, J., De Decker, S., Verschuren, D., & De Batist, M. (2017). A revised classification and terminology for stacked and amalgamated turbidites in environments dominated by (hemi) pelagic sedimentation. *Sedimentary Geology*, 357, 72-82.

Waldmann, N., Anselmetti, F.S., Ariztegui, D., Austin, J.A., Pirouz, M., Moy, C.M., Dunbar, R., (2011). Holocene mass-wasting events in Lago Fagnano, Tierra del Fuego (54°S): implications for paleoseismicity of the Magallanes-fagnano transform fault. *Basin Research* 23, 171-190.

# Chapter 7

## General conclusions

This work was strongly based on the analysis of a new dataset of multibeam bathymetry, high-resolution seismic reflection, sediment echo-sounder, and sedimentary cores, collected during the ATACAMES scientific cruise along the Ecuadorian margin. In this study, analysis of all the seismic data were complemented by the use of oil seismic data recorded every 4 kilometers along the trench (data owned by the “Secretaría de Hidrocarburos del Ecuador” and accessible through an agreement between this institution and IRD).

This study was focused on the analysis of the sedimentary filling of the subduction trench in relation with the gravitational processes along the Ecuadorian margin. The aim was to characterize the deformation of the margin in the short term (several seismic cycles) and in the middle term (Quaternary scale). This study confirms that the margin of Ecuador, which extends only 600 km long, is a strongly segmented margin considered from the morphological point of view (arrival of the Carnegie ridge), and the source and quantity of the sediment supply, rather than from the point of view of the great earthquakes recorded in the sedimentary deposits of the trench. This study illustrates that the sediments of the subduction trench are excellent recorders of the deformation of the active margins.

This study allowed us:

To specify the nature and distribution of the sediments of the sedimentary filling of the trench. The study of regional morphology and trench infilling (through petroleum profiles) allowed us to identify three segments: a northern segment and a southern segment characterized by a continental slope with numerous morphological markers of destabilization and a consequent sedimentary filling in the trench. A central segment with a smooth slope, full of gullies but with few major destabilizations and a very small sedimentary infilling in the trench, and sometimes absent. In a second step, the study of the sedimentary cores combined with the interpretation of the Chirp profiles revealed in the trench the presence, since the last glacial maximum, of various sedimentary deposits (turbidites, hemipelagites, volcanoclastic deposits, homogenites, slumps and debris flow). Hemipelagites, turbidites and homogenites are present in all segments. The turbidites are coarser and sandy with a higher frequency in the central segment. The mass transport deposits are located mainly in the north and south segments, while the volcano-clastic deposits are mainly present in the central segment. The distribution of these sedimentary facies along the trench is related to the subduction of the Carnegie Ridge which controls the individualization of the three segments, as well as the nature and lateral distribution of the sediments along the trench. Due to shallower deposition conditions, the central segment facing the Carnegie Ridge, mainly consists of sandy and silty turbidites in a proportion of 2:1 compared to other segments. Its position relative to the volcanoes of the (nearer) volcanic arc could explain the concentration of volcanoclastic deposits. The southern and northern segments, affected by the subduction of isolated seamounts, show more debris flows and mass transport deposits.

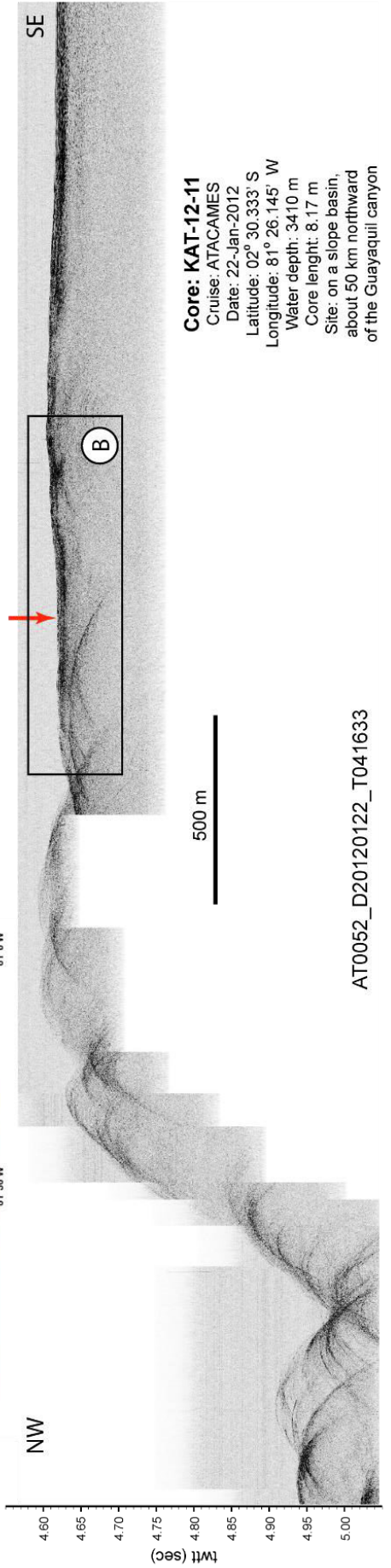
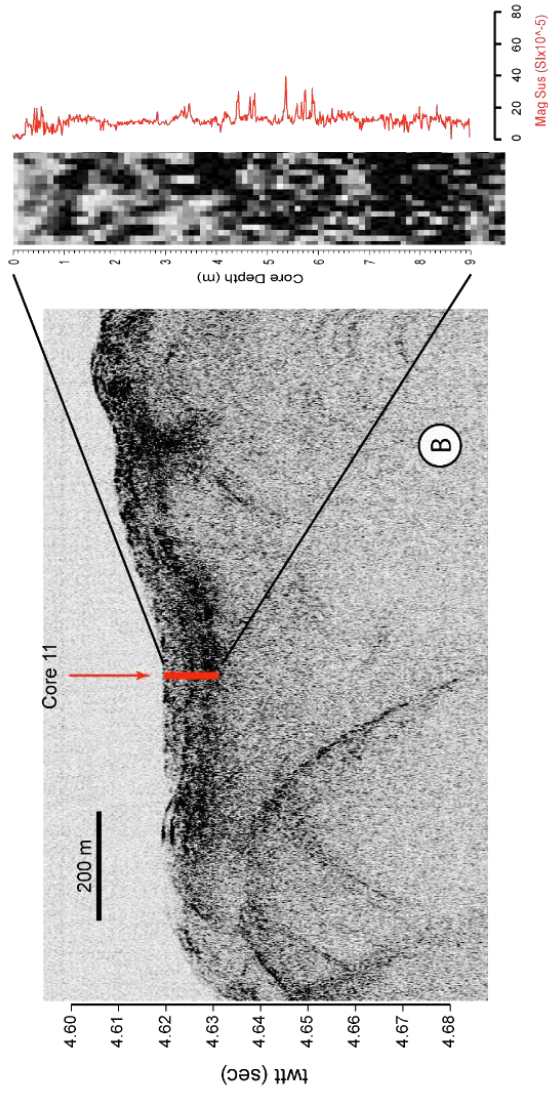
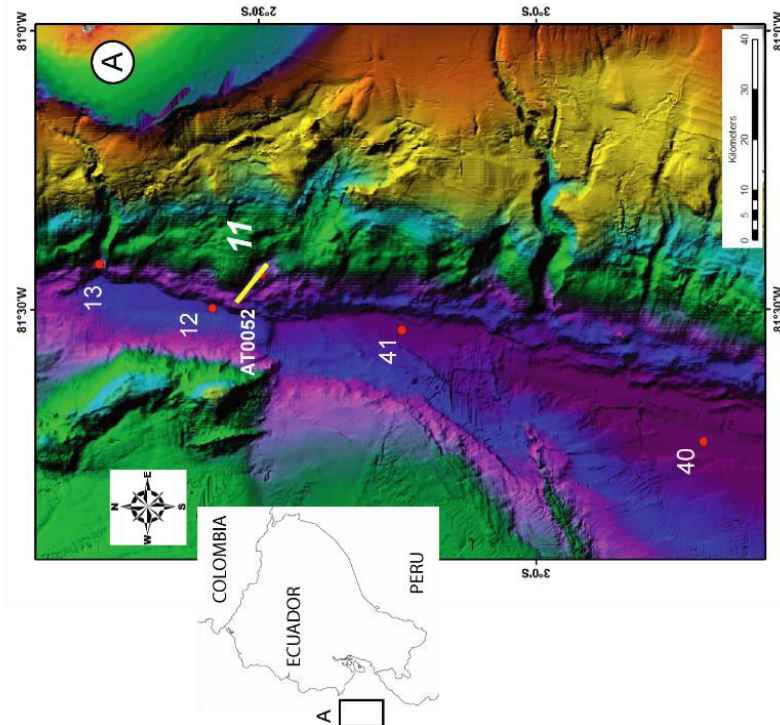
To show the importance of the destabilization of the slope for sedimentation in the trench. A detailed reconstruction of the emplacement and chronology of the destabilization of the margin and associated massive gravitational landslides was carried out in a sector of successive subduction of seamounts. We have specified the role of the impact of seamount subduction on the sedimentation of the margin by studying the formation, the evolution and the filling of the Ayampe basin, a deep reentrant created 1.45 Ma. ago which is characterized by a flexing of the continental slope accompanied by normal faults and gravitational tectonic initiated by separation levels. In this area, the sequence of gravitational events has been identified, reconstructed and dated. It consists of mass deposits, debris flows, megaturbidites and turbidites correlated with the successive subduction of four seamounts that locally accentuate frontal erosion. This study provided a better understanding of the dynamics of frontal erosion and discussed the relationships between deformation mechanisms and sedimentation along active subduction margins. The analysis of the landslides and their age-dating shows a quasi-permanent destabilization of the whole slope in connection with the compression at the front of the margin.

In the northern sector of the trench we firstly specify the modalities of mass sediment transfers. The analysis of the oil seismic profiles together with a detailed analysis of the morphology allowed us to determine the distribution, the source of the slided masses and their relationship with the level of deformation of the margin. The analysis of the petroleum profiles reveals that the rocks forming the major escarpments, which feed the largest mass-slides, did not undergo the same sequence of deformation. In the South the subduction of the seamounts fractured "pervasively" over a large area and a great thickness of the rocks. This diffuse fracturing of the rocks, during the passage of a seamount in subduction, associated with an intense circulation of fluids, will strongly weaken the rocks over a large surface and a great thickness. In the north, the escarpments are, on the contrary, controlled by faults and thus the fracturing and embrittlement of the rocks appear limited, in the space, to the fault's areas. Between the faults, the original structure of the deposits is conserved, suggesting that, in the absent of faulting, the rocks would keep their structures, coherence and even would be less fragile. The few landslides highlighted in the northern sector, higher up the slope, did not reach the trench but stopped at mid-slope, probably reflecting a fairly cohesive nature of the materials involved, with few fluids, and therefore a short run on the slope. Similarly, in the North of the segment the MTDs are large and few in numbers, and one of them shows kilometric size blocks. In the South the MTDs are more frequent and less bulky. Thus, in our study, we observed a very sharp segmentation along this margin segment of both escarpments, the deformation of the rocks along them and the signature in the trench of the resulting landslides. The lower continental slope is the main source of MTDs. Subduction of seamounts and regional faulting are undoubtedly the main factors of the pre-conditioning slope instability. These two tectonic contexts probably respond differently to earthquake occurrences and may explain the heterogeneity of the sedimentary records in this trench segment.

In the northern sector of the trench we have in a second time search the presence of possible paleo-seismological indicators where large historical earthquakes were recorded. At the rupture zones of 1942 and 2016, no major river supplies sediment to the slope and trench so that the continental slope may not be sufficiently recharged in sediment between two earthquakes, resulting in an incomplete paleo seismic archive. The analysis of Chirp and sedimentary cores allowed us to identify 13 MTDs and/or megaturbidites that are distributed in four spatially disconnected series. A preliminary sedimentation rate model based on radiocarbon core dating permit us to propose new MTD/megaturbidite correlations along the northern segment of the margin; in particular U0, U1 and U2 could be related to the recurrence of large earthquakes ranging 600-700 years proposed by Migeon et al., 2017. Additional dates are needed to confirm this sequence. Finally, the sedimentary analysis of megaturbidites shows a complex sequence that involves several stages of implementation. In this work three hypotheses are presented (triggering multiple sedimentary destabilizations, tsunamis and/or Seiche effect) without being able to propose a model that integrates all observations.

Annexe 1: Core sites

Core 11

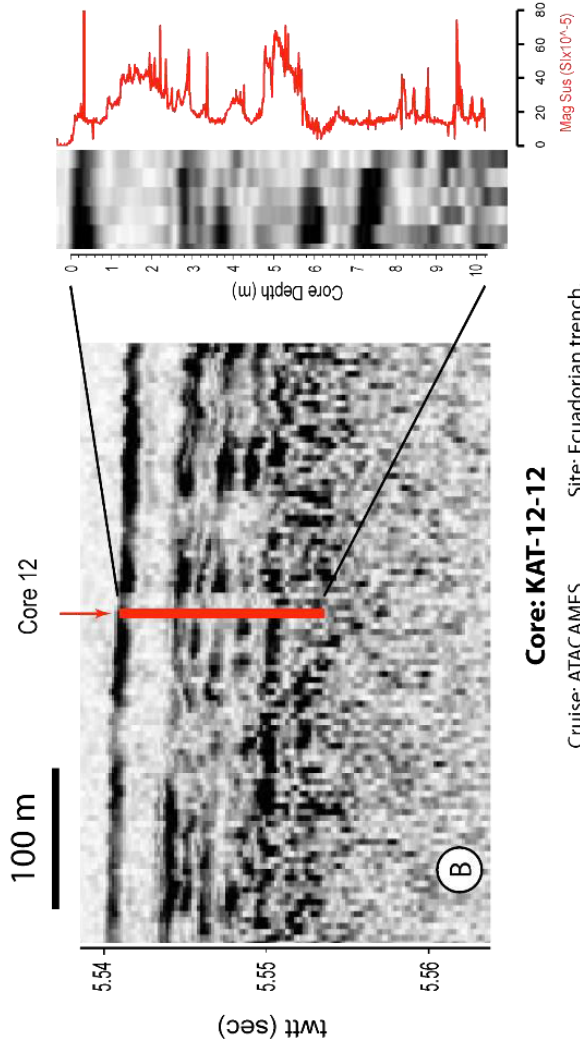
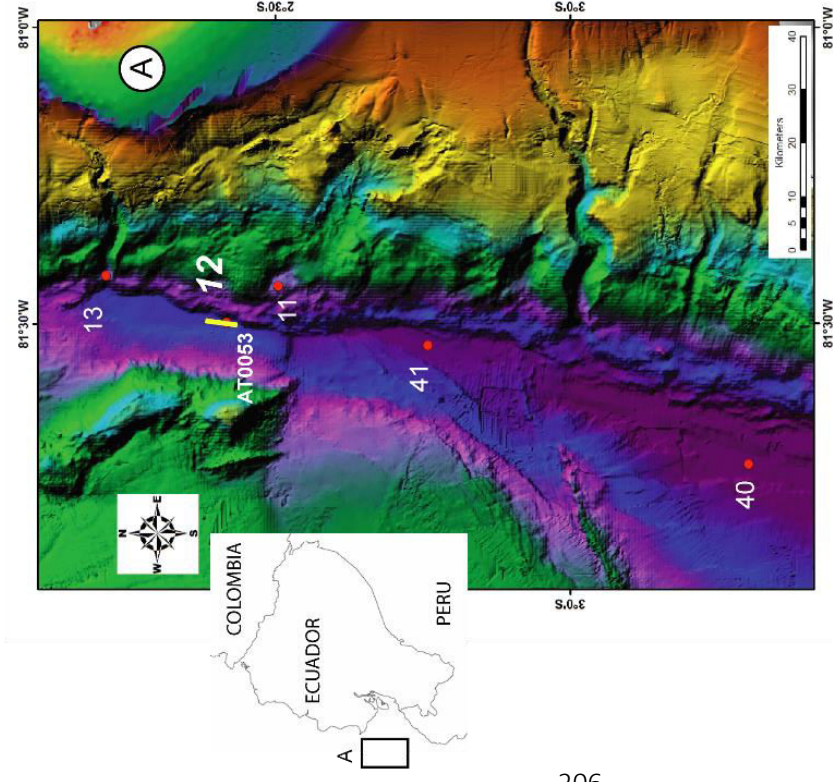


**Core: KAT-12-11**  
 Cruise: ATACAMES  
 Date: 22-Jan-2012  
 Latitude: 02° 30.333' S  
 Longitude: 81° 26.145' W  
 Water depth: 3410 m  
 Core length: 8.17 m  
 Site: on a slope basin,  
 about 50 km northward  
 of the Guayaquil canyon

AT0052\_D20120122\_T041633



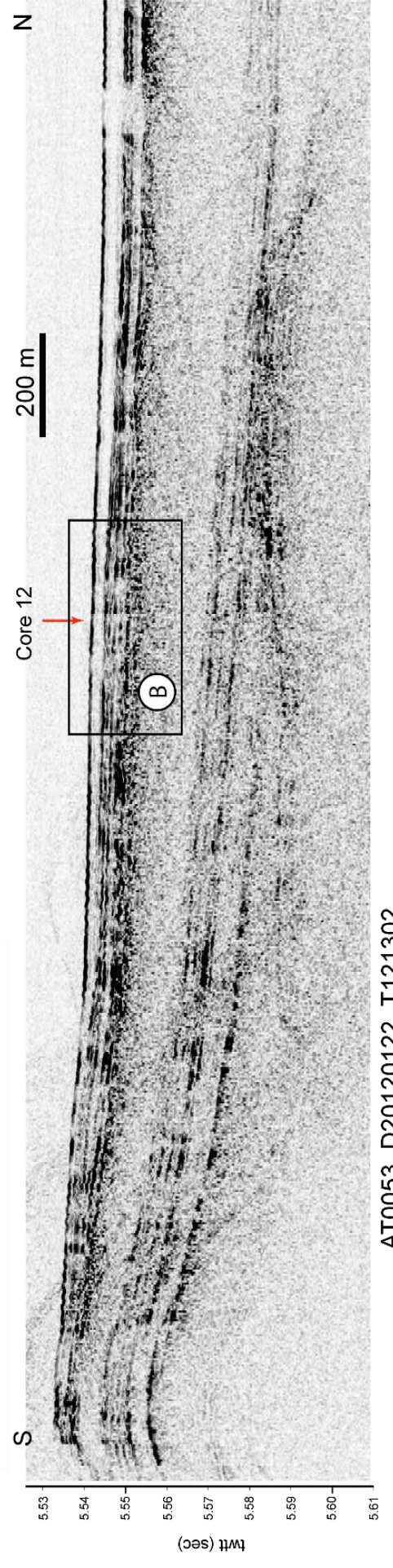
Core 12



**Core: KAT-12-12**

Cruise: ATACAMES  
 Date: 22-Jan-2012  
 Latitude: 02° 25.074' S  
 Longitude: 81° 29.852' W  
 Water depth: 4104 m  
 Core length: 10 m

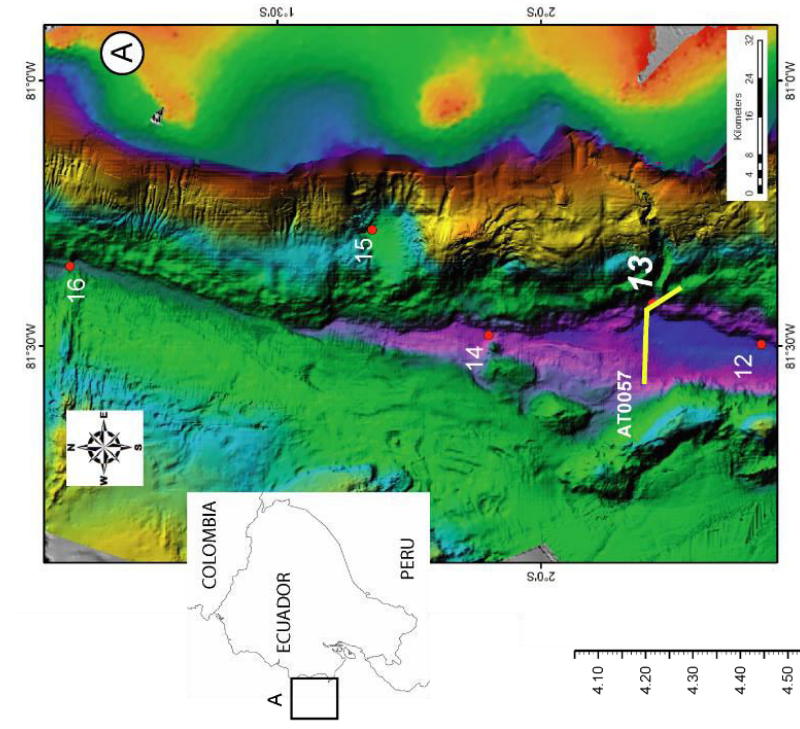
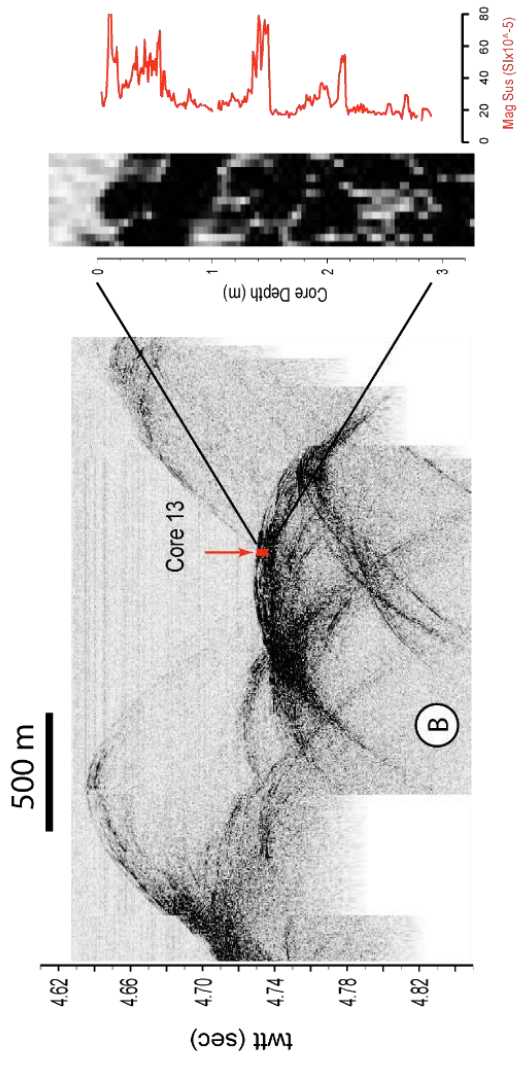
Site: Ecuadorian trench,  
 about 20 km south of the  
 Santa Elena canyon, left side of  
 the Salinas seamounts



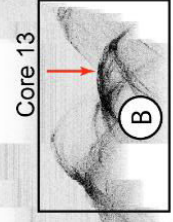
AT0053\_D20120122\_T121302



Core 13



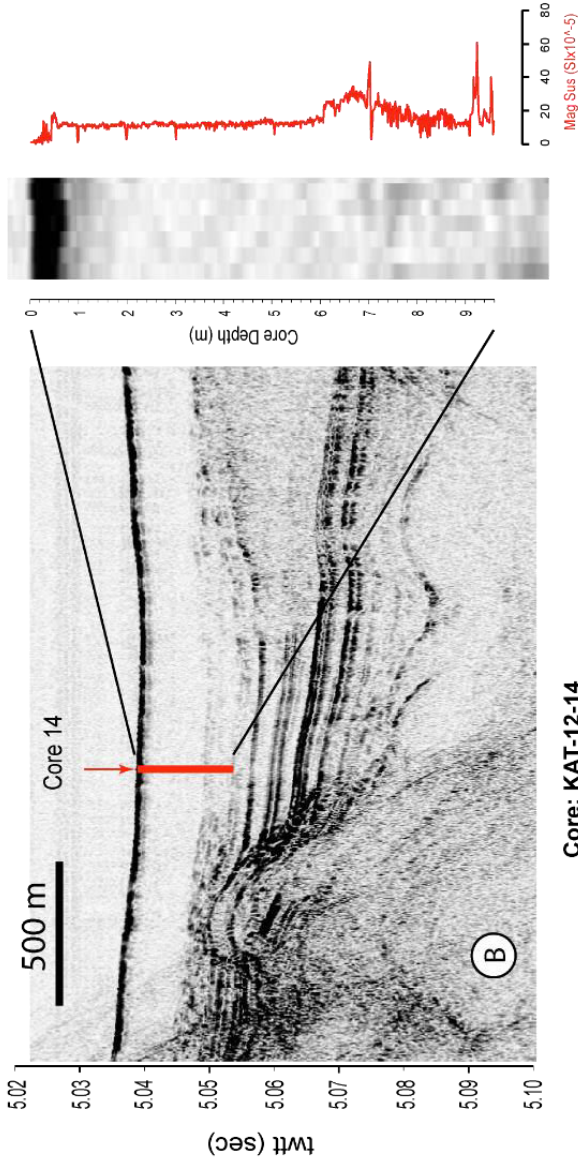
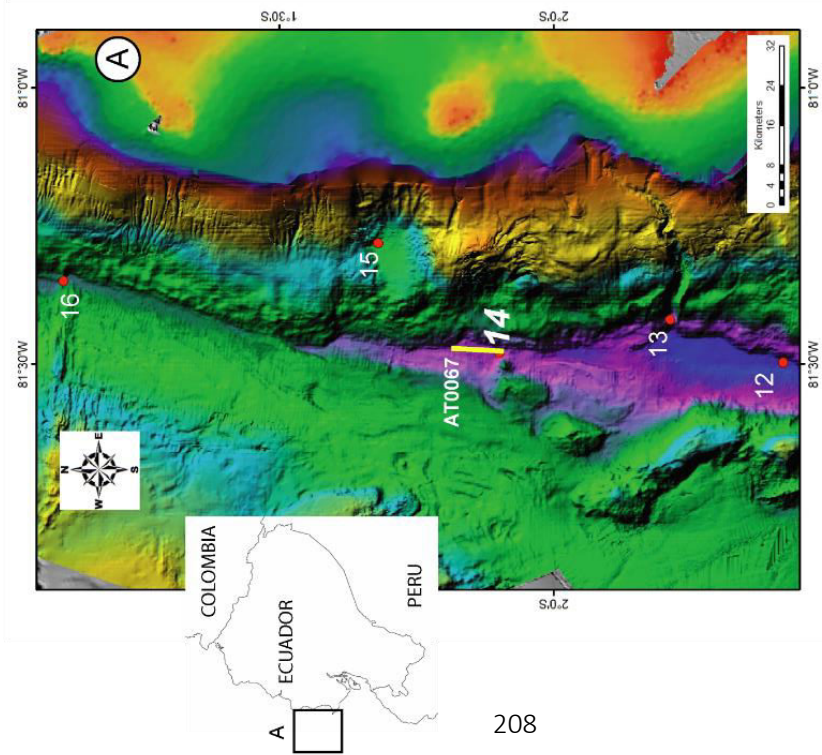
**Core: KAT-12-13**  
 Cruise: ATACAMES  
 Date: 23-Jan-2012  
 Latitude: 12° 12.776' Svw  
 Longitude: 81° 25.138' W  
 Water depth: 3475 m  
 Core length: 2.92 m  
 Site: Ecuadorian trench, on the river mouth of the Santa Elena canyon



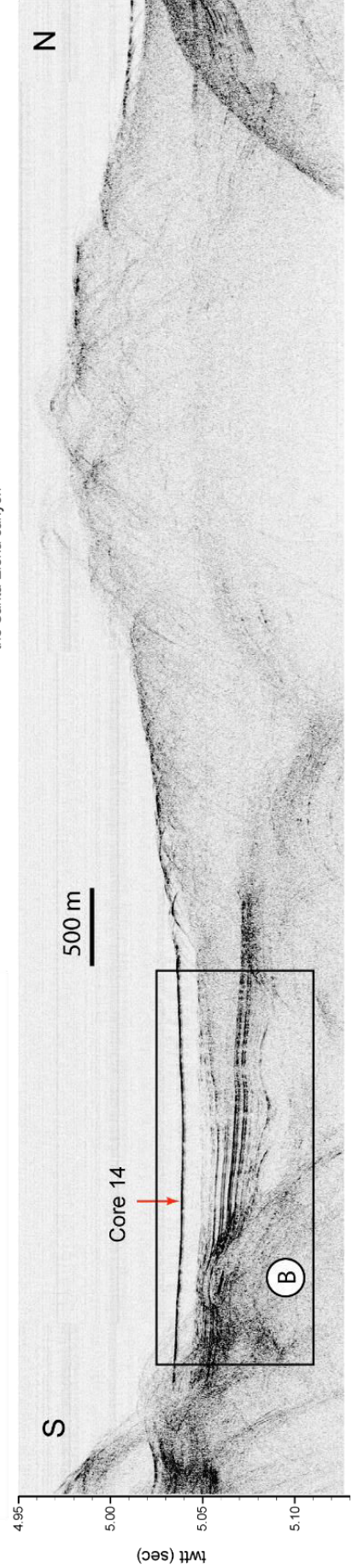
2 km

AT0057\_D20120122\_T203557

Core 14



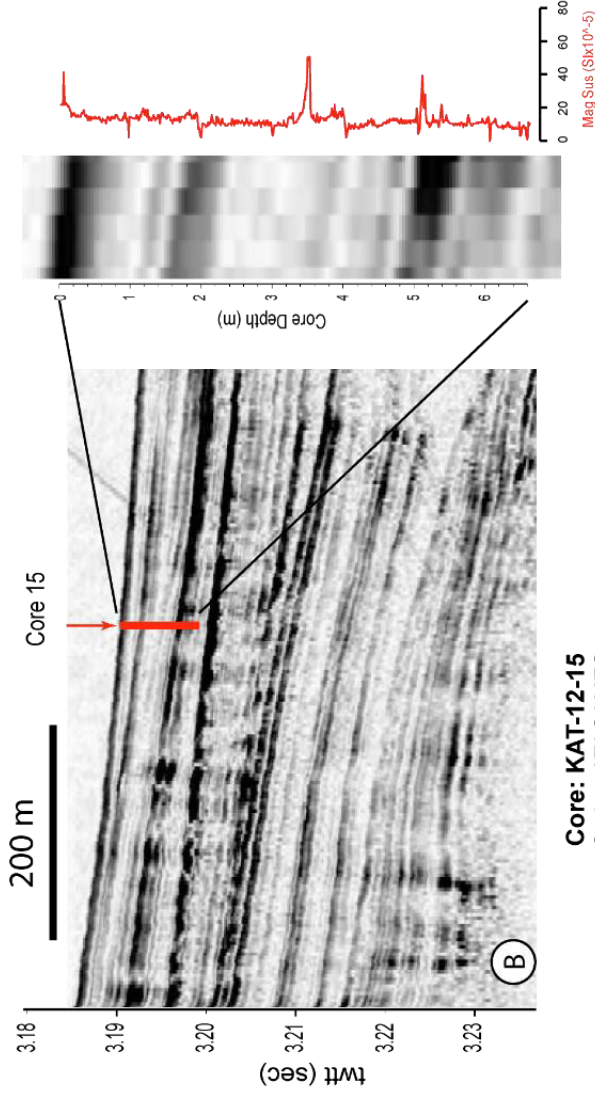
**Core: KAT-12-14**  
 Cruise: ATACAMES  
 Date: 23-Jan-2012  
 Latitude: 01° 54.048' S  
 Longitude: 81° 28.814' W  
 Water depth: 3709 m  
 Core length: 9.47 m  
 Site: Ecuadorian trench,  
 about 35 km northward of  
 the Santa Elena canyon



AT0064\_D20120123\_T200501



Core 15



**Core: KAT-12-15**

Cruise: ATACAMES

Date: 23-Jan-2012

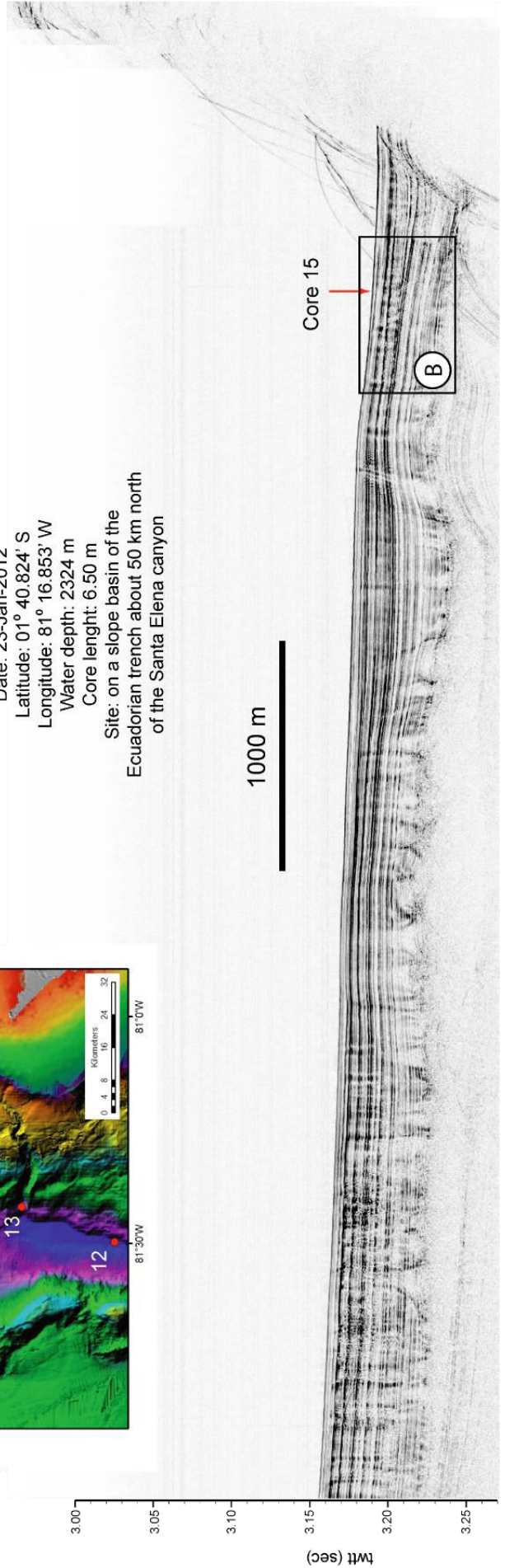
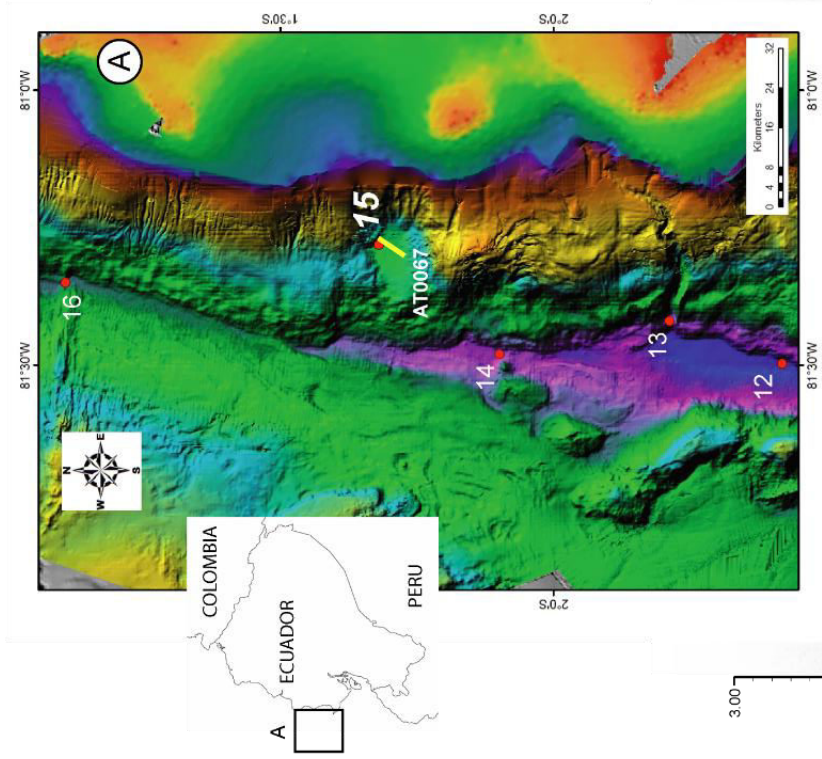
Latitude: 01° 40.824' S

Longitude: 81° 16.853' W

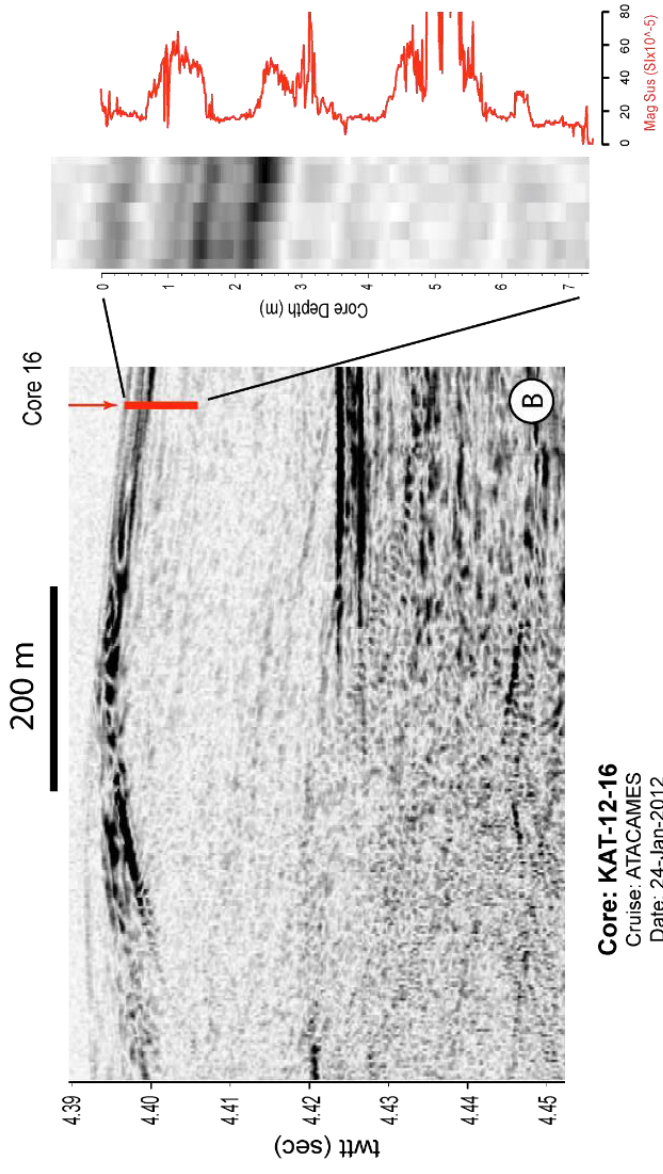
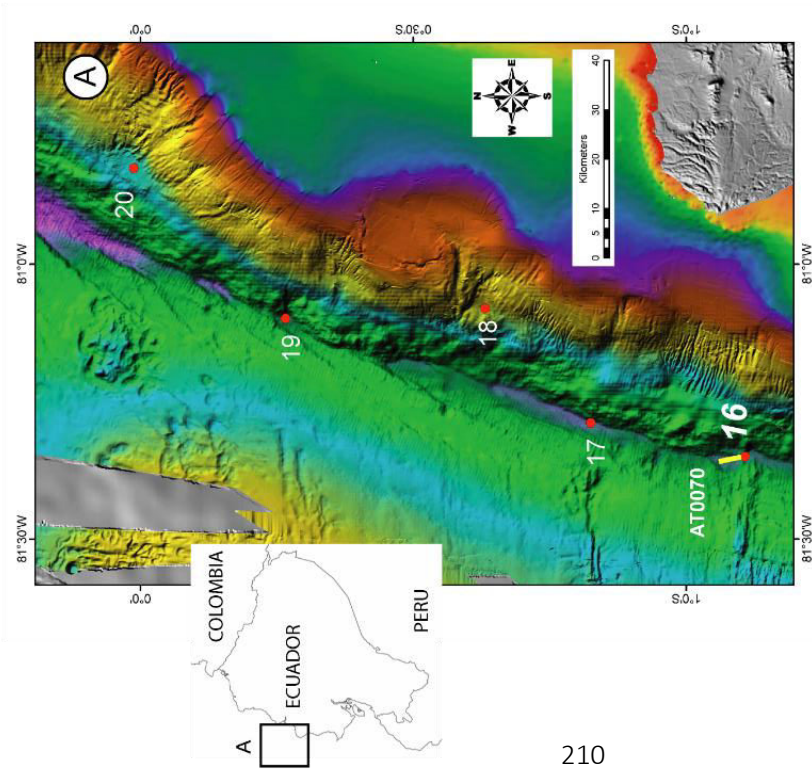
Water depth: 2324 m

Core length: 6.50 m

Site: on a slope basin of the Ecuadorian trench about 50 km north of the Santa Elena canyon

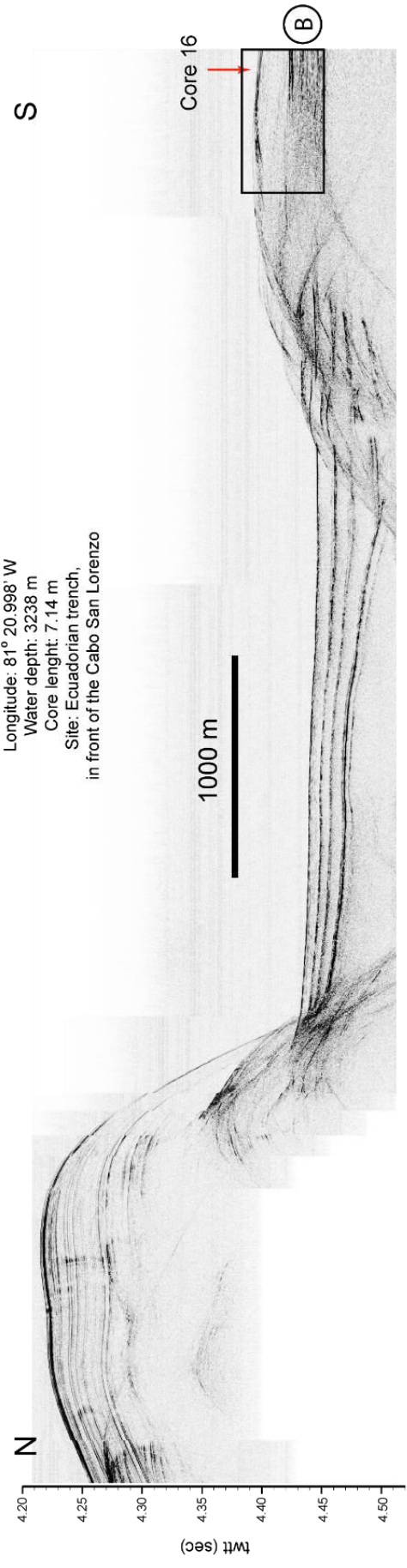


Core 16



**Core: KAT-12-16**

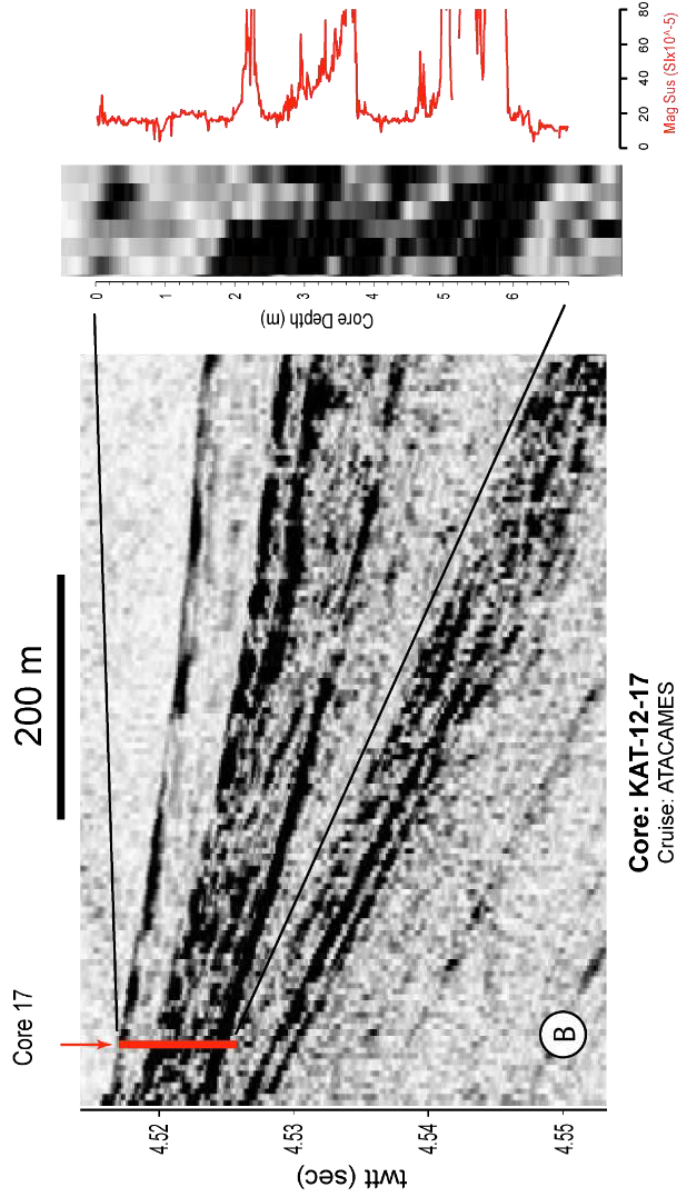
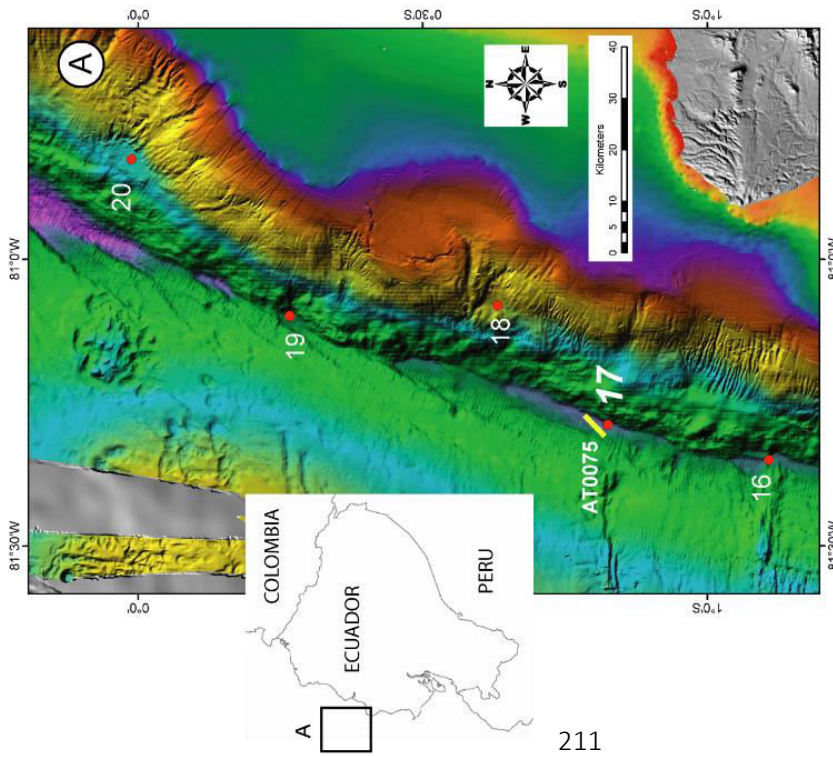
Cruise: ATACAMES  
 Date: 24-Jan-2012  
 Latitude: 01° 06.481' S  
 Longitude: 81° 20.998' W  
 Water depth: 3238 m  
 Core length: 7.14 m  
 Site: Ecuadorian trench,  
 in front of the Cabo San Lorenzo



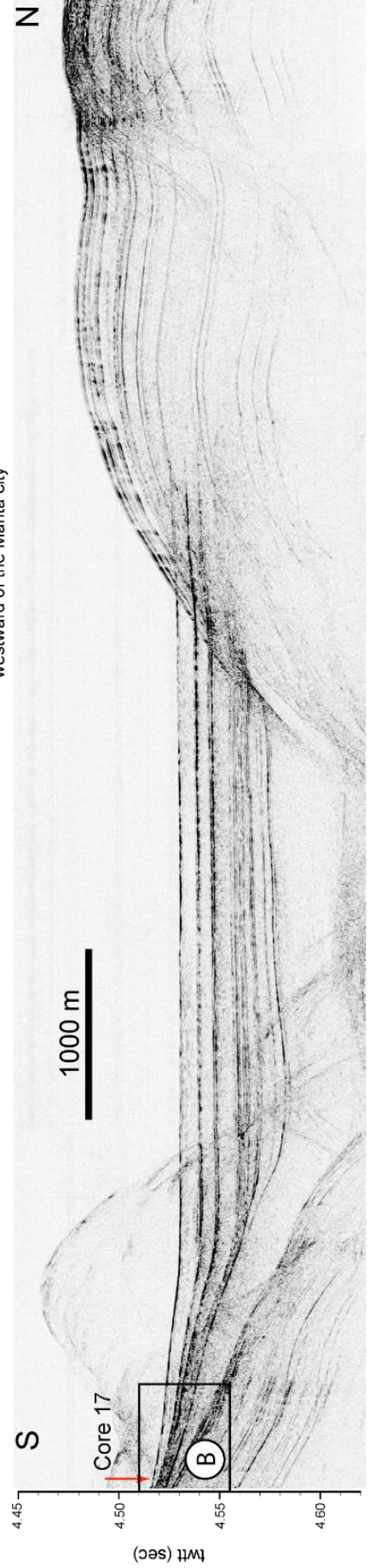
AT0070\_D20120124\_T065648



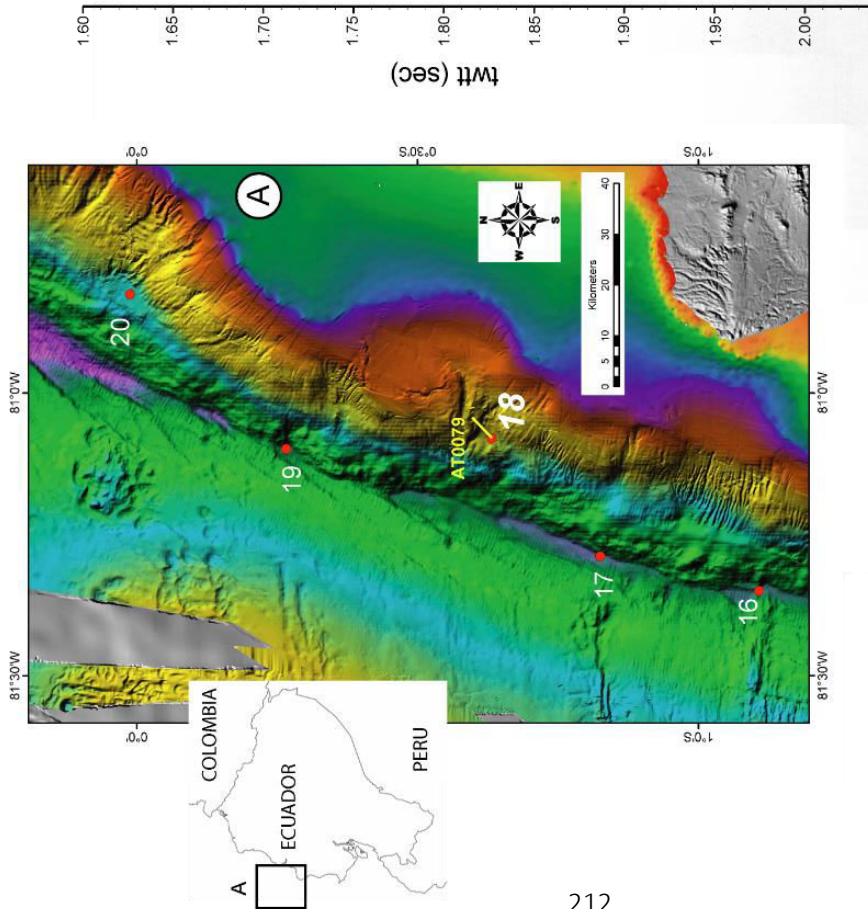
Core 17



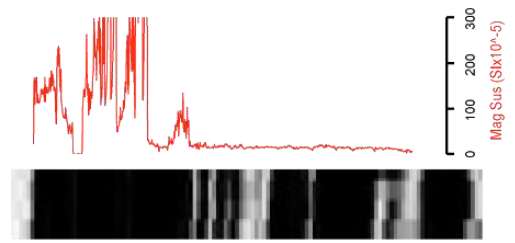
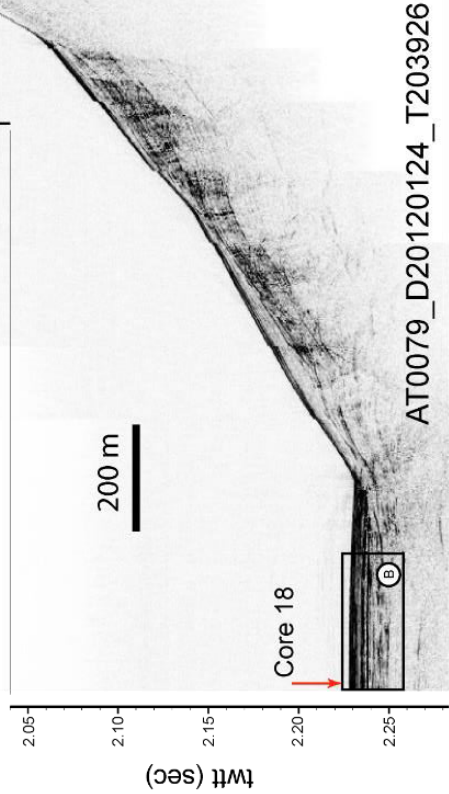
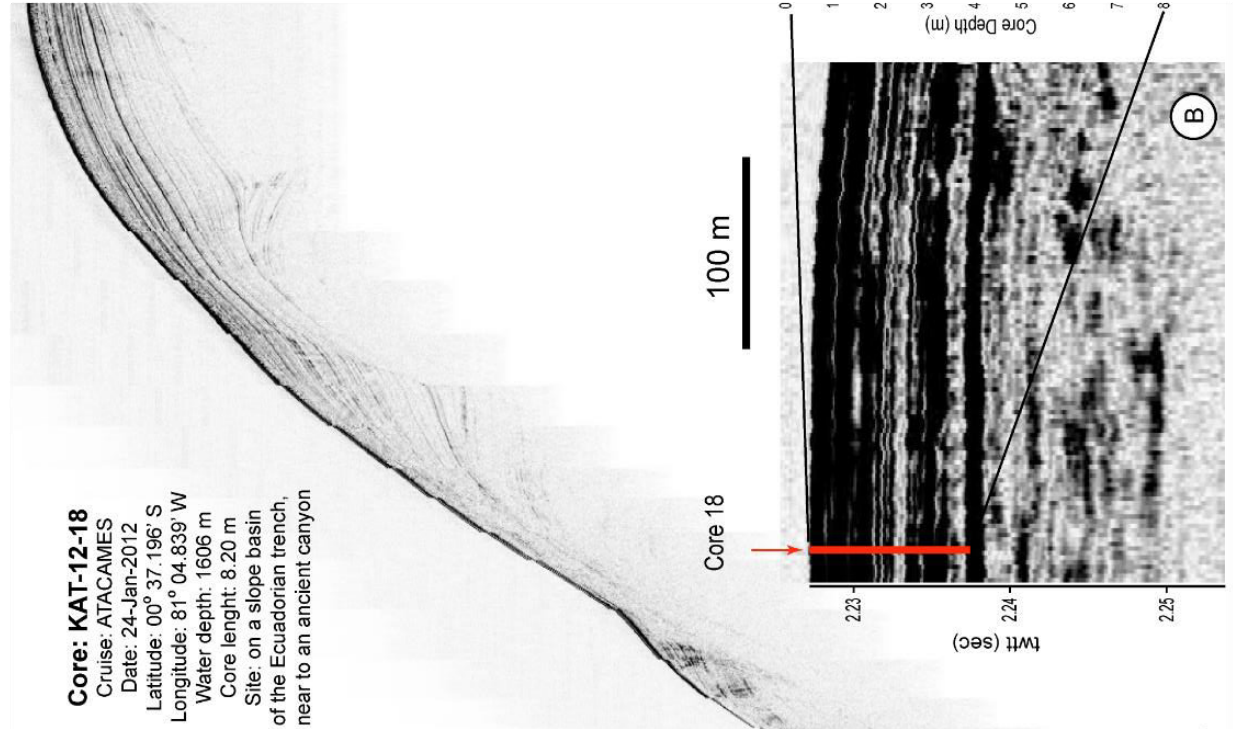
**Core: KAT-12-17**  
 Cruise: ATACAMES  
 Date: 24-Jan-2012  
 Latitude: 00° 49.530' S  
 Longitude: 81° 17.330' W  
 Water depth: 3324 m  
 Core length: 6.71 m  
 Site: Ecuadorian trench,  
 westward of the Manta city



Core 18

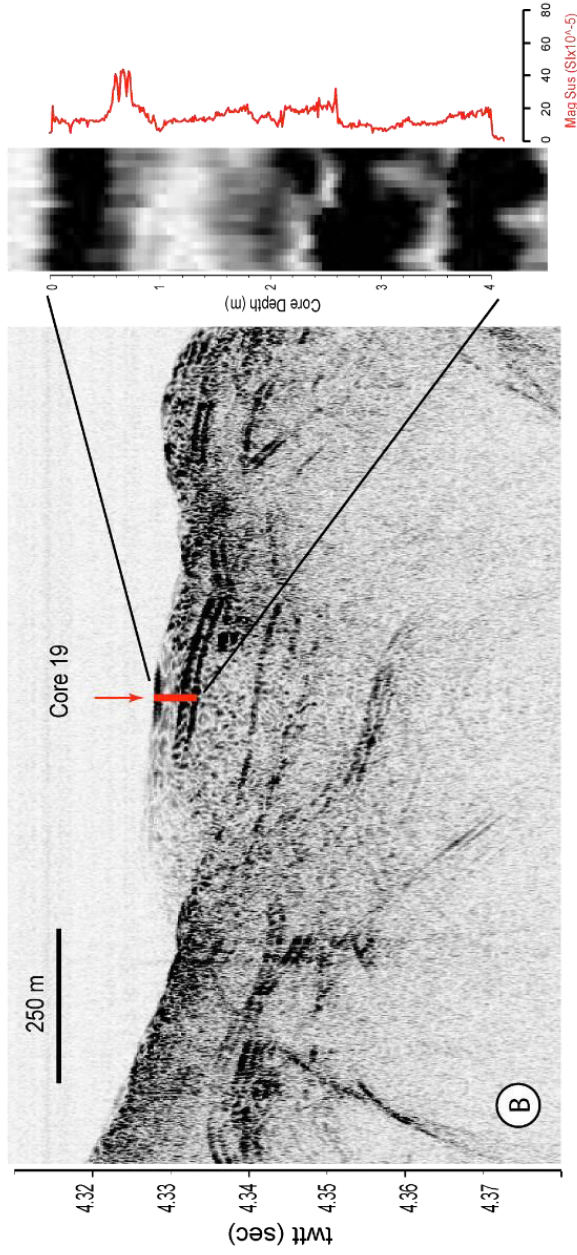
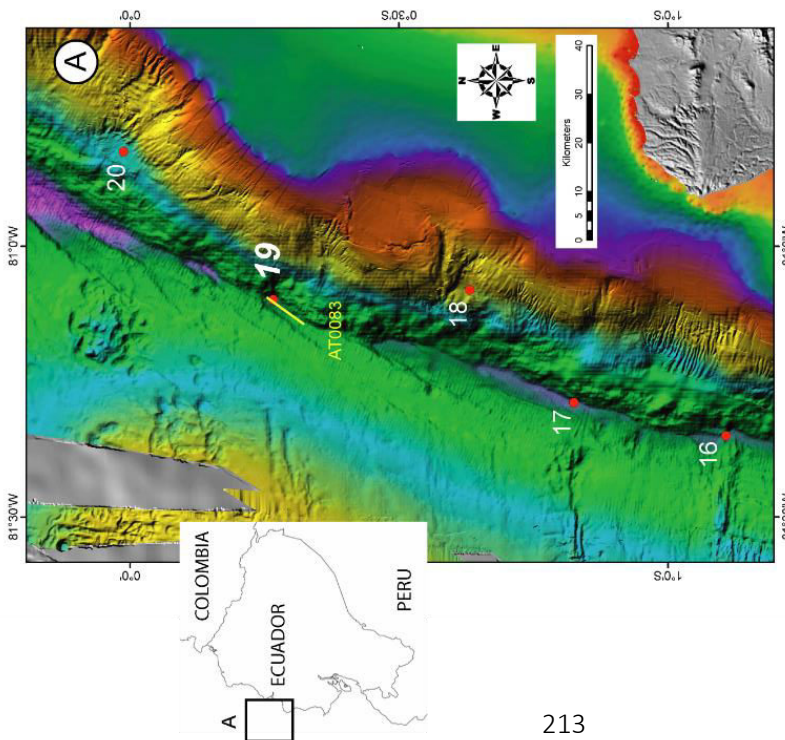


**Core: KAT-12-18**  
 Cruise: ATACAMES  
 Date: 24-Jan-2012  
 Latitude: 00° 37.196' S  
 Longitude: 81° 04.839' W  
 Water depth: 1606 m  
 Core length: 8.20 m  
 Site: on a slope basin of the Ecuadorian trench, near to an ancient canyon

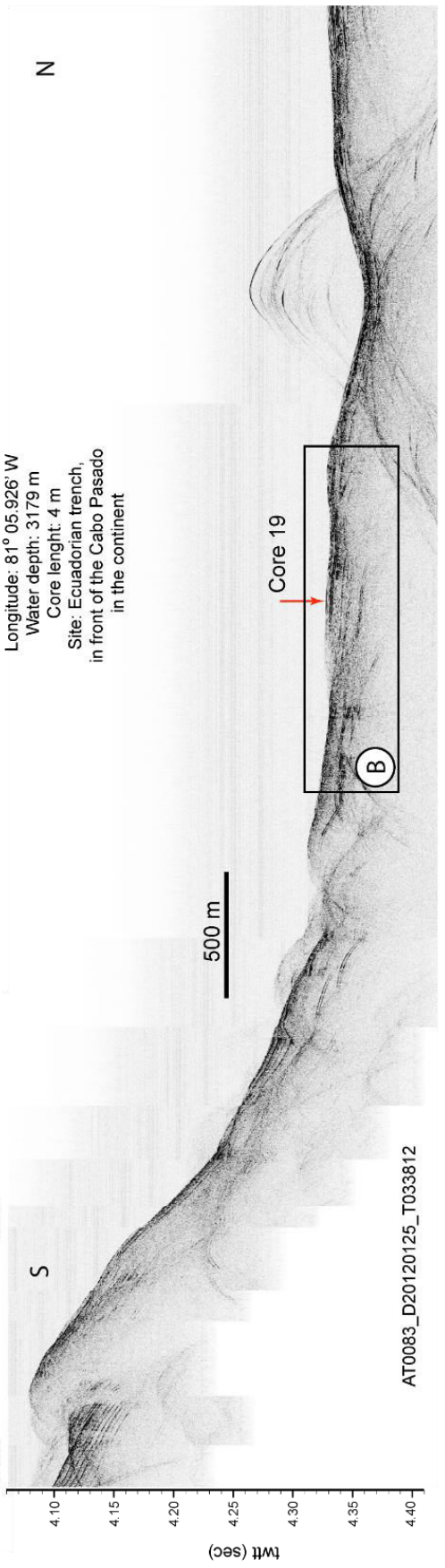




Core 19

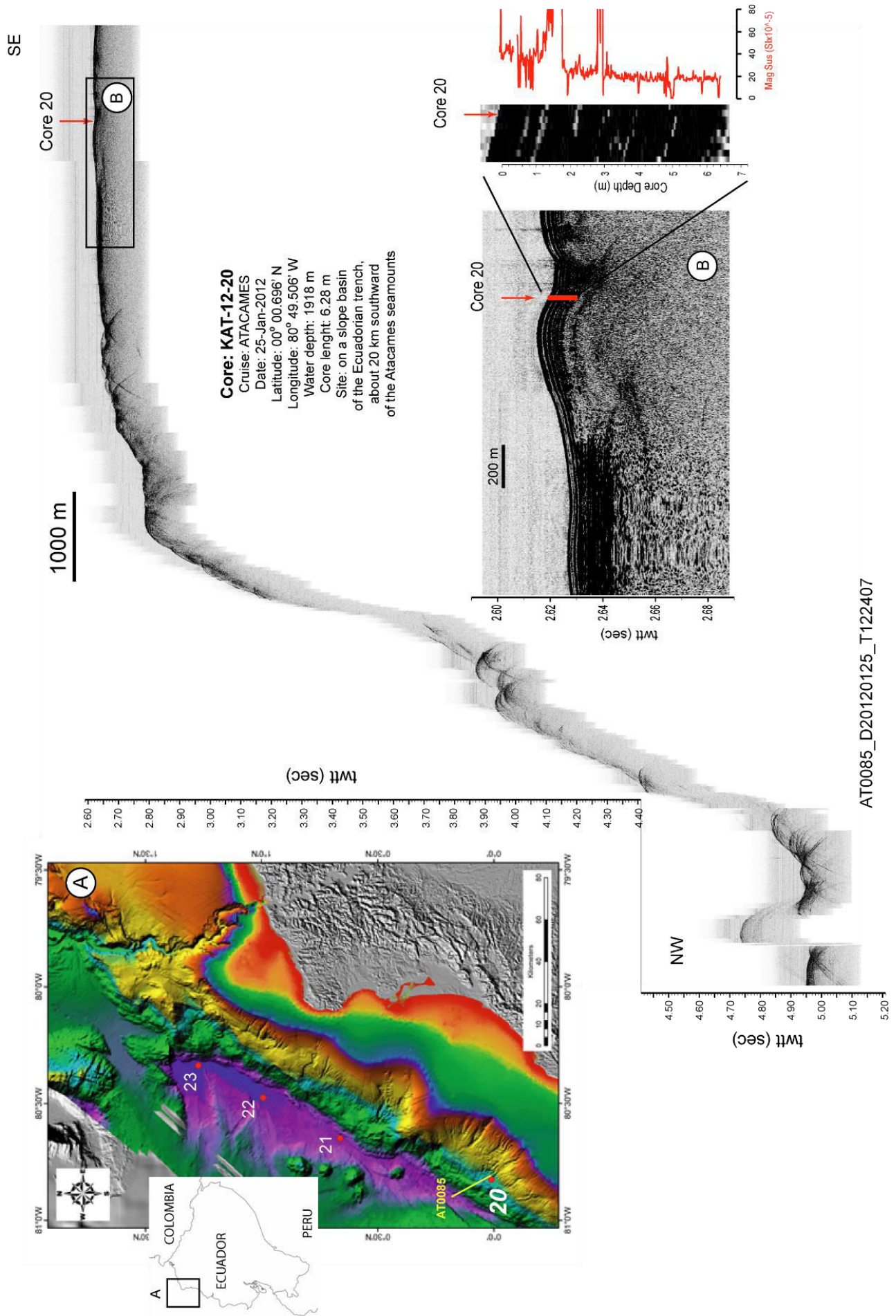


**Core: KAT-12-19**  
 Cruise: ATACAMES  
 Date: 25-Jan-2012  
 Latitude: 00° 16.008' S  
 Longitude: 81° 05.926' W  
 Water depth: 3179 m  
 Core length: 4 m  
 Site: Ecuadorian trench,  
 in front of the Cabo Pasado  
 in the continent



AT0083\_D20120125\_T033812

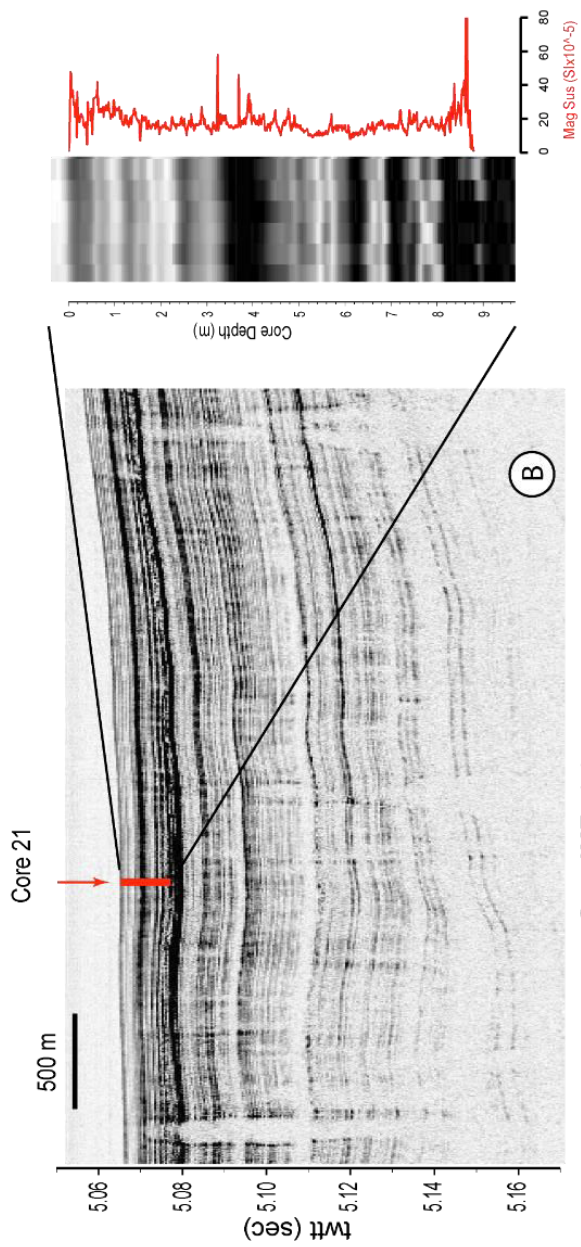
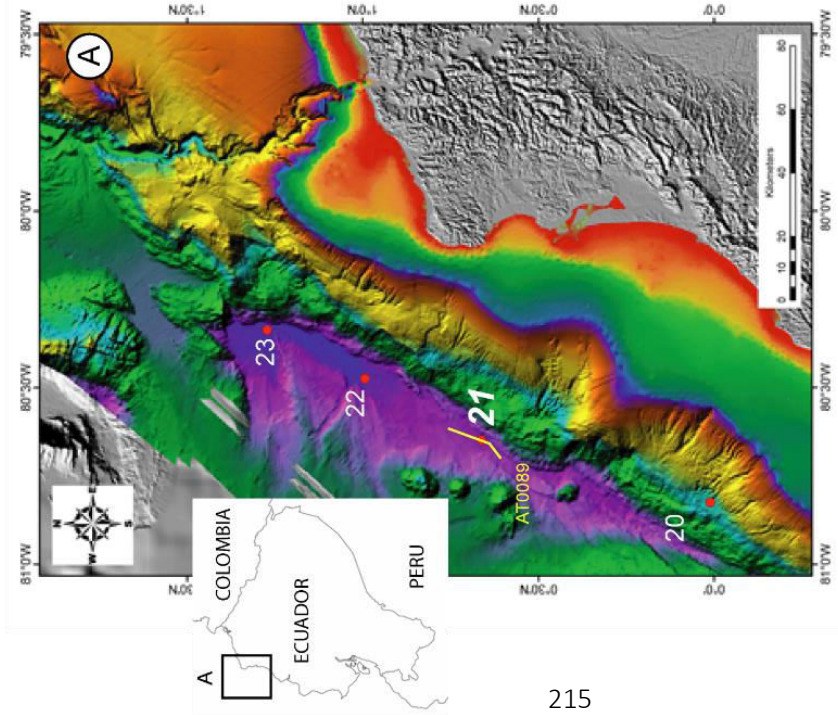
Core 20



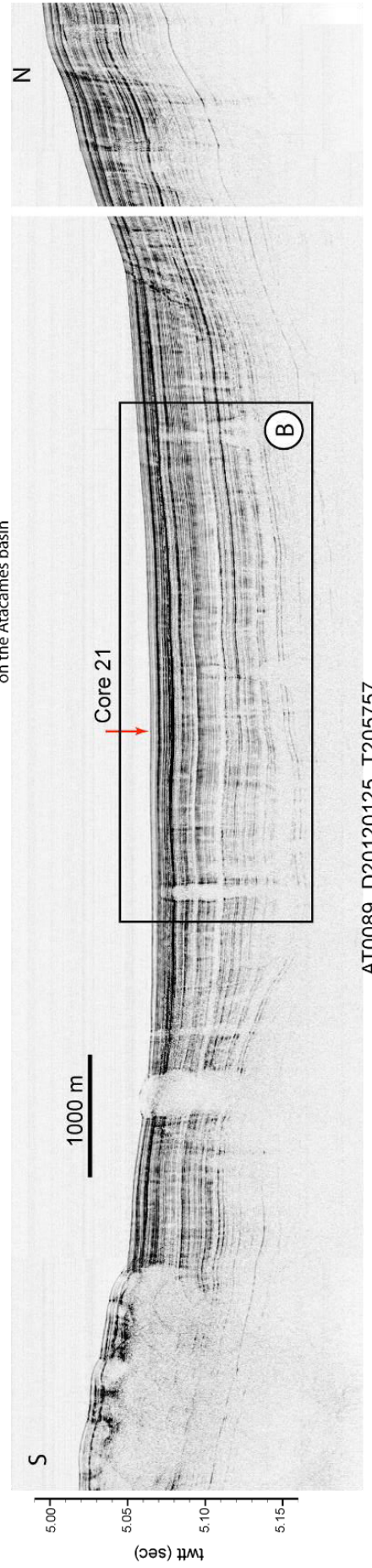
AT0085\_D20120125\_T122407



Core 21



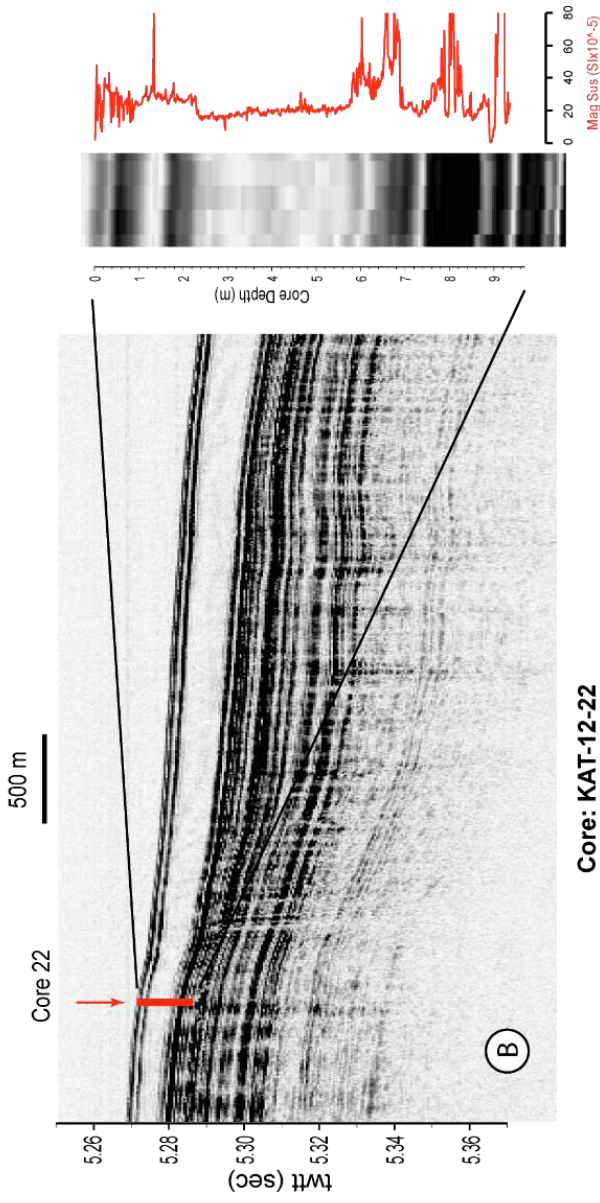
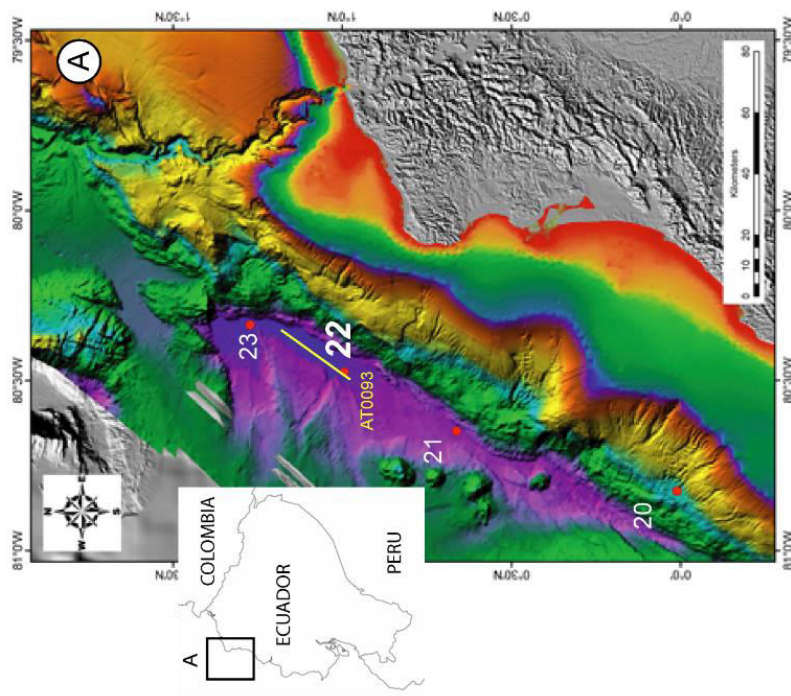
**Core: KAT-12-21**  
 Cruise: ATACAMES  
 Date: 25-Jan-2012  
 Latitude: 00° 39.819'N  
 Longitude: 80° 38.922'W  
 Water depth: 3802 m  
 Core length: 8.63 m  
 Site: Ecuadorian trench,  
 on the Atacames basin



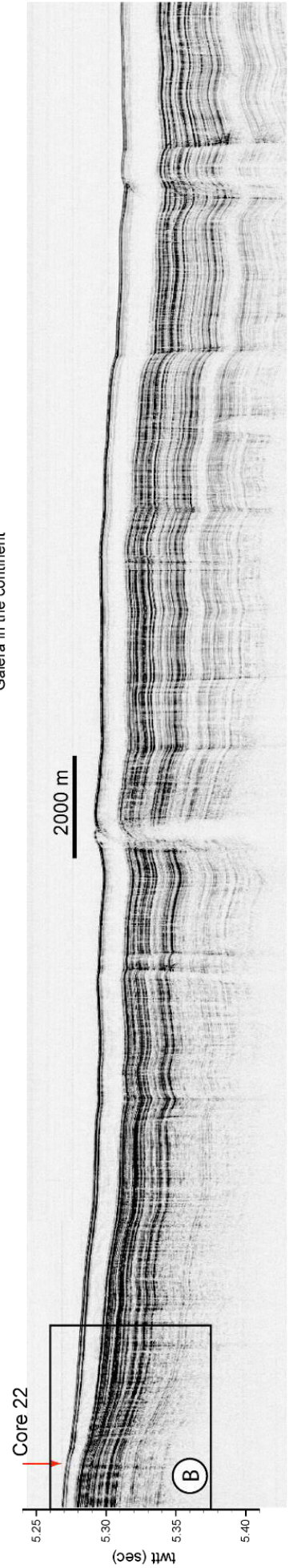
AT0089\_D20120125\_T205757



Core 22

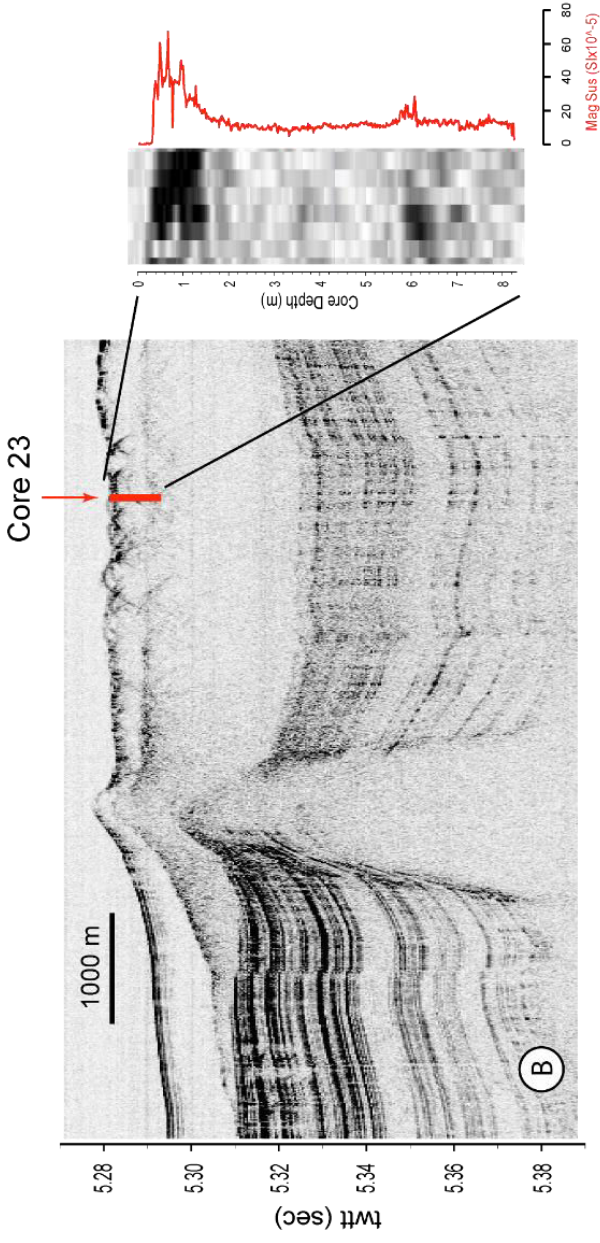
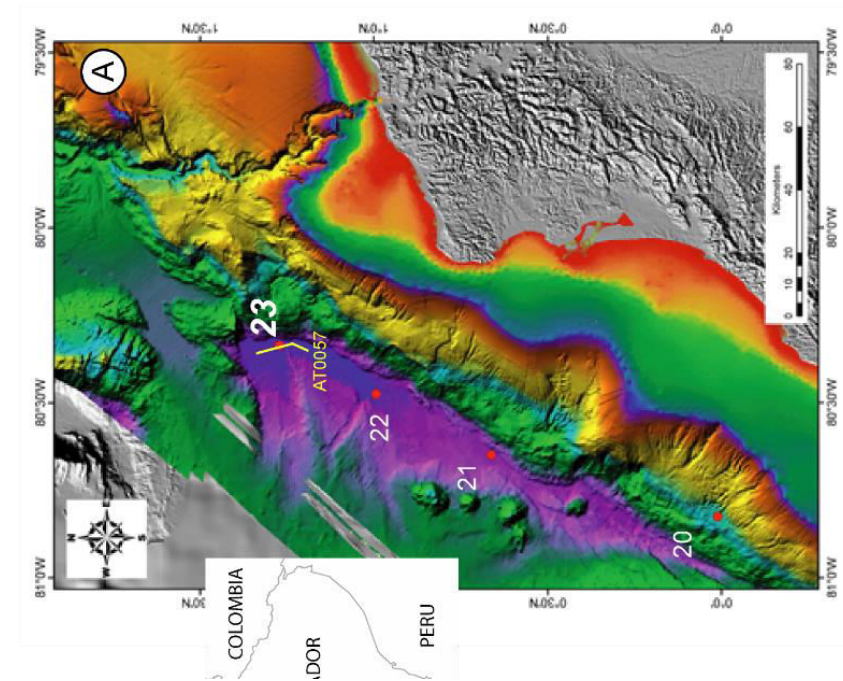


**Core: KAT-12-22**  
 Cruise: ATACAMIES  
 Date: 26-Jan-2012  
 Latitude: 00° 59.686' N  
 Longitude: 80° 28.491' W  
 Water depth: 3962 m  
 Core length: 8.98 m  
 Site: Ecuadorian trench,  
 in front of the Punta  
 Galera in the continent



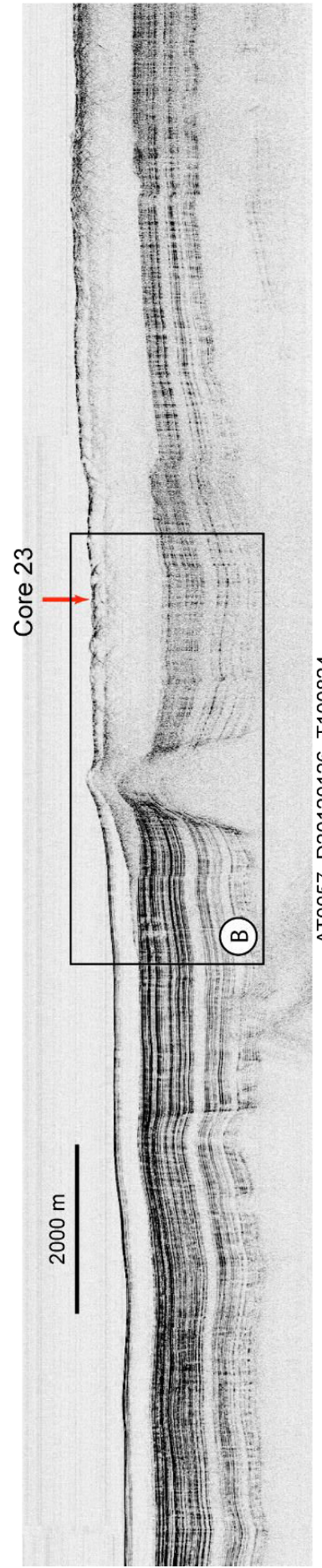


Core 23



**Core: KAT-12-23**

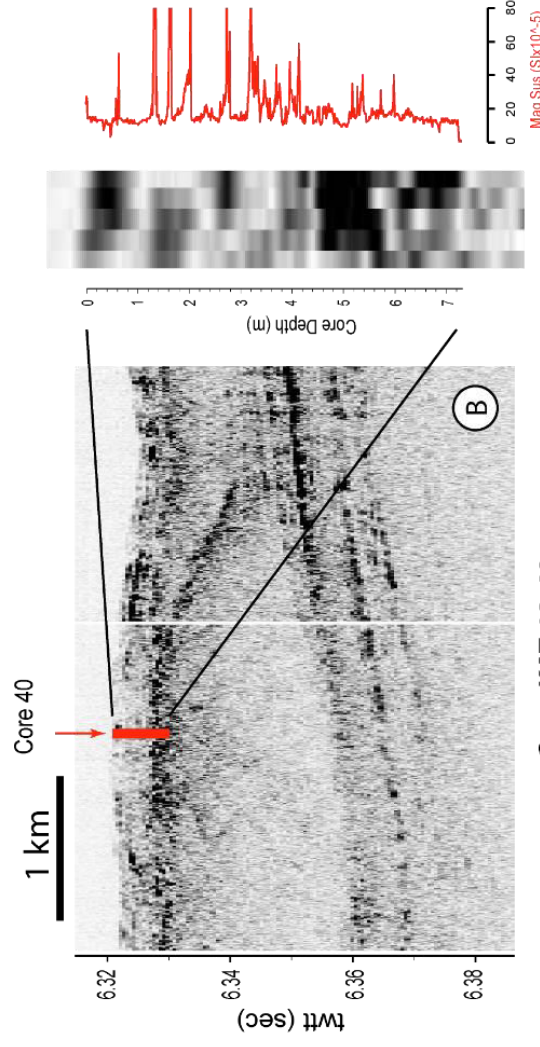
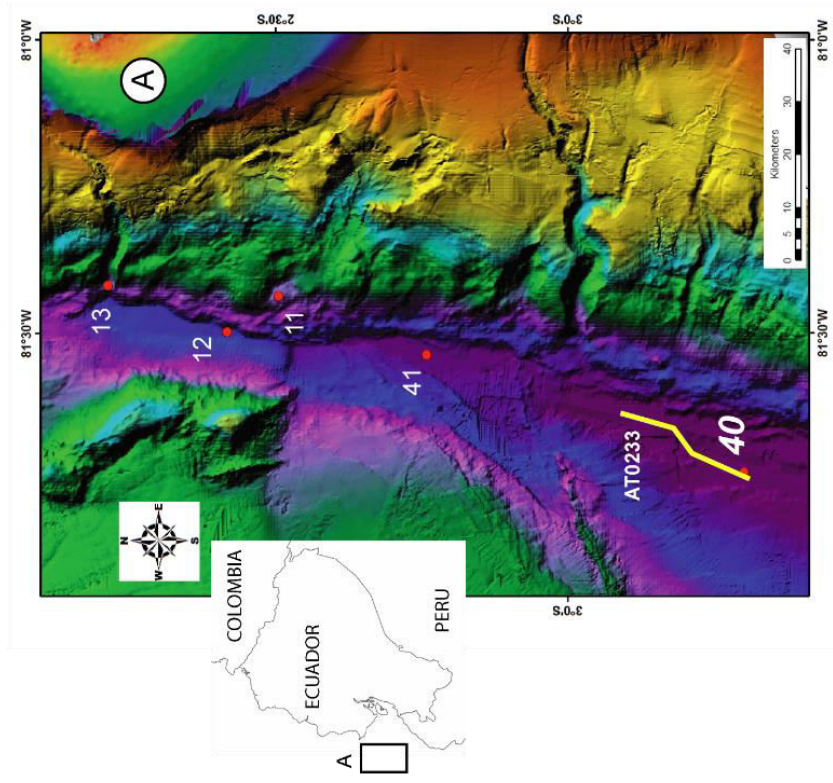
Cruise: ATACAMES  
 Date: 26-Jan-2012  
 Latitude: 01° 16.387' N  
 Longitude: 80° 20.206' W  
 Water depth: 3973 m  
 Core length: 8.18 m  
 Site: Ecuadorian trench,  
 about 10 km southward  
 of the Galeras seamounts



AT0057\_D20120126\_T100824

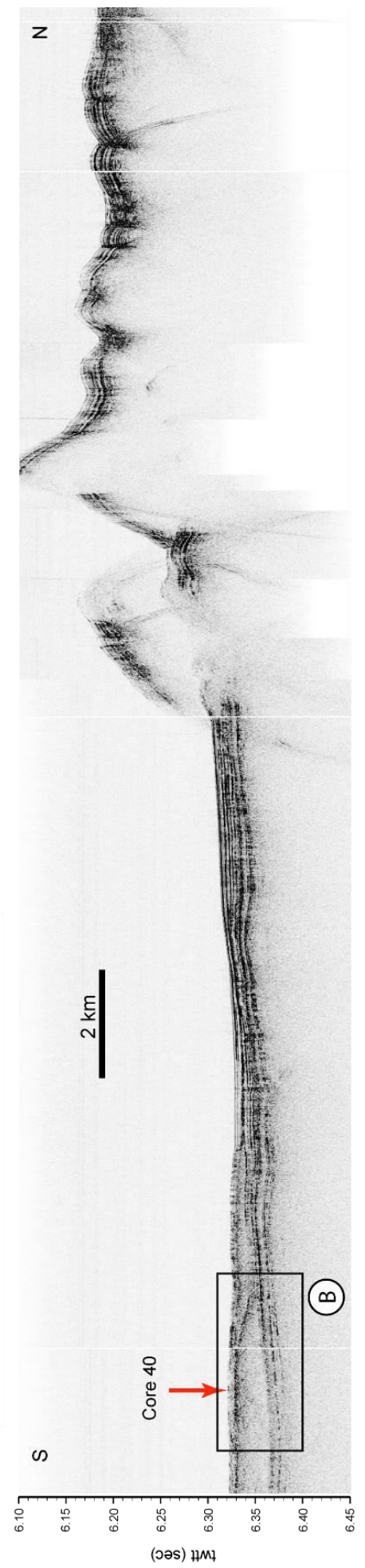


Core 40



**Core: KAT-12-40**

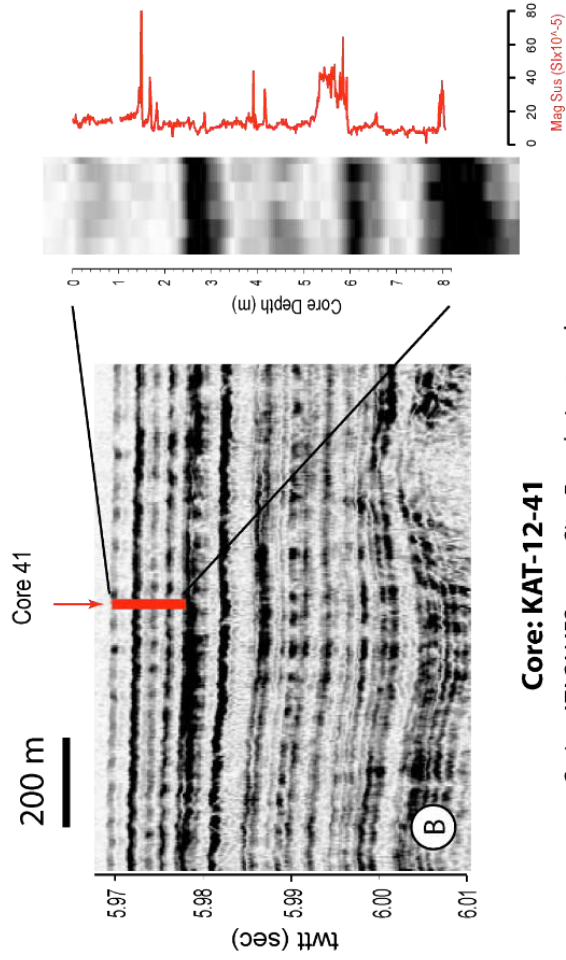
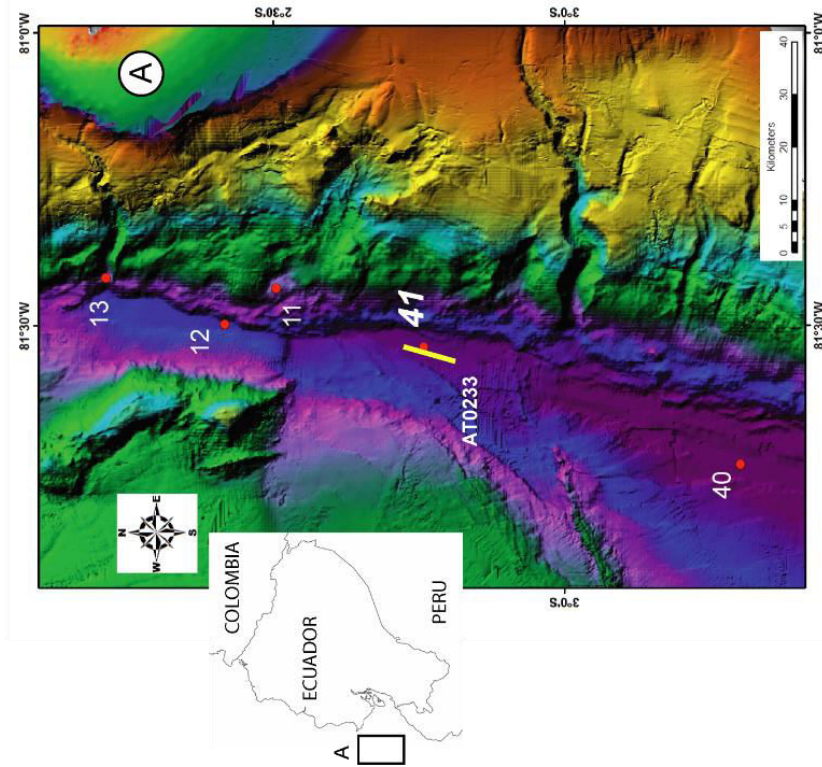
Cruise: ATACAMES  
 Site: Ecuadorian trench,  
 about 30 km southward  
 of the Guayaquil canyon  
 Date: 13-Feb-2012  
 Latitude: 03° 18.150' S  
 Longitude: 81° 44.185' W  
 Water depth: 4698 m  
 Core length: 7.77 m



AT0233\_D20120213\_T231719

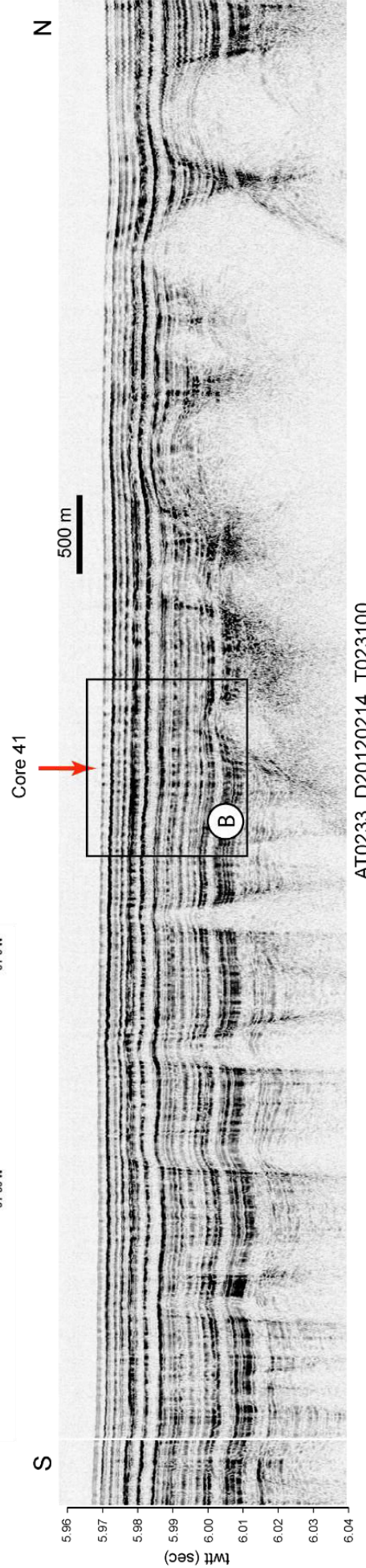


Core 41



**Core: KAT-12-41**

Cruise: ATACAMES Site: Ecuadorian trench,  
 Date: 14-Feb-2012 about 20 km north  
 Latitude: 02° 45.555' S of the Guayaquil canyon,  
 Longitude: 81° 32.218' W in front of the Gulf  
 Water depth: 4422 m of Guayaquil.  
 Core length: 7.77 m




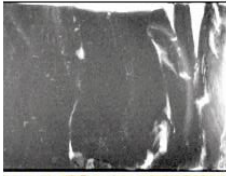
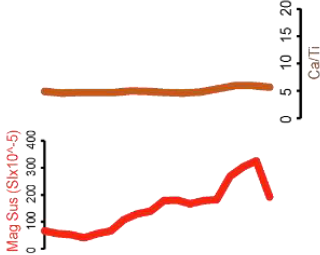




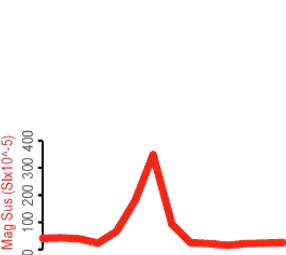



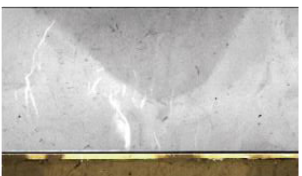
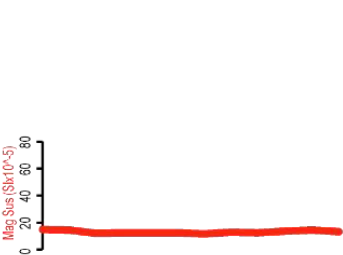


AT0233\_D20120214\_T023100


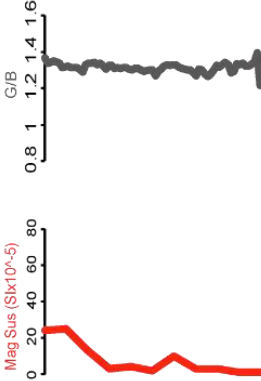


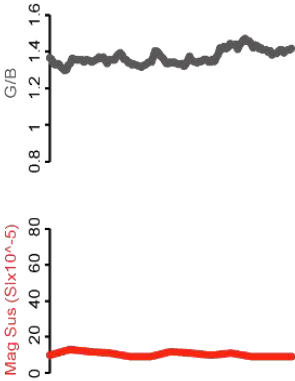
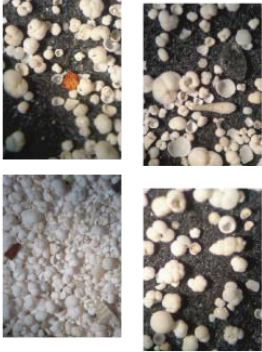
## Annexe 2: Facies Diagrams

Color symbology	High-resolution photographs	X-ray images	Petrophysical parameters	Micro-facies photographs	Description
					<p>Average density 2.49 g/cc, average MS 27.38 SI</p> <p>Olive grayish homogenous clay to silty clay</p> <p>Moderately to highly bioturbated</p> <p>Presence of foraminifers planctonics and benthics, diatoms</p> <p>Degree of reflectivity: medium</p> <p>No sedimentary structures except bioturbation</p> <p>Minerals: few quartz and ferromagnesian grains</p>
					<p>Average density 2.2 g/cc, average MS 25 SI</p> <p>Olive grayish homogenous clay</p> <p>Moderately to highly bioturbated</p> <p>Rare foraminifers</p> <p>Degree of reflectivity: medium</p> <p>No sedimentary structures except bioturbation</p> <p>There is not evidence of minerals</p>
					<p>Average density 2.43 g/cc, average MS 19.86 SI, with by places sharp increases to 30SI</p> <p>Olive grayish clay to silty clay with no bioturbation and rare foraminifers</p> <p>Degree of reflectivity: medium</p> <p>Thin horizontal to low angle lamination</p> <p>Similar to facies 1 except for the lamination and lack of bioturbation</p>



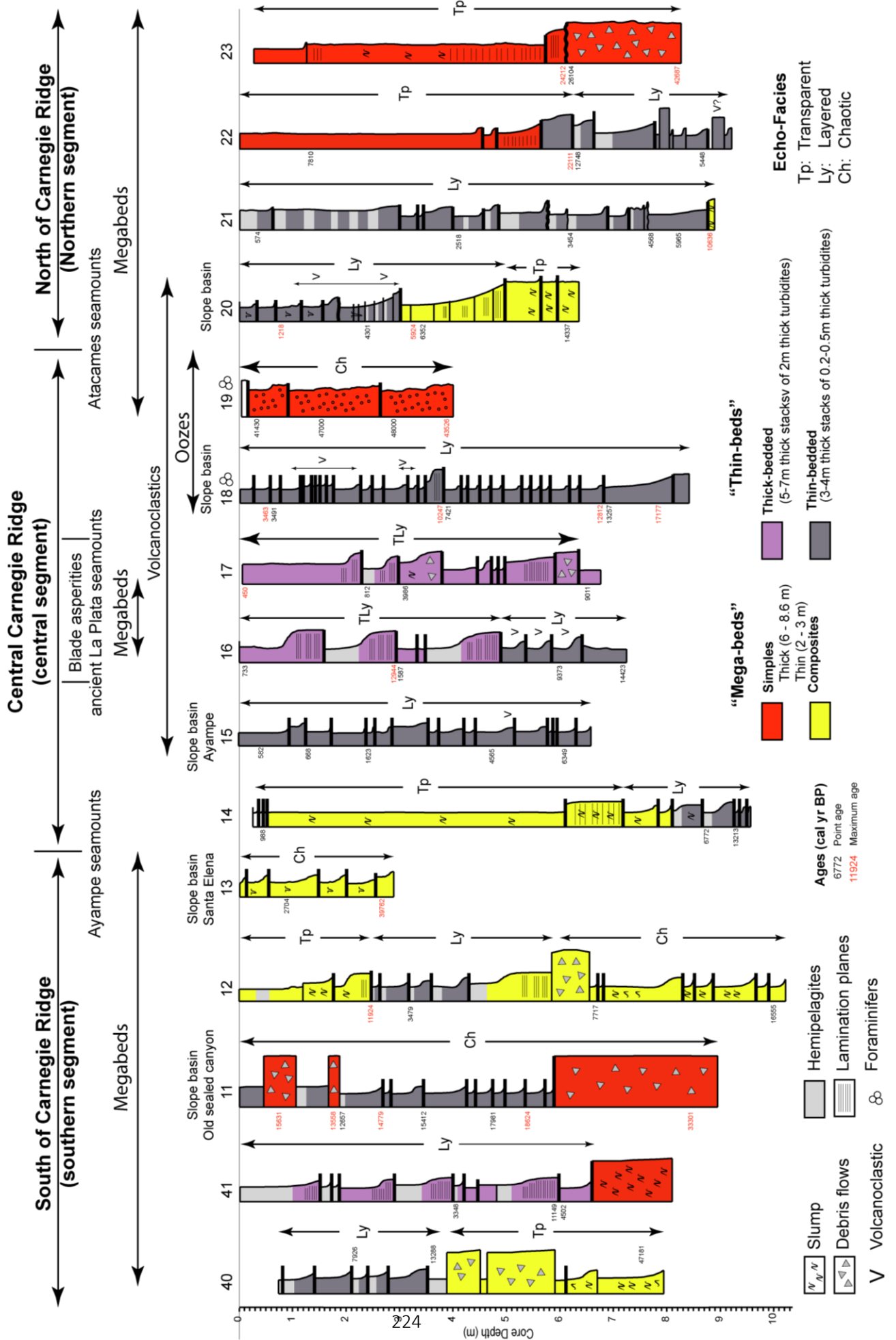
Color symbology	High-resolution photographs	X-ray images	Petrophysical parameters	Micro-facies photographs	Description
Facies 4 (T4)			<p>Mag Sus (<math>6 \times 10^{-5}</math>) vs G/B: Values range from ~30 to 50. Ca/Ti vs G/B: Values range from ~5 to 15. Median Q50 vs G/B: Values range from ~5 to 10.</p>		<p>Average density 2.49 g/cc, average MS 35.40 SI Olive grayish clay to silty clay Rare foraminifers Degree of reflectivity: low to medium. low reflectivity is represented by the dark grayish silty laminations No or rare bioturbation Remnants of low angle laminations, flame and convolute structures and syndimentary microfolds Similar to facies 2 but more structured, showing intercalations of dark grayish silty clay laminations</p>
Facies 5 (T3)			<p>Mag Sus (<math>6 \times 10^{-5}</math>) vs G/B: Values range from ~30 to 50. Ca/Ti vs G/B: Values range from ~5 to 15. Median Q50 vs G/B: Values range from ~5 to 10.</p>		<p>Average density 2.48 g/cc, average MS 37.70 SI Olive grayish silty clay to silt Rare foraminifers No bioturbation Degree of reflectivity: low to medium. Low reflectivity is represented by the dark grayish silty laminations Planar horizontal to low angle or rippled laminations with low angle erosion surfaces</p>
Facies 6 (T0-T2)			<p>Mag Sus (<math>6 \times 10^{-5}</math>) vs G/B: Values range from ~30 to 50. Ca/Ti vs G/B: Values range from ~5 to 15. Median Q50 vs G/B: Values range from ~5 to 10.</p>		<p>Average density 2.66 g/cc, average MS 78.20 SI Darkish olive grey massive to laminated silt to silty sand Degree of reflectivity is Low representing dark grayish silty laminations Rich in foraminifers No bioturbation Fining up sand to silt, massive at base and then horizontal to low angle or ripple lamination Quartz, mica and shell bioclasts</p>

Color symbology	High-resolution photographs	X-ray images	Petrophysical parameters	Micro-facies photographs	Description
	<p><b>Facies 7</b> (volcanoclastic T4-T6)</p>  		 	 <p style="text-align: right; font-size: small;">source: sample 22-9-72</p>	<p>Average density 2.51 g/cc, average very high MS 180 SI Brownish massive volcanogenic silt (tephra) No bioturbation, no foraminifers Degree of reflectivity is medium to high reflectivity Quartz, ferromagnesian minerals (biotite) Erosion surfaces at base and top T4-T6 (tephra) horizons of Stow</p>
	<p><b>Facies 8</b> (volcanoclastic T2-T3)</p>  		 	 <p style="text-align: right; font-size: small;">Source: sample 21-10-12</p>	<p>Average density 2.15 g/cc, high average MS 200 SI Light brownish bioclastic sand with intercalations of black volcanogenic ferromagnesian sand laminae Shell hash of microfossils of benthic and planktonic forams, radiolarians Volcanic ash both base and top is characteristic in this facies Bioturbation Degree of reflectivity is medium Erosion surfaces at base and top Quartz and ferromagnesian minerals T2-T3 (bio+tephra) horizons of Stow</p>
	<p><b>Facies 9</b> (debris flow)</p>  		 	 <p style="text-align: right; font-size: small;">Source: sample 23-7-50</p>	<p>Average density 2.43 g/cc, average MS 13.36 SI Olive grayish massive silty clay to silt with brown and yellow mottling, which represent relicts of centimetric to decimetric clasts No bioturbation Plenty of microfossils: benthic and planktonic forams, diatoms and radiolarians Medium to high reflectivity where high reflectivity is represented by the clear, transparent grayish silt Quartz</p>

Color symbology	High-resolution photographs	X-ray images	Petrophysical parameters	Micro-facies photographs	Description
	<p><b>Facies 10 (slump)</b></p> 			 <p style="text-align: right; font-size: small;">Source: sample 21-10-26</p>	<p>Average density 2.2 g/cc, average MS 10 SI  Yellowish to whitish silt over a sharp erosive base.  The white color is similar to tephra layers, but the values of magnetic susceptibility are very low.  No bioturbation  Presence of microfossils: benthic and planktonic forams, diatoms  Medium to high reflectivity  Presence of quartz and biotite  Soft deformation structures like in slump deposit</p>
	<p><b>Facies 11 (carbonate ooze)</b></p> 			 <p style="text-align: right; font-size: small;">Source: sample 19-1-6</p>	<p>Average density 2.58 g/cc, average MS 10 SI  Yellowish massive bioclastic sand  Almost exclusively shells of microfossils: benthic and planktonic forams and radiolarians  No bioturbation  Traces of ferromagnesian minerals  Massive to poorly laminated with erosion surfaces  Ooze deposit</p>



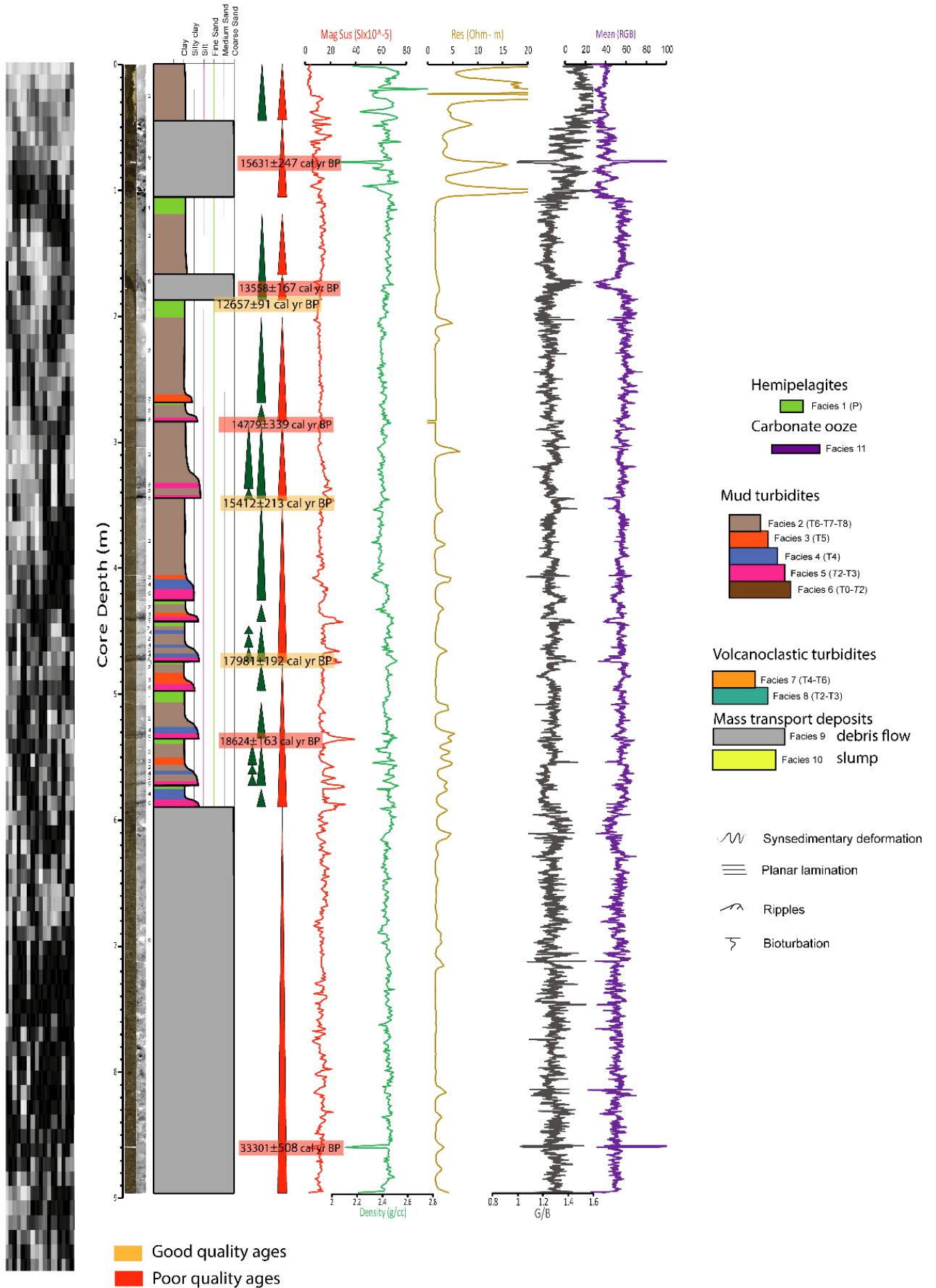
# Annexe 3: Sedimentary cores



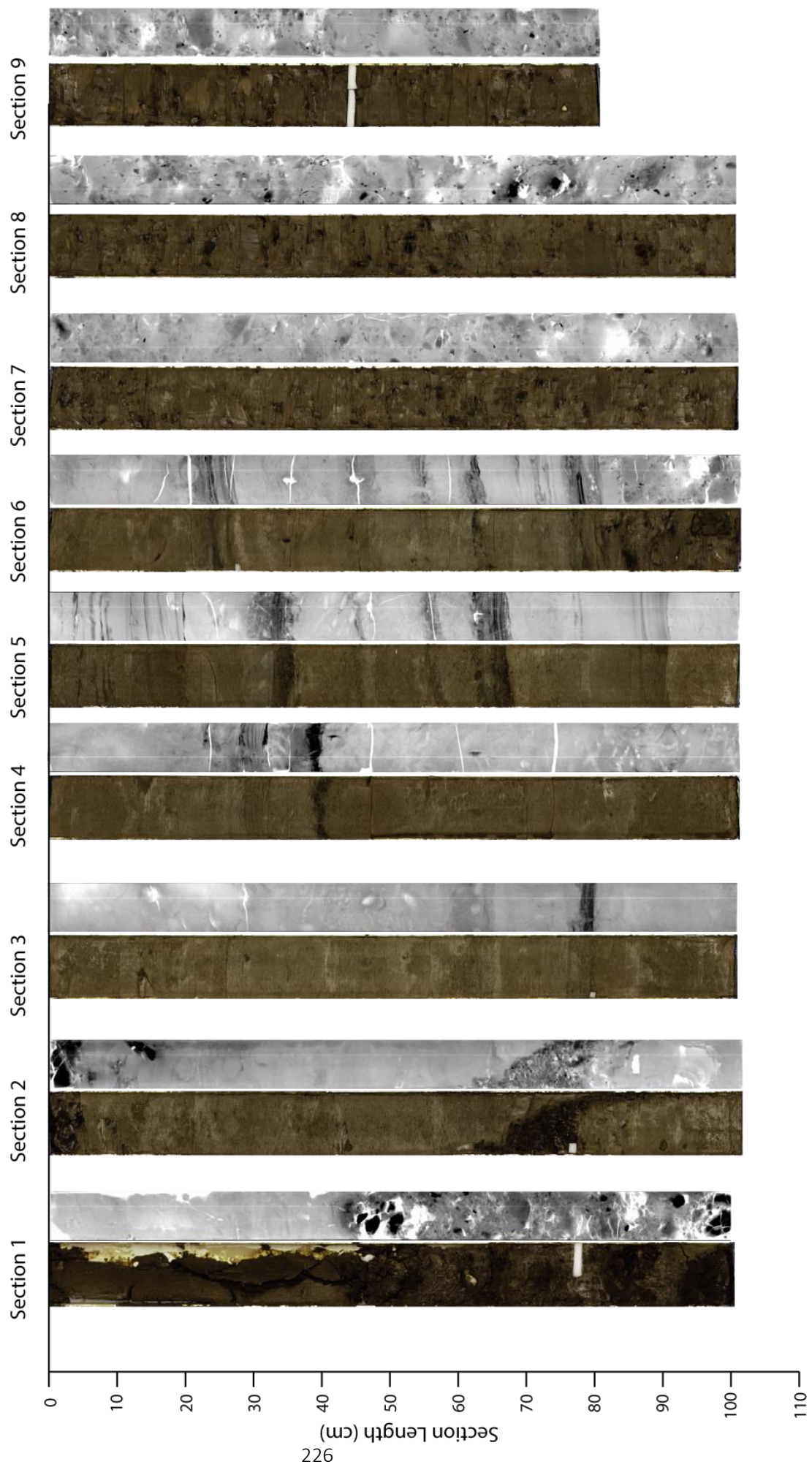
**Core: KAT-12-11**

Cruise: ATACAMES  
 Date: 22-Jan-2012  
 Latitude: 02° 30.333' S  
 Longitude: 81° 26.145' W  
 Water depth: 3410 m

Core length: 8.17 m  
 Site: on a slope basin,  
 about 50 km northward  
 of the Guayaquil canyon



KAT-12-11



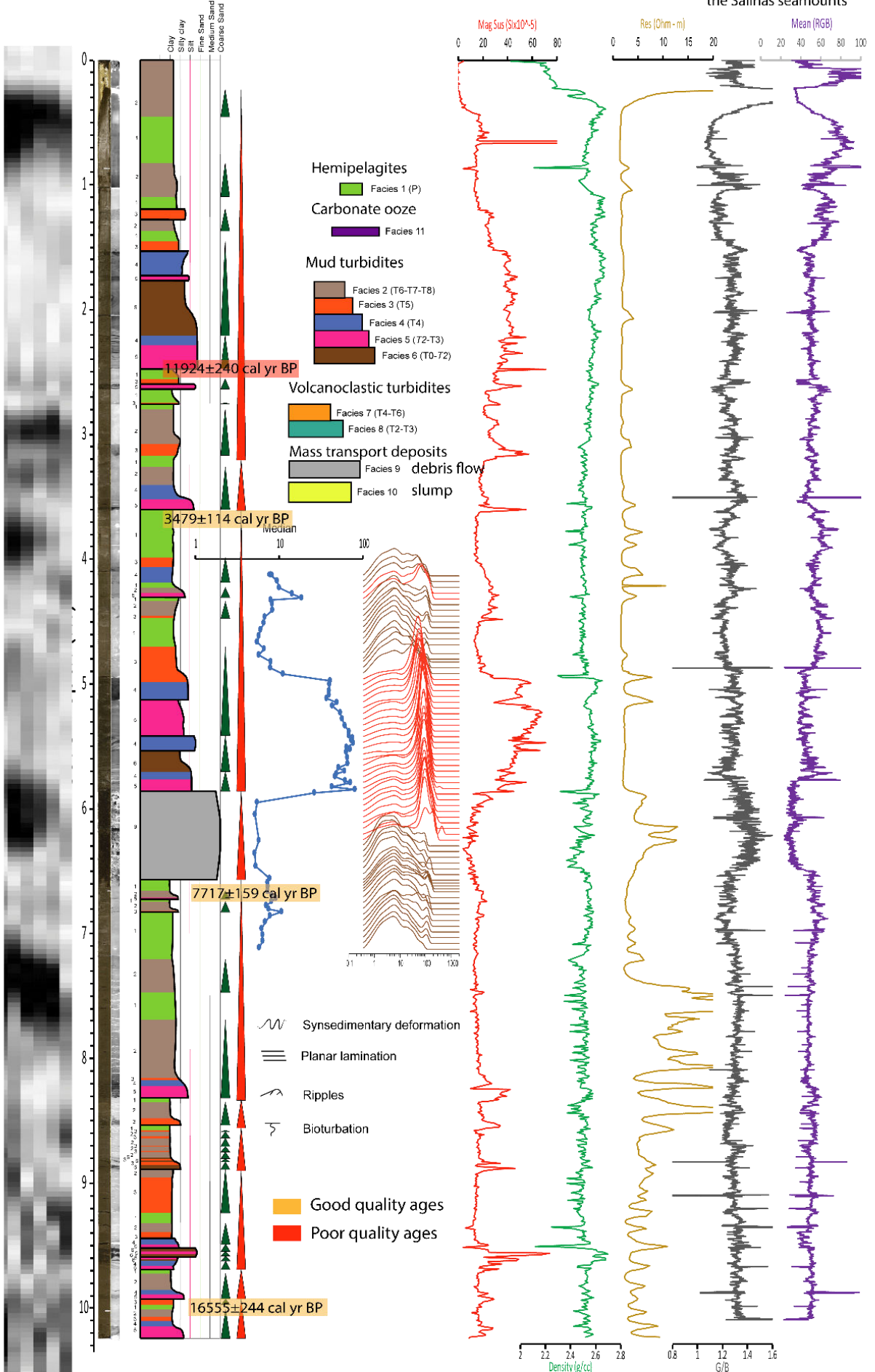
Core: KAT-12-12

Cruise: ATACAMES  
Date: 22-Jan-2012

Latitude: 02° 25.074' S  
Longitude: 81° 29.852' W

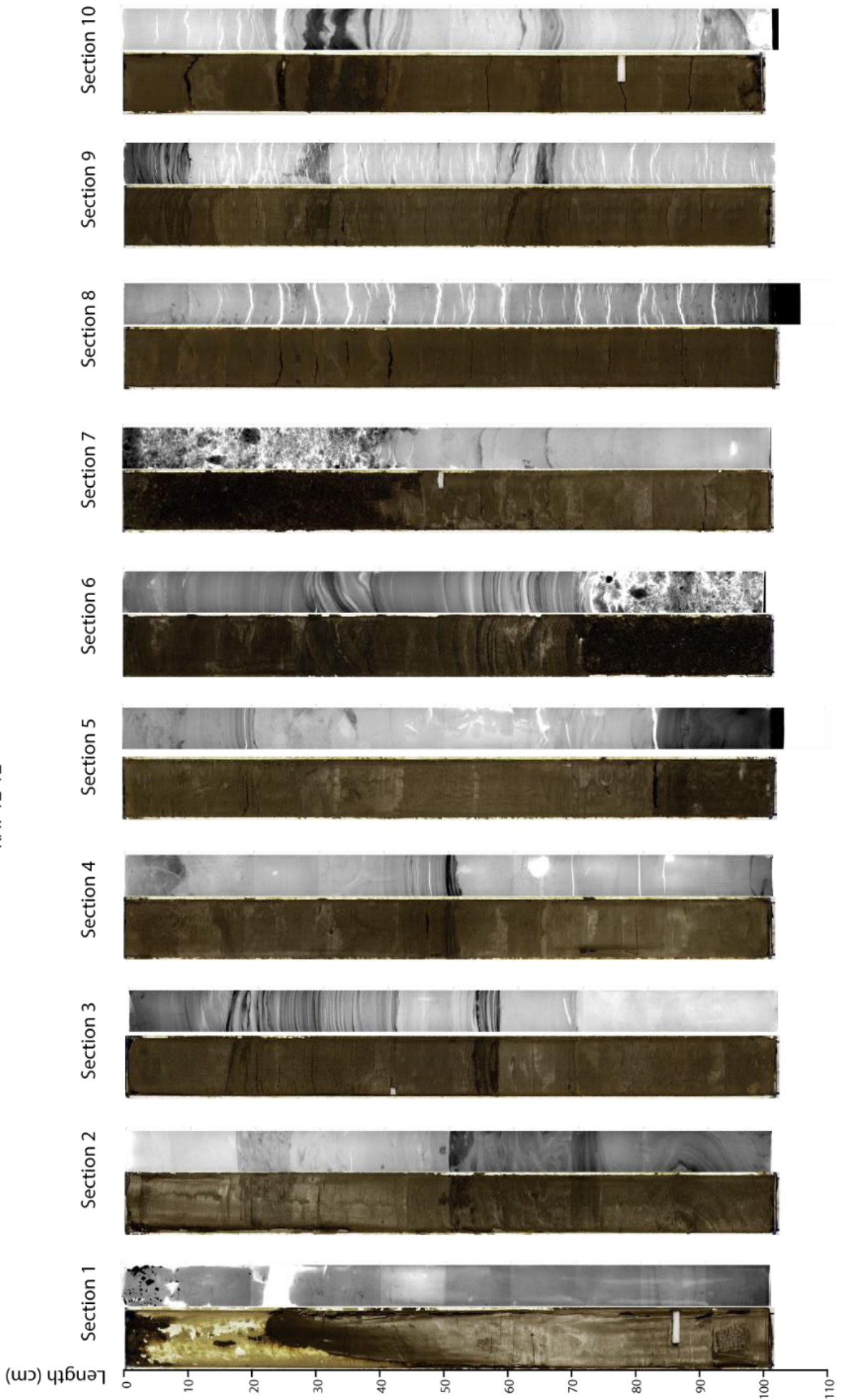
Water depth: 4104 m  
Core length: 10 m

Site: Ecuadorian trench,  
about 20 km south of the  
Santa Elena canyon, left side of  
the Salinas seamounts





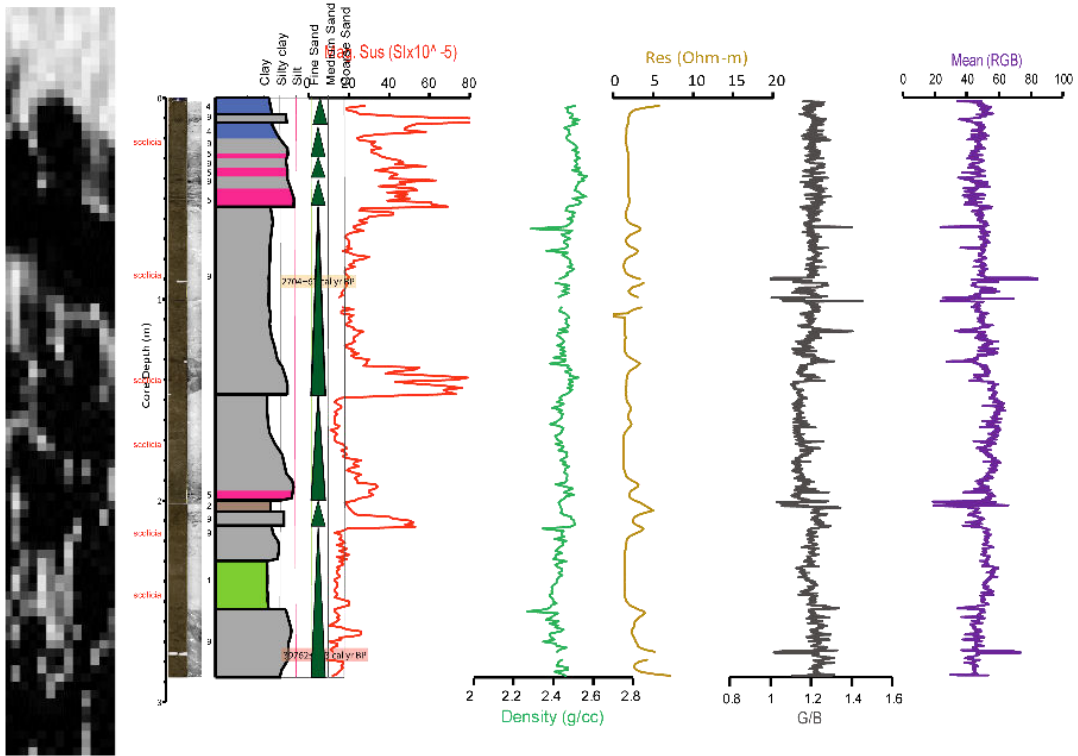
KAT-12-12





**Core: KAT-12-13**

Cruise: ATACAMES  
 Date: 23-Jan-2012  
 Latitude: 12° 12.776' S  
 Longitude: 81° 25.138' W  
 Water depth: 3475 m  
 Core length: 2.92 m  
 Site: Ecuadorian trench,  
 on the river mouth of  
 the Santa Elena canyon



Good quality ages  
 Poor quality ages

Hemipelagites  
 Facies 1 (P)  
 Carbonate ooze  
 Facies 11

**Mud turbidites**

Facies 2 (T6-T7-T8)  
 Facies 3 (T5)  
 Facies 4 (T4)  
 Facies 5 (T2-T3)  
 Facies 6 (T0-T2)

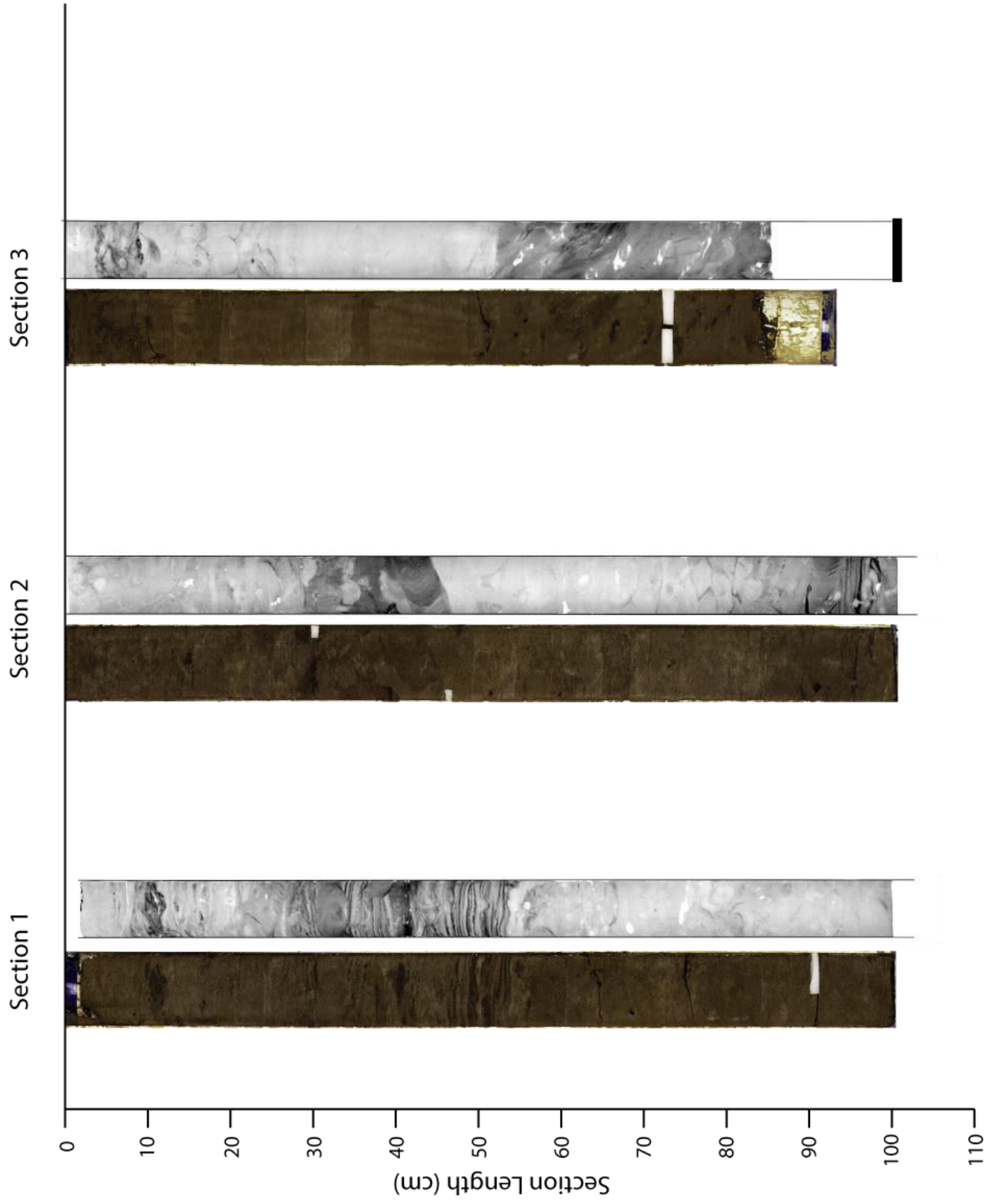
**Volcanoclastic turbidites**

Facies 7 (T4-T6)  
 Facies 8 (T2-T3)

Mass transport deposits  
 Facies 9 debris flow  
 Facies 10 slump

Synsedimentary deformation  
 Planar lamination  
 Ripples  
 Bioturbation

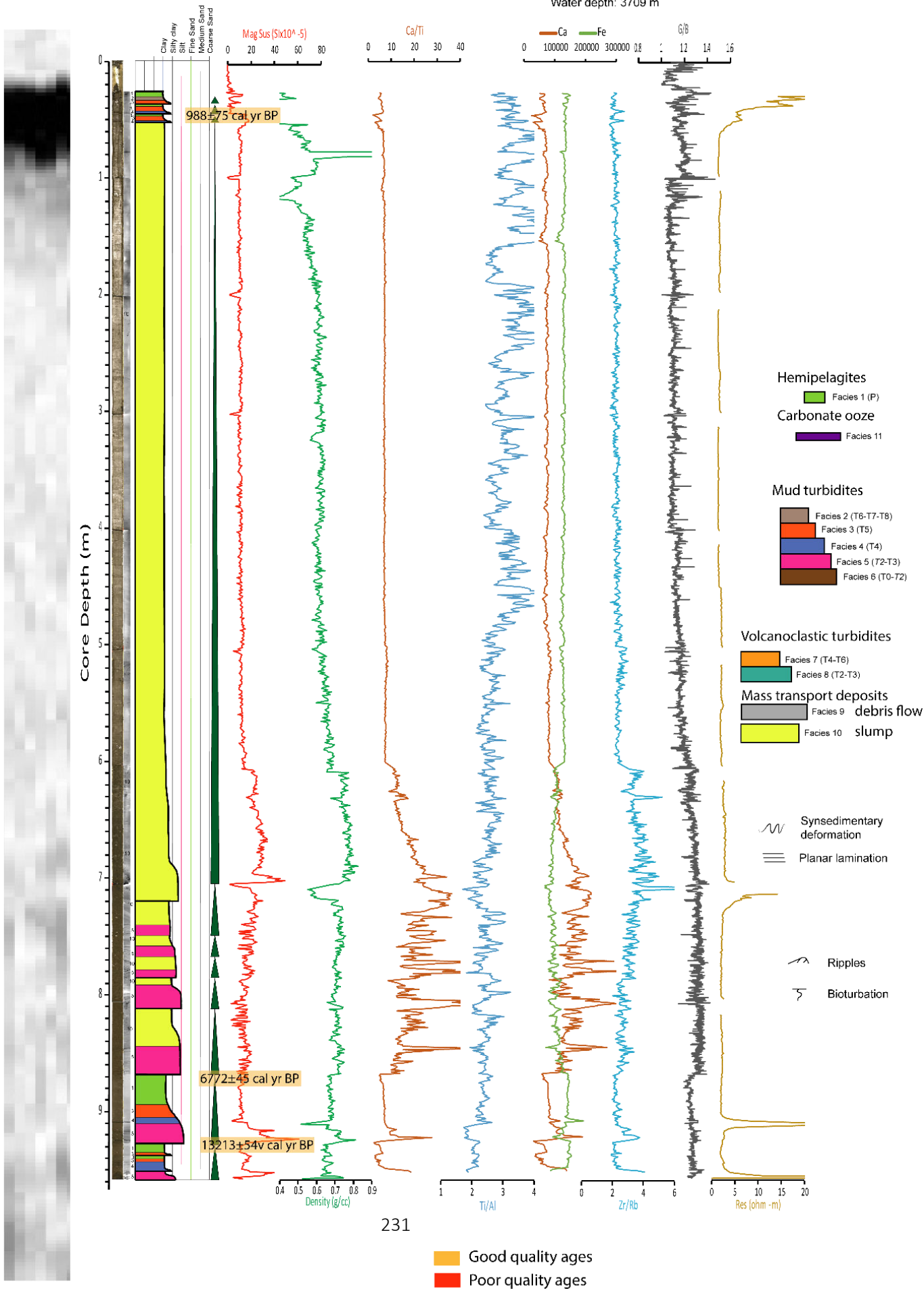
KAT-12-13



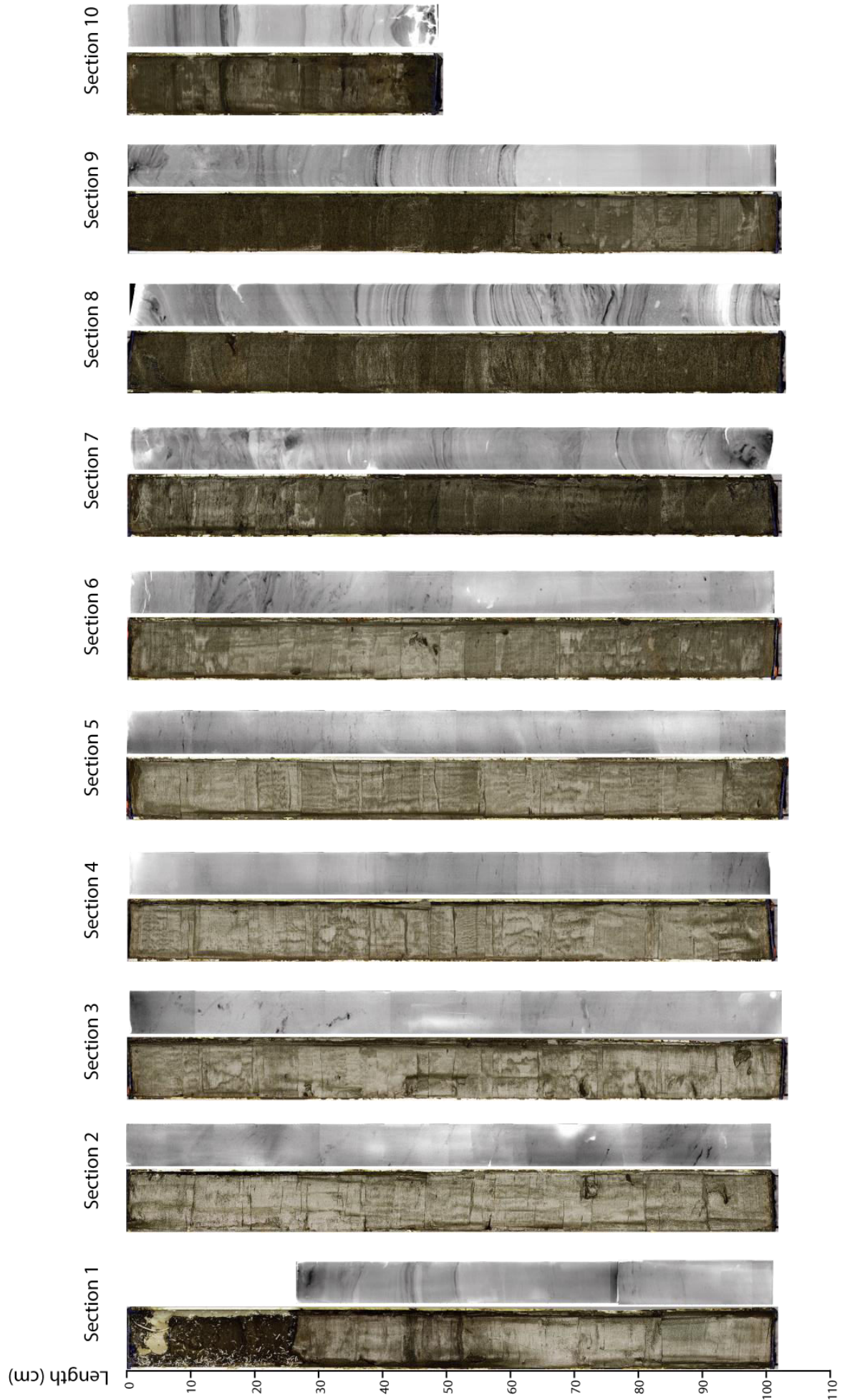
**Core: KAT-12-14**

Cruise: ATACAMES  
 Date: 23-Jan-2012  
 Latitude: 01° 54.048' S  
 Longitude: 81° 28.814' W  
 Water depth: 3709 m

Core length: 9.47 m  
 Site: Ecuadorian trench,  
 about 35 km northward of  
 the Santa Elena canyon

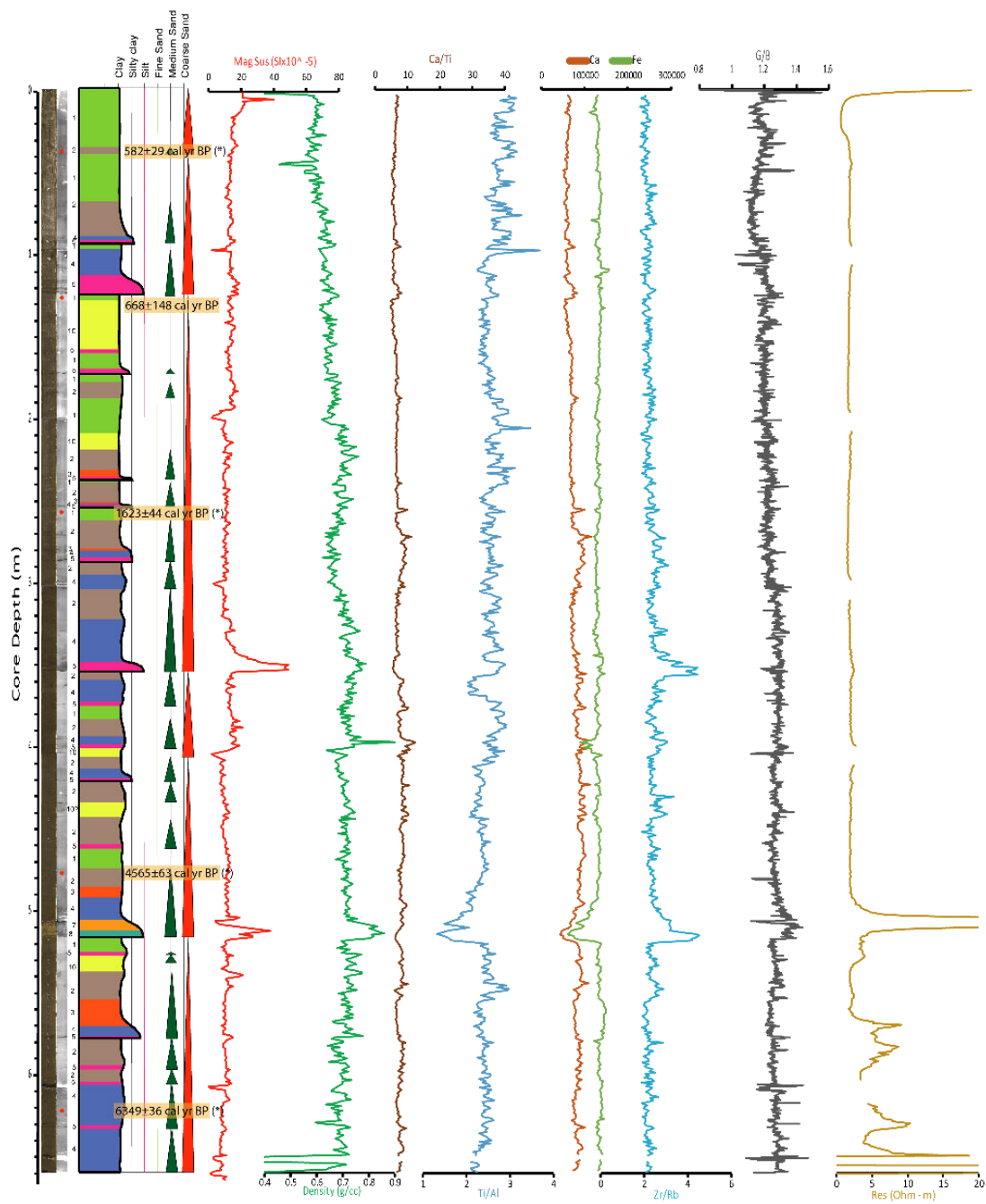
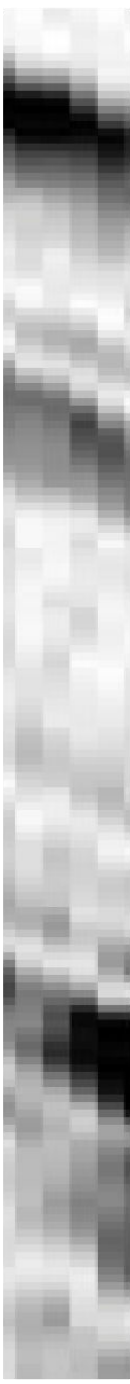


KAT-12-14





**Core: KAT-12-15**  
 Cruise: ATACAMES  
 Date: 23-Jan-2012  
 Latitude: 01° 40.824' S  
 Longitude: 81° 16.853' W  
 Water depth: 2324 m  
 Core length: 6.50 m  
 Site: on a slope basin of the  
 Ecuadorian trench about 50 km north  
 of the Santa Elena canyon



(\*) Ages from Durand (2014)

Good quality ages  
 Poor quality ages

**Hemipelagites**  
 Facies 1 (P)  
**Carbonate ooze**  
 Facies 11

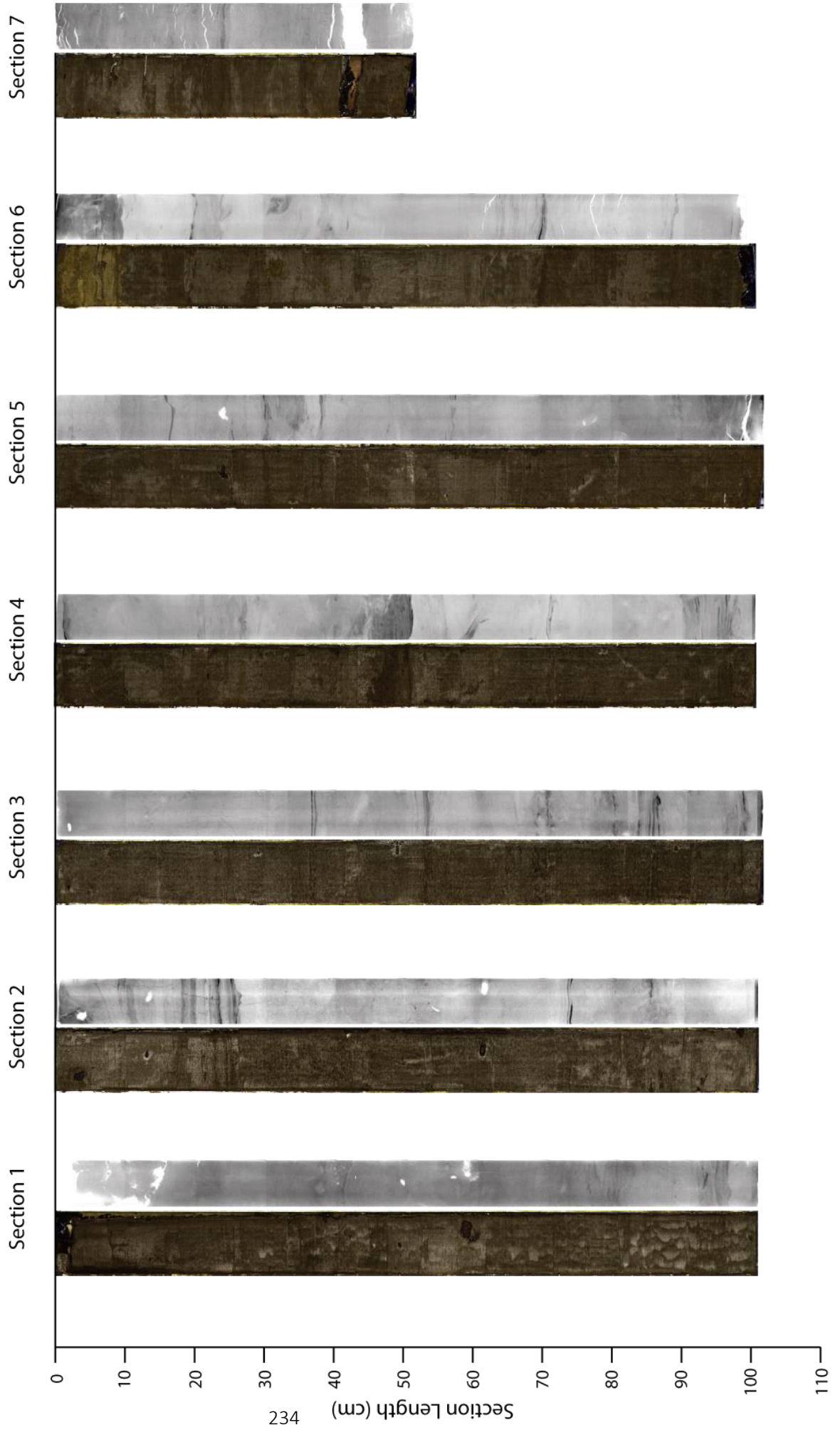
**Mud turbidites**  
 Facies 2 (T6-T7-T8)  
 Facies 3 (T5)  
 Facies 4 (T4)  
 Facies 5 (T2-T3)  
 Facies 6 (T0-T2)

**Volcanoclastic turbidites**  
 Facies 7 (T4-T6)  
 Facies 8 (T2-T3)  
**Mass transport deposits**  
 Facies 9 debris flow  
 Facies 10 slump

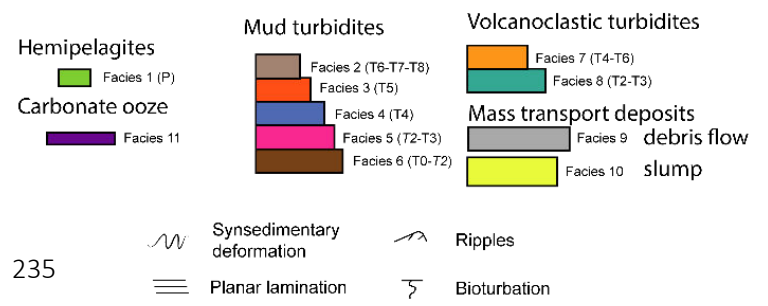
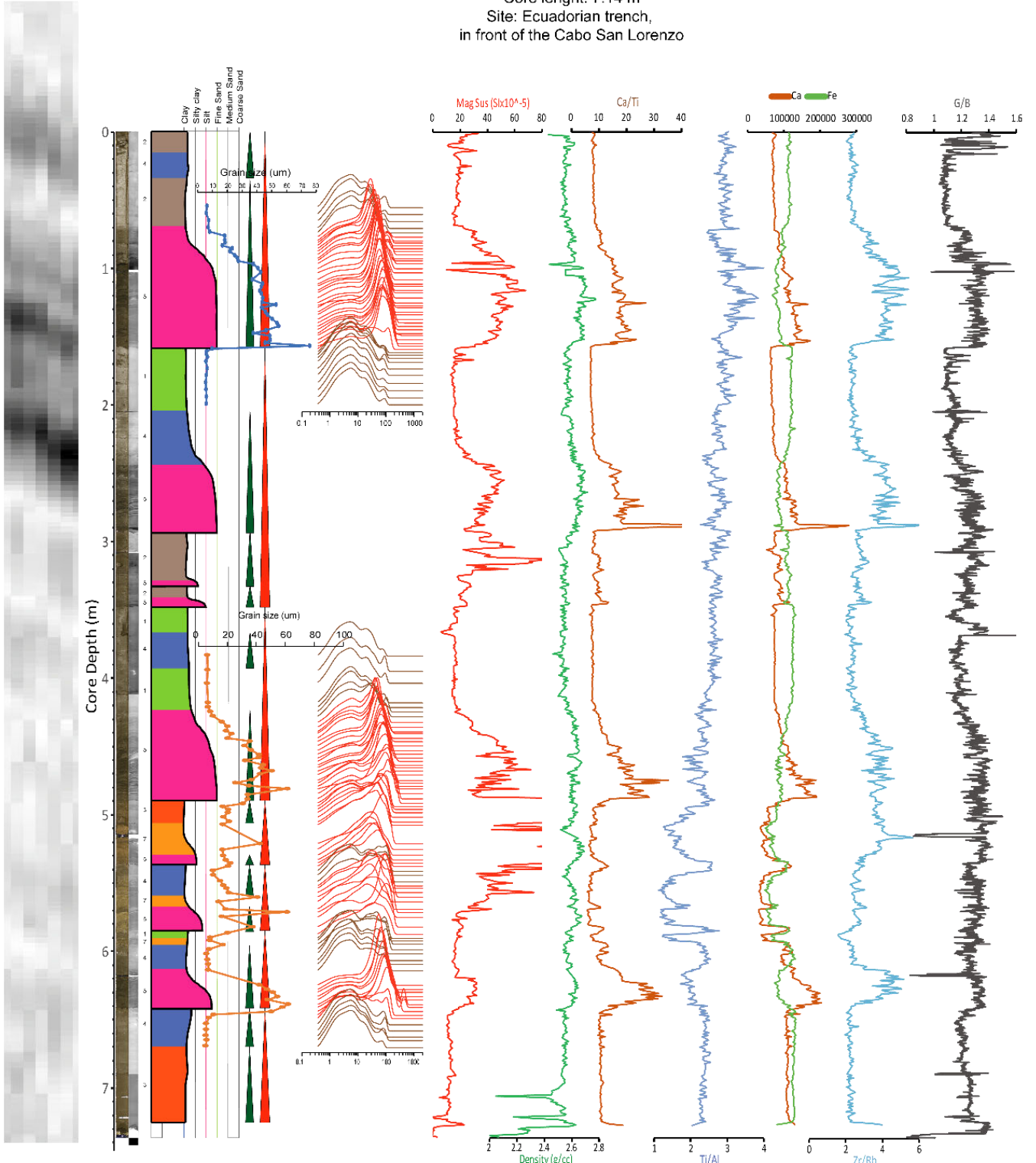
Synsedimentary deformation  
 Ripples  
 Planar lamination  
 Bioturbation



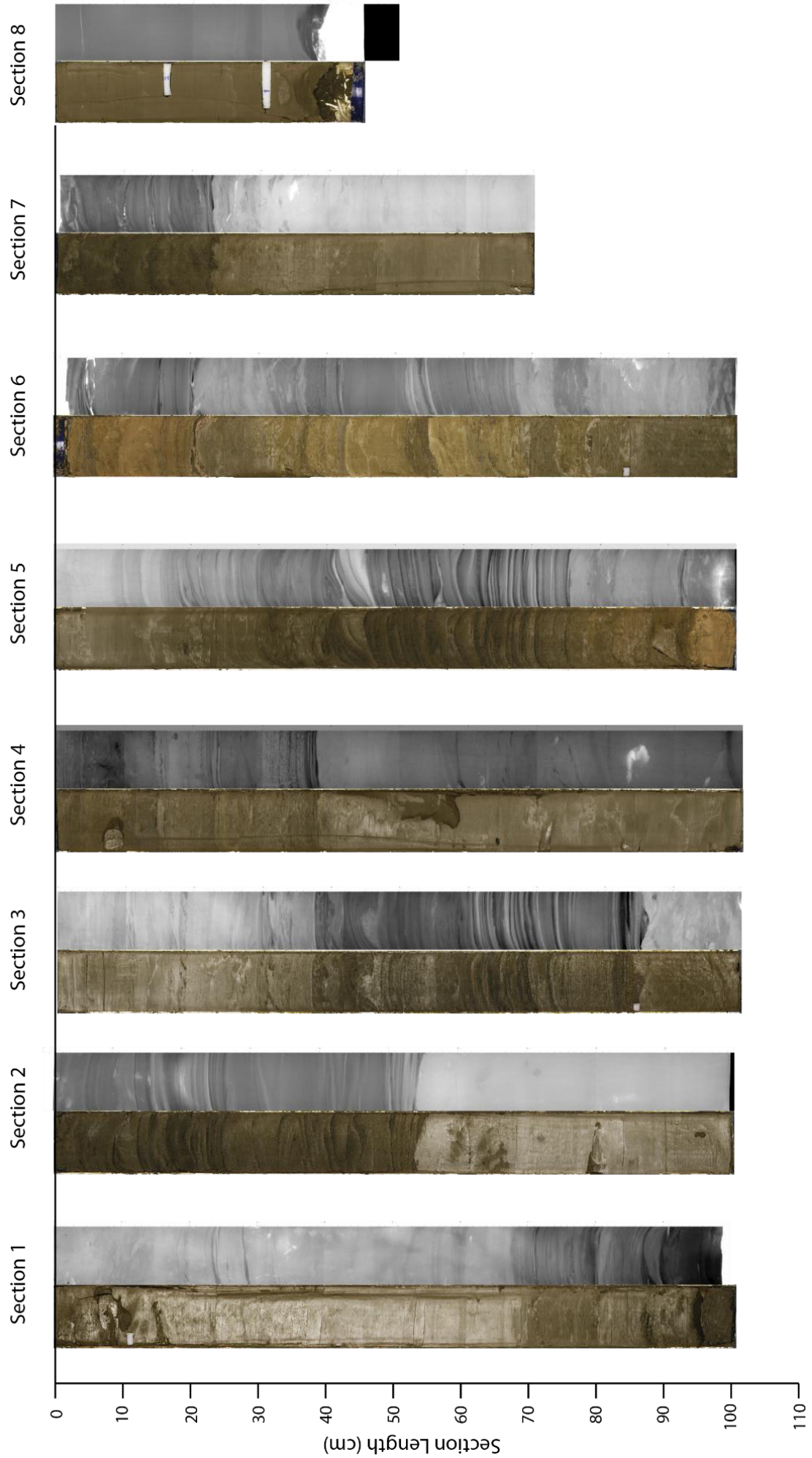
KAT-12-15



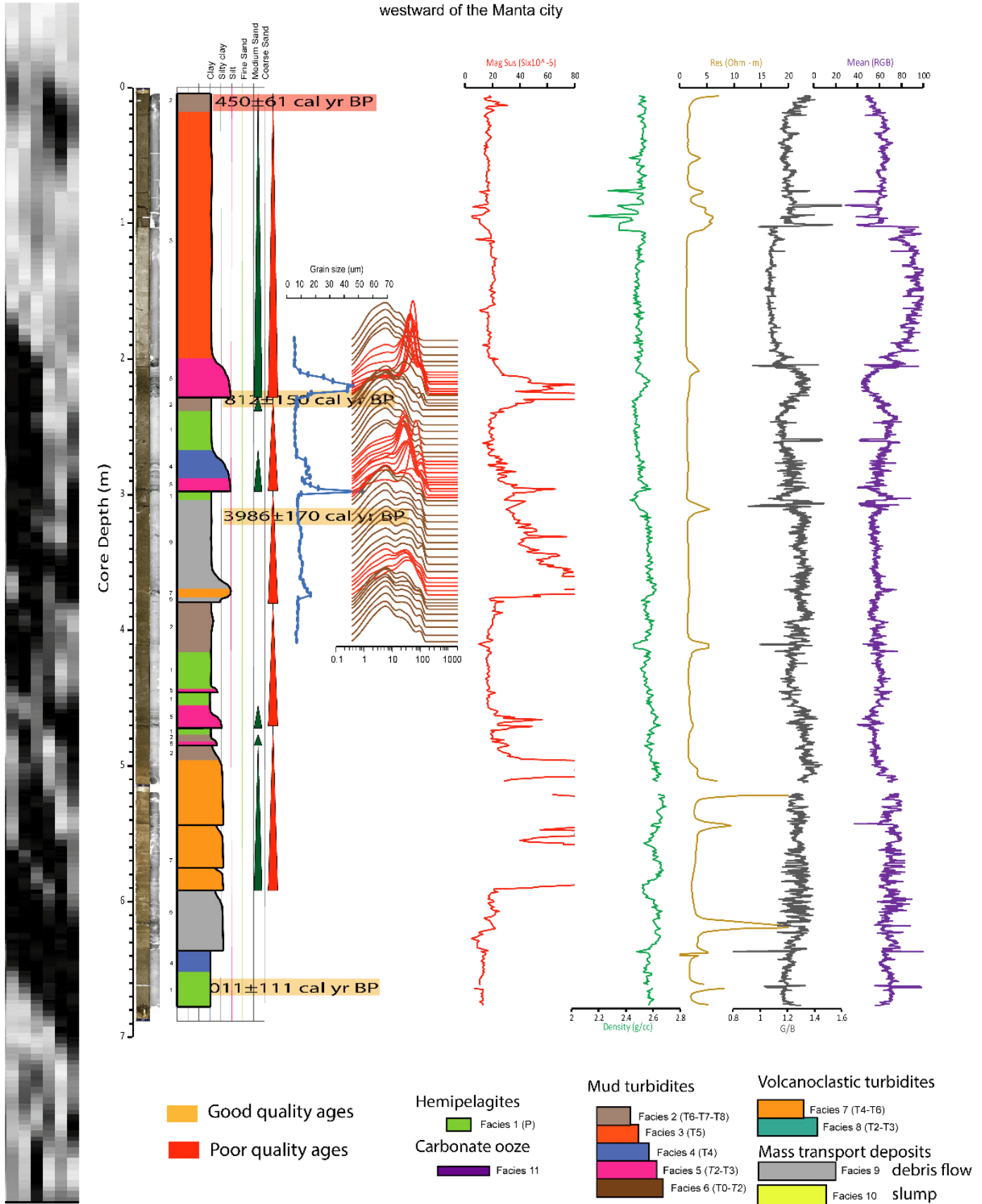
**Core: KAT-12-16**  
 Cruise: ATACAMES  
 Date: 24-Jan-2012  
 Latitude: 01° 06.481' S  
 Longitude: 81° 20.998' W  
 Water depth: 3238 m  
 Core length: 7.14 m  
 Site: Ecuadorian trench,  
 in front of the Cabo San Lorenzo



KAT-12-16



**Core: KAT-12-17**  
 Cruise: ATACAMES  
 Date: 24-Jan-2012  
 Latitude: 00° 49.530' S  
 Longitude: 81° 17.330' W  
 Water depth: 3324 m  
 Core length: 6.71 m  
 Site: Ecuadorian trench,  
 westward of the Manta city



Good quality ages  
 Poor quality ages

Hemipelagites  
 Carbonate ooze

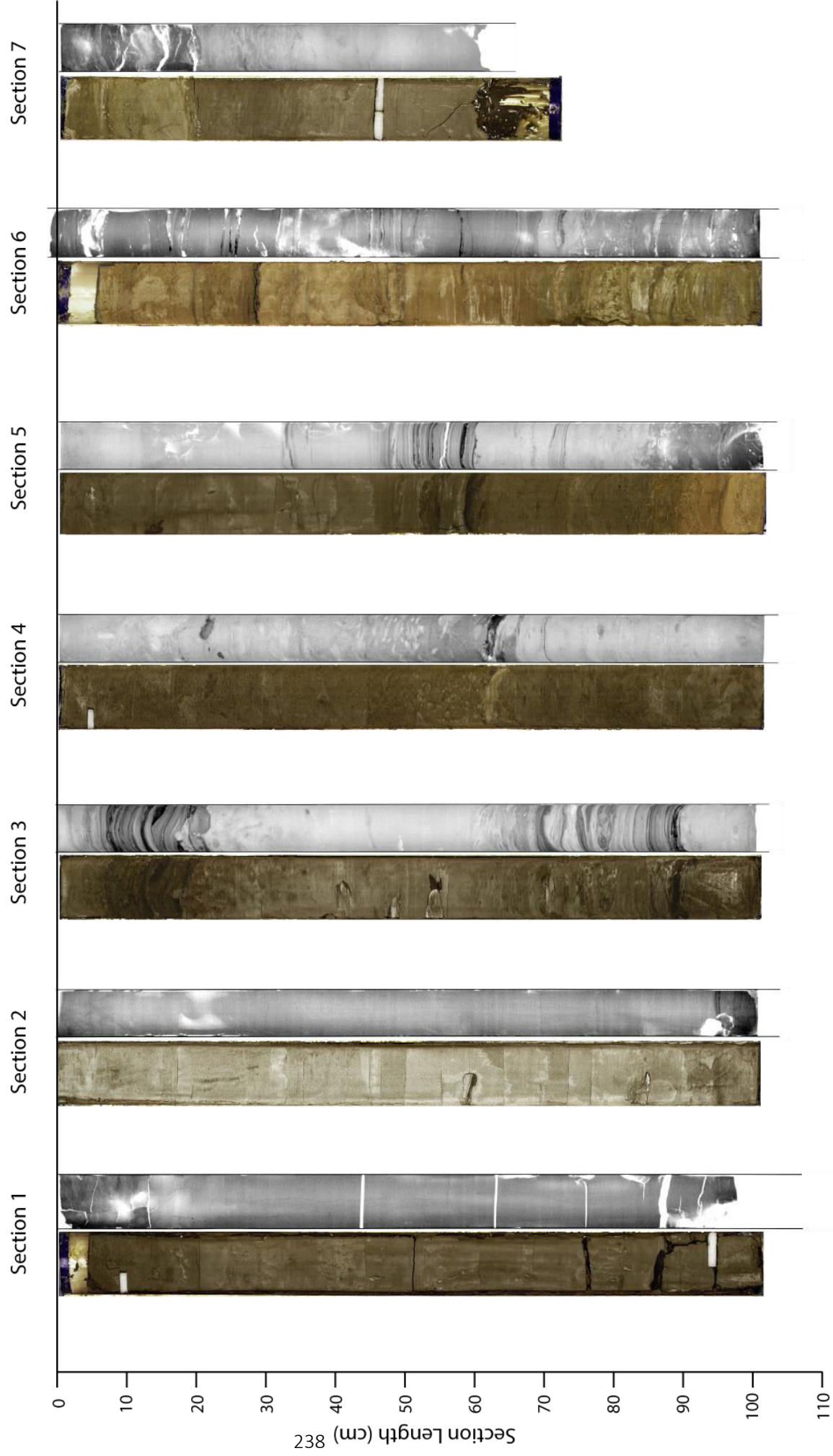
Mud turbidites  
 Facies 2 (T6-T7-T8)  
 Facies 3 (T5)  
 Facies 4 (T4)  
 Facies 5 (T2-T3)  
 Facies 6 (T0-T2)

Volcanoclastic turbidites  
 Facies 7 (T4-T6)  
 Facies 8 (T2-T3)  
 Mass transport deposits  
 debris flow  
 slump  
 Facies 9  
 Facies 10

Symsedimentary deformation  
 Planar lamination  
 Ripples  
 Bioturbation



KAT-12-17

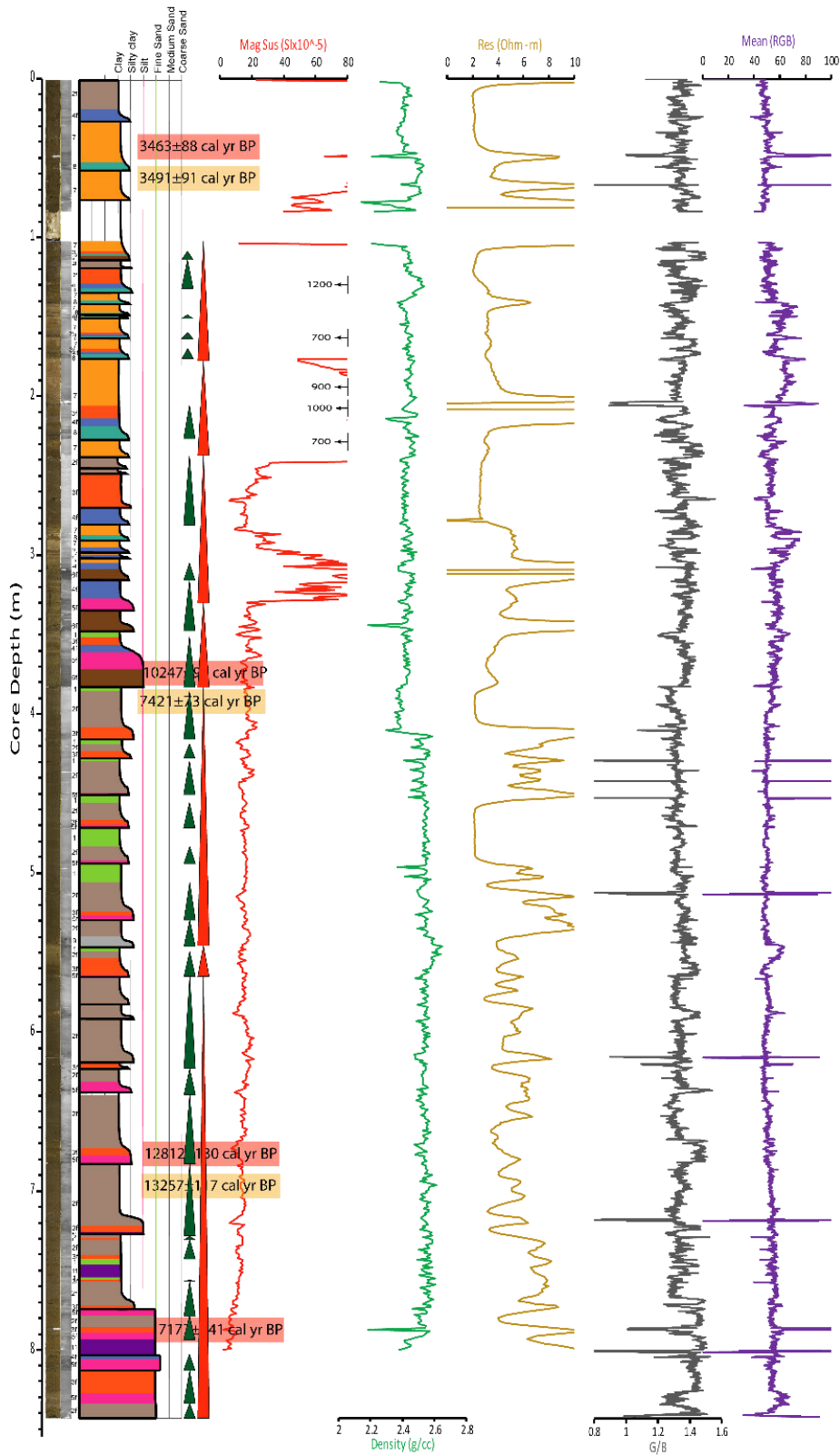




**Core: KAT-12-18**

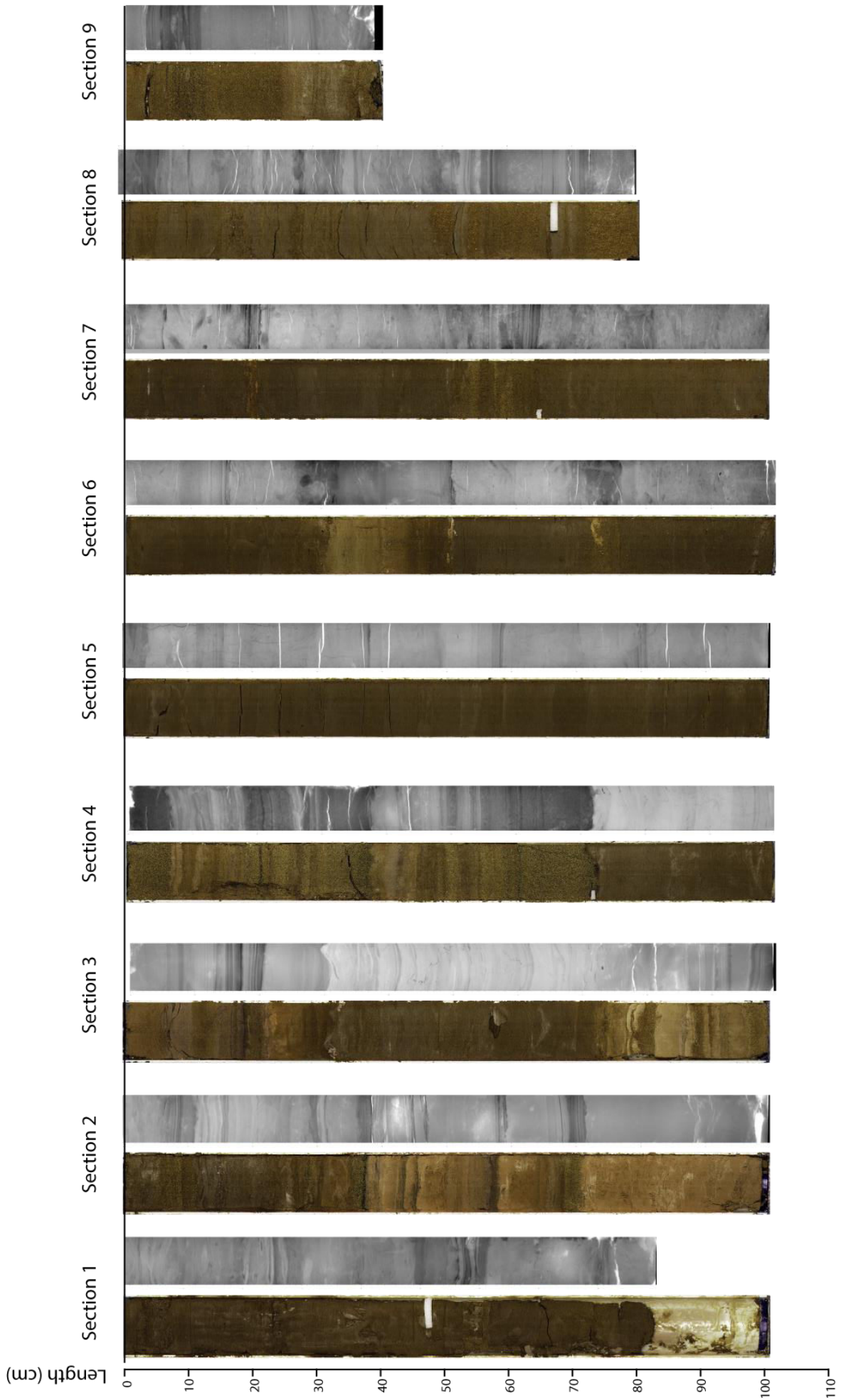
Cruise: ATACAMES  
 Date: 24-Jan-2012  
 Latitude: 00° 37.196' S  
 Longitude: 81° 04.839' W  
 Water depth: 1606 m

Core length: 8.20 m  
 Site: on a slope basin  
 of the Ecuadorian trench,  
 near to an ancient canyon

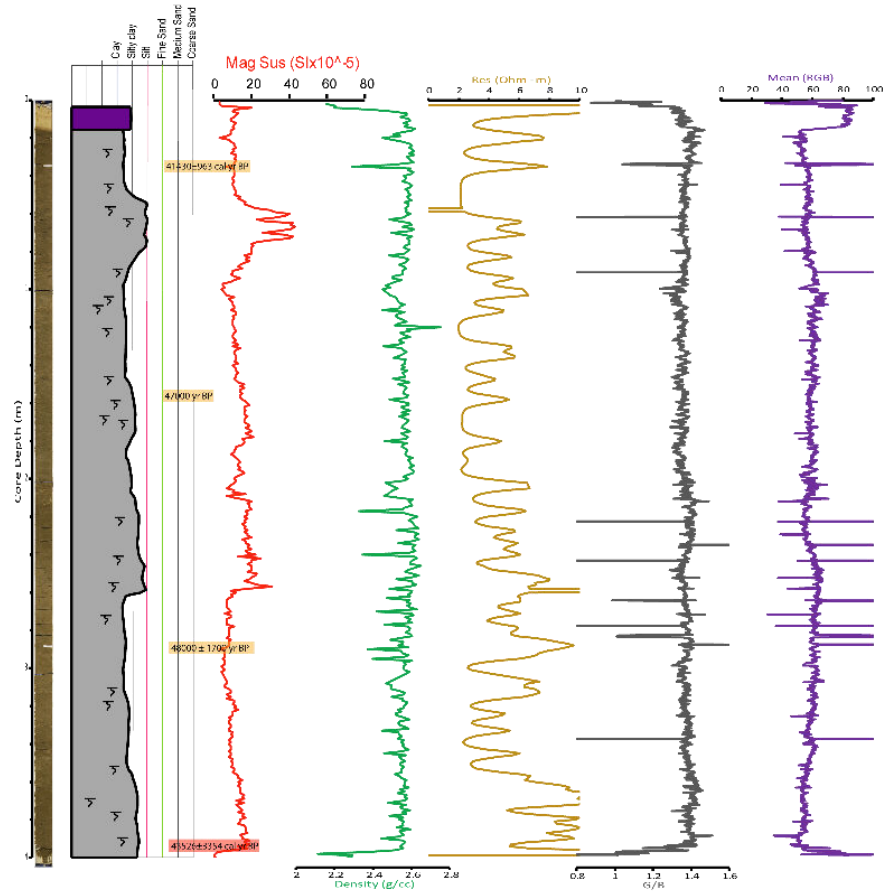


Good quality ages	Poor quality ages	Hemipelagites Facies 1 (P)	Mud turbidites Facies 2 (T6-T7-T8) Facies 3 (T5) Facies 4 (T4) Facies 5 (T2-T3) Facies 6 (T0-T2)	Volcanoclastic turbidites Facies 7 (T4-T6) Facies 8 (T2-T3)
Synsedimentary deformation	Planar lamination	Carbonate ooze Facies 11	Mass transport deposits debris flow	Facies 10 slump
Ripples	Bioturbation			

KAT-12-18



**Core: KAT-12-19**  
 Cruise: ATACAMES  
 Date: 25-Jan-2012  
 Latitude: 00° 16.008' S  
 Longitude: 81° 05.926' W  
 Water depth: 3179 m  
 Core length: 4 m  
 Site: Ecuadorian trench,  
 in front of the Cabo Pasado  
 in the continent



Good quality ages  
 Poor quality ages

Hemipelagites

Facies 1 (P)

Carbonate ooze

Facies 11

Mud turbidites

Facies 2 (T6-T7-T8)

Facies 3 (T5)

Facies 4 (T4)

Facies 5 (T2-T3)

Facies 6 (T0-T2)

Volcanoclastic turbidites

Facies 7 (T4-T6)

Facies 8 (T2-T3)

Mass transport deposits

Facies 9 debris flow

Facies 10 slump

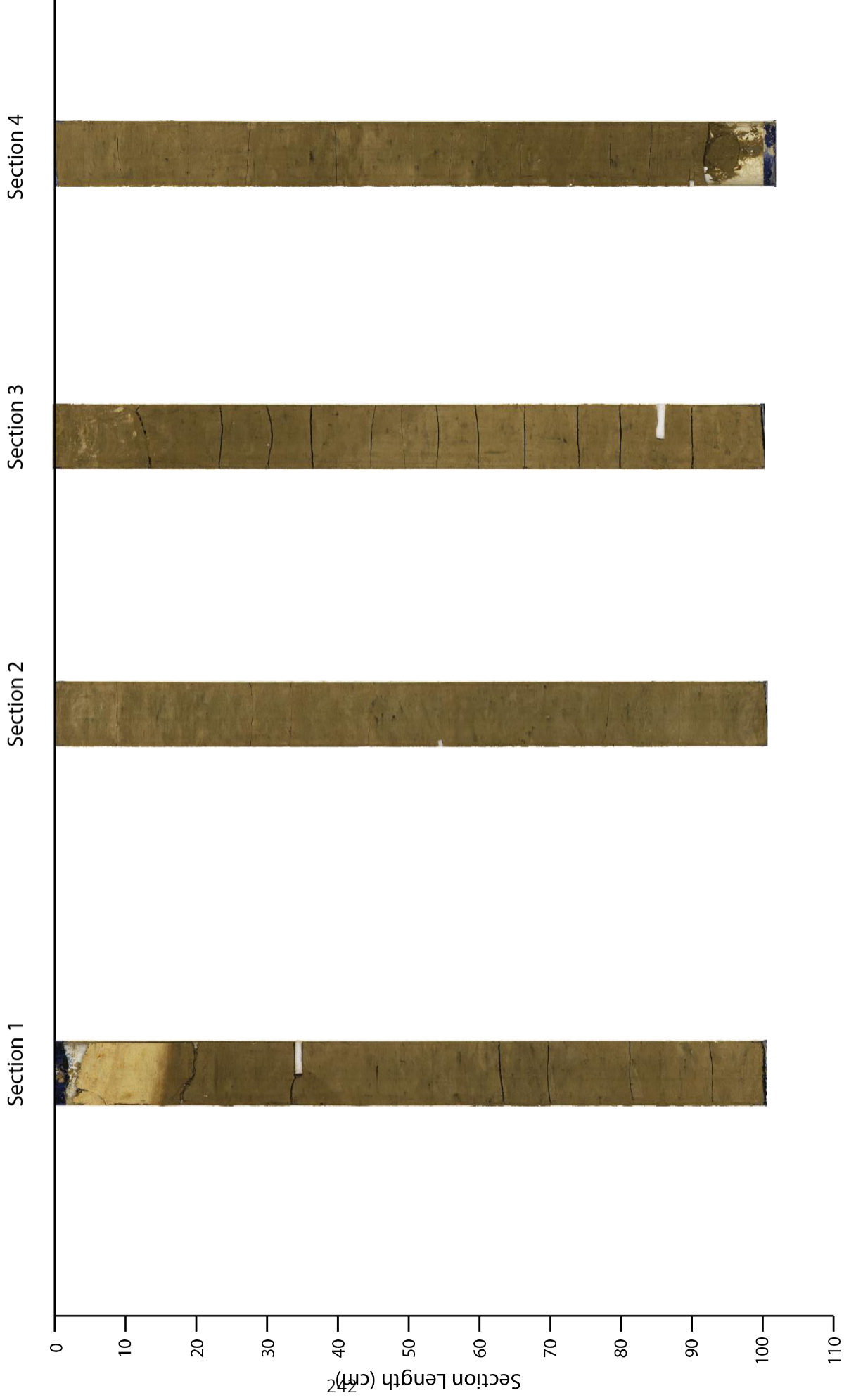
Synsedimentary deformation

Ripples

Planar lamination

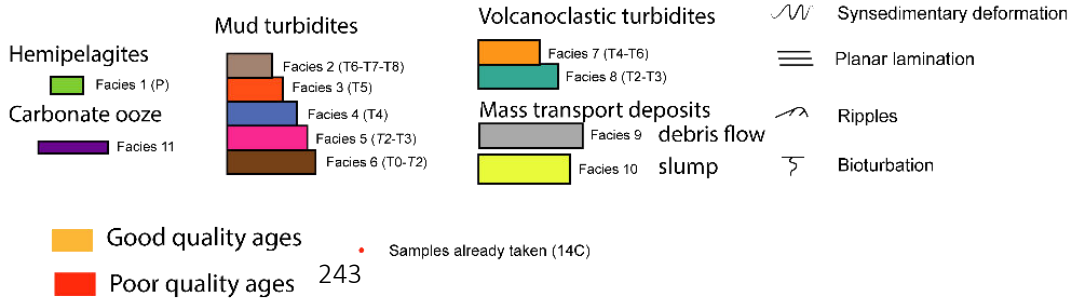
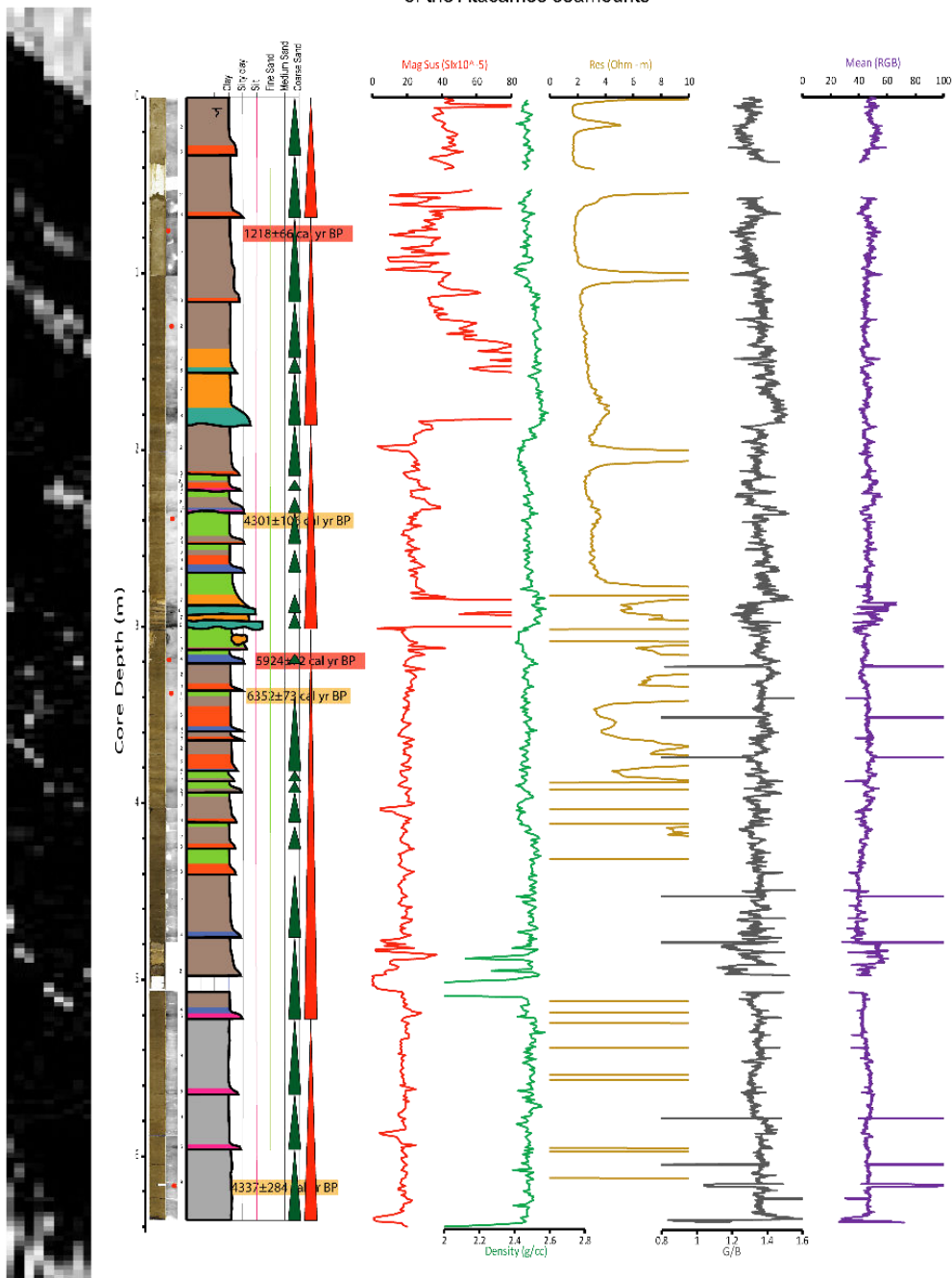
Bioturbation

KAT-12-19



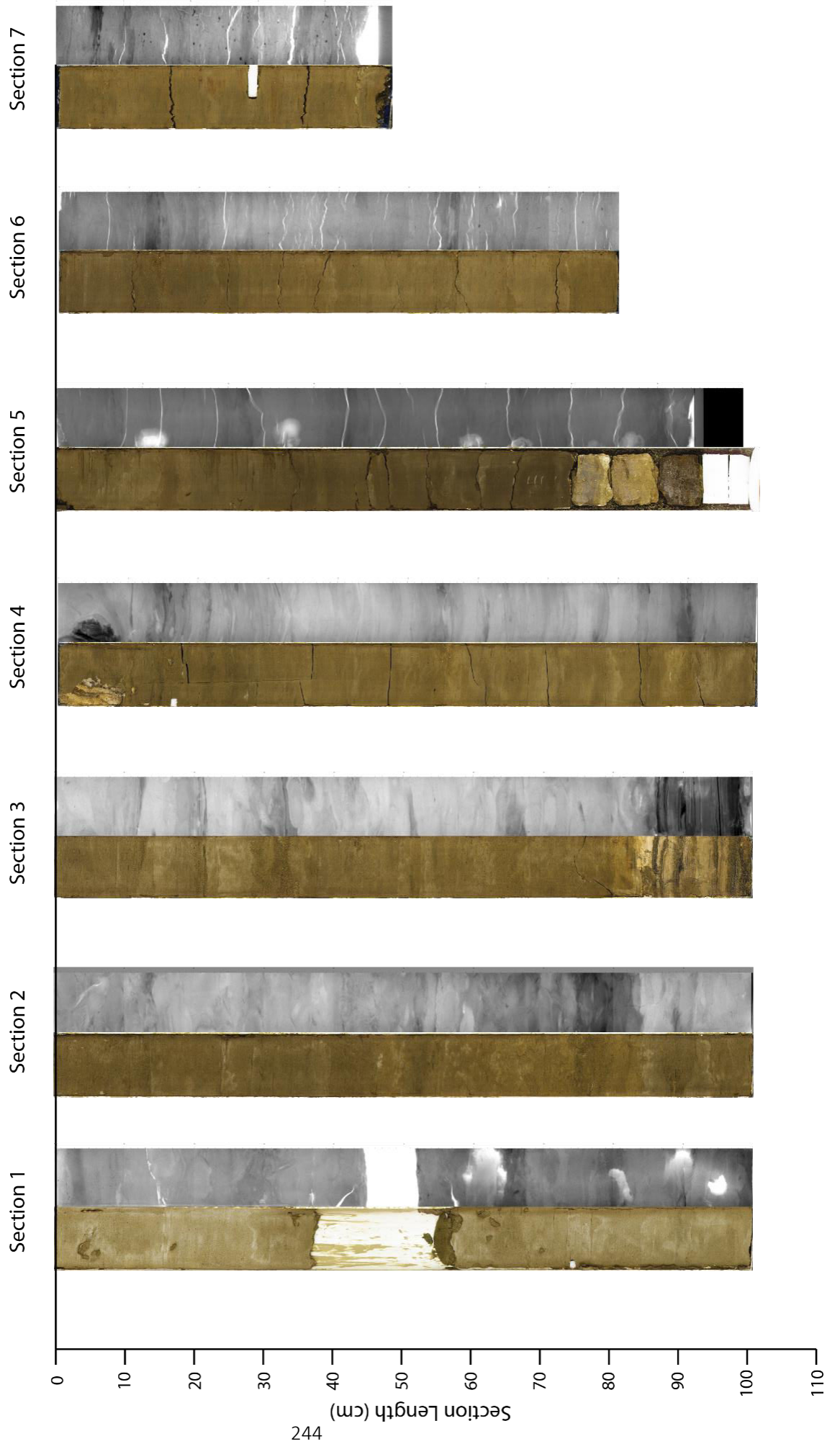
# Core: KAT-12-20

Cruise: ATACAMES  
 Date: 25-Jan-2012  
 Latitude: 00° 00.696' N  
 Longitude: 80° 49.506' W  
 Water depth: 1918 m  
 Core length: 6.28 m  
 Site: on a slope basin  
 of the Ecuadorian trench,  
 about 20 km southward  
 of the Atacames seamounts





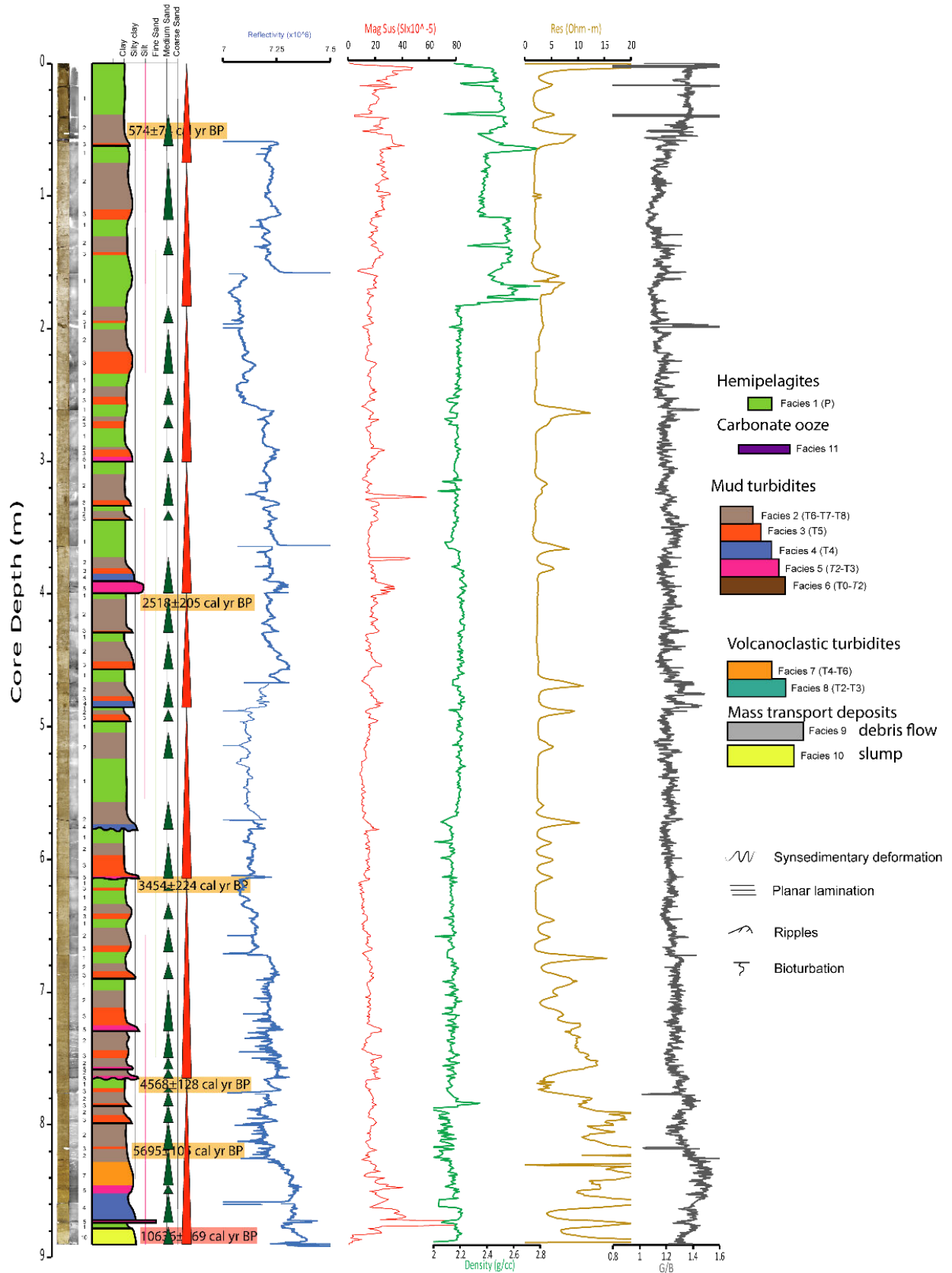
KAT-12-20



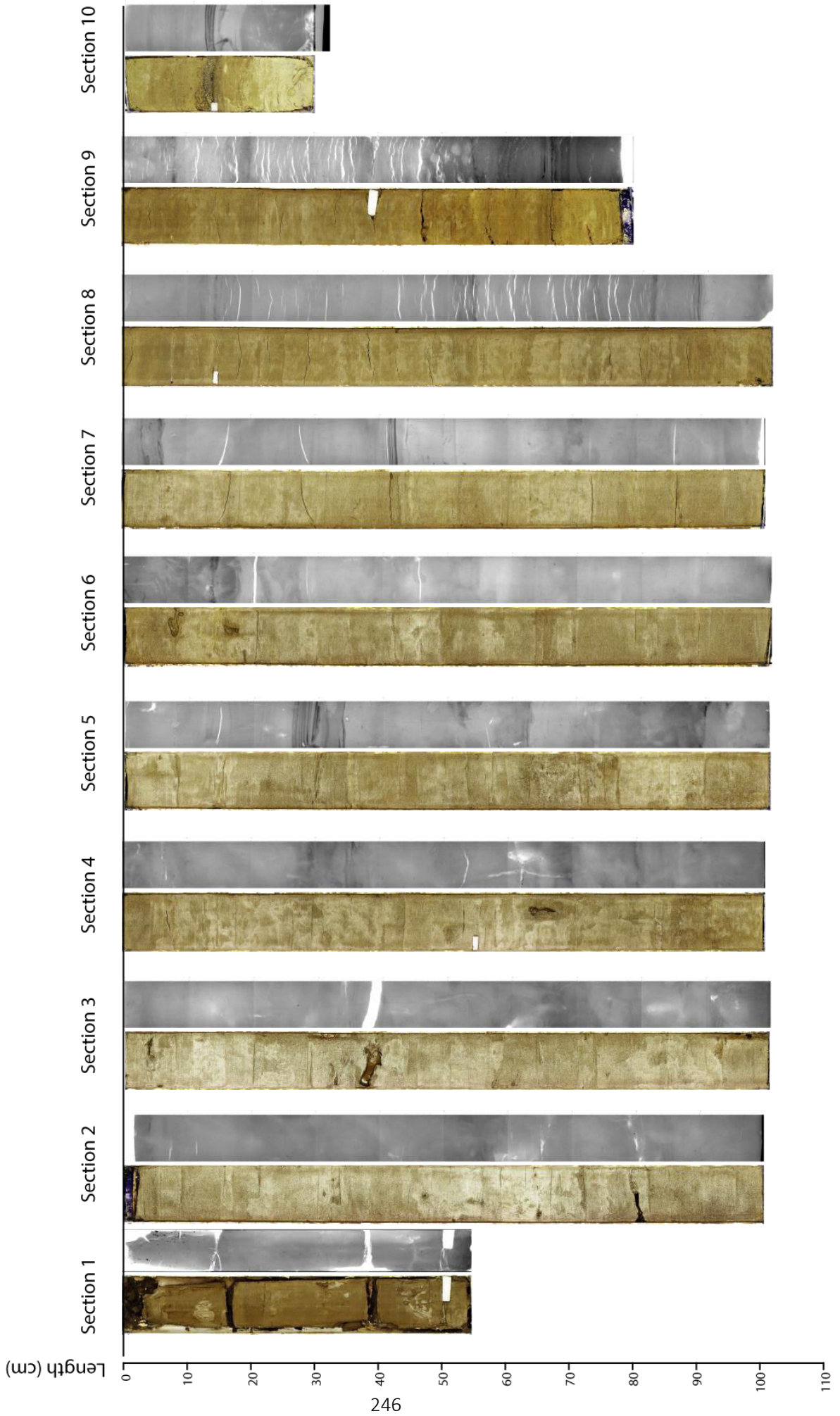
# Core: KAT-12-21

Cruise: ATACAMES  
 Date: 25-Jan-2012  
 Latitude: 00° 39.819'N  
 Longitude: 80° 38.922'W

Water depth: 3802 m  
 Core length: 8.63 m  
 Site: Ecuadorian trench,  
 on the Atacames basin



KAT-12-21



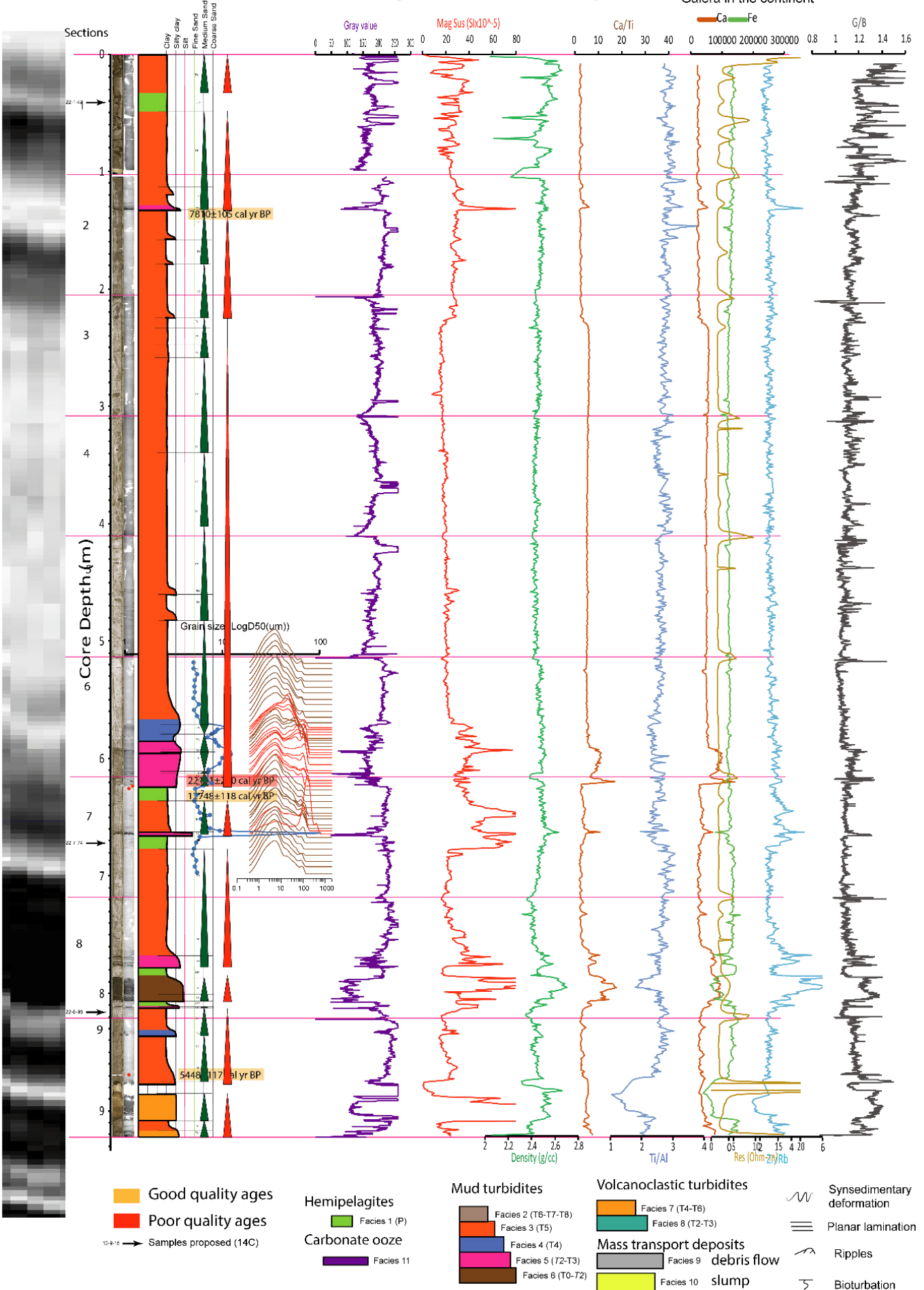


**Core: KAT-12-22**

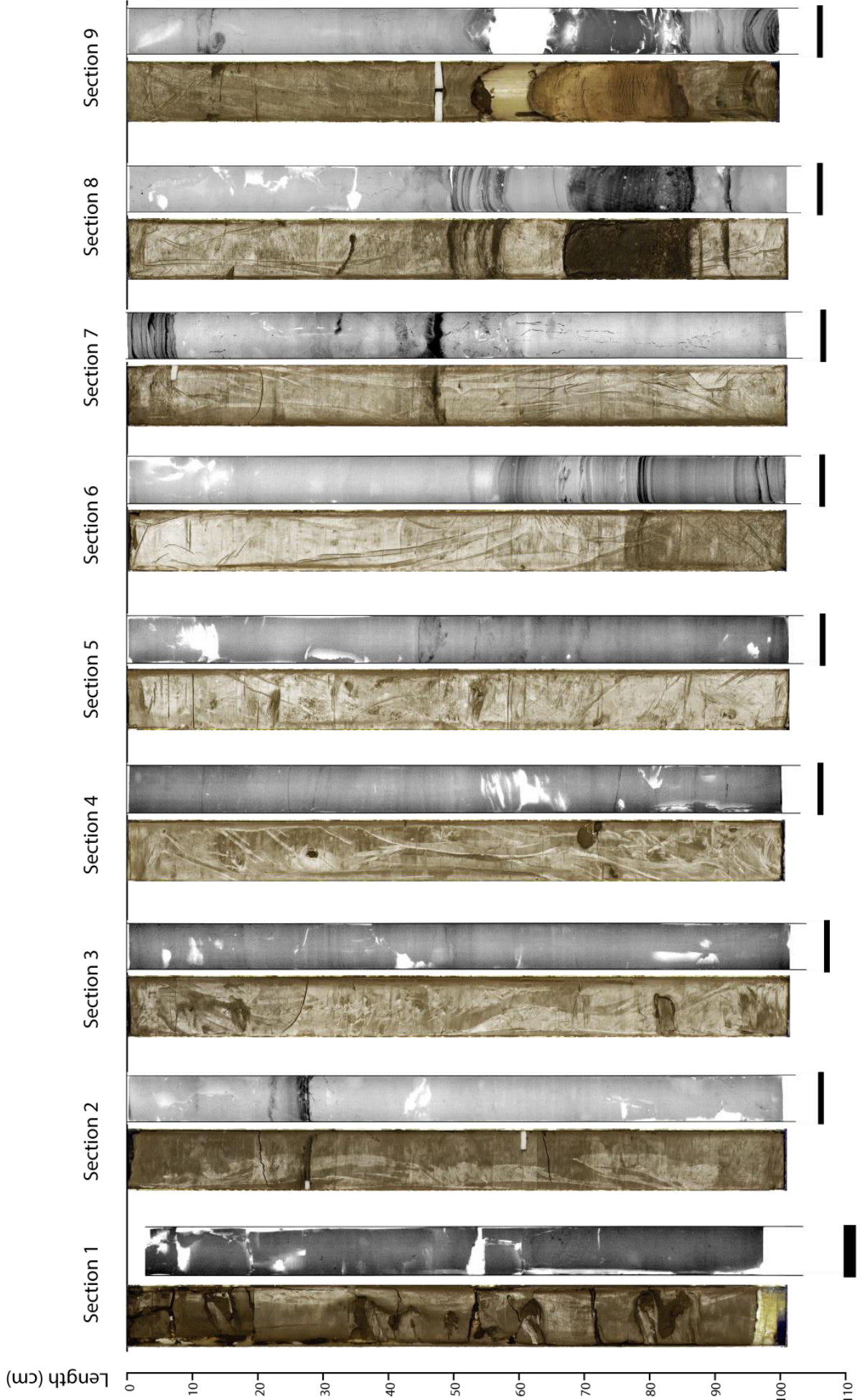
Cruise: ATACAMES Latitude: 00° 59.686' N  
 Date: 26-Jan-2012 Longitude: 80° 28.491' W

Water depth: 3962 m  
 Core length: 8.98 m

Site: Ecuadorian trench,  
 in front of the Punta  
 Galera in the continent



KAT-12-22



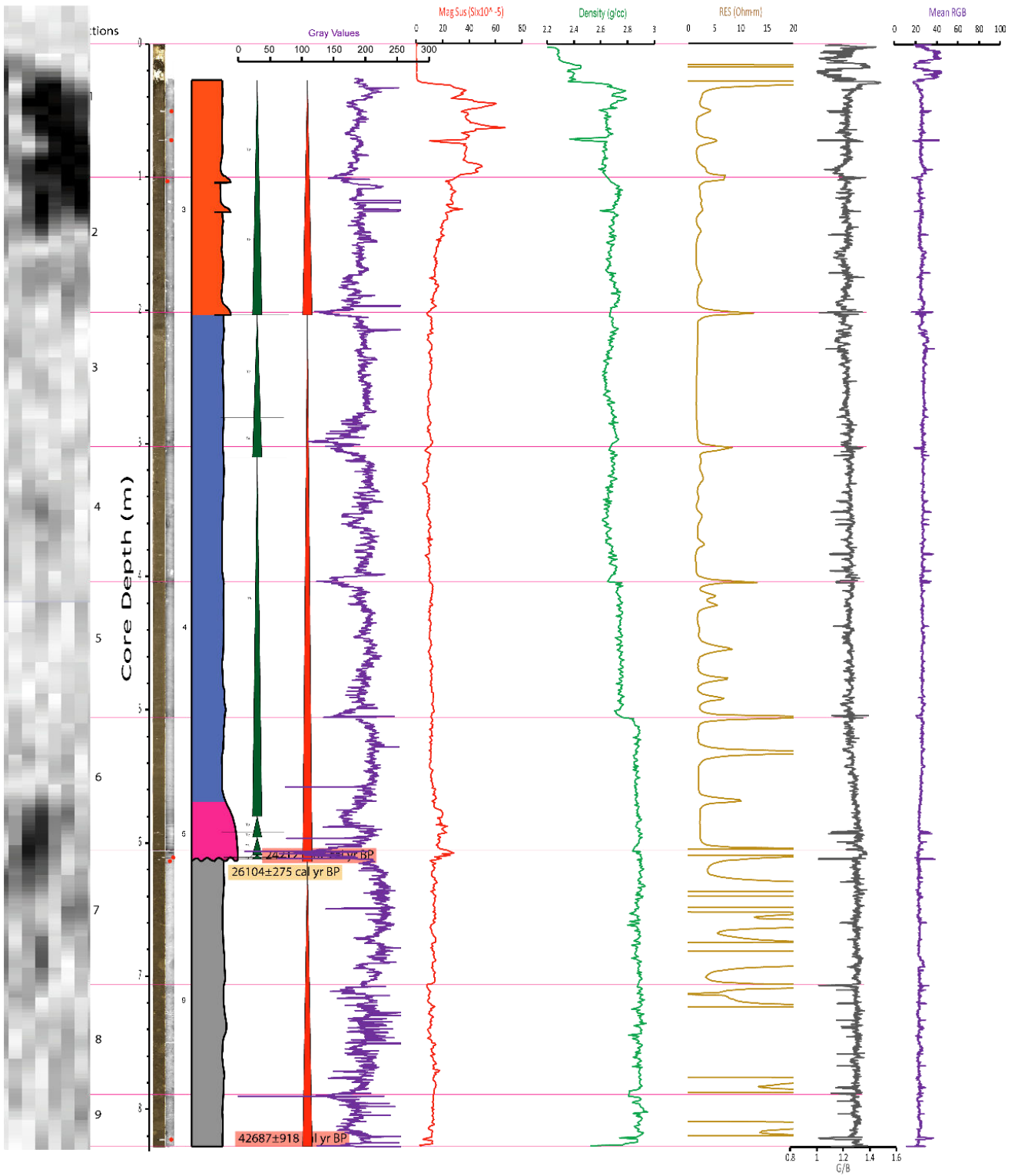


# Core: KAT-12-23

Cruise: ATACAMES  
 Date: 26-Jan-2012  
 Latitude: 01° 16.387' N  
 Longitude: 80° 20.206' W  
 Water depth: 3973 m  
 Core length: 8.18 m

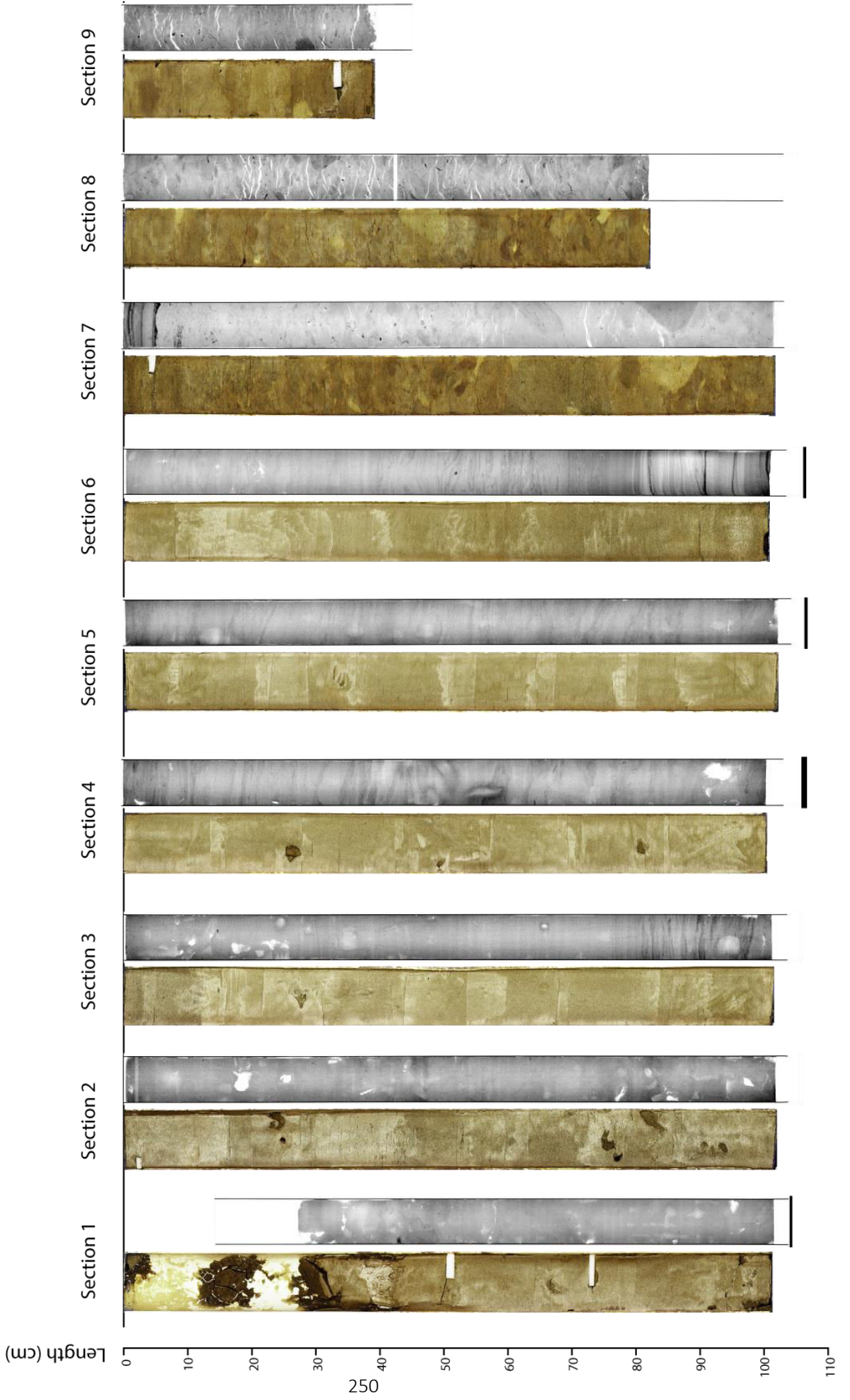
Site: Ecuadorian trench,  
 about 10 km southward  
 of the Galeras seamounts

KAT-12-23



- |   |   |  |  |   |
|---|---|--|--|---|
| <span style="display:inline-block; width:15px; height:15px; background-color:orange; border:1px solid black;"></span> Good quality ages         | <span style="display:inline-block; width:15px; height:15px; background-color:lightgreen; border:1px solid black;"></span> Hemipelagites<br>Facies 1 (P) | <span style="display:inline-block; width:15px; height:15px; background-color:lightblue; border:1px solid black;"></span> Mud turbidites<br>Facies 2 (T6-T7-T8) | <span style="display:inline-block; width:15px; height:15px; background-color:lightorange; border:1px solid black;"></span> Volcanoclastic turbidites<br>Facies 7 (T4-T6) | <span style="display:inline-block; width:15px; height:15px; border-bottom:1px solid black;"></span> Synsedimentary deformation    |
| <span style="display:inline-block; width:15px; height:15px; background-color:red; border:1px solid black;"></span> Poor quality ages            | <span style="display:inline-block; width:15px; height:15px; background-color:purple; border:1px solid black;"></span> Carbonate ooze<br>Facies 11       | <span style="display:inline-block; width:15px; height:15px; background-color:lightred; border:1px solid black;"></span> Facies 3 (T5)                          | <span style="display:inline-block; width:15px; height:15px; background-color:lightgreen; border:1px solid black;"></span> Facies 8 (T2-T3)                               | <span style="display:inline-block; width:15px; height:15px; border-bottom:3px double black;"></span> Planar lamination            |
| <span style="display:inline-block; width:15px; height:15px; background-color:gray; border:1px solid black;"></span> Samples already taken (14C) |   | <span style="display:inline-block; width:15px; height:15px; background-color:blue; border:1px solid black;"></span> Facies 4 (T4)                              | <span style="display:inline-block; width:15px; height:15px; background-color:gray; border:1px solid black;"></span> Mass transport deposits<br>Facies 9                  | <span style="display:inline-block; width:15px; height:15px; border:1px solid black; border-radius:50%;"></span> Pebbles (1-10 cm) |
|   |   | <span style="display:inline-block; width:15px; height:15px; background-color:lightblue; border:1px solid black;"></span> Facies 5 (T2-T3)                      | <span style="display:inline-block; width:15px; height:15px; background-color:yellow; border:1px solid black;"></span> debris flow<br>Facies 10                           | <span style="display:inline-block; width:15px; height:15px; border:1px solid black; border-radius:50%;"></span> Bioturbation      |
|   |   | <span style="display:inline-block; width:15px; height:15px; background-color:lightblue; border:1px solid black;"></span> Facies 6 (T0-T2)                      | <span style="display:inline-block; width:15px; height:15px; background-color:yellow; border:1px solid black;"></span> slump  |   |

KAT-12-23

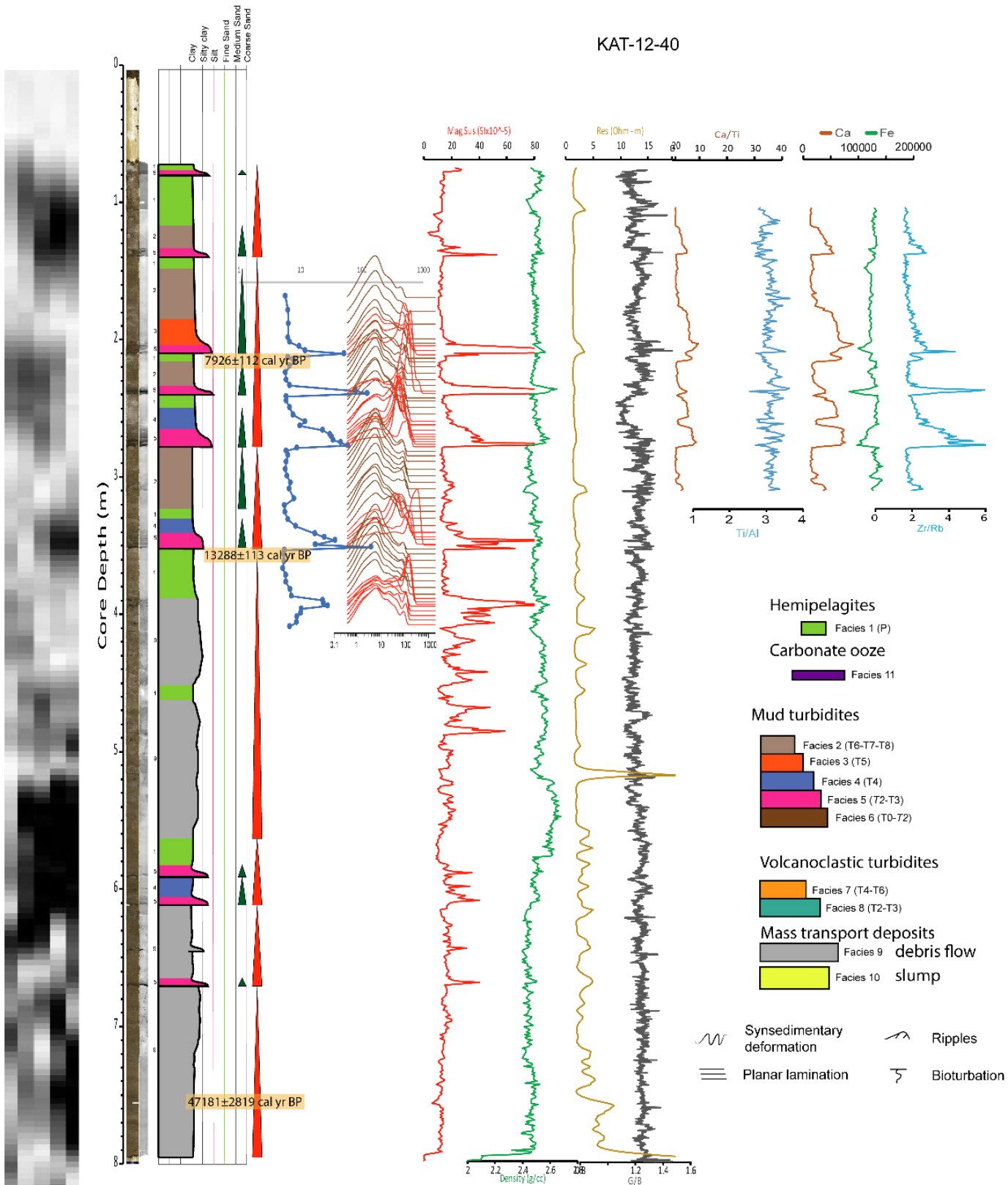


# Core: KAT-12-40

Cruise: ATACAMES  
 Date: 13-Feb-2012  
 Latitude: 03° 18.150' S  
 Longitude: 81° 44.185' W  
 Water depth: 4698 m

Site: Ecuadorian trench,  
 about 30 km southward  
 of the Guayaquil canyon

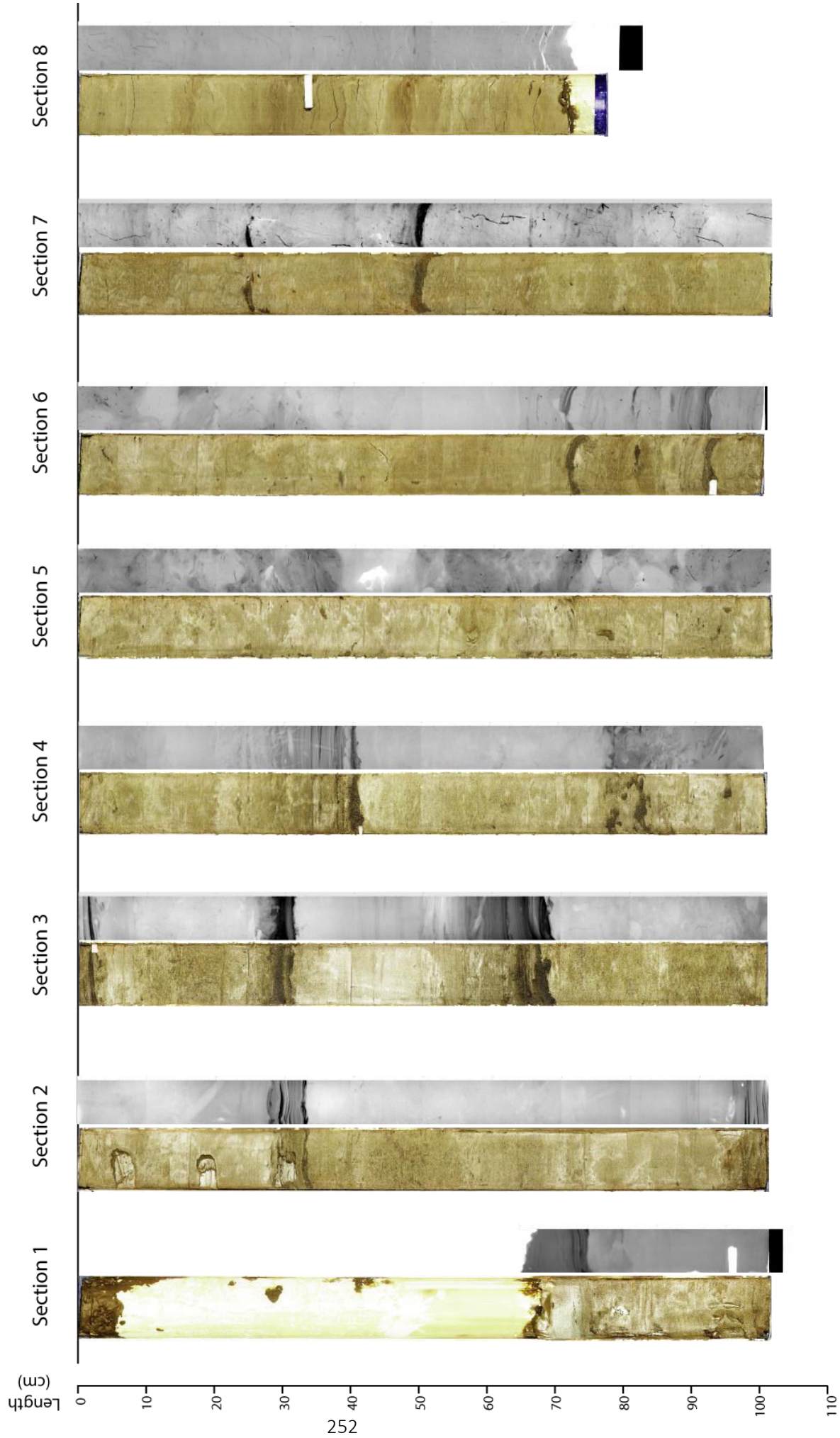
Core length: 7.77 m



Good quality ages  
 Poor quality ages



KAT-12-40

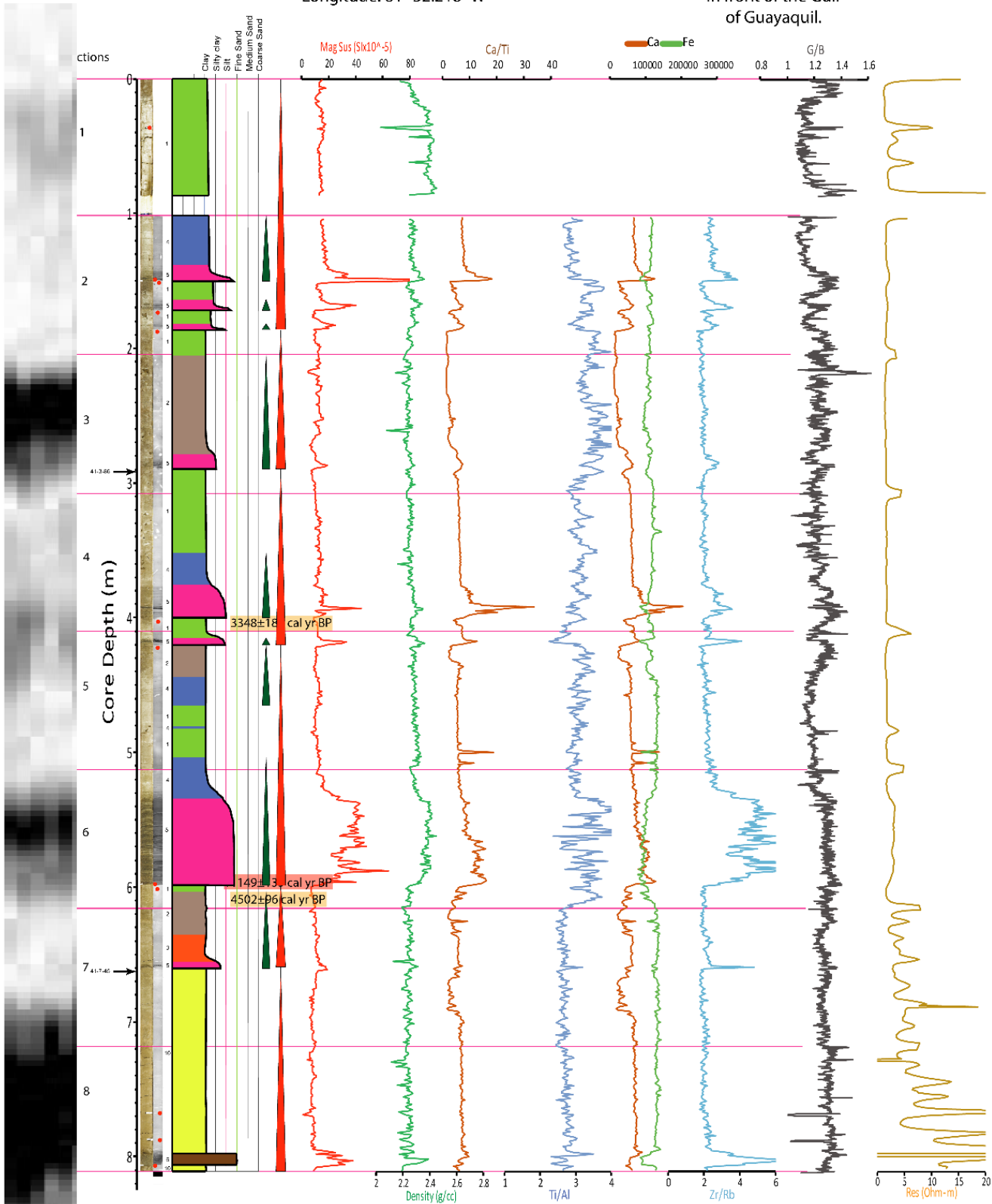


**Core: KAT-12-41**

Cruise: ATACAMES  
 Date: 14-Feb-2012  
 Latitude: 02° 45.555' S  
 Longitude: 81° 32.218' W

Water depth: 4422 m  
 Core length: 7.77 m

Site: Ecuadorian trench,  
 about 20 km north  
 of the Guayaquil canyon,  
 in front of the Gulf  
 of Guayaquil.

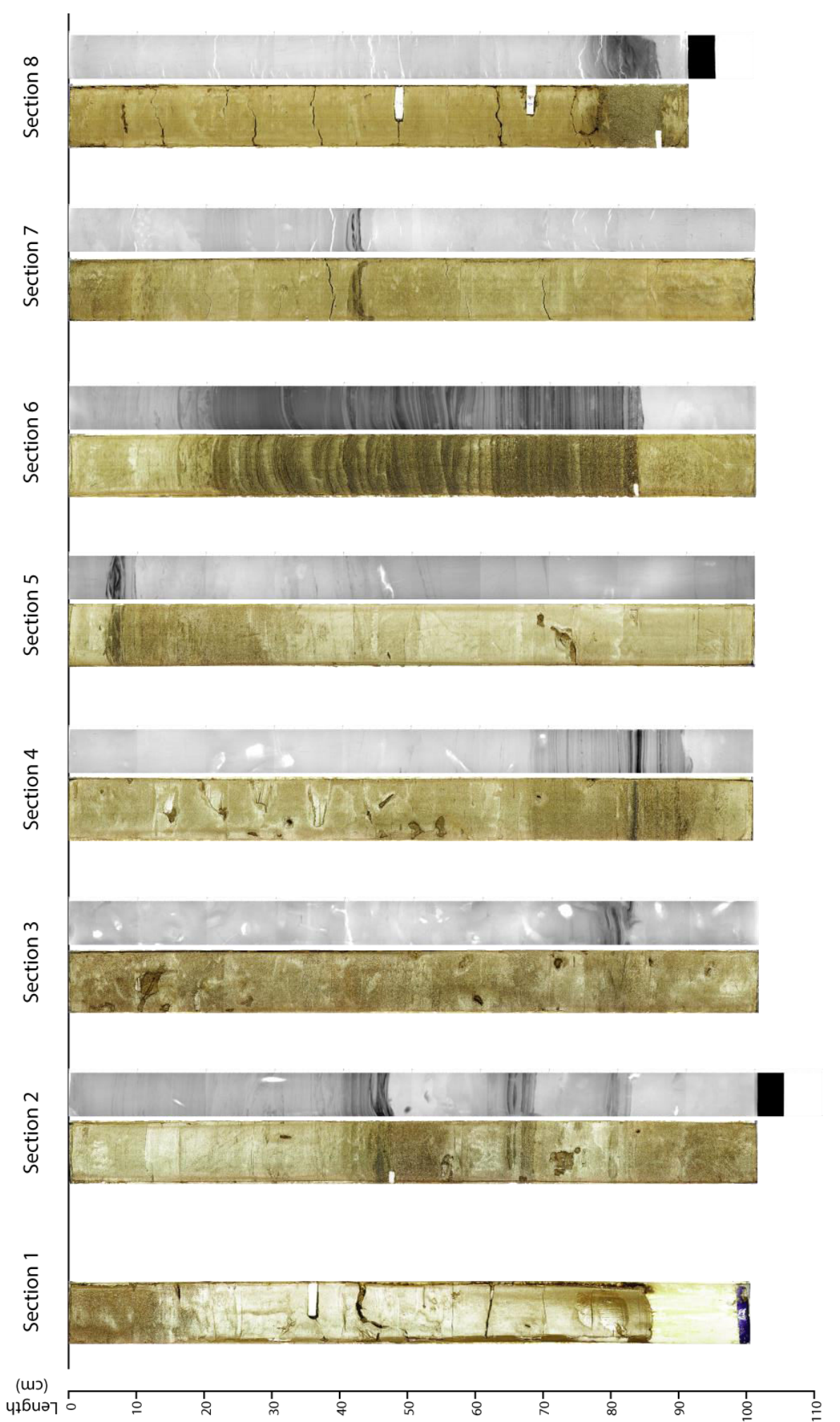


■ Good quality ages  
■ Poor quality ages  
● Samples already taken (14C)  
→ Samples proposed (14C)

<p><b>Hemipelagites</b></p> <ul style="list-style-type: none"> <li><span style="color: green;">■</span> Facies 1 (P)</li> </ul> <p><b>Carbonate ooze</b></p> <ul style="list-style-type: none"> <li><span style="color: purple;">■</span> Facies 11</li> </ul> <p> <span style="color: blue;">~</span> Synsedimentary deformation  <span style="color: blue;">≡</span> Planar lamination             </p>	<p><b>Mud turbidites</b></p> <ul style="list-style-type: none"> <li><span style="color: grey;">■</span> Facies 2 (T6-T7-T8)</li> <li><span style="color: orange;">■</span> Facies 3 (T5)</li> <li><span style="color: blue;">■</span> Facies 4 (T4)</li> <li><span style="color: pink;">■</span> Facies 5 (T2-T3)</li> <li><span style="color: brown;">■</span> Facies 6 (T0-T2)</li> </ul> <p> <span style="color: blue;">~</span> Ripples  <span style="color: blue;">∩</span> Bioturbation             </p>	<p><b>Volcanoclastic turbidites</b></p> <ul style="list-style-type: none"> <li><span style="color: orange;">■</span> Facies 7 (T4-T6)</li> <li><span style="color: green;">■</span> Facies 8 (T2-T3)</li> </ul> <p><b>Mass transport deposits</b></p> <ul style="list-style-type: none"> <li><span style="color: grey;">■</span> Facies 9 debris flow</li> <li><span style="color: yellow;">■</span> Facies 10 slump</li> </ul>
---	--	---



KAT-12-41



## Annexe 4: Age dating

Core	Sample's reference	Age (yr BP)	Error age BP	Cal yr BP age median (2-sigma) ( $\Delta R=29$ )	Error Age BP ( $\Delta R=29$ )	Location along core (m)
KAT-12-11	12-11-I*	13500	50	15631	247	0.815
	11-2*	12130	60	13558	167	1.840
	11-2-85	11175	45	12657	91	1.915
	11-3*	12970	50	14779	339	2.855
	11-4-43	13330	50	15412	213	3.525
	11-5-68	15210	60	17981	192	4.535
	11-6*	15790	70	18624	163	5.385
	12-11*	29570	220	33301	508	8.595
KAT-12-12	12-3*	10645	50	11924	240	2.480
	12-4-53	3615	45	3479	114	3.640
	12-7	7270	80	7717	159	6.680
	12-12	14140	50	16555	244	10.030
KAT-12-13	12-13-I*	2950	30	2704	63	0.920
	12-13*	35650	410	39762	953	2.770
KAT-12-14	14-1 @	1470	30	988	75	0.620
	14-2 @*	6330	30	6757	94	8.390
	14-3 @*	11740	45	13204	109	9.280
KAT-12-15	15-1 @*	1015	30	576	58	0.400
	15-2-27	1130	80	668	148	1.340
	15-2 @	2075	30	1614	85	2.170
	15-3 @	4425	30	4541	114	4.760
	15-4 @	5955	30	6339	68	6.190
KAT-12-16	16-1	1220	30	733	72	0.120
	16-3*	11510	60	12944	174	2.910
	16-3-87	2040	35	1587	99	2.940
	16-6	8735	35	9373	90	6.000
	12-16	12770	80	14423	380	7.180
KAT-12-17	17-1*	845	30	450	61	0.080
	17-3-23	1300	80	812	150	2.310
	17-4	4010	60	3986	170	3.140
	12-17	8435	35	9011	111	6.650
KAT-12-18	12-18-I*	3600	30	3463	88	0.470
	18-1-59	3630	30	3491	91	0.600
	18-4*	9420	40	10247	99	3.860
	18-4-74	6940	30	7421	73	3.880
	18-7*	11385	45	12812	130	6.820
	18-7-69	11810	50	13257	117	6.910
	12-18-VIII*	14540	60	17177	241	7.770
KAT-12-19	12-19-I	37490	570	41430	963	0.350
	19-2	47000		47000		1.560
	12-19-III	48000	1700	48000	1700	2.900
	19-4*	40100	1900	43526	3354	3.950
KAT-12-20	20-1*	1685	30	1218	66	0.760
	20-3-37	4235	30	4301	106	1.930
	20-4*	5565	30	5924	72	3.220
	20-4-36	5970	30	6352	73	3.470
	12-20	12740	50	14337	284	6.200
KAT-12-21	12-21-I	1010	50	574	74	0.520
	21-5-36	2810	90	2518	205	4.060
	21-7-47	3590	90	3454	224	6.150
	21-8-94	4440	30	4568	128	7.690
	12-21	5360	35	5695	105	8.180
	21-10*	9750	60	10636	169	8.730
KAT-12-22	22-7*	18680	100	7810	105	1.280
	22-2-29	7375	40	22111	260	6.190
	22-7-9	11295	45	12748	118	6.240
	12-22	5130	40	5448	117	8.670
KAT-12-23	23-7*	20580	110	24212	282	6.205
	23-7-6	22280	130	26104	275	6.255
	12-23*	39090	630	42687	918	8.420
KAT-12-40	40-3	7500	50	7926	112	2.090
	40-4	11845	45	13288	113	3.530
	12-40	45900	2600	47181	2819	7.540
KAT-12-41	41-4-92	3500	70	3348	180	4.070
	41-6-84	4390	30	4502	96	6.000
	41-6*	10170	50	11149	135	6.060
Hemipelagites samples			41			
Base of turbidites samples (*)			25			

**Title : Nature and origin of sedimentary deposits in the Ecuador subduction trench : paleoseismological implications**

**Keywords :** Ecuador ; subduction trenches ; deep marine sedimentation ; turbidites ; hemipelagites ; tephtras ; debris flows ; homogenites ; slumps ; ooze carbonate deposits ; sedimentary cores ; high-resolution photographs ; X-Ray imagery ; XRF data ; petrophysical properties ; sedimentary facies ; sedimentary processes ; echo-facies ; 14C age dating ; normal faults ; inverse faults ; seamounts

**Abstract :** Recent deep marine sedimentation in subduction trenches is characterized by the inter-stratification of hemipelagic and turbidite sediments locally interbedded with debris flow, which can result from continental slope shaking triggered by earthquakes. The active margin of Ecuador comprises tectonic erosion that contributes to the formation of a deep trench filled by a complex suite of sedimentary facies. Gravity flow sedimentation is ubiquitous along the margin and facies range from laterally continuous m-thick mass transport deposits to isolated cm-thick turbidites intercalated with hemipelagite, volcanoclastics and tephra. In this study we show interpretation of swath bathymetry, high-resolution seismic profiles and petrophysical data from cores. The objective is to describe the morphologic complexity on the Ecuadorian border of the Nazca plate where a set of deep marine asperities is subducting at different scales, and their consequences on the distribution of sediments in the different sub-basins. Ecuadorian margin comprises three geomorphological segments: The northern segment, northward of the Carnegie Ridge, is characterized by a wide (5-10 km) and deep trench (3800 – 4000 m), a gentler gullied continental slope and a shelf (10-40 km wide) with active subsidence. The central segment facing the Carnegie Ridge, is strongly influenced by the subduction of the Carnegie ridge which induces a narrow (0–5 km wide) and shallow trench (3100 – 3700 m depth), a steep and gullied slope with no canyons and a 15–40 km wide shelf characterized by areas with active subsidence and uplift. Finally, the southern segment, southward of the Carnegie Ridge, presents a wide (5–10 km) and deep (4000–4700 m) trench, a starved continental slope with well-defined canyon systems and a wide subsiding shelf (20–50 km). The sedimentary dynamics along the margin is evaluated by the analysis of 15 cores.

Visual description, high-resolution photographs, X-Ray imagery, XRF data and petrophysical properties led to the identification of 11 sedimentary facies that characterize seven sedimentary processes: turbidites, hemipelagites, tephtras, debris flows, homogenites, slumps, and ooze carbonate deposits. Age of the deposits is defined by radiocarbon age dating of hemipelagic sediments. Ages range from 500 to 48,000 years BP. High-resolution seismic profiles allow definition of three echo-facies: transparent, layered and chaotic. Transparent echo-facies is mainly associated to homogenite deposits, layered echo-facies is associated to the turbiditic-hemipelagic interbedded deposits and chaotic echo-facies is associated to reworked gravity flow deposits. The trench fill represents a lacunar but important record of the subduction margin history. Large eastward debris flows in the lower two sequences of the trench fill are provided by the trench outer wall as a results of slope failures along normal faults due to the downward bending of the oceanic plate. The sediment of the upper sequence of the trench fill draping the trench floor, are largely provided by the inner trench wall strongly controlled by the Carnegie Ridge. As a result, depth, frequency, thickness, composition and lateral disposition of the deposits vary greatly from those at north and south. The large, simple mega-beds like slump, debris flows and homogenites are located at the northern and southern segments. They were triggered by large regional faults in the North and enhanced by the activity of sets of splay faults in the South overhanging the seafloor at the slope toe. Small-size, fluid rich events were triggered by subduction of isolated seamounts at the edges of the Carnegie Ridge due to frequent but small destabilizations of an inner trench wall preconditioned by the impacts of successive seamounts. Sets of partly volcanoclastic turbidites in central segment might have been triggered by the complex interaction of slope and continental shelf deformation by seamount subduction

**Titre : Nature et origine des dépôts sédimentaires de la fosse de subduction d'Equateur : Implications paléosismologiques**

**Mots clés :** Equateur ; fosses de subduction ; sédimentation marine ; dépôts de turbidite ; hémipélagites ; téphras ; dépôts de coulées de débris ; homogénites ; slumps ; dépôts de carbonate de ooze ; carottes sédimentaires ; photographies à haute résolution ; l'imagerie par rayons X ; données XRF ; propriétés pétrophysiques ; faciès sédimentaires ; processus sédimentaires ; echo-faciès ; datation 14C ; failles normales ; failles inverses ; monts sous-marins

**Résumé :** La sédimentation marine récente dans les fosses de subduction est caractérisée par l'interstratification de sédiments hémipélagiques et de turbidites localement intercalées avec les coulées de débris, qui peuvent résulter de la destabilisation des pentes continentales par de tremblements de terre. La marge d'Equateur est constituée par une forte érosion tectonique qui contribue à la formation d'une fosse profonde remplie d'une suite complexe de faciès sédimentaires. La sédimentation par écoulements gravitaires est omniprésente le long de la marge et les faciès vont de dépôts de transport de masse d'épaisseur métriques latéralement continus à des turbidites d'épaisseur centimétriques isolées intercalées avec des couches d'hémipélagites, de volcanoclastiques et de téphras. Nous présentons l'interprétation de la bathymétrie, des profils sismiques à haute résolution et des données pétrophysiques des carottes sédimentaires. L'objectif de cette étude est de décrire la complexité morphologique à la frontière équatorienne de la plaque de Nazca où un ensemble d'aspérités marines profondes ont subducté à différentes échelles, et ses conséquences sur la distribution latérale des sédiments dans les différents sous-bassins. La marge équatorienne comprend trois segments géomorphologiques: Le segment nord, situé au nord de la crête Carnegie, est caractérisé par une large (5-10 km) et profonde fosse (3800-4000 m), une pente continentale ravinée et une plate-forme (10-40 km de large) avec subsidence active. Le segment central en face de la crête de Carnegie montre une fosse étroite (0-5 km de large) et peu profonde (3100-3700 m), la pente escarpée et ravinée, sans canyons, et plateau continental étroit de 15 à 40 km de large caractérisé par des zones d'affaissement et de soulèvement actifs. Enfin, le segment sud, situé au sud de la crête Carnegie, présente une large (5-10 km) et profonde fosse (4000-4700 m), une pente continentale pauvre en sédiments avec des systèmes de canyons bien définis et une large plate-forme de subsidence (20-50 km).

La dynamique sédimentaire le long de la marge est évaluée par l'analyse de 15 carottes sédimentaires dont la description visuelle, les photographies à haute résolution, l'imagerie par rayons X, les données XRF et les propriétés pétrophysiques conduisent à l'identification de 11 faciès sédimentaires caractérisant 7 processus sédimentaires: dépôts de turbidite, hémipélagites, téphras, dépôts de coulées de débris, homogénites, des slumps et des dépôts de carbonate de ooze. Les âges des dépôts sont définis par la datation au radiocarbone des sédiments hémipélagites. Les âges vont de 500 à 48000 ans BP. Les profils sismiques à haute résolution permettent de définir 3 echo-faciès: transparent, stratifiés et chaotiques. Le facies transparent est principalement associé aux dépôts d'homogénites, le facies stratifié est associé aux dépôts interstratifiés turbiditique-hémipélagique et le facies chaotique est associé à des dépôts gravitaires grossiers. Le remplissage de la fosse représente un enregistrement lacunaire mais important de l'histoire de la marge de subduction. De grandes coulées de débris se déplaçant vers l'est dans les deux séquences inférieures du remplissage de la fosse sont initiées le long de la paroi extérieure de la fosse, le long de grandes failles normales dues à la flexion de la plaque océanique subductante. Les sédiments de la séquence supérieure du remplissage qui nappent la fosse sont plus largement fournis par la paroi interne de la fosse mais avec un fort contrôle de la ride de Carnegie. En conséquence, la profondeur, la fréquence, l'épaisseur, la composition et la disposition latérale des dépôts sédimentaires varient grandement entre le nord et le sud. Les grands méga-lits simples, les slumps, les coulées de débris et les homogénites sont situés dans les segments nord et sud. Ils sont déclenchés par de grands escarpements de failles régionales, dans le Nord